LiMAT-2001

Proceedings of the Second International Conference on Light Materials for Transportation Systems (LiMAT-2001) held at Pusan, Korea, May 6~10, 2001

Volume I

Edited by

Nack J. Kim, POSTECH

C.S. Lee, POSTECH

D. Eylon, University of Dayton

DISTRIBUTION STATEMENT A:
Approved for Public Release -
Distribution Unlimited

20020114 155

Organized by

Center for Advanced Aerospace Materials
Pohang University of Science and Technology

Co-organized by

Korea Institute of Machinery and Materials
Research Center for Aircraft Parts Technology, Gyeongsang National Univ.

Sponsored by

The Korean Institute of Metals and Materials (KIM)
The Minerals, Metals and Materials Society (TMS)
US Air Force Office of Scientific Research/Asian Office of
Aerospace Research and Development (AFOSR/AOARD)
The Office of Naval Research International Field Office (ONRIFO)
Korea Science and Engineering Foundation (KOSEF)
Technology Innovation Center for Metals and Materials (TICM), POSTECH
Pohang Iron and Steel Company
Hyundai Motor Company

Published in Aug., 2001 by:
Center for Advanced Aerospace Materials
Pohang University of Science and Technology
San31, Hyoja-dong, Pohang 790-784, Korea
Tel: +82-54-279-2141, 2820
Fax: +82-54-279-2399

ISBN 89-85510-01-0

Printed in The Republic of Korea

REPORT DOCUMENTATION PAGE

Form Approved

OMB No. 0704-0188

The public reporting burden for this collection of information is estimated to average 1 hour per response, including the time for reviewing instructions, searching existing data sources, gathering and maintaining the data needed, and completing and reviewing the collection of information. Send comments regarding this burden estimate or any other aspect of this collection of information, including suggestions for reducing the burden, to Department of Defense, Washington Headquarters Services, Directorate for Information Operations and Reports (0704-0188), 1215 Jefferson Davis Highway, Suite 1204, Arlington, VA 22202-4302. Respondents should be aware that notwithstanding any other provision of law, no person shall be subject to any penalty for failing to comply with a collection of information if it does not display a currently valid OMB control number.

PLEASE DO NOT RETURN YOUR FORM TO THE ABOVE ADDRESS.

1. REPORT DATE *(DD-MM-YYYY)*	2. REPORT TYPE	3. DATES COVERED *(From - To)*
04-01-2002	Conference Proceedings	06-05-01 – 09-05-01

4. TITLE AND SUBTITLE

Light Materials for Transportation System (LiMat-2001)

5a. CONTRACT NUMBER

F6256200M9105

5b. GRANT NUMBER

5c. PROGRAM ELEMENT NUMBER

6. AUTHOR(S)

Conference Committee

5d. PROJECT NUMBER

5e. TASK NUMBER

5f. WORK UNIT NUMBER

7. PERFORMING ORGANIZATION NAME(S) AND ADDRESS(ES)

Pohang Univeristy of Science and Technology
San 31, Hyoja-dong, Nam-gu
Pohang 790-784
Korea (South)

8. PERFORMING ORGANIZATION REPORT NUMBER

N/A

9. SPONSORING/MONITORING AGENCY NAME(S) AND ADDRESS(ES)

AOARD
UNIT 45002
APO AP 96337-5002

10. SPONSOR/MONITOR'S ACRONYM(S)

AOARD

11. SPONSOR/MONITOR'S REPORT NUMBER(S)

CSP-001013

12. DISTRIBUTION/AVAILABILITY STATEMENT

Approved for public release; distribution is unlimited.

13. SUPPLEMENTARY NOTES

14. ABSTRACT

This proceedings emanates from an interdisciplinary materials conference, the objective of which was to provide a forum for scientific exchange among materials researchers from the aerospace, automotive, civil, marine, and rail-transportation industries. The theme of need to develop improved lightweight materials is common to each of those industries. Papers within the proceedings focus on titanium, magnesium, and aluminum alloys, intermetallics, and metal/ceramic composites. Emphasis is placed on fabrication, mechanical properties, microstructural studies, corrosion, and fundamental modeling.

15. SUBJECT TERMS

Aerospace Materials

16. SECURITY CLASSIFICATION OF:			17. LIMITATION OF ABSTRACT	18. NUMBER OF PAGES	19a. NAME OF RESPONSIBLE PERSON
a. REPORT	b. ABSTRACT	c. THIS PAGE			Thomas D. Kim
U	U	U	UU	1144	19b. TELEPHONE NUMBER *(Include area code)* +81-3-5410-4409

PREFACE

During the last several decades, considerable efforts have been made in light materials research for applications in transportation systems. Although the impetus for this comes from the various needs depending on the type of transportation system, one common goal is to develop transportation system with improved performance. For the automotive industry in particular, ever increasing restrictions on the fuel consumption and pollutant emission have placed a great demand to the automobile manufacturers to produce automobiles with reduced weight. Using light materials can be a viable solution to this challenge and it is expected that the demand for the light materials will continue to grow.

As such, this conference aims to review and update all aspects of the science and technology of light materials for applications in various transportation systems. The first conference on Light Materials for Transportation Systems was held in Kyoungju, Korea in 1993 (LiMAT-93). After 8 years following the first conference, the second conference is being held under the theme of "Development of Better Air, Sea and Land Transportation Light Materials for the 2000's" with an emphasis on technology transfer from aerospace to sea and land transport to help improve performance, cost and reliability. We believe that it is timely appropriate and also important to review our efforts on the light materials research, and to redirect our future research efforts.

We would like to express our deep gratitude to The Korean Institute of Metals and Materials (KIM), The Minerals, Metals and Materials Society of USA (TMS), US Air Force Office of Scientific Research/Asian Office of Aerospace Research and Development (AFOSR/AOARD), The Office of Naval Research International Field Office (ONRIFO), Korea Science and Engineering Foundation, Pohang Iron and Steel Co., Hyundai Motor Co., Technology Innovation Center for Metals and Materials (TICM) of Pohang University of Science and Technology, who have co-sponsored our conference.

Aug., 2001

Nack J. Kim
C.S. Lee
D. Eylon
LiMAT-2001 Organizing Committee

SESSION CHAIRMEN

S.H. Ahn
Research Institute of Industrial Science and Technology
(KOREA)

S. Ankem
University of Maryland
(USA)

E.S. Balmuth
Lockheed Martin Aeronautics Co.
(USA)

Y.W. Chang
Pohang Univ. of Science and Technology
(KOREA)

K.M. Cho
Pusan National University
(KOREA)

W.S. Cho
Hyundai Motor Company
(KOREA)

D.M. Dimiduk
Air Force Research Laboratory
(USA)

D. Eliezer
Ben Gurion University of the Negev
(ISRAEL)

O.S. Es-Said
Loyola Marymount University
(USA)

E. Evangelista
University of Ancona
(ITALY)

D. Eylon
University of Dayton
(USA)

D.S. Han
Hyundai Motor Company
(KOREA)

D. Hua
Northeastern University
(P.R.CHINA)

S.M. Hur
Agency for Defense Development
(KOREA)

S.K. Hwang
Inha University
(KOREA)

O.M. Ivasishin
Institute for Metal Physics
(UKRAINE)

C.G. Kang
Pusan National University
(KOREA)

H. Kikukawa
Japan Aircraft Development Corporation
(JAPAN)

J.G. Kim
Sungkyunkwan University
(KOREA)

S.S. Kim
Gyeongsang National University
(KOREA)

H. Kwon
Kookmin University
(KOREA)

E.W. Lee
Naval Air Systems Command
(USA)

J.C. Lee
Korea Institute of Science and Technology
(KOREA)

S.Y. Lee
Korea Institute of Machinery and Materials
(KOREA)

K. Nakasa
Hiroshima University
(JAPAN)

M. Niinomi
Toyohashi University of Technology
(JAPAN)

C.G. Park
Pohang Univ. of Science and Technology
(KOREA)

Y.H. Park
Tohoku National Industrial Research Institute
(JAPAN)

S.L. Semiatin
Air Force Research Laboratory
(USA)

K.S. Shin
Seoul National University
(KOREA)

T. Shinoda
Nagoya University
(JAPAN)

C. Suryanarayana
University of Central Florida
(USA)

H.G. Suzuki
National Research Institute for Metals
(JAPAN)

L. Wagner
Technical Univ. of Brandenburg at Cottbus
(GERMANY)

TABLE OF CONTENTS

Volume I

PLENARY LECTURES

The Advanced Materials and Technology in the Next Generation Vehicles (INVITED) 3
W.S. Cho

Applications, Benefits, and Implementation of Ti-6Al-4V Castings (INVITED) 5
E.W. Lee, C.S.C. Lei and W.E. Frazier

Friction Stir Welding: Emphasis on Aircraft and Space Applications (INVITED) 15
K.V. Jata

The R&D Actives on Light Alloys and Their Applications in Transport Systems in China (INVITED) 23
Z. Lian

Structural In-Situ Composites at Very High Temperatures (INVITED) 31
S. Hanada, T. Suzuki, K. Yoshimi and N. Nomura

Session I : TITANIUM ALLOYS

Enhancement of Mechanical Properties by Alloying and Processing in Titanium Base Alloys (INVITED) 41
Y.T. Lee, S.E. Kim, Y.T. Hyun and H.W. Jeong

Thermomechanical Control Processes of Titanium Alloys (INVITED) 49
H.G. Suzuki

High Strength Microstructural Forms in Beta Alloys Intended for Automotive Application (INVITED) 57
O.M. Ivasishin and S. Fox

The Ordering Behavior of Supersaturated Metastable Phase in Beta-Ti Alloys 65
B.H. Choe, B.H. Lee, B.G. Jung, T.H. Lee, C.G. Lee, S.J. Kim and Y.T. Lee

Influence of Cooling Rate From a Temperature within the Beta Phase Region on Tensile Properties and Phase Constitution of Ti-Fe-Cr Alloys for Technical Aids 73
M. Ikeda, S. Komatsu, M. Ueda, T. Imose and K. Inoue

Effect of Preform Microstructure on Constitutive Behavior of Ti-6Al-4V under Conventional Hot-Working Conditions (INVITED) 79
S.L. Semiatin and T.R. Bieler

Characteristics of Titanium Silicides Formed by Hip in Ti-Fe-Si Alloys 91
H.W. Jeong, S.E. Kim, Y.T. Hyun and Y.T. Lee

The Role of Filler Material in 360°Cold Bending Ti-6Al-4V Large-Diameter Seamless Tube 97
S.M. Hur and J.S. Park

Microstructure and Properties of Titanium-Based Materials Sintered from TiH_2 Powder 105
H.H. Shin, H.L. Park and S.N. Chang

Effects of Precipitated Intermetallics on Fracture Characteristics of Ti-6Al-2Sn-2Zr-2Mo-2Cr-Si (INVITED) 111
M. Niinomi, K. Fukunaga, G. Tono, J. Koike, D. Eylon and S. Fujishiro

Correlation of Microstructure with Quasi-Static and Dynamic Deformation Properties of Ti-6Al-4V Alloy 119
D.G. Lee, C.-S. Lee, S.H. Kim, S.H. Lee and C.S. Lee

Effect of Microstructure on Fracture Behavior of β-Rich α+β Type Titanium Alloy with High Superplastic Formability 127
Gunawarman, M. Niinomi, K. Fukunaga, D. Eylon, S. Fujishiro and C. Ouchi

A New Method for Detection and Quantification of Fretting Fatigue Damage (INVITED) 133
E.B. Shell and D. Eylon

Characterization of Accumulated Fatigue Damage in Ti-6Al-4V Using Nonlinear Acoustics and TEM 141
J.L. Maurer, J. Frouin, S. Sathish and D. Eylon

Cycle Deforming Behavior and Structure Observation of Ti-2Al-2.5Zr Alloy at –196 °C 147
Y. Zhentao and D. Ju

Recent Developments on the Low-Temperature (298 – 458K) Creep Deformation Behavior of Titanium Alloys (INVITED) 153
S. Ankem and D. Doraiswamy

High Temperature Deformation Behavior of Ti40 Burn Resistant Titanium Alloy 161
Y.Q. Zhao, K.Y. Zhu, H.L. Qu, H.Wu and L. Zhou

A Study on the Machining Characteristics in Turning of Ti-6Al-4V Alloy – Tool Wear Experiment with Carbide Tool K10 – 167
W.P. Hong, H.C. Kim and D.J. Lee

Session II : MAGNESIUM ALLOYS

New Magnesium Alloys for Automobile Applications (INVITED) 175
D. Eliezer and E. Aghion

New Semisolid Process of Magnesium Alloys 185
T. Motegi, E. Yano and N. Nishikawa

Rheological and Flow Behavior of Semi-Solid AZ91D Magnesium Alloy (INVITED) 191
C.D. Yim, S.H. Lee and K.S. Shin

Fabrication of Bulk Mg-Cu-Ag-Y Glassy Alloy by Squeese Casting 199
E.S. Park, H.K. Lim, W.T. Kim and *D.H. Kim*

Fatigue in Wrought and Cast Magnesium Alloys (INVITED) 205
L. Wagner, J. Wendt and M. Hilpert

Effect of Test Environment on Fatigue Crack Propagation Behavior of AZ91D Magnesium Alloy 215
H.C. Jung and K.S. Shin

The Effect of Ca Addition on the Microstructure, Mechanical and Corrosion Properties in Mg-Zn Alloy 221
B.Y. Hur, J.P. Eom, S.G. Lim and *K.W. Kimm*

Strip Casting of Mg Alloys 225
S.S. Park, Y.S. Park and Nack J. Kim

Session III : FUNDAMENTAL ISSUES

Copper Concentration inside Guinier-Preston (I) Zone Formed in an Al-Cu Alloy 235
M. Takeda, Y. Nagura and A. Igarashi

Effect of Damage Growth on Sheet Metals Forming 241
Y.S. Kim and S.Y. Won

Advanced Indentation Approach to Characterize Micro-Mechanical Properties of Small-Volume Materials 247
Y. Choi, Y.H. Lee, J.H. Ahn and D. Kwon

Ab Initio Study on Generalized Stacking Fault Energy of Basal Plane in Magnesium 255
T. Uesugi, M. Kohyama, M. Kohzu and K. Higashi

Mechanically Alloyed Magnesium Alloys for Hydrogen Storage 261
C. Suryanarayana, E. Ivanov and I.G. Konstanchuk

A Microstructural Model for the Prediction of High Cycle Fatigue Life Based on the Small Crack Theory 269
J.S. Park, S.H. Park and C.S. Lee

Trace and Control of Binder Removal Processes from MIM Compacts by Simultaneous Application of Thermogravimetry and Mass Spectrometry 275
T. Senda, K. Suzuki and Y. Kankawa

Addressing Urgent Mass Reduction Requirements by the Use of Lightweight Components 281
M. Leary and C. Burvill

Optimal Material Selection for Finite Life Automotive Suspension Applications 287
M. Leary and C. Burvill

Session IV : FORMING

Textures and Structures of Asymmetrically Rolled Aluminum Sheets (INVITED) 297
D.N. Lee, S.H. Kim and K.H. Kim

Evolution of Anisotropy in Precipitation Hardening Al-Li 2090-T8E41 Alloy 305
H. Garmestani, S. R. Kalidindi, C. Fountain, L. Williams, E.W. Lee and O.S. Es-Said

Through-Thickness Variation of Microstructure and Texture in High Speed Hot Rolling of Aluminum and Aluminum Alloy Sheet 311
T. Sakai, S.H. Lee and Y. Saito

Texture Evolution of the Al Sheet Processed by Continuous Confined Strip Shearing Based on Equal Channel Angular Pressing 317
J. Lee, H.K. Seok, J.H. Han, J.Y. Suh and H.I. Lee

Elongation-Control Rolling of Wires with Asymmetric Cross Section 325
H. Utsunomiya, Y. Saito, M. Ueyama and R. Souba

Effect of Preform Shape on a Surface Grain Coarsening Behavior at the Hammer-Forged Al7050 331
Y.S. Lee, J.H. Lee and Y.S. Choi

Light Weight Aluminum Forged Suspension Parts for Automobile 337
Y. Inagaki

Characteristics of Strain Profile at Hydroformed Al Tubes 343
S.Y. Lee, Y.J. Jo, S.M. Sohn, M.Y. Lee and Y.S. Kim

The Hemming Process for Aluminum Body Sheet 349
K. Noda, Y. Takaki and H. Konishi

Inhomogeneous Deformation Behaviour during Equal Channel Multi-Angular Pressing 355
H.S. Kim and M.H. Seo

Plastic and Superplastic Forming of Aluminium Based Metal Matrix Composites for Transport Applications (INVITED) 361
F.Bardi, P. Cavaliere, L. Ceschini, A. Morri, S. Spigarelli and E. Evangelista

An Anlaysis of Gas Pressure Forming of Superplastic Al 5083 Alloy 369
C.K. Syn, M.J. O'Brien, D.R. Lesuer and O.D. Sherby

Hot Forming Related Properties of Al 6061/Al_2O_3 and Al 2618/Al_2O_3 Composites 375
M. Vedani and E. Gariboldi

Particle Weakenging in High-Strain-Rate Superplastic Powder-Metallurgy Processed 2124 and 6061 Aluminum Composites 381
W.J. Kim and K.B. Kim

Determination of Superplastic Properties of AlCuAgMgZr Alloys Prepared from Various Techniques 387
J. Dutkiewicz, P. Malczewski J. Kuśnierz and T.G. Nieh

Fracture and Superplasticity in Hyper-eutectic Al-20Si Alloy with Coarse Primary Silicon Phase 393
A. Shan, I.G. Moon, J.W. Park and Y.H. Park

Improving the Superplastic Properties of an Aluminum Alloy Using Equal-Channel Angular Pressing 399
S.W. Lee, M. Furukawa, Z. Horita and T.G. Langdon

High Strain Rate Superplasticity (HSRS) in Aluminum Based Alloys and Composites for Automotive and Aircraft Applications 405
Y.H. Han, R.S. Mishra and A.K. Mukherjee

High Strain Rate Superplasticity of Mg-Li- Zn Alloy 411
S.W. Lim, T. Imai, J. Mao, T. Choh and Y. Nishida

Superplastic Formability of Fine-Grained AZ61 and AZ31 Magnesium Alloy Sheets and Deformation Mechanism Maps for Magnesium Alloys 417
S.W. Chung and W.J. Kim

Superplastic Deformation Behavior of Fe-Al Intermetallic Alloys 423
J.H. Song, T.K. Ha, H.T. Lim and Y.W. Chang

Session V : JOINING

Development of High Deposition Rate Double Wire MIG Welding Process For Aluminum Alloy (INVITED) 431
T. Shinoda, J. Nakata and H. Miyauchi

Effect of Alloy Elements on Solidification Discontinuities of EB Welded High Tensile Aluminum Alloys 439
S.W. Kim and C.H. Lee

Underwater Friction Welding of A6061 Aluminum Alloy 445
K. Katoh and H. Tokisue

Diffusion Bonding in Pure Magnesium 451
H. Somekawa, M. Kohzu and K. Higashi

Effect of the Pulse Frequency on Solidification Crack Sensitivity of TIG Welded AZ31 Magnesium Alloy 457
T. Asahina, H. Tokisue and K. Katoh

Mechanical Properties and Interface Reaction in Brazed Joint of Titanium and Stainless Steel 463
S.C. Kwon, H.J. Yim, S.H. Kim and Y.Y. Kim

Brazaing Process and Microstructures of Al/Ti Brazed Joint 469
W.H. Sohn, S.I. Cha, H.H. Bong and S.H. Hong

Session VI : SPECIAL SESSION ON JAPAN'S NEDO

Nedo'S R&D Program on Key Technology for Innovative Low-Cost and Lightweight Structures 477
Y. Ito

R&D Scheme and Objectives for Innovative Aircraft Structures 483
A. Yahata, M. Kadoya and H. Kikukawa

Innovative Nose Section of Fuselage Structures Applied by Friction Stir Welding (FSW) of the Aluminum Alloy and Large Thin Casting of Improved Aluminum Alloy 489
Y. Hirose, T. Tsujimoto, K. Kosugi, M. Imuta and H. Fukagawa

Application of Manufacturing Processes for Monolithic Structure to Wing Leading Edge 495
T. Jinishi, M. Matoba, S. Ohashi, M. Ochi and A. Yahata

Volume II

Session VII : ALUMINUM ALLOYS

Enhancement in Strength and Fatigue Resistance of 6061Al Alloy Produced by Equal-Channel Angular Pressing 503
J.K. Kim, C.S. Chung, T.Y. Park, C.W. An and W.J. Kim

Computational Thermodynamic Optimization of Aluminum Base Metallic Glass Systems 509
M.C. Gao, R.E. Hackenberg and G.J. Shiflet

Crystallization Behavior of Al-Mm-Ni-Fe Amorphous Alloys 517
H.W. Jin, K.M. Lim and C.G. Park

Synthesis and Thermal Stability of Nanocrystalline Al-Mg Alloys 523
F. Zhou, D.H. Shin and E.J. Lavernia

Growth Kinetics of Primary Al Nanocrystals in Al-Ni-Nd Alloy 529
S.H. Kim, S.B. Lee and Nack J. Kim

DSC and HRTEM Study of Precipitation in Al-Mg-Si Alloys 535
K. Matsuda, H. Matsui, K. Terayama, Y. Uetani and S. Ikeno

Stress-Assisted Nucleation of Ω Precipitate in Al-Cu-Mg-Ag Alloys 541
S. Muraishi, S. Kumai and A. Sato

A Study on the Structural Characteristics and Tensile Properties of Al-Si Alloys Utilizing Strip Casting Method 547
S.L. Kuan, T.S. Lui, L.H. Chen and J.M. Song

Effects of Mn Addition on Microstructure and Mechanical Properties of Strip Cast Al6061 Alloy 553
Y.S. Park and Nack J. Kim

A Review of the Effect of Retrogression and Reaging on Aluminum Alloy 7249 559
K. Koziar, P. Fleck, G. Davila, E. Fromer, M. Leal, H. Pech, J. Foyos, E.W. Lee, B. Sarkar and O.S. Es-Said

Effect of Retrogression and Reaging on Bake Hardenability in Al-Mg-Si-(Cr, Be) Alloys 565
K.D. Woo, J.S. Lee, C.H. Yang, H.C. Park and S.W. Kim

Influence of Retrogression and Reaging (RRA) Treatments to an Al-Li-Cu-Mg-Zr Alloy on Mechanical Properties and Stress Corrosion Cracking Behaviour. 571
K.S. Ghosh, K. Das and U. K. Chatterjee

Effects of Excess Silicon Content on the Ageing Behaviour of Solution-Treated Al-Mg-Si Alloys 577
Y. Ohmori, Y. Matsuura, K. Nakai and S. Kobayashi

Effect of Over-Aging on the Microstructure and Mechanical Properties of Cu, Ni Containing AC8A Aluminum Casting Alloy 583
S.W. Kwon, D.W. Suh, Y.R. Im, H.C. Lee, J.K. Yang and K.H. Ryu

Application of Aluminum Alloy 2297 in Fighter Aircraft Structures (INVITED) 589
E.S. Balmuth

Mechanical Property of Super-High Strength Aluminum Alloys 597
K. Osamura, H. Adachi, J. Kusui and K. Yokoe

The Effects of Chemical and Microstructure on Axial Compressing Property of Extruded Al-Mg-Si Alloys 603
H. Kawai and M. Hirano

Microstructure and Elevated-Temperature Strength of P/M $Al_{90-x}Fe_xCr_2Ti_2$ (x=3, 4, 5) Alloys 609
H.M. Kimura, A. Inoue and K. Sasamori

Effect of Si Addition on the Microstructure and Creep Properties of the Mechanically Alloyed Al-10Ti Alloy 615
C.J. Choi, J.K. Park and B.K. Kim

Texture Analysis of Aluminum Plate Produced by ECAP 621
S.M. Baeck, H.K. Seok, J.C. Lee, D.I. Kim, H.C. Lee and K.H. Oh

Microstructural Evolution during ECA Pressing of Commercial 5083 Al Alloy and Its Mechanical Properties (INVITED) 627
S.Y. Chang, J.G. Lee, K.T. Park and D.H. Shin

Grain Refinement and Strengthening of 6061 Aluminum Alloy by Accumulative Roll-Bonding Process 635
S.H. Lee, Y. Saito, T. Sakai, H. Utsunomiya and N. Tsuji

Refinement of Intermetallic Compounds in Al-Fe Alloys by LTMT Process 641
C.Y. Lim, H.W. Kim, J.M. Lee and S.B. Kang

Mechanical Properties of Al-Mg-Sc and Commercial Aluminum Alloys after Equal-Channel Angular Pressing 647
M. Furukawa, S.W. Lee, Z. Horita and T.G. Langdon

Fracture Toughness of Various Zones in Weldments of 6082 Al Alloys 653
V.A. Mosneaga, T. Kobayashi and H. Toda

Study on Microstructures and Mechanical Properties in Electromagnetic Cast and Direct Chill Cast Al Alloys 659
S.W. Kim, H. Hao, U.J. Lee, K.D. Woo and J.Z. Jin

Tensile Ductility and Tear Resistance of A356 Aluminum Alloys Fabricated by Conventional and Semi-Liquid Casting Process 665
S. Kumai, T. Tanaka, S.W. Han, A. Sato and S.W. Kim

A Study on the Fabrication Process, Compression Strength and Sound Absorption Properties of Al Foam in Pot Furnace 671
B.Y. Hur, H.J. Ahn, D.C. Choi and S.Y. Kim

Development of Light-Weight Al Scroll Compressor for Car Air Conditioner 675
J.M. Park, J.K. Ahn, H.B. Im, C.S. Ha, I.D. Choi, K.M. Cho and I.M. Park

Hydrogen-Assisted Deformation and Fracture Behavior of Al8090 681
W.K. Jang, S.S. Kim and K.S. Shin

Fracture Behavior of AA6061 Aluminum Alloy Under Resonant Vibration 689
J.H. Horng, J.L. Hu, T.S. Lui and L.H. Chen

Deformation Behavior of a Spray-Cast Hypereutectic Al-25Si Alloy 695
T.K. Ha, J. Kim, W.J. Park, E.S. Lee, S.H. Ahn and Y.W. Chang

Acoustic Emission from Fatigue Crack Extension in Corroded Aluminum Alloys 701
K.W. Nam, S.H. Ahn and A.K. Mal

Short and Long Fatigue Crack Growth Behavior in Al-7%Si-0.4%Mg Alloy Castings 707
S.W. Han, S. Kumai and A. Sato

Fatigue Crack Propagation Behavior of A356 Squeeze Cast Alloy 713
S.H. Kim and K.H. Rhee

Session VIII : INTERMETALLICS

Gamma Titanium Aluminides: Alloys, Processing & Scale-Up (INVITED) 721
D.M. Dimiduk, H.A. Lipsitt and M.J. Blackburn

Advances in Synthesizing Methods of Ti-Based Intermetallics from Elemental Powders (INVITED) 729
H.S. Park, Y. Wu, Y. Park, D. Lee and S.K. Hwang

Mechanical Properties and Microstructure Observation of TiAl+Nb Alloy 737
Y.Q. Yan, L. Zhou, W.S. Wang and G.Z. Luo

Effect of B Addition on the Continuous Cooling Transformation Behavior of Ti-45.5at.%Al Alloy 743
S.K. Kim, J.S. Kim and J.K. Park

Effects of Low Cycle Fatigue Test Parameters on $\alpha_2 \rightarrow \gamma$ Phase Transformation at the Grain Boundary in Lamellar TiAl Alloy 749
Y.S. Park and S.W. Nam

High Temperature Deformation Behavior of Fine Duplex Gamma TiAl Alloy 755
J.H. Kim, D.H. Shin and C.S. Lee

Creep, Creep-Fatigue and Continuous Fatigue Deformation Characteristics of Lamellar TiAl Alloy (INVITED) 761
S.W. Nam, Y.S. Park and S.J. Yang

A Comparative Study of the Creep Resistance Improvement between the Interstitial Alloying Elements and Different Heat Treatments for TiAl Alloys 769
S.J. Yang, S.W. Nam and S.K. Hwang

Effect of Lamellar Spacing on the Fatigue Crack Propagation Resistance of Fully Lamellar γ-TiAl Alloy 775
H.J. Kim and C.S. Lee

In-Situ Observation of Fatigue Crack Propagation of Ti-Al Intermetallics 781
H. Suzuki, A. Nozue and M.N. Tamin

The Optimum Thickness of Coating Film for the Fatigue Strength of Surface Modified TiAl Intermetallic Alloy 787
H. Suzuki, Y. Watanabe, M. Ikenaga and K. Ikenaga

Surface Strengthening for Optimizing Fatigue Performance of Gamma Titanium Aluminides at Ambient and Elevated Temperatures 793
J. Lindemann, D. Fagaraseanu and L. Wagner

Alloy Design of Gamma Titanium Aluminides 799
K. Hashimoto

Fabrication of Ti_3Al-xNb (x=0, 3, 7, 11, 13 at%) Powder Compacts Manufactured by Pulse Discharge Sintering 805
W. Fang, S.H. Ko and Y.H. Park

Synthesis of Ti-Based Intermetallic Compounds and Their Composite Using Shock Compression 811
J.S. Lee, K. Hokamoto and K.S. Kumar

Improved Room and High Temperature Mechanical Properties of an Orthorhombic Ti_2AlNb-Based Alloy 817
M. Hagiwara, S. Emura and F. Tang

Microstructure and Tensile Ductility of Fe-40Al with High Boron Content 823
J.H. Lee, S.I. Kwun, W.S. Lee, Y.H. Kim and J.W. Byeon

Synthesis of Nickel Aluminides via Vacuum Plasma Spraying with Self-Propagating High-Temperature Synthesis 829
Y.G. Jeong, S.J. Park and H.K. Lee

Session IX : COMPOSITE MATERIALS

Methodologies to Design the Interfaces in SiC/Al Composites (INVITED) 837
J.C. Lee

Tensile Properties and Microstructures of 7075 Al/SiC_p Composite Fabricated by Pressureless Infiltration Technique 845
K.B. Lee, H.S. Sim and H. Kwon

Microstructure and Thermal Properties of Compositionally Graded Al-SiC_p Composites 851
N.B. Choi, J.I. Hwang, I.M. Park, I.D. Choi and K.M. Cho

Preparation of SiC/2024 Composites by Semisolid Casting 857
X. Meng, H. Ding, Y. Chen and J. Wen

Influence of ECA Pressing on Microstructure and Mechanical Properties of P/M SiC_w/6061 Al Alloy Composite 863
S.Y. Chang, S.K. Ryu, D.H. Shin, H. Tezuka and T. Sato

In-Situ Synthesis of Al/Al_3Ti Composites by MA-PDS Process 869
Z. Sun, Q. Wang, H. Hashimoto, Y.H. Park and T. Abe

Microstructural Evolution of Al/Al_3Fe Composites by Plasma Synthesis Method 875
J.M. Lee, S.B. Kang, C.Y. Lim, C.Y. Eum, T. Sato, H. Tezuka and A. Kamio

Dynamic Softening of Al-18Si Composite during Hot Deformation 881
S.I. Kim, C.H. Han, H.I. Lee and Y.C. Yoo

Tailoring the Hypereutectic Al-Si-Xs Composites as a Structural Material Requiring High Young's Modulus 887
H.K. Seok, J.Y. Suh, D.S. Shin, H.I. Lee and J.C. Lee

Particles Refinement in Aluminum Composite Slurry Formed by Liquid/Particles Reaction and Its Wear Properties 893
M. Tsujikawa, M. Hino and M. Kawamoto

Dry Sliding Wear Behavior of Aluminum Alloy Matrix Composites Reinforced with Carbide Particles Produced by a Pressureless Infiltration Technique 899
S.H. Kim, H.C. Park, H. Kwon and Y.S. Kim

Effect of Residual Stress on the Wear Properties of SiC_p/6061Al Composites 905
H.J. Kim, C.G. Kim, L.S. Oh and J.H. Cheon

Active Control of Crack Closure Acts by the Shrinkage Effect of Shape Memory TiNi Fiber Embedded/Polymer Matrix Composite 911
A. Shimamoto, C.C. Lee and H. Isui

The Properties and Microstructures of TiC_p Particle Reinforced Titanium Matrix Composites 917
Z. Lian, M. Xiaonan, Z. Yongqing, Z. Liying and A. Vassel

Mechanical Properties of SCS-6/Ti-15V-3Cr-3Sn-3Al Titanium Matrix Composites 923
H. Izui, A. Tada and T. Furukawa

Mechanical and Fracture Behaviors of $(Al_2O_3+SiC_p)$/AZ91 Hybrid Mg Matrix Composite 929
I.M. Park, K.M. Cho, I.D. Choi and C.S. Ha

Session X : CORROSION & SURFACE TREATMENT

Corrosion Attacks of Aluminum Wire in a Solution Contaminated by Combustion Gas of Chemical Waste 937
O. Seri

Changes in Oxide Film Characteristics of Magnesium Alloy by the Addition of Calcium and Minor Element 943
B.S. You, M.H. Kim, W.W. Park and I.S. Chung

Corrosion Models in Mg Alloys with Residual and Concentrated Stresses 949
S.I. Tanaka and S. Iwata

The Effect of SiC and Si_3N_4 Additions on the Oxidation Resistance of TiAl Alloys 955
D.B. Lee, K.B. Park and J.J. Moon

TEM Observation of Initial Oxidation Behaviour of Nb Ion Implanted TiAl 961
S. Taniguchi, Y.C. Zhu, K. Fujita and N. Iwamoto

Investigation of Passivity and Its Breakdown on Al_3Ti Alloys in 3.5 wt.% NaCl Solution 967
Y.J. Yu and J.G. Kim

High Temperture Sulfidation and Oxidation of Sputter-Deposited Nb-Al-Si Coatings 973
D.B. Lee, G.Y. Kim and W.S. Shim

Effect of Molybdenum on the Corrosion Behavior of Iron-Aluminides in Thiosulfate-Chloride Solution 977
Y.S. Choi and J.G. Kim

A Study of Composite Coating of Cr Evaporation and Pack Cementation to Improve High Temperature Oxidation Resistance of TiAl Alloys 983
D.J. Jung, H.G. Jung and K.Y. Kim

Titanium and Aluminum Coatings with Supersonic Free-Jet PVD 991
A. Yumoto, F. Hiroki, I. Shiota and N. Niwa

Fabrication and Thermo-Mechanical Properties of Functionally Graded Thermal Barrier Coatings 997
J.H. Kim, Y.M. Rhyim and C.G. Park

Low Pressure Carburizing of Ti-6Al-4V Alloy 1003
J.H. Kim, C.H. Shin and S.W. Kim

Nitriding and Boronizing of Titanium and Titanium Alloys and Evaluation of Surface Strength 1009
K. Nakasa, X. Yan and M. Kato

Intensified Plasma-Assisted Processing of Pure Ti and Ti-6Al-4V Alloy 1015
E.I. Meletis

Evaluation of Corrosion on Aluminum Alloy Airframe Structures under Protective Coatings Using Acoustic and Thermographic Techniques 1021
J. Hoffmann, S. Sathish and N. Meyendorf

Microstructure and Mechanical Properties of Ti-6Al-4V Alloy Surface-Alloyed Materials Fabricated by High-Energy Electron Beam Irradiation 1027
K.J. Euh, J.M. Lee and S.H. Lee

Session XI : MELTING/CASTING

The Expanding Family of Aluminium Grain Refiners for the Wrought and Foundry Industries 1037
D.A. Boot and P. Fisher

Filling Limitation and Mechanical Properites for Different Gate Positions in Semi-Solid Forming Process of Aluminum Alloys 1043
C.G. Kang, P.K. Seo and Y.I. Son

Comparison of Innovative Induction Heating for Aluminum Alloys and Metal Matrix Composites in Semi-Solid Forming Process 1049
H.K. Jung and C.G. Kang

Microstructural Evolution and Deformation Behaviour of 2014 Aluminium Alloys in the Semi-Solid State 1055
D.S. Han, I.C. Stone and B. Cantor

Microstructural Control for Thixotrpic Al Alloy by Horizontal Continuous Casting Process Using Electromagnetic Stirring 1061
K.B. Kim, D.Y. Lee, Y.K. Seon, H.I. Lee and D.S. Shin

Interfacial Reactions between Mold Materials and Molten Titanium Aluminide 1067
M.G. Kim, S.Y. Sung, T.W. Hong, Y.I. Bae and Y.J. Kim

POSTER PRESENTATION

Effect of Silicon on Microstructure and Mechanical Properties of TiAl Base Alloys 1075
S.E. Kim, F. Sun, Y.T. Lee and M. Yamaguchi

Development of Fine Microstructure of B.390 Casting Alloy by the Modification of Ca Amount 1081
H.J. Kim, M.K. Kim, B.H. Jung and K.J. Son

Plasma Nitriding Properties of Ti-aluminide Intermetallic Compounds Fabricated by Hot-Pressing 1087
J.Y. Son and Y.W. Park

High Resolution Electron Microscopic Study of the δ'/G.P.zone Complex Precipitate Structure in an Al-Li-Cu-Mg-Zr Alloy 1093
K.H. Lee, Y.H. Lee, Y.J. Lee and K. Hiraga

Eutectic Bonding of Al6061 Alloy Using Cu Insert Metal 1101
S.Y. Shin, D.C. Cho, C.H. Lee, M.W. Ko and K.S. Shin

Rotation-Cylinder Method for Mass-Production of Lightweight Mg-Ni Hydrogen Absorbing Alloys 1109
W. Ha, T.W. Hong, S.K. Kim, S.G. Lee and Y.J. Kim

Drilling of Magnesium AM60B Alloy by Use of PVD Coated Tools 1115
E. Gariboldi, P. Locati and M. Vedani

High Efficient Drilling of Aluminum Alloys 1121
K. Sakurai1, K. Adachi, G. Kawai and K. Ogawa

Selection of Optimum Welding Conditions for A6061 Aluminum Alloy Friction Welding by Neural Networks 1127
G. Kawai, T. Sawai, T. Kurozawa, Y. Yamamoto, H. Yamaguchi and K. Ogawa

Evaluation of Corrosion Fatigue Pitting Damage on 2024-T3 1133
Y.I. Yoon, V. Chandrasekaran, D.W. Hoeppner and Y.H. Hwang

Characteristics of Semi-Solid Processed Al-Based Alloys for Automobile Applications 1139
S.Y. Lee, B.S. Kim, B.Y. Lee, S.Y. Lee and H.J. Lee

AUTHOR INDEX

PLENARY LECTURES

THE ADVANCED MATERIALS AND TECHNOLOGY IN THE NEXT GENERATION VEHICLES

Won Suk Cho*

*Materials Development Lab.
Research & Development Division for
Hyundai Motor Company & Kia Motors Corporation
772-1, Jangdug-Dong, Hwasungshi , Korea 445-850

Recent legislative and environmental pressures on the automotive industry to produce light-weight fuel efficient vehicles with lower emissions have led to a requirement for traditional steel components to be replaced by advanced materials such as aluminium, magnesium and metal matrix composites. Those social pressures have also led to a claim for conventional vehicles to be replaced by the next generation vehicles such as electric vehicles, hybrid electric vehicles, fuel cell vehicles and 3 liter car etc. This has led to a complete re-analysis of the design and manufacturing routes, with the emergence of advanced technologies as a viable process for the production of high volume, low cost, high integrity automotive components. In this lecture the development and application of advanced materials and key technologies including the next generation vehicles will be described and discussed in terms of vehicle performance and cost effectiveness. The research activities described illustrates the benefits of tailoring of design, processing and materials suitable for EV, HEV, FCEV and 3 Liter Car etc.

APPLICATIONS, BENEFITS, AND IMPLEMENTATION OF TI-6AL-4V CASTINGS

Eui W. Lee, Charles S. C. Lei and William E. Frazier

Naval Air Systems Command
Aerospace Materials Division
Patuxent River, MD 20670

ABSTRACT

Increased attention has been given to the use of structural Ti-6Al-4V castings on navy aircraft because of their potential to reduce weight and cost. Advanced castings have improved mechanical properties and reduced mechanical property variability. Combined, these improvements have put the use of a casting factor (an additional safety factor used only for cast components) in the design of structural cast components into question. Consequently, the Navy has partnered with the Air Force and the commercial sector in order to address impediments to the wide spread use of castings. Two round robin studies are described. The first explores the affect of Beta Vs. Mil annealed heat treatments on fatigue properties. The second is focused on the development of reliable design data for cast, thick section Ti-6Al-4V. It was concluded that the fatigue properties of Beta Vs. Mil annealed Ti-6Al-4V castings were comparable for thin section castings. Further, caution should be exercised in using AMS-4985 minimum property values for the design of thick Ti-6Al-4V investment cast components as minimum property values listed may not be achieved.

1. INTRODUCTION

In an environment of reduced DoD spending on new weapon systems and an aging fleet of Navy aircraft, the NAVAIR Team is engaged in efforts to reduce the cost and increase the readiness of products delivered to the Fleet. The implementation of advanced structural casting technology is an important facet of this work. The use of structural castings permits the consolidation of sub-components, parts, and fasteners greatly reducing both the acquisition cost and the maintenance cost of the structure.

Over the past decade, the use of investment castings has increased on both commercial and military aircraft because they lower cost and save weight. Advanced castings technology now permits the replacement of complex multi-piece components. Part counts, joint materials, labor and weight is significantly reduced through the use of structural cast components. For example, a one-piece transmission adapter made from investment cast titanium which has been successfully implemented on V-22 Osprey. The cast transmission adapter is originally fabricated by joining eight parts and 395 fasteners, and the cost is reduced by $50, 000. Thick, investment cast parts of 180 Kg have become a reality due to the high quality casting process. Also, welded titanium castings are being implemented on newly developed military aircraft to replacing mechanically and adhesively joined components.

The Navy uses a rigorous process in order to certify and qualify materials and structures in order to ensure safety of flight and full mission capability of Naval aviation weapon systems [1]. A building block process is practiced in which validated engineering data and concepts provide the foundation for continued technological development and innovation. The customer's cost, schedule, and performance requirements-expectations must be carefully considered. The down selection of appropriate technologies for immediate use or further research and development is based upon a risk assessment that takes into account many factors including: technological maturity, lessons learned, the sponsor budget and schedule constraints, affordability, return on investment, and life cycle cost impact. Importantly, thoughtful consideration and affirmative answers to three important questions is essential: 1. Has the materials technology been developed and standardized? 2. Has the materials technology been fully characterized? 3. Has the materials technology been demonstrated? Presently, unlike wrought alloys, each structural titanium casting must be independently qualified.
The implementation of structural castings requires the following critical issues are addressed:

- Heat treatment optimization,
- the development adequate design allowable test data, specifications and standards
- the elimination of the casting (safety) factor by designers to account for uncertainty in material properties.
- the development of an adequate understanding of the effect of defects (porosity, shell inclusions, especially the halo zone) on mechanical properties especially fatigue and fracture toughness
- the development of satisfactory nondestructive inspection (NDI) techniques for the inspection of thick section casings and for the detection of shell mold inclusion
- a reduction in the cost and time associated with the qualification of structural castings.

A casting (safety) factor has traditionally been used to offset inconsistencies in mechanical properties. Recent advances in our understanding of casting technology, improvements in foundry practices, and advances in process control have greatly reduced the variability of mechanical properties of cast structures [2]. Figure 1 illustrates the type of quality improvement realized in advanced investment cast properties as compared to those of traditional castings. Major improvements have been made in design allowable properties. Typically, 99% of the data must exceed the design allowable at a 95% confidence level. As a result of improvements made in the design allowable strength levels, the cost and weight of structural castings can be significantly reduced. Some navy acquisition programs, for example the F/A-18E/F, are actively working to demonstrate the possibility of designing components with a casting factor of 1.0, i.e., without a casting factor. ONR has also established an exploratory development (6.2) and manufacturing technology programs in order to develop affordable titanium and aluminum castings technology for advanced navy aircraft [3]. The exploratory development program was designed to elucidate the process of void closure, that is healing, that occurs during the hot isostatic pressing (HIP) of titanium and aluminum alloy castings [3]. This effort led to the first round-robin program examining the affect of heat treatment on mechanical properties of titanium castings, and the establishment of design allowable database. A parallel endeavor is being conducted under the Navy

International Cooperative Program (NICOP). It's purpose to characterize the affect of shell-mold inclusions and weld joining on the mechanical properties of the thick titanium castings.

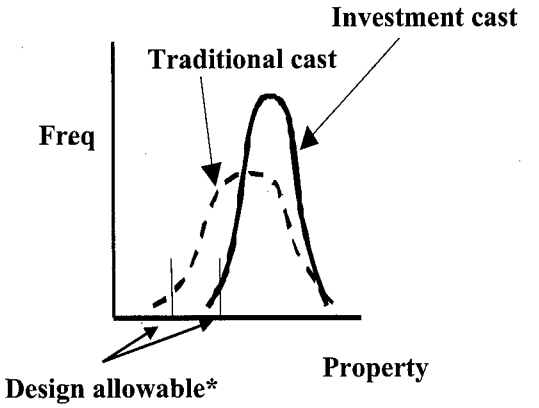

***99% of the data exceeds the design allowable limit with a 95% confidence level**

Figure 1. Scattering data of cast materials

The lack of design allowable data led to the formation of a government-industry steering group, TICAS, that has worked with the MIL HDBK-5 Committee in order to develop statistical substantiated test data suitable for inclusion in MIL HDBK-5 [4]. Participation in the TICAS Committee has grown, and now consists of the following members: Air Force, Navy, Boeing, Lockheed-Martin, Northrop Grumman, PCC, IMT and HOWMET. The committee has sponsored two round-robin studies in order to help facilitate the wide-spread use of structural castings on aircraft.

2. F18 EJECTOR BLOCK TITANIUM CASTING ROUND-ROBIN

The purpose of the first round-robin was to determine the effect of heat treatment on the mechanical properties, especially fatigue, of cast Ti-6Al-4V components. Two heat treatments were investigated: Mil Anneal, and Beta Solution Treatment and Overaged (BSTOA). In the aerospace industry, most of critical structural titanium castings are required to be hot isostatically pressed (HIP) and BSTOA before they can be used for structural parts. Annealing serves primarily to increase the fracture toughness, room temperature ductility, creep resistance, and the dimensional and thermal stability, In order to reduce manufacturing cost, an investigation was conducted into whether mill-annealed, HIPed, titanium castings perform as well as BSTOA, HIPed titanium castings. Due to the lack of specifications for designers to use, the government-industry casting steering group in conjunction with MIL HDBK-5 Committee conducted a round-robin test program.

Mill anneal is a general-purpose treatment given to all mill products. This process is a simple treatment consisting of annealing around 800 °C for 2-4 hours and air cooling. BSTOA patented by Boeing Company, is widely used for titanium alloys. This treatment consists of annealing above 1000 °C for a period and rapid cooling. Subsequently, the alloy is annealed at about 850 °C and then air-cooled. This unstable phase partially decomposes upon aging. Figure 2 illustrates the mill anneal and BSTOA heat treatment processes [5].

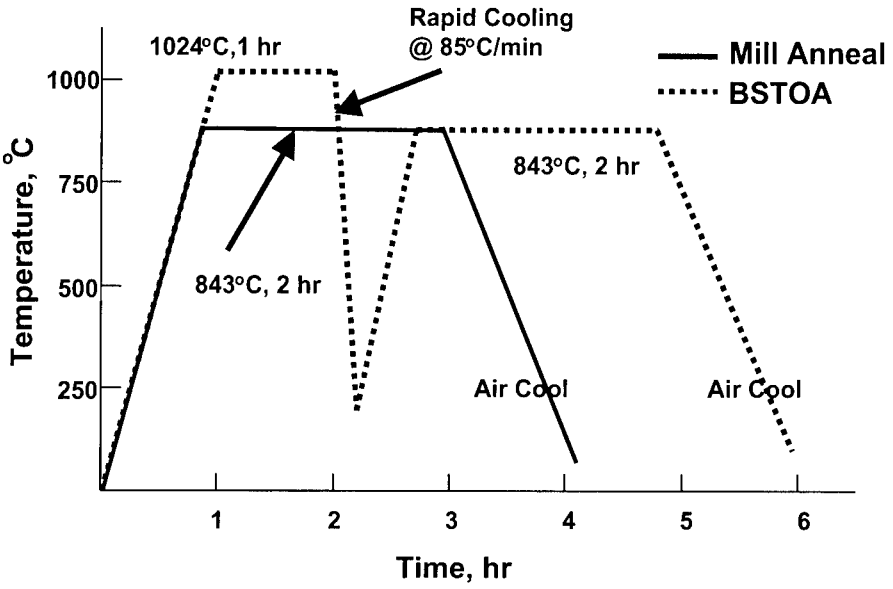

Figure 2. Titanium heat treatment process: Mill Anneal and BSTOA

Eighteen F-18 titanium aft ejector blocks were cast by HOWMET. Nine aft ejector blocks were mill-annealed, while the other nine were BSTOA. One mill- annealed ejector block and one BSTOA ejector block were distributed to round-robin test participants (NAVY, AIR FORCE, BOEING, LOCKHEED-MARTIN, and HOWMET). Mechanical properties, such as tensile yield strength, ultimate tensile strength, fatigue life, fatigue crack growth rate and fracture toughness, were examined and compared. Four tensile, twelve high cycle fatigue, two fatigue crack growth and two fracture toughness specimens were cut and machined from each ejector block. A total of 20 tensile, 60 high cycle fatigue, 10 fracture toughness and 10 fatigue crack growth tests were performed by the participants. Mechanical properties were evaluated using ASTM standards: 1. tensile properties, ASTM E8; 2. high cycle fatigue, ASTM E466; 3. fracture toughness, ASTM E399; and 4. fatigue crack growth ASTM E647.

2.1 Tensile Properties:

The tensile test results, including yield strength, ultimate tensile strength, modulus and elongation are summarized in Table 1. The average, mean properties of both the mill-annealed and BSTOA test specimens are comparable, e.g., mil annealed and BSTOA treated casting have ultimate tensile strengths of 943 & 949 MPa respectively. A preliminary statistical analysis of the tensile results is also present in Table 1. The average mean value of

the mil annealed and BSTOA processed material are comparable. However, the standard deviation observed for the mil annealed material is significantly greater than that of the BSTOA. The effect is to reduce the minimum values (used by designers), e.g., the mil annealed and BSTOA minimum yield strengths are 729 and 796 MPa respectively.

Table 1. Population Means and Standard Deviation of Tensile Properties

	Mil Anneal				BSTOA			
Property	**UTS, MPa**	**YS, MPa**	**E, GPa**	**EL, %**	**UTS, MPa**	**YS, MPa**	**E, GPa**	**EL, %**
Average	942	841	116	12.2	949	851	115	11.5
Standard Deviation	20.2	33.7	3.2	2.29	16.0	16.5	3.0	2.16
N_{sample}	19	19	15	19	19	19	15	19
N_{lots}	3	3	3	3	3	3	3	3
Minimum*	875	729	105	4.6	896	796	104	4.3

Minimum: 99% of the population of values is expected to equal or exceed the minimum value with a confidence of 95%.

$$\text{Minimum} = \bar{X} - \sigma k_{99}$$

Where $\bar{X}$ = sample mean

σ = standard deviation

k_{99} = one-sided tolerance-limit factor

2.2 High Cycle Fatigue Test

The fatigue life (number of loading cycles to failure) is plotted against the maximum applied stress for mill-annealed specimens and BSTOA specimens as shown in Figure 3. Results from five different organizations show similar fatigue life with slightly less scattering for BSTOA specimens. Figure 3 also shows the fatigue limit of mill-annealed specimens is similar to that of BSTOA specimens, with the fatigue limit of 503 MPa. BSTOA does not provide any high cycle fatigue life advantage over mill-anneal.

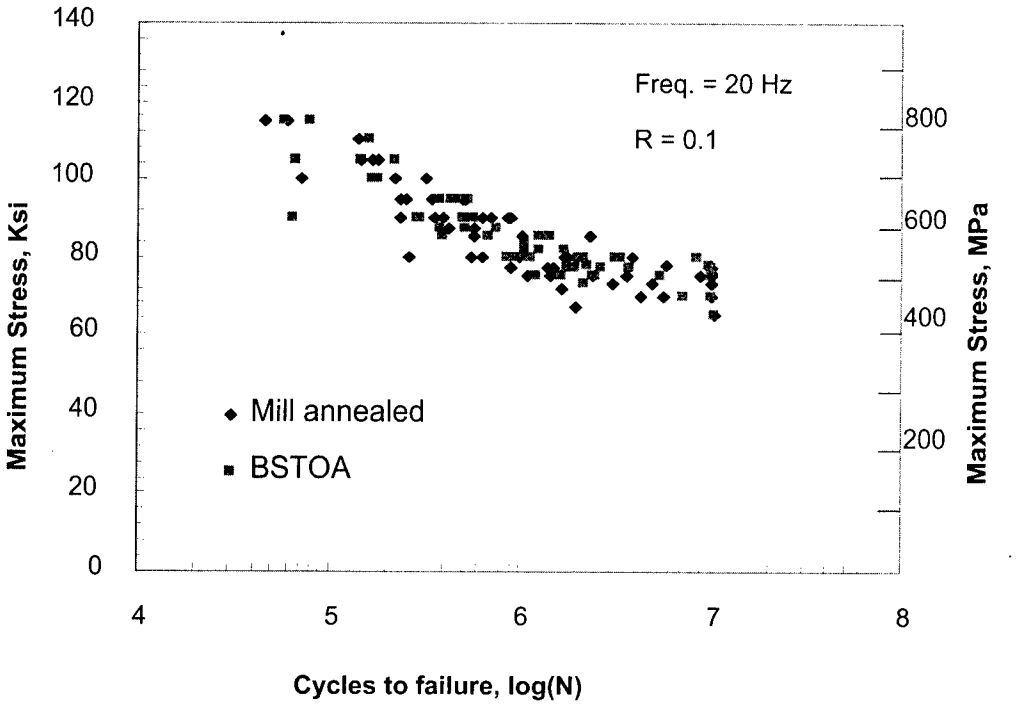

Figure 3. Comparison of high cycle fatigue: Mill Annealed vs BSTOA

2.3 Fatigue Crack Growth

Figure 4 shows the similar crack growth rate from five different organizations for mill annealed specimens and BSTOA specimens. It is observed that the fatigue crack growth behavior of mill-annealed specimens is comparable to that of BSTOA specimens

2.4 Fracture Toughness

Table 2 shows the mean fracture toughness values compiled from five different organizations for mill-annealed specimens. The average mean fracture toughness values were 82.3 and 82.7 MPa $m^{1/2}$ for mil annealed and BSTOA respectively. The population mean and standard deviation are also presented in Table 2. The standard deviation observed for the mil annealed alloy was one-third that of the BSTOA.

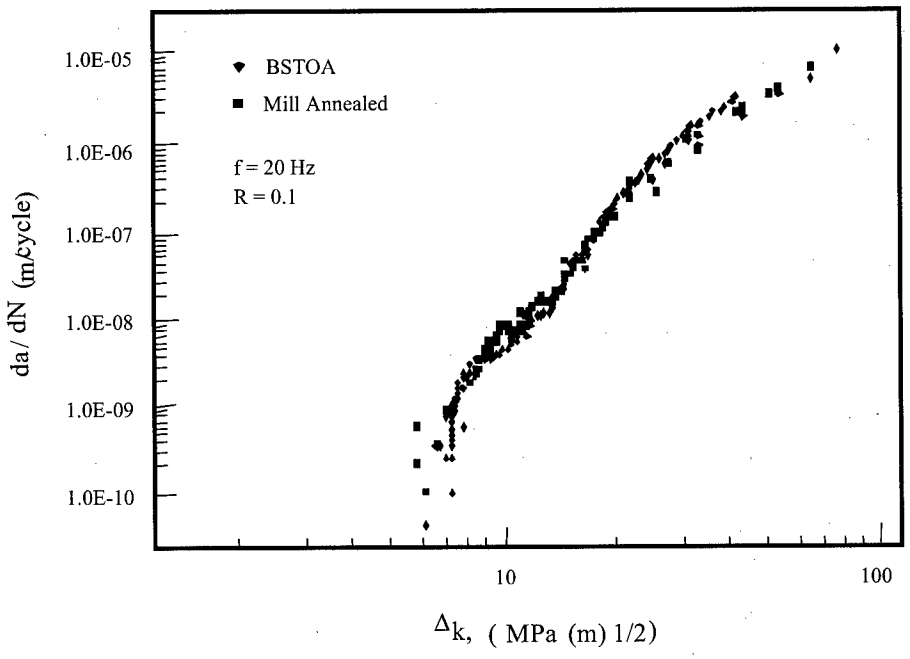

Figure 4. Comparison of fatigue crack growth rate: Mill Annealed vs BSTOA

Table 2. F18 Ejector Block Fracture Toughness Values: Population Mean and Standard Deviation

Property	**Mil Anneal Kq, MPa $m^{1/2}$**	**BSTOA Kq, MPa $m^{1/2}$**
Mean	82.0	82.7
Standard Deviation	1.9	6.6
N_{sample}	9	10
N_{lots}	3	3

2.5 Discussion of results

Prior studies have shown superior high cycle fatigue resistance for BSTOA castings over mill annealed castings. The results of this round-robin test program do not support that assessment. There are several factors that could explain this difference: 1. The location on the casting from which the specimen is taken is very important. Castings with different cross-sectional areas exhibit different cooling rates during solidification. This factor can result in slightly different microstructures and grain sizes, which affect mechanical properties. 2. Different heat treatment parameters such as annealing and cooling times and temperatures can change

the microstructure as well as mechanical properties; and 3. the results of the present round-robin work are being compared with a mechanical property data base established more than a decade ago. As compare to a decade ago, improved compositional and process controls are used to produce today's advanced titanium castings. The microstructures of as-cast material produced today are more uniform and contain fewer defects. Consequently, the enhanced diffusion rates achieved during the high temperature beta anneal may not be needed to achieve adequate compositional homogeneity.

3. 50.8 mm THICK Ti-6Al-4V CASTING ROUND-ROBIN

Large airframe structures are frequently produced from thick, wrought, plate, extrusions, and forgings. In order to reduce the cost of these large structures, net-shape casting technology and manufacturing practices are being exploited. However, large, thick cast components have historically been prone to defects, such as porosity and shell mold inclusions. The consequence is that traditional thick castings exhibited considerable range of static and dynamic mechanical properties.

The purpose of the second round-robin investigation, sponsored by the TICAS committee, was to evaluate the properties of 50.8 mm thick mil-annealed Ti-6Al-4V castings. The mil-anneal heat treatment was selected because of the satisfactory fatigue results achieved in the first round-robin study. The second round-robin work is in progress and the data and results presented here are preliminary.

The participants in the testing phase of this round-robin are the Air Force, Navy, Boeing, Lockheed Martin, Northrop Grumman, IMT and CTC. Ten heats of Ti-6Al-4V blocks measuring 50 mm x 100 mm x 200 mm were cast: 5 by Howmet and 5 by PCC. From the material, 200 tension, 50 compression, 100 bearing, and 50 shear specimens were prepared and tested. The following standard test methods were applied: 1. Tensile Properties, ASTM E8; 2. Compression, ASTM E9; 3. Shear strength, ASTM B769, and 4. Bearing Strength, ASTME238. The test results will be evaluated and included in MIL-HDBK-5.

3.1 Tensile Properties

The tensile test results, including yield strength, ultimate tensile strength, modulus and elongation are summarized in Table 3. Both ultimate strength and modulus show consistent value with a small standard deviation. While yield strength and total elongation show relatively large deviation due to one or two sets of extreme experimental results. The ultimate tensile strength of the 50.8 mm thick casting (the second round-robin) was nearly 30 MPa lower than that of the F-18 ejector block. Elongation of the second round-robin test is greatly reduced, compared to that of the first round-robin test. Finer grain size due to relatively fast cooling of the first round-robin test samples may contribute to higher strength, larger elongation and less scattering.

3.2 Compression, Shear, and Pin-Bearing Strength

Table 3 also shows the compressive yield strength, shear strength, and Pin-Bearing Strengths for the 50.8 mm thick titanium castings. The results are from five different organizations and seven heats of mill-annealed specimens. Population statistics for the mechanical properties of the 50.8 mm thick Ti-6Al-4V castings are presented in Table 3 as well.

Table 3. Population Statistics for the 50 mm Thick Ti-6Al-4V Cast Round-Robin

Property	**UTS,** MPa	**YS,** MPa	**E,** GPa	**Elong.** %	**CYS,** MPa	**S,** MPa	**BS,** MPa e/d=1.5	**BS,** MPa e/d=2.0
Average	913	840	118	6.39	904	655	1470	1766
STD	18.9	34.4	6.9	1.58	29.2	28.8	87.6	99.1
N_{sample}	177	176	136	177	36	46	67	45
N_{lots}	9	9	7	9	7	9	9	6
Minimum	864	751	99.8	2.3	817	572	1226	1478

Minimum: 99% of the population of values is expected to equal or exceed the minimum value with a confidence of 95%.

$$\text{Minimum} = \overline{X} - \sigma k_{99}$$

Where

$\overline{X}$ = sample mean

σ = standard deviation

k_{99} = one-sided tolerance-limit factor

4. SUMMARY

The application of advanced titanium investment castings in aircraft is increasing. The principle drivers for their use are the potential for lower acquisition and maintenance costs. Although the Navy has implemented large structural investment castings (e.g., the V22 transmission adapter), the cost and time associated with qualifying castings is a significant impediment to their wide-spread use. This paper presents the results of two round-robin studies conducted by TICAS, a Navy-Industry Titanium Casting Consortium. The objective of the first round-robin was to assess the affect of the BSTOA and Mil Anneal heat treatments on the mechanical properties of investment cast Ti-6Al-4V. It was concluded that these heat treatments yield similar results and the less expensive Mil Anneal heat treatment can be used when cost is a driver. The objective of the second round-robin was to develop a statistical substantiated, materials allowable, data base for 50.8 mm "thick" Ti-6Al-4V investment castings. The data is currently being analyzed by the Mil HDBK-5 Committee.

ACKNOWLEDGEMENT

The authors appreciate the efforts by all the participants including the Air Force, Lockheed Martin, Boeing, Lockheed Martin, IMT, CTC, Northrop Grumman, PCC and Howmet. Their contributions made this work possible. We also extend our sincere appreciation to the MILHDBK-5 Committee for their support in committee meetings and data inclusion.

REFERENCES

1. William E. Frazier, Donald Polakovics, and Wayne Koegel, "Qualification of Metallic Materials and Structures for Aerospace Applications," JOM. (33)(11) (March 2001), 16-19

2. Dale McLellan, "Understanding Casting Factors in Aircraft Components," Modern Casting, October 1994.

3. Charles Lei, Eui Lee, and William E. Frazier, "Effect of HIP on the Cast Aluminum," JOM. November 1997.

4. MIL-HDBK-5, "Metallic Materials and Elements for Aerospace Vehicle Structures," (DoD, March 1998)

5. Charlie R. Brooks, Heat Treatment, Structure and Properties of Nonferrous Alloys (Metals Park, Ohio: ASM), pp.361-376.

FRICTION STIR WELDING: EMPHASIS ON AIRCRAFT AND SPACE APPLICATIONS

Kumar V. Jata

Air Force Research Laboratory
Materials and Manufacturing Directorate
AFRL/MLLM, 2230 Tenth Street
WPAFB, Ohio 45433, USA

ABSTRACT

Friction stir welding (FSW) is evolving extremely rapidly as a viable and affordable technology to join metallic alloys to manufacture structures for use in transportation systems. Automotive, aircraft, space and ship building industries have been actively pursuing this technology for the last six to eight years to join aluminum alloys, steels and recently titanium alloys. Research work is progressing at a vigorous pace on all fronts, including novel tool design, optimization of process parameters to produce mechanical properties equal to or better than fastened structures, and process models to understand and guide the FSW process. This paper focuses primarily on high strength aluminum alloys, aluminum-lithium alloys and a titanium alloy that have applications in aircraft and space transportation.

1. INTRODUCTION

Friction stir welding (FSW) was invented at The Welding Institute (TWI) in 1991 [1]. Numerous researches and engineering publications are showing that this technology may have excellent weight and cost benefits and be highly attractive for efficiently joining aluminum structures. FSW can join aluminum alloys fairly rapidly (~4mm/s) with low heat input requiring no shielding gases and costly filler materials. The Aerospace industry currently uses a significant amount of fastener technology to join metallic structures and it is well known that a large cargo aircraft or a large commercial jet airliner has millions of fasteners. Thus elimination of fasteners will provide considerable weight savings. However, issues such as crack initiation, crack growth and corrosion that originate at fastener holes are well understood. Damage tolerance prediction methodologies, operations and maintenance issues are also well established for riveted/fastened structures. In a similar vein, space industry employs fusion/arc welding for aluminum cryotanks; weld repair methods and cryogenic-property databases are well established for the fusion welding process. For FSW to replace these well established joining technologies not only will it have to be better understood for predictable microstructure-property relationships, corrosion and failure modes but also life cycle benefits will have to be convincingly demonstrated. Secondly, databases will have to be generated for predictable properties to qualify FSW before it can be inserted into transportation systems. There is still a lack of available engineering design data which limits commercialization of FSW for aerospace and space applications. This paper will focus on the research findings in the areas of microstructure and properties of aluminum alloys and the Ti-6Al-4V alloy.

2. MICROSTRUCTURE EVOLUTION

Microstructure of friction stir welds of aluminum alloys is well characterized and described in details in the literature [2-8]. Under an optical microscope the weld zone is seen to consist of a nugget region/stir zone in which the grains are fine and recrystallized. Adjacent to the weld nugget is a thermomechanically affected zone (TMAZ) in which grains retain the original pancake shape but are highly deformed (curved/bent). Next to the TMAZ zone is the heat affected zone (HAZ) in which grains retain the original shape and size of the parent material grains. When a precipitation hardened Al alloy is friction stir welded in a T6 or T7 temper several significant changes occur at the precipitate and dislocation scale which can be resolved with a TEM. Careful analysis shows that the strengthening precipitates in the weld nugget region go back into solution because here the temperature excursions exceed the solution heat treatment temperature of the alloy. A high dislocation density is also found in the weld nugget region. In the HAZ, the effect of the temperature excursion is to coarsen the precipitates that result in an overaged or an annealed microstructure. For example, for the 7050-T7451 alloy it is shown that precipitates and the precipitate free zone in the HAZ coarsen by a factor of five compared to the parent material. Similar observations have been made for an Al-Li-Cu alloy (Al-1.8Li-2.7Cu-0.3Mg) AF/C458, as shown here in Figure 1. Significant coarsening of the precipitates, T_1, Al_2CuLi is observed (the weld nugget was slightly artificially aged to bring out the δ' precipitates). During friction stir welding the crown side of the weld makes direct contact with the rotating shoulder whereas the root side contacts the backing plate. Therefore, there is excess heat generation on the crown side that is conducted away through the root side. Similarly, on the advancing side of the tool (relative velocity between tool and work piece is maximum) thermocouple measurements show that the heat generation is slightly lower than on the retreating side (relative velocity between tool and work piece is minimum). Therefore, there is a variation in the size of the microstructure constituent along the through-the-thickness direction from the crown side to the root side of the weld. A variation in the microstructure also exists between the retreating side and the advancing side. Jata and Semiatin [6] showed that the grains in the weld nugget region evolve through a continuous dynamic recrystallization process and that the large refinement in grain size compared to the parent material can be explained by the Zenner-Hollomon parameter that is dependent on temperature and imposed stress.

When the grain size of the starting material is very fine such as in powder metallurgy (P/M) alloys and P/M MMCs, friction stir welding does not show a grain refinement of the matrix grains. In fact matrix grain size increases due to hot working of the microstructure and as mentioned above can be explained by the Zener-Hollomon parameter analysis. Mishra et.al. [9] have recently conducted a study on the 7093/15vol% SiC + 10% pure aluminum (used as ductile phase reinforcement) joined by FSW. Microstructure of this MMC is shown here as an example, Figure 2. The optical micrograph shows a transverse section of the weld containing an "onion ring" type of weld nugget (originating from the threads in the tool pin). SEM micrographs of the parent material show the banded Al reinforcement (that was added to this MMC as a ductile phase) and the SiC reinforcement. SEM micrograph of the weld nugget clearly shows that the size of the SiC reinforcements is similar to that of the parent material indicating that there is no breakage of the SiC reinforcements due to friction stir welding. Some authors have indicated that there is excessive tool wear during friction stir welding of Al MMCs and that iron particles from the FSW tool pin can be found in the microstructure.

3. MECHANICAL PROPERTIES

Much of the FSW work on Al alloys reported in the literature has been performed on peak and overaged tempers (T6, T8 and T7). When Al alloys are FS welded the HAZ exhibits the lowest hardness consistent with the severely coarsened precipitate microstructure in this zone, Figure 3. Several experiments have shown that it is impossible to recover the weld hardness when the alloys are joined in a peak and overaged tempers unless they are re-solution heat-treated (SHT) and artificially aged. However, as shown in Figure 3, when Al–Li alloy AF/C458 was FS welded in the T3 temper, appropriate heat treatment can be used to recover the hardness (without resolving to SHT) and bring the hardness of the weld close to the parent material. The recovery of hardness by aging at low temperature without SHT has advantages since high temperatures employed for SHT followed by a quench can distort parts and introduce residual stresses. In the case of AF/C458, friction stir welding was performed on the T3 temper and then the weld was aged at 150 C for 24 hours. Tensile properties transverse to the weld direction provided a yield of 280 MPa, ultimate strength of 380 MPa with an elongation of 5 percent. In comparison, the parent AF/C458-T8 has a yield of 480 MPa, ultimate of 540 MPa and an elongation of 9%. Friction stir welding can therefore provide opportunities to work with various starting tempers and tailor weld properties to suitable needs.

Figure 1. Bright and dark field micrographs showing precipiates in weld nugget and the heat affected zone in Al-Li alloy AF/C458 at similar magnification. (As mentioned before, FSW puts the precipitates in the weld nugget back into solution. Here the weld zone was slightly heat treated to bring out the weld zone precipitate microstructure)

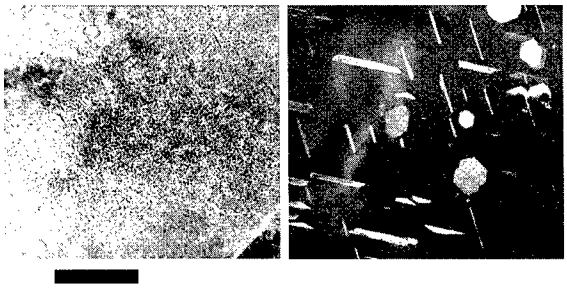

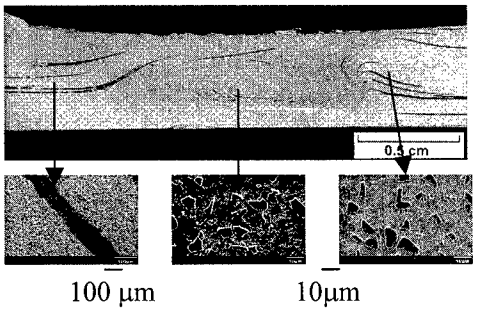

Figure 2. Optical micrograph showing a transverse section of friction stir welded 7093/15vol.%SiC MMC and SEM micrographs showing a band of pure aluminum reinforcement and SiC reinforcement that is similar size in both the weld nugget and matrix (i.e. no breakage of SiC reinforcement).

In a comprehensive study of AF/C458-T8 for space applications mechanical properties were obtained on the parent material and welded joints, prepared through variable polarity plasma arc (with the best available filler material for Al-Li alloys) and friction stir welding. For space applications it is required that the material exhibits increasing strength and increasing ductility at cryogenic temperatures. Therefore properties were obtained at room, liquid nitrogen and

liquid helium temperatures to study the behavior of the welds. As shown in Figure 3, the strength and elongation behavior of the friction stir welds is similar to the unwelded material. It is also seen that the elongation of FSW material not only surpasses the VPPA welds but also exceeds that of the base material at liquid nitrogen and liquid helium temperatures. For Al-Li alloys the increase in ductility at cryo temperatures has been attributed to slip homogenization. The microstructural modifications produced in the FSW welds are conducive to slip homogenization.

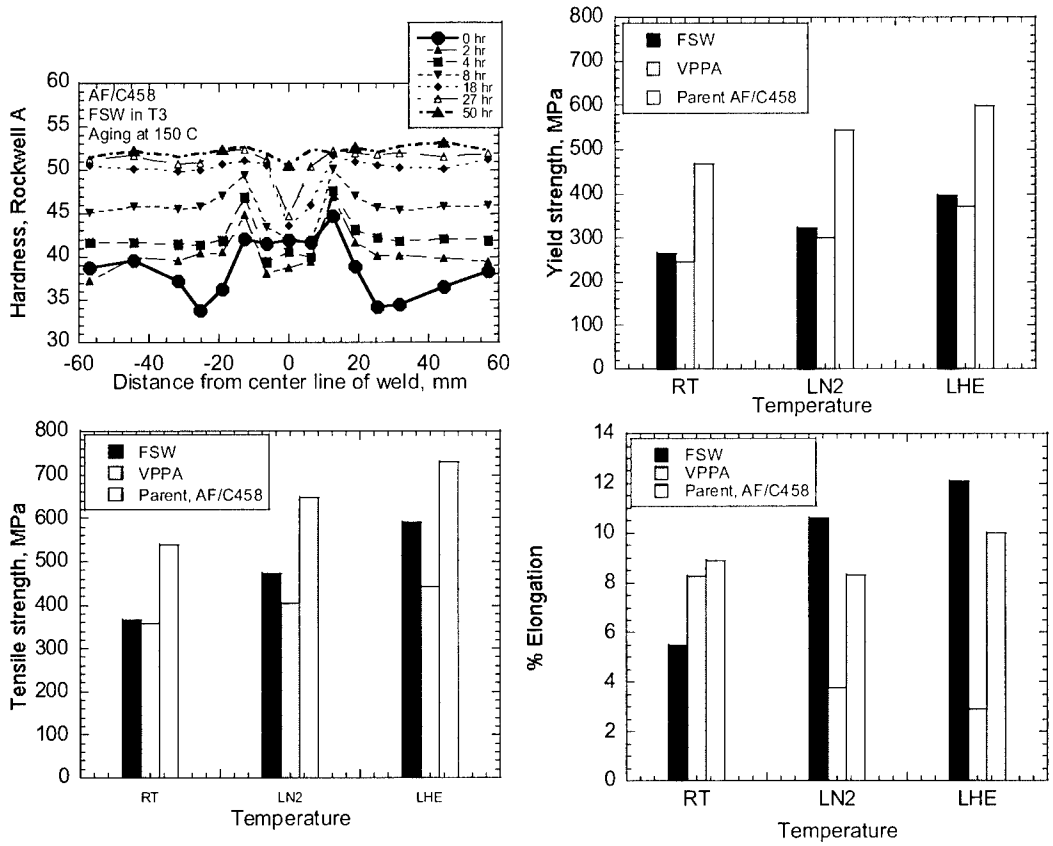

Figure 3 Hardness measurements of friction stir welded Al-Li alloy AF/C458 showing variation of hardness across the weld and it's recovery as a function of aging time at 150C. Bar graphs showing the yield, ultimate strength and % elongation in the parent Al-Li alloy and comparison to friction stir welded and variable polarity plasma arc welding.

4. RESIDUAL STRESSES

Residual stresses in general can have a significant effect on fatigue crack growth (FCG) and stress corrosion cracking (SCC). Since friction stir welding is a solid state process it is anticipated that the residual stress generated will be much smaller than the stresses generated in fusion welding and hence have much lower effects on FCG and SCC properties. Several investigators have measured residual stresses on welds in Al alloys, aluminum-lithium alloys such as AF/C458, 2195 [10,11]. Measurements parallel to the weld direction (longitudinal components), perpendicular to the weld (transverse component) and also through the thickness of the weld have been measured. A single picture that clearly ties the deformation

heating and accommodation of the stresses between the hot weld and the surrounding elastically stressed metal has not yet emerged. However, measurements show that the residual stresses are indeed small. In the case of Al-Li alloy C458, James et.al. [10] showed that the longitudinal and transverse stress components in the weld nugget are compressive and range between 20 to 70 MPa. In the TMAZ and HAZ regions the transverse component becomes slightly tensile but the longitudinal stress component stays compressive. Residual stresses up to 100 MPa have been measured for a 7050-T7451 alloy. For this alloy, the transverse component changes little in magnitude with respect to distance from centerline of weld but the longitudinal component remains compressive and a maximum value of–100 MPa is observed. Residual stress measurements made on Ti-6Al-4V alloy are shown here as an example, Figure 4. The Ti alloy was welded with travel speeds up to 1.7 mms^{-1} using a tool pin of length 5.08 mm and a shoulder 19.05 mm in diameter [12]. Thermocouples attached to the tooling and work piece at various locations show temperatures in the range of 830-1000C. The parallel stress component on the root side of the plate stays predominantly compressive whereas the crown side and the interior of plate exhibit tensile stresses. On the other hand the transverse component stays mostly compressive on both the crown and root sides with the interior of the plate exhibiting slightly tensile stresses. Although the residual stresses generated during FSW are lower than that in fusion welding their effect on the fatigue crack growth, particularly, near threshold is being investigated.

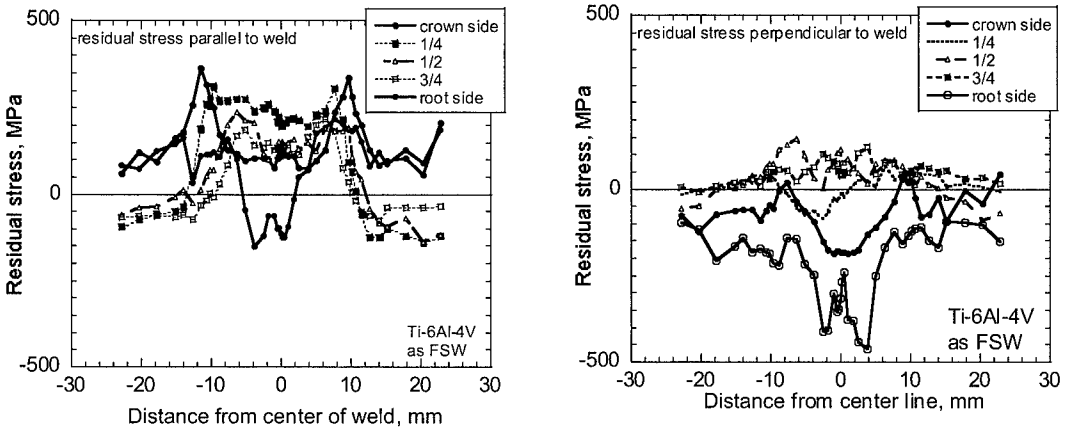

Figure 4. Residual stress variation in a Ti-6Al-4V friction stir weld. Longitudinal and parallel residual stress components at various locations transverse to the weld and through the thickness.

5. FATIGUE CRACK GROWTH AND TOUGHNESS

Residual stresses can have significant good and bad effects on critical load bearing structures, therefore, a study of damage tolerance of FSW welds is important. Fatigue crack growth (FCG), R-curve behavior and crack growth modes are some of the pertinent issues for aircraft structures, and similarly, if friction stir welding is used for cryotankage fracture toughness and FCG of FSW welds at cryo temperatures are important design factors. Fatigue crack growth in friction stir welds of Al-Li alloy AF/C458 was carried out using compact tension C(T) and extended compact tension EC(T) specimen geometry to understand the role of

microstructure and residual stress effects. Initial work was performed on understanding how fatigue cracks propagate in the weld nugget and HAZ regions of the friction stir welds.

Figure 5 shows the results for the AF/C458 alloy. The compact tension geometry shows a very large increase in FCG thresholds in the weld nugget as well as in the HAZ. Although the fatigue crack in the weld nugget propagated along the original crack plane the solution heat treated microstructure of the weld nugget and the beneficial compressive residual stresses present in the weld nugget pushed the FCG threshold way above that of the parent material. The HAZ result which also appears to be better than the baseline material is misleading since the crack grew severely out of plane and therefor the data are not valid. Because the crack growth was so out of plane, it was decided to choose a EC(T) specimen geometry. The EC(T) specimen is a conducive geometry for materials in which cracks grow out of plane. As shown, the initial conclusion from the EC(T) work is that the beneficial residual stress effects are washed out when the specimen geometry is changed from a C(T) to a EC(T) geometry.

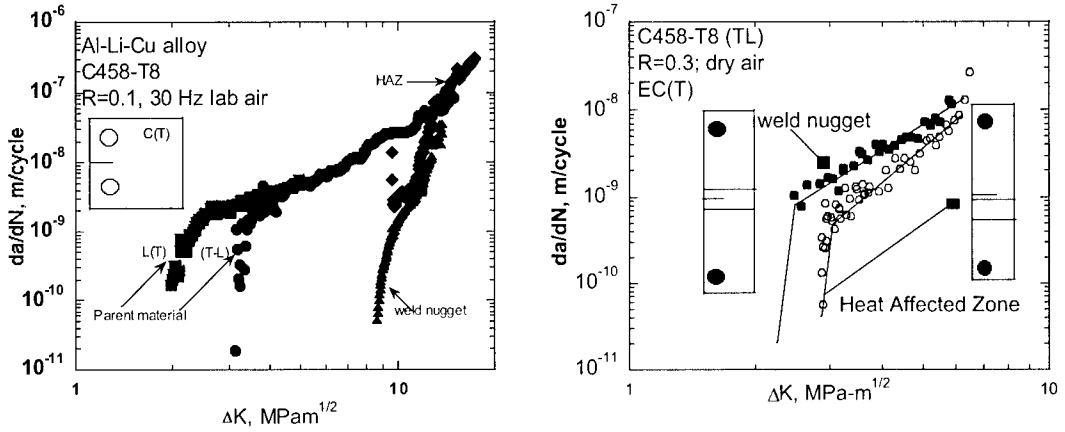

Figure 5. Comparison of fatigue crack growth rates in the parent Al-Li C458 to the rates in the weld nugget and heat affected zone. (a) Data obtained using compact tension specimen, C(T), (b) data obtained using Extended compact tension geometry.

FCG work was also carried out on the alloy 7050. As shown in Figure 6, it is found that the FCG rates in the weld nugget are faster and the FCG rates in the heat-affected zone are slower than the base material, at low R-ratios. At high R-ratio, as expected the FCG curves almost collapse into a single curve. The 7050 work shows that in the weld nugget in spite of the presence of compressive residual stress FCG rate was faster than the base material. For FCG in the weld nugget it was concluded that the fine grain size and grain boundary fracture negated the beneficial effects of the compressive residual stresses. For the heat affected zone compressive residual stresses dominated over the coarsened microstructure present in the HAZ and FCG rates were slowed down compared to the parent material. At high R-ratio the K_{max} level is high enough to remove the beneficial effects of the compressive residual stresses. Details of this investigation are provided in reference [7].

Another experiment was performed on the 7050 alloy to confirm the residual stress contamination of the FCG behavior. A C(T) and a middle crack tension M(T) specimen geometry were employed to study the behavior of FCG at low and high R-ratio with the same load shedding rate. The HAZ was chosen as the region where the crack would propagate.

Results in Figure 6 show that for the C(T) geometry at low load ratio the crack growth rates are far superior and at high R-ratio the benefit disappears, (as anticipated). However, when the M(T) specimen is used both the low and high R-ratio provide conservative values corresponding to the C(T) data at high R-ratio. These results suggest that the M(T) specimen geometry minimizes the residual stress effect and the misleading results.

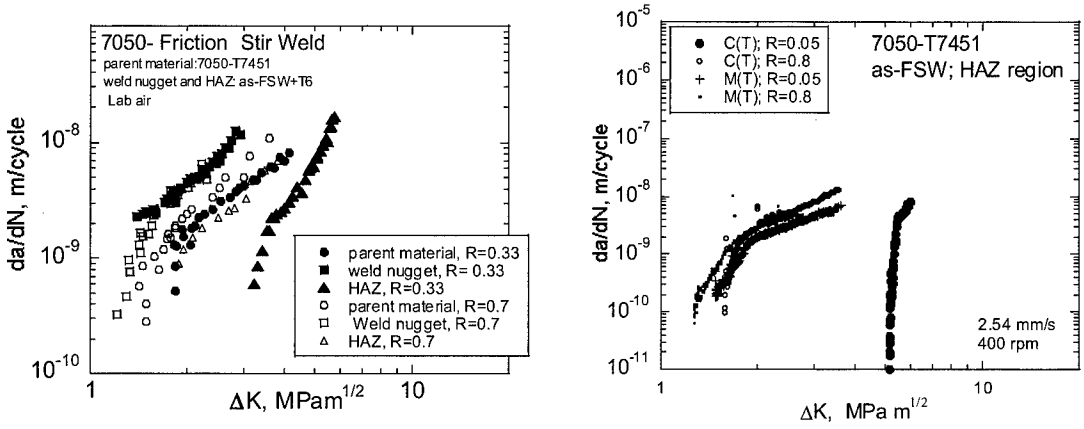

Figure 6. FCG results on the alloy 7050 using a EC(T) geometry at R-ratio of 0.33 and 0.7. Effect of specimen geometry, C(T) vs. M(T) on fatigue crack growth rate in 7050 alloy, R-ratio, 0.05 and 0.8. All results are for crack propagating in the heat-affected zone.

6. FRICTION STIR PROCESSING

The starting parent material microstructure lying under the FSW tool pin is completely broken down during FSW. Microstructure consists of fine grains (1 to 20 μm) with high angle grain boundaries and is therefore amenable to superplasticity during high temperature deformation. Mishra et.al. [13] have demonstrated superplastic-type elongations on alloy 7075 at various strain rates and temperatures and recently on aluminum-lithium alloy AF/C458. Seetharaman et.al. [14] have shown moderate to high strain rate sensitivity exponent for the stir zone material of 7050-T7451 alloy at 400 C and in the strain rate 10^{-5} to 10^{-2} range. These works demonstrate that the FSW tooling can be used for producing localized superplasticity.

7. SUMMARY & CONCLUSIONS

Friction stir welding is evolving rapidly as a commercial tool for joining aluminum alloys. This paper has made an attempt to show that high strength aluminum alloys that are important to aircraft and space transportation but are difficult to join by conventional means can be joined using FSW. Huge changes in microstructure occur. However, mechanical properties of FS joined materials are promising. It is important to keep in mind that many of the high strength aluminum alloys and associated tempers have been developed by the aluminum industry for specific aerospace applications to meet needs of stress corrosion cracking, damage tolerance and /or strength properties. Therefore, when these alloys are taken off-the-shelf and friction stir welded a knockdown in properties has to be expected and resultant properties may not always be the best. Comparisons should be judicious and can only be

made to the best available welding method. A systematic approach using various starting tempers of the alloys heat treatments to recover lost properties needs to be taken and examined at a fundamental metallurgical understanding level to fully exploit FSW. FCG results at a coupon level have been discussed here, and it is clear that residual stresses can contaminate the true FCG rate. Prediction of damage tolerance properties at a structural element and component scale will have to include residual stress effects. Stress corrosion cracking in thick plate FS welded aluminum and also corrosion in FS welded sheet material is important but has not received enough attention. A brief mention has also been made in this paper of the work performed in the area of friction stir welding as a technique to provide superplastic properties in the stir zone of the weld region. Much work needs to be done in this area to take this concept to the next stage. An example is provided in this paper that shows Ti alloys can be joined using FSW. The usefulness of joining Ti, (which can be easily diffusion bonded) in terms of cost and weight benefits is, however, not clear. Work that is being done in the areas of corrosion, castings dissimilar metals joining and process modeling has not been mentioned in this paper as most of this work is still evolving and beyond the scope of this paper.

8. REFERENCES

1. W.M. Thomas, E.D.Nicholas, J.C. Needham, M.G. Church, P. Templesmith and C.J. Dawes, International Patent application No. PCT/GB92/02203 and GB Patent Application No. 9125978.8 , 1991.
2. M.W. Mahoney, C.G. Rhodes and W.H. Bingel, Metallurgical and Materials Transactions, 1998, vol. 24, no.2, pp. 1955-1964.
3. G. Liu, L.E. Murr, C-S. Niou, J.C. McClure and F.R. Vega, Scripta Materialia, 1997, vol. 37, no.3, pp. 355-361.
4. L.E. Murr, G. Liu and J.C. McClure, J of Mater. Sci. Letters 1997, (16), pp. 1801-1803.
5. T.J. Linert, R.J. Gryllis, J.E. Gould and H. L. Fraser, in Hot Deformation of Al Alloys-II, Eds. T. R. Bieler, L. A. Lalli and S. R. MacEwen, TMS 1998, pp.149-158.
6. K.V. Jata and S.L. Semiatin, Scripta Materialia, 2000, Vol. 43, No.8, pp.743-749
7. K.V. Jata, K.K. Sankaran and J. J. Ruschau, Metallurgical and Materials Transactions, Vol.31 A, September 2000, pp. 2181-2192
8. Heinz, Birgit Skrotzki and Gunther Eggeler, in Aluminum Alloys, Their Physical and Mechanical Properties, Part 3, Proceedings of the 7th International Conference ICAA7, Charlottesville, Virginia, April 9-14, 2000, Materials Science Forum, volume 331-337, 2000, pp1757-1762
9. Mishra et.al., University of Missouri, Rolla, USA
10. M. James, M.W. Mahoney and D. Waldron, Proceedings of the 1st. International Symposium on Friction Stir Welding, Thousand Oaks, CA, 1999
11. M.A. Sutton, A.P. Reynolds, D.Q. Wang and C.R. Hubbard Journal of Engineering Materials and Technology, In Press, 2001
12. T. Lienert, K.V. Jata, R. Wheeler, V. Seetharaman, Proceedings of the International Conference on Joining of Advanced and Specialty Materials III, 2000, In Press eds. M. Singh, J.E. Indacochea, J.N. DuPont and T.J. Lienert
13. R.S. Mishra et.al. Scripta Materiala, Vol. 42, 2000, pp.163-168
14. V. Seetharaman, K.V. Jata and S.L Semiatin Proceedings of the Second Friction Stir Welding Symposium held at Gothenburg, Sweden, June 26-28, 2000, TWI, U.K. (Session 10, Paper 1), pp.1-10

THE R&D ACTIVITIES ON LIGHT ALLOYS AND THEIR APPLICATIONS IN TRANSPORT SYSTEMS IN CHINA

Zhou Lian

Northwest Institute for Nonferrous Metal Research
(P.O.Box 51 Xi'an 710016, Shaanxi, China)

ABSTRASCT

The R&D situations and activities on light alloys are very active in China, and special alloys are developed. Five Ti alloy systems are constituted as high strength, high temperature, corrosion resistance and shipbuilding ones. High strength, Al-Li alloys, and Al-based composite are developing. Some Mg alloys are also developed with the systems of RE addition, burn-resistance and damped. The Industry systems of Al, Mg and Ti have been formed during the past ten years. The production of light metals has been increased rapidly recent years. An estimated potential market for the light metals in the next 5 years is also given. In the new century, the R&D of light alloy and their application on transportation systems will get more active as the developing economy in China.

1. INTRODUCTION

Light metals, here mainly referred to Aluminum, magnesium and titanium, play an important role in the national economy and modern technology. Their resources in the Earth's crust are abundant, among which Al is the third most abundant resource in the Earth, and one of the most widely used metal materials in the world. Mg is the eighth most abundant resource in the Earth and one of the lightest metals in the common use. Ti ranks the ninth and is one of very important light metals.

China is abundant in Ti, Al and Mg and is one of the countries with the most abundant resources in the world. Recently proven Ti, Al and Mg deposits in China are 8.7×10^8t, 21.8×10^8t and 79.7×10^8t respectively. All of these lay a good foundation for developing Al, Mg and Ti industry.

2. RESEARCH PROGRESS OF TI ALLOYS

The main Ti research units in China include Northwest Institute for Nonferrous Metal

Research (NIN), Beijing Institute of Aviation Materials (BIAM), Beijing General Research Institute for Nonferrous Metals (BGRIN) and Institute of Metal Research (IMR) etc. Five series of Ti alloys (nearly 80 different designations of alloys) have been developed through hard working for 40 years.

The Ti alloys used for fasteners are always considered as one of the main research directions[2]. In order to meet the different requirements from air planes, different strength grades of Ti alloys for fasteners have been developed, such as TC4, TB2, Ti-15-3, β_{III}, β 21S etc. New type of different Ti alloys with different strength used for fasteners at different temperatures have been researched also in recent years, such as BT16, TC6, Ti-26 etc. Their typical properties are shown table 1.

Table 1 Typical mechanical properties of Ti alloys used for fasteners in China

Designation	Composition	σ_b (Map)	$\sigma_{0.2}$ (Map)	δ (%)	Remark
TC4	Ti-6Al-4V	900~993	830~924	14	Using up to 300℃
TB2	Ti-3Al-5Mo-5V-8Cr	1000~1400		20~7	
TB3	Ti-3.5Al-10Mo-8V-1Fe	1370		8	Using up to 300℃ easy to cold upset
Ti-15-3	Ti-15V-3Cr-3Al-3Sn	787	773	21.5	UTS is 1310Mpa after aging plasticity deformation over 5%
β_{III}	Ti-11.5Mo-6Zr-4.5Sn	841~1260	765~1190	18~8.0	
β_{21S}	Ti-15Mo-3Al-2.7Nb-0.25Si	905	887	13	
BT16	Ti-3Al-4.5V-5Mo	883	778	25	Using up to 300℃
TC6	Ti-5Al-2.5Cr-2Mo-1Fe	1100		18	Using up to 500℃ Easy to cold upset
Ti26	Ti-15V-3Cr-3Sn-3Al-Nb-Zr	1250		15	Using up to 500℃ Easy to cold upset

In the area of Ti alloys used for shipbuilding, their designations, strength grades and application scope have been specified [1~3]. Ti alloys with different strength scope used for shipbuilding were formed, among them four Ti alloys e.g. Ti-31, Ti-75, Ti80 and Ti-B19 have good toughness, easy to cold deform, good weldability, corrosion resistance to seawater, and can meet the different requirements from the different parts of ships. The comprehensive properties are similar to these of Timetal 5111, U.S.A.

High temperature Ti alloys are one of the hot researching fields. The special contribution of China is to add rare earth elements (RE) to Ti alloy to improve the properties [1~2]. Different alloys with RE have been developed, such as Ti55, Ti-633G, Ti60, Ti600 and 7715D, among which Ti600 has good comprehensive properties in the temperature from 600℃ to 650℃.

especially, its creep property is better than that of Timetal 834(Table 2). Important progress on the research of burn resistant Ti alloys has been made in recent years. Ti40 is a new type of burn resistant alloy which has good comprehensive mechanical properties and satisfied burn resistance being similar to Alloy C. Its high temperature oxidation mechanism is studied and oxidation model is proposed recently [4~5].

Table 2 Mechanical Properties of high temperature Ti-alloys

Alloy	Tensile strength at RT				Tensile at 600℃				Creep at 600℃			σ_{100}^{600} MPa
	σ_b MPa	$\sigma_{0.2}$ MPa	δ %	ψ %	σ_b MPa	$\sigma_{0.2}$ MPa	δ %	ψ %	σ_b MPa	T h	ε_3 %	
Ti600	1068	1050	11	13	745	615	16	31	150	100	0.03	
Ti60	1100	1030	11	18	700	560	14	27	150	100	0.1	350
Timet 834	1070	960	14	20	680	550	15	50	150	100	0.1	340
Ti1100	960	860	11	18	630	530	14	30	150	100	0.1	300
BT36	1080		10	15	640				147	100	0.2	335

A great deal of work on particle reinforced Ti matrix composites have been done in recent years, and some progresses have been made. The reinforcing particles TiC, TiB etc are selected as reinforcing particles which are added to high temperature Ti alloys by using mechanical alloying and melting etc to produce particle reinforced Ti matrix composites. Among them, TP650 composite developed by NIN has good comprehensive properties[6] (Table3), which can be applied to friction-resistant automobile parts.

Table 3 Typical mechanical properties of TP650

Tensile at RT				Tensile at 600℃				Tensile at 650℃			
σ_b MPa	$\sigma_{0.2}$ MPa	δ %	RA %	σ_b MPa	$\sigma_{0.2}$ MPa	δ %	RA %	σ_b MPa	$\sigma_{0.2}$ MPa	δ %	RA %
1330	1280	5	13	775	652	18	31	681	562	24	39

The requirements from transportation systems for low cost Ti alloys are more and more urgent. Low cost TAFS Ti alloy developed by NIN can reduce the cost by 20%, which can be used for automobile parts. Its tensile strength, yield strength, elongation, reduction in area, elastic modulus and HRC were 995MPa, 853MPa,19%, 26%, 381KJ m^{-2} and 127Gpa, respectively.

3. PROGRESS IN RESEARCH OF AL ALLOYS

By putting much effort in investigation of Al alloys for several decades 23 grades of Al casting alloys, 3 grades of Al-Si casting alloys and 143 designations of processed Al alloys products have been developed in China. A great progress in research of new types of Al alloys has been made in recent years[7].

Al-Li alloys are possessed of low density, high elastic modulus and high strength, and more

attention to which is paid extensively, several institutes and universities are being engaged in the research of this field actively. Eight medium strength and weldable Al-Li alloys, such as Al-1.5Li-4.4Mg-0.2Ag-0.12Zr etc. and high strength alloys such as Al-1.9~2.4Li-2.0~2.4Cu-1.0~1.5Mg-0.6~0.13Zr etc. have been developed successively. Melting and casting equipment with 6t capacity and relevant technologies for large scale ingots have been set up in China, by which qualified ingots with of $\Phi 310 \times 1800$mm can be produced.

Chinese researchers have conducted investigating of Al-based composite materials for a long time. B/Al composite materials and SiC/Al composite tubes were developed successfully by BIAM and IMR etc. Fruitful research on non-continuos fiber reinforced Al based materials have won some achievements.

Foamed Aluminum is investigated by many units in China, the foamed Aluminum prepared has superior properties to conventional Al alloys in the aspects of elastic modulus and thermal conductivity. Their values are 1/50~1/100 and 1/500 of those of conventional Al alloys respectively. It is also a superior shock absorption and heat insulation material. The associated technologies are transferred to industrial sectors for production in industrial scale at the present time.

Aluminum parts of heat exchanger by semi-solidification die forging can be formed into the shape as complex as that by casting method, and meanwhile maintain nearly the same mechanical properties as those of castings[8].

4. PROGRESS IN RESEARCH OF MAGNESIUM ALLOYS

Research and development of Magnesium and its alloys began in the end of 1950's in China, with human-being paying more attention to environment and energy resources in 1990's, development of Magnesium and its alloys comes to a new hot stage.

Effective research on new type of magnesium alloys has been conducted in China in recent years. The alloys containing rare earth elements, such as ZM3, ZM6 have been listed in China national specifications. Ce-containing magnesium alloy ZM3 has typical mechanical properties: σ_b=140MPa, $\sigma_{0.2}$=99MPa, δ =2.5%(R.T), σ_b=130MPa, $\sigma_{0.2}$=30MPa(below 250 ℃). Alloy ZM6 taking Nd as main alloying composition has also very good mechanical properties both in room temperature and in high temperature. New Magnesium alloy GQMZ96-Mg-9.0~9.5Al-3.5~4.0Zn-0.15~2.0Ag-0.2~0.3Mg possesses even higher tensile strength and elongation, as well as dramatic higher yield strength [8~11]. The property comparison of several magnesium alloys are listed in Table 4.

Investigation of burn-resistant magnesium alloys is now being conducted in China. The ignition temperature is increased by 250℃ for Mg-Be-RE alloy developed by researchers in Shanghai Jiao Tong University, the alloy has nearly the same mechanical properties as those of alloy AM91D.

Another new damping alloy ZMJD-15 has been developed in China. It is a Mg-Zn system alloy containing Zr, Nd, Mn with mechanical properties of $\sigma_b \geqslant 165$MPa, $\delta \geqslant 5$ and specific resistance $\Psi \geqslant 45\%$, and may have good prospect of application in transportation

vehicles to fulfil demands of shock absorption and noise reduction.

Table 4 The properties comparison of several magnesium alloys

Designation	Country	σ b/MPa	σ 0.2/MPa	δ /%
ZM5	China	157	93	3
ZM6	China	157	118	1.5
TL-WV03010	Germany	220	110	2--6
AZ91D	USA	230	130	5
GQMZ96	China	220	162	7

5. PROGRESS IN PROCESSING TECHNOLOGY OF LIGHT METALS

In order to raise and improve the level of the processing technology and equipments, China Rare Metal Material Processing Engineering Research center has been set up since 1994, thus an important base of R&D of metal materials has been formed at home.

In producing of Ti alloy, a new processing technology of step by step rolling is developed in the present time. A lot of Ti processed products with perfect performances have been turned out.

Important progress in producing Ti powder by Hydride-Dehydride process (HDH) has been made in NIN. By means of the process, the Ti powder with satisfied performances, low cost and low content of oxygen has been produced. HDH Ti powder is suitable to be used in manufacturing auto parts or components.

There are three heavy-duty aluminum works in China. They can produce various sorts of processed products including plates, sheets, foils, rods, profiles, forgings and castings etc., and total production capacity with 2,000,000t/a, and can provide cold sheet with 2500mm width and foil with 2000mm width[12].

6. STATUS OF LIGHT METAL INDUSTRY IN CHINA

The light metal industry in China has been developed to a greater scale for 40 years. The urgent demand of transportation system to lightening promotes further developing of Al, Mg, Ti industries in China. Fig.1 shows their output increase.

The statistics show that the outputs of Al and Mg in China increase in the speed of 10% and 12% a year. The annual consumption of Ti, Al and Mg are 2000, 3,020,000 and 24, 000, and among them transportation systems occupies 2.3%, 11.2% and 30% respectively in 2001. The output of Al don't satisfy the requirement of Chinese market, the annual import reaches about 100,000~200,000 tons per year. While the output of Mg exceeds the domestic demand, and 85% of the output is exported, and thus it is benefit for the development of Mg in the

transportation systems. It is predicated the output of Al and Mg will be increased by 15% and 12%, respectively, and their consumption will be increased by 10% and 12% respectively [13].

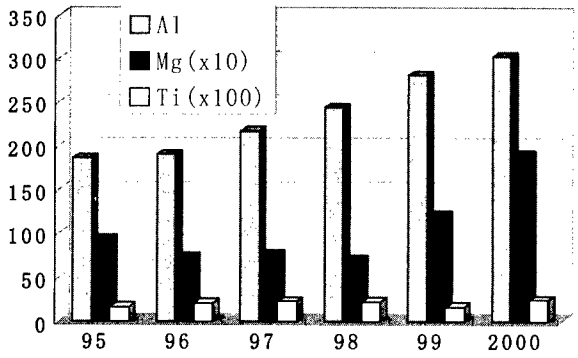

Fig.1 Output of Al, Mg and Ti in recent five years

7. APPLICATION OF LIGHT METALS IN TRANSPORT SYSTEMS

7.1 Airplane

Titanium, aluminum and magnesium are the main materials applied in the field of means of transportation. The amount of Al used in a plane in China is about 80 percent of the plane weight, the quantity of Ti is about 2~3 percent and the amount of Mg is as much as that of Ti. Various components of airplane are made of Al, Ti and Mg. Aluminum and magnesium alloys, especially some processed rare-earth-doped casting alloys are used as engine cabin in some outer place, while more titanium is used in engines.

7.2 Shipping

Metals for shipping require excellent toughness and ductility, weldability and corrosion resistance, and are mainly used for manufacturing the structures of the hull, the components of the engines and the instruments for navigation. China has researched a series of processed Ti alloys and casting Ti alloys for shipping. Al alloys can meet the different requirements in hull, rib, badkstay, aeration pipeline, steamer pump, heat exchanger, propellers, parts of communication meters and so on. In addition, a double-lulls passenger ships made of welding Al alloy (120 persons can be carried) has already run

7.3 Vehicle

Since 1990s, the industry of land communication has been developed quite rapidly due to the need of energy saving and environment protecting. The output of automobiles, especially cars,

increase persistently by 20 percent per year. In 1996, 2616 of passenger trains were produced, 40% more than that of 1990. In 1998, the China Nation Railway Ministry put forward a project of investing 250 billions RMB to quicken the passenger train speeds.

Among Al materials used for auto industry, castings are accounted for about 80%, forging are about 1~3%, balance are the processed materials. They are mainly applied to jars of engines, derailed, wheels, top board of bodywork, crossbeam of framework and other parts. Aluminum used for passenger trains is another important application field [14].

It is estimated that Al alloy used as carriage material may decrease 1/5 of carriage weight, which is much favorable for increasing the speed of trains. Plenty of LF21, LY12 and rust resistance aluminum are used to produce the parts of motorcycle such as top board of bodywork, window blind, inner wall, floor and gearing box etc. More than 30 lines of producing Al alloy wheels have been built in China, the output exceeds 9 millions pieces per year. In order to satisfy the demands in high quality Al alloy for transportation system, the main producers are rebuilding the existing lines or preparing to construct new lines in China. At the same time, the auto manufacturers are engaging in increasing the application and exploitation in pivotal components, such as parts of engine, underpants, and letting gas system made of titanium, and the core of steering wheel, lid of cylinder, clutch, brake pedal bracket and so on made of magnesium. Many of components have passed the formal trail run at the present, and will be put into production soon. The bases for producing and industrialization for Mg alloy and its products will be built in Shen Zhen and Qing Dao in 2001 respectively, which will promote the development of Chinese magnesium industry further.

It is forecasted that the demands of cars in Chinese market will increase by 16.4% per year during the coming ten years. It will reach 2.5 million in 2005. Assuming 110Kg of Al, 3Kg of Mg and 0.28Kg of Ti are used in each car, the total amount will achieve 275,000t Al, 7500t of Mg and 70t of Ti respectively.

7.4 Other Applications

China is a big country in producing and consuming bicycles. Since the beginning of 1990s, China has started the trial-producing Al, Mg and Ti components for top grade, handsome, light-duty bicycles. The rims, brake handlebar and frame etc are made of aluminum alloys. The whole Al bicycles (10kg of weight only), the whole Mg and the Ti bicycles made in China have been sold in market. The frame, handle bar(even wall thickness or variation in diameter and wall thickness) made of Ti-3Al-2.5V, and cushion spring and some standard components made of TC4 and Ti-230 alloy have become the steady products in mainland and Tai Wan of China. Many top grade bicycles made of Ti have been exported to more than ten countries and areas including Europe, America and Australia etc. In 1992, 5000 bicycles were exported from Shan Jing Company in Tai Wan.

Furthermore, Al and Mg alloys have also been applied in motorcycles in a large quantity. The wheels of motorcycles made of Al alloy achieved 4.5~5 million per year, about 24% of the total motorcycles in 1996.

8. CONCLUSIONS

Within the past few yeas, a lot of work in the fields of the research, production, design and application of light alloys have been done in China. A great progress on the application of the alloys in transportation has been made, the institutions and factories dealing with the research on aluminum, titanium and magnesium-based alloy materials have won great achievements and become the most active field of R&D of metal materials in China. Thus in the new century China will strengthen the study of above mentioned field, devote herself to develop new type of Ti, Al, Mg and their alloy materials with low costs, and high performances, to be engaged in the application of new precious fabrication technologies and near-shape forming technology etc., to make the coordination among materials and their products as well as modes of life and relation to their environment so as to meet the requirement of transportation-developing.

REFERENCE

1. Zhou Lian, in Proceedings of the 9th World Conference on Titanium 2000,Vol,10-18.
2.L Zhou, J Deng, in Proceedings of Xi'an international titanium conference, 1999, vol.1, 52~64
3. G.X.Luo, R.Z.Liu. Mater. Sci. Eng.A. A280(2000),pp. 25~29
4. Y.Q.Zhao, L.Zhou, Mater, Sci. Eng.A, A267(1999), pp.167~170
5. Y. Q.Zhao, H.L.Qu, Rare Metal Materials and Engineering, No.1 2001 pp.35~39
6. L.Zhou, X.N.Mao, Y.Q.Zhao etal. (published in this conference) .
7.Yu Shibin,Processing technology of light metals, No.9(2000),pp4~7
8.Chen Jiahua, Light metals, No.2(2000), pp3~7
9. Yu Kun, Li Wenxiang, Special casting and Nonferrous Metal alloys, No.1(2001)
10. Bai Jingqin, Zhao Pifeng. Research on new Mg alloy--GQMZ96,
11. Zhai Chunquan, Zeng Xiaoquan, Materials for Mechanical Engineering, No.1(2001)
12.Liu Yan, Processing technology of light metals, No.5(2000),pp41~45
13.Zhou Hongzhang, Proceddings of the fourth conference of Chinese nonferrous metal society, 1999, pp.1~5
14. Liu Jin'an, Shichuan nonferrous metals, No4(2000), pp.1~4

STRUCTURAL IN-SITU COMPOSITES AT VERY HIGH TEMPERATURES

S. Hanada, T. Suzuki, K. Yoshimi and N. Nomura
Institute for Materials Research, Tohoku University, Sendai 980-8577, Japan

ABSTRACT

Recent studies on structural in-situ composites for applications at very high temperatures above the maximum operating temperature of Ni base superalloys are reviewed in this paper focusing on intermetallics and carbides reinforced by refractory alloys. Especially emphasis is placed on ZrC/Mo in-situ composites with high strength at elevated temperatures and good fracture toughness at ambient temperature.
ZrC/Mo in-situ composites with hyper-eutectic (Mo-30, 40, 50mol%ZrC) and eutectic (Mo-16mol%ZrC) compositions were synthesized by arc-melting blended Mo and ZrC powders and their microstructures and mechanical properties were investigated. The hyper-eutectic composites consist of coarse primary ZrC particles and eutectic containing fine ZrC particles in Mo solid solution, while the eutectic composite is composed of fine ZrC particles distributed in Mo solid solution, forming some colonies. Yield stresses above 1500 K at a strain rate of 1.7×10^{-4} s^{-1} for the hyper-eutectic composites are around 400~800 MPa, which are higher than those of monolithic ZrC. Mo-40ZrC exhibits good creep strength as compared with advanced ceramic matrix composites. Fracture toughness K_Q values at room temperature for the hyper-eutectic composites are 12~15 MPa$\sqrt{m}$, which are much higher than those for monolithic ZrC.

1. INTRODUCTION

Development of structural materials at very high temperatures over Ni base superalloys has been recognized to be one of key technologies to solve environmental problems in various industrial fields. To aim at solving the problems advanced structural materials such as refractory intermetallics or ceramics have been investigated mainly because of their high strength at elevated temperatures. However, most of them have low fracture toughness at ambient temperature. In spite of many efforts to increase the fracture toughness by incorporating a ductile phase reinforcement, most studies have not succeeded in increasing the fracture toughness without sacrificing high temperature strength. There are two processes to incorporate a ductile phase in brittle intermetallics or ceramics. One is an ex-situ process in which a ductile phase is artificially introduced, and the other is an in-situ process in which a ductile phase is formed during high temperature synthesis. As a result, the interface between two phases is unstable in ex-situ composites, thereby producing other phase(s) through interfacial reaction on holding at high temperature, while the interface in in-situ composites is very stable at high temperature. Therefore, in-situ composites are more promising as structural materials at very high temperatures. Refractory intermetallic base in-situ composites were extensively investigated in the systems of Nb_3Al/Nb_{ss} [1-3] and Nb_5Si_3/Nb_{ss} [4-6], where Nb_{ss} denotes Nb solid solution. A considerably good balance between high temperature strength and room temperature fracture toughness has been attained by controlling alloy composition and microstructure. By contrast, few studies have been reported for ceramic base in-situ composites, although some carbides are known to be equilibrated with refractory alloys in phase diagrams at high temperatures [7].

2. Nb_3Al/Nb_{ss} IN-SITU COMPOSITES

Nb_3Al having a low density (7.26Mg/m^3) and a high melting temperature (2333K) exhibits high strength at elevated temperatures above 1450K; about 800 MPa at 1470K and 500 MPa at 1570K at a strain rate of $10^{-4}s^{-1}$. Monolithic Nb_3Al alloys are further strengthened at high temperatures by alloying with Ta, Mo and W [8]. Therefore, it is strongly suggested that Nb_3Al base alloys are promising as high-temperature structural materials. It is known, however, that monolithic Nb_3Al alloys are very brittle at ambient temperatures because of their complex crystal structure and limited slip systems. It has been clearly shown in the binary Nb_3Al/Nb_{ss} in-situ composites that the incorporation of Nb_{ss} in equilibrium with Nb_3Al lowers the brittle-ductile transition temperature (BDTT) significantly [9] and simultaneously increases the fracture toughness at room temperature [10], while reducing high-temperature strength. The incorporation of fine Nb_{ss} particles can lead to an increase in toughness at room temperature from 1-2 MPa$\sqrt{m}$ for monolithic Nb_3Al to 5-7 MPa$\sqrt{m}$ for the in-situ composites [10-13]. Microstructure control by isothermal forging and heat treatment for Nb_3Al/Nb_{ss} in-situ composites alloyed with Si produced multi-phase alloys consisting of Nb_3Al, Nb_{ss} and Nb_5Si_3, which possessed fracture toughness above 12 MPa$\sqrt{m}$ at room temperature [14].
Nb_3Al/Nb_{ss} in-situ composites have been studied with ternary additions of Ti, Ta, Mo and W to increase their high-temperature strength without lowering their fracture toughness at ambient temperatures. Mechanical properties of the constituent phases were investigated as a function of the alloying concentration. Monolithic Nb_{ss} at room temperature is strengthened by alloying with Ti, Al or Mo and not by Ta, while monolithic Nb_3Al at high temperatures is strengthened by alloying with Ta, Mo and W [8] and weakened by Ti [15]. The high-temperature strength of ternary Nb_3Al/Nb_{ss} in-situ composites was measured at 1470K and at a strain rate of $10^{-4}s^{-1}$ as a function of volume percent of the Nb_3Al phase [15]. The yield stress of Mo-containing composites was higher than that of the binary composites throughout the composition range investigated. By contrast, the yield stress of Ti-containing composites is lower than that of the binary composites throughout the composition range investigated. On the other hand, the yield stress of Ta-containing composites is higher than those of the binary composites at a high volume percent of the Nb_3Al phase and is similar to them at low volume percent. These results on the composites can be interpreted in terms of the rule of mixture of Nb_3Al and Nb_{ss}. Creep strength of Nb_3Al/Nb_{ss} in-situ composite is significantly increased by Mo addition, especially when its microstructure is controlled so as to consist of directionally elongated grains. The obtained creep strength is higher than that of other refractory intermetallic alloys such as $MoSi_2$ and $(Cr,Mo)_3Si/(Cr,Mo)_5Si_3$ alloys [15].

3. Nb_5Si_3/Nb_{ss} IN-SITU COMPOSITES

Nb_5Si_3/Nb_{ss} in-situ composites have high potential as very high-temperature structural materials, since both the phases have relatively low densities (Nb_5Si_3: 7.09 Mg/m^3, Nb: 8.57 Mg/m^3) and high melting temperatures (Nb_5Si_3: 2757K, Nb: 2742K). In addition, Nb_5Si_3 can be equilibrated with Nb_{ss} in a wide temperature range. Hot extrusion of a cast ingot consisting of primary coarse Nb_{ss} particles and fine eutectic of Nb_{ss} and Nb_5Si_3 produced the directional microstructure in which primary Nb_{ss} particles are elongated to the extrusion direction. The fracture toughness at room temperature of this composite exceeds 20 MPa$\sqrt{m}$ in the crack propagation direction perpendicular to the extrusion direction [16]. Yield stress of this binary composite is not so high at elevated temperature in spite of the high toughness value, since Nb_{ss} with a very low solubility of Si becomes very weak with increasing temperature. High-temperature strength is remarkably increased by alloying with Mo [17,18], W or Mo+W [17], as shown in Fig. 1. It should be noted that yield stress of Nb-16Si-10Mo-15W is higher than that of monolithic Nb_5Si_3. This result suggests that both Nb_5Si_3 and Nb_{ss} phases are

remarkably solid solution strengthened by Mo and W alloying.

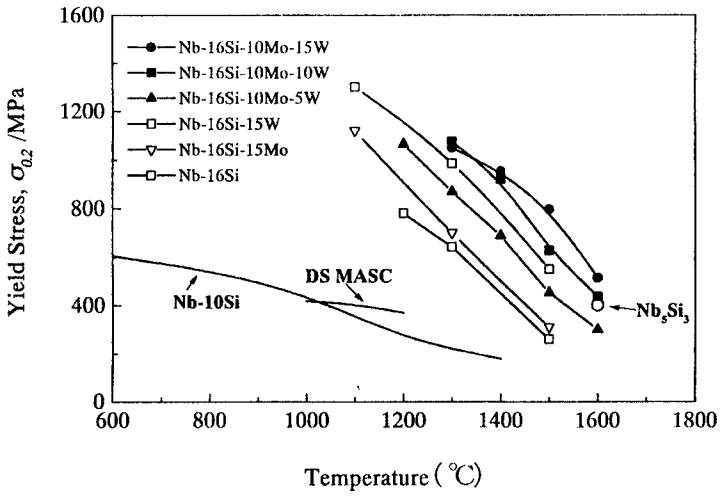

Fig. 1 Temperature dependence of compressive yield stress for Nb_5Si_3/Nb_{ss} in-situ composites as a function of alloying content.

The fracture toughness of arc-melted Nb_5Si_3/Nb_{ss} in-situ composites is increased to ~ 12 MPa $\sqrt{m}$ by controlling alloying composition, as shown in Fig. 2 [18].

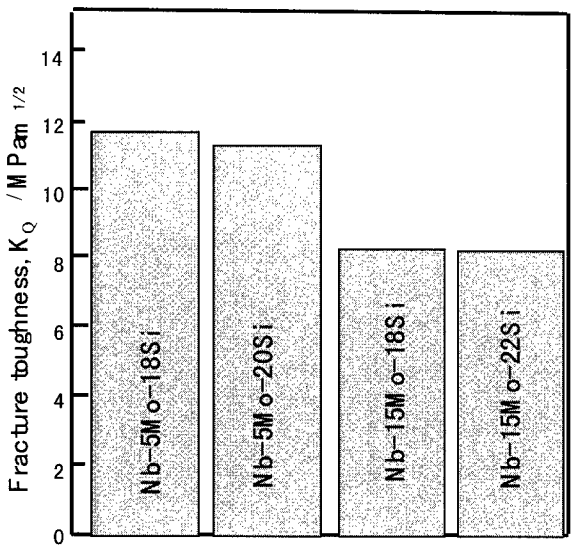

Fig. 2 Fracture toughness at room temperature for Mo-alloyed Nb_5Si_3/Nb_{ss} in-situ composites with various compositions.

4. ZrC/Mo_{ss} IN-SITU COMPOSITES

Monolithic ZrC having a high melting temperature of 3640K and a low density of 6.9

Mg/m^3 is known to possess high strength at very high temperatures. According to the phase diagram of Mo-Zr-C system [19], ZrC is in equilibrium with bcc Mo(Zr) at high temperature such as 1673 K. It is expected, therefore, that fracture toughness of ZrC/Mo in-situ composite can be increased by increasing a volume fraction of the ductile bcc phase and controlling microstructure.

Mo and ZrC powders with nominal compositions Mo-16, 30, 40 and 50mol%ZrC were blended in a cross-rotary mixer and arc-melted in an Ar atmosphere. The arc-melted buttons were homogenized at 1873 K for 70 h. Microstructure was observed with a scanning electron microscope (SEM) and a transmission electron microscope (TEM). Phase identification and chemical analysis were performed by an X-ray diffractometer (XRD) and an electron probe microanalyzer (EPMA). Rectangular compression samples with the dimension of 2 mm x 2 mm x 5 mm were prepared by electro-discharge machining (EDM) and polishing with SiC paper. Compression tests were conducted in vacuum at temperatures from room temperature to 1773K at an initial strain rate of $1.7 \times 10^{-4}\ s^{-1}$. Fracture toughness measurements were carried out by three-point bending test using the single-edge notched beam specimens. Rectangular bend specimens have the dimension of 3 mm x 6 mm x 30 mm and the span length is 24 mm. A thin notch was introduced at the center of the bend specimens by EDM using a 100 μm diameter wire. The cross head speed in bending is $8.3 \times 10^{-6}\ m \cdot s^{-1}$.

XRD and EPMA analysis indicated that homogenized ZrC/Mo in-situ composites consist of ZrC and bcc Mo solid solution (Mo_{ss}). In Mo-40ZrC dark dendritic phase corresponding to primary ZrC particles greater than 10 μm and bright phase containing very fine particles of eutectic are observed in a SEM micrograph, as shown in Fig. 3(a) [20]. A TEM micrograph of Fig. 3(b) shows that the eutectic is composed of fine ZrC particles less than 1 μm and Mo_{ss} with grain sizes of 3-5 μm. Similar microstructures were observed in Mo-30ZrC and Mo-50ZrC. Fig. 4(a) shows a SEM micrograph of Mo-16ZrC, where fine ZrC particles are distributed in Mo_{ss}, forming some colonies with sizes of several 10 μm. A very small amount of bulky ZrC particles are observed in Fig. 4(a), indicating that the composition is close to the eutectic one. A TEM micrograph of Fig. 4(b) shows that the fine ZrC particles consist of short fibers with an average diameter of about 600 nm. The fibers have neither apparent preferential growth direction nor orientation relationship.

Temperature dependence of compressive yield stresses (0.2% proof stress) for Mo-30ZrC, Mo-40ZrC and Mo-50ZrC is shown in Fig. 5 [21], where data for Mo-40TiC [22] and

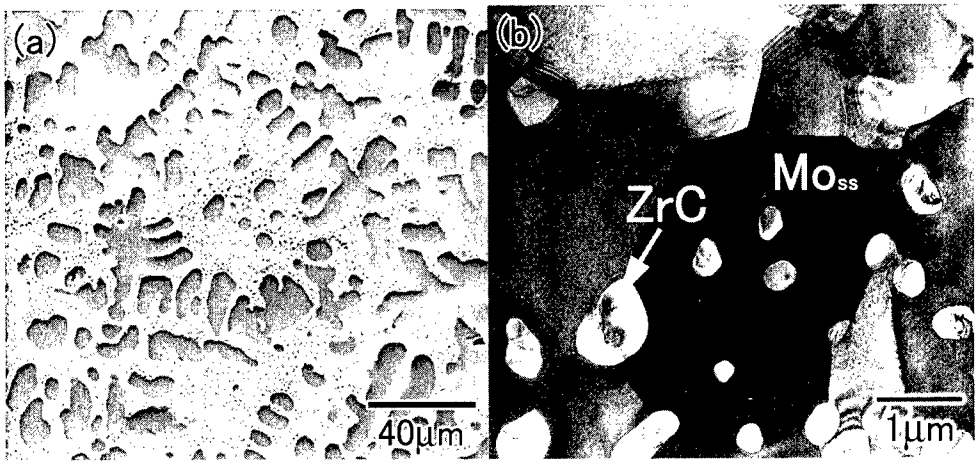

Fig. 3 (a) SEM and (b) TEM micrographs of Mo-40mol%ZrC.

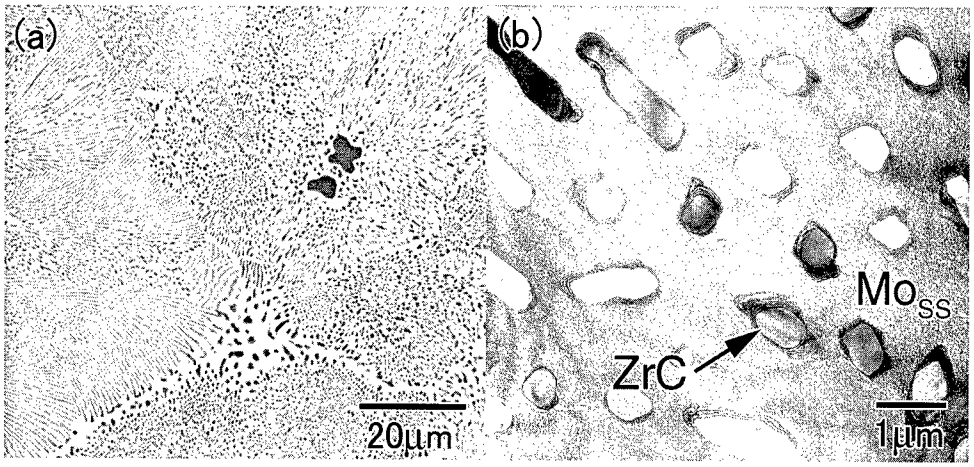

Fig. 4 (a) SEM and (b) TEM micrographs of Mo-16mol%ZrC.

monolithic ZrC [23] are also included for comparison. It is evident that yield stresses of Mo-40ZrC and Mo-50ZrC are higher than those of Mo-40TiC and monolithic ZrC above 1300 K. The different grain sizes of Mo_{ss} (3-5 μm for Mo-40ZrC and several 10 μm for Mo-40TiC), solid solution strengthening of Mo by Zr and solid solution strengthening of ZrC

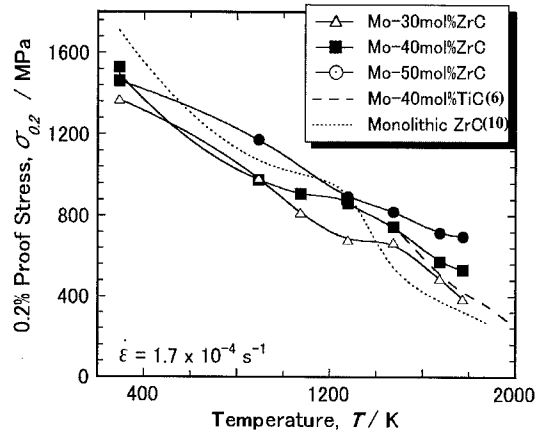

Fig. 5 Temperature dependence of 0.2% proof stress for Mo-30, 40, 50mol%ZrC. Data for Mo-40TiC and monolithic ZrC are included for comparison.

by Mo may be concerned with the high yield stress of Mo-40ZrC. Fig. 6 shows the applied stress dependence of minimum strain rate in log-log plots for Mo-40ZrC at 1673, 1773 and 1873 K, where data of Mo-40TiC are also included for comparison. Creep strength of Mo-40ZrC is higher than that of Mo-40TiC, which is consistent with the result of compression tests in Fig. 5. Clearly, a linear relationship holds between minimum strain rate and applied stress. Stress exponents given by the gradient of the log minimum creep rate vs. log applied stress plot are 4.5, 4.8 and 4.3 at 1673, 1773 and 1873 k, respectively. The apparent activation

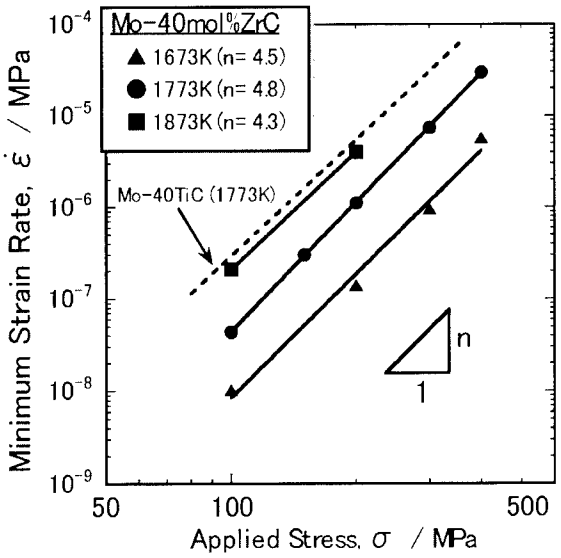

Fig. 6 Applied stress dependence of minimum strain rate for Mo-40mol%ZrC at 1673, 1773 and 1873K.

energy for creep is calculated to be 510 kJ/mol at applied stresses of 200 and 300 MPa, which is close to the activation energy for the self diffusion of Mo in pure Mo, 488 kJ/mol. Fig. 7 shows a typical TEM micrograph of Mo-40ZrC crept to 3% strain at 1673 K and 200 MPa. The micrograph is taken at a region of eutectic. Dislocation networks are formed in Mo_{ss} between fine ZrC particles. Hence, the creep deformation is controlled by recovery occurring in Mo_{ss}. Most dislocations touching ZrC particles in Fig. 7 are found to be perpendicular to the ZrC/Mo_{ss} incoherent interface, implying that attractive force is operating between the dislocations and ZrC particles. Thus, the high creep strength is attributable to this interaction of dislocations with ZrC particles.

Fracture toughness K_Q values of Mo-16ZrC, Mo-30ZrC and Mo-40ZrC at room temperature are evaluated to be 12.7, 14.7 and 13.9 MPa$\sqrt{m}$, respectively. This result means that the

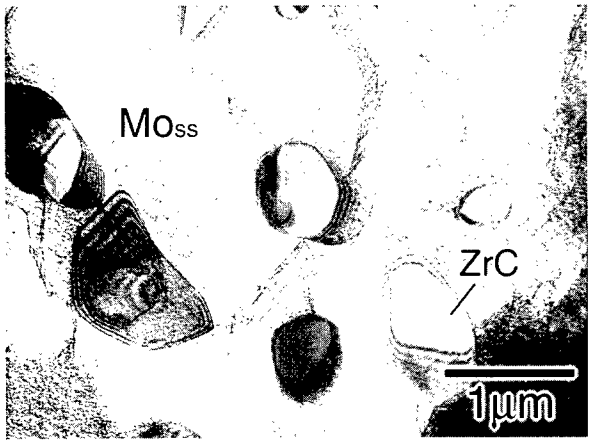

Fig. 7 A TEM micrograph of Mo-40mol%ZrC crept to 3% strain at 1673K and 200MPa.

incorporation of Mo_{ss} in ZrC increases fracture toughness significantly, as compared with monolithic ZrC (1-3 MPa$\sqrt{m}$). Fig. 8 shows a SEM micrograph indicating crack propagation on a sample surface of Mo-30ZrC bend tested. One can see that cracks propagate in a zig-zag manner partially along colony boundaries and many ligaments of Mo_{ss} are produced. Therefore, the crack deflection and ligament formation are responsible for the increase in

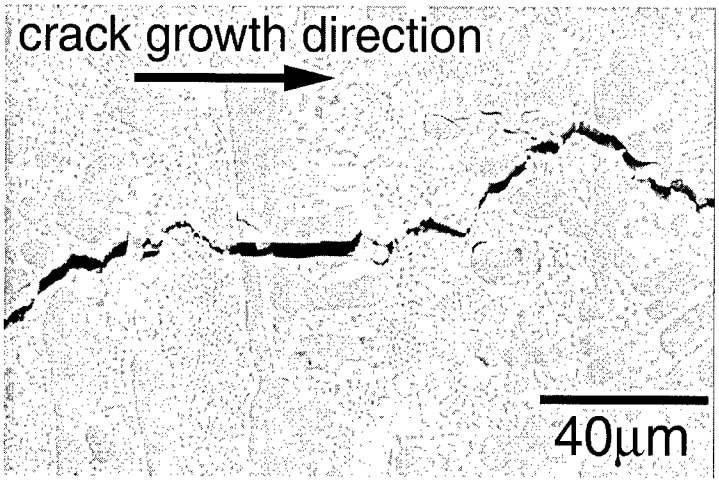

Fig. 8 SEM micrograph indicating crack propagation in Mo-30mol%ZrC after three point bending.

fracture toughness. Fig. 9(a) shows a SEM micrograph of fracture surface indicating that primary ZrC particles are fractured by transgranular cleavage. A SEM micrograph in a eutectic region at a high magnification in Fig. 9(b) shows the pull-out of ZrC particles indicating decohesion at the interface between Mo_{ss} and ZrC. This weak interfacial bonding may lead to the increased fracture toughness at room temperature in addition to crack deflection and ligament formation.

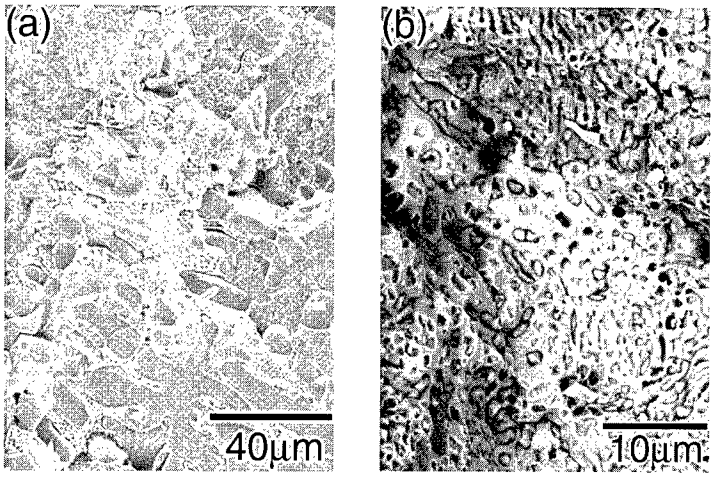

Fig. 9 SEM micrographs of fracture surface indicating (a) cleavage fracture at ZrC particles and (b) pull-out of ZrC particles at eutectic in Mo-30mol%ZrC.

5. SUMMARY

High strength at elevated temperatures above 1500K and good fracture toughness at ambient temperature are achieved in refractory intermetallic-base in-situ composites of Nb_3Al/Nb_{ss} and Nb_5Si_3/Nb_{ss} alloyed with Mo.
Arc-melted ZrC/Mo_{ss} in-situ composites with hyper-eutectic compositions (Mo-30, 40 and 50 mol%ZrC) consist of coarse primary ZrC particles and eutectic containing fine ZrC particles in Mo_{ss}, while the composite with eutectic composition (Mo-16mol%ZrC) is composed of fine ZrC particles distributed in Mo_{ss}, forming some colonies. Yield stresses above 1500K at a strain rate of $1.7 \times 10^{-4} s^{-1}$ for the hyper-eutectic composites are around 400~800 MPa, which are higher than those of monolithic ZrC. Mo-40ZrC exhibits good creep strength as compared with advanced ceramic matrix composites. Fracture toughness K_Q values at room temperature for the hyper-eutectic composites are 12~15 MPa$\sqrt{m}$, which are much higher than those for monolithic ZrC.

References

[1] R. Gnanamoorthy and S. Hanada : Mater. Sci. Eng., A207 (1996), pp. 129-134.
[2] T. Tabaru and S. Hanada : Intermetallics, 6 (1998) pp. 735-739.
[3] T. Tabaru and S. Hanada : Intermetallics, 7 (1999) pp. 807-819.
[4] M.G. Mendiratta et al. : Metall. Trans., 22A (1991), pp. 1573-1583.
[5] C.L.Ma et al. : Mater. Trans., JIM, 41 (2000), pp. 444-451.
[6] C. L. Ma et al. : Mater. Trans., JIM, 41 (2000), pp. 719-726.
[7] S. Hanada et al. : Properties of Complex Inorganic Solids 2, ed. A. Meike et al., Kluwer Academic/Plenum Publishers, 2000, pp. 393-400.
[8] Y. Murayama and S. Hanada : Scripta Metall., 37 (1997) 949-953.
[9] Y. Murayama et al. : High-Temperature Ordered Intermetallic Alloys V, ed. I. Baker et al., MRS, 1993, pp. 95-106.
[10] L. Murugesh et al. : Intermetallic Matrix Composites II, ed. D.B. Miracle et al., MRS, 1992, pp. 433-438.
[11] D.L. Davidson and D.L. Anton : High-Temperature Ordered Intermetallic Alloys V, ed. I. Baker et al., MRS, 1993, pp. 95-106.
[12] C.D. Bencher et al. : Intermetallics, 4 (1996) pp. 23-29.
[13] R. Gnanamoorthy et al. : Scripta Mater., 34 (1996) 999-1003.
[14] Y. Murayama et al. : J. Japan Inst. Metals, 63 (1999) 1519-1526.
[15] T. Tabaru and S. Hanada : Intermetallics, 6 (1998) 735-739.
[16] M.G. Mendiratta et al. : Metall. Trans., 22A (1991) 1573-1583.
[17] C.L. Ma et al. : High-Temperature Ordered Intermetallic Alloys IX, ed. J. Schneibel et al., MRS, 2000, in press.
[18] W.Y. Kim et al. : to be published.
[19] P. Villars : Handbook of Ternary Phase Diagram, vol.6, ASM, 1995, pp. 7138.
[20] T. Suzuki et al. : Mater. Trans., JIM, 41(2000) 1164-1167.
[21] T. Suzuki et al. : J. Japan Inst. Metals, 64 (2000) 1082-1088.
[22] N. Nomura, K. Yoshimi and S. Hanada: Mater. Trans., JIM, 41 (2000), pp. 1599-1604.
[23] R. Darolia and T.F. Archbold: J. Mat. Sci., 11 (1976), pp. 283-290.

Session I

TITANIUM ALLOYS

ENHANCEMENT OF MECHANICAL PROPERTIES BY ALLOYING AND PROCESSING IN TITANIUM BASE ALLOYS

Yong-Tai Lee, Seung-Eon Kim, Yong-Taek Hyun, Hi-Won Jeong

Korea Institute of Machinery and Materials
66, Sangnam, Changwon, Kyungnam, 641-010, KOREA

ABSTRACT

A new high strength titanium alloy system with low cost alloying elements, such as Al, Fe, Si, has been recently developed. Combination of Al, Fe and Si yielded a basket-weave microstructure with reduced colony size. The optimum composition range for the best mechanical properties was identified to be Ti-(4~6)Al-4Fe-(0.5~1)Si. The yield and ultimate tensile strengths of the alloys were superior to those of TIMETAL 62S as well as Ti-6Al-4V at room and elevated temperatures up to 400 °C.

A new processing technology in the directional solidification of TiAl base alloys has been recently developed as well. DS ingots consisting of fully lamellar microstructure parallel to the DS growth direction and of columnar grains rotated each other with respect to a longitudinal axis were successfully fabricated with a size of 16 mm in diameter and 50 mm in length, using a polycrystalline seed technology. Fracture toughness of the DS TiAl alloys was superior to that of single crystalline TiAl alloys in a short transverse orientation and comparable to that in a crack arrest orientation.

In the present study, fatigue crack growth behavior of Ti-6Al-2Sn-4Zr-6Mo (Ti6246) alloy were also investigated. The fatigue crack growth was not sensitive to loading waveform but to test environments.

I. INTRODUCTION

Titanium alloys have been spotlighted over 50 years for military applications, especially for fighters and submarine, because of their excellent specific strength and corrosion resistance. Since the end of cold war, their uses have been expanded toward civil applications, such as automobile, chemical and power plant, biomedical device, accessory, sports-leisure and so on. The variety in uses needs low cost as well as good properties of the alloys. For the past several years, we have concentrated on new alloy development with low cost elements and enhancement of mechanical properties by new processing. This review will discuss about our recent efforts and results for alloying and processing of titanium base alloys. In addition, an evaluation technology of fatigue crack propagation behavior in titanium alloys will be mentioned.

In alloying, a newly developed Ti-Al-Fe-Si alloy system will be described. The role of Al, Fe and Si has been known to be an alpha stabilizer, a beta stabilizer and a precipitation hardener, respectively, in conventional titanium alloys. Although a similar alloy, TIMETAL 62S, has already been developed, The combining effect of Al, Fe and Si on microstructures and mechanical properties has never been yet studied systematically in titanium alloys. We have clarified the effect of the alloying elements in binary, ternary and quaternary system respectively.

In processing, we have employed a new concept so called polycrystalline seed in directional solidification of TiAl base alloys and have made a success to enhance the mechanical properties and reduce the anisotropy of the lamellar microstructure. Mechanical properties of TiAl alloys depend upon their microstructure represented by a fully lamellar microstructure

consisting of TiAl(γ) and $Ti_3Al(\alpha_2)$ phase layers or a duplex microstructure consisting of lamellae(γ/α_2) and γ grains. Microstructure control is a key factor to improve mechanical properties of the alloys. Many studies have shown that the fully lamellar microstructure yields good fracture toughness and elevated temperature strength compared to the duplex microstructure [1-4]. However, the fully lamellar microstructure is usually accompanied by large grain size that results in poor ductility. Moreover, from the previous studies on the PST single crystals that the entire ingot consists of only a single lamellar grain, the lamellar microstructure has shown a significant anisotropy in mechanical properties [5-8]. This review will delineate how to figure it out by employing a new concept in directional solidification.

Meanwhile, in the present study, fatigue crack growth behavior of Ti-6Al-2Sn-4Zr-6Mo (Ti6246) alloy was also investigated. Ti6246 is the promising alloy for the compressor disk part of a jet engine at a high operating temperature around 500°C. Therefore, evaluation of the fatigue crack growth behavior is very important. This review will cover the effect of environment on the fatigue crack growth rates of Ti6246 for each loading waveform.

2. Alloy Development

In the previous study, the effect of the iron and silicon element on the mechanical properties of Ti-Fe-Si alloy has been investigated. The tensile strengths of the Ti-Fe-Si alloy containing 0.5-2wt% of the iron element were not higher than those of Ti-Si binary alloys which did not containing the iron element. The tensile strength of the Ti-Fe binary alloy increased with the increasing contents of the iron, but that of the Ti-xFe-ySi ternary alloy showed the minimums at the range of 0.5-1wt% Fe with the increasing contents of the silicon. Moreover, the gap between the maximum and the minimum decreased with the increasing contents of the iron. It is suggested that these minimums may attribute to competitive working. The positive working is the strengthening by the solid solution of Fe, Si, and the increase of α/β phase boundary, and the fine precipitates of the titanium silicides, and the negative working is the deteriorating by the coarse precipitates of the titanium silicides of which size are 1μm over. The fraction of the coarse titanium silicides increased with the increasing contents of the iron because the iron reduced the solubility limit of the silicon in titanium matrix. So, the tensile strengths of Ti-(0.5~2)Fe-(0.5~4)Si alloys were lower than those of Ti-(0.5~4)Si alloys because the negative working was dominant over the positive working. The optimum composition was identified to be a range of Ti-4Fe-(0.5-1)Si in Ti-Fe-Si ternary system.

Ti-4Fe-(0.5-1)Si alloy was modified by addition of Al to improve the mechanical properties. Fig. 1 shows the optical micrographs of Ti-4Fe-0.5Si-(2,4,6)Al. The fraction of α phase increased with increasing contents of Al because Al is α-stabilizer. In particular, it was remarkable that the β grain size of the alloy containing more than 4wt% Al decreased dramatically.

Fig. 2 (a) shows the tensile properties of Ti-4Fe-(0.5,1)Si-(2,4,6)Al alloys at ambient temperature. The tensile strength of the alloys increased linearly with increasing contents of Al and the elongation did not decreased. Moreover, the alloys containing 1wt% Si had the higher strength than the alloy containing 0.5wt% Si. However, the elongation of Ti-4Fe-1Si-(2,4,6)Al alloy was lower than that of Ti-4Fe-0.5Si-(2,4,6)Al alloys. The lower elongation of Ti-4Fe-1Si-(2,4,6)Al alloy was due the coarse silicide formed at grain boundary. The ultimate tensile strength of Ti-6Al-4Fe-0.5Si was higher than that of Timetal 62S (beta rolled and annealed at 700°C for 2hrs), as indicated by dotted line in Fig. 2.[9]

Fig. 2 (b) shows the tensile properties of Ti-4Fe-(0.5,1)Si-(2,4,6)Al alloys at 400°C. As the contents of Al increased, the tensile strength of Ti-4Fe-0.5Si-(2,4,6)Al alloys increased without decreasing elongation. On the contrary, the tensile strength of Ti-4Fe-1Si-(2,4,6)Al alloys increased, but the elongation decreased. Though Timetal 62S was tested at 300°C, the ultimate tensile strength of Ti-6Al-4Fe-0.5Si was higher than that of Timetal 62S, as indicated by dotted line in Fig. 2.[9]

Ti-6Al-4Fe-0.5Si alloy has more contents of Fe, and Si than those of Timetal62S. Fe

increased the fraction of β phase, solid solution, and interphase boundary, and Si increased the fine precipitates of titanium silicides. Therefore, the strengths of Ti-6Al-4Fe-0.5Si at ambient temperature and 400 °C were higher than those of Timetal62S because of the solid solution strengthening, interphase boundary strengthening, and precipitates strengthening

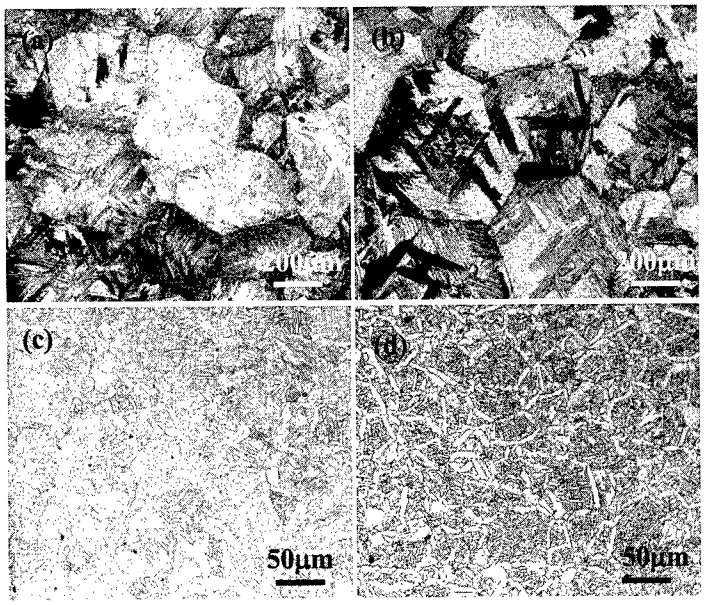

Fig. 1. Optical micrographs of as HIPed Ti-Al-Fe-Si alloys. (a) Ti-4Fe-0.5Si, (b) Ti-2Al-4Fe-0.5Si, (c) Ti-4Al-4Fe-0.5Si, (d) Ti-6Al-4Fe-0.5Si

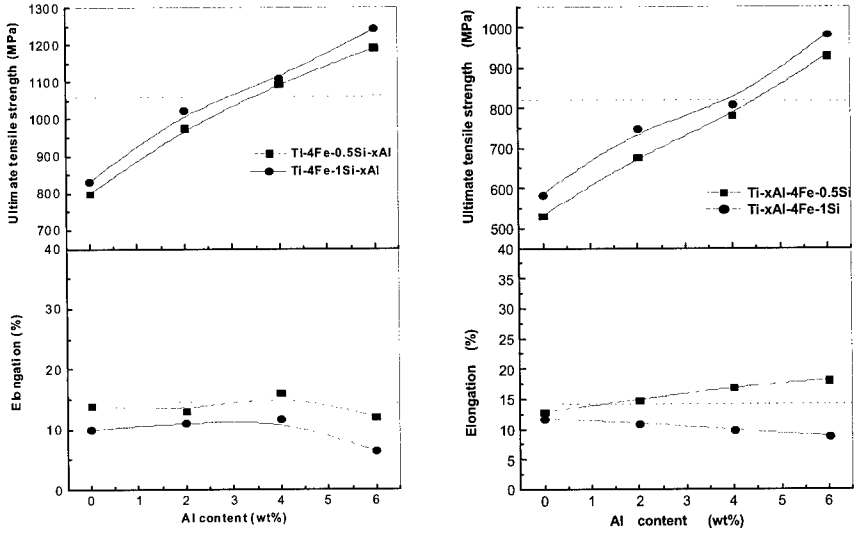

(a) (b)

Fig. 2. Ultimate tensile strength and elongation of Ti-(2,4,6)Al-4Fe-(0.5,1)Si at ambient temperature(a) and at 400 °C(b). The dotted lines correspond to those of TIMETAL 62S.

Fig. 3 shows the fractographs of Ti-6Al-4Fe-(0.5,1)Si alloys fractured at 400°C. The fractograph of Ti-6Al-4Fe-0.5Si showed a dimple fracture. However, the fractograph of Ti-6Al-4Fe-1Si showed an intergranular fracture. This result shows that the coarse titanium silicides hindered the sliding of the α/β phase boundary. Therefore, the elongation of Ti-4Fe-1Si-xAl alloys decreased with increasing contents of Al because the area of grain boundary increased by grain refinement gave the heterogeneous nucleation sites for titanium silicides.

In the present study, the optimum composition was the Ti-6Al-4Fe-0.5Si alloy which showed the higher tensile strength at ambient and high temperature without decreasing elongation.

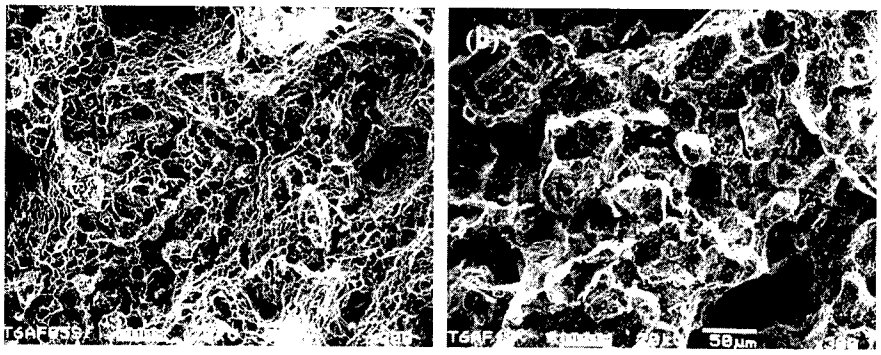

Fig. 3. Fractographs of Ti-6Al-4Fe-(0.5,1)Si alloys fractured at 400°C. (a) Ti-6Al-4Fe-0.5Si, (b) Ti-6Al-4Fe-1Si

3. Directional Solidification

Concerning the microstructure control by directional solidification(DS) process in TiAl base alloys, many efforts[10-14] have been made to obtain rotated columnar grains and aligned lamellar microstructure parallel to the growth axis of DS ingot, because such a microstructure is expected to not only enhance mechanical properties but also reduce the anisotropy of the lamellar microstructure. However, no success had been actually achieved because lamellar orientation depends on solidification path and crystallographic orientation relationship among the phases[15] . Suppose that the alloy has $\beta - \alpha - \gamma$ solidification path, final lamellar orientation in DS ingot should be aligned at 0° and/or 45° with respect to the DS growth direction owing to the $\beta - \alpha$ and $\alpha - \gamma$ orientation relationship denoted as follows; $(110)_\beta // (0001)_\alpha$, $<111>_\beta // <1120>_\alpha$ and $(0001)_\alpha // (111)_\gamma$, $<1120>_\alpha // <110>_\gamma$ [16]. If the alloy solidifies tracing $\alpha - \gamma$ solidification path, final lamellar orientation in DS ingot should be aligned at 90° only with respect to the DS growth direction owing to the unique $\alpha - \gamma$ orientation relationship.

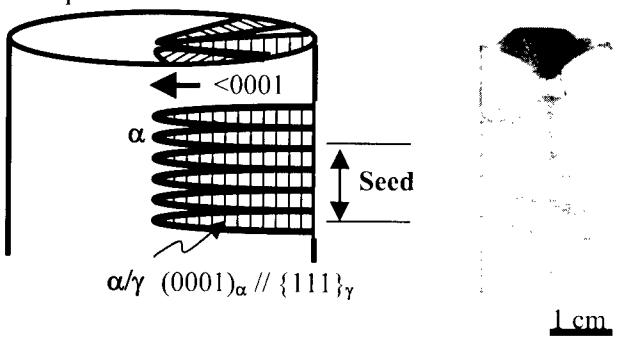

Fig. 4. Schematic illustration for the polycrystalline seed concept in a conventionally cast ingot and a macrostructure of seed ingot.

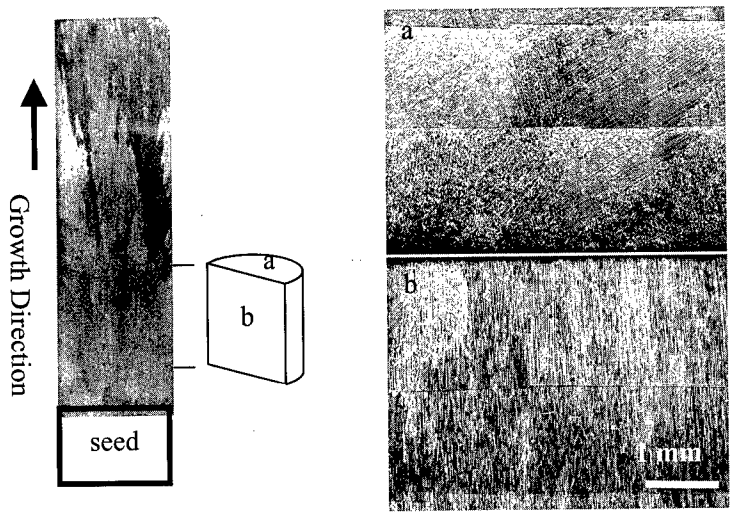

Fig. 5. Macrostructure of the directionally solidified ingot grown at a velocity of 5 mm/h, and microstructures in transverse(a) and longitudinal(b) section of the ingot.

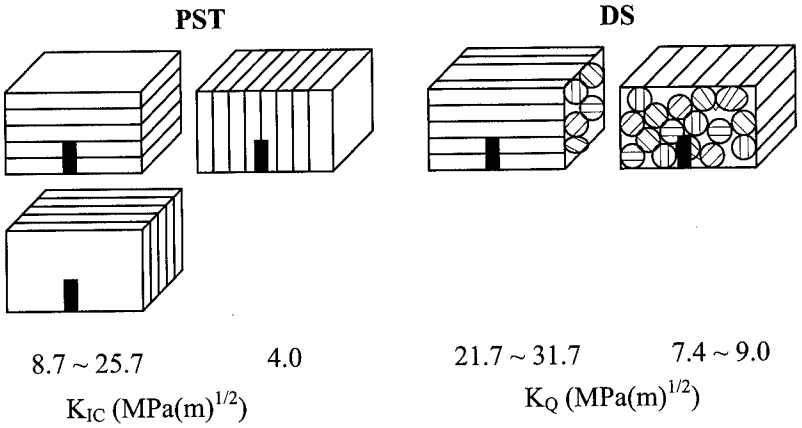

Fig. 6. schematic illustrations for comparison in fracture toughness of the PST single crystal and the DS alloys with notch geometry.

Based on the $\alpha - \gamma$ solidification path and conventionally cast ingot microstructure, the polycrystalline seed having radial columnar grains perpendicular to a seeding direction. Furthermore, fully lamellar microstructure parallel to the seeding direction were made as shown in Fig. 4. Ti-43Al-3Si was selected as a seed alloy composition for this purpose because the alloy solidifies through $\alpha - \gamma$ solidification path, moreover lamellar microstructure is very stable up to near melting temperature during reheating.

As a result of directional solidification using the polycrystalline seed, a successful DS ingot having fully lamellar microstructure parallel to the longitudinal axis as well as rotated columnar grains with respect to the longitudinal axis were obtained at a growth velocity of 5 mm/h, as shown in Fig. 5.

Fig. 6 shows schematic illustrations for comparison in fracture toughness of the PST single

crystal and the DS alloys with notch geometry. For the crack arrest/divide mode, in the PST alloys, fracture toughness varies in a wide range from 8.7 to 25.7 MPa(m)$^{1/2}$ with crystallographic orientation. On the contrary, in the present DS alloy, fracture toughness with a value of 21.7~31.7 MPa(m)$^{1/2}$ was not significantly affected by crystallographic orientation. For the short transverse mode, fracture toughness of the DS alloy was much higher than that of the PST alloys. This must be because columnar grains have a rotated orientation with each other.

4. Fatigue Crack Growth Behavior of Ti6246 alloy

The Ti-6Al-2Sn-4Zr-6Mo(in wt%, Ti6246) alloy used in this study was forged from billet to pancake geometry at 40°C above the β transus. The resulting microstructure showed a Widmanstätten structure, consisted of both aligned α plates and a basketweave structures. The fatigue crack propagation tests were carried out under load control on a servo-hydraulic test machine. The tests were conducted at 500°C in air and vacuum. Two types of loading, trapezoidal load waveform and dwell waveform, were used.

In order to understand the effect of loading cycles on fatigue crack growth in Ti6246 alloy, da/dN-ΔK plots are presented in Fig. 7 in various environmental conditions. A direct comparison can be made between dwell and trapezoidal loading from these fatigue crack growth curves. The growth rates are nearly identical in vacuum. However, the fatigue crack growth rates of Ti6246 with dwell loading were higher than those with trapezoidal loading in air, particularly in intermediate and high ΔK regimes, as shown in Fig. 7(a). The trend observed in Fig. 7 suggests that the effect of dwell loading is mainly due to the environmental effect. At 500°C, the creep-fatigue interaction is believed to be the major mechanism for the environmental effect.

The data in Fig. 7 were replotted in Fig. 8 to demonstrate the effect of environment on the fatigue crack growth rates of Ti6246 for each loading waveform. No considerable effect of environment on fatigue crack growth rates between in air and in intermediate vacuum was observed. High vacuum, however, showed substantially reduced fatigue crack growth rates. Despite the difference in absolute da/dN value at the same applied ΔK, both dwell and trapezoidal waveforms showed the same trend. The similar environmental effect between air and an intermediate vacuum has been often observed in various alloy systems[17].

Fig. 9 shows the SEM fractographs of the fatigue-fractured CC specimen, tested at 500°C in air with a trapezoidal loading waveform. In low ΔK regime (approximately 15MPa$\sqrt{m}$), as shown in Fig. 9(a), both cleavage feathers and striations were observed. In high applied ΔK

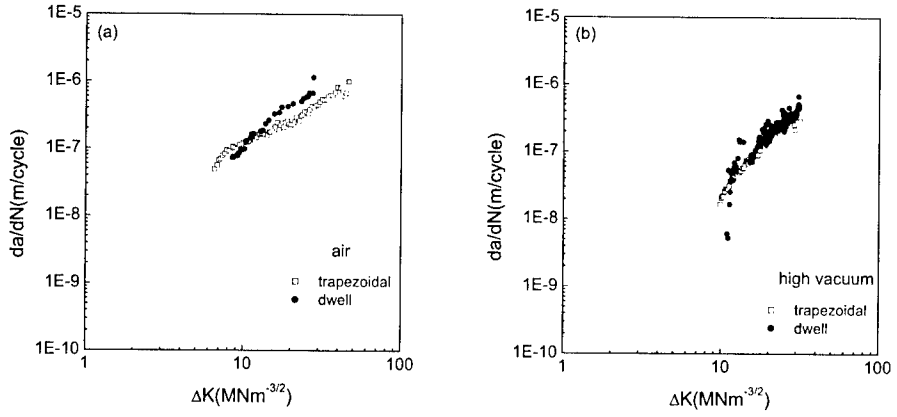

Fig. 7. Effect of waveform on fatigue crack growth behavior of Ti6246 tested at 500°C and in (a) air and (b) vacuum, respectively.

regime, on the other hand, a considerable amount of oxides were observed on the fracture surface, along with some secondary cracks. Most of these secondary cracks were appeared to follow the α/β interfaces. Some secondary cracks, which cut through the α plates, were sometimes observed.

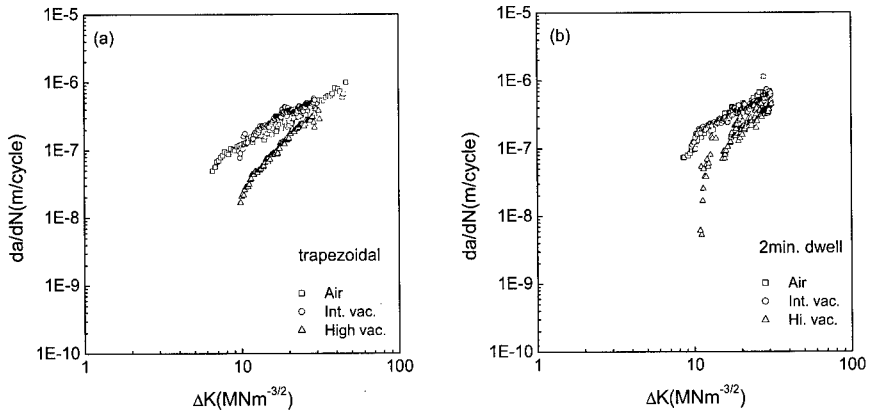

Fig. 8. Effect of environment on fatigue crack growth behavior of Ti6246 tested at 500°C and in various environments with (a) trapezoidal waveform and (b) dwell waveform, respectively

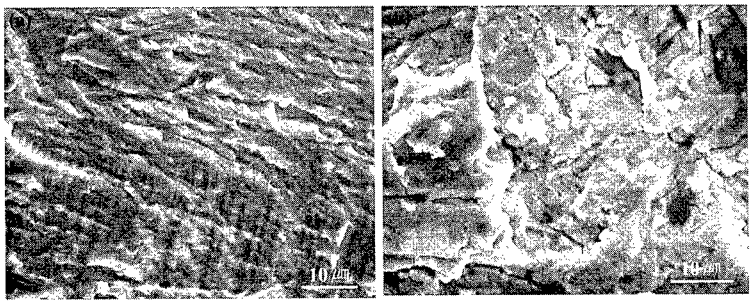

Fig. 9. SEM fractographs of Ti6246 tested in air. The pictures were taken in (a) low ΔK and (b) high ΔK regime, respectively.

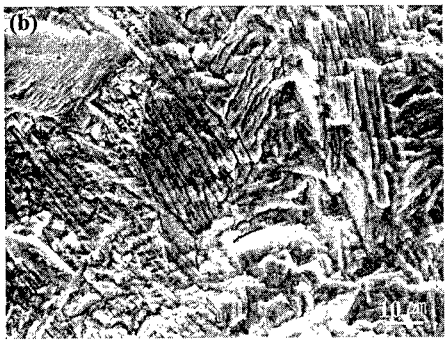

Fig. 10. SEM fractographs of Ti6246 tested in vacuum

The present study indicated that the fracture morphology of the CC specimens tested in vacuum, as shown in Fig. 10, was rather different from that in air, particularly in high ΔK

regime. The fracture occurred predominantly by crystallographic cracking, and the crack appeared to be deflected at certain microstructural discontinuities. It is considered that one of these microstructural discontinuities can be the boundary between basketweave structure and aligned α structure.

5. SUMMARY

1) A new high strength titanium alloy system with low cost alloying elements, such as Al, Fe, Si, has been recently developed. The optimum composition range for the best mechanical properties from room temperature up to 400°C was identified to be Ti-(4~6)Al-4Fe-(0.5~1)Si.

2) Directionally solidified TiAl base alloys that have not only fully lamellar microstructure parallel to the longitudinal axis, but also rotated columnar grains with respect to the longitudinal axis were successfully obtained using a polycrystalline seed. Fracture toughness of the DS alloy was superior to the single crystal PST alloy and the anisotropy was also reduced.

3) No considerable effect of environment on fatigue crack growth rates between in air and in intermediate vacuum was observed. High vacuum, however, showed substantially reduced fatigue crack growth rates. The fatigue crack growth rates of Ti6246 with dwell loading were higher than those with trapezoidal loading in air, particularly in intermediate and high ΔK regimes

REFERENCE

1.M. Yamaguchi and H. Inui in: R. Darolia, J. J. Lewandowski, C. T. Liu, P. L. Martin, D. B. Miracle and M. V. Nathal (Eds.), Structural Intermetallics, TMS, Warrendale, PA, 1993, pp.127.
2.Y-W. Kim, J. Met. 46 (1994) 30.
3.D. M. Dimiduk in: Y-W. Kim, R. Wagner and M. Yamaguchi (Eds.), Gamma Titanium Aluminides, TMS, Warrendale, PA, 1995, pp. 3.
4.C. T. Liu and P. J. Maziasz, Intermetallics 6 (1998) 653.
5.T. Fujiwara, A. Nakamura, M. Hosomi, S. R. Nishitani, Y. Shirai and M. Yamaguchi, Phil. Mag. A61 (1990) 591.
6.H. Inui, M. H. Oh, A. Nakamura and M. Yamaguchi, Acta Metall. Mater. 40 (1992) 3095.
7. H. Inui, K. Kishida, M. Misaki, M. Kobayashi, Y. Shirai and M. Yamaguchi, Phil. Mag. A72 (1995) 1609.
8. S. Yokoshima and M. Yamaguchi, Acta Metall.Mater. 44 (1996) 873.
9. R. Boyer, G. Welsch and E.W. Collins : Materials Properties Handbook, Titanium Alloys, ASM, 1994
10. D. R. Johnson, H. Inui and M. Yamaguchi, Acta Metall. Mater. 44 (1996) 2523.
11. D. R. Johnson, Y. Masuda, H. Inui and M. Yamaguchi, Acta Metall. Mater. 45 (1997) 2523.
12. D. R. Johnson, Y. Masuda, H. Inui and M. Yamaguchi, Mater. Sci. & Eng. A239-240 (1997) 577.
13. D. R. Johnson, H. Inui and M. Yamaguchi, Intermetallics 6 (1998) 647.
14. D. R. Johnson, Y. Masuda, Y. Shimada, H. Inui and M. Yamaguchi in: M. V. Nathal, R. Darolia, C. T. Liu, P. L. Martin, D. B. Miracle, R. Wagner and M. Yamaguchi (Eds.), Structural Intermetallics, TMS, Warrendale, PA, 1997, pp.287.
15. M. C. Kim, M. H. Oh, J. H. Lee, H. Inui, M. Yamaguchi and D. M. Wee, Mater. Sci. & Eng. A239-240 (1997) 570.
16. M. J. Blackburn in: R. I. Jaffee and N. E. Promisel (Eds.), The Science, Technology and Application of Titanium, Pergamon Press, Oxford, 1970, pp. 633.

Thermomechanical Control Processes of Titanium Alloys

Hirowo G.Suzuki

National Research Institute for Metals
1-2-1 Sengen, Tsukuba, 305-0047, Japan

ABSTRACT

Microstructural control is one of the most important parameter to achieve high quality product of titanium alloys. In this report, several kinds of processing variables are summarized based on our work. In the beginning, the processing for Ti-6Al-4V is described and one of the application for the pressure vessel of deep sea of 10Km is presented. Beta-quenching together with repeated α- β and β thermomechanical processing to the VAR ingot was necessary to get homogeneous α - β duplex microstructure, resulted in the high strength and high toughness products. Ti-6Al-6V-2Sn alloy shows very high hardenability and thus easy to obtain equiaxed α - β duplex microstructure by repeated hot working in the α - β region. One of the drawback of this alloy is that the alloying elements of both Fe and Cu segregate during VAR casting and top part of the ingot(finally solidifying area) shows almost two times higher content than the average. In order to diminish this segregation, we introduced diffusion treatment at high temperature, which consists of hot working at α - β region and up-quenching to 1523K and keeping for 48h to accelerate the downhill diffusion of Fe and Cu elements. The strengthening of β alloy, Ti-15V-3Cr-3Sn-3Al is controlled by the precipitation of α particles. Our finding is that homogeneous precipitation of α on the quenching-in-vacancy is accelerated by the fairly higher temperature solution treatment such as 1573K and aging. Finally the most economical and efficient production process,i.e., strip casting and hot direct rolling process is discussed. This process will become the main production process in the 21 century.

1. INTRODUCTION

Thermomechanical control process (TMCP) has been initiated in the steel industries in England and Japan in 1960's and 1970's[1]-[4]. The main purpose is to strengthen and toughen the steel products through the grain refinement, control of γ–α decomposites as well

as precipitation such as carbonitrides. Intentional control of the hot rolling schedule(temperature and reduction rate) and thermal history (cooling rate and holding time or heating rate) changes the transformation kinetics, recrystallization behavior and precipitation characteristics. Steel industries have managed TMCP quite successfully because the factories equipped with high power rolling mill and computer control system.

Nowadays this idea is commonly applied to other metallic materials as far as possible. Titanium alloys also belong to this category. Concerning with the microstructural control of titanium alloys, there are many excellent papers[5]-[8]. Very recent review on this matter is found in the special issue of thermomechanical processing and metallurgy of titanium alloy[9].

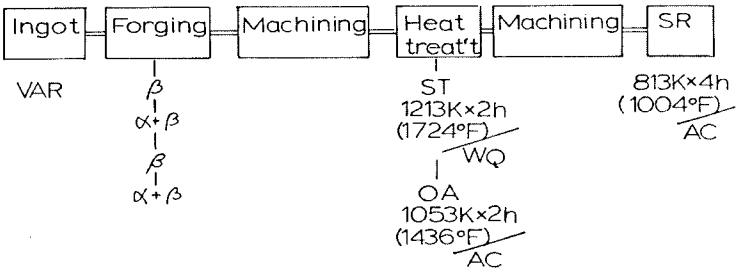

Fig.1 Manufacturing process of the pressure proof vessel made of forged Ti-6Al-4V alloy

In this paper, several applications of TMCP to get high quality of alloy products have been described based on our research.

2. DEVELOPMENT OF PRESSURE PROOF VESSEL FOR DEEP SEA BY Ti-6Al-4 V (α–β ALLOY)[10]

Because of high strength with low density and strong resistance to sea water, titanium alloys have potent applicability to ocean development. The pressure proof vessel for Japanese submarine using for scientific research, "Shinkai 6500" was made by Ti-6Al-4V ELI, which was α–β processed plate by hot rolling, hot stage creep forming to semisphere and EB welding[11].

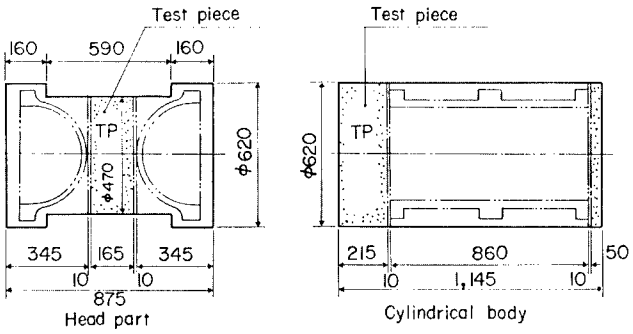

Fig.2 Forged product and size of test piece (unit : mm)

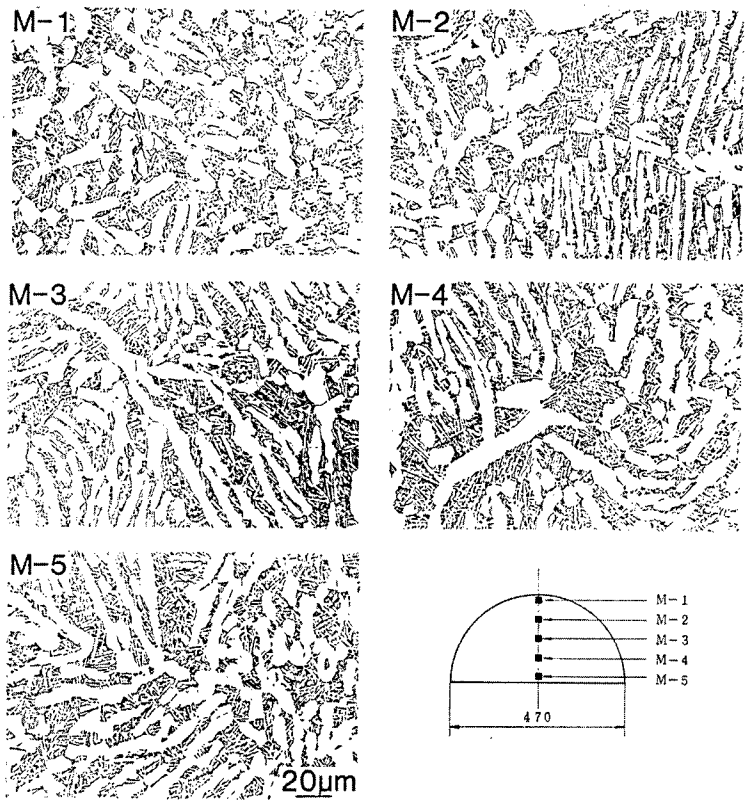

Fig.3 Microstructures of the as forged head part (positions are schematically shown)

In this time, the development of the pressure proof vessel for non-man operating submarine exploration of 10km deep sea level is aimed. It necessitates to have high strength to resist the pressure of 10km deep sea, severe corrosion resistivity and also light weight to make the vehicle mobile easily. Thus, conventional Ti-6Al-4V was selected as a starting material and only the process of the hot forging and heat treatment was applied to refine the microstructure with no preferential crystal texture.

Double melted VAR ingot was sliced into two pieces (0.6mϕ-0.8mL,-1.2mL) and each of them was forged into the head and body parts with almost the same forging operation. Manufacturing procedure is shown in Fig.1. The product size and the position of test pieces taken are shown in Fig.2. Forging was operated to produce fine equiaxed α - β microstructure through the product by keeping the diameter almost the same with that of the original ingot. Therefore, more than 15 times of heating and forging were repeated. Initial heating temperature was 1423K and decreased gradually to insure the recrystallization to get fine grain and ended up with the heating temperature of 1203K and forged about 70% in the α - β region. After rough machining, solution treatment and overaging (ST-OA) was applied to attain the aimed mechanical properties. Final heat treatment of stress relieving (SR) was done

after finish machining. Fig.3 shows the microstructure of the as forged cross section of the head product. It consists of the α and transformed β structure. Hydrostatic pressure test at designed value was done and succeeded in fracturing within 1% of the designed value.

3. TMCP TO DIMINISH THE β-FLECKS IN Ti-6Al-6V-2Sn(α–β ALLOY) [12]

Ti-6Al-6V-2Sn alloy shows very high hardenability and thus easy to obtain equiaxed α - β duplex microstructure by repeating hot working in the α - β region. One of the drawback of this alloy is that the alloying elements of both Fe and Cu segregate during VAR casting and top part of the ingot (finally solidifying area) shows almost two times higher content than the average. Segregation can be reduced during VAR process by either (1) providing an artificial concentration gradient to the consumable electrode[13], or controlling the melting to create a shallow pool in the final stage of VAR[14]. However, fairly large zones enriched with Fe and Cu may be found at the top position in large diameter ingots. Both Fe and Cu are β stabilizers leading to enriched zone of β-flecks[15]. It is necessary to cut off one third or one half of the ingot as scrap. This paper describes a new technique to reduce zones of Fe and Cu related β- flecks by applying TMCP process.

Fig.4 β-fleck band in the mid-thickness of T-662 plate

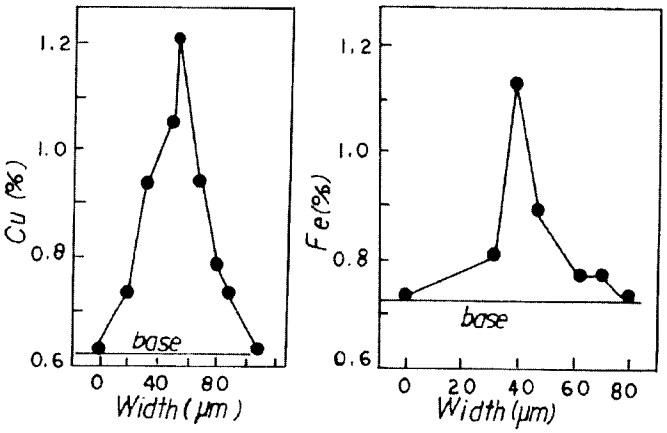

Fig. 5 Results of EPMA showing Cu and Fe segregation in the β-fleck in Ti-662 plate

VAR double melted ingot of Ti-6Al-6V-2Sn(Ti-5.4%Al-5.5%V-2%Sn-0.63%Cu-0.73%Fe-0.18%O) was used in this study. In the conventional manufacturing process, α–β processing was repeated to obtain an equiaxed fine α in the matrix of transformed β structure after the ingot was forged in the β region to break down the cast structure. The β transus of this heat was 1203K for a region free from β-lecks.The microstructure at the positions of mid-thickness in the top surface in the α–β processed plate is shown in Fig.4. Equiaxed α–β microstructure was obtained in the slab surface region, while fine lamellar structure was appeared in the mid-thickness position, indicating the lowering of β transus due to the enrichment of β stabilizing elements. The EPMA analysis of this region is shown in Fig.5, which showed segregation of both Fe and Cu to levels as high as 1.2mass% in the β-fleck region.

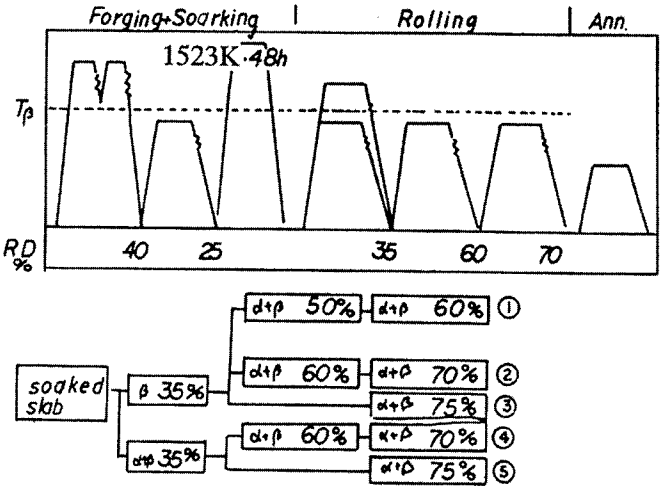

Fig.6 Newly developed thermomechanical treatment for Ti-662 plate.

In the newly developed process, slabs were put into a high temperature soaking furnace and then hot rolled under the various conditions after α–β forging as shown in Fig.6. It was found that the homogeneization treatment at higher temperature, i.e.1503K-48h, after β and α–β forging was more effective to get a segregation-free slab. The slabs were sealed in a pure titanium (CP Ti) box with a wall thickness greater than 10mm to prevent oxidation. The distribution of Fe and Cu is quite homogeneous

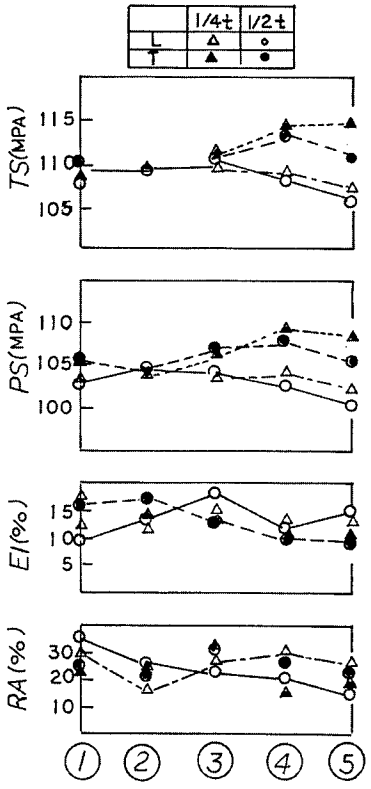

Fig.7 Tensile properties for the 50mm thick plate subjected to various thermomechanical processings shown in Fig.6

and sharp segregation of these elements disappeared through the thickness direction by this process. Tensile properties at room temperature are shown for the various thermomechanical processings in Fig.7. These data were taken after annealing at 1013K-40min. The best combination of strength and ductility was obtained after the process ②, i.e., after high temperature soaking, β cogging and two times of α–β rolling.

4. HIGH TEMPERATURE SOLUTIONING OF Ti-15V-3Cr-3Sn-3Al(β ALLOY)[16]

One of the most popular β type titanium alloy, Ti-15V-3Cr-3Sn-3Al, shows an excellent cold workability and cold formability. High strength is attained by the solutioning just above

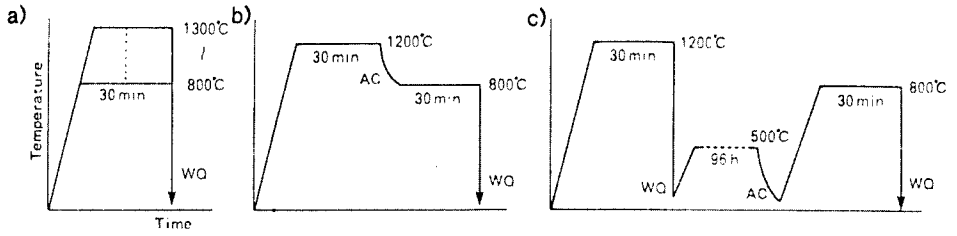

Fig.8 Patterns of the solution treatment used in the experiment. (a) 1-step solution treatment (800 ~ 1300°C, 30 min, water quenching), (b) 2-step solution treatment (1200°C, 30 min, air cooling to 800°C + 800°C, 30 min, water quenching), (c) 3-step solution treatment (1200°C, 30 min, water quenching + 500°C, 96 h, air cooling + 800°C, 30 min, water quenching).

the β transus, rapid cooling to retain the metastable β phase at room temperature, and subsequent aging in the α–β region, where α phase precipitates in the β matrix. There are many reports to discuss the precipitation behavior of α phase by aging[17]-[18]. However very limited studies on the effect of solutioning temperature have been reported[19].

The alloy used was Ti-15%V-3.03%Cr-3.09%Sn-3.3%Al-0.06%Fe-0.08%O, which was double melted by VAR and β transus was 1013K. Hot rolled plate of 10mm in thickness was sliced into small pieces of 100mmx70mm and they were solution treated with the various heat patterns as shown in Fig.8. The effect of solutioning temperature on the age hardening behaviors is shown in Fig.9. It is clearly shown that higher temperature of solutioning accelerates age hardening. The difference between one-step and two-step solutionings is due to the density of quenching-in vacancies. Solutioning at 1473K produces high density of quenching-in vacancies during quenching, which act as a nucleation site for the homogeneous precipitation of α phase. The denuded zone became quite visible in the specimen of two-step solutioning, where vacancies are annihilated at grain boundary during holding at 1073K. Thus, homogeneous precipitation becomes difficult in the vicinity of grain boundary and denuded zone is formed. One of the application of this process is surface hardening by lazer irradiation[20].

5.FUTURE PROCESS[21]

For the drastic reduction of production cost keeping with high quality of titanium alloys, it is necessary to develop a new manufacturing process such as continuous casting and hot direct rolling(CC-DR process). It has been studied the mechanical properties of steels at elevated temperature. Based on this result, crack-free sound steel products have been produced by continuous casting and hot direct rolling. By the analogical studies of titanium alloys, the possibility of the production by continuous casting is presented.

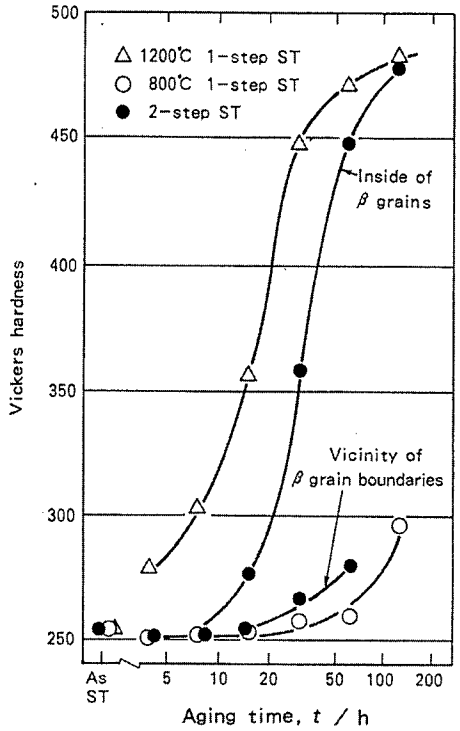

Fig.9 Age hardening behavior at 300°C in the 2-step solution treated specimens. Hardness measurements are conducted for the inside of the β grains and the vicinity of the β grain boundaries separately. In the figure, the age hardening behavior in the 1-step solution treated specimens at 800 and 1200°C is also plotted for reference.

Acknowledgements:

Author would like to express my sincere thanks to NIPPON STEEL CORP., and his peoples including senior researcher, Dr.H.Fujii and managing director, Mr.K.Kako of their supports and corperation. Thanks are extended to Prof.D.Eylon, Director of Materilas Sci. Dept. of Univ. of Dayton, USA. For his important comment and advice.

REFERENCES

1. J.J.Jonas, C.M.Sellars and McG.Tegart,Met.Rev.,14(1969),pp1
2. H.J.McQueen and J.J.Jonas, in Deformation of Materials,ed.R.J.Arsenault(1975), Academic Press, pp393
3. I.Kozasu, I.Shimizu and H.Kubota, Trans.ISIJ.,11(1971),pp1367
4. H.Sekine and T.Maruyama, Seitetu-Kenkyu,289(1976),pp43
5. J.Albrecht and G.Lutjering, in Titan'99, Science and Technology,Rrussia(1999), pp363-374, pp390-397
6. D.Eylon and S.R.Seagle, ibid, pp37-47
7. G.Lutjering, in Titan'98, Xi'an Inter.Titanium Conf, ed L.Zhou and D.Eylon (1998),pp1-20

8. I.Weiss and S.L.Semiatin, ibid, pp206-232
9. D.Eylon et al, Thermomechanical Processing and Metallurgy of Titanium Alloys, Special issue of Materials Sci.& Eng.,A243(1998)
10. H.G.Suzuki, H.Fujii, N.Yamada, M.Yamamoto and M.Kobayashi:The development of high pressure vessel for 10km submarine exploration, 6th World Conf. On Titanium, 1988,p477-482
11. Technical Report of Mitsubishi Heavy Industry 23(1986,7), No.4
12.H.G.Suzuki, S.Ishikawa, N.Noda, K.Kaku, Y.Kako and N.Yamada, in Titanium '92, Science and Technology,TMS,1993,pp489-495
13. H.B.Bomberger and F.H.Froes, in Titanium Technology, ed F.H.Froes, D.eylon and H.B.Bomberger(1985),pp25
14.H.Hayakawa, N.Fukuda, T.Udagawa, M.koizumi, H.G.Suzuki and T.Fukuyama, ISIJ International,31(1991),pp775
15. A.Mitchell, Materials Sci & Eng.,A243(1998),pp257-262
16.H.Fujii and H.G.Suzuki, Materials Transactions, JIM.,34(1993),373-381
17.P.Bania, G.A.Lenning and J.A.Hall, in Beta Titan Alloys in the 1980's, ed R.R.Boyer, H.W.Rosenberg, AIME,NY(1984),pp209
18.M.Okada, Tetsu-to-Hagane,76(1990),pp614
19.Chen Hai-Shan, in Titan '80, Science and Technology, H.Kimura, AIME., NY(1980),pp1591
20.H.Fujii, I.Takayama and H.G.Suzuki, Proc.1st Japan SAMPE, Japan(1989),pp93-98
21. H.G.Suzuki and D.Eylon: Hot ductility of titanium alloy: a challenge for continuous casting process, Materials Sci & Eng., A243(1998), pp126-133

HIGH STRENGTH MICROSTRUCTURAL FORMS IN BETA ALLOYS INTENDED FOR AUTOMOTIVE APPLICATION

Orest M. Ivasishin* and Stephen Fox**

* Institute for Metal Physics, 36 Vernadsky str., Kyiv 03142, Ukraine
** TIMET Henderson laboratory, Henderson, Nevada, USA

ABSTRACT

Due to higher than in alpha-beta alloys amounts of beta-stabilizing elements beta titanium alloys are capable of being heat treated to very high strength through solid solutioning followed by aging. High strength levels are particularly attractive for an efficient application of beta alloys in the automotive industry as materials for springs since weight and space advantages achieved with using titanium springs are directly related to the strength. Metallurgical problem remains however, in that the high strength material should be ductile enough to provide fabricability and to assure a resistance against a brittle fracture during service life. This requirement is strongly complicated by non-monotonic grain-size dependence of ductility exhibited by beta alloys, which predicts a nearly brittle behaviour if the beta-grain size exceeds some critical value depending, in turn, on the strength level desired.
In this work a combination of cold or warm work and rapid annealing has been used to generate in beta alloy TIMETAL ®LCB optimized microstructural forms hardened in excess of 1500 MPa whilst maintaining a range of grain sizes small enough to keep a reasonable ductility giving rise to their wider applications in suspension components.

1. INTRODUCTION

Titanium alloys offer significant design advantages over conventional materials for many automotive applications which, however, with a few exceptions, has not yet been acceptable in the general marketplace because of high cost of titanium. The cost penalty is being diminished by developing a concept of low cost titanium alloys [1]. In particular, low cost metastable beta alloy TIMETAL®- LCB (nominal composition Ti–6.8Mo-4.5Fe-1.5Al-$0.15O_2$) has been developed recently which formulation cost is reduced essentially to parity with commercially pure titanium by using a relatively cheap steel-making master alloy. On the other hand, the higher the performance benefits of the titanium alloys than the more attractive they are for other than aerospace industries and the wider their application is likely to be. One of the excellent examples of maximized benefits is related to application of beta-titanium alloys in automotive suspension components. Their unique combination of high strength, low elastic modulus, and low density results in springs designed to be both lighter and smaller than springs conventionally made of steels [2]. This is an area where titanium alloys are currently undergoing testing for application in series cars. Both weight and space efficiency of titanium springs are proportional to squared torsional stress allowed. Thus, there is significant benefit in developing manufacturing and heat treatment approaches that

maximize the strength that can be realized in the component. If the density and dispersion of precipitates is high enough, strengths in excess of 1500 MPa can be achieved in beta alloys, but such a condition has very limited application because ductility in this case generally is very low. A reasonable ductility of high strength beta alloys can be expected only if the beta grain size falls below some critical value, typically well below 100 μm [3]. Therefore, refinement of grain size is a key point in improving the strength/ductility balance in beta alloys. Small β grain size can be provided in so-called bi-modal microstructures conventionally processed by sub-transus deformation and heat treatment. Drawback of bi-modal microstructures consists in that they are highly textured and laminated and, therefore, their fracture under torsional stresses is often fibrous [4]. To avoid this, equiaxed microstructures achieved by finish rolling or solution treatment above the transus would be appreciated if they met the above requirement for the small beta grain size. At present, fully beta transformed fine-grained microstructure can be achieved only with a rapid heat-treating (RHT), key point in which is a rapid heating (RH) of equiaxed α +β microstructures above beta transus, high enough to fully dissolve primary alpha phase while preventing single-phase beta grains from essential growing. The present paper is aimed to review the attempts to apply the RHT to TIMETAL®-LCB and characterize its microstructure and some of the mechanical properties which could be attractive for application in automotive suspension elements.

2. MATERIALS AND EXPERIMENTAL PROCEDURE

Two batches of commercial TIMETAL®-LCB produced by TIMET Corp., USA were studied. The first was received as a 45 mm thick plate that was then rolled down to 9 mm below beta transus temperature at 750°C, followed by annealing at 730°C, 2h. Such processing resulted in a formation of fine equiaxed (α+β) microstructure (Fig. 1, a). The second was received as wires 14.6 (coil #1) and 8.6 mm (coil #2) in diameter that had been processed via full-scale trial production routes in the α +β and β fields respectively (Fig. 1, b and c). Blanks 8×8 mm in cross-section and 100 mm long were cut from plate material in the rolling direction. These as well as wire blanks 100 mm long of coil materials were rapidly heated above beta transus with direct electric resistance technique (50 Hz). Primary information for processing fine-

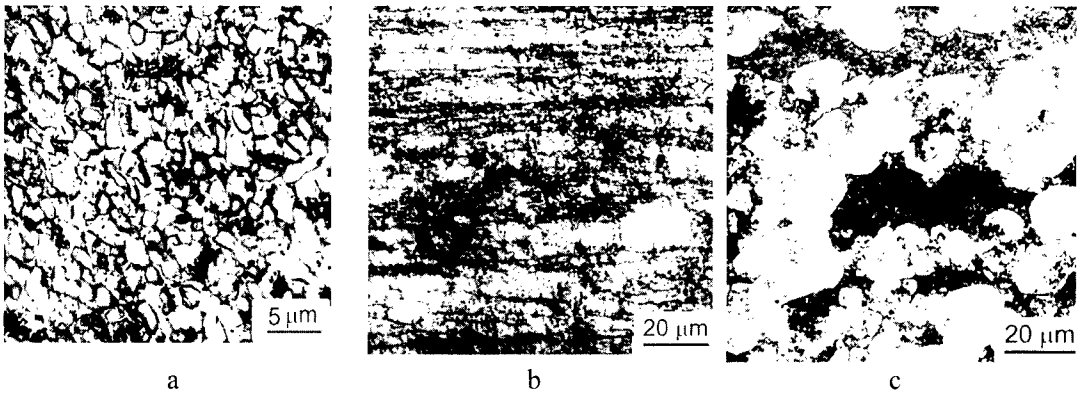

a b c

Fig. 1. Initial microstructures of (a) plate, (b) coil#1, and (c) coil#2 TIMETAL®-LCB materials.

grained beta microstructures was gained from a heating rate dependency of beta transus (Fig.

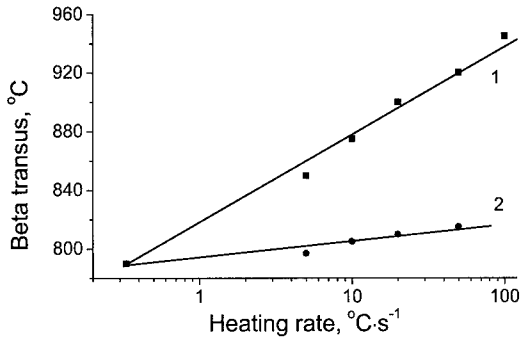

Fig. 2. Beta transus as a function of a heating rate for (1) plate and (2) coil#1 materials.

2). The beta transus of plate and coil #1 materials shifted up linearly with logarithm of heating rate. The effect that has its origin in a diffusion controlled migration of α/β boundary during the $\alpha+\beta\rightarrow\beta$ transformation [5] was much less pronounced for coil #1 material in which α grains of phase was found to be fewer and finer. No heating rate dependence of beta transus was measured for coil #2 material since this was single-phase beta, and no α precipitation occurred during RH. Preliminary experiments showed that the same beta-grain size could be achieved with various combinations of heating rate and temperature. Having in mind a possible industrial application of RHT, heating rate of 20 Ks^{-1} was chosen as the most reasonable, the peak temperature being determined for each particular material. Following the RH all blanks were cooled to obtain 100% metastable β phase. It was found by X-ray diffraction that in given cross-sections, both water quenching (WQ) and air cooling (AC) were efficient in preventing the β phase from decomposition upon cooling. However, since precipitation kinetics at subsequent aging is known to be strongly affected by vacancy density, which, in turn, depends on cooling rate, both WQ and AC cooling procedures were tried. Aging was performed at various temperatures in 500-600^{0}C range to achieve a different level of strength. To avoid microstructural inconsistency due to an interrelation between precipitation of ω and α phases, a fixed heating rate of 15 $Kmin^{-1}$ to aging temperature was used. To have a reference condition for comparison with RHT, the materials were also heat treated using the recommended [4] conventional $\alpha+\beta$ STA heat treatment of 760°C, 0.5h/WQ/538^{0}C, 8h. Tensile tests were performed at room temperatures. To compare the uniformity of properties through the cross-section of coil#1 material, tensile specimens were machined either from core or rim of heat-treated blanks. Only core tensile specimens were prepared from coil #2 material. After some heat treatments, fatigue tests were also performed. The microstructures were examined by light and transmission electron microscopy. X-ray diffraction was used to determine phase compositions.

3. EXPERIMENTAL RESULTS AND DISCUSSIONS

3.1 Plate material.

Reference $\alpha+\beta$ STA treatment of plate material led to a formation of a bi-modal type microstructure in which primary α phase was distributed in a precipitation hardened β phase (Fig. 3). Small equiaxed beta grains sometimes were pinned by a primary α phase. Although mostly an equiaxed morphology of primary α phase was evident, a strong crystallographic texture was observed.

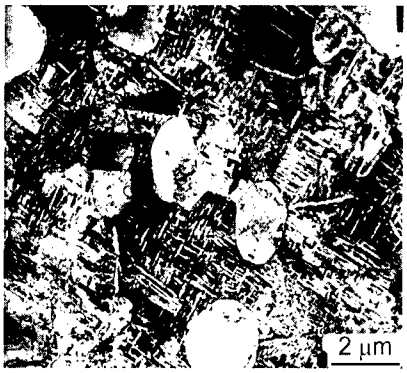

Fig. 3. Microstructure of plate material after reference α+β STA treatment. TEM.

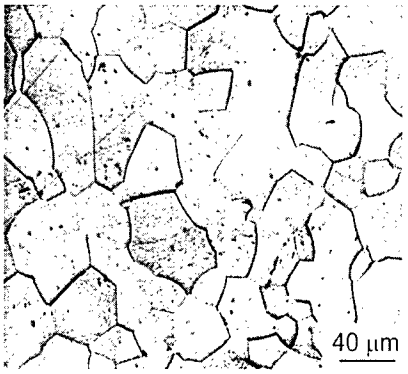

Fig. 4. Microstructure of plate material after solute solution treatment by rapid heating to 930 °C. LM.

Rather uniform 100% β microstructure with average grain size of about 50 μm formed by RH with rate of 20 Ks^{-1} to 930°C (Fig. 4). Overheating 30 K above beta transus was necessary to eliminate remnants of the largest primary α grains. At subsequent aging, precipitation occurred in β phase. Increase in aging temperature and/or aging time led to coarsening of α-lamellae and in formation of continuous layer of grain-boundary α phase [6].

Mechanical properties of the plate material after some selected treatments are presented in Table 1. Initial microstructure has an attractive combination of strength and ductility due to high rolling reduction and a relatively low annealing temperature resulted in that part of work hardening remained in the material. After reference treatment, strength remarkably increased whilst ductility remained very reasonable. WQ was advantageous in strength and in ductility as compared to AC, presumably due to a higher density of vacancies affecting the precipitation behavior in the metastable β phase.

After isothermal β STA treatment (not shown in Table 1), the material was totally brittle and fractured generally at stresses below yield stress level at all aging temperatures in 538 to 600°C range. This was not unexpected with a grain size of about 300 μm. After RHT, material received a reasonable amount of ductility confirming the noted viewpoint that the strength/ductility balance of beta alloys with fully β transformed microstructure is strongly grain-size dependent. With a fixed beta-grain size of about 50 μm, temperature and time of aging were the major parameters changing a fracture mode from nearly brittle to well ductile. Aged at 538°C, 8h condition (not shown in Table 1) that was generally stronger compared to reference treatment, above 1400 MPa level, but insufficiently ductile. The former was due to 100% precipitation hardened microstructure. However, high internal stresses arising from a precipitation of fine α phase resulted in a premature fracture along the grain boundaries even if grains were as small as 50 μm. Increasing of ageing temperature to 580-600°C led to a significantly better ductility. At equal aging times, precipitates after 580°C aging were finer resulting in a higher strength, as compared to 600°C aging. Optimal duration of aging at 580 and 600°C felt between 2 and 4 hours since longer times were decreasing the strength level while not contributing to the increase in ductility.

Table 1. Mechanical Properties of ***TIMETAL®* LCB** plate.

##	Treatment	$\sigma_{0.2}$, MPa	UTS, MPa	A_5, %	RA, %	10^7 HCF strength, MPa
1	Annealed (equiaxed)	1061	1112	11.3	36	600
2	760 °C, 2h/AC/538 °C, 8h	1240	1300	6.2	20	NM
3	760°C, 2h/WQ/538°C,8h	1303	1333	7.2	14	NM
4	RHT/WQ/580°C,8h	1250	1260	5.6	13	NM
5	RHT/AC/580°C,8h	1323	1340	6.6	20	NM
6	RHT/WQ/600°C,2h	1330	1350	9.2	29	820
7	RHT/WQ/600°C,4h	1248	1268	10.5	31	NM
8	RHT/WQ/600°C,8h	1210	1220	12.7	22	NM
9	RHT/AC/600°C,8h	1200	1250	11.9	30	740

Generally, the above results showed that at selected aging parameters the strength/ductility balance achieved with RHT used was equivalent to or better than that achieved with reference α+β STA treatment. However, the absence of primary α and its associated texture may lead to properties that are more isotropic. On the other hand, if a goal for a given application is more appealing and requires an yield stress in excess of 1400 MPa that could be achieved with lower aging temperatures, a microstructure with even finer than 50 μm beta grains is necessary. However, it would require a special improvement in a preliminary thermomechanical processing of the material to gain a finer dispersion and uniformity of starting α+β microstructure.

High cycle fatigue strength of the plate material in various conditions related well to the tensile strength (see Table 1) with ratio value being of about 0.6 that is typical for beta alloys.

3.2 Coil #1 material.

As-received microstructure of coil #1 material was of a laminated type (see Figure 1, b), in which very fine equiaxed α phase 1-2 μm in size was unevenly distributed in highly elongated grains of β matrix. Bands were narrower and better defined in close to surface areas indicating of more severe deformation here. The variability in microstructure was reflected in the tensile properties achieved by reference heat treatment for the surface and core (Table 2).

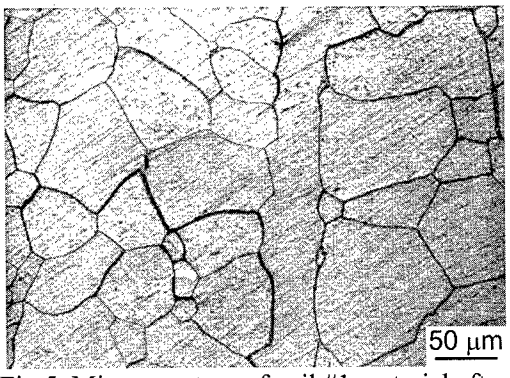

Fig.5. Microstructure of coil #1 material after solid solution treatment by rapid heating to 930°C. LM.

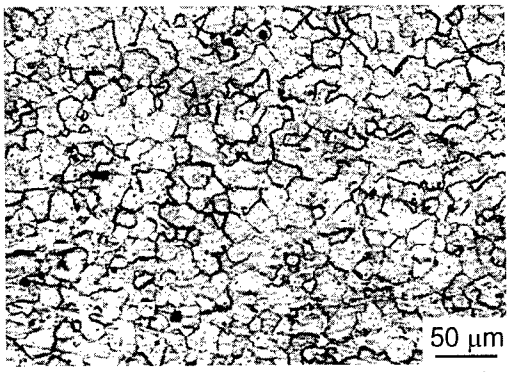

Fig.6. Microstructure of coil #2 material after solid solution treatment by rapid heating to 850°C. LM.

To fully dissolve the primary α but still keep beta grains moderate in size, RH to 920°C was employed. This temperature was chosen as that at which new beta grains formed throughout the whole volume. The fact that the starting microstructure varied significantly from one location to another gave rise to a variation in grain size after RH. Since, the beta transus temperature in RH was not reached simultaneously and, therefore, grain growth commenced at different stages of the heating cycle. This non-uniformity is well illustrated by the presence of high aspect ratio grains which remained from starting microstructure and were not fully consumed by other grains during their growth (Fig. 5). An average β grain size 65 μm was achieved; smaller grain sizes were impossible to fix by RH because of noted non-uniformity. Mechanical properties of coil #1 material achieved with RHT using final aging at 580 °C are also presented in Table 2. These are similar to the properties after the reference heat treatment. Some variation in elongation and reduction of area data between the core and surface locations, less pronounced than after reference heat treatment, may be related to the variation in the original microstructure development between the surface and core of the wire. An attempt to increase the strength of the coil #1 material by employing lower aging temperatures resulted in embrittlement. This was expected for this grain size from the grain size dependence of ductility presented in [3].

Table 2. Mechanical properties of coil #1 material

##	Location	YS, MPa	UTS, MPa	A_5, %	RA, %
Reference (α+β)-STA treatment					
1	Core	1340	1380	13	36
2	Surface	1320	1360	5	9
RHT/WQ + 580°C, 8h					
3	Core	1340	1370	5	25
4	Surface	1320	1360	6.9	12

3.3 Coil #2 material.

The as-received microstructure of coil #2 material showed non-uniform dynamic recrystallization of β phase (see Fig. 1, c). Again, core and near surface areas differed, in this case - in degree of recrystallization and beta grain size. The strength of core of the coil #2 material in the reference condition was slightly higher and with lower ductility as compared to the coil #1 (Table 3). The former is due to remaining dislocation substructure in the unrecrystallized part. For the RH a peak temperature of 850°C was selected for coil #2 material. This was lower than for coil#1 material because no primary α phase to be dissolved was present in the starting microstructure. The RH was needed only to complete the recrystallization. Consequently, smaller β grain sizes, around 20 μm in average, were achieved (Fig. 6). When aged at the same temperature as coil #1, the RHT coil #2 material exhibited a better ductility at the same level of strength. Finer beta grain microstructure allowed an extension of strength/ductility combination to higher strength values with aging at lower temperatures while keeping the ductility quite reasonable (see Table 3).

Table 3. Mechanical properties of coil #2 material

##	Treatment	YS, MPa	UTS, MPa	A_5, %	RA, %
1	Reference α+β STA treatment	1370	1390	2.8	13
2	RHT/WQ /580°C, 8h;	1335	1365	8.3	32.5
3	RHT/WQ/560°C, 8h;	1350	1385	5.8	37
4	RHT/WQ/538°C, 8h;	1450	1460	5.0	19

3.4 Material preliminary processed by cold deformation in solid solution treated condition.

Based on the above results from RHT of the plate and two coil materials, further improvement in strength/ductility balance could be expected with reducing the grain size below 20 um. It has already been noted that to reach this goal with rapid heating approach in plate and coil materials with the initial microstructures provided remained difficult because of their non-uniformity. Cold deformation of beta alloys that have been heat treated in the β phase field in conjunction with rapid recrystallization annealing (RRA) was another approach used in this work to produce beta grains smaller than 20 micrometers. Experiments were conducted with coil #2 material that was solution treated either in a furnace at 820°C, 0.5 h (beta-grain size 90 μm) or by rapid heating (beta-grain size 20 μm), both followed by WQ. Following the solid solution treatment, the materials were cold drawn with a total reduction of either 50% or 70%. Cold drawn materials were then rapidly heated (20 Ks^{-1}) to produce recrystallization, water quenched from peak temperatures and finally aged. Aging was also done for solid solution treated specimens.

Owing to a specific mechanism of recrystallization, at which new grains nucleated mostly on old-grain boundaries, the resulting microstructures were found to be strongly dependent on the beta-grain size in the initial solid solution condition. Much finer resulting grain sizes after cold drawing and rapid recrystallization annealing were produced with an initial grain size of 20μm (Fig. 7). For the same starting microstructure, higher reduction degree caused in finer beta grains. It is worth noting that higher reduction resulted in a more uniform beta-grain microstructure. Improvement in the properties was observed for all starting microstructures (Table 4). The material with a 90-μm grain size that exhibited brittle behavior in the directly aged condition had an attractive combination of strength and ductility after the grain

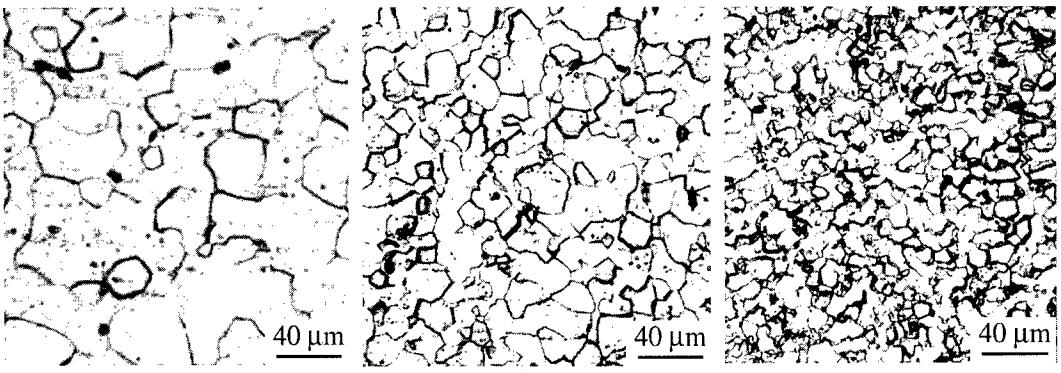

Fig. 7. Recrystallized microstructure: (a) furnace solid solutioning, reduction 50%; (b) solid solutioning by rapid heating, reduction 50%; (c) solid solutioning by rapid heating, reduction 70%.

refinement to 30 μm achieved by cold deformation and RRA. Even higher properties resulted from this approach applied to starting 20 μm microstructure. The finest grain size achieved was 7 μm. The strength values of or in excess of 1600 MPa were the result of the high density of fine α precipitates produced by low-temperature aging. The improvement in ductility may be attributed to the fine and very uniform beta-grain microstructure. This represents a significant overall improvement in strength/ductility balance achieved in this alloy.

Table 4. Mechanical properties of coil #2 material in cold drawn/recrystallized conditions.

# #	Solid solution	Reduction	Recrystallization	β-grain size, μm	Aging	YS, MPa	UTS, MPa	A_5,%	RA, %
1	Furnace	50	RRA	30	538 °C, 8h	1395	1425	6.8	24
2	RH	50	RRA	12	538 °C, 8h	1420	1470	8.2	22.5
3	RH	70	RRA	7	538 °C, 8h	1475	1490	10.3	25.5
4	RH	70	RRA	7	520 °C, 8h	1600	1625	6.0	20.0
5	RH	70	RRA	7	500 °C, 8h	1615	1690	4.2	13.5

4. CONCLUSIONS

Above presented results completely confirm the suggestion on overwhelming influence of beta-grain size on ductility of high-strength beta alloys. Finer beta-grain microstructure allows to strengthen beta alloys without the loss in ductility. RHT approach allows to control mechanical property balance of beta-titanium alloys within a wider range of the properties as compared to conventional heat treatments. Strength level of 1300÷1350 MPa can be obtained with beta-grain size of about 50 μm easily attained by RHT of alloys thermomechanically processed in alpha+beta field. Further increase in strength requires beta-grain size to be smaller than 50 μm, what can be achieved by RHT of alloys carefully processed in single-phase beta field. Even more attractive balance of the mechanical properties can be obtained if RHT is combined with a preliminary cold deformation.

REFERENCES

1. P.J. Bania, in Beta titanium alloys in the 1990's, D. Eylon, R.R. Boyer and D.A. Koss, eds., TMS, Warrendale, PA (1993), pp. 3-14.
2. S. R. Seagle, R. Bajoratis and C. F. Pepka, in Designing with Titanium, The Institute of Metals, London, UK (1986), pp.166-171.
3. O.M. Ivasishin and R.V. Teliovich, Mat. Sci. and Eng., Vol. A263 (1999), pp. 142-154.
4. P.G. Allen, P.J. Bania, A.J. Hutt, Y. Combres, in Titanium'95, Science and Technology, Vol. II, The Inst. of Materials, Birmingham, UK, (1996), pp. 1680-1687.
5. V.N. Gridnev, O.M. Ivasishin and P.E. Markovsky, Metal Science and Heat Treatment, Vol. 25 (1-2) (1985), pp.43-47.
6. O.M. Ivasishin et al., in Titanium'99, Science and Technology, Vol. I, CRISM "Prometey", Saint-Petersburg, Russia, (2000), pp.505-512.

The Ordering Behavior of Supersaturated Metastable Phase in Beta-Ti Alloys

Byung-Hak Choe, Baek-Hee Lee, Byung-Gil Jung, Tae-Ho Lee*,
Chang Gil Lee*, Sung-Joon Kim* and Yong-Tai Lee*

Dept. of Metall. Engineering, Kangnung National Univ., Kangnung 210-702, Korea
* Korea Institute of Machinery & Materials, Changwon 641-010, Korea

ABSTRACT

A phase originated in solid solution and quenched state of beta-Ti alloys has long been recognized as a metastable structure containing unusual phenomena, and is not well understood. This paper reviews a new regularity generated in metastable phase of supersaturated state. It may be induced by the electron charge distribution and atomic bonding between matrix and solute atoms, causing the tweed structure. Then this proposes new phase transformation criteria to assist in assessing the lattice regularity of tweed and diffraction patterns.

1. INTRODUCTION

When solid solution treated alloy at the high temperature is quenched to room temperature, supersaturated structure of matrix was induced by constraining of solute atoms. Although such supersaturated state does not undergo a definite lattice transformation like martensite transformation in steel, it has an ordering formation in lattice. It is considered that the ordering behavior of supersaturated solution is not the common behavior of order-disorder transformation, and it may cause a new regularity on matrix lattice [1,2,3,4]. We tried to discuss the abnormal structure due to ordering behavior of supersaturated solution, while it has the same lattice with the stable phase composed in high temperature. In order to study the ordering behavior, the microstructure and diffraction were mainly investigated by transmission electron microscope about commercially used β-Ti alloys and Cu added steel.

2. EXPERIMENTAL PROCEDURES

Ti-15-3 and β-C alloys in the form of 12mm diameter rod were obtained from TIMET company in United States. The nominal compositions of Ti-15-3 and β-C alloys are Ti-15V-3Cr-3Sn-3Al and Ti-3Al-8V-6Cr-4Mo-4Zr in weight percent, respectively. The specimens for experiment were heated to 788℃ in Ti-15-3 rods and 750℃ in β-C rods, and water quenched. After solid solution treatment and quenching (STQ), the specimens were in-situ. aged in hot stage TEM at 450℃ of two phases region temperature of α and β.

3. RESULTS

3.1 Supersaturated state of metastable phase

The new regularity in supersaturated matrix is observed at diffraction pattern considerably, and the abnormal patterns about supersaturated state of Ti-15-3, β-C and Ti_3Al-Nb are shown in Fig.1. The diffraction patterns due to the metastable state phase are not normal composed by spot streaks and satellites, but They have a regular shape related to main spots of stable phase. Such diffraction patterns may be caused by supersaturated solute atoms in matrix, and they look like diffraction pattern of ω phase in Ti alloys [5,6].

All the TEM micrographs of the supersaturated matrix have the almost same characteristics as shown in Fig.1. There are long stripes in all figures of three alloys. It is twin-like structure defined as tweed, which can be induced by elastic strain field in supersaturated matrix. The tweed structure is distinguished from twin as considered Fig.1, which does not reach behavior of plastic deformation.

Such formation of spot satellites with streaks and shape of tweed in supersaturated state has been already studied in shape memory alloys [2,3,4]. Fig.2 is the micrographs of NiAl alloy studied by Wayman. The micrographs of tweed and spot satellites with streaks of difrraction pattern in matrix are similar to metastable β-Ti alloys mentioned above (Fig.1). Especially in diffraction pattern of NiAl, spot satellites are located at 1/3 and 2/3 point between main spots.

The regularity in diffraction pattern and the distinctive microstructure of tweed are also demonstrated in Cu added steel. Fig.3 shows the microstructure and diffraction pattern of Fe-1Cu alloy in supersaturated state of solute atoms of Cu. It can be seen that obvious diffraction patterns are made up like ordered lattice as shown in Fig.1, even though there are not compounds such as carbide in matrix. The shape of supersaturated matrix has the winding structure of tweed in the figure.

The new regularity on diffraction pattern of supersaturated state is commonly applied in Ti-15-3, β-C, Ti_3Al-Nb and Fe-1Cu alloys as mentioned above. The common characteristics of such alloys may come from phase instability due to supersaturated solute atoms retained in matrix. It is believed that this phenomena could happen to more various alloys that have unchangeable lattice structure even in supersaturated state. The new regularity inflicted by supersaturated state was described at discussions.

3.2 Stable state of phase

Supersaturated state means the condition of metastable state. If driving force such as heating or stress are inflicted on the metastable state, the metastable state can be changing to stable state.

By heating, the metastable phase changes to stable state because the phase undergoes sufficient solid solution of solute atoms at high temperature. Also in process of slow cooling after solid solution, the stable phases of α and β are retained by enough diffusion of solute atoms. The stress inflicted on metastable structure can also influence on the phase transformation to the stable structure such as martensite which is composed of definite plastic deformation of twin or stacking faults.

Such phase transformation from metastable to stable state has several common features. In solidified Ti-Al-Cr alloys by rapid quenching, the diffuse ω phase transforms to crystalline ω phase during annealing after STQ. This phase transformation behavior is similar with $\alpha+\beta$ precipitation behavior in aging after supersaturated solid solution in metastable β-Ti alloys [1,6].

Also the 9R martensite structure of steels and α' martensite of β-Ti alloys in subzero quenching after solid solution treatment have the similarity with the phase transformation from metastable to stable phase [7,8,9].

It means that the regularity induced in supersaturated state of all the above mentioned alloys depends on a fixed formula at the phase transformation from metastable to stable phase. If the unknown regularity of supersaturated state should be defined, a new stand point about evolution of compound in aging, crystallization of amorphous, and martensite phase transformation will be identified.

4. DISCUSSION

The unknown regularity takes place in supersaturated state causes a new lattice periodicity to the metastable structure. However, the new lattice period is different from general order-

disorder transformation. General ordered lattice means regular arrangement between A and B atoms in condition of enough solute atoms and diffusion time, but supersaturated state does not have enough time for regular arrangement.

In ordering behavior of metastable lattice at supersaturated state, the distribution of charge electrons, i.e., free electrons distributed in mixture of A and B atoms plays an important major role.

Solid solution treated alloys in high temperature are composed of disordered mixture of A and B atoms. When the state was quenched to room temperature, it is being maintained the single β phase that A and B atoms was mixed irregularly as solid solution state. However, new charge density periods of electrons can be built up in the as-quenched alloys by orbital distribution, which is participated in atomic bonds, or the number of valence electrons of A and B atoms.

This is charge density wave (CDW) induced in supersaturated state [10,11,12]. The CDW has a favorable shape in one dimension but the shape and structure are obscure in two or three dimension. If CDW is formed in supersaturated state, it can change even lattice structure. It is lattice displacement wave (LDW). In case of CDW conforms to LDW, free energy is decreased and the phase stability is increased. Futhermore, new energy gap is formed in regular wave, and new Brillouin zone is created on Ferimi surface by beam diffraction especially in the points of 1/3 and 2/3 between main lattice points (Fig.4).

This is interpretation for the new regularity of supersaturated state. The premartensite behavior in shape memory alloys was interpreted by this mechanism, but there are no more studies about other alloys including such regularity until now. The alloys, which the regularity occurs, are mainly composed of bcc lattice structure and it is also demonstrated that the shape of supersaturated state has the morphology of tweed structure due to lattice distortion.

The lattice distortion, which is formed in supersaturated state of metastable phase, is consequently induced by elastic strain field due to charge density wave in atomic bonding between solution and solute atoms. Then the elastic field causes the distinctive shape of matrix, tweed, which is given by the elastic deformation. The tweed is not twin but limited in elastic deformation as twin-like.

When 1% of Cu is added to plain carbon steel, a pretty special phenomenon on regularity of lattice structure takes place in microstructure and diffraction pattern. The phenomenon was caused by soluble limit of Cu atoms in Fe matrix at the quenched state after solid solution, because the enough soluble Cu in γ -fcc of high temperature was retained to supersaturated state of α -bcc iron in room temperature.

Being able to generate obvious diffraction pattern of ordered lattice by adding only 1% of Cu, as shown in Fig.3, is considered by pinning effect of Cu atom between CDW and LDW in Fig.5. The CDW may have been already built up in α -Fe structure and move independently

above the bcc lattice in Cu free steel, then there is no specific regularity of matrix structure. However, in Cu added steel, the CDW formed above lattice can be cohered to LDW on lattice even with only 1% of Cu, and finally a new lattice wave accompanied by lattice regularity is created.

It is the explanation for diffraction pattern of ordered lattice in supersaturated state of Cu added steel as shown in Fig. 3(b). It is considered that tweed of the stripe shapes, as shown in Fig. 3(a), is also caused by pinning effect between CDW and LDW, which is consistent with a favorable shape in one dimension such as tweed lines.

It is anticipated that the regularity of supersaturated state may occur in more various alloys. It is needed to investigate the new discussed regularity of lattice structural wave and the formation of elastic strain field in metastable phase of supersaturated state.

5.CONCLUSIONS

1) A new regularity of lattice, which is induced by the charge electron distribution and the atomic bonding between matrix and solute atoms, is generated in metastable phase of supersaturated state.

2) The regularity of lattice structure causes the ordered spots at 1/3 and 2/3 or 1/2 between main matrix spots in diffraction patterns.

3) The regularity of supersaturated state originates from specific elastic strain field due to lattice distortion within elastic deformation range.

4) It is considered that the CDW and LDW model may be applied to the metastable phases of β-Ti alloys, and a preferable direction in one dimension by electron charge wave may make the tweed structure.

REFERENCES

1. B.H. Choe, J.H. Choi, S.C. Lee, S.J. Kim and Y.T. Lee, Scripta Materialia, 39, 749 (1998).
2. I. M. Robertson and C. M. Wayman, Philosophical Magazine, 48, 421 (1983).
3. I. M. Robertson and C. M. Wayman, Metallurgical Transactions A, 15A, 1353 (1984).
4. C. M. Hwang, M. Meichle, M. B. Salamon and C. M. Wayman, Res Mechanica, 10, 1 (1984).
5. D. Banerjee, A. K. Gogia, T. K. Nandi and V. A. Joshi. Acta, 36, 871 (1988).
6. G. Shao and P. Tsakiropoulos, Acta mater. 48 3671 (2000).
7. P. J. Othen, M. L. Jenkins, G. D. W. Smith and W. J. Phythian : Philosophical Magazine

Letters, 64 (1991) 383
8. N. Maruyama, M. Sugiyama, T. Hara and H. Tamehiro : Mater. Trans. JIM, 40 (1999) 268
9. P. J. Othen, M. L. Jenkins, G. D. W. Smith : Philosophical Magazine A, 70 (1994) 1
10. G. M. Michal, P. Moine and R. Sinclair, Acta Metallurgica, 30, 125 (1982).
11. P. Moine, G. M. Michael, and R. Sinclair, Acta Metallurgica, 30, 109 (1982).
12. Y. Yamada, Proc. Int. Conf. on Martensitic Transformations, Japan Inst. Metals, 89 (1986).

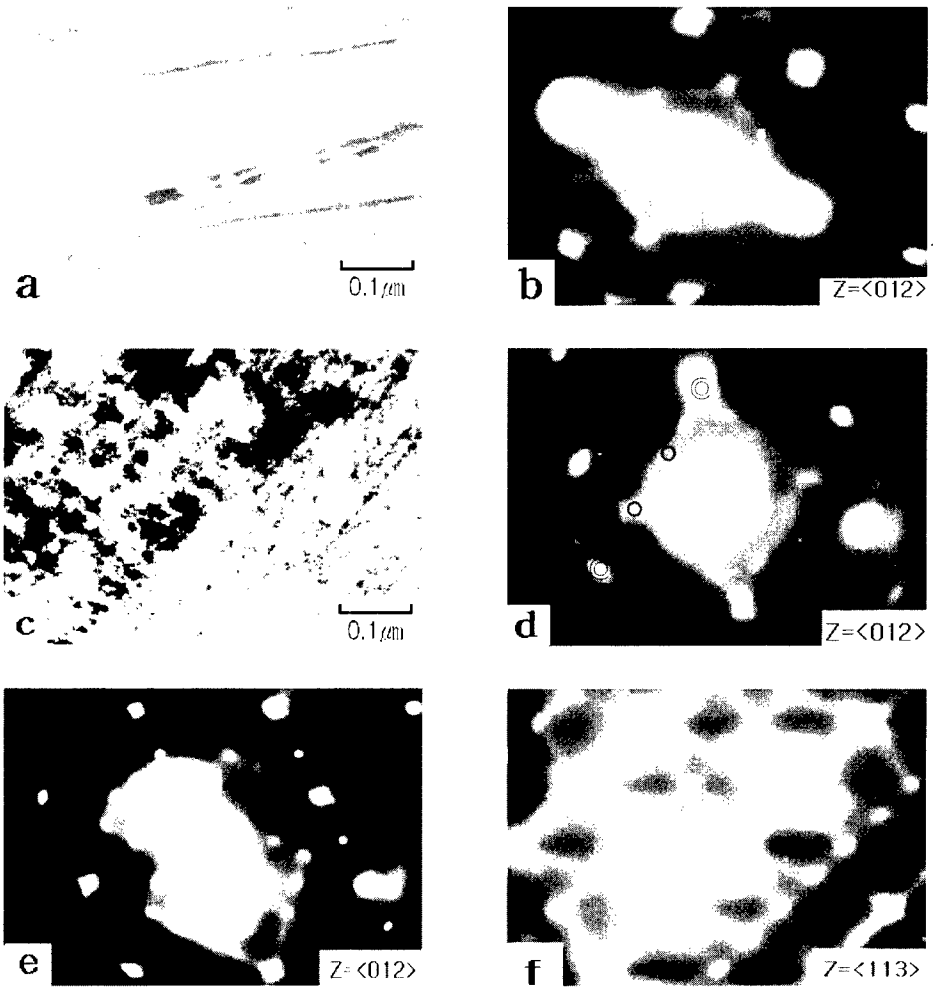

Fig.1 Transmission electron micrographs of Ti alloys :
(a), (b) Ti-15-3, (c),(d) β - C and (e), (f) Ti_3Al-Nb alloy

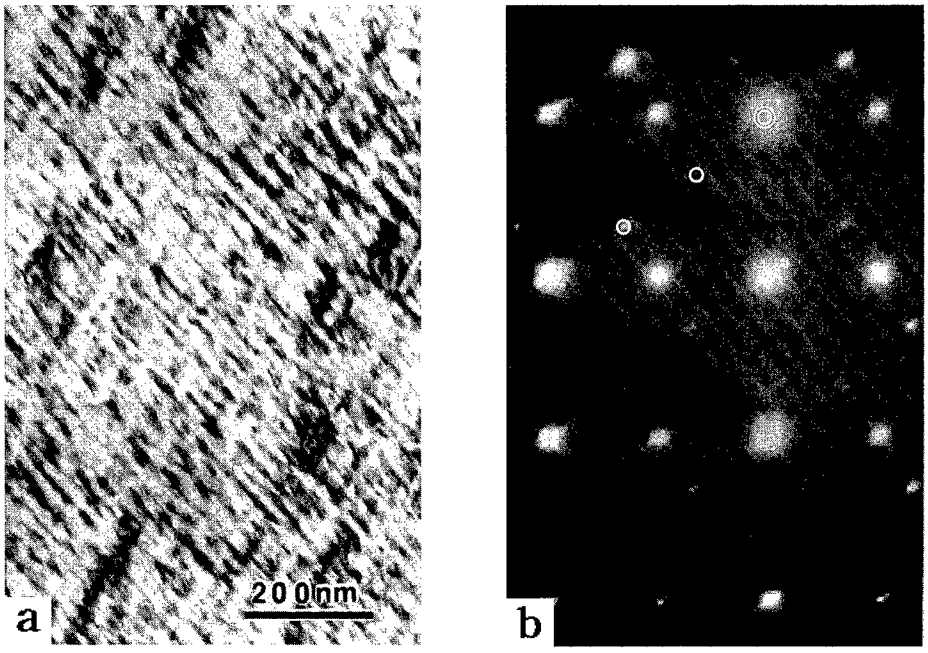

Fig.2 Typical feature of tweed in NiAl of a shape memory alloy ; (a) tweed structure consisted of 10nm thickness layer boundaries, (b) diffraction pattern combined by spot satellites located in the points of 1/3 and 2/3 between main spots.

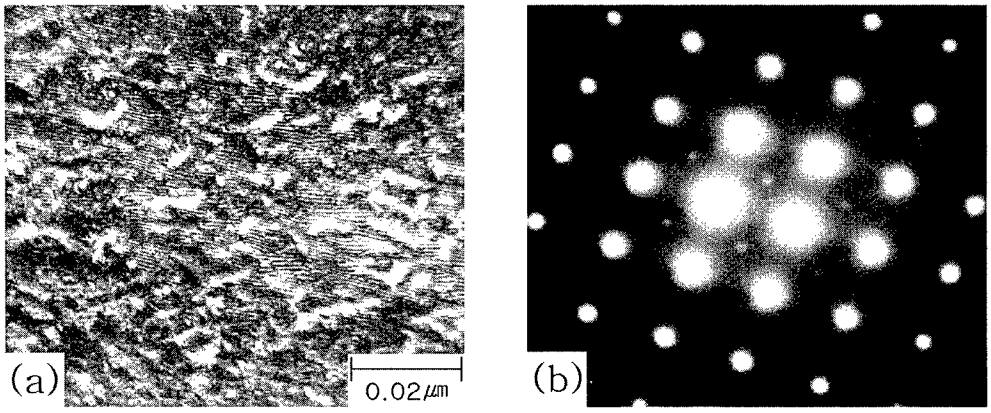

Fig.3 Microstructures of a Cu-doped steel at the state of solid solution treatment and quenching : (a) Modulated structure composed of fine striations and (b) superlattice diffraction spots, z = <001>, in ferrite matrix.

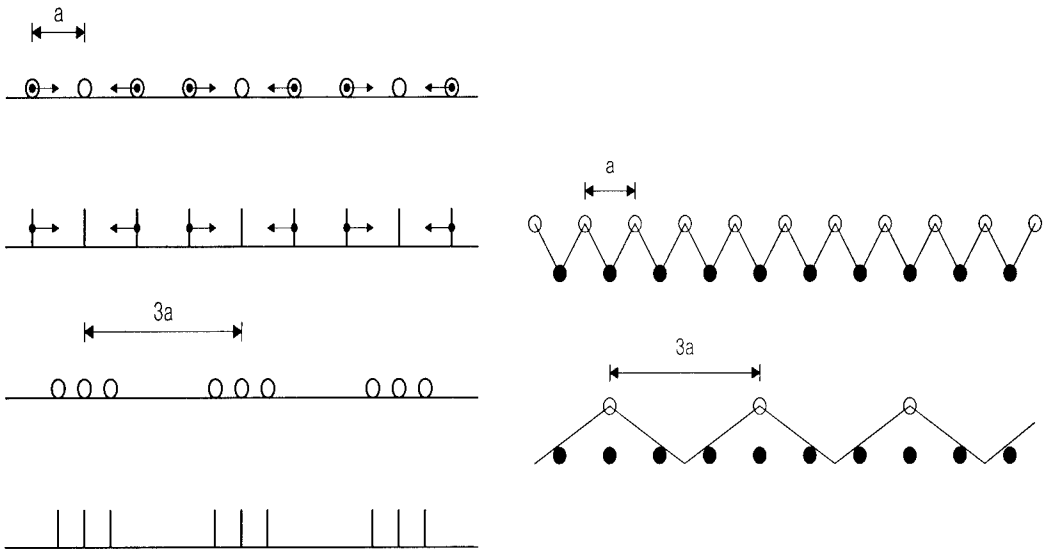

(a) Lattice Displacement Wave (b) Charge Density Wave

Fig.4 Schematic diagrams of (a) Lattice Displacement Wave and (b) Charge Density Wave models which show a new periodicity of three times of lattice parameter, i.e. 3a,

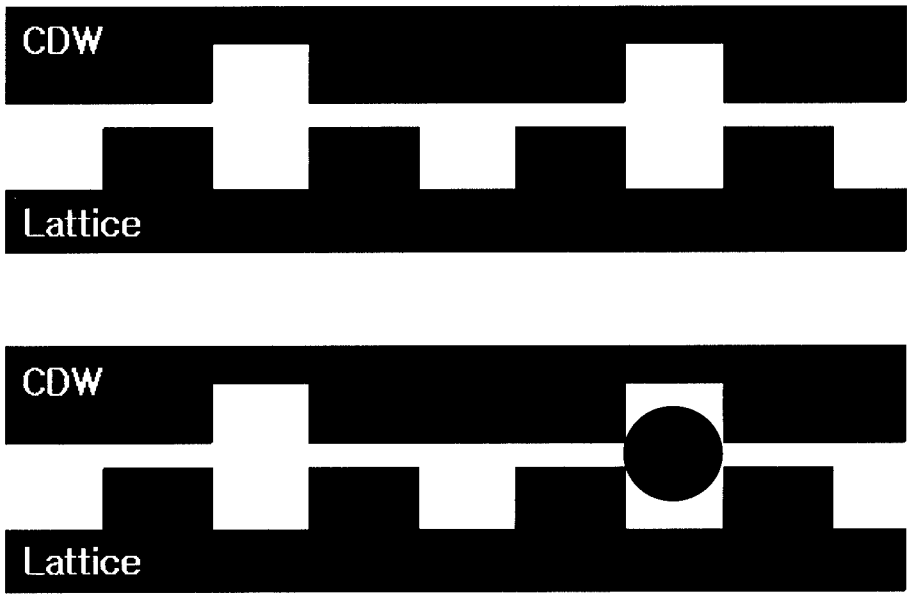

Fig.5 Pinning effect by an impurity Cu atom in Cu added steel matrix.

INFLUENCE OF COOLING RATE FROM A TEMPERATURE WITHIN THE BETA PHASE REGION ON TENSILE PROPERTIES AND PHASE CONSTITUTION OF Ti-Fe-Cr ALLOYS FOR TECHNICAL AIDS

Masahiko IKEDA[a], Shin-ya KOMATSU[*], Mitsuhide UEDA[**], Toru IMOSE[**] and Koichiro INOUE[***]

*Department of Mats. Sci. &.Eng., Kansai University,3-3-35, Yamate-cho, Suita, Osaka 564-8680, JAPAN
**Graduate student of Kansai University,
*** Daido Steel Co. LTD.

ABSTRACT

The influence of cooling rate on phase constitution and tensile properties of Ti-3.1Fe-5.1Cr and Ti-4.3Fe-7.1Cr alloys was investigated by electrical resistivity and Vickers hardness measurements, X-ray diffraction, optical microstructure observation and tensile testing.

In only Ti-3.1Fe-5.1Cr alloy quenched at an average cooling rate of $25Ks^{-1}$, reflections from isothermal omega phase were identified, whereas only reflections from beta phase were identified by XRD with no reflections of isothermal omega phase present in Ti-3.1Fe-5.1Cr alloy cooled at other cooling rates and Ti-4.3Fe-7.1Cr alloy quenched at all cooling conditions. HV for Ti-3.1Fe-5.1Cr alloy cooled at three different cooling rates, i.e. $60Ks^{-1}$, $48Ks^{-1}$ and $31Ks^{-1}$, was about 350 and HV of Ti-4.3Fe-7.1Cr alloy cooled at all cooling conditions was around 320. Therefore, quench sensitivity of Ti-4.3Fe-7.1Cr alloy is lower than that of Ti-3.1Fe-5.1Cr alloy..

Tensile strength and reduction in area of Ti-3.1Fe-5.1Cr alloy cooled at three different cooling rates (except for $25Ks^{-1}$) showed about 1200MPa, 15% and 45%, respectively. About 1050MPa in σ_B and 60% in ϕ were obtained in all quenched Ti-4.3Fe-7.1Cr alloys, respectively. The strength/ductility balances of both Ti-Fe-Cr alloys are comparable with those of developed beta titanium alloys, e.g. Ti-15V-3Cr-3Sn-3Al alloy.

1. INTRODUCTION

In some countries, especially Europe, e.g. Italia, Sweden, German and UK, the population of elderly people tends to increase [1]. In Japan, it is expected that people aged 65 and older will become 27% in 2020, after only 19 years [1]. Thus, there is need to develop support equipments for the elderly. For disabled people, of course, it is also important to develop the support equipment, e.g. wheelchairs, with lightweight, high strength and good biocompatibility. In the near future, the market for wheelchairs with attached electrical driving and controlling systems will increase. Thus, frame materials having higher specific strength, ratio of tensile strength to density, for wheelchairs will be demanded. Though beta titanium alloys are suitable materials for the application mentioned above because of high

specific strength, these alloys are costly [2]. Therefore, it is necessary that new beta titanium alloys with reasonable cost will be developed for welfare applications, e.g. wheelchairs.

The present authors developed a low cost beta Ti alloy by using low cost ferro-chromium alloy as alloying materials, i.e. Ti-Fe-Cr alloys having a good balance between tensile strength and ductility in the solution treated and quenched state [3]. However, since diffusion coefficients of Fe and Cr in beta Ti are higher than the self-diffusion coefficient of Ti [4], it is expected that volume fraction of retained beta phase at room temperature decreases with increase in specimen size. In beta quenched Ti-5mass%Fe beta alloys with 20mm diameter and 70mm length, it was revealed that reflections from isothermal omega phase were identified by X-ray diffraction and that tensile specimens failed without plastic deformation [5]. In Ti-Fe-Cr alloys having a volume fraction of omega above a critical value, tensile properties will be compromised due to the isothermal omega precipitation during quenching. Therefore, it is important to study about the effect of specimen size, i.e. cooling rate, on phase constitution and tensile properties of Ti-Fe-Cr alloys cooling from a temperature within beta single phase, for application to welfare equipment.

In this study, by using four different sized specimens, i.e. varying cooling rate by changing specimen size, the influence of cooling rate on tensile properties and phase constitution was investigated in Ti-Fe-Cr alloys having values of e/a (electron/atom ratio) between 4.20 and 4.28.

2. EXPERIMENTAL PROCEDURES

Ti-3.1Fe-5.1Cr (e/a=4.20) and Ti-4.3Fe-7.1Cr (e/a=4.28) alloys were melted by Plasma Progressive Casting Furnace Process [6], PPC and then Vacuum Arc Remelting Process, VAR in Daido Steel Co. LTD. **Table 1** shows alloy code and chemical composition of the alloys used in this study. Obtained ingots were hot forged at a suitable temperature in to round bar about 25 mm in diameter and about 1000 mm in length. Four deferent diameter bar specimens, i.e. 10mm, 15mm, 20mm and 25mm diameter, with 70mm length were machined.

Table 1 Alloy code and chemical composition (mass%) of alloys used in this study

Alloy code	Fe	Cr	O	C	N
Ti-3.1Fe-5.1Cr	2.93	4.89	0.14	0.010	0.005
Ti-4.3Fe-7.1Cr	4.21	6.93	0.14	0.011	0.008

All bar specimens were heat-treated at 1173K for 3.6ks and quenched in to iced water, STQ. After STQ, All specimens were machined to tensile test specimens with 4mm diameter and 60mm in gage length. Before tensile tests, resistivity of all tensile test specimens was measured at room and liquid nitrogen temperature, ρ_{RT} and ρ_{LN} [3]. Tensile tests were performed with a cross head speed $5 \times 10^{-5} ms^{-1}$ [3]. After tensile tests, the microstructure of specimens prepared from the grip section of the test peaces was observed in an optical microscope (OM). Phase constitution was identified by X-ray diffraction (XRD) and Vickers hardness (HV) was measured on the same specimen as used for OM [3]. Fracture surfaces were also observed by SEM [3]. The method for cooling curve measurement is as follows Thermocouple was set near the center of the specimen's body. The specimen was heated up to 1173K and held for 3.6ks and then was quenched into iced water. At the same time, cooling curve of the specimen of Ti-3.1Fe-5.1Cr alloy only was measured by digital thermometer and pen-recorder. Though thermal properties, e.g. specific heat capacity, of

Ti-4.3Fe-7.1Cr are not the same value as those of the Ti-3.1Fe-5.1Cr alloy, the expected difference of those values was small. Thus average cooling rates of Ti-3.1Fe-5.1Cr alloy calculated between 1073 and 473K were also applied to results of Ti-4.3Fe-7.1Cr alloy. **Figure 1** shows cooling curves of four different sized specimens, respectively. Average cooling rates between 1073K and 473K are $60Ks^{-1}$ in 10mm diameter, $48Ks^{-1}$ in 15mm diameter, $31Ks^{-1}$ in 20mm diameter and $25Ks^{-1}$ in 25mm diameter specimens, respectively.

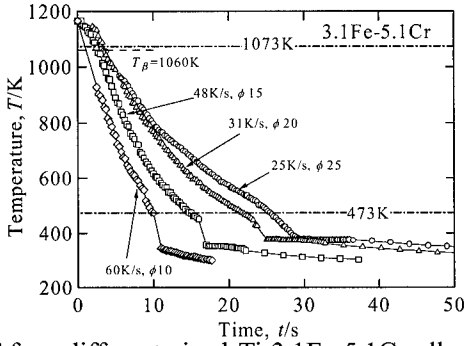

Fig.1 Cooling curves of four different sized Ti-3.1Fe-5.1Cr alloy specimens after solution treatment at 1173K for 3.6ks.

RESULTS and DISCUSSION

Figure 2 shows optical microstructures of Ti-3.1Fe-5.1Cr and Ti-4.3Fe-7.1Cr alloys cooled by $25Ks^{-1}$ and $60Ks^{-1}$, respectively. In both alloys in STQed state, the structures were single phase beta with equaxed grains. Average grain size was about 270μm in Ti-3.1Fe-5.1Cr alloy and about 160μm in Ti-4.3Fe-7.1Cr alloy irrespective of specimen size, respectively. Reflections from only β phase were only identified in alloys except for STQed Ti-3.1Fe-5.1Cr alloy specimen in 25mm diameter, in which reflections from isothermal ω phase were identified.

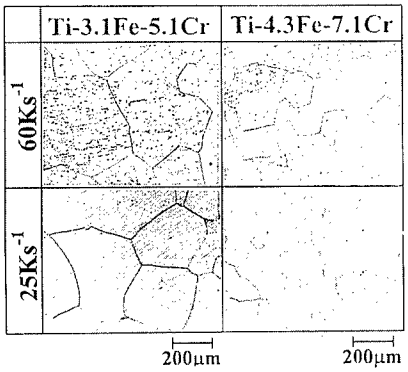

Fig. 2 Examples of optical micrographs of Ti-3.1Fe-5.1Cr and Ti-4.3Fe-7.1Cr alloys cooled at two different average cooling rates, i.e. $25Ks^{-1}$ and $60Ks^{-1}$, respectively.

Figure 3 shows changes in resistivity ratio (ρ_{LN}/ρ_{RT}) and HV as function of average

cooling rate. Resistivity ratio and HV of small sized flat bar specimens with about 3mm width, about 3mm height and about 50mm length were also shown in this figure for comparison. In Ti-3.1Fe-5.1Cr alloys, resistivity ratio decreased with decrease in average cooling rate down to $31Ks^{-1}$ and drastically decreased at $25Ks^{-1}$. This decrease of resistivity ratio is due to isothermal omega precipitation. In Ti-4.3Fe-7.1Cr, resistivity ratio also decreased with decrease in average cooling rate. However a drastic decrease did not appear, in even specimens cooled at $25Ks^{-1}$. From the above results, it is considered that either isothermal omega did not precipitate or the volume fraction of isothermal omega phase was very low, in even in specimens quenched at $25Ks^{-1}$. Values of ρ_{LN}/ρ_{RT} of Ti-3.1Fe-5.1Cr and Ti-4.3Fe-7.1Cr alloys cooled at $60Ks^{-1}$ were the same as values of the small sized flat bar specimens, i.e. 1.064 and 1.071, respectively. HV of Ti-4.3Fe-7.1Cr alloy specimens cooled at each cooling rate used in this study were almost the same value as that of the flat bar specimen. In Ti-3.1Fe-5.1Cr alloy, HV values of specimens cooled at a cooling rate above $31Ks^{-1}$ were almost same value as the flat bar Ti-3.1Fe-5.1Cr specimen, whereas HV of specimen cooled at $25Ks^{-1}$ was about 400 which was higher than that of other sized round bar specimens. This result is suggested that isothermal omega phase precipitated during cooling at $25Ks^{-1}$ in Ti-3.1Fe-5.1Cr alloy specimen.

By comparison of XRD profiles between Ti-3.1Fe-5.1Cr and Ti-4.3Fe-7.1Fe alloys cooled at $25Ks^{-1}$, it is considered that quench sensitivity of the Ti-4.3Fe-7.1Cr alloys will be lower than that of the Ti-3.1Fe-5.1Cr alloy. This will cause that beta phase stability of the former to be higher than the latter.

Figure 4 shows changes of tensile strength, σ_B, elongation, δ, and reduction in area, ϕ, of Ti-3.1Fe-5.1Cr and Ti-4.3Fe-7.1Cr alloys as function of average cooling rate. In Ti-3.1Fe-5.1Cr alloy, σ_B, δ and ϕ were almost the same values irrespective of cooling rate above $31Ks^{-1}$, i.e. about 1.2GPa, 15% and 45%, respectively.

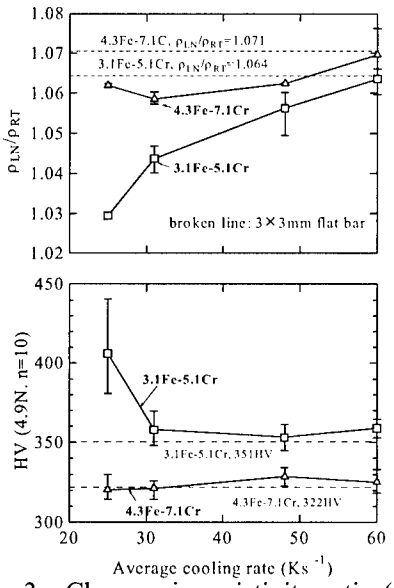

Fig. 3 Changes in resistivity ratio (ρ_{LN}/ρ_{RT}) and Vickers hardness (HV, load; 4.9N) of Ti-3.1Fe-5.1Cr and Ti-4.3Fe-7.1Cr alloys with average cooling rate respectively.

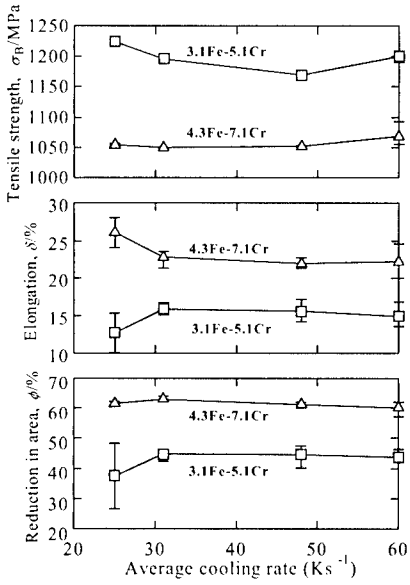

Fig. 4 Tensile strength (σ_B), elongation (δ) reduction in area (ϕ) of Ti-3.1Fe-5.1Cr and Ti-4.3Fe-7.1Cr alloys changed at average cooling rate, respectively.

σ_B of Ti-3.1Fe-5.1Cr alloy cooled at $25Ks^{-1}$ was slightly higher than those of the alloys cooled at an average cooling rate above $31Ks^{-1}$, while δ and ϕ of the former were slightly lower that the latter alloys. In Ti-4.3Fe-7.1Cr alloy, σ_B and ϕ were almost the same value irrespective of cooling rate, around 1050MPa and 60%. δ of specimens cooled at $31Ks^{-1}$ and higher rates was almost same value, about 23%, except for specimen cooled at $25Ks^{-1}$ having 26% in δ. Average σ_B of Ti-4.3Fe-7.1Cr alloy was lower that that of Ti-3.1Fe-5.1Cr alloy, while average δ and ϕ of the former alloy were higher that those of the latter. **Figure 5** shows fracture surfaces of Ti-3.1Fe-5.1Cr alloy cooled at $25Ks^{-1}$ (indicating as "A" in Figure 7) and Ti-4.3Fe-7.1Cr alloys cooled at $25Ks^{-1}$, respectively. In Ti-3.1Fe-5.1Cr alloy, intergranular fracture was partially observed. While, dimples which are characterized as ductile fracture were observed on the whole fracture surface in Ti-4.3Fe-7.1Cr alloy.

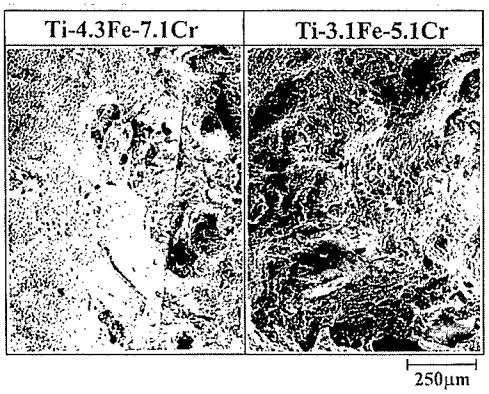

Fig. 5 Fracture surfaces of Ti-3.1Fe-5.1Cr (A) and Ti-4.3Fe-7.1Cr alloys cooled at $25Ks^{-1}$, respectively.

Figure 6 shows the relation between ϕ and σ_B of Ti-3.1Fe-5.1Cr and Ti-4.3Fe-7.1Cr alloys cooled by various cooling rate. The band of strength/ductility balance for developed beta Ti alloys reported by Kawabe et al. [6] is also shown in this figure. Data for tensile strength/reduction in area obtained in this study lie within the band. From the above results, Ti-3.1Fe-5.1FeCr alloy is appropriate material for applications with relatively higher strength, while Ti-4.3Fe-7.1Cr alloy is suitable material for applications with relative higher ductility.

CONCLUSIONS

The influence of cooling rate on phase constitution and tensile properties of Ti-3.1Fe-5.1Cr and Ti-4.3Fe-7.1Cr alloys was investigated by electrical resistivity and Vickers hardness measurements, X-ray diffraction, optical microstructure observation and tensile tests.

In only Ti-3.1Fe-5.1Cr alloy quenched by $25Ks^{-1}$ as average cooling rate, were reflections from isothermal omega phase identified by XRD and 400 HV. While reflections from only beta phase were identified by XRD without reflections of isothermal omega phase in Ti-3.1Fe-5.1Cr alloy cooled by other cooling rates and in all quenched Ti-4.3Fe-7.1Cr alloys. HV for Ti-3.1Fe-5.1Cr alloy cooled at three different cooling rates, i.e. $60Ks^{-1}$, $48Ks^{-1}$ and $31Ks^{-1}$, was about 350 and HV of Ti-4.3Fe-7.1Cr alloy cooled at all cooling conditions was

around 320. Therefore, the quench sensitivity of Ti-4.3Fe-7.1Cr alloy is lower than that of Ti-3.1Fe-5.1Cr alloy. Tensile strength and reduction in area of Ti-3.1Fe-5.1Cr alloy cooled at three different cooling rates except for $25Ks^{-1}$ showed about 1200MPa, 15% and 45%, respectively.

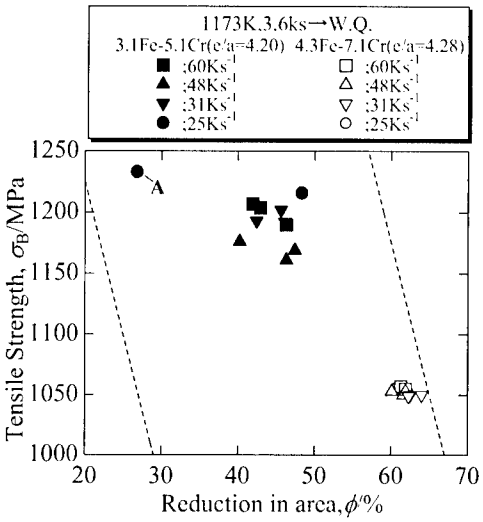

Broken line: σ_B-ϕ balance band of commercial β Ti alloys[6].

Fig. 6 Relationship between reduction in area (ϕ) and tensile strength (σ_B) of Ti-3.1Fe-5.1Cr and Ti-4.3Fe-7.1Cr alloys in various cooled states. The strength/ductility balance band for developed beta Ti alloys reported by Kawabe et al.[6] is also shown in this figure.

About 1050MPa in σ_B and 60% in ϕ were obtained in all quenched Ti-4.3Fe-7.1Cr alloys, respectively. The strength/ductility balances of both Ti-Fe-Cr alloys are comparable with those of developed beta titanium alloys, e.g. Ti-15V-3Cr-3Sn-3Al alloy.

Acknowledgments

One of Authors, M. Ikeda, extends special thanks to Professor H. M. Flower at Imperial College of Science, Technology and Medicine for very kind and useful advice and suggestions on this paper. Part of this research was financially supported by Kansai University Research Grants (Grant-in-Aid for Faculty Joint Research Program, 1999).

REFERENCES

1. Home page of Japan Ministry of Health and Welfare, Now Ministry of Health, Labour and Welfare.
2. Private communication, Mr. H. Ito of The Japan Titanium Association
3. M. Ikeda, S. Komatsu, T. Imose and K. Inoue, "Effect of chromium content on electrical resistivity and tensile properties of Ti-Fe-Cr alloys," Materials Science and Technology, 16(6), 605-608, (2000).
4. H. Nakajima and M. Koike, "Diffusion in titanium," ISIJ Intl., 31(8), 757-766, (1991).
5. K. Inoue, M. Ikeda and S. Komatsu, "The influence of cooling rate and iron content on mechanical properties of quenched beta Ti-Fe alloys," CAMP-ISIJ, 12, 537, (1999).
6. Y. Kawabe and S. Muneki: "Strength and toughening of titanium alloys," ISIJ Intl. 31(8), (1991), 785-791

EFFECT OF PREFORM MICROSTRUCTURE ON CONSTITUTIVE BEHAVIOR OF Ti-6Al-4V UNDER CONVENTIONAL HOT-WORKING CONDITIONS

S.L. Semiatin* and T.R. Bieler‡

*Air Force Research Laboratory, Materials and Manufacturing Directorate, AFRL/MLLMP, Wright-Patterson Air Force Base, OH 45433-7817 USA
‡ Michigan State University, Department of Materials Science and Mechanics, East Lansing, MI 48824-1226 USA

ABSTRACT

Isothermal, hot compression tests were conducted on Ti-6Al-4V to establish the effects of various microstructural features on the constitutive behavior of alpha/beta titanium alloys during conventional hot-working processes. A number of lots of material were prepared to systematically vary microstructural features including colony size, alpha plate thickness, globular-alpha grain size, and the volume fraction of colony alpha and globular alpha. Hot compression tests were conducted at subtransus temperatures of 815°C, 900°C, and 955°C and strain rates between 10^{-1} and 10 s^{-1}. For samples with a fully transformed colony microstructure, plastic flow characterized by a peak stress at low strains followed by extensive flow softening was observed. Such behavior was found to be dependent on alpha platelet thickness (through a Hall-Petch-like effect) and crystallographic texture, but relatively insensitive to colony size per se. For samples with a globular alpha microstructure, the flow curves exhibited a broad maximum at low strains followed by a relatively small amount of flow softening which was attributed to a weak Hall-Petch effect and/or texture softening. The bimodal microstructures revealed stress-strain curves between that of the fully transformed and fully globular microstructures, thus suggesting a rule-of-mixtures behavior.

1. INTRODUCTION

The design of bulk hot-working processes for alpha/beta titanium alloys often relies on models such as that based on finite element analysis. Input data to these models include descriptions of material constitutive behavior and the nature of friction and heat transfer at the tooling-workpiece interface. It is well known that the stress-strain relations that are used to quantify constitutive behavior depend strongly on preform microstructure [1-4]. For example, alloys with a colony microstructure show a sharp peak stress at low strains followed by substantial flow softening. By contrast, globular-alpha microstructures often exhibit near-steady-state flow, i.e., a broad flow-stress maximum followed by weak or no flow softening. A full explanation of the various flow softening behaviors has yet to be put forth. This may be ascribed to the complex interrelation of constitutive behavior and the evolution of substructure, microstructure, and texture during hot working.

The objective of the present work was to clarify the effect of preform microstructure and crystallographic texture on the plastic flow behavior of a typical alpha/beta titanium alloy, Ti-6Al-4V. For this purpose, isothermal hot compression tests were conducted on various lots of material in order to systematically vary the colony size and alpha plate thickness (for

transformed microstructures), the globular alpha grain size (for equiaxed and bimodal microstructures), and crystallographic texture (relative to the compression axis). By this means, the design of a general framework for describing constitutive behavior under conventional hot working conditions was begun.

2. MATERIALS AND PROCEDURES

2.1 Materials

Two lots of Ti-6Al-4V (whose compositions are listed in Table 1) served as the program materials for the present investigation. They were received in the form of bar or plate material which had been subtransus hot rolled. The beta-transus (temperature at which alpha + beta $\rightarrow$ beta) was determined to be 995°C for both lots of material via a technique comprising heat treatment followed by optical metallography. The beta-approach curve was also measured via a series of heat treatments. From this evaluation, the volume fraction of alpha phase was determined to be 0.83, 0.50, and 0.20 at temperatures of 815, 900, and 955°C, respectively.

Table 1. Composition (Weight Percent) of Ti-6Al-4V Program Materials

Product Form	Al	V	Fe	O	C	N	H	Ti
Hot-Rolled Bar	6.08	4.02	0.22	0.18	0.02	0.01	0.005	Balance
Hot-Rolled Plate	6.09	3.95	0.18	0.19	0.02	0.01	0.010	Balance

The two lots were given different heat treatments or thermomechanical processing sequences to develop a variety of microstructures with controlled textures. Sections of the hot-rolled *bar* were beta annealed and controlled cooled (per the temperatures in Table 2) to obtain samples to assess the effect of colony/grain size (Table 3, Figure 1) on constitutive behavior of the transformed microstructure. Designated as Bar-A and Bar-B, these two microstructural conditions both had alpha-plate thicknesses of ~ 1 μm and a layer of grain-boundary alpha ~ 3 μm thick. Pole figures for both microstructures were very similar. They exhibited relatively strong alpha phase textures (~ 7 x random) with two major components – one with the basal poles parallel to the bar axis and one with the basal poles rotated ~ 30° from the transverse (radial) direction toward the bar axis.

Sections of the hot-rolled *plate* were used in the as-received (bimodal, or BiM, microstructure) condition or given a heat treatment to develop a fully-globular-alpha (FG) or colony-alpha (BACC) microstructure in order to establish the effect of phase volume fraction (and texture) on stress-strain behavior. The specific heat treatments and resulting microstructures (at hot working temperatures) are summarized in Tables 2 and 3, respectively, and Figure 2. The crystallographic textures of these samples are discussed in the Results section below.

Sections of the hot-rolled plate were also subjected to a series of additional hot rolling steps and final heat treatments (Table 2) to obtain transformed or fully-globular microstructures with various alpha lath/platelet thicknesses or alpha grain sizes (Figure 3) and thus to determine the effect of such structural variations on plastic flow. Nominal values of the alpha lath/platelet thicknesses or alpha grain sizes at hot working temperatures are listed in Table 3; precise values for these structural parameters were determined by water quenching

samples preheated at various hot-working temperatures. These microstructures were designated as A, B, C (Widmanstatten/colony alpha) and D, E (globular alpha). The

Table 2. Processing Sequences for Ti-6Al-4V Program Materials

As-Received Product Form	I.D.	Processing Sequence*
Hot-Rolled Bar	Bar-A	HT: 1040°C/2 min. + 815°C/10 min. + air cool
Hot-Rolled Bar	Bar-B	HT: 1040°C/12 min. + 815°C/10 min. + air cool
Hot-Rolled Plate	BiM	None (used as-received)
Hot-Rolled Plate	FG	HT: 955°C/60 min. + furnace cool
Hot-Rolled Plate	BACC	HT: 1065°C/15 min. + 940°C/5 min. + 815°C/15 min. + air cool
Hot-Rolled Plate	A	TMP + HT: 1040°C/60 min. + water quench
Hot-Rolled Plate	B	TMP + HT: 1065°C/15 min. + 940°C/5 min. + 815°C/15 min. + air cool
Hot-Rolled Plate	C	TMP + HT: 1040°C/60 min. + furnace cool to RT + 970°C/4h + furnace cool to RT
Hot-Rolled Plate	D	TMP + HT: 900°C/60 min. + furnace cool to 810°C + air cool
Hot-Rolled Plate	E	TMP + HT: 970°C/8h + furnace cool

*TMP ≡ beta annealed (1040°C) + water quenched + hot rolled at 870°C to 60 percent reduction in thickness; HT ≡ heat treated; RT ≡ room temperature

Table 3. Microstructures of Ti-6Al-4V Program Materials at Hot-Working Temperatures

I.D.	Microstructure
Bar-A	Colony alpha; beta grain size ≈ 100 μm; colony size ≈ 50 μm
Bar-B	Colony alpha; beta grain size ≈ 400 μm; colony size ≈ 150 μm
BiM	Bimodal: ~12 μm alpha grains in a transformed beta matrix
FG	Fully globular: ~15 μm alpha grains in a beta matrix
BACC	Colony alpha: beta grain size ≈ 600 μm; colony size ≈ 150 μm; alpha platelet thickness ≈ 1 μm
A	Widmanstatten alpha: beta grain size ≈ 500 μm, alpha lath thickness ≈ 0.6 μm
B	Colony alpha: beta grain size ≈ 500 μm; colony size ≈ 150 μm; alpha platelet thickness ≈ 1.0 μm
C	Colony alpha: beta grain size ≈ 500 μm; colony size ≈ 150 μm; alpha platelet thickness ≈ 6.4 μm
D	Fully globular: ~3 μm alpha grains in a beta matrix
E	Fully globular: ~9 μm alpha grains in a beta matrix

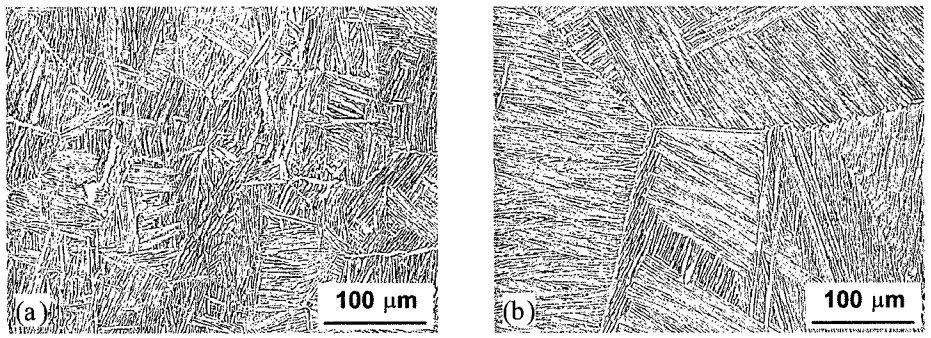

Figure 1. Optical micrographs of colony alpha microstructures in Ti-6Al-4V bar stock: (a) Bar-A and (b) Bar-B.

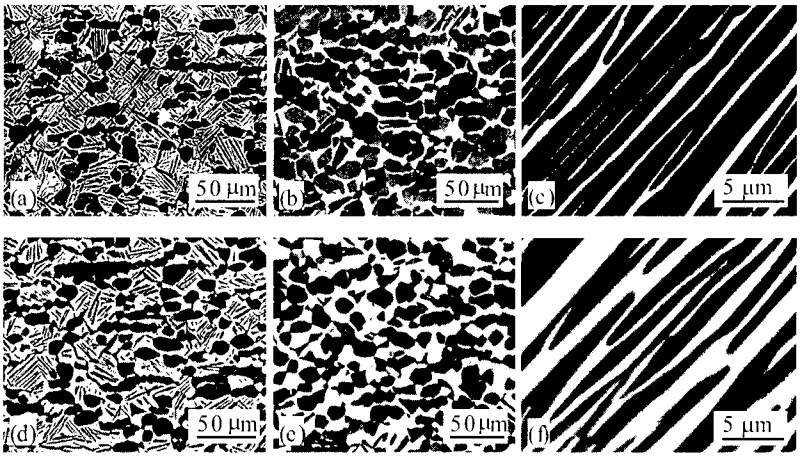

Figure 2. Backscattered-electron micrographs of (a,d) bimodal (BiM), (b,e) fully globular alpha (FG), and (c,f) colony alpha (BACC) microstructures developed in heat-treated Ti-6Al-4V plate following water quenching from (a,b,c) 815°C, (d,e,f) 900°C. The dark phase is alpha; the light phase is beta.

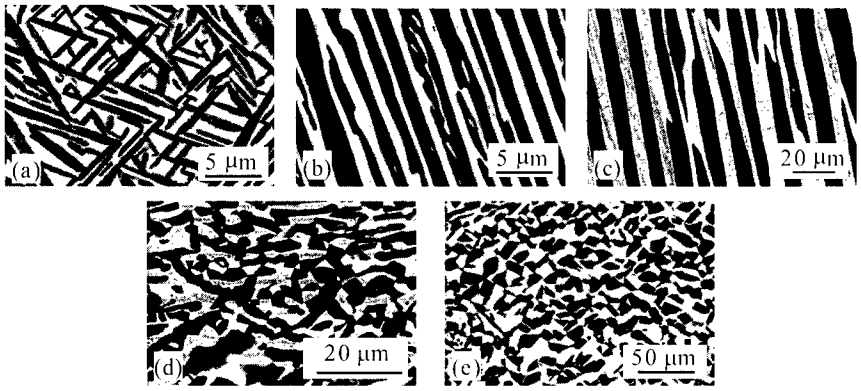

Figure 3. Backscattered-electron micrographs of Ti-6Al-4V microstructures developed in thermomechanically processed plate following water quenching from 900°C: (a) A, (b) B, (c) C, (d) D, and (e) E. See Tables 2 and 3 for processing details and description of microstructures.

crystallographic textures of the A, B, and C samples were similar to each other, and the textures of the D samples were similar to those of the E samples.

2.2 Hot Compression Tests

Isothermal, hot compression tests were conducted on the various lots of Ti-6Al-4V to determine the effect of preform microstructure and texture on plastic flow behavior at conventional hot forging temperatures and strain rates. For this purpose, cylinders measuring 10-mm diameter x 15-mm height were machined. The cylinder axis/compression direction was cut (i) parallel to the bar axis (Bar-A, Bar-B samples), (ii) at 0°, 45°, or 90° to the rolling direction (L, 45, or T directions) or in the short transverse (ST) direction (BiM, FG, BACC samples), or (iii) parallel to the rolling direction (A, B, C, D, E samples). The ends of each compression specimen were grooved for retention of the glass lubricants used during upset

testing. Samples were heated to a test temperature of 815, 900, or 955°C, soaked for 10 minutes, and then compressed under either constant-strain-rate or strain-rate-jump conditions in a set of induction-heated tooling. The constant-strain-rate tests, used to determine flow curves, comprised a 2:1 height reduction at a strain rate of 0.1, 1, or 10 s^{-1}. The strain-rate-jump tests (for determining the strain rate sensitivity of the flow stress) were conducted to a 3:1 height reduction using a strain-rate range of 0.1 $\leftrightarrow$ 0.5 s^{-1}; the strain rate was alternated at true-height-strain increments of 0.05.

For the constant-strain-rate tests, flow curves were estimated from load-stroke measurements (after correcting for machine compliance) assuming uniform, constant volume deformation. Finite-element-method (FEM) analysis of the isothermal, hot compression test [5] has shown that this method of data reduction provides a relatively good estimate of constitutive behavior for flow-softening materials despite the inherent nonuniformities in strain and strain rate that are present in the test.

3. RESULTS AND DISCUSSION

The principal results of this investigation were the measured flow curves for Ti-6Al-4V with various microstructures. The discussion that follows is broken into sections on the flow behavior of the colony alpha, globular alpha, and bimodal microstructures.

3.1 Colony-Alpha Microstructure

Effect of Colony Size on Flow Behavior. The effect of colony-alpha size on stress-strain behavior (with fixed alpha-plate thickness and crystallographic texture) is illustrated in Figure 4 for materials Bar-A and Bar-B (Tables 2, 3, Figure 1). All of the flow curves exhibited a well-defined peak flow stress at low strains (~ 0.03) followed by noticeable flow softening and near steady-state flow at strains of the order of 0.7. For a given temperature and strain rate, the flow curves for the Bar-A and Bar-B microstructures were essentially identical with the small differences being attributable to experimental scatter.

The absence of an effect of colony size on plastic flow behavior suggests that previous hypotheses [1,6] that flow softening is due to bending and kinking of the lamellar structure are incorrect. If such flow nonuniformities were important, one might expect different peak stresses for the Bar-A and Bar-B materials whose alpha platelet length-to-thickness ratios vary by a factor of approximately three. By analogy with the von Karman theory of plastic buckling [7], such differences would be expected to give rise to noticeably different behaviors at the onset of lamellar kinking/bending, i.e., near the peak stress, an effect not observed.

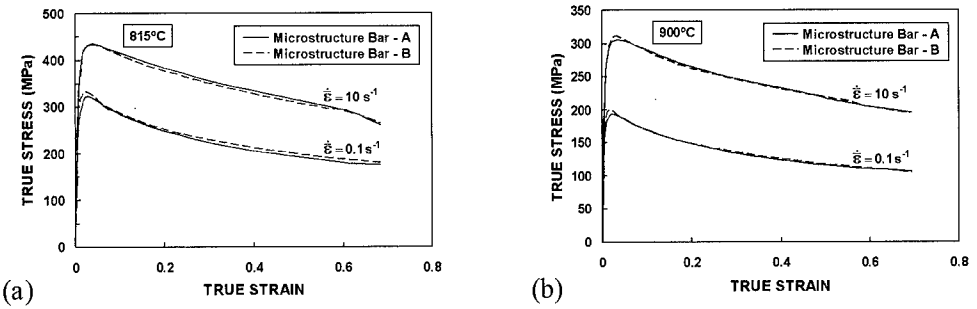

Figure 4. True stress-true strain curves for Ti-6Al-4V colony-alpha samples with microstructures Bar-A and Bar-B tested at (a) 815 C or (b) 900 C and strain rates of 0.1 or 10 s^{-1}.

The absence of a colony-size dependence of the flow behavior also suggests that plastic flow is controlled by processes occurring at a scale much finer than the grain or colony size, i.e., by the glide and climb of dislocations. Measured values of the strain-rate sensitivity of the flow stress of 0.15 to 0.25 for the Bar-A and Bar-B materials deformed at conventional hot-working temperatures and strain rates supports this conclusion as well. Further insight into deformation mechanisms for the colony microstructure is provided in subsequent sections.

Effect of Alpha Lath/Platelet Thickness on Flow Behavior. The effect of alpha lath/platelet thickness (at fixed grain/colony size and texture) on flow behavior is shown in Figure 5 using data from hot compression tests on samples cut from plate material with microstructures A, B, C (Tables 2, 3, Figures 3a-c). The shapes of the flow curves and the magnitudes of the flow stresses are very similar to those for the colony microstructure tests on the bar material (Figure 4). Strain-rate-jump-test data for the A, B, C samples also indicated that deformation at conventional hot-working temperatures and strain rates was controlled by dislocation glide/climb processes. Of greater import, however, is the noticeable effect of lath/platelet thickness on the peak flow stress $\overline{\sigma}_p$, but minimal effect on the steady state flow stress $\overline{\sigma}_{ss}$ at large strains.

The peak stress behavior is further quantified in the Hall-Petch-type plots in Figure 6. Here, the stresses have been plotted versus the inverse square root of the measured alpha

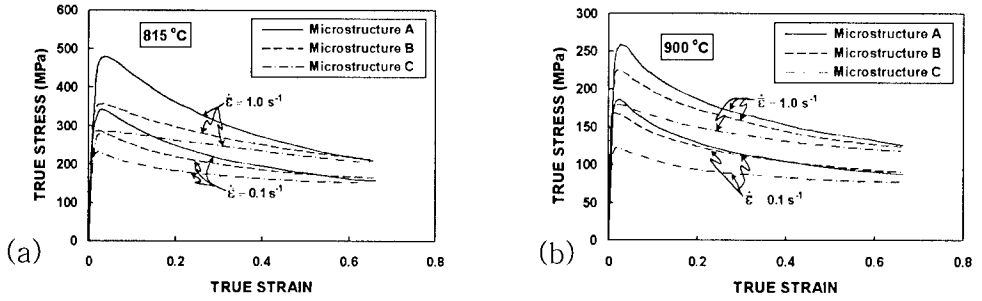

Figure 5. True stress-true strain curves for Ti-6Al-4V colony-alpha samples (microstructures A, B, C) with different alpha lath/platelet thicknesses tested at (a) 815°C or 900°C and strain rates of 0.1 or 1.0s^{-1}.

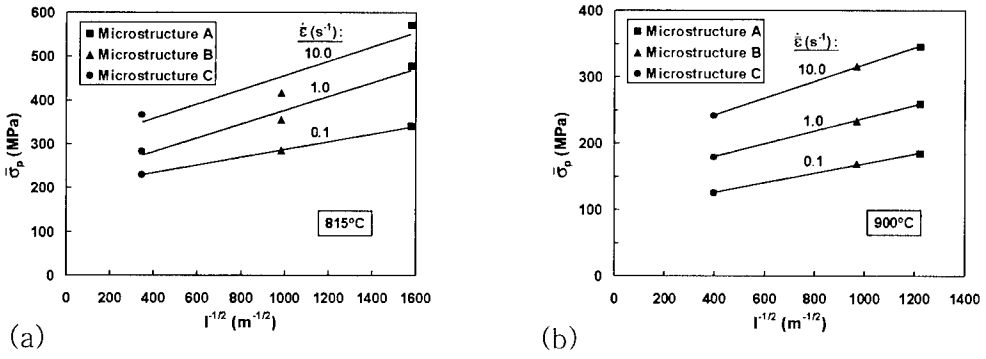

Figure 6. Plots of peak stress versus the inverse square root of the alpha lath/platelet thickness for colony-alpha samples (microstructures A,B,C) tested at (a) 815°C or 900°C.

lath/platelet thickness $\left(\ell^{-1/2}\right)$ at test temperatures of 815°C and 900°C at which the volume fraction of the (stronger) alpha phase is equal to or greater than 0.5. The $\bar{\sigma}_p$ results follow an approximately linear dependence on $\ell^{-1/2}$ which may be represented by the following expression [8]:

$$\bar{\sigma}_p = M_p \left(\tau_o + k_s \ell^{-1/2}\right), \tag{1}$$

in which M_p denotes the Taylor factor for the measured texture at low strains (≈ 3), τ_o is the apparent lattice (friction) stress for the alpha/beta microstructure in the absence of microstructural-scale effects, and k_s is a Hall-Petch-type constant which quantifies the effect of lath/platelet thickness and hence alpha-beta interfaces on strength. Taking $M_p = 3$, the data in Figure 6 yield values of k_s between approximately 0.025 and 0.055 MPa$\sqrt{m}$ with higher values found at lower temperatures and higher strain rates (Table 4). In previous work [9], these measurements were shown to be comparable to those predicted by the Eshelby (mechanistic) analysis for Hall-Petch strengthening due to grain-size effects [10]. Per this model, the observed decrease of k_s with increasing temperature and decreasing strain rate can be ascribed to (i) the decrease of shear modulus with increasing temperature and (ii) the decrease of barrier strength with decreasing strain rate, respectively.

Table 4. Hall-Petch Constants (k_s) Based on Peak Flow Stress Data for Ti-6Al-4V

Microstructure	Temperature (°C)	$k_s \left(\text{MPa}\sqrt{m}\right)$ at $\dot{\bar{\varepsilon}} \left(s^{-1}\right) =$		
		0.1	1.0	10.0
Colony Alpha	815	0.0296	0.0526	0.0547
Colony Alpha	900	0.0242	0.0322	0.0424
Globular Alpha	815	0.0203	0.0456	0.0605
Globular Alpha	900	0.0153	0.0305	-----

The data in Figure 5 and Equation (1) also provide a framework for quantifying the source of flow softening during conventional hot working of Ti-6Al-4V with a colony (or Widmanstatten) alpha microstructure. If it is hypothesized that slip transmission across alpha-beta interfaces serves as the source of dynamic globularization of the colony microstructure, flow softening may thus be attributed to the loss of Hall-Petch (interface) strengthening. The steady-state flow stress $\bar{\sigma}_{ss}$ is then simply the following:

$$\bar{\sigma}_{ss} = M_{ss}\, \tau_o - \Delta\bar{\sigma}_h, \tag{2}$$

in which M_s denotes the Taylor factor for the deformed texture, and $\Delta\bar{\sigma}_h$ is the change in flow stress due to deformation heating. In Reference 11, texture calculations revealed that the change in Taylor factor with strain is small (i.e., $M_{ss} \approx M_p$ to a first order). Hence, taking the difference of Equations (1) and (2) leads to the relation:

$$\left(\bar{\sigma}_p - \bar{\sigma}_{ss}\right) \approx M_p\, k_s \ell^{-1/2} + \Delta\bar{\sigma}_h. \tag{3}$$

Estimates of the overall level of flow softening based on Equation (3) (using measured values for k_s and ℓ, and assuming $M_p \approx 3$) agree well with measured levels such as those shown in Figure 5. Furthermore, a hybrid microstructural-/phenomenological-based flow curve for the post-peak-stress behavior may be obtained using Equations (1) and (2) and fitting an exponential curve to the data between the peak and steady state stresses viz.:

$$\bar{\sigma} = \bar{\sigma}_{ss} + \left(\bar{\sigma}_p - \bar{\sigma}_{ss}\right) \exp\left[-a\left(\bar{\varepsilon} - \bar{\varepsilon}_p\right)\right] . \qquad (4)$$

In Equation (4), $\bar{\varepsilon}$ and $\bar{\varepsilon}_p$ denote strain and the strain at the peak stress, respectively, and a is curve-fitting constant whose value is approximately equal to 3 for Ti-6Al-4V.

Effect of Texture on Flow Behavior. The effect of crystallographic texture on the flow behavior of the colony microstructure was elucidated by stress-strain data for compression tests on samples cut from various test directions in plate heat treated to obtain the BACC microstructure (Tables 2, 3, Figures 2c, f). To this end, attention was focussed on the texture of the alpha phase because of its much higher strength than the beta phase [12, 13]. Inverse pole figures for the four compression directions (Figure 7) revealed substantial crystallographic anisotropy. The compression axis was close to the [0001] direction for L (RD) and T (TD) compression tests. In contrast, the 45° and ST samples had their compression axes close to $\langle 2\bar{1}\bar{1}0 \rangle$ - or $\langle 10\bar{1}2 \rangle$ - type directions. This variation in inverse pole figures was mirrored in the BACC flow curves, examples of which are shown in Figure 8 for a strain rate of 0.1 s^{-1}. Irrespective of test temperature, the peak stresses for the L and T tests were higher than those for the ST and 45° tests. From a qualitative standpoint, the higher peak stresses for the L and T directions can be rationalized on the basis of the [0001] texture component, which is especially strong for the L experiments (Figure 7). Compression along [0001] requires the activation of <c+a> slip, which is known to involve much higher critical resolved shear stresses than the activation of prism <a> or basal <a> slip [14].

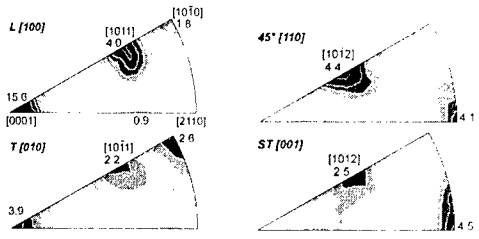

Figure 7. Inverse pole figures for the alpha phase of Ti-6Al-4V with the BACC (colony-alpha) microstructure.

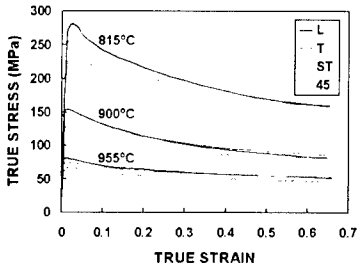

Figure 8. True stress-true strain curves for Ti-6Al-4V samples with a colony-alpha (BACC) microstructure cut from various directions (L, T, 45 , ST) of a heat-treated plate and tested at 0.1 s^{-1}.

To quantify the relation between texture and peak stress, crystal-plasticity modeling is required. For this purpose, the Los Alamos Polycrystal Plasticity (LApp) code [15] has been applied to estimate Taylor factors (M) for specific measured textures [16]. For the BACC texture, such calculations predicted a variation of peak flow stress with test direction of approximately 10 percent, rather than the observed value of 18 percent shown in Figure 8. Therefore, more advanced codes, such as that based on the viscoplastic self-consistent approach, are needed.

Figure 8 also shows that the amount of flow softening varies with test direction in such a way that comparable steady state flow stresses are achieved at large strains. In this regard, LApp calculations [11] revealed differences in texture *hardening* that explain these observations. After correcting for such differences, the likelihood of a purely microstructural source of flow softening, whose magnitude is independent of test direction and texture changes, was surmised (and quantified as discussed in the previous section).

3.2 Globular Alpha Microstructure

The principal microstructure variable that may affect the plastic flow of the globular-alpha microstructure is the alpha grain size. Sample flow curves for globular alpha samples with the same texture, i.e., microstructures D and E (Tables 2 and 3, Figures 3d, e) are shown in Figure 9. The corresponding strain-rate-jump tests revealed rate sensitivity values between 0.10 and 0.20 at strain rates of 0.1 s^{-1} or greater and temperatures of 815, 900, and 955°C. Thus, the flow response is typical of that of a material deforming by dislocation glide/climb processes.

The flow curves (Figure 9) all showed a peak stress followed by flow softening and near steady-state flow at large strains, much like the results for the colony microstructure. However, for the globular-alpha samples, the peak-stress maximum was much broader and the magnitude of the flow softening was much less.

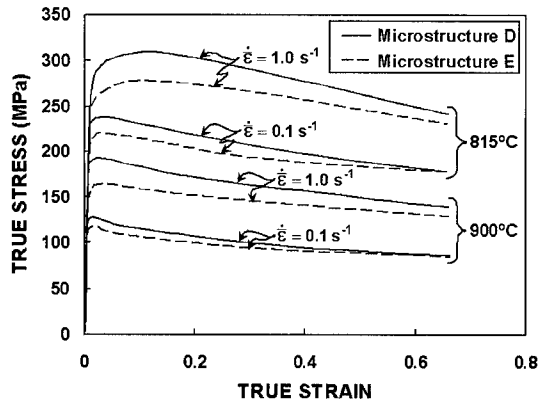

Figure 9. True stress-true strain curves for Ti-6Al-4V globular-alpha samples (microstructures D, E) with different alpha grain sizes tested at 815°C or 900°C and strain rates of 0.1 or 1.0 s^{-1}.

A Hall-Petch analysis, similar to that described above for the colony-alpha samples, was done using the peak stress values for the globular-alpha flow curves. Although based on results for only two alpha grain sizes, the k_s values (Table 4) were very similar to those measured for the colony-alpha microstructure at comparable temperatures and strain rates. Thus, the influence of alpha-beta interface strengthening on plastic flow in the dislocation glide/climb regime can be concluded to be similar for both microstructures.

The source of the broader flow stress maximum and the interpretation of the overall levels of flow softening for the globular alpha microstructure are not as readily identifiable as was the case for the colony alpha microstructure. Several factors that should be considered are the nature of the alpha-beta interface and the influence of deformation heating and texture hardening on flow softening. With regard to the first factor, the alpha-beta interface for the globular alpha microstructure is *incoherent* and thus may retard the kinetics of slip transmission that appear to control flow softening. Slip transmission may be conjectured to initiate rapidly for the colony microstructure and thus give rise to the sharper peak stress behavior observed. Secondly, because of the relatively coarse alpha grain sizes in the globular microstructures, the amount of flow softening due to the loss of alpha-beta interface strength via a slip-transmission mechanism would be small. Such small amounts are comparable to the levels of flow softening due to deformation heating. Thus, the determination of the precise magnitude of each influence is difficult even in the absence of the additional confounding effect of texture hardening/softening, whose quantitative impact must rely on advances in texture modeling.

3.3 Bimodal Microstructure

The flow curves of the bimodal microstructure (BiM) of Ti-6Al-4V (Tables 2, 3) were found to lie between those of the fully globular (FG) and colony microstructures (BACC) *when the comparison was made at fixed crystallographic texture.* Such a comparison was feasible for the case of L direction compression tests for the BiM and FG microstructures and the T direction BACC microstructure, as indicated by the inverse pole figures for the alpha phase in Figure 10. In each material, [0001], $[10\bar{1}1]$, and $[10\bar{1}0]$ texture components of comparable magnitudes were found along the compression axis.

A comparison of the BiM 'L', FG 'L', and BACC 'T' flow curves at 815°C, 0.1 s^{-1} is shown in Figure 11. At this temperature, the globular alpha grain size was ~ 12-15 μm in both the BiM and FG microstructures, and the alpha platelet thickness was ~ 1 μm in the BACC microstructure and the transformed (colony-alpha) matrix phase of the BiM microstructure. Furthermore, the volume fraction of globular and colony alpha phases in the

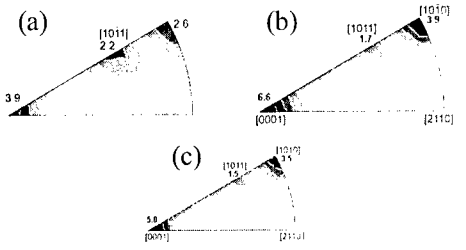

Figure 10. Inverse pole figures (IPFs) for the alpha phase of Ti-6Al-4V with the(a) colony-alpha (BACC), (b) fully globular alpha (FG), or (c) bimodal (BiM) microstructures. The IPFs are for the (a)transverse (T) or (b,c) longitudinal (L) directions in sections of heat-treated plate.

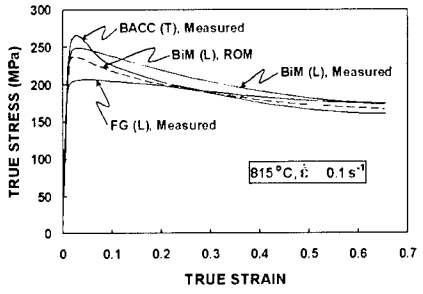

Figure 11. Comparison of measured true stress-true strain curves for Ti-6Al-4V samples with colony-alpha (BACC), globular-alpha (FG), or bimodal (BiM) microstructures tested along the transverse (BACC) or longitudinal (FG, BiM) directions at 815°C and a strain rate of 0.1 s^{-1}. The predicted (rule-of-mixtures) flow curve for the BiM microstructure is compared to the measurement.

BiM material were approximately 0.40 and 0.60, respectively. Using these volume fractions and the measured flow curves for the FG and BACC microstructures, a rule-of-mixtures (ROM) flow curve was calculated and found to be in fair agreement with the measured one (Figure 11). This agreement can be conjectured to be a result of two factors. First, the two constituents of the BiM microstructure deform similarly at 815°C; i.e., an isostrain state of deformation is enforced. Second, the flow response of the FG flow curve used in the ROM is essentially that of a single-phase alpha, with little influence of the beta matrix. This conclusion is reasonable in view of the large volume fraction of alpha at 815°C (~ 0.83) and the fact that the strength of the alpha phase at this temperature is approximately three times that of the beta phase [12, 13].

The estimation of the flow curves for the bimodal microstructure at a higher temperature (i.e., 900°C) using the ROM yielded only fair agreement. This behavior may be attributed to the neglect of the increased influence of the beta matrix of the fully globular structure on its flow curve, or a factor which must be eliminated in assessing the contribution of the globular alpha phase flow stress in the bimodal microstructure.

4. SUMMARY AND CONCLUSIONS

The plastic flow behavior of Ti-6Al-4V was measured using isothermal, hot compression testing of samples with various microstructural conditions. Tests were conducted at temperatures and strain rates at which deformation was controlled by dislocation glide and climb processes. The following conclusions were drawn from this work:

(i) The plastic flow of Ti-6Al-4V with a colony-alpha microstructure is independent of grain/colony size but greatly affected by alpha lath/platelet thickness and crystallographic texture, particularly at low strains. The loss of Hall-Petch-like interface strengthening can explain the magnitude of the observed flow softening.

(ii) A comparable Hall-Petch-like effect is seen in the flow curves for Ti-6Al-4V with a globular-alpha microstructure. The quantification of the flow softening possibly associated with the loss of Hall-Petch strengthening in this microstructure is difficult because of its small magnitude (at typical alpha grain sizes) and the confounding effects of deformation heating and texture hardening/softening.

(iii) The plastic flow behavior of the bimodal microstructure in Ti-6Al-4V *at low hot working temperatures* (~ 815°C) follows a rule-of-mixtures relation to the flow curves of the fully globular and colony microstructures, thus implying isostrain deformation of the constituent phases.

5. ACKNOWLEDGEMENTS

This work was conducted as part of the in-house research activities of the Metals Processing Group of the Air Force Research Laboratory's Materials and Manufacturing Directorate. The support and encouragement of the laboratory management and the Air Force Office of Scientific Research (Dr. C.S. Hartley, program manager) are gratefully acknowledged. One of the authors (TRB) was supported through Air Force Contract No.

F33615-94-C-5804. The assistance of P. Fagin in conducting the experimental work and L.A. Farmer in preparing the manuscript is also much appreciated.

REFERENCES

1. S.L. Semiatin and G.D. Lahoti, *Metall. Trans. A*, Vol. 12A (1981), pp. 1705-1717.
2. E.B. Shell and S.L. Semiatin, *Metall. Mater. Trans. A*, Vol. 30A (1999), pp. 3219-3229.
3. H.J. Rack and A. Wang, in *Titanium '92: Science and Technology*, F.H. Froes and I. Caplan, eds., TMS, Warrendale, PA, 1993, pp. 1379-1386.
4. S. Guillard, M. Thirrukkonda, and P.K. Chaudhury, in *Advances in the Science and Technology of Titanium Alloy Processing*, I. Weiss, R. Srinivasan, P.J. Bania, D. Eylon, and S.L. Semiatin, eds., TMS, Warrendale, PA, 1996, pp. 93-100.
5. S.I. Oh, S.L. Semiatin, and J.J. Jonas, *Metall. Trans. A*, Vol. 23A (1992), pp. 963-975.
6. R.M. Miller, T.R. Bieler, and S.L. Semiatin, *Scripta Mater.*, Vol. 40 (1999), pp. 1387-1393.
7. A. Nadai, *Theory of Flow and Fracture of Solids*, Vol. I, McGraw-Hill, New York, 1950, chapter 23.
8. R. Armstrong, I. Codd, R.M. Douthwaite, and N.J. Petch, *Phil. Mag.*, Vol. 7 (1962), pp. 45-58.
9. S.L. Semiatin and T.R. Bieler, paper submitted to *Acta Mater.*, 2001.
10. J.D. Eshelby, *Phys. Stat. Solidi*, Vol. 3 (1963), pp. 2057-2060.
11. S.L. Semiatin and T.R. Bieler, communication submitted to *Metall. Mater. Trans. A*, 2000.
12. I. Weiss and S.L. Semiatin, *Mater. Sci. Eng. A*, Vol. A263 (1999), pp. 243-256.
13. I. Weiss and S.L. Semiatin, *Mater. Sci. Eng. A*, Vol. A243 (1998), pp. 46-65.
14. N.E. Paton, J.C. Williams, and G.P. Rauscher, in *Titanium Science and Technology*, R.I. Jaffee and H.M. Burte, eds., Plenum Press, New York, 1973, pp. 1049-1069.
15. J.S. Kallend, U.F. Kocks, A.D. Rollett, and H.-R. Wenk, *Mater. Sci. Eng. A*, Vol. A132 (1991), p. 1.
16. S.L. Semiatin and T.R. Bieler, paper submitted to *Metall. Mater. Trans. A*, 2000.

CHARACTERISTICS OF TITANIUM SILICIDES FORMED BY HIP IN TI-FE-SI ALLOYS

Hi-Won Jeong, Seung-Eon Kim, Yong-Taek Hyun and Yong-Tai Lee

Korea Institute of Machinery and Materials, Changwon 641-010, Korea

ABSTRACT

Silicon addition in titanium alloys generally results in solid solution hardening by silicon itself and precipitation hardening by titanium silicides. The morphology and distribution of the titanium silicides depend upon the alloy chemistry or the heat treatment condition, and play an important role in improving the mechanical properties of the alloys. In this study, the morphology and crystallographic characteristics of the titanium silicides in the Ti-Fe-Si alloy system were studied.

Three types of silicides were found in the alloys ; (1) interconnected chain-like silicides at grain boundary, (2) coarse silicides over 1μm, (3) fine silicides smaller than 0.2μm.

Ti_3Si was dominant in cast + HIP condition while Ti_5Si_3 was dominant in as-cast state. It is recognized that $Ti_5Si_3 \rightarrow Ti_3Si$ transition occurred by the peritectoid reaction and it may be promoted by the pressure during HIP. However, in the case of the fine silicides, Ti_3Si and Ti_5Si_3 were found simultaneously even after HIP. Such a fine silicide was found to have a crystallographic orientation relationship with β matrix.

1. INTROCUCTION

Silicon is generally added in commercial titanium base alloys with a range from 0.08 to 0.5wt% to improve the high temperature mechanical properties and the oxidation resistance of the alloys. Si usually exists as an element itself or a titanium silicide precipitate. Titanium silicide can be formed during solidification and also during subsequent heat treatment. The morphology of the titanium silicide depends upon the alloy chemisty or the heat treatment condition, and plays an important role in improving the mechanical properties.

Ti_5Si_3 is a typical silicide in Zr-free alloys, while $(Ti, Zr)_5Si_3$(called S1) and $(Ti, Zr)_2Si$(called S2) are found in Zr-bearing alloys. Pietrikowsky first observed Ti_5Si_3 in 1951, and Ti_5Si_3 was originally considered to be the most titanium-rich silicide by Hansen.[1,2] Since Ti_3Si was first reported by Schubert and Von Rossteuscher in 1964, Ti_3Si has been known to be a most titanium-rich silicide stable below 1170°C. They proposed that Ti_5Si_3 was replaced by Ti_3Si through a peritectoid reaction. However, the peritectoid reaction was so sluggish that the replacement was only partially occurred by the heat treatment at 1000 °C for 72hrs, followed by aging at 750 °C for 20hrs. It was also observed by Svenchnikov *et al.* that Ti_3Si phase formed through a peritectoid reaction by the heat treatment at 1220 °C for 120hrs, followed by aging at 1000 °C for 115hrs. However they did not observe the Ti_3Si formation by the heat treatment at 1220 °C for 120hrs, followed by aging at 800 °C for 200hrs. They also stated that the peritectoid reaction was incomplete even at 1000 °C[2].

In preliminary study, we observed that Ti_5Si_3 was totally replaced by Ti_3Si through a hot isostatic pressing at 900 °C for 2hrs in Ti-Fe-Si alloys. The morphology of titanium silicide was changed by the alloy chemisty and HIP, and affected the mechanical properties of Ti-Fe-Si alloys. Although many studies have been conducted about the crystallographic characteristics of Ti_5Si_3, $(Ti, Zr)_5Si_3$, and $(Ti, Zr)_2Si$ formed by aging in various alloy systems, that of titanium silicide formed by HIP in Ti-Fe-Si system has never been reported.

Therefore, the present study concentrated on investigating the morphology and the crystallographic characteristics of titanium silicide formed by HIP as a function of alloy chemistry in Ti-Fe-Si alloys.

2. EXPERIMENTAL PROCEDURE

The ternary systems, Ti-Fe-Si, simultaneously containing 0.5, 1, 2, 4 wt% of Fe and Si were designed. The 40g buttons of these alloy systems were manufactured in the vacuum arc remelting furnace which employed a water-cooled copper hearth, non-consumable tungsten electrode. The high purity of argon was used to provide a protective inert atmosphere, and the titanium getter was melted to eliminate all interstitial gases like oxygen and nitrogen from the furnace atmosphere before the designed alloys being melted. This process was repeated five times, and the buttons were inverted on each melting to ensure the homogeneity. The melted button-shaped ingots were cast into rod-shaped ingots (8.5mm in diameter and 65mm in length) with a centrifugal casting device, which employed a non-consumable tungsten electrode, permanent copper mold, triggering system by the springs. In centrifugal casting the high purity of helium was used as atmosphere. The rod-shaped ingots were hot-isostatic-pressurized at 900°C, 100MPa for 2hrs.

The microstructures of the alloys were examined by an optical microscope and a scanning electron microscope(JSM-5800). The samples were etched in Kroll solution. A thin slices were prepared for TEM (JEOL-2010) and mechanically ground to about 100μm and electrolytically thinned using a twin jet polishing unit in a solution containing 10vol% perchloric acid in methanol at –30° C. The accelerating voltage of TEM was 200keV.

3. RESULTS AND DISCUSSION

Fig. 1 shows the scanning electron micrographs of the as-cast and the as-HIP'ed Ti-4Si alloy, respectively. The plate-like titanium silicides formed at the prior β grain boundary of the as-cast ingots transformed into the interconnected chain-like titanium silicides.

Fig. 2 shows the X-ray diffraction patterns of the as-cast and the as-HIP'ed Ti-4Si alloy. Indexing of the XRD peaks for the as-cast Ti-4Si alloy showed that Ti_5S_3 was found only as the silicide phase. However, those were replaced by the new peaks of the as-HIP'ed alloy. It is obvious from Fig. 1 and Fig. 2 that hot isostatic pressing changed the morphology and chemistry of titanium silicide of the as-cast alloy. As a result of XRD and TEM analysis, the new phase were corresponding to Ti_3Si phase.

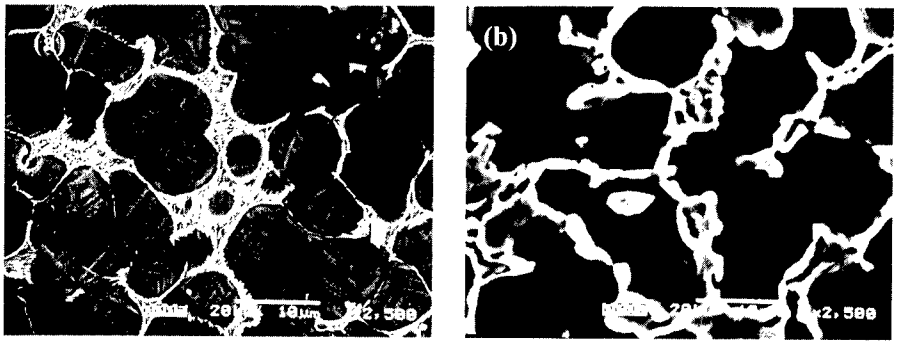

Fig. 1 SEM micrographs of Ti-4Si alloy. (a) as-cast, (b) as-HIP'ed

Fig. 3 shows the morphology of titanium silicides after hot-isostatic pressing. There were three kinds of titanium silicides as follows;(1) the chain-like titanium silicides formed at β grain boundary, (2) the coarse titanium silicides of over 1μm in size, (3) the fine titanium silicides of smaller than 0.2 μm. Only the fine titanium silicides of smaller than 0.2μm were found in the alloy containing 0.5wt% of silicon. The fraction of the coarse silicides increased with increasing Si content.

Fig. 4 shows a TEM bright field image, and a SAD pattern for the coarse titanium silicide bigger than 1μm. This silicide was identified as Ti_3Si which has a tetragonal structure (space

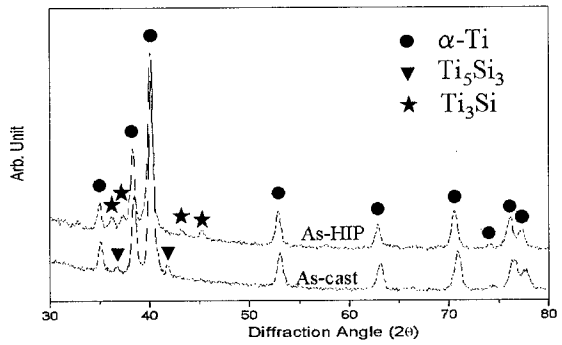

Fig. 2 XRD analysis of the as-cast(lower) and the as-HIP'ed(upper) Ti-4Si alloy.

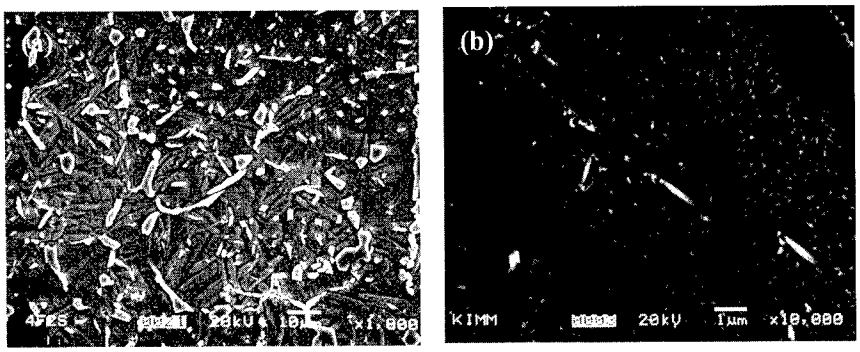

Fig. 3 Silicides morphology of Ti-4Fe-2Si. (a) Chain-like and coarse silicides, (b) fine silicides

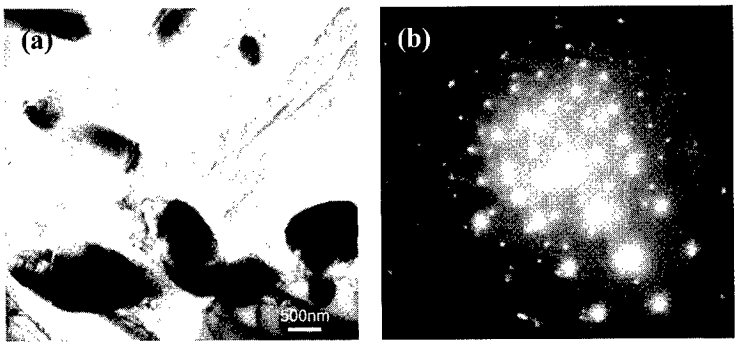

Fig. 4 A TEM image (a) and a SAD pattern (b) for the coarse titanium silicide bigger than 1μm in as-HIP'ed Ti-4Fe-2Si alloy. zone axis is $[2\bar{1}\bar{1}3]_\alpha$ and $[123]_t$, respectively.

group : $P4_2/n$, a=1.0196nm, c=0.5097nm)[3] and did not have any crystallographic orientation relationship with matrix.

Fig. 5 shows TEM bright field and dark field image, and a SAD pattern for the fine silicide below 0.2μm in as-HIP'ed sample. The silicides were identified as a hexagonal Ti_5Si_3 (designated as h) (space group : $P6_3/mcm$, a=0.74610(3)nm, c=0.51508(1)nm)[3] or a tetragonal Ti_3Si (designated as t). Fig. 5 (b) is the dark field image of Ti_5Si_3 of which zone axis is $[2\bar{1}\bar{1}6]$.

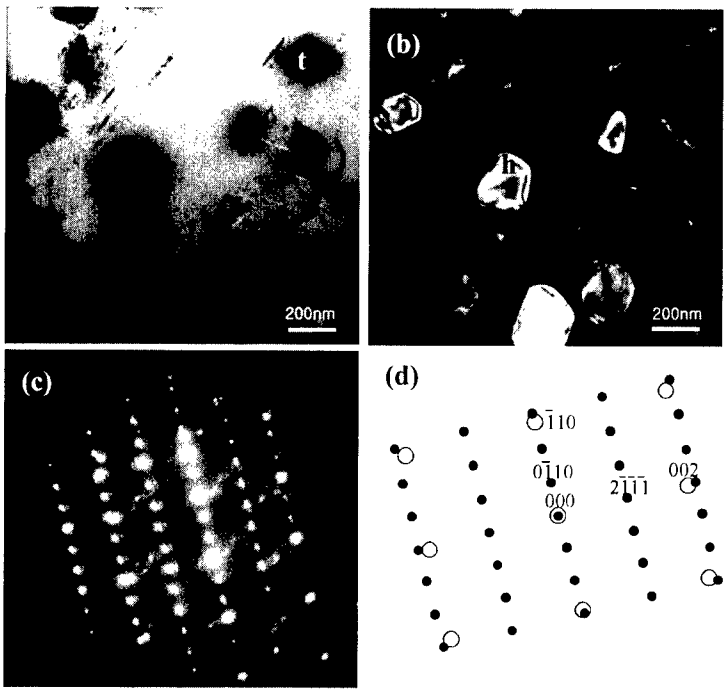

Fig. 5 Transmission electron micrographs and SAD pattern for titanium silicide below 0.2μm in as-HIP'ed Ti-4Fe-2Si alloy. (a) Bright field image, (b) Dark field image, (c) SAD pattern of Ti_5Si_3 and matrix, zone axis : $[110]_\beta$, $[2\bar{1}\bar{1}6]_h$

Ti_5Si_3 had the following orientation relationship with matrix, as shown in Fig. 6.

$$[110]_\beta // [2\bar{1}\bar{1}6]_h,\ (1\bar{1}0)_\beta // (01\bar{1}0)_h$$

Fig. 6 shows a stereographic projection based on the composite SAD pattern in Fig. 5 (c). When the [110] direction of β matrix is parallel to the $[2\bar{1}\bar{1}6]$ of Ti_5Si_3, the closest direction [111] of matrix and the [0001] of Ti_5Si_3 are misoriented by 0.6°. The SAD pattern was also examined from the [111] direction shown in Fig. 7. It was clear that the [111] and the [0001] were also parallel. The difference of 0.6° can be attributed to the c/a ratio of Ti_5Si_3 and thus it can be negligible.

By the way, Ping *et al.* has reported the following orientation relationship between Ti_5Si_3 and β-matrix.[5]

$$[001]_\beta // [11\bar{2}3]_h,\ (\bar{1}10)_\beta // (1\bar{1}00)_h,\ (110)_\beta // (\bar{1}\bar{1}22)_h$$

This relationship is consistent with that of the present study, as shown in the stereographic projection in Fig. 7.

Fig. 8 shows a SAD pattern of titanium silicide that was not diffracted in the dark field image, as shown in Fig. 5 (b). This phase was identified as a tetragonal Ti_3Si and had an orientation relationship with β-matrix as follows.

$$[001]_\beta // [111]_t,\ (110)_\beta // (\bar{1}10)_t$$

When the [001] direction of β matrix was parallel to the [111] direction of Ti_3Si, the closest direction of matrix, $[1\bar{1}1]$ and the $[\bar{1}\bar{1}2]$ direction of Ti_3Si were parallel. From these

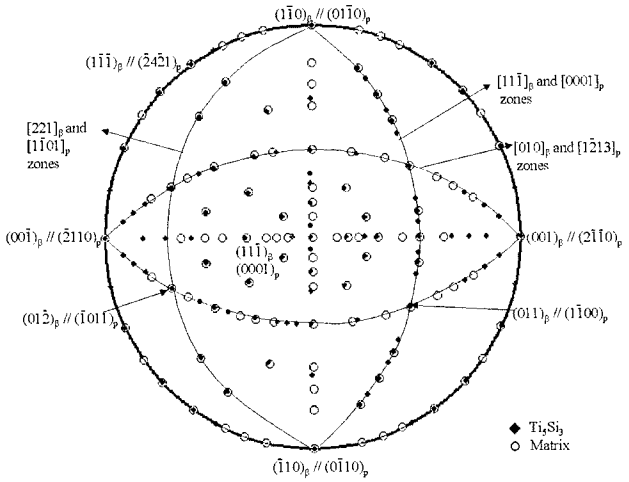

Fig. 6 Stereographic projection of β Ti matrix and Ti_5Si_3 based on $[110]_\beta // [2\bar{1}\bar{1}6]_h$.

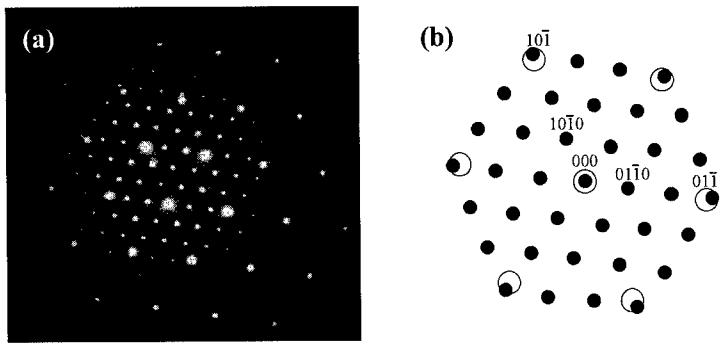

Fig. 7 SAD pattern for the Ti_5Si_3 and β matrix in the as-HIP'ed Ti-4Fe-2Si alloy. zone axis : $[111]_\beta$, $[0001]_h$

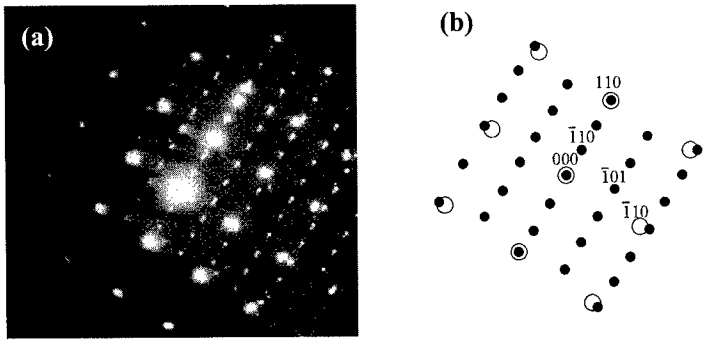

Fig. 8 SAD pattern for the Ti_3Si and β matrix in the as-HIP'ed Ti-4Fe-2Si. zone axis : $[001]_\beta$, $[111]_h$

orientation relationships, it was thought that the fine Ti_5Si_3 and Ti_3Si formed and grew at the closest plane {110} and direction <111> of β matrix.

Pretorius[4] has reported that Ti_5Si_3 formed earlier than any other phases in titanium-rich part of Ti-Si binary because this is congruent phase. Many studies have showed that Ti_5Si_3 formed first and Ti_3Si formed through subsequent heat treatment at high temperature and for a long time. Salpadoru suggested that this phenomenon be due to the very sluggish peritectoid reaction of $\beta+Ti_5Si_3 \rightarrow Ti_3Si$. However, Ti_3Si formed by HIP at 900°C for 2hrs, which are relatively low temperature and short time, in present study. This may be attributed to the pressure of 100MPa during HIP. It was thought that the pressure promoted the peritectoid reaction during HIP.

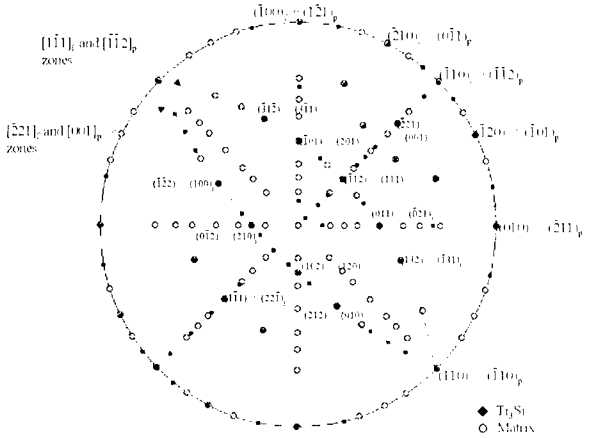

Fig. 9 Stereographic projection of fine Ti_3Si and β Ti matrix based on $[001]_\beta // [111]_t$.

4. SUMMARY

The study on characteristics of titanium silicides formed by HIP in Ti-Fe-Si alloys is summarized as follows.

1) The pressure promoted the peritectoid reaction related to the formation of Ti_3Si during HIP.
2) Three types of silicides were found in the Si-bearing titanium alloys ; (1) interconnected chain-like silicides at grain boundary, (2) coarse silicides bigger than 1μm, (3) fine silicides smaller than 0.2μm.
3) The fine silicide was identified to be Ti_5Si_3 and Ti_3Si and had a crystallographic orientation relationship with β matrix as follows.

$$[110]_\beta // [2\bar{1}\bar{1}6]_h,\ [111]_\beta // [0001]_h,\ (1\bar{1}0)_\beta // (01\bar{1}0)_h.$$
$$[001]_\beta // [111]_t,\ (110)_\beta // (\bar{1}10)_t$$

REFERENCE

1. K. Schubert, K. Raman, W. Von Rossteuscher : Naturwissenschaften, **5** (1964) 506
2. N.H. Salpadoru, H.M. Flower : Metall. Trans. A, **26A** (1995) 243
3. P. Villare, L. Calvert : Pearson's Handbook of Crystallographic Data for Intermetallics phases, 2nd editon, ASM, Ohio **4** (1991)
4. R. Pretorius, T.K. Marais, C.C. Theron : Mater. Sci. & Eng., **10** (1993) 1
5. D.H. Ping, G.P. Li, Y.G. Wang, Y.D. Yu, D.X. Li, H.Q. Ye : Mater. Letters **24** (1995) 121

THE ROLE OF FILLER MATERIAL IN 360°COLD BENDING Ti-6Al-4V LARGE-DIAMETER SEAMLESS TUBE

Hur, Sun-Moo*, Park, Jong-Seung**

* Principal researcher and ** Senior researcher in Agency for Defense Development,Yuseong P.O.Box 35-5,Taejon City 305-600,SEOUL, KOREA

ABSTRACT

The 360°bending of Ti-6Al-4V large diameter seamless tube(OD >60 mm and wall thickness >4.0 mm) has been achieved at room temperature without heating. Cerro Tru^{TM}(Bi-42Sn) was used as a filler to get : (1) Improved ovality of tube after bending, and (2)enhanced consistency of wall thickness during bending. As compared to lead or sand, Cerro Tru^{TM} has a low melting point(138℃), density(8.7g/cm^3) and a tensile strength of 56 MPa so that the 360° cold bending of Ti-6Al-4V large diameter seamless tube might be possible. The resultant ovality(out of roundness)obtained was 1.28%, compared with 7.16% without applying Cerro Tru^{TM}.

1. INTRODUCTION

Since the early 1970's Ti-3Al-2.5V has been standard for titanium hydraulic tubing. Recently[1,2],however,seamless tube was produced from Ti-6Al-4V(Ti-64) alloy ,which has 20 ~ 30% increase in strength[4,5] and specific strength(i.e. the ratio of strength to density) over Ti-3Al-2.5V.

Since the internal pressure, P of a tube vessel can be described as

$$P = 2t\sigma_{UTS}/OD \quad \cdots\cdots (1)$$

(t=wall thickness of tube, σ_{UTS} =tensile strength of tube, OD=outer diameter of tube)

about 20 ~ 30% increase in internal pressure for Ti-64 tube vessel over Ti-3Al-2.5V can be applied.

Ovality in tube bending is defined as

$$\% \equiv 100 \times (D_{max} - D_{min})/D_{nom}, \quad D_{nom} \equiv (D_{max} + D_{min})/2,$$

where D_{max} and D_{min} refer to the maximum and minimum tube diameter, respectively. Ovality[7] limitations in tube bending for aerospace applications are also influenced by the formability of Ti-64. To improve ovality, lead and sand[9] would normally be employed as a filler. However, they have been found to be ineffective in large-diameter Ti-64 tube with large wall thicknesses. Cerro Tru^{TM} is found to be effective as a filler for that purpose[8] (Fig.3).

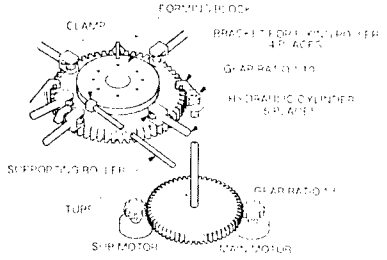

Fig.1.Schematic view of the rotary 360° bending machine

Recently, the 360°bending of Ti-6Al-4V large diameter seamless tube(OD >60 mm and wall thickness >4.0 mm) at room temperature without heating has been achieved through a two-step process[8]. The first step is 360° bending by a powered rotary bender(Fig.1). Spring back, which measures the distance between two ends of the tube after removal of the supporting rollers, is subsquently eliminated by the second or finishing step, which comprises repeated bending processes with a controlled small strain rate by a powered three-roll bender(Fig.2). Fig.3 shows the flow of the cold bending processes, where process I represents bending without a filler.

But tube wall thicknesses, t undergo changes during bending process, i.e. increase or decrease, the magnitude of which are not known, but important since the minimum(i.e. not nominal) value of t in vessel determines the rupture pressure of the vessel[Eq.1] .

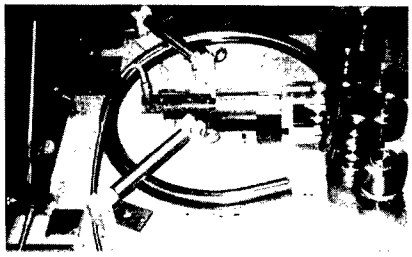

Fig.2. The three-roll bending machine for the elimination of tube spring back[8].

The effect of a filler, Cerro Tru^{TM} on ovality and variation of wall thicknesses of tube, during the 360°cold bending of Ti-6Al-4V large diameter seamless tube are discussed.

2. Ti-6Al-4V LARGE-DIAMETER SEAMLESS TUBE

Table1 and Table 2 show chemical compositions, mechanical properties and size of seamless tube, respectively.

Table 1.Chemical compositions of seamless tube(%)

C	Al	V	Fe	O	N	H	Ti	OT	Remark
.032/ .029	6.27/ 6.34	4.22/ 4.19	.22	.18/ .16	.031/ .030	.0027/ .0021	Bal	.06	Y.0010

Table2.Mechanical properties and size of seamless tube

UTS (MPa)	.2%YS (MPa)	%El	RA(%)	Size(mm)	
				OD	t*
1,018.5	936.6	16.4	42.0	62.37	4.4
* t ± 10 %					

3. 360° COLD BENDING OF Ti-6Al-4V LARGE-DIAMETER SEAMLESS TUBE

Fig.3 shows the flow sheet of 360° cold bending processes of Ti-64 large diameter seamless tube for the two cases including and excluding application of Cerro Tru™ as a filler. After bending step surface of tube was cleaned in the solution of nitric acid and hydrofluoric acid after removal of Cerro Tru™. The inner surface of tube was then visually inspected through endoscope. Finally penetration test was performed for detection of crack of the bent tube.

	Process I	Process II(CT™ process)	Remarks
1	Ti-64 Seamless tube(Annealed)	Ti-64 Seamless tube(Annealed)	Thickness & ovality
2	none	To fill the tube with Cerro Tru™ by melting and pouring into preheated tube with a capped end.	150 °C
3	360° bending of the tube in the powered rotary bending machine	360° bending of the tube filled with Cerro Tru™ in the powered rotary bending machine	Allowing resultant spring back
4	To eliminate the spring back in the three-roll bender through application of controlled strain rate.	To eliminate the spring back in the three-roll bender through application of controlled strain rate.	The finishing step of bending
5	none	To melt Cerro Tru™ out in low temperature(150 °C) after cutting the capped portion of tube	Thickness & ovality

6	none	To clean the inner and outer surfaces of the tube in the solution of nitric and hydrofluoric acid	
7	none	Visual inspection through endoscope coupled with monitor	
8	Penetration test in order to detect potential cracks nondestructively	Penetration test in order to detect potential cracks nondestructively	
9	Ti-64 seamless tube bent 360° ready for stress relieving treatment.	Ti-64 seamless tube bent 360° ready for stress relieving treatment.	

Fig.3. Flow sheet of 360° cold bending processes of Ti-64 large diameter seamless tube.

4. MESUREMENT OF WALL THICKNESS OF TUBE

Fig.4. **Position of wall thickness measurement**

Before bending the wall thickness of tube was measured on the 4-equally spaced point(0°, 90°, 180°, 270°) along axial direction, every 30cm along longitudinal direction of the tube using PANAMETRICS 260L plus which uses Tranducer (PANMETRICS, Type D790SM, 10 MHZ). After bending the same measurement was performed on 4 places, including inner, upper, outer and lower points(Fig.4) along axial direction every 10 cm along longitudinal direction of the torus. The estimated error in measurement was 1/100 mm, and performed before and after bending as shown in Fig.3 for two processes respectively.

5. IMPROVEMENT OF OVALITY THROUGH APPLICATION OF Cerro Tru™

Table 3. Properties of Cerro Tru™ {values in( ) refer to values for lead}

Composition	58%Bi,42%Sn	Melting Point(°C)	138 (340)
Density(g/cm^3)	8.7(11.34)	Tensile Strength(Mpa)	56

Ovality[7](out of roundness) of tube was measured before and after each step of bending. The results of improvement of ovality through the application of Cerro Tru™ are shown in Table 4. Requirement for ovality of Ti-64 tubing after bending has not been established[6,7]. But it's limit is 3%[7] for commercially pure titanium. Ovality of Ti-64 tubing after 360°bending with application of Cerro Tru™ was found 1.28%, whereas that without Cerro Tru™ was measured 7.16%. No reaction was found between Cerro Tru™ and Ti-64 tube during processing.

Table 4. Measurement of ovality of tube

		Ovality(%)	Remarks
Reference[7]		3 for CP Ti	No data for Ti-64 seamless tube
Ti-64 seamless tube filled with CerroTru™	Starting material	0	Seamless tube as received
	After first bending	0.96	
	After 2nd bending	**1.28**	**7.16%** ,ovality without applying CT™

6. IMPROVEMENT OF WALL THICKNESS VARIATION OF TUBE DURING BENDING THROUGH APPLICATION OF Cerro Tru™

Fig.5 shows the variation in thickness of tube before(Fig.5-1) and after(Fig.5-2) bending for the process I, i.e. **without application** of **Cerro Tru™** . As had been estimated from geometrical constraint of tube during bending, there were no significant changes in t for upper and lower part of tube, but t in outer part showed decrease and t in inner part increase due to the increase of tube length in outer part. Table 5 shows the summary of quantitative variations in t during the bending process I . Overall thinning in outer portion is 11%,compared to 1% thickening in inner portion.In the other part, length of tube increased after bending, due to plastic deformation which tube experience between forming block and supporting roller during bending. The increment in the length of 2,320mm tube was 72mm,which corresponds to 3.1% of the original length and is believed to be from overall thinning of tube.

Fig.6 shows the variation in thickness of tube before(Fig.6-1) and after(Fig.6-2) bending for the process II ,i.e. **with application** of **Cerro Tru™** . The overall trends in

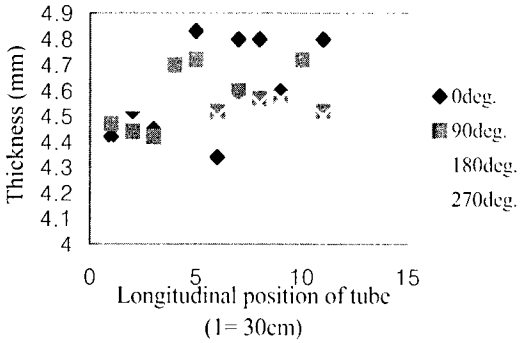

Fig. 5-1.Thickness of tube prior to bending(process I)

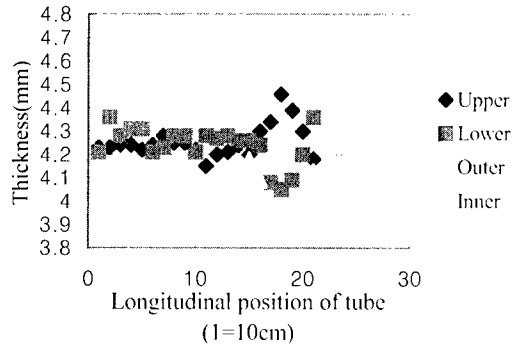

Fig. 5-2. Thickness of tube after bending(processI)

Table5. Variation of tube thickness before and after bending(process I)(mm)

		average	minimum	maximum
Before bending		4.55 (1.00)	4.32 (0.95)	4.83 (1.06)
After bending	outer	4.05 (0.89)	3.90 (0.86)	4.83 (1.06)
	inner	4.58 (1.01)	4.48 (0.98)	4.72 (1.04)

Values in( ) refer to relative value with respect to average of starting material

the variation of thickness are similar with those in bending process I(Fig.5), but no overall thickening in the inner part of torus was found (table 6)and the overall magnitude of thinning in outer part was far smaller than that in bending process I. The increase in t of inner part of torus and decrease in t of outer part beyond 1,500mm shown in Fig.6-2 are believed to be due to role of CT^{TM} in tube during bending,i.e. might have played as an inner roller during repeated bending.

From table 5 and 6, role of CT^{TM} in tube during bending may be said to contribute to

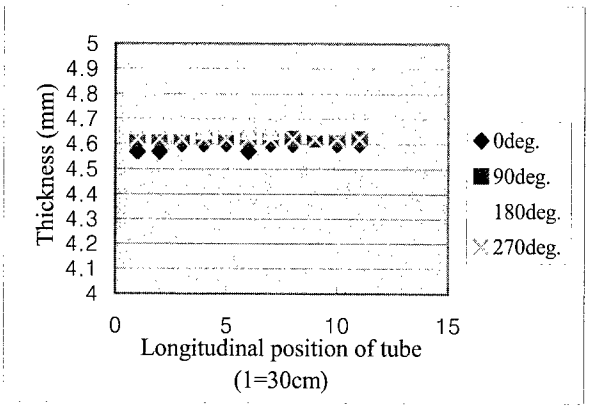

Fig. 6-1. Thickness of tube prior to bending(process II)

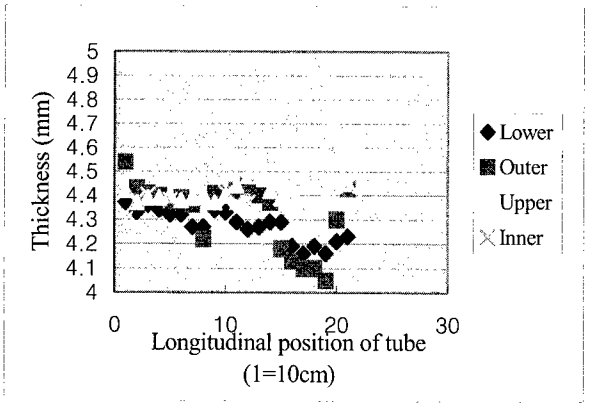

Fig. 6-2. Thickness of tube after bending(process II)

Table6. Variation of tube thickness before and after bending (process II)(mm)

		average	minimum	maximum
Before bending		4.62 (1.00)	4.57 (0.99)	4.67 (1.01)
After bending	outer	4.32 (0.95)	4.05 (0.88)	4.54 (0.98)
	inner	4.52 (0.98)	4.30 (0.93)	4.91 (1.06)

Values in( ) refer to relative value with respect to average of starting material

reduce magnitude of discrepancy in thickness before and after bending for some range of length of tube.

When considering the 3.10% increase in length of tube, maximum 14% decrease in thickness of outer portion of tube after bending, these dimensional changes should be taken account into for the optimum design of a vessel .

7. CONCLUSIONS

- The ovality of Ti-6Al-4V large-diameter seamless tube after 360°cold bending was 1.28% by employing CT™ as a filler, compared to 7.16% without a filler.
- During 360°cold bending Ti-6Al-4V large-diameter seamless tube, the tube thickness showed decrease in the outer point of torus whereas increase in the inner point.
- With applying CT™ as a filler the overall magnitude of tube thickness variation after bending decreases compared to that without applying CT™.
- When considering the 3.10% increase in length of tube and maximum 14% decrease in thickness of outer portion of tube during bending, these dimensional changes should be taken account into for the optimum design of a vessel .

REFERENCES

1. S. Meredith and P. Finden, "Production of Seamless Ti-6Al-4V Tubing", Titanium 95: Science and Technology, Proceedings of the 8th World Conference on Titanium, Edited by P.A.Blenkinship, W.J.Evans and H.M.Flower, The Institute of Materials, 1996, P.755~762.
2. M. Koch, H.Sibum, H.Jelenak and E.Planker, "Seamless Thin-walled TiAl6V4 Tubes Manufactured by Flow-Forming Process", Titanium92: Science and Technology Edited by F.H.Froes and I.Caplan, The Minerals, Metals & Materials Society, 1993,P1429~1436.
3. L.L. Kollmorgen, "Titanium Tube Bending (Technical Paper NO.616)", American Society of Tool and Manufacturing Engineers, Collected Papers, Metal Forming, Book4, Library Ed., The Boeing Company, Seattle,1964,Vol.64.
4. Metals Handbook, 9th Ed. Vol. 14, April 1988, ASM International.
5. Materials Properties Handbook : Titanium Alloys, Ed. By R. Boyer, G.Welsch & E.W.Collings, ASM International, 1994, P605.
6. MIL-STD-1627C(SH),"Bending of Pipe or Tube for Ship Piping Systems", 30. September .1994 Commander, Naval Sea Systems Command, SEA 03R42 , 2531 Jefferson Davis Hwy, Arlington, VA 22242-5160 USA.
7. MS 33611,"Tube Bend Radii", April.1983, Commander, Naval Air Systems Command, Hwy 547, Lakehurst, NJ 08733-5100 USA.
8. Sun-Moo Hur and Jong-Seung Park," The 360° Cold Bending of Ti-6Al-4V Large-Diameter Seamless Tube", JOM, Vol.51, No.6 ,June 1999, p.28~30.
9.Avitzur,Betzalel : Handbook of Metal-Forming Processes,p475,1983, John Wiley & Sons, Inc..

MICROSTRUCTURE AND PROPERTIES OF TITANIUM-BASED MATERIALS SINTERED FROM TiH_2 POWDER

Hyunho Shin, Hong-Lae Park and Soon-Nam Chang

Ground Systems Development Center
Agency for Defense Development, Daejon 305-600, Korea

ABSTRACT

Two kinds of titanium-based samples with 0 and 45vol% TiC have been fabricated from titanium hydride (TiH_2) powder by hot pressing. After the processing, the TiH_2 starting powder has been transformed to titanium matrix in both samples with a hardly identifiable amount of TiH_2 in X-ray diffraction pattern. Microstructure and both static and dynamic compressive strength of the two samples have been characterized. The sintered TiH_2 specimen cooled in a fast-cooling hot press instrument shows an alpha prime microstructure. The addition of titanium carbide into TiH_2 fosters the formation of an acicular alpha in the titanium-based matrix and shows an evidence of carbon contamination of matrix from TiC, based upon scanning electron microscopy. The sintered TiH_2 and TiH_2-45vol%TiC sample show 0.2% offset yield strength of 1008 and 1446MPa, respectively, in a static compressive mode (strain rate of 1×10^{-3}/s) and dynamic (strain rate of 4×10^{3}/s) compressive strength of 1600 and 2060MPa, respectively, at ~3% strain.

1. INTRODUCTION

Numerous research on titanium-based materials have been performed for the purpose of applying these materials to light weight transport systems and others[1]. Used bulk titanium can be recycled to prepare titanium powder by the hydride dehydride (HDH) process[2-3] which involves hydration of the bulk titanium to form TiH_2, followed by pulverization and subsequent dehydration to form titanium powder. Titanium powder and the interim product TiH_2 powder by such a process are commercially available[4].
In a preliminary study of the authors' work group[5], the sinterability of TiH_2 powder was shown to be promising as compared to titanium powder, when tested using a small size specimen (~ϕ20×10mm). In the present work, TiH_2 powder and TiH_2-45vol%TiC powder mixture have been hot pressed on a large scale (~ϕ100×15mm) and then microstructure and mechanical properties of the titanium-based materials are characterized.

2. EXPERIMENTAL PROCEDURE

2.1 Sample Fabrication

Table I shows chemical composition of the raw materials[3] used in this study. In order to fabricate monolithic titanium-based disk, an appropriate amount of as-received TiH_2 powder (-200mesh) was shifted into BN-coated graphite mold (inner diameter ~ϕ100mm), followed by hot pressing at 980°C and 19.6MPa for 4 min. For the preparation of TiC reinforced titanium-based composite sample, as-received TiH_2 (-200mesh) and 45vol% TiC (-200mesh) powders were mixed by ball mill for 3hrs. Then an appropriate amount of the powder mixture

was applied to the same graphite mold, for subsequent hot pressing at 1100°C and 19.6MPa for 4 min. After sintering, both samples were cooled in hot press instrument down to 500°C, followed by air cooling thereafter. The samples were located near bottom support surface of the hot press instrument where the cooling water effect was notable during furnace cooling. The final size of the sintered specimen was ~ϕ100×15mm.

Table I. Chemical composition of raw materials (wt%)

	Fe	Mn	Mg	Si	N_2	O_2	H_2
TiH_2	0.019	0.009	0.0025	0.033	0.05	0.5~0.6	3~4
TiC	0.04	0.0015	0.002	0.02	0.08	0.5	0.035

2.2 Characterization

The sintered specimens were cut to ~ϕ20×10mm from a central portion of the sintered body by electro-dynamic wire cutting. Density of the sample was determined by water immersion method based on Archimedes' principle using the cut sample. The flat surface of the specimen normal to the hot pressing direction was further polished for microstructure characterization using scanning electron microscopy (Philips, Model XL30 FEG, The Netherlands). Qualitative X-ray diffraction analysis (continuous scan, 3°/min, RIGAKU, Japan) was also performed on a polished surface of the specimen for the identification of the crystalline phases in the sintered body.

2.3 Mechanical Property Test

A portion of the fabricated sample near center was cut to ~ϕ6×12mm shape and the flat surfaces were machined to be parallel for the static compressive strength test (Instron, Model 8502, U.S.A.). The loading direction of the compressive test was the same as the hot pressing direction during fabrication. MoS_2 and Teflon lubricants were applied to both flat specimen surfaces so that the specimen-fixture set up was: upper support plate/MoS_2/Teflon/specimen/ Teflon/MoS_2 /lower push plate. Nominal strain rate of the specimen was 1×10^{-3}/sec.
A split Hopkinson pressure bar (SHPB) instrument was used for the determination of the dynamic compressive strength of the specimen. Other central portion of the fabricated sample was cut to ~ϕ8×4mm shape and both flat surfaces were machined to be parallel. The thickness direction of the cut specimen was the direction of hot pressing during sample fabrication and it was the same as the loading direction in SHPB test. The material of the striker, incident, and output bar was maraging steel grade 350 and their diameter was 14.98mm. The velocity and length of the striker bar were ~16m/sec and 370mm, respectively. The type of the strain gauges applied at the center of the incident and output bars was ED-DY-031CF-350 (Micro-measurement, Inc.). The stress and strain information of the specimen in dynamic mode was obtained from the strain gauges attached on the surface of the output and incident bars, respectively, both of which measure transmitted and reflected strain signals, respectively[6].

3. RESULTS AND DISCUSSION

3.1 Densification and Phase Evolution

Fig.1 shows X-ray diffraction pattern of the fabricated samples and TiH_2 starting powder as a comparison standard. As apparent from Fig.1, the TiH_2 phase (JCPDF card No. 25-982 and 25-983) in the starting powder has been transformed to titanium phase after sintering while TiH_2 phase is unappreciable in XRD. The JCPDF card identified that the chemical composition of the titanium hydride was $TiH_{1.924}$ while raw material blending during processing was based upon its nominal composition TiH_2.
Density of the hot pressed TiH_2 and TiH_2-45vol%TiC were 4.06 and 4.50g/cm^3, respectively. These are 90.1 and 95.3% of theoretical density, respectively, assuming complete conversion

of TiH_2 to Ti in the matrix. If the processing temperature of the TiH_2 powder sample had been higher than 980°C like the TiH_2-45vol%TiC sample (1100°C), the densification could have been fairly enhanced.

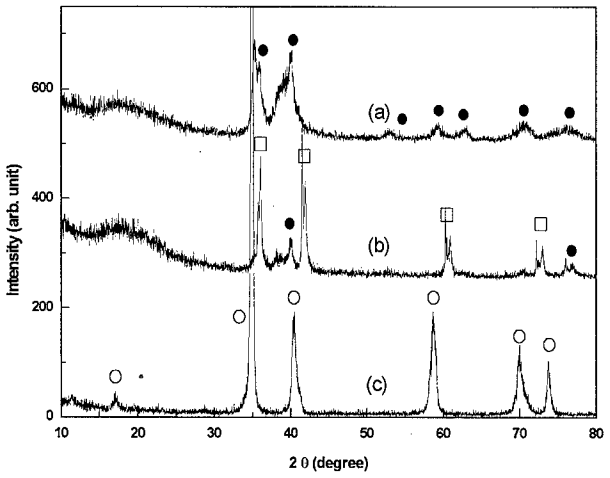

Fig.1. X-ray diffraction pattern from (a) sintered TiH_2, (b) TiH_2-45vol%TiC, and (c) TiH_2 starting powder. •: Ti, □:TiC, and O: TiH_2

3.2. Microstructural Evolution

Fig.2 shows microstructures of studied specimens. Kim et al.[2] reported that when pressurelessly sintered TiH_2 was cooled in a vacuum furnace where heat conduction (cooling) was more limited than hot press, the specimen yielded an equiaxed alpha grains. However, as can be seen in Fig.2(a), hot pressed TiH_2 in this work results in an alpha prime (martensite) titanium microstructure. This is because the cooling of the specimen was fairly fast due to the specimen location in the hot press instrument as aforementioned in section 2.1.

Figs.2(b)-2(d) show the effect of TiC addition on the microstructure of the titanium based matrix (The microstructures of TiH_2-15vol%TiC and TiH_2-30vol%TiC sample are additionally presented in this work to clarify the effect of TiC addition into TiH_2). In Fig.2(b), dark areas are TiC and relatively gray areas with bright needles are titanium-based matrix. As can be seen in Figs.2(b)-2(d), the addition of TiC yields an acicular alpha in the matrix and the length to diameter ratio of the acicular alpha decreases with TiC addition.

Concerning the salient difference in microstructures of the matrix of the two specimens (alpha prime in sintered TiH_2 and acicular alpha with the addition of TiC into TiH_2), at least the following two reasons would be associated. First, in Figs.2(b)-2(d), the boundary regions of TiC phase is less dark than the interior of TiC in the secondary electron SEM, implying the contamination of the titanium-based matrix by carbon from TiC. Since carbon is an alpha stabilizer[7], addition of the carbon source (TiC) into the matrix is interpreted to foster the beta to alpha transformation during fairly fast cooling in the same hot press instrument. This would inhibit martensitic transformation, resulting in the acicular microstructure in the TiC-added titanium-based composite samples. Second, since the heat capacity of the TiC ceramic (50.3J/mol K at room temperature) is higher than the metallic titanium matrix (26.3J/mol K at room temperature), the addition of TiC in the matrix is expected to lower the cooling rate of the composite sample as compared to the sintered TiH_2 sample. This may ensure enough time for beta to alpha transformation during cooling, resulting in the acicular alpha microstructure in the titanium-based matrix with TiC.

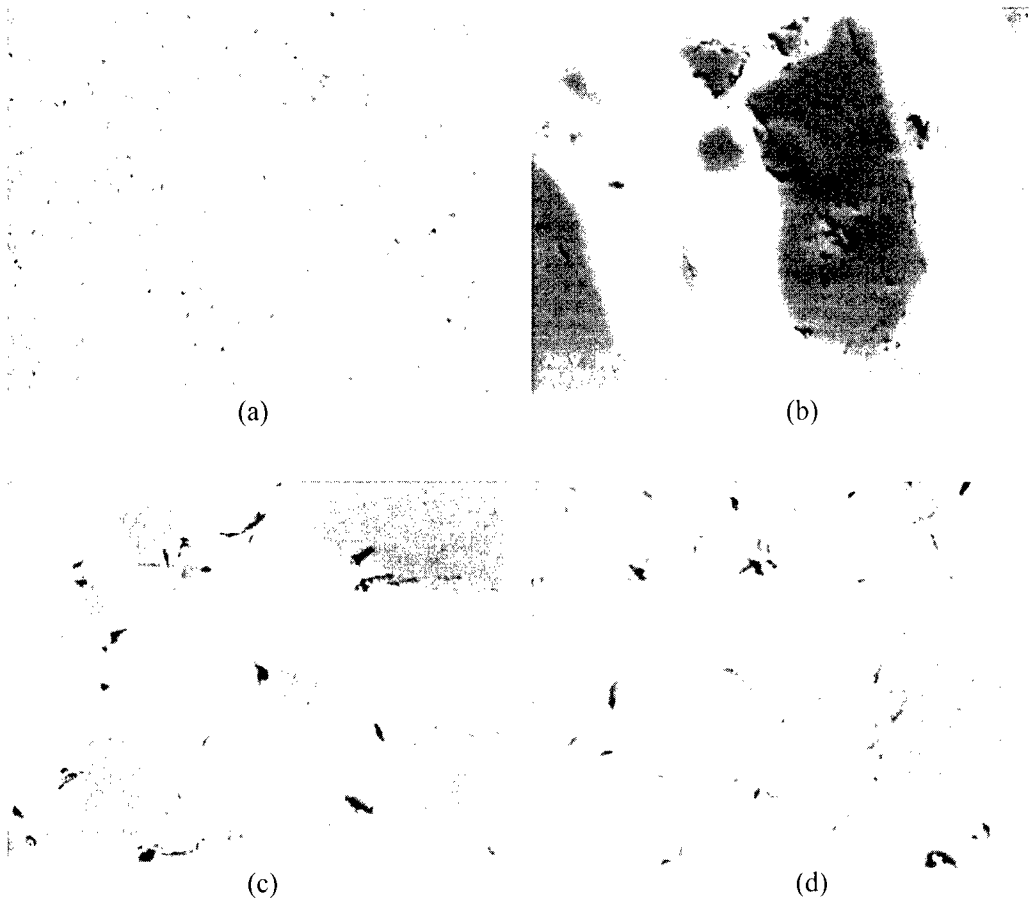

Fig.2. Scanning electron microscopy image of sintered (a)TiH_2, (b) TiH_2-15vol%TiC, (c) TiH_2-30vol%TiC, and (d) TiH_2-45vol%TiC.

3.3. Mechanical Properties

Fig.3 shows the static compressive test results at 1×10^{-3}/s nominal strain rate. In Fig.3, stress-strain curves for two TiH_2-45vol%TiC specimens (solid lines in (b)) are so close that they are hardly identifiable. Average values of 0.2% offset yield strength of sintered TiH_2 and TiH_2-45vol%TiC samples are 1008 and 1446MPa, respectively, indicating 143.5% values for TiH_2-45vol%TiC sample. Compressive strength of TiC ceramic is ~2050MPa. Bearing the obtained value of TiH_2 strength in mind, the application of the rule of mixture for compressive strength of TiH_2-45vol%TiC leads to 1477MPa, indicating fair agreement with the experimental value, 1446MPa. The lower experimental value would be associated with the microstructural change of the matrix (alpha prime to acicular alpha) with the addition of TiC.

Fig.4 shows the dynamic compressive test results at 4×10^{3}/s nominal strain rate. As shown in the figure, two TiH_2 samples indicate initial peak stress of ~1600MPa at ~3.1% strain and total failure occurs at ~10% strain. Gabelotaud et al.[8] reported that dislocation free pure alpha titanium showed stress of ~600MPa at 3% strain and total failure strain over 20% when tested at 10^{3}/s strain rate. Thus the studied titanium material sintered from TiH_2 is shown to retain much higher dynamic strength and lower failure strain than pure titanium. Magnusen et al.[9] reported that porosity in titanium matrix lowered total failure strain and dynamic strength, implying that these values of the studied titanium from TiH_2 (90.1% theoretical density) could be increased by an enhanced densification at a higher temperature.

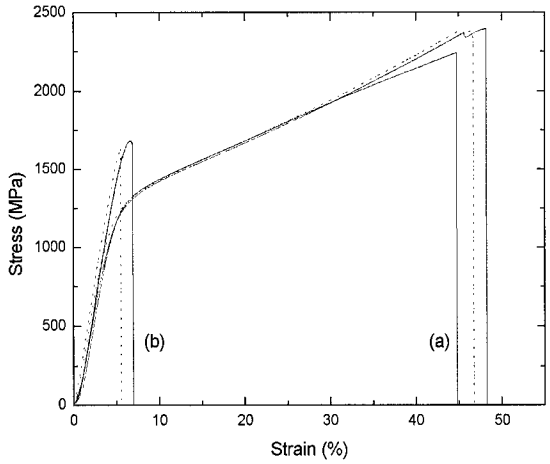

Fig.3. Static compressive stress-strain diagram for sintered (a) TiH_2 and (b) TiH_2-45vol%TiC. Solid lines: MoS_2+Teflon lubricant and dash dot dot lines: MoS_2 lubricant.

The strength level of the studied material sintered from TiH_2 is comparable to that of Ti-6Al-4V alloy which with equiaxed alpha grain structure (~5μm) shows flow stress of 1700MPa[10] at 4% strain when tested at 10^3/s strain rate. While dynamic compressive stress-strain diagram for the 6-4 composition is not found in the reference [10] and [11] (only a stress level at a fixed strain is available), Lee's dynamic stress-strain diagram[12] shows that Ti-6Al-4V alloy forged at 1000°C and another sample heat treated at 950°C for 1hr and at 538°C for 4hrs have an initial maximum stress levels of 1620 and 1650MPa, respectively, both at 4~5% strain. Based on Maiden and Green's work[11], the Ti-6Al-4V alloy has flow stress as high as ~1930MPa at 4% strain and 10^3/s strain rate and this would be due to the different microstructure of the alloy as pointed out by Follansbee and Gray[10].
The TiH_2-45%TiC samples show initial peak stress of 2060MPa at 2.85% strain as shown in Fig. 4. The total failure strain of this sample has been decreased as compared to TiH_2 sample while initial peak stress has been about 129% level.

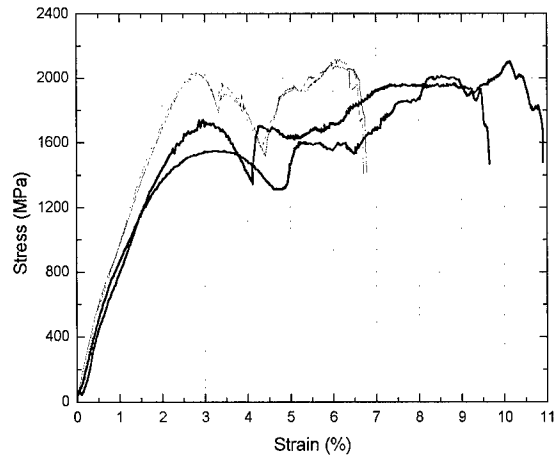

Fig.4. Dynamic compressive stress-strain diagram for sintered (a) TiH_2 (thick curves) and (b) TiH_2-45vol%TiC (thin curves) samples.

4. CONCLUSIONS

Two types of titanium-based materials have been fabricated by hot pressing TiH_2 and TiH_2-45vol%TiC powder mixture and their microstructure and both dynamic and static compressive mechanical properties have been uncovered. Both hot pressed samples form titanium phase in matrix with a barely identifiable amount of TiH_2 in X-ray diffraction pattern. TiH_2 sample cooled in a fast-cooling hot press instrument resulted in an alpha prime microstructure in the sintered body while TiH_2-45vol%TiC composition yielded an acicular titanium microstructure in the matrix. The diffusion of alpha stabilizer carbon from TiC into the matrix has been interpreted as one of the reason for such a microstructural difference. The sintered titanium-based samples with 0 and 45vol%TiC show 0.2% offset yield strength of 1008 and 1448MPa, respectively, in a static compressive mode (strain rate of 10^{-3}/s) and a dynamic compressive strength (strain rate of 4×10^{3}/s) of 1600 and 2060MPa, respectively.

ACKNOWLEDGMENT

The authors are grateful for the technical support from and helpful discussions with Drs. W.B. Kim and K.S. Choi at Korea Institute of Geology, Mining and Minerals, Dr. H. Ha at Sejong Materials Co., Ltd., Inchon, Korea.

REFERENCES

1. M.J. Donachie, Jr.: Titanium - A Technical Guide, ASM International, 1988.
2. W.B. Kim, H.S. Yu, and K.S. Choi, KIGAM Research Report, KR-98(C)-28, Korea Institute of Geology, Mining and Materials, (1998).
3. W.M. Mueller, J.P. Blackledge, and G.G. Libowitz: Metal Hydrides, Academic Press, New York and London, (1968).
4. H. Ha, private communications, Sejong Materials Co., Ltd., Inchon, Korea.
5. H. Shin, H.L Park, and S.N. Chang, unpublished work.
6. P.S. Follansbee, in Materials Testing, Metals Hand Book, Vol. 8, 9th ed., pp. 198-203, American Society for Metals, Metals Park, OH (1985).
7. M.J. Donachie, Jr., Titanium and Titanium Alloys, American Society for Metals, Metals Park, OH (1982).
8. S. Gabelotaud, C. Nguy, P. Bensussan, M. Berveiller, and P. Lipinski, in Shock-Wave and High-Strain-Rate Phenomena in Materials, M.A. Meyers et al. eds., American Physical Society, Dekker, New York (1992).
9. P.E. Magnusen, P.S. Follansbee, and D.A. Koss, in Technical Report No.25 (AD-A148670), The Office of Naval Research, Contract No. N00014-76-C-0037, NR 031-756 (1984).
10. P.S. Follansbee and G.T. Gray, III, Metall. Trans. A, Vol.20A(1989), pp.863-874.
11. C.J. Maiden and S.J. Green, J. Appl. Mech., Vol.33, (1966), pp.496-504.
12. Y.Y. Lee, private communication, Agency for Defense Development, Korea.

EFFECTS OF PRECIPITATED INTERMETALLICS ON FRACTURE CHARACTERISTICS OF Ti-6Al-2Sn-2Zr-2Mo-2Cr-Si

Mituso Niinomi*, Kei-ichi Fukunaga*, Genzo Tono**, Junichi Koike***, Daniel Eylon**** and Shiro Fujishiro*****

*Department of Production Systems Engineering, Toyohashi University of Technology, Toyohashi 441-8580, Japan
**Graduate School, Toyohashi University of Technology, Toyohashi 441-8580, Japan
***Department of Materials Science, Faculty of Engineering, Tohoku University, Sendai 980-8579, Japan
****Graduate Materials Science, The Universtiy of Dayton, OH 45469-0240, USA
*****Formerly Asian Office of Aerospace R & D, United States Air Force of Scientific Research, Tokyo 106-0032, Japan

ABSTRACT

Ti-6Al-2Sn-4Zr-2Mo-0.1Si (Ti-62222S) is highly expected to be widely used for structural aircraft materials because Ti-62222S shows both characteristics of α type alloys with excellent high temperature strength and creep resistance, and $\alpha + \beta$ type alloys with high fracture toughness and high strength. The intermetallics, Ti_3Al and silicides, precipitated in Ti-62222S during aging treatments decrease the strength and fracture toughness. However, the effect of each intermetallic on fracture characteristics of Ti-62222S is not yet clearly understood. Therefore, the fracture characteristics of Ti-62222S with only Ti_3Al or only silicides precipitated by aging treatment were investigated with relating the matrix microstructure.

0.2% proof stress, tensile strength and elongation of the as-received material are much better than those of the aged materials. 0.2% proof stress and tensile strength of the material with only Ti_3Al precipitated by aging treatment are better than those of the material with only silicides precipitated by aging treatment. Static fracture toughness of the material with only silicides is better than that of the material with only Ti_3Al. The intergranular fracture appears in the material with only Ti_3Al. Coarsening of Widmanstätten α structure and increasing ductility of β phase during aging is considered to be effective for increasing static fracture toughness.

1. INTRODUCTION

Titanium alloys are attracting attention due to their excellent specific strength as well as

excellent corrosion resistance and fatigue characteristics. In the field of developing titanium alloys for airplane, Ti-6Al-2Sn-4Zr-2Mo-Si (Ti-62222S) has been developed in RMI Titanium Inc. as a titanium alloy combining the characteristics of the α-type alloy, which has excellent high temperature strength and creep resistance, and the α + β type alloy, which has high toughness and high strength [1-3]. Ti-62222S has greater strength, greater elasticity, greater toughness, and more excellent damage tolerant characteristics than Ti-6Al-4V [4-7]. However, it has been reported that when Ti-62222S is subjected to a certain heat treatment, intermetallic compounds of Ti_3Al and silicide precipitate, and such compounds lower the toughness and strength. In that case, only the case where Ti_3Al and silicide precipitate simultaneously has been reported [8], where which intermetallic compound affects the toughness and strength more strongly is not well understood and how the changes in the precipitation volumes of such compounds affect the same characteristics is not yet examined.

In this study, therefore, aging processes [9] for various lengths of time to precipitate intermetallic compounds of Ti_3Al and silicide separately were applied to Ti-62222S. Tensile tests and static fracture toughness tests were then carried out on the aged Ti-62222S, and the effects of precipitated intermetallics on fracture characteristics were compared and examined.

2. EXPERIMENTAL PROCEDURE

2.1 Material and Aging Process

Materials used in this study were rolled sheets of Ti-62222S made by RMI Titanium Inc. The chemical composition of Ti-62222S is shown in Table 1. The materials were subjected to heat treatment of three stages: β solution treatment, α - β stabilizing treatment, and aging process (1261 K - 3.6 ks, Fan cool + 1200 K - 3.6 ks, Fan cool + 811 K - 28.8 ks, Air cool) by RMI Titanium Inc. (hereinafter referred to as as-received material). The as-received materials were subjected to two types of heat treatment in this study. The heat treatment was carried out in order to precipitate Ti_3Al only. In this heat treatment process, materials were keeping at 913 K for 14.4, 28.8 and 57.6 ks, respectively and then cooled in air (hereinafter referred to as aging process). On the other hand, the heat treatment process was carried out to precipitate silicide only. In this process, materials were keeping at 1088 K for 7.2, 14.4 and 28.8 ks, respectively and then quenched into water (hereinafter referred to also as aging process). The β transus of this alloy is round 1250 K.

Table 1 Chemical composition of Ti-62222S (mass%)

Al	Sn	Zr	Mo	Cr	Si	Fe	O	N	H	Ti
5.44	1.99	1.99	2.16	2.06	0.16	0.09	0.11	0.006	62(ppm)	bal.

2.2 Microstructural Observation

Small specimens with a size of 10 x 10 x 10 mm^3 were cut from the as-received material and aged materials. They were buff polished after undergoing wet polishing with emery paper and then etched with 3%HF + 10%HNO_3 solution. Microstructural observations were performed on those specimens using a light microscope. On each material that was subjected

to either process to precipitate Ti_3Al or silicide, constitutional phases were identified using the X-ray diffraction analysis. More detailed observations of microstructures were performed using a transmission electron microscope, TEM.

2.3 Specimen and Testing Method

From as-received and each aged material, tensile test specimens with its tensile direction aligned with the rolling direction were machined. Static fracture toughness test specimens with its longitudinal direction aligned with the rolling direction were also machined. The tensile tests were performed using an Instron-type testing machine at a cross-head speed of 8.3×10^{-8} m/s in the atmosphere of room temperature. A fatigue crack was introduced to the specimen for the static fracture toughness test in accordance with ASTM E813 [10]. The static fracture toughness tests were performed using an Instron-type testing machine at a cross-head speed of 5.0×10^{-6} m/s in the atmosphere of room temperature.

2.4 Observation of Fracture Surface

Observation of fracture surface after the static fracture toughness tests were performed using a scanning electron microscope, SEM. In that case, if a intergranular fracture appears, the ratio of the transgranular ductile fracture surface area (dimple fracture surface) to the total fracture surface area was evaluated from the SEM fractograph of fracture surface using an image analyzer.

3. RESULTS AND DISCUSSION

3.1 Microstructure

From X-ray diffraction analysis, on the as-received material, besides the diffraction peaks of α and β phases, there was the diffraction peak of Ti_3Al also. The intensity of this peak slightly increased after aging at 913 K and it further increased as the aging time at the same temperature increased indicating that the volume fraction of Ti_3Al increased with the progress of aging. The diffraction peak of Ti_3Al disappeared by the aging holding for 7.2 ks at 1088 K and then the diffraction peak of silicide appeared. The intensity of this peak increased as the aging time increased indicating that the volume fraction of silicide increased with the progress of aging.

Figure 1 shows light micrographs of the as-received material and each aged material. The

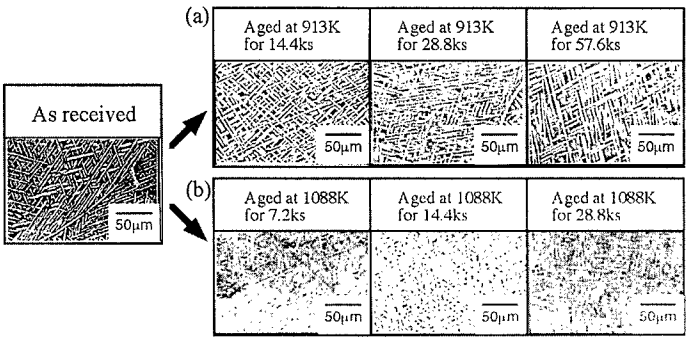

Fig.1 Optical micrographs of Ti-62222S conducted with aging treatments for precipitation of (a) Ti_3Al only and (b) silicide only versus aging time.

microstructure of the as-received material consists of Widmanstätten α phase and β phase. The microstructures of both aged materials show Widmanstätten α structure similar to that in the microstructure of the as-received material, although here are slight differences in the morphology of Widmanstätten α structure. The area fraction and aspect ratio of Widmanstätten α phase increased further during either aging process and they increased further as the aging time increased.

Figure 2 shows the TEM bright field images of the as-received material and the materials aged at 913K and 1088K, respectively. In this case, a trend that the area of β phase decreases as the aging time increases can be seen. The microstructures of the specimens aged at 913K for 14.4 ks and 28.8 ks show precipitates that seem to be fine α phase in the β phase. The α phase that precipitates in this way in the β phase forming Widmanstätten α structure is defined as the precipitated acicular α phase. Since the observation of the precipitated acicular α phase has been performed in such an area where it can be observed as clearly as possible, an area considerably greater than the average area of precipitated acicular α phase (β area) is shown here as a representative one. The aspect ratio of the precipitated acicular α phase of the specimen aged at 913K for 14.4 ks is smaller than that obtained from aging at the same temperature for 28.8 ks. Further, in the specimen aged at 913K for 57.6 ks, no precipitated acicular α phase is observed. It is considered that this is because distribution of elements in the β phase area further advances as aging progresses and the precipitated acicular α phase disappears, in other words, the growth of the Widmanstätten α phase is further promoted.

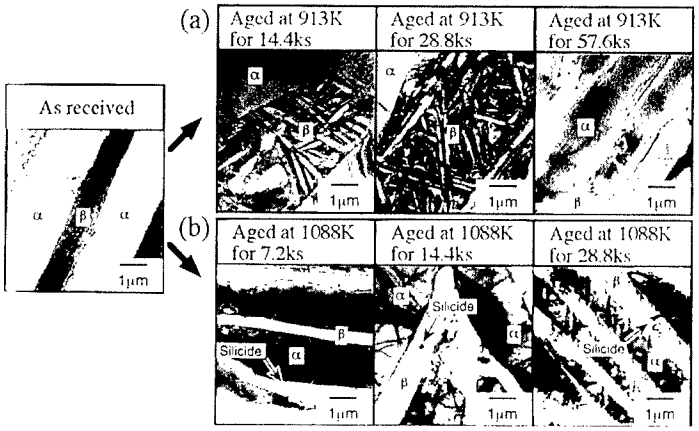

Fig.2 Bright field images of Ti-62222S conducted with aging treatments for precipitation of (a) Ti_3Al only and (b) silicide only versus aging time.

At 1088 K, on the other hand, after being aged for 7.2 ks, particles are already detected in the β phase area. These particles were mainly precipitating in the β phase. Chemical composition of these particles were evaluated to be $(Ti,Zr)_5Si_3$ by EDX. The size of these particles increased as the aging time increased. In the selected area electron diffraction pattern on the specimen aged at 1088 K for 7.2 ks, on the other hand, no diffraction spots corresponding to the diffraction spots of Ti_3Al were detected between α phase diffraction spots. Therefore, it can be seen that only silicide precipitates in the material aged at 1088 K. Moreover, in this case, no precipitated acicular α phase is observed in every aging time.

From the selected area electron diffraction patterns of α phase of the as-received material and the material aged at 913 K for 14.4 ks, a relatively weak diffraction spots was observed between α phase diffraction spots. These diffraction spots were the diffraction spots of Ti_3Al. Therefore, it could be considered that Ti_3Al precipitated in the as-received material and in the

material aged at 913K. However, in the dark field image of these diffraction spots, existence of a particle that seemed to be Ti_3Al was not detected. It is considered that this is because very small cluster of Ti_3Al with long range order structure is exist and its structure is changed according to the time.

3.2 Tensile Characteristic

0.2% proof stress, $\sigma_{0.2}$, and tensile strength, σ_B versus aging time are shown in Fig. 3 for the as-received material and each aged material, respectively. 0.2% proof stress and tensile strength of Ti-62222S are the greatest in the as-received material, while they are lowered under every aging condition. It is considered that the causes of this phenomenon are the coarsening of the Widmanstätten α according to the increase in the area fraction and aspect ratio of the Widmanstätten α phase and the precipitation of Ti_3Al or silicide during aging process. Since, in the material subjected to the aging process for precipitating Ti_3Al, in particular, intergranular cracking can be detected after the aging process as will be described later, it can be considered that intermetallic compounds have considerably large influence to lower the ductility, i.e. elongation.

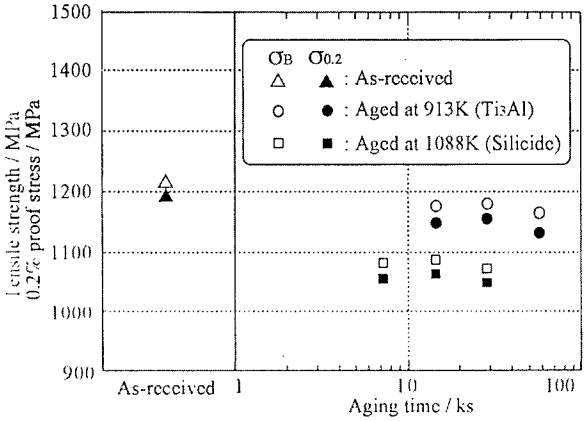

Fig.3 Tensile strength and 0.2% proof stress of Ti-62222S conducted with various heat treatments.

The tensile strength and 0.2% proof stress of the material subjected to the aging process for precipitating silicide are lower than those of the material subjected to the aging process for precipitating Ti_3Al. Further, in the aged materials, regardless to the aging processes, tensile strength and 0.2% proof stress tend to decrease slightly as the aging time increases.

Since intergranular fracture tends to decrease as the aging time increases in the material subjected to the aging process for precipitating Ti_3Al as will be also described later, it can be understood that the increase in elongation along with the increase in aging time is due to the increase in the plastic deformability of the matrix, that is, β phase. Although many of fine precipitated acicular α phases appeared in the β phase at the initial stage of aging, they disappeared as the aging time increased leaving β phase only. In other words, it is considered that, although the plastic deformation of β phase is suppressed at the initial stage of aging due to the precipitation strengthening by precipitated acicular α phase, precipitated acicular α phase in β phase disappears as the aging time increases, and then the plastic deformability of β phase increases.

In the material subjected to the aging process for precipitating silicide, no precipitated acicular α phase in β phase was observed as already shown in Fig.2. Therefore, it cannot be considered that precipitated acicular α phase influences the plastic deformability of β phase. In this case, as described above, a trend that the volume of precipitated silicide increases with the increase in the size as the aging time increases was recognized. Therefore, although it is

considered that stress concentration to silicide increases as the aging time increases, it is also considered that the effect of silicide on the precipitation strengthening of β phase decreases and the plastic deformability of β phase increases. Therefore, the increase in elongation along with the increase in aging time in this case is a result obtained from the fact that the influence of the latter exceeded the influence of the former.

3.3 Static Fracture Toughness

Figure 4 shows the values of static fracture toughness, J_{IC}, of the as-received material and each aged material.

The value of static fracture toughness of Ti-62222S in either aged material is lower than that in the as-received material.

The value of static fracture toughness of Ti-62222S lowers after undergoing aging process in either material subjected to the aging process for precipitating intermetallic compound of Ti_3Al or silicide. It is considered that this is because local stress concentration to the precipitated Ti_3Al or silicide occurred. In the specimen with precipitated Ti_3Al, in particular, it can be considered that the main cause of lowered fracture toughness is that the intergranular cracks occur as will be described later leading to the local stress concentration to the grain boundary.

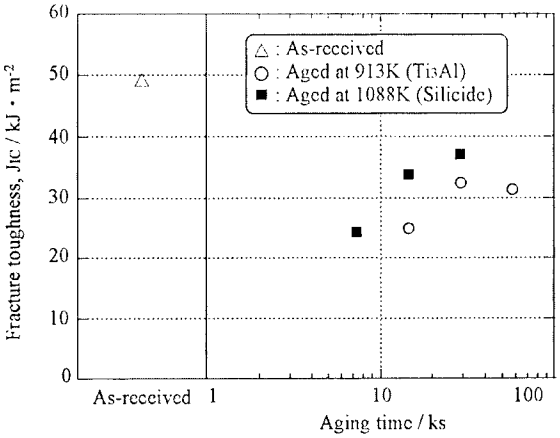

Fig.4 Fracture toughness, J_{IC}, of Ti-62222S conducted with various heat treatments.

In both materials, however, although the value of static fracture toughness lowers when subjected to aging, the value of static fracture toughness increases as the aging time increases. In general, in Widmanstätten α structure, the value of static fracture toughness increases as the microstructure becomes coarser [11]. In this study, while the volume fraction of intermetallic compound tended to increase as the aging time increased as described above, microstructure also became coarser. Further, elongation also increased as the aging time increased. While the increase in volume fraction of precipitated intermetallic compounds leads to a lower value of fracture toughness, the increase in coarseness of Widmanstätten α structure, the increase in aspect ratio of Widmanstätten α phase, and the increase in ductility (elongation) lead to a greater value of fracture toughness. In other words, it is said that the increase in coarseness of Widmanstätten α structure and the increase in aspect ratio of Widmanstätten α phase lead to extrinsic toughening such as toughening caused by stress release due to the formation of microcracks and toughening caused by lowered effective stress intensity factor at the crack tip due to the deflection of cracks [11]. On the other hand, it is said that the increase in ductility leads to intrinsic toughening, which is the increasing crack tip plastic blunting [11]. Therefore, it is considered that the reason why the value of fracture

toughness increases as the aging time increases is that the above mentioned extrinsic and intrinsic toughening exceed lowering toughness due to the precipitation of intermetallic compounds.

Moreover, material subjected to aging for precipitating Ti_3Al tends to have a smaller value of fracture toughness than the material subjected to aging for precipitating silicide.

3.4 Fracture surface morphology

Figure 5 shows the typical SEM fractographs of the fracture surfaces near the fatigue pre-cracks of the static fracture toughness tested specimens of the as-received material and the materials subjected to aging for precipitating Ti_3Al or silicide, respectively. The photographs on the upper and lower sides of this figure are the photographs of low and high magnifications, respectively.

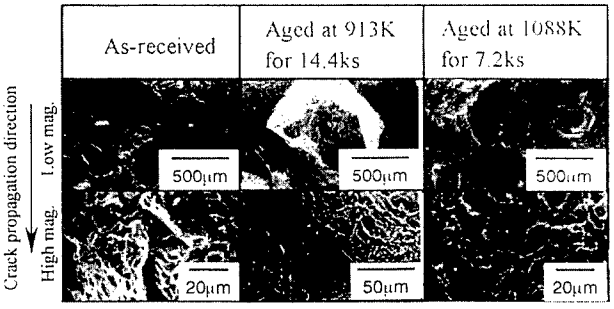

Fig.5 Typical SEM fractographs of Ti-62222S in static fracture toughness tested specimens.

Fracture surface of the as-received material shown in Fig.5 mainly shows transgranular fracture morphology. On the fracture surface of the material subjected to aging for precipitating Ti_3Al only, on the other hand, intergranular cracking is seen, and on the photograph of fracture surface of high magnification, striped patters are seen on that intergranular fracture surface. This intergranular cracking was seen at any aging time, and decreased as the aging time increased. The ratio of intergranular fracture surface to the total fracture surface tends to decrease as the aging time increases and transgranular fracture becomes dominant. Further, the fracture surface of the specimen subjected to the aging process tended to become rougher as the aging time increases.

It can be seen that the fracture surface of the material subjected to the aging process to precipitate silicide only shows transgranular fracture morphology with no intergranular cracking. Furthermore, the photograph of fracture surface of high magnification clearly shows the dimple fracture surface morphology. Also in this case, the fracture surface of the material subjected to aging tended to become rougher as the aging time increased.

4. SUMMARY

Aging process to precipitate metallic compound, Ti_3Al or silicide only, was applied to the Ti-62222S, and after performing observation of microstructure, tensile tests and static fracture toughness tests of the specimens, the following results have been obtained:

(1) The volume fraction of intermetallic compounds Ti_3Al and silicide increases with increasing aging time.

(2) 0.2% proof stress and tensile strength tend to be the greatest in the as-received material

and lower after being subjected to the aging process to precipitate intermetallic compound, Ti_3Al or silicide. 0.2% proof stress and tensile strength of the material subjected to the aging process to precipitate Ti_3Al only are greater than those of the material subjected to the aging process to precipitate silicide only.

(3) The value of static fracture toughness tends to be the greatest in the as-received material and lower after being subjected to the aging process to precipitate Ti_3Al or silicide only but increases as the aging time increases. The value of static fracture toughness of the material subjected to the aging process to precipitate silicide only is greater than that of the material subjected to the aging process to precipitate Ti_3Al only.

(4) Although intergranular fracture surface appears on the fracture surface of the material subjected to the aging process to precipitate Ti_3Al only, the ratio of that area in the total area decreases as the aging time increases. In the material subjected to the aging process to precipitate silicide only, fracture surface shows the transgranular dimple fracture surface morphology. Further, in either aged material, the roughness of the fracture surface increases as the aging time increases.

(5) It is considered that, although the precipitation of intermetallic compound, Ti_3Al or silicide, by aging process lowers the value of fracture toughness, the increasing rate of the value of fracture toughness due to the increase in coarseness of Widmanstätten α structure and increase in plastic deformability of β phase exceed the decreasing rate of the value of fracture toughness due to the increase in the volume fraction of intermetallic compounds as the aging time increases, and thus a trend that the value of fracture toughness increases is shown.

REFERENCES

1. D. J. Evans, T. F. Broderick, J. B. Woodhouse and J. R. Hoenigman, Materials Science and Engineering, A213(1996), pp. 37 - 44.
2. J. R. Wood, P. A. Russo, M. F. Welter and E. M. Crist, Materials Science and Engineering, A243(1998), pp. 109 - 118.
3. X. D. Zhang, J. M. K. Wiezorek, W. A. Baeslack III, D. J. Evans and H. L. Fraser, Acta Matellurgica, 46(1998), pp. 4485 - 4495.
4. A. W. Wilson and J. M. Howe, Metallurgical and Materials Transaction A, 29A(1998), pp. 1585 - 1592.
5. M. J. Donachie-Jr., Titanium-A Technical Guide, ASM International, Materials Park, OH, USA, (1988), p. 418.
6. G. W. Kuhlman, K. A. Rohde and A. K. Chalrabarti, Titanium 92, TMS, Warrendale, PA, USA, (1992), pp. 1371 - 1378.
7. R. Boyer, G. Welsch and E. W. Collings, Mechanical Properties Handbook Titanium Alloys, ASM International, Materials Park, OH, USA, (1994), p. 584.
8. R. Boyer, Materials Science and Engineering, 1996, A213, pp. 103 - 114.
9. D. J. Evans and T. F. Broderick, Titanium'95: Science and Technology, The Institute of Materials, London, UK, (1995), pp. 2413 - 2420.
10. Standard Test Method for J_{IC}, A measure of fracture toughness, ASTM Designation E813-89, Philadelphia, PA, USA, (1997).
11. M. Niinomi, Materials Science & Technology, 66(1996), pp. 21 - 28.

CORRELATION OF MICROSTRUCTURE WITH QUASI-STATIC AND DYNAMIC DEFORMATION PROPERTIES OF Ti-6Al-4V ALLOY

Dong-geon Lee, Chang Sup Lee, Sangho Kim, Sunghak Lee, and Chong Soo Lee

Center for Advanced Aerospace Materials
Pohang University of Science and Technology Pohang, 790-784 Korea

ABSTRACT

The present study aims at investigating correlation of microstructures with quasi-static and dynamic deformation properties of a Ti-6Al-4V alloy. Quasi-static and dynamic torsional tests were conducted using a torsional Kolsky bar for Widmanstätten, equiaxed, and bimodal microstructures, which were processed by different heat treatments, and then the test data were analyzed in relation to microstructures, tensile properties, and fracture modes. Quasi-static torsional properties showed a tendency similar to tensile properties, and ductile fracture occurred in all the three microstructures. Under dynamic torsional loading, maximum shear stress of the three microstructures was higher and fracture shear strain was lower than those under quasi-static loading, but the overall tendency was similar. In the Widmanstätten and equiaxed microstructures, adiabatic shear bands were found in the deformed region of the fractured specimens. The possibility of the adiabatic shear band formation under dynamic loading was quantitatively analyzed, depending on how plastic deformation energy was distributed to either void initiation or adiabatic shear banding. It was found most likely in the equiaxed microstructure, whereas least likely in the bimodal microstructure.

1. EXPERIMENTAL

A Ti-6Al-4V alloy plate of 900×900×50 mm was used, and its chemical composition is Ti-6.19Al-4.05V-0.19Fe-0.12O-0.02C-0.01N-0.004H (wt.%). This alloy plate was subjected to different heat treatments to obtain Widmanstätten, equiaxed, and bimodal microstructures[1,2]. The Widmanstätten microstructure was obtained by holding at 1050 °C, above the β transformation temperature, for 1 hour followed by furnace cooling, while the equiaxed microstructure by holding at 950 °C, the $\alpha+\beta$ region, for 1 hour followed by furnace cooling. For the bimodal microstructure, equiaxed α and martensite were first obtained by holding at 950 °C, above the martensitic transformation temperature (Ms), for 1 hour followed by water quenching, which was then aged for 24 hours at 600 °C and air cooled.

Tensile bars were machined with a gage length of 30 mm and a gage diameter of 5 mm, and tensile tests were conducted at a strain rate of 10^{-3} sec^{-1}. Fracture surfaces were observed by a scanning electron microscope (SEM) after the tests.

Thin-walled tubular specimens used for quasi-static and dynamic torsional tests have a

gage length of 2.5 mm and a gage thickness of 280 ㎛ as shown in Figure 1(a). The torsional Kolsky bar consists of a pair of 2-meter long 2024-T6 aluminum bars with a diameter of 25.4 mm (Figure 1(b)) [3]. In the dynamic torsional test, a certain amount of torque is stored between a clamp and a dynamic loading pulley, and then the clamp is fractured, at which time an elastic shear wave is momentarily transmitted into the specimen, deforming it. In the quasi-static torsional test, the incident bar is fixed by a clamp, and then the specimen is deformed slowly at a strain rate of about 10^{-4} sec^{-1} by transmitting power to the bar by a motor. Detailed descriptions of the dynamic and quasi-static torsional testing are provided in references [3,4,5].

2. RESULTS AND DISCUSSION

2.1. Microstructure

Figures 2(a) through (c) are optical micrographs of the Widmanstätten, equiaxed, and bimodal microstructures, respectively. In the Widmanstätten microstructure, α phases are formed in 8~10 ㎛ thickness along prior β grain boundaries, and colonies of lath-type β and α lamellar structure are present inside prior β grains (Figure 2(a)). Prior β grain size, colony size, and thickness of α platelets were measured to be 300 ~800 ㎛, 100~350 ㎛, 5~6 ㎛, respectively. In the equiaxed microstructure, about 10 vol.% of β is present at triple points of α grains, and volume fraction and grain size of α are about 90% and 19 ㎛, respectively (Figure 2(b)). The bimodal microstructure consists of tempered martensite and α, together with a small amount of residual β, as shown in Figure 2(c). Primary α grain size was measured to be 19 ㎛, and volume fractions of tempered martensite, α, and β were measured to be 52%, 38%, and 10%, respectively.

2.2. Tensile Properties

Tensile data of the three microstructures are listed in Table 1. Yield and tensile strengths increase in the order of Widmanstätten, equiaxed, and bimodal microstructures, while elongation increases in the order of bimodal, Widmanstätten, and equiaxed microstructures. Elongation of the Widmanstätten microstructure is relatively low because deformation at colony boundaries and boundary α phases occurs with ease [6]. The equiaxed microstructure shows excellent tensile strength and elongation of 959 MPa and 15%, respectively, due to the presence of equiaxed, fine α grains. Although the bimodal microstructure shows comparatively higher yield and tensile strengths than the equiaxed microstructure due to the formation of tempered martensite, elongation is lower because the reduction in volume fraction of α significantly affects the ductility.

2.3. Quasi-static Torsional Properties

Figure 3 presents shear stress-shear strain curves obtained from the quasi-static torsional test. From these curves, maximum shear stress, shear strain at maximum shear stress point, and fracture shear strain were measured, and are summarized in Table 2. All three microstructures show a low level of strain hardening after yielding, and stress

continues increasing with straining, reaching eventual fracture. Maximum shear stress increases in the order of Widmanstätten, equiaxed, and bimodal microstructures, and shows a similar tendency to tensile strength, roughly satisfying the relationship of $\sigma = \sqrt{3}\,\tau$ when compared with tensile strength. Fracture shear strain also shows a tendency similar to elongation.

Figures 4(a) through (c) are SEM micrographs of the deformed area (central area of the gage section) beneath the fracture surface of the quasi-statically fractured torsional specimens. In the Widmanstätten microstructure, many voids are initiated at α/β interfaces or boundary α phases, and their number decreases gradually as it gets deeper from the fracture surface (Figure 4(a)). Some voids are observed even at considerable distance from the surface. Voids are initiated mainly at interfaces between α and β distributed at triple points of α phases for the equiaxed microstructure (Figure 4(b)) and at interfaces between α and tempered martensite for the bimodal microstructure (Figure 4(c)).

2.4. Dynamic Torsional Properties

Figure 5 shows shear stress-shear strain curves obtained from the dynamic torsional test. When the values of maximum shear stress, shear strain at maximum shear stress point, and fracture shear strain under both dynamic and quasi-static loading conditions are compared as shown in Table 2, maximum shear stress is higher and fracture shear strain is lower under dynamic loading, but the same tendency overall is shown. Stress increases but strain decreases under dynamic loading over the case of quasi-static loading because of the strain rate hardening effect in general. The Widmanstätten and equiaxed microstructures show slow strain rate hardening with considerable plastic deformation after yielding. But in the bimodal microstructure, high strain rate hardening is shown with a little plastic deformation and fracture occurs fast after reaching maximum shear stress.

SEM observations of the deformed area beneath the fracture surface of the dynamically fractured torsional specimens are shown in Figures 6(a) through (c). In the Widmanstätten microstructure, voids are initiated at α/β interfaces or boundary α phases. Near the fracture surface, an adiabatic shear band formed weakly in a direction perpendicular to the torsional stress direction is found as marked by arrows in Figure 6(a). In the equiaxed microstructure, a localized shear zone of about 20 μm in thickness is formed along the fracture surface because shear strain is concentrated along the center of the gage section (Figure 6(b)). The number of voids initiated near the fracture surface is largely reduced, compared with the quasi-static torsional test. In the bimodal microstructure, localized shear deformation is not observed, but many voids are generated as in the case of quasi-static loading as indicated by arrows in Figure 6(c).

2.5. Adiabatic Shear Band

One of the characteristics that appear when dynamic loading is applied to the Ti-6Al-4V alloy is the formation of adiabatic shear bands [7,8,9]. In the Widmanstätten microstructure, adiabatic shear bands are weakly developed vertical to the shear stress direction, and α grains of the equiaxed structure are elongated along the shear direction

long enough to cover up grain boundaries, forming seriously deformed area as shown in Figures 6(a) and (b). In the bimodal microstructure, adiabatic shear banding is not observed at all. In order to quantitatively interpret the possibility of the adiabatic shear band formation, the number of voids per unit area in the deformed region beneath the fracture surface was measured, and the results are shown in Figures 7(a) through (c). In the quasi-static torsional specimens, the number of voids descends in the order of bimodal, Widmanstätten, and equiaxed microstructures. This indicates that void initiation is related to the number or the area of interfaces initiating voids. Voids are mostly initiated at α/β interfaces or boundary α phases for the Widmanstätten, at interfaces between α and β distributed at triple points of α grains for the equiaxed, and at interfaces between α and tempered martensite for the bimodal microstructure. Because of the presence of tempered martensite in addition to α and β in the bimodal microstructure, void initiation sites are plenty, whereas they are scarce because of the meagre presence of β in the equiaxed microstructure. Thus, the number of voids decreases in the order of bimodal, Widmanstätten, and equiaxed microstructures.

Under dynamic loading, which does not allow enough time for voids to initiate at void initiation sites and to grow, the number of voids in all of the three microstructures is smaller than that under quasi-static loading. Particularly in the Widmanstätten and equiaxed microstructures, the number of voids is far reduced from that under quasi-static loading. The bimodal microstructure does not show outstanding change in the number of voids with loading conditions, and has more voids than the other two microstructures. In order to interpret these results, the concept of energy required for dynamic deformation was introduced.

In the Widmanstätten and equiaxed microstructures, considerable plastic deformation occurs up to the maximum shear stress point as shown in Figure 5, and thus large plastic deformation energy is stored inside the specimen. This deformation energy works as driving force for ductile fracture through void initiation, growth, and coalescence, and is also partly used for adiabatic shear banding. When part of deformation energy is used for the formation of adiabatic shear bands under dynamic loading, deformation energy required for void initiation is thus reduced as much. Adiabatic shear bands are formed in the Widmanstätten and equiaxed microstructures under dynamic loading. Since driving force for void initiation is reduced as much as deformation energy used for the adiabatic shear band formation, the number of voids is drastically reduced than the case of quasi-static loading (Figures 7(a) and (b)). In the equiaxed microstructure having a few void initiation sites, the number of voids decreases further, promoting instead the formation of adiabatic shear bands in which shear strain is concentrated at the center of the gage section. In the Widmanstätten microstructure, many voids are initiated at colony boundaries, boundary α phases, and α/β interfaces, consuming much of deformation energy. Thus, the possibility of the adiabatic shear band formation is lower than that in the equiaxed microstructure. In the bimodal microstructure having the largest interfacial area, deformation energy is largely consumed for void initiation, thereby forming no adiabatic shear bands.

Depending on how deformation energy is distributed and consumed for either void initiation or adiabatic shear banding, the possibility of the adiabatic shear band formation can be evaluated. Despite excellent mechanical properties of the equiaxed

microstructure, the possibility of the crack initiation due to adiabatic shear banding should be considered when Ti alloys having the equiaxed microstructure are dynamically deformed.

3. SUMMARY

Quasi-static torsional properties of the Widmanstätten, equiaxed, and bimodal microstructures showed a similar tendency to tensile properties. Voids were initiated at α/β interfaces or boundary α phases in the Widmanstätten, at interfaces between α and β distributed at triple points of α grains in the equiaxed, and at interfaces between α and tempered martensite in the bimodal microstructure. Under dynamic torsional loading, maximum shear stress of the three microstructures was higher and fracture shear strain was lower than under quasi-static loading, but the overall tendency was similar. The number of voids under dynamic loading was smaller than that under quasi-static loading. In the Widmanstätten and equiaxed microstructures, adiabatic shear bands were found in the seriously deformed region beneath the fracture surface. The possibility of the adiabatic shear band formation under dynamic loading was quantitatively analyzed, depending on how plastic deformation energy was distributed to either void initiation or adiabatic shear banding. It was found most likely in the equiaxed microstructure, whereas least likely in the bimodal microstructure. Therefore, the possibility of the crack initiation due to adiabatic shear banding should be considered in advance of high-speed deformation processing of the equiaxed structure which was highly prone to adiabatic shear banding.

ACKNOWLEDGMENTS

This work has been supported by the Agency for Defense Development. The authors thank Dr. Sun Moo Hur of Agency for Defense Development for his helpful discussions on the dynamic deformation behavior.

REFERENCES

1. M. Mier and A.K. Mukherjee, Scripta Metall. Mater., Vol. 24(1990), pp. 331-336.

2. S. Yadav and K.T. Ramesh, Mater. Sci. Eng., Vol. A203(1995), pp. 140-153.

3. Metals Hand Book, 9th Ed., ASM, Metals Park, Ohio, Vol. 8(1990), pp. 218-224.

4. K.A. Hartley, J. Duffy, and R.H. Hawley, J. Mech. Phys. Solids, Vol. 35(1987), pp. 283-301.

5. D.-K. Kim, S. Lee, and H.-S. Song, Metals and Materials, Vol. 5(1999), pp. 211-223.

6. F.S. Lin, E.A. Starke, S.B. Chakrabortty, and A. Gysler, Metall. Trans. A, Vol. 15A (1984), pp. 1229-1246.

7. H.A. Grebe, H-r. Pak, and M.A. Meyers, Metall. Trans. A, Vol. 16A(1985), pp. 761-775.

8. K. Cho, S. Lee, S.R. Nutt, and J. Duffy, Acta Metall., Vol. 41(1993), pp. 923-932.

9. C.G. Lee and S. Lee, Metall. Mater. Trans. A, Vol. 29A(1998), pp. 227-235.

Table 1. Room-temperature tensile results of the three microstructures of the Ti-6Al-4V alloy.

Microstructure	Yield Strength (MPa)	Ultimate Tensile Strength (MPa)	Elongation (%)
Widmanstätten	829	897	12.7
Equiaxed	872	959	15.1
Bimodal	1070	1134	10.7

Table 2. Quasi-static and dynamic torsional properties of the three microstructures.

Loading Condition	Microstructure	Maximum Shear Stress (MPa)	Shear Strain at Maximum Shear Stress Point	Fracture Shear Strain
Quasi-Static	Widmanstätten	470	0.13	0.14
	Equiaxed	523	0.15	0.16
	Bimodal	655	0.11	0.12
Dynamic	Widmanstätten	608	0.10	0.17
	Equiaxed	663	0.11	0.18
	Bimodal	742	0.08	0.16

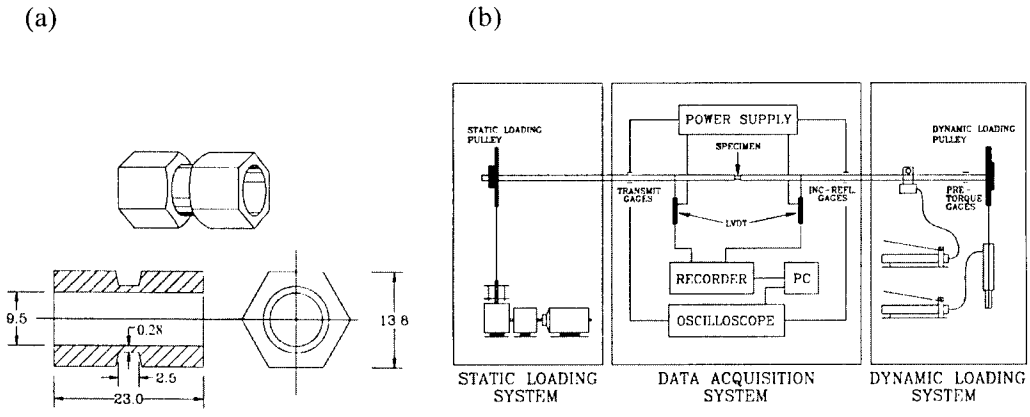

Fig. 1. (a) Shape and dimensions of the thin-walled tubular specimen used for the torsional test. (unit: mm) (b) Schematic drawing of the torsional Kolsky bar.

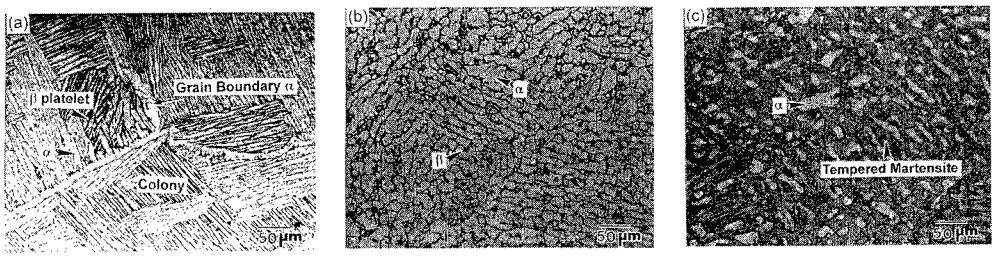

Fig. 2. Optical micrographs of (a) Widmanstätten, (b) equiaxed, and (c) bimodal microstructures.

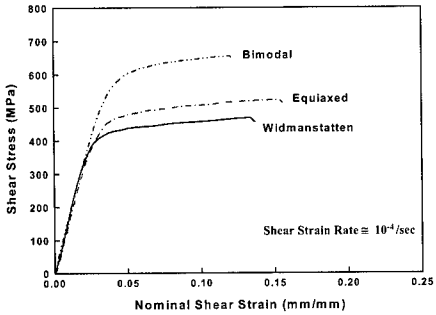

Fig. 3. Shear stress-shear strain curves obtained from the quasi-static torsional test.

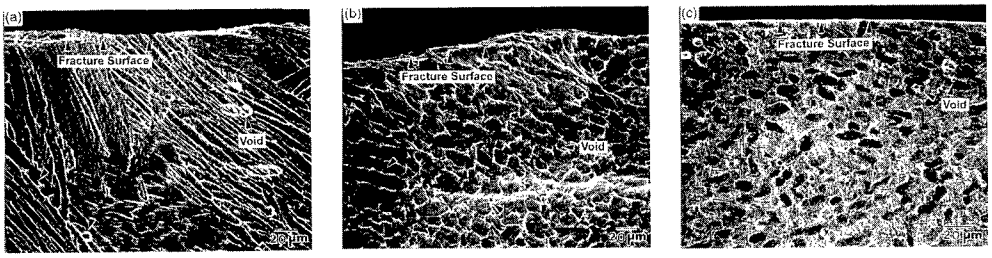

Fig. 4. SEM micrographs of the deformed area (the central area of the gage section) of the quasi-statically fractured torsional specimens for (a) Widmanstätten, (b) equiaxed, and (c) bimodal microstructures.

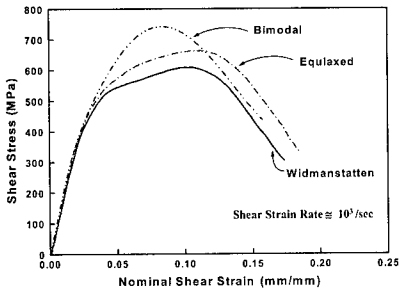

Fig. 5. Shear stress-shear strain curves obtained from the dynamic torsional test.

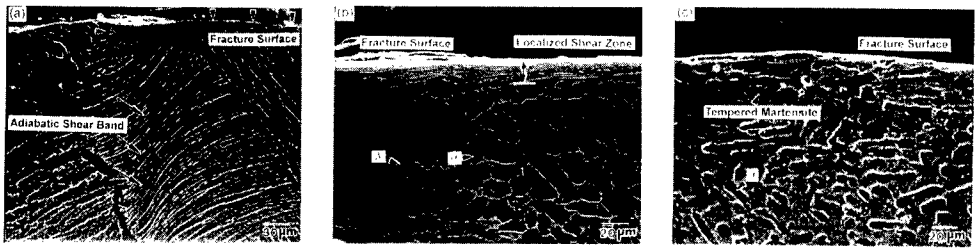

Fig. 6. SEM micrographs of the deformed area (the central area of the gage section) of the dynamically fractured torsional specimens for (a) Widmanstätten, (b) equiaxed, and (c) bimodal microstructures.

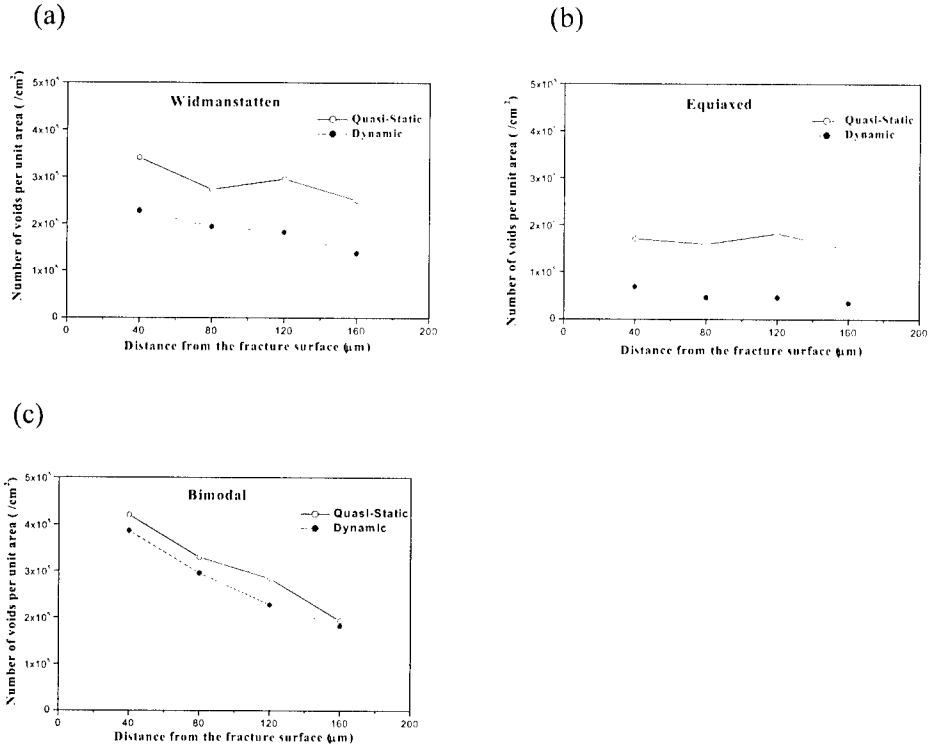

Fig. 7. Number of voids per unit area as a function of distance from the fracture surface for (a) Widmanstätten, (b) equiaxed, and (c) bimodal microstructures.

EFFECT OF MICROSTRUCTURE ON FRACTURE BEHAVIOR OF β-RICH α+β TYPE TITANIUM ALLOY WITH HIGH SUPERPLASTIC FORMABILITY

Gunawarman[a], Mitsuo Niinomi[a], Kei-ichi Fukunaga[a], Daniel Eylon[b], Shiro Fujishiro[c] and Chiaki Ouchi[d]

[a] Toyohashi University of Technology, Toyohashi 441-8580, Japan.
[b] University of Dayton, Dayton, OH 45469-0240, USA.
[c] Former AOA R&D, USAFOSR, Tokyo 106-0032, Japan.
[d] Former NKK Co. Now: Tohoku University, Sendai 980-8579, Japan.

ABSTRACT

The β rich α+β type Ti-4.5Al-3V-2Mo-2Fe alloy is a promising candidate alloy for high-speed aircrafts, helicopter blades and any other structural applications due to its excellent superplastic and mechanical properties, and low manufacturing cost. For getting high performance alloy, a better understanding between microstructure and mechanical properties is needed. In this study, the effect of microstructure on mechanical properties of the rolled plate of the high superplastic formable titanium alloy, Ti-4.5Al-3V-2Mo-2Fe, was investigated. Particular attention was paid to the effect of secondary phase within prior β grain on fracture toughness. A variety of microstructures containing different types of secondary phases were obtained by solution treating the alloy at various temperatures in α+β field followed by subsequent treatments such as water quenching, air-cooling, furnace-cooling, slow furnace-cooling and duplex-annealing treatments. The types of secondary phases are martensite α, acicular α, plate-like α and no secondary phase. It was found that the fracture toughness, J_{IC}, and strength strongly depend on the type of secondary phase. The fracture toughness increases with coarsening secondary phase that leads to increasing extrinsic toughening effect. A relatively better balance of strength, elongation and toughness is given by the microstructure containing coarse acicular α and plate-like α resulting from duplex-annealing and furnace-cooling treatments, respectively, after solution treatment at near β transus.

1. Introduction

The β-rich α+β type titanium alloy, Ti-4.5Al-3V-2Mo-2Fe, has been developed for improving superplastic properties of the most popular titanium alloy, Ti-6Al-4V. By employing smaller content of α stabilizer (4.5 %Al) but higher content of β stabilizer (3%V, 2%Mo and 2%Fe) in the present alloy, its β transus as well as its superplastic temperature is reduced about 100 K lower than that of Ti-6Al-4V [1-3]. This reduction obviously leads to lowering its manufacturing cost. Previous comparative studies on mechanical properties showed that the fatigue and tensile properties of the present alloy is superior to that of Ti-6Al-4V [2,3]. Due to these advantages, it has been then promoted as a candidate alloy for structural applications such as high-speed aircrafts, helicopter blades and non-structural applications such as golf club heads [4-6].

For α+β type titanium alloys, it is well known that α+β annealed alloys provide good fatigue and tensile properties, but gives relatively lower fracture toughness. Previous studies demonstrated that the fracture toughness, K_{IC} [7] and J_{IC} [8], have minimum value at 1123 K when the alloy was air-cooled after solution treatment in α+β field. Although the fracture toughness can be improved by coarsening acicular α phase through duplex-annealing treatment, the minimum value is still bequeathed at 1123K [8]. Our recent study on the effect

of cooling rate after solution treatment on fracture toughness showed that the relatively higher fracture toughness can be achieved by conducting either water-quenching or furnace-cooling treatment instead of air-cooling treatment [9]. Since mechanical properties are strongly related to microstructures, it is important to understand the relationship between microstructure and mechanical properties in order to get the high performance alloy. For this purpose, microstructural observations were carried out on the fractured specimens using a scanning microscope, a transmission electron microscope, and X-ray diffraction to study the microstructural factors of controlling the fracture toughness. Particular attention was paid to investigate the role of the local and continuous secondary phase on fracture toughness.

2. Experimental procedures

The material used in this study was 12.5 mm thick rolled plate of Ti-4.5Al-3V-2Mo-2Fe alloy. The alloy contained (by mass) 4.47 % Al, 3.00% Al, 1.86% Mo, 1.96% Fe, 0.1% O, 0.01% C. 0.01% N, 0.0036% H and balance Ti. Fracture toughness specimens with the final size of 10 x 10 x 55 mm^3 and tensile test specimens with the final size of 4 mm in gauge diameter and 20 mm in a gauge length were taken along the rolling direction of the plate as schematically shown in Fig. 1(a). These specimens had been previously heat treated at solution treatment temperatures between 1103 K and 1173 K in α+β field for 3.6 ks followed by subsequent treatments such as water-quenching (WQ), air-cooling (AC), furnace-cooling (FC), slow furnace-cooling (SFC), and duplex annealing (DA) as schematically shown in Fig. 1b. Solution treatment was carried out in an evacuated quartz tube. The cooling rates of WQ, AC, FC and SFC were around 200 Ks^{-1}, 10 Ks^{-1}, 0.1 Ks^{-1}, and 0.05 Ks^{-1}, respectively.

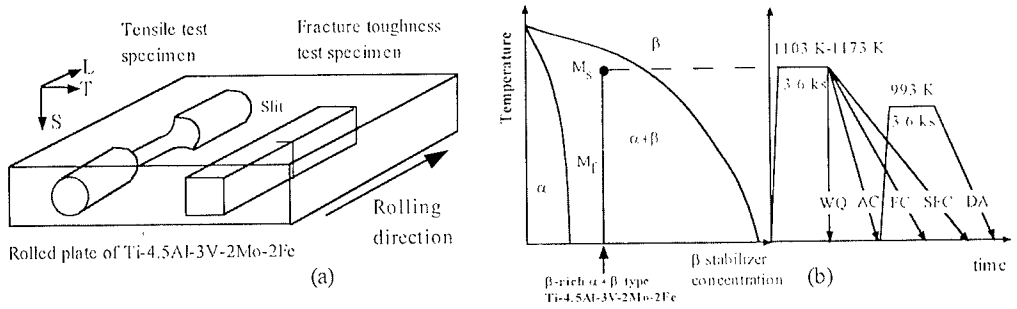

Fig. 1. Schematic illustrations of (a) specimens, and (b) heat treatment conditions.

Fatigue pre-crack was introduced into the slit tip according to ASTM E813. The fracture toughness tests were carried out according to ASTM E813 using an Instron-type testing machine at room temperature in air. The elastic plastic fracture toughness parameter at the crack initiation point, J_{in}, was evaluated using the procedures described in the previous report [8]. J_{in} was judged to be the elastic-plastic fracture toughness, J_{IC}, when J_{in} satisfied the valid conditions for J_{IC}. Tensile tests were carried out Instron-type testing machine at a crosshead speed of 8.3 × 10^{-6} m/s at room temperature in air. Microstructural observations were conducted on the fractured specimens using a scanning electron microscopy (SEM), a transmission electron microscopy (TEM) and X-ray diffraction (XRD).

3. Experimental results and discussion

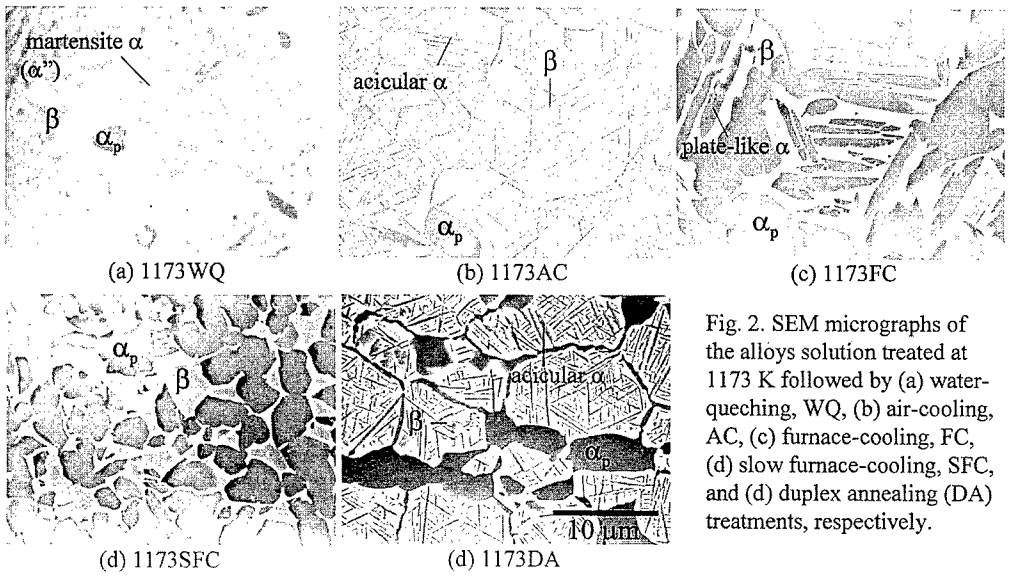

Fig. 2. SEM micrographs of the alloys solution treated at 1173 K followed by (a) water-quecheing, WQ, (b) air-cooling, AC, (c) furnace-cooling, FC, (d) slow furnace-cooling, SFC, and (d) duplex annealing (DA) treatments, respectively.

3.1. Effect of heat treatment condition on microstructure

Typical SEM micrographs of the heat-treated alloys are shown in Fig.2. The microstructures contain primary α phase, α_p, (the dark phase) and different types of secondary phases (the needle or plate like phase) in matrix β (the bright phase). Both the secondary phase and matrix β are found within prior β grain. The secondary phase types are martensite α (orthorhombic α"), acicular α, plate like α and no or lack secondary phase observed in WQ, AC and DA, FC and SFC specimens, respectively.

Variations of microstructural parameters of the secondary phases, which were measured on SEM and TEM micrographs by using an image analyzer, for the indicated secondary phase (subsequent treatment) and the indicated solution treatment temperature are shown in Fig. 3. It is clearly seen that volume fraction and size (width) of secondary phase increase with increasing solution treatment temperature.

3.2. Effect of heat treatment condition on the mechanical properties

Variations of the fracture toughness, J_{IC}, and calculated flow stress, σ_f, and the tensile strength, σ_B, and elongation, El, for the given heat treatment conditions are shown in Fig. 4. The flow stress was calculated by using tensile stress, σ_B and yield stress, $\sigma_{0.2}$, as $(\sigma_B + \sigma_{0.2})/2$. It is well known that, in the case of elastic-plastic fracture mechanics, fracture toughness can be related to flow stress. The tensile strength is known, in general, inversely related to the elongation.

Figure 4a shows that J_{IC} and σ_f strongly depend on heat treatment conditions. The dependence of J_{IC} and σ_f on the subsequent treatment appears to increase with increasing solution treatment temperature. However, for SFC specimen, J_{IC} and σ_f are nearly independent of solution treatment temperature. It is clearly seen that, in general, J_{IC} increases with decreasing σ_f. This is a general trend in the relationship between fracture toughness and flow stress. The increment of J_{IC} and the decrement of σ_f strongly depend on the subsequent treatment. It can be seen that the significant increase in fracture toughness with slight decrease in flow stress is given by FC treatment. While, the slight increase in fracture toughness of WQ specimen is resulted from remarkable decrease in flow stress. It can be also

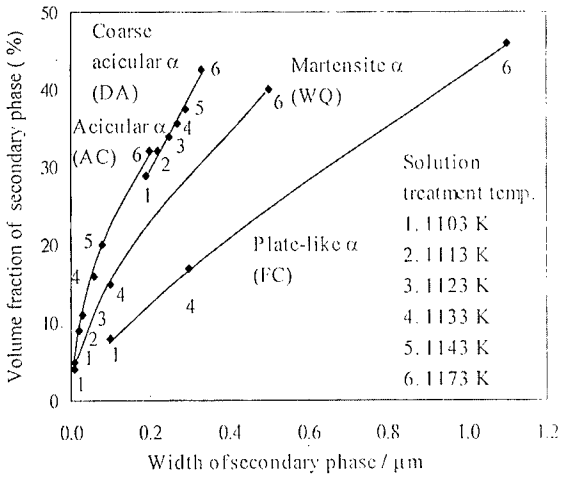

Fig. 3. Variations of volume fraction and width of secondary phase for indicated heat treatment conditions

seen that there is an exception in AC treatment, where the fracture toughness increases with increasing flow stress for solution treatment temperature between 1123 K and 1143 K when the observed microstructure contains a mixture of local and continuous structures of acicular α. It is suggested that the local acicular α provides secondary phase strengthening while the continuous one provides crack deflection toughening mechanism.

Figure 4b shows that the elongation is inversely related to the tensile strength for the given heat treatment condition except for WQ specimen. In WQ, the elongation appears to increase considerably with increasing tensile strength. The significant increment of elongation as decreasing tensile strength mainly due to the deformation-induced martensite, DIM, is found. XRD analysis showed that the matrix β in water-quenched specimens has low stability. The low stable matrix β transforms to martensite α (orthorhombic α") during testing and results in the high ductility and tensile strength, but low yield stress (0.2% proof stress). Such tensile properties characteristics are commonly observed in titanium alloy when DIM occurs [10]. DIM is found to decrease with either decreasing solution treatment temperature or lowering cooling rate as the result of decreasing stability of β phase.

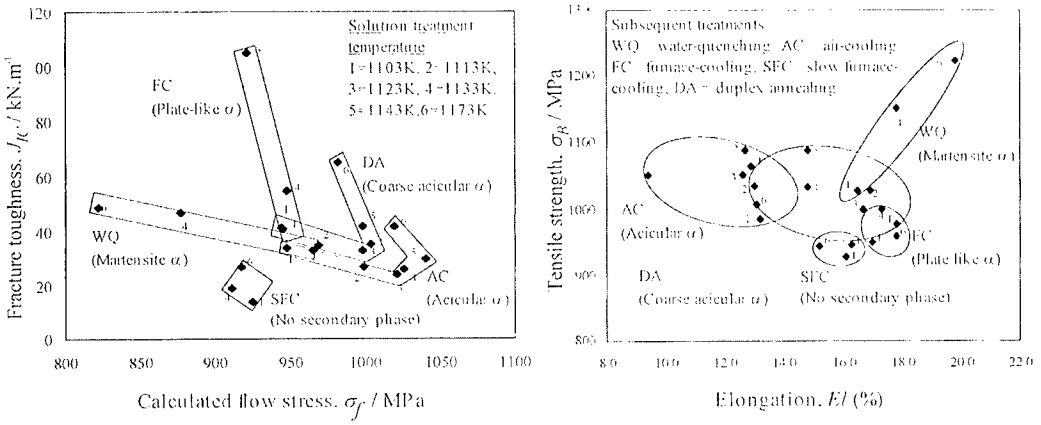

Fig. 4. Variations of (a) fracture toughness, J_{IC}, and flow stress, σ_f, and (b) tensile strength, σ_B, and elongation, El, for the indicated subsequent treatment (the observed secondary phase type).

3.3. Relationship between microstructure and fracture toughness

Figure 4a shows that the fracture toughness of microstructure containing no or lack secondary phase observed in SFC specimens, in general, is lower than that of microstructures containing secondary phase observed in WQ, AC, DA and FC specimens. Briggs *et al.* [11] reported that the low stress corrosion threshold, K_{ISCC}, in the slow-cooled Ti-6V-4VELI is due

Fig. 5. TEM micrograph showing the absence of either α_2 or ω precipitate in 1173SFC specimen.

to α_2 (Ti_3Al) phase. Bird *et al.* [12] reported that the low fracture toughness, K_{IC}, in the slow-cooled Timetal-21s alloy is related to the formation of ω phase. This indicates that the main reason for lowering fracture toughness for those type alloys is the presence of the well-known hard and brittle phase, α_2 or ω phase. However, TEM analysis of the present alloy shows that there are no such phases characterized in the SFC specimen (Fig. 5). The observed low tensile strength and high elongation for SFC specimen (Fig. 4) can indirectly indicate the absence of the α_2 and ω phase in this specimen. The reasons for the absence of such phases or precipitates in the present alloy are due to its low content of α stabilizer (4.5%Al and 0.1%O) and not so high β stabilizer (3.5%V, 2%Fe and 2%Mo). These factors suppress the formation of α_2 and ω phase, respectively during slow-cooling treatment. It is well known that α_2 and ω phases are commonly found in the high α stable alloys such as titanium aluminides and high β stable alloys such as β type titanium alloys, respectively. Therefore, it can be concluded that the low fracture toughness in the SFC specimen is the absence of secondary phase (martensite α, acicular α or plate-like α) in matrix β. The absence of the secondary phase causes the absence of extrinsic toughening mechanism in this specimen as reported in the previous report [9].

The relatively high fracture toughness in WQ, AC, DA and FC specimens are found to be mainly due to the secondary phase. It is seen in Fig. 4 that the presence of martensite α in WQ specimen (1103WQ) increases fracture toughness. The increase of fracture toughness is more pronounced when the observed DIM increases (1133WQ and 1173WQ). This indicates that both martensite α and DIM contribute to increase fracture toughness. The soft martensite α is suggested to absorb a part of energy and, as a consequence, much more energy is needed for crack tip opening. While, stored energy for the transformation of retained β to martensite α during deformation is believed to be the main reason for causing the increase of fracture toughness due to DIM. The increase of fracture toughness in the microstructures containing acicular α and plate-like α phases (AC, DA and FC specimens) is due to increasing crack deflection [8,9]. The increase of fracture toughness is more pronounced by coarse secondary phase because of micro-cracking and crack branching toughening mechanisms as observed in 1173FC specimen (Fig.6).

It can be seen in Fig. 4 that a relatively better balance of fracture toughness, and tensile strength and ductility is given by microstructure containing coarse acicular α (DA) or plate-like α (FC). The highest level of fracture toughness, i.e. at the level around 100 kNm^{-1} is given by furnace-cooling treatment with a cooling rate around 0.1 ks^{-1} from 1173 K. However, a slight decrease in cooling rate, that is, the slow furnace-cooling treatment with a cooling rate around 0.05 Ks^{-1} from 1173 K instead of furnace-cooling treatment, causes a significant decrease in fracture toughness

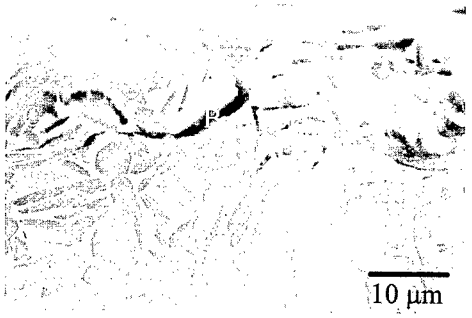

Fig. 6. SEM micrograph showing crack deflection (A), crack branching (B) and micro-cracking (C) in 1173FC specimen.

although almost no change in strength and ductility is found. The decrease of fracture toughness is mainly due to the absence of extrinsic toughening mechanism, as a result of the absence of secondary phase in the microstructure of the slow furnace-cooled specimen.

4. Conclusions

Fracture toughness, J_{IC}, and tensile properties of β-rich α+β type Ti-4.5Al-3V-2Mo-2Fe alloy were evaluated in the microstructures containing different types of secondary phases in matrix β resulting from different cooling rates from various solution treatment temperatures in α+β field. The following results were obtained.

(1) The types of secondary phases observed in WQ, AC and FC and SFC specimens are martensite α (α"), acicular α and plate-like α, respectively. While, SFC specimen has matrix β that contains no or lack secondary phase. Beside, deformation-induced martensite (α") is observed water-quenching specimen after testing.

(2) The fracture toughness of specimen having microstructure lacking secondary phase, in general, is inferior to that having microstructure containing secondary phase.

(3) The absence of extrinsic toughening mechanism as a result of the absence of secondary phase is found to be the main reason for lowering fracture toughness in the microstructure lacking secondary phase.

Acknowledgements

The authors would like to thank to Air Force Office of Scientific Research Asian of Aerospace R&D for financial support under Grant No F49620-96-0183 and to Japan Titanium Association for encouraging this study.

REFERENCES

1. R. Boyer, G. Welsch, and E.W. Collings, eds., Materials Properties Handbook: Titanium Alloys, ASM International, Materials Park, OH, USA, 1994.
2. M. Ishikawa, O. Kuboyama, M. Niikura, and C. Ouchi, Titanium '92: Science and Technology, F. H. Froes and I. Caplan, eds., vol.2, 1993, pp. 141-148.
3. T. Fujita, M. Ishikawa, S. Hashimoto, K. Minakawa, and C. Ouchi, Beta Titanium Alloy in the 1990s, D. Eylon, *et al.* eds., TMS, Warrendale, PA, USA, 1993, pp. 61-307.
4. W. D. Brewer, R.K. Bird and T.A. Wallace, Mat. Sci. Engng., A243(1998), pp. 299-304.
5. C. Ouchi, Metallurgy and Technology of Practical Titanium Alloys, S. Fujishiro, D. Eylon and T. Kishi eds., TMS, Warendale, PA, USA, 1994, pp. 37-44.
6. A. Ogawa, M. Niikura, C. Oichi, K. Minakawa, and M. Yamada, Journal of Testing and Evaluation, 24(1996), pp. 100-109.
7. A. Ogawa, K. Minakawa, and S. Takagi, Titanium '95: Science and Technology, P. A. Blenkinsop, *et. al.* eds., The Institute of Materials, vol.2, 1996, pp. 1251-1258.
8. Gunawarman, M. Niinomi, K. Fukunaga, D. Eylon, S. Fujishiro and C. Ouchi, Mat. Sci. Engng., A308(2001), pp. 216-224.
9. Gunawarman, M. Niinomi, K. Fukunaga, D. Eylon, S. Fujishiro and C. Ouchi: Journal of Material and Product, Proc.of 2nd ISAEM Conference, Guilin, P.R. China, 2000, in press.
10. M. Niinomi, T. Kobayashi, I. Inagaki and A.W. Thompson; Metall. Mat. Trans., A 21(1990), pp.1733-1744.
11. R.D. Briggs, Advances in the Sci. and Tech. of Titanium Alloy Processing, I. Weiss *et al.* eds., TMS, Warrendale, PA, USA,1997, pp. 413-420.
12. R.K. Bird, T.A. Wallace and W.D. Brewer: Advances in the Sci. and Tech. of Titanium Alloy Processing, I. Weiss *et al.* eds., ibid, pp. 473-479.

A NEW METHOD FOR DETECTION AND QUANTIFICATION OF FRETTING FATIGUE DAMAGE

E.B. Shell*, D. Eylon**

* Center for Materials Diagnostics, University of Dayton, Dayton, OH 45469-0121, USA
** Graduate Materials Program, University of Dayton, Dayton, OH 45469-0240, USA

ABSTRACT

A new method has been developed for detection and quantification of fretting fatigue damage in gas turbine engine alloys. Profilometry data taken by white light interference microscopy was used to evaluate the likelihood of crack initiation in fretted surfaces. Crack initiation in fretting samples was preceded by two precursors. First, an increase in the surface roughness in the slip region followed by an increase in the population and power of closely spaced asperities. The combination of these two factors has led to a detection and quantification method capable of differentiating between the slip and stick regions in a fretted component. A Fretting Fatigue Damage Parameter (FFDP) has been established that can be measured and used to assess the localized degree of damage of a component. When used in cooperation with a life prediction methodology, the FFDP may be used to calculate residual life in laboratory samples. In addition, the FFDP may be used in field inspections during maintenance and as a criterion for removal of parts from service. This could lead to the development of more reliable depot nondestructive evaluation (NDE) techniques for fretting fatigue prone components.

1. INTRODUCTION

Fretting fatigue has long been recognized as an important mode of failure in the service of mechanical components that are not intended to have a relative motion, but because of vibrational loads or deformations experience minute cyclic relative motions [1]. Such damage can result in a considerably lower component life. Fatigue strength under fretting fatigue conditions may be as low as 30% of the plain fatigue strength, depending upon the material and loading conditions [2]. This increased rate of damage accumulation, along with the unpredictability of the actual conditions experienced in use, necessitate a means for non-destructive examination of the surface and prediction of the remaining service life.

Fretting fatigue is a surface and near-surface phenomena. Thus, surface NDE techniques may be particularly useful in the detection of fretting fatigue damage. However, this may be complicated by the initial surface conditions of the material. Because fretting damage is a very localized phenomenon, techniques developed to detect fretting damage must have a reasonably high spatial resolution. Although much research has been devoted to the understanding of fretting mechanisms, no characterization methodologies have been established for quantifying the level of fretting damage.

1.1 Need for an Improved Fretting Damage Detection Method

Currently, the procedure for the inspection of fretting fatigue critical components (e.g., as turbine engine fan blades and disks) is simply a visual inspection for the presence of any large surface irregularities during depot inspections. This led to the removal of many blades and disks either: (1) before there was a substantial amount of fretting damage, or (2) due to less dangerous surface deformation such as sliding wear.

In addition, this criterion has been proven ineffective when compared to laboratory-tested samples. In fact, laboratory-testing conditions frequently lead to failure in samples where the roughness of the surface is less than 3 μm, well below what could be called a "large surface irregularity" during inspection. A new method that would allow for a better understanding of the fretting process is, therefore, needed. This may be achieved through observation of the inherent changes that may be universally observed, leading to the ability to quantify fretting damage and calculate residual component life.

1.2 Concept of Precursor Damage Detection

Because fretting fatigue is a surface and near-surface phenomena, surface NDE techniques, particularly optical techniques, lend themselves to the detection and characterization of fretting damage. Most surface techniques are specifically designed for the detection of surface cracks. However, because high strength materials, such as titanium and nickel-based alloys, have relatively low fracture toughness, methods that are used to detect cracks are inherently unsafe and require frequent inspection. In fact, some high strength materials may not form a detectable crack before 95-99% of life has expired.

Instead of crack detection, it may be more beneficial to assess the material on the basis of the *likelihood of* or *potential for crack initiation*. This may be accomplished by evaluating the condition of the surface through such parameters as roughness and asperity spacing. These parameters relate, on a microscopic level, the material surface finish to the very localized stress concentration at the bases of the asperities geometry and spacing.

It is postulated that through fretting action, the morphology of these asperities changes. This change allows, through an analysis of the roughness and the spacing between adjacent asperities, an inference to be made as to the condition of the material and the changes that have occurred due to the vibrational loading of the sample. The fretting damage level may then be evaluated through profilometric observations and analysis based on the non-destructive characterization of the asperities on the surface.

1.3 Fracture Mechanics Basis for Profilometric Damage Criteria

The theoretical basis for a profilometric description of fretting damage accumulation lies in the fracture mechanics that may be used to describe the stress field, on a microscopic level, near the surface of the material. An equation that may be used to describe the stress intensity at the front of a semi-elliptical flaw on the surface of a sample is: $K \propto \sigma \sqrt{(a/\rho)}$, where $\boldsymbol{\sigma}$ is the applied stress, **a** is the length of flaw, and $\boldsymbol{\rho}$ is the radius of curvature of the elliptical flaw. In a two-dimensional analysis of asperities on the surface of a sample this equation may be applicable. In this case, we cannot accurately measure the radius of curvature of the asperity bases. However, we can make an inference into the curvature at the bases of the asperities based upon the spacing between asperities. The average radius of curvature between adjacent asperities is then directly proportional to the average spacing between asperities. For every

sample there will be a continuous range of asperity spacing present on the surface of the material. However, the range of most interest is that of a low asperity spacing that would lead to a smaller radius of curvature and, thus, higher localized stress intensity near the surface.

As for the investigation of the asperity height, it is impractical to analyze each individual asperity. But, we can use the calculated roughness of given area of analysis to provide a statistical inference of the average asperity height, which is directly proportional to the surface roughness of the material.

Combining the asperity spacing and surface roughness over a given area leads to a better understanding of crack initiation from fretting fatigue-related surface damage.

2. MATERIALS AND PROCEDURES

2.1 Materials

The forging stock for the material used on this work was a double VAR melted Ti-6Al-4V 63.5mm diameter bar stock from Teledyne Titanium produced in accordance with AMS4928, and supplied in mill-annealed condition: 705°C/2 hr/AC [3]. Chemistry was acceptable in accordance with AMS4928 as shown in Table 1, as well as the beta-transus temperature as determined by DTA.

Table 1: Chemistry of Teledyne Titanium Heat No. TE01

Element	Ti	Al	V	Fe	O	N	Transus °C
Top	bal.	6.27	4.19	0.20	0.18	0.012	990
Bottom	bal.	6.32	4.15	0.18	0.19	0.014	1003
AMS4928	bal.	5.50-6.75	3.50-4.50	0.30 max	0.20 max	0.050 max	-------

The 63.5mm diameter bar stock was cut into 200 400mm long forging performs forged in one campaign in a 400mm long closed-end channel-die, with the intended plate size of 400x150x20mm on an 8,000 ton mechanical press. Dies were initially heated to 150°C. Glass-lubricant coated bars were preheated to 940°C +/- 10°C for 30 minutes in a continuous furnace and rapidly transferred to the press. After a one stroke forging, pieces were air-cooled. The average strain rate at impact (for plain strain case) was calculated to be 9/sec. Forging was followed by a vacuum anneal at 700°C/2hr to stabilize microstructure and normalize hydrogen content that might have been picked up during de-scaling, and followed by 930°C/1hr ST and another 700°C/2hr vacuum anneal. This practice is similar to the one used for forging gas turbine engine fan-blades, and resulted in a duplex microstructure with 60vol% equiaxed primary alpha (Fig.1) with good fatigue strength. Tensile results of one plate at $5x10^{-4}(s^{-1})$ are shown in Table 2. The higher modulus in the transverse direction indicates processing texture.

Table 2: Room temperature tensile results of plate #7

Location	Orientation	UTS (MPa)	YS (MPa)	El (%)	Modulus (GPa)
Center-long	L	976	929	21.2	116
Center-long	L	981	931	19.0	124
center-trans	T	997	947	21.0	121
center-trans	T	993	937	19.2	134

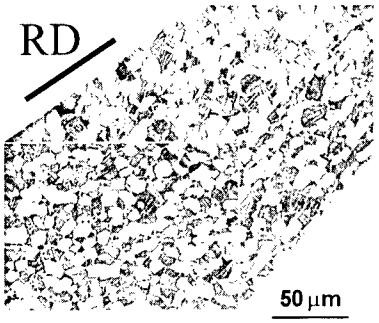

Fig.1 Ti-6Al-4V microstructure used in this study.

2.2 Mechanical Testing

Details of the fretting fatigue procedures are provided elsewhere [4]. In brief, the test system is an axial fatigue test machine in which the gripping system allows the development of a slip region on the sample's surface. The samples measure 100 mm in length, 10 mm in width, and 2 mm in thickness. The sample is clamped at each end by two flat pads (25.4 mm in length), also machined from the same Ti-6Al-4V plate. When a cyclic stress is applied, a slip and stick zone is developed on the sample. The samples were tested using a variety of surface finish conditions. These included samples that were finished with a RMS#8 finish and samples that were carefully polished, both tested with Ti-6Al-4V fretting pads.

2.3 Profilometry

White light interference microscopy was used to measure the surface topography before and after the samples were subjected to load. This fast technique is capable of a lateral surface resolution of 0.2 μm and a vertical/height resolution of 3 nm. The details of the instrument are provided elsewhere [5].

From the surface height maps, two evaluations of the data are performed. (a) A Fourier transform of the surface from which the Power Spectral Density (PSD) can be plotted against Spatial Frequency is calculated. It has been postulated that fretting fatigue cracks initiate when the surface features reach a critical spatial frequency. As the concentration of high spatial frequencies in the surface increases, cracks are able to initiate easier. (b) The roughness of the sample is evaluated; either quantitatively by a roughness calculation or qualitatively by viewing a line-scan of the sample surface.

From the profilometry data, the inherent spatial frequencies of the surface can be investigated. Looking at the asperity spacing gives some insight into the likelihood of crack initiation. So, instead of looking at the data in the spatial domain, it would be more useful to investigate the spacing of the surface asperities by transforming the data into the frequency domain. This enables the observation of local decreases in the asperity spacing that are present in the slip region of fretting samples. The PSD-spatial frequency plot is generated by a Fourier Transform of the 3-dimensional height data. This effectively transforms the data from the space domain to the frequency domain, which enables an easier evaluation of the inherent frequencies of the data set. Because the sample surface is nominally flat, the maximum PSD occurs as the spatial frequency approaches zero, which represents a perfectly flat surface. The higher range of spatial frequencies corresponds to small, closely spaced asperities. This PSD plot represents a spatial frequency spectrum over the entire field of view

of the sample. So, when using this data to determine the presence of slip regions, care must be taken to ensure that the sampling area and the reference area are uniform. If this is not the case, the PSD levels for the data set will only be an average of the entire field. Likewise, when determining fretting damage levels in a given area, the percentage of slip versus stick regions must be taken into account to determine the true degree of damage.

3. RESULTS AND DISCUSSION

The profilometry data resulted in two types of information; (a) the power spectral density, which is the Fourier decomposition of the measured surface into its component spatial frequencies, and (b) the surface roughness. While an increase in surface roughness due to asperity yielding and microwelding is often associated with fretting fatigue damage [6], the samples used in this study already had a machining roughness on the order of that expected due to fretting wear. So, while a slight increase in roughness was seen, more promising results are shown based upon the PSD data.

3.1 PSD-Spatial Frequency Analysis

Profilometric data has been proven effective in the qualitative detection of fretting fatigue and fretting wear. By taking profilometry data from non-contacted, slip, and stick regions of the same sample, differences in the Power Spectral Density (PSD) of the surface data may be seen. PSD-Spatial Frequency plots, such as that shown in Fig. 2, have shown that regions that are damaged by fretting action contain a higher PSD value at higher spatial frequencies than areas subjected solely to fatigue (non-contact region) or areas that were in the stick regime. As can be seen, at very low spatial frequencies, all regions have high PSD values, indicating that all regions are nominally flat. However, as higher spatial frequencies are considered, an order of magnitude difference is seen between the slip and non-contact regions.

It is postulated that high spatial frequency asperities may be associated with fretting fatigue crack initiation. So two related conclusions may be formed: (a) an area that has been fretted will have a higher density of high spatial frequency asperities, and (b) an area that has a

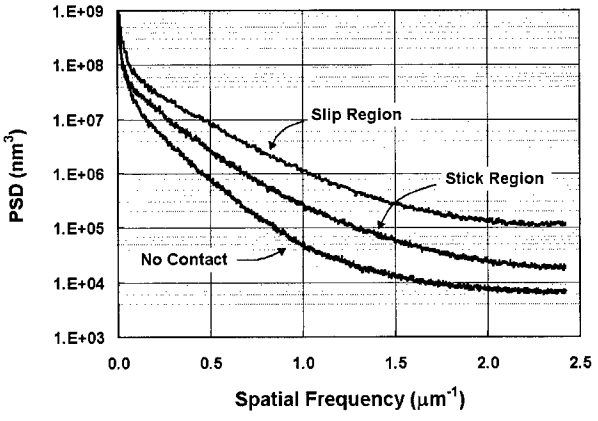

Fig.2 PSD data for the partial slip, stick, and non-contact regions of a fretting fatigue laboratory sample.

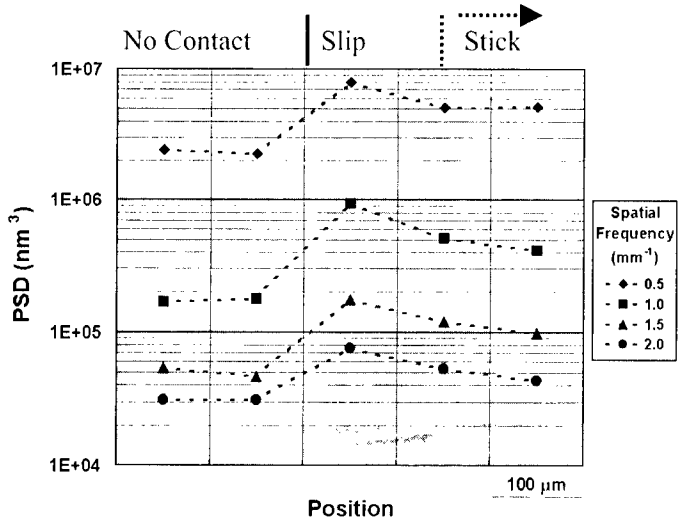

Fig.3 PSD data plotted at discrete spatial frequencies. The slip zone can be seen in the background of the chart.

higher density of high spatial frequency asperities is likely to initiate cracks sooner. This is justified by imagining each area between asperities as a stress concentration area. As the frequency of the asperities gets higher, the average radius of curvature of the valleys between the asperities decreases, thereby increasing the localized stress concentration factor at the surface. These characteristics enable the detection of possible crack initiation sites at the surface of the material through spatial frequency analysis before crack initiation occurs. The detection of localized fretting damage can be seen in the following example. A scan of the surface of a laboratory fretting fatigue sample is taken. The fretting scar is clearly visible in the data shown in the background of Fig. 3. The data set is then separated into subsets as shown by the gridlines. A PSD plot is generated from each of these regions. To better compare the surface from stick, slip, and non-contacted regions, the PSD is compared for discrete spatial frequencies (0.5, 1.0, 1.5, and 2.0 μm^{-1}). This enables a relative comparison between adjacent regions in the sample. The data clearly shows that the slip region may easily be detected through profilometry measurements. The PSD of the slip region is 2.5 to 7 times higher than the non-contact region, decreasing as the measurement is obtained back into the stick region.

3.2 Fretting Fatigue Damage Parameter

Beyond using PSD data for the detection of fretting fatigue damage, PSD analysis is promising in the quantification of fretting damage. This quantification is accomplished by observing the relative differences between the fretted region and the region subjected solely to plain fatigue. As seen in Fig. 4a, scans taken from samples of similar damage levels are not identical, possibly the result of slightly different initial surface conditions. However, by normalizing the fretting data with respect to data from the non-contact region (Fig. 4b), a Fretting Fatigue Damage Parameter (FFDP), is derived: $FFDP = PSD_{slip} / PSD_{NC}$. The deviation of this parameter above unity is representative of the damage level of the area examined and may be used to quantify the damage. It is thought that this parameter relates directly to the likelihood of crack initiation relative to the starting condition of the material.

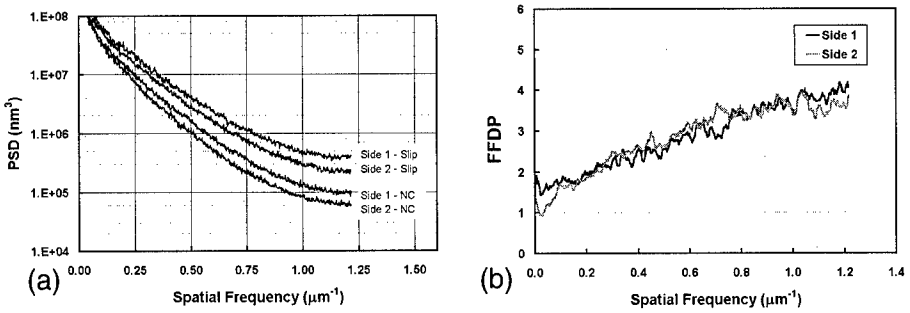

Fig.4 (a) Data taken from the slip and non-contact regions from two sides of a specimen. Both sides were subjected to identical loading conditions but experienced slightly different machining conditions. (b) Data from two slip regions normalized with respect to the non-contacted surface data. Both sides exhibit identical degrees of damage.

3.3 Quantification of Damage and Residual Fatigue Life Predictions

The development of a refined quantification tool based upon PSD analysis presents a number of challenges. The primary difficulty in developing a calibrated technique for the prediction of residual life in components is the inability to actually determine the true fractional life of a specific area. Because most fretting fatigue experiments do not yield uniform damage across the slip line, there is a question as to what damaged area should be considered for determination of the overall sample residual life. In fact, due to non-uniform damage, only the area that is the most damaged will ultimately initiate the final failure and should be considered at the nominal fractional life. This leads to another obstacle to making quantitative measurements for life prediction purposes: the difficulty involved in using an area analysis to search for a relatively localized phenomenon. In any sample or component subjected to fretting fatigue, generally only a small region is subjected to the most severe conditions. As a result, manually searching for this most damaged area is extremely time consuming. However, a methodology based upon these techniques could implement computer analysis of a large image to: first, break up the image into smaller, discrete regions; second, perform a Fourier transform on each of these smaller regions; finally, through comparison of the PSD curves determine the region representative of the highest degree of damage. This method has been (roughly) performed manually for one sample. In this case, the sample was scanned along the leading edge of the slip line as seen in Fig 5. The resulting data, shown for a few spatial frequencies, shows that the FFDP is highest within 2 mm of both edges of the sample. This increased level of damage near the edge corresponds to the location of crack initiation as seen in failed test samples and should be used for residual life calculation [7].

4. CONCLUSIONS

The objective of this work was to develop a new tool for the detection of fretting fatigue damage in Ti-6Al-4V. In addition, characteristics of fretting fatigue damage were investigated in order to develop damage quantification techniques. From this work, the following conclusions were made: .

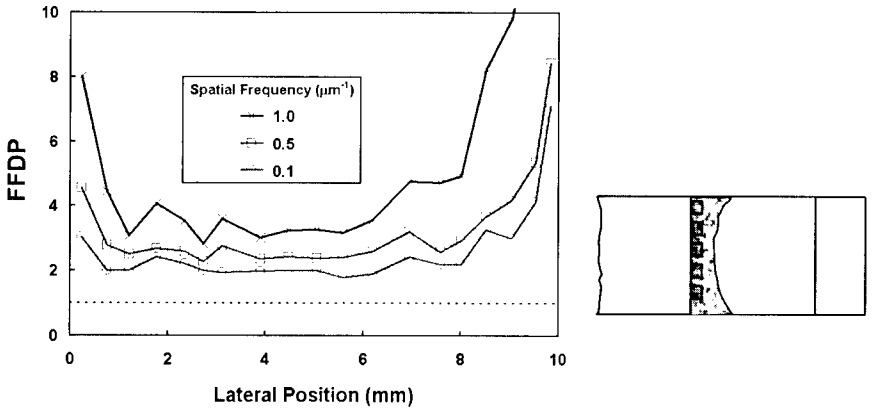

Fig.5 Variation of the FFDP across the slip region of a fretting sample. The schematic shows the location of the scans in the slip region.

1. PSD-spatial frequency analysis has proven effective in the detection of fretting fatigue damage. Differentiation between the slip, stick, and non-contact regions is possible with this NDE technique.

2. The surface roughness increases in the slip zone compared to the non-contact and stick zones. However, the machining lines and pre-existing roughness of the samples prevent this measurement from being a reliable method of slip region detection.

3. Initial attempts at quantification have proven difficult due to the extremely localized nature of failure initiation due to fretting fatigue. The technology is available that would permit this method to be used as a NDE tool. However, further refinement and computerized data analysis of the damaged region must be utilized for this method to be a mature, reliable damage quantification technique.

4. A Fretting Fatigue Damage Parameter (FFDP) has been developed that may be used to quantify the level of damage in a component.

ACKNOWLEDGEMENTS

Effort sponsored by the Defense Advanced Projects Agency (DARPA) Multidisciplinary University Research Initiative (MURI), under Air Force Office of Scientific Research grant number F49620-96-1-0442. The cooperation of A. Hutson, Dr. T. Nicholas, Dr. S. Mall, Prof. M Niinomi, and Prof. S. Gustafson in providing samples for examination is also greatly appreciated.

REFERENCES

[1] J.A. Collins, Failure of Materials in Mechanical Design. John Wiley & Sons, NY, 1981.
[2] R.A. Antoniou, T.C. Radtke, Mat. Sci. Eng. A237 (1997) 229-240.
[3] D. Eylon, "Summary of the Available Information on the Processing of the Ti-6Al-4V HCF/LCF Program Plates"; UDRI report, October 1998, UDRI, University of Dayton, Dayton, Ohio.
[4] A.L. Hutson and T. Nicholas, Int. J. of Fatigue 21 (1999) 663-669.
[5] J.L. Schroeder, D. Eylon, E.B. Shell and T.E. Matikas, in Nondestructive Methods for Materials Characterization, MRS, Fall Meeting, Symposium S, (1999) Paper No. S2.3.
[6] O. Vingsbo and S. Soderberg, Wear 126 (1988) 131.
[7] A. Hutson, unpublished research conducted at Wright-Patterson Air Force Base, 1999.

Characterization of Accumulated Fatigue Damage in Ti-6Al-4V Using Nonlinear Acoustics and TEM

J.L. Maurer*, J. Frouin**, S. Sathish**, D. Eylon*

* Graduate Materials Program, University of Dayton, Dayton, OH 45469-0240, USA
** Center for Materials Diagnostics, University of Dayton, Dayton, OH 45469-0121, USA

ABSTRACT

Life prediction methodologies for aerospace components subjected to fatigue, require understanding and quantification of accumulated damage prior to failure. Most studies are associated with the understanding of crack initiation, propagation and the final fracture stage mechanisms and relating them to various life prediction models. However, damage detection at the pre-initiation stage, may allow a better prediction of *residual life* and better judgement about component repair and retirement. The objective of this work was to generate controlled damage in Ti-6Al-4V forged plate material in a duplex microstructural condition, and characterize the stages of damage using transmission electron microscopy (TEM). The microscopy results from the controlled damage samples were used to interpret the results from nonlinear acoustics (NLA) measurements on the fatigued material. The results show a clear correlation of the dislocation density measurements and local nonlinear acoustic measurements on the deformed material. This could lead to a method to estimate the accumulated damage in components in which the cyclic history is not well defined and prediction of residual life.

1. INTRODUCTION

Unpredictable failures of titanium alloy engine components, such as fan blades, in both military and civil aviation have recently highlighted the importance of understanding and predicting fatigue failure. Nondestructive techniques that measure the degradation of mechanical properties of materials undergoing fatigue are extremely important in the prediction of remaining fatigue life of materials. Most of the techniques available at the present time are still in the experimental stage and while useful in the basic understanding of fatigue processes, cannot be used as a characterization tool. However, nonlinear acoustic (NLA) data shows large changes as accumulated damage due to fatigue increases [1,2,3]. For this reason, nonlinear acoustics is thought to be a promising tool for both characterization and determination of fatigue damage levels and residual life.

2. MATERIALS AND PROCEDURES

2.1 Materials

The material selected for this study is a forged Ti-6Al-4V plate, which is part of a larger HCF/LCF program [4,5]. The microstructure studied in this work was a duplex microstructure shown in Figure 1. This material was very carefully prepared, processed and

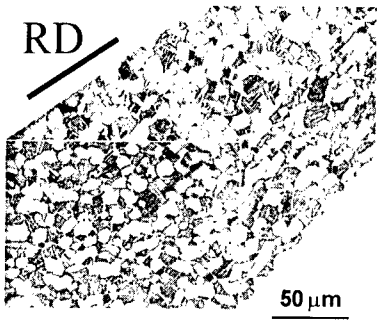

Fig.1: Ti-6Al-4V microstructure used in this study.

characterized to provide conditions as close as possible to the microstructure found in forged titanium alloy fan blades [4]. This duplex microstructure has about 60% equiaxed primary alpha phase and 40% fine lamellar transformed alpha plates. The slight directionality in the long axis of the plate simulates an actual Ti-6Al-4V fan blade microstructure. In addition, this microstructure is an ideal microstructure for a good combination for crack initiation and crack propagation resistance. The equiaxed alpha-phase provides good tensile ductility and as a result, good resistance to crack initiation [6]. On the other hand, the lamellar secondary alpha-phase will slow crack propagation and therefore increase the fatigue crack propagation resistance [7,8].

2.2 Mechanical Testing

To enable damage characterization by nondestructive methods, such as nonlinear acoustics, it is advantageous to initially use test conditions which create high levels of damage and which can be done under well-controlled conditions. In low cycle fatigue the material is undergoing plastic deformation that leads to generation, motion, and rearrangement of dislocations [8]. It is such internal damage conditions that may enable observation of internal changes in the characteristics of the material by nondestructive characterization techniques.

When the characterized damage at a certain percentage of fatigue life is compared to service damage components, a methodology for residual life prediction can be developed. As a result, *fractional fatigue life tests* were conducted for the LCF condition. The average fatigue life at certain test conditions was established, followed by characterization of the damage observed with TEM at those conditions.

For the fatigue damage generation, a Servo-hydraulic machine with capability of cycling at frequencies up to 100 Hz was utilized. Special grips were designed to allow simultaneous testing of mechanical loading and nonlinear acoustic detection of the samples. This capability allowed for in-situ, real-time monitoring of fatigue experiments through observation of the changes in nonlinear acoustic parameters due to fatigue cycles. Fatigue specimens were cylindrical smooth samples with a grip diameter of 14 mm and a gauge diameter of 7.5 mm (Figure 2).

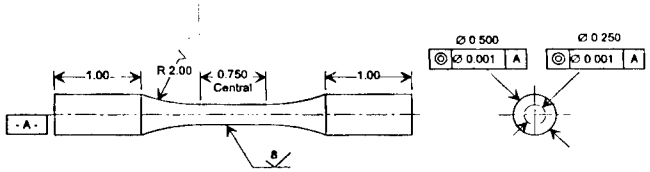

Fig.2: Schematic of fatigue specimens.

The fatigue tests were conducted in laboratory air and at room temperature with a stress ratio of 0.1. Table 1 shows the test conditions.

Table 1: Summary of fatigue testing conditions.

	Maximum Stress (MPa)	Frequency (Hz)	Ave. Fatigue Life (cycles)
Low Cycle Fatigue	850	1	34,545
High Cycle Fatigue	620	10	1,934,789

2.3 Nonlinear Acoustics

A block diagram of the experimental arrangement for the piezoelectric f-2f method is shown in Figure 3 [9]. This is a relatively simple and straightforward measurement technique for an in-situ study of the fatigue process. A tone burst signal generator and a power amplifier were used to inject sound waves with longitudinal mode in the specimen at a frequency of 10 MHz. A 10 MHz high power bandpass filter was placed between the power amplifier and the transducer to make sure that unwanted harmonic signals were filtered out. The same transmitting transducer was used to detect the fundamental signal as it was reflected from the other end of the specimen. In order to receive the second harmonic signal from the other end of the specimen, a 20MHz transducer was attached. After the second harmonic signal was detected, it was fed to a linear IF amplifier through a 20 MHz bandpass filter. Both fundamental and second harmonic amplitudes were measured with a digital oscilloscope. NLA measurements were conducted during online fatigue experiments and also at localized points on broken fatigue specimens.

The nonlinearity parameter, β, is calculated for each sample. When a pure longitudinal acoustic wave with a fundamental frequency, f, propagates through material, some of the energy is converted to higher order harmonic signals due to the inherent nonlinear elastic behavior of the material. The second harmonic signal is particularly strong and can be used to measure the nonlinearity parameter, β, which is defined as [3]:

$$\beta = (8/ak^2)\,[A_2/(A_1)^2]$$

where A_1 and A_2 are the amplitudes of the fundamental and second harmonic signals respectively. Also, **k** is the wave number and **a** is the length of the sample.

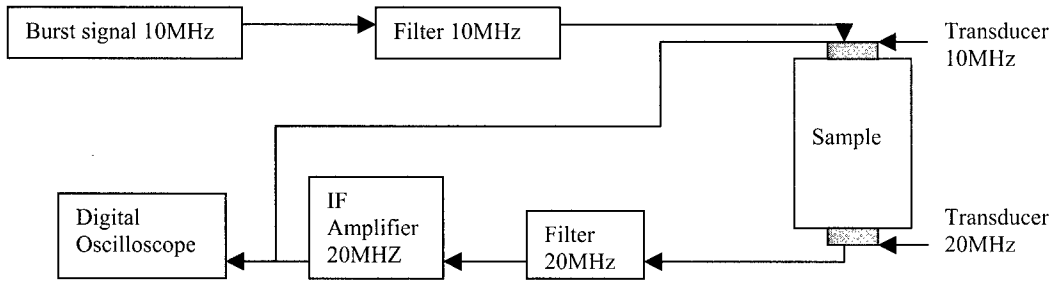

Fig.3: Block diagram of the experimental setup for NLA parameter measurements.

2.4 Transmission Electron Microscopy

Transmission electron microscopy was done on a Phillips microscope. TEM samples were prepared from the fatigue specimens in a very controlled, precise manner so that no new deformation is introduced into the material. First, the 2-mm section of the fatigue specimen is ground with 400-grit paper to 125-150 micron thickness. Next, a 3-mm diameter disk is core drilled from the section. The disk is then dimpled so a 25-micron thick region exists in the center of the disk. Finally, the disk is placed in an ion mill until a small perforation develops in the center of the disk. It is around this perforation that the transmission electron microscopy is conducted.

3. RESULTS AND DISCUSSION

Transmission electron microscopy was conducted on fractured fatigue samples and partial life samples to characterize the types and amounts of damage occurring in the material during the fatigue experiments. The TEM material from the partial life samples was always taken from a slice perpendicular to the direction of deformation from the middle of the gauge section. The fractured samples were sectioned into 2 mm slices up the gauge length away from the fracture surface (designated by an 'F' in Figure 4), thus providing graded imaging of the internal damage.

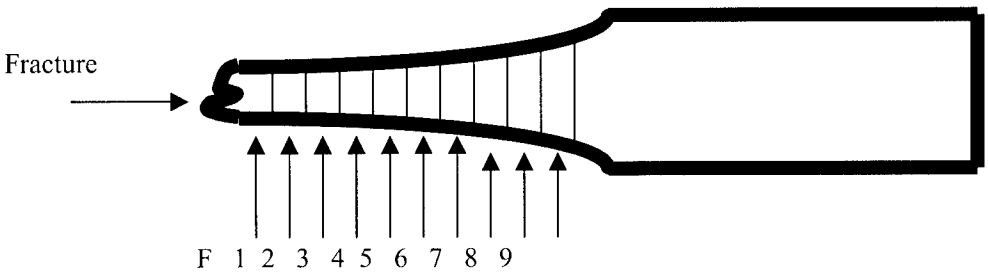

Fig.4: Diagram illustrating the sectioning of the fractured fatigue samples.

3.1 Online Nonlinear Acoustic and TEM Results for LCF

In-situ, real-time nonlinear experiments were preformed during the course of two separate LCF tests. Figure 5 displays the results of the nonlinearity parameter plotted against the number of fatigue cycles with TEM results from partial life samples [9]. As can be seen, the test was reproducible, as the curve for the two tests are almost identical in nature. Figure 6 shows the dislocation density measurements for LCF partial life samples. The online, in-situ NLA tests on the duplex microstructure for LCF conditions tend to follow the dislocation density curve generated from TEM analysis of the partial life LCF samples. However, at 90% of life the dislocation density curve increases drastically, while the nonlinearity parameter curve plateaus. The NLA measurements of the material do not detect this increase in accumulated damage at the end of life. It appears that a saturation point is reached beyond which a distinction cannot be made a differentiation cannot be made from one level of damage to another. This is thought to be due to the acoustic signal having to travel through the entire length of the sample, including material that has not experienced significant deformation due to fatigue.

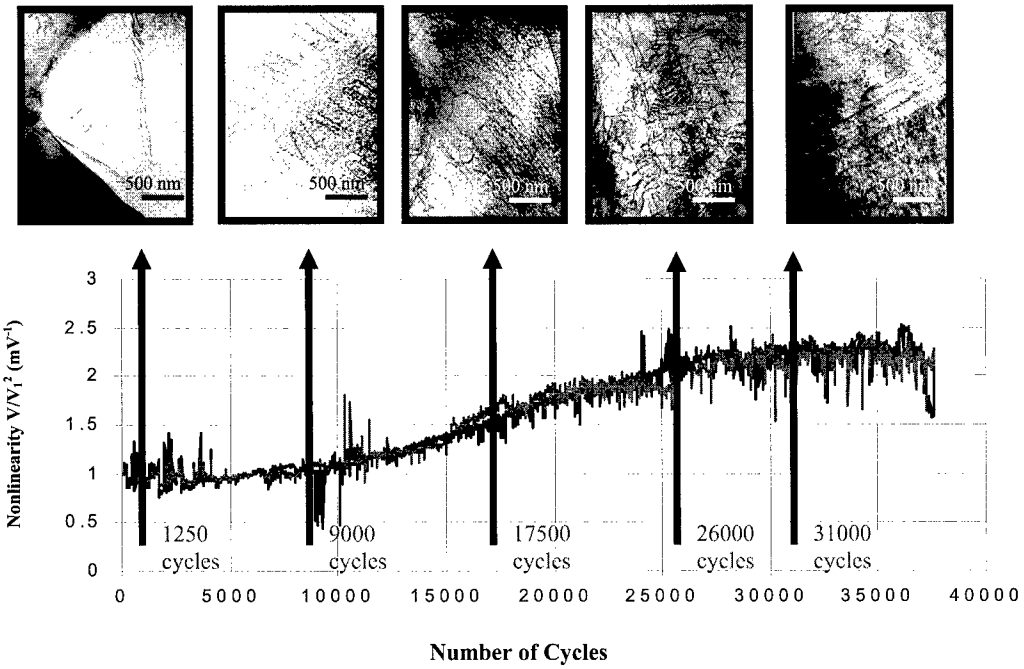

Fig.5: Nonlinearity parameter vs. LCF cycles for online NLA measurements with accompanying TEM micrographs showing the levels of internal damage.

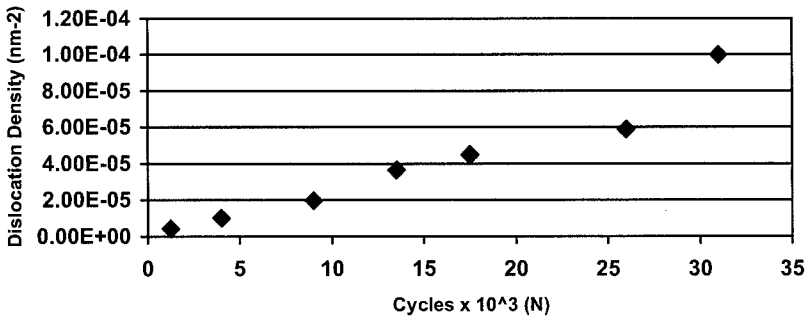

Fig.6: Dislocation density vs. number of LCF cycles.

3.2 Localized Nonlinear Acoustic and TEM Results for LCF

Dislocation density values were compared to NLA measurements made on fractured LCF duplex samples and plotted as a distance from the fracture surface to the grip section (Figure 7). The results revealed that the nonlinearity parameter curve follows the trend of the dislocation density curve; the curves lay almost on top of each other for the LCF condition. Both the dislocation density and the nonlinearity parameter grew at an exponential rate as the fracture surface was approached. The nonlinear acoustic measurements definitely appear to be detecting the amount of accumulated damage in the fatigued material, indicating that nonlinear acoustics could be a viable nondestructive evaluation tool for samples where the history is not well-defined.

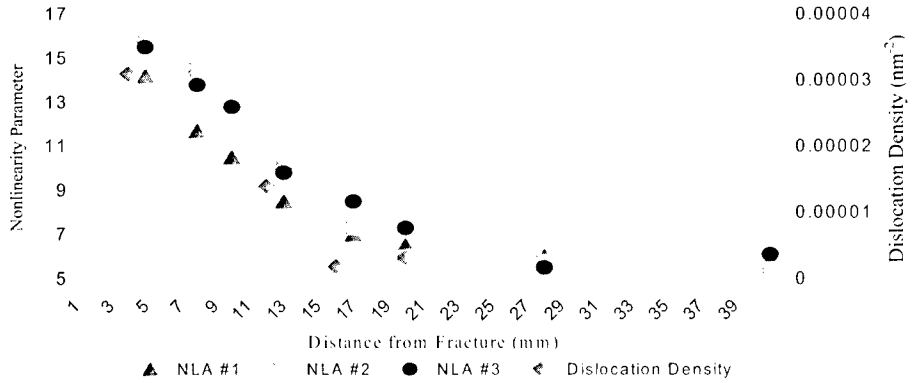

Fig.7: Comparison of the dislocation density and nonlinearity parameter measurements on broken LCF samples.

4. CONCLUSIONS

The objective of this work was to analyze accumulated microstructural fatigue damage by using TEM to explain the changes in the nonlinear acoustic signal produced during online fatigue experiments in the crack precursor stage, and localized NLA measurements on broken fatigued samples. The nonlinear acoustic signal was shown to exhibit a reproducible, characteristic curve with the continuation of the online fatigue cycling process. However, the online NLA measurements were not able to distinguish any change in the internal damage past 60% of fatigue life. The localized NLA measurements in contrast correlated extremely well with the dislocation density measurements along the fractured fatigue samples. By calibrating this nonlinear acoustic signal with the microstructural changes observed by TEM, it may be possible to develop a nondestructive technique to relate the level of internal damage in the material and to predict residual life of the component.

ACKNOWLEDGEMENTS

The authors wish to thank the Ohio Space Grant Consortium, the DAGSI and the Clare Boothe Luce Foundation for the aid during the course of this work. In addition, the help of Dr. T. Nicholas of AFRL in obtaining the material, facilitating the processing and providing helpful discussions on the fatigue results is highly appreciated. This work was supported by the DARPA-MURI grant number F49620-96-1-0442. Finally the authors wish to thank for following individuals for all of their help and efforts: Bob Wheeler, Scott Apt, Tim Campbell, Ed Klosterman, and Cindy O'Brien.

REFERENCES

[1] FROUIN, J., S. SATHISH, T.E. MATIKAS, and J.K. NA. Waiting publication in Journal of Materials Research.
[2] CANTRELL, J.H. and W.T. YOST, Journal of Applied Physics, 81, 2957 (1997).
[3] BUCK, O. In Review of Progress in QNDE, Vol. 9, eds. D.O. Thompson and D.E. Chimenti, (New York: Plenum, 1990) p. 1677.
[4] EYLON, D. "Summary of the Available Information on the Processing of the Ti-6Al-4V HCF LCF Program Plates." Report prepared for the PRDA V Meeting, February 1998, San Antonio, TX.
[5] E.B. SHELL and D. EYLON, "A New Method for the Detection and Quantification of Fretting Fatigue Damage." A paper in this Conference Proceedings.
[6] EYLON, D. and C.M. PIERCE, Metallurgical Transactions A, Vol. 7A, (1976), p. 111-121.
[7] EYLON, D., J.A. HALL, C.M. PIERCE and D.L. RUCKLE, Metallurgical Transactions A, Vol. 7A, (1976), p. 1817-1826.
[8] EYLON, D. and P.J. BANIA, Metallurgical Transactions A, Vol. 9A, (1978), p. 1273-1279.
[9] FROUIN, J., T.E. MATIKAS, S. SATHISH, and J.K. NA, Proceedings SPIE Nondestructive Evaluation of Aging Materials and Composites III, Vol. 3585, (1999), p. 107-116.

CYCLE DEFORMING BEHAVIOR AND STRUCTURE OBSERVATION OF Ti-2Al-2.5Zr ALLOY AT –196 °C

Yu Zhentao Deng Ju

Northwest Institute for Nonferrous Metal Research
P. O. Box 51, Xi'an, Shaanxi 710016, CHINA

ABSTRACT

The cycle deforming behavior of Ti-2Al-2.5Zr alloy with its tube specimens (as annealed) was investigated at –196 °C. The effects of stress ratio R, stress amplitude σ_a, cycle number N on cyclic deforming behavior and fatigue properties etc. were analyzed. The stress~strain curve equations under tensile and cyclic loading, and the prediction equations of fatigue-life were got. According to LM、SEM and TEM observation, the regularity of twin formation, fatigue fracture features and dislocation configurations under cyclic deforming were discussed. The results show: during cycle deforming of Ti-2Al-2.5Zr alloy, the cyclic deforming behavior behave as cycle hardening as R=0, -0.5 and -1. There are large quantities of dimples, secondary cracks and fatigue striations in fatigue fractures of Ti-2Al-2.5Zr alloy, and some facets and holes also exist among them. The cyclic deforming is alternately controlled by slip and twinning, and twins of the $\{01\ \bar{1}2\}$, $\{11\ \bar{2}1\}$, $\{11\ \bar{2}2\}$, $\{11\ \bar{2}3\}$ have been found.

Keyword: Cycle deforming behavior, Microstructure, Ti-2Al-2.5Zr alloy, –196 °C

1. INTRODUCTION

Ti-2Al-2.5Zr alloy (TA16) is one kind of single –phase α Ti alloy with hexagonal close-packed (HCP) structure that is mainly applied as tube system. Since the symmetry of its slip system in space is lower, thus the deforming mode is very complicated. It is thought the prism slip is main plastic deforming pattern[1], but prism slip cannot supply enough slip systems to meet the coordinated deforming condition, so it can mot explain the fine plasticity of TA16 at RT. Twinning is also important deforming mode for HCP metal at cryogenic temperature[2]. And the deforming characteristics of the tube are somewhat different from the plate and rod materials because of their different shape, texture etc[3].

In the present work, the cyclic deforming behavior of TA16 alloy were investigated at -196°C with tube specimen under different stress ratio R, stress amplitude σ_a and cycle number N. The comparative analysis and microstructure observation were also performed.

2. EXPERIMENTAL PROCEDURE

The TA16 rolled tube (Φ13×2, as-annealed) with equiaxial structure were machined into LCF specimens according to GB/T13239-91 and GB6399-86 of Chinese national standard

(See Fig.1, Tab.1). LCF tests at -196°C were conducted with MTS 810±250KN fatigue tester. Experimental parameters are as follows: (1) constant stress control, stress ratio R=0.1, -0.5 and –1, (2) Maximum stress $\sigma_{max}=0.70\sigma_b^{-196}\sim0.95\sigma_b^{-196}$, (3) triangle wave, (4) 0.5Hz. Tests were stopped when the specimens were broken, or above 20000 cycles in liquid nitrogen. The fatigue fracture, microstructure and dislocation configuration were observed by LM (McF2), SEM (JEOL JSM-5800) and TEM (JEOL-200CX).

Table.1 Chemical compositions and mechanical properties ofTi-2Al-2.5Zr at -196°C

Elements	Al	Zr	Fe	Si	C	N	H	O	Ti
Composions	2.0	2.5	0.03	<0.04	0.02	0.01	0.003	0.07	Balance
Tensile properties	-196°C: σ_b=923.5Mpa, σ_s=795.8Mpa, δ_5=42%								

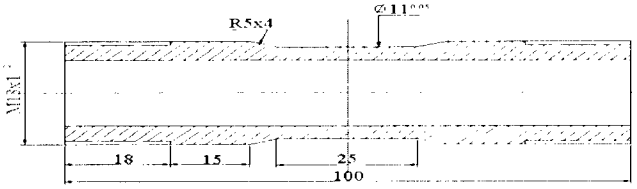

Fig.1. Specimen diagram for low cycle fatigue test at -196°C

3. RESULTS AND DISCUSSION

3.1 Cyclic deforming behavior

The peak strain amplitude ε_a ~ cycle N curves of TA16 alloy are shown in Fig2. It is found the cyclic deforming regularity is little different at different R and σ_a values, but mostly appears as early cyclic softening, then stabilizing, up to fracture, and the cyclic stabilizing duration decreases with the increase of σ_a values.

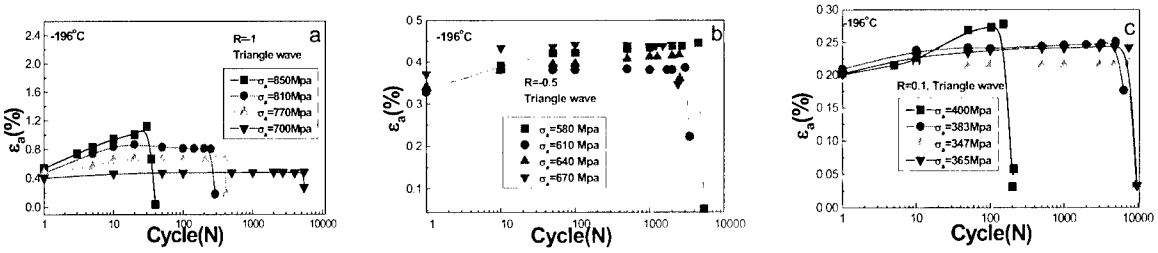

Fig.2 Curves of ε_a vs N of Ti-2Al-2.5Zr alloy tube

Fig.3 shows the σ ~ ε curves of monotonic and cyclic deforming comparison of Ti-2Al-2.5Zr alloy tube. It is found the σ ~ ε curves of cyclic deforming at different R values are below that of monotonic tension, therefore Ti-2Al-2.5Zr alloy appears as cyclic hardening. Since the ε_a~ N and σ ~ ε curves of Ti-2Al-2.5Zr alloy tube are different, the equations of σ ~

ε and fatigue life prediction equations are also different (see Table 2,3).

Fig.3. Stress ~ strain curves of tensile and cyclic deformingof Ti-2Al-2.5Zr alloy

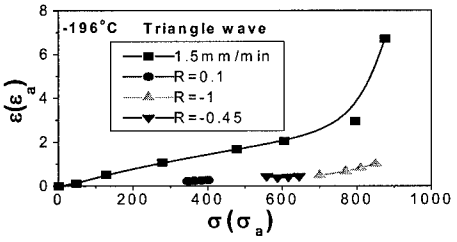

Table2 The cyclic stress ~ strain relations of Ti-2Al-2.5Zr alloy

specimen	temperature (°C)	Loading mode	Fit equation	Correlative coefficient (%)	Standard error
tube	-196	V=6mm/min	$\sigma=6401.5(\varepsilon_p)^{0.71}$	95.5	0.1343
tube	-196	Δ, 3Hz R = – 1	$\Delta\sigma=1052.8(\Delta\varepsilon_p)^{0.06}$	99.5	0.0042
Tube	-196	Δ, 3Hz R =0.1	$\Delta\sigma=600.8(\Delta\varepsilon_p)^{0.06}$	93.0	0.0105
Tube	-196	Δ, 3Hz R = -0.5	$\Delta\sigma=3449.5(\Delta\varepsilon_p)^{0.23}$	97.7	0.0097

Table3 The fatigue life prediction equations of Ti-2Al-2.5Zr alloy

Specimen	temperature (°C)	Loading mode	Fit equation	Correlative coefficient (%)	Standard error
Tube	-196	Δ, 3Hz R = – 1	$\Delta\varepsilon_{t/2}=2.2\times10^{-6}(2N_f)^{-0.17}+2.85(2N_f)^{-0.9}$	98.7	0.0866
			$\Delta\varepsilon_p\cdot N_f^{0.9}=3.033$	99.0	0.1384
Tube	-196	Δ, 3Hz R = 0.1	$\Delta\varepsilon_{t/2}=3.9\times10^{-7}(2N_f)^{-0.04}+0.005(2N_f)^{-0.13}$	94.4	0.1249
			$\Delta\varepsilon_p\cdot N_f^{0.13}=0.0098$	93.5	0.0518
Tube	-196	Δ, 3Hz R = – 0.5	$\Delta\varepsilon_{t/2}=1.5\times10^{-7}(2N_f)^{-0.125}+7.6\times10^{6}(2N_f)^{-2.6}$	99.6	0.0255
			$\Delta\varepsilon_p\cdot N_f^{2.6}=2.5\times10^{6}$	99.5	0.049

3.2 Microstructure observation and analysis

The tests show that there are few twins occurrence under low σ_a and N at R=0.1 and –0.5, whereas more twins under high σ_a and N. There are more twins under different σ_a and N values at R=-1(Fig.4). Therefore the twinning has been important plastic deforming mode at cryogenic temperature (-196°C).

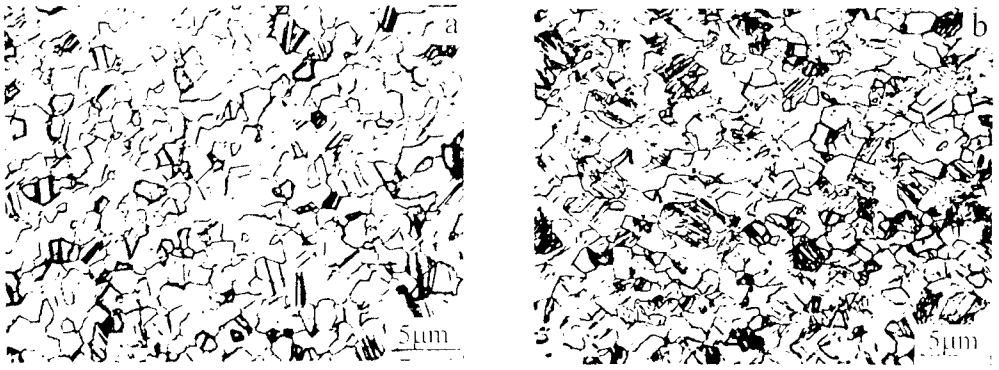

(a) σ_a=810MPa N=50, R=-1(200×) (b) σ_a 810MPa N_f 286, R -1(200×)

Fig 4 cyclic deforming twins observed in Ti-2Al-2.5Zr alloy

The fatigue fracture at -196°C show crack spreading in transgranular mode. In crack spreading region, the typical features were more small dimples, secondary cracks, fatigue striations and some holes, facets. Which are related to the values of R, σ_a (see Fig.5). The large quantities of dimples, secondary cracks and fatigue striations absorb much energy, and thus crack spreading is blocked. This shows Ti-2Al-2.5Zr alloy possesses very fine plasticity in cryogenic temperature.

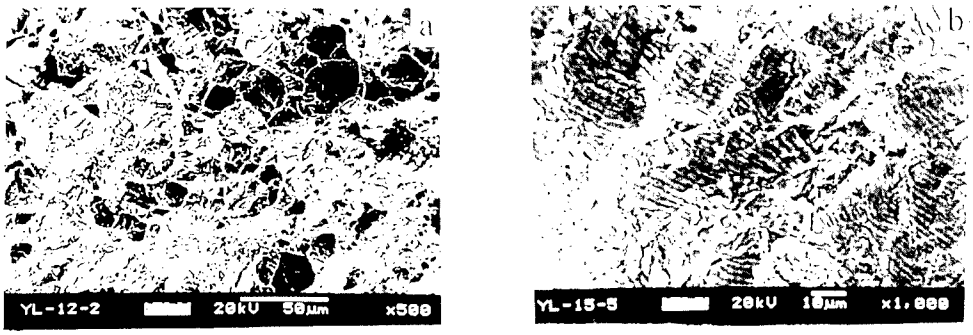

(a) σ_a 558MPa , R= -0.5 (b) σ_a=645MPa, R= -0.5

Fig.5 Fatigue fracture features of Ti-2Al-2.5Zr alloy with SEM

TEM observation on foils taken from fatigued specimens displays that there were much more twins and dislocations under higher σ_a and N values, whereas less dislocations and no twins at lower σ_a and N values. There appeared dislocation lines, clusters, cell, net, vein and ladder-like structure etc. which belong to <a > or <c+a> type dislocations (Fig.6a, b), and stacking fault (Fig.6c) and subgrain boundary slip (Fig.6d) were also found. There were also various twins, including secondary twins inside big twin, twin-twin interaction and Twin-slip interaction etc. (Fig.6e~g). The above-mentioned twins had been defined with $\{10\bar{1}2\}$, $\{11\bar{2}1\}$, $\{11\bar{2}2\}$, $\{11\bar{2}3\}$ (Fig.6h).

It is proved α-Ti (such as Ti-2Al-2.5Zr) alloy belongs to wave-like slip materials, but its cyclic deforming behavior is similar to that of plane-like slip materials[4], Which its cyclic deforming behavior is related with the loading mode, amplitude, wave, temperature and

deforming history etc. It is also found that HCP metal is easy to twin and difficult to slip when the temperature lower. Therefore single slip or twin deforming mode cannot completely explain the cyclic deforming behavior of Ti-2Al-2.5Zr alloy at –196°C. The twinning has been one of important deforming modes other than slip deforming[5-8]. The twinning is to be formed on the condition unfavouring for slip. On the other hand, twinning facilitates the unfavourably oriented grain for slip and twin to reorient into a more favorable position upon slip. Therefore, the total plastic strain can be increased significantly by the advent of twinning. So it can concludes the cyclic deforming of Ti-2Al-2.5Zr alloy is controlled with alternate deforming between slip and twinning. In this paper, the twinning-detwinning appearance (Fig.6g) has been found with which can support the above-mentioned conclusions.

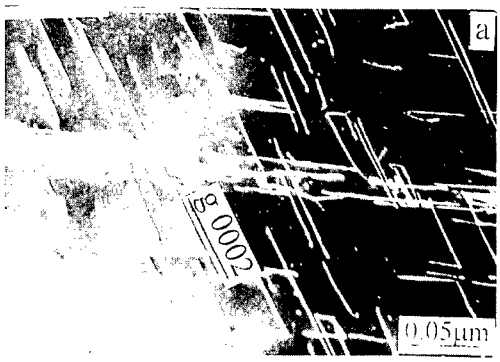

(a): <c+a> type dislocation net

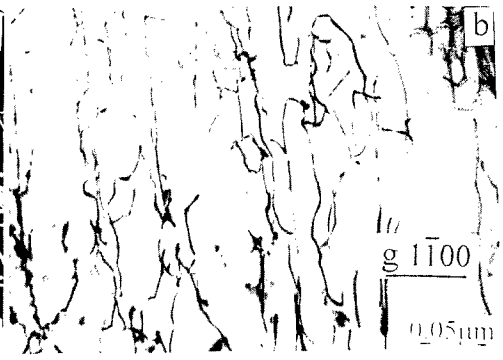

(b): <a> type dislocation

(c): stacking fault

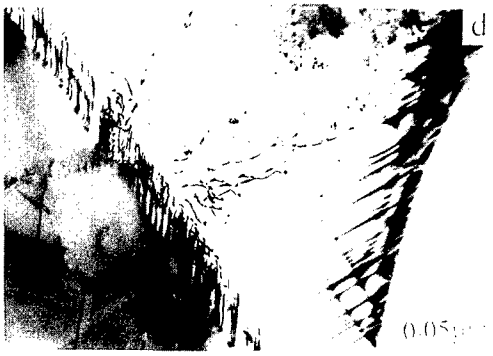

(d): subgrain boundary and its slip

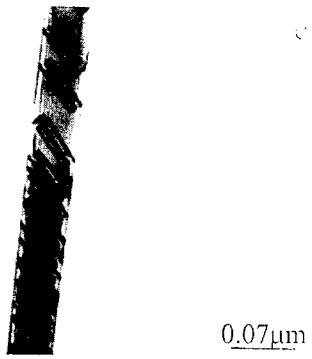

(e) secondary twin

(f) twin-twin interaction

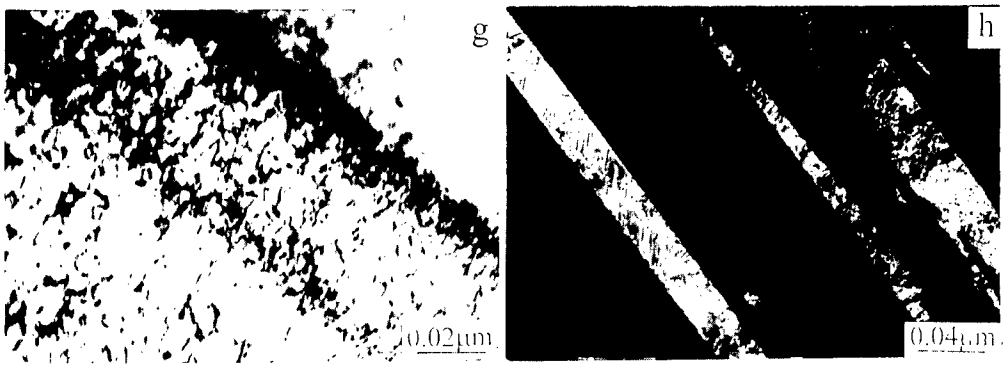

(g) twin-slip interaction (h) $\{10\bar{1}2\}$type twin

Fig. 6 The typical dislocation patterns in Ti-2Al-2.5Zr alloy fatigued at –196°C

4. CONCLUSIONS

(1) During cyclic deforming at –196°C, Ti-2Al-2.5Zr alloy appears cyclic hardening at different stress ratios.

(2) Twinning occurrence in Ti-2Al-2.5Zr alloy is much related to stress ratio, stress amplitude and cycle number.

(3) The fatigue fractures of Ti-2Al-2.5Zr alloy mainly consist of large quantities of dimples, secondary cracks, fatigue striations, and some facets and holes also exist among them.

(4) The plastic deforming modes at –196°C comply with the alternate deforming mechanism between slip and twinning. The <a>, <c+a>type slip and $\{10\bar{1}2\}$, $\{11\bar{2}1\}$, $\{11\bar{2}2\}$, and $\{11\bar{2}3\}$ twin have been observed.

REFERENCE

1. Xiao Lin, Rare Metal. Mater. Eng., 24(6) (1995), 21
2. Xiao Lin, Cuo Huifang and Gu Haicheng, Strength of Materials, Oikawa et.al. (eds.), The Japan Institute of Metals (1994), 163
3. Yu Zhentao, Zhou Lian, Deng Ju etc., Material Science and Engineering A, A280 (2000), 192
4. Xiao Lin, Gu Haicheng, Rare Metal. Mater. Eng., 27(2) (1998), 69
5. Yang Guanjun, Cai Xuezhang, Du Yu etc. Acta Metallurgical Sinica (supp1.1), 35(1) (1999), S475
6. Liu Junliang, Lin Dongliang, Wang Yu etc., Acta Metallurgical Sinica 35(1) (1999), 41
7. O.U.mezawa, K. Nagai and K. Ishikawa, Material Science and Engineering A 129 (1990) 223
8. Cao Guoying, Cao Houyi, Liu Changsheng etc, Journal of uniuersity of Science and Technoloty Beijing, 15 (1) (1993) 86

RECENT DEVELOPMENTS ON THE LOW-TEMPERATURE (298 – 458K) CREEP DEFORMATION BEHAVIOR OF TITANIUM ALLOYS

Sreeramamurthy Ankem, Durgalakshmi Doraiswamy

Materials Science and Engineering
University of Maryland, College Park, MD 20742-2115

ABSTRACT

Titanium alloys find many technologically important applications particularly in aerospace, bio-medical, consumer goods, and automotive industries. Understanding their behavior under prolonged exposure to stresses at low temperatures is very essential. Major developments have occurred in regard to the deformation behavior of α, β, and α-β titanium alloys. Some of the important observations made in the creep deformation behavior of these alloys include time-dependent-twinning phenomenon in α and β alloys; effects of grain size, β phase stability, stress levels and microstructure on the creep behavior. This paper attempts to review these developments and suggest optimal microstructures for improved creep-resistance.

1. INTRODUCTION

Titanium alloys (α, β, and α-β) are technologically important and they find applications in a number of areas including aerospace, chemical, naval and bio-medical. Their attractive properties include low density, high fracture toughness, excellent corrosion resistance, and biocompatibility. The selection of the type of alloy for a given application depends on the property requirements. Some of the titanium alloys are prone to creep degradation and follow varying deformation mechanisms depending on the type of alloy. The deformation mechanisms depend on alloying elements and microstructure, and the final mechanical properties, which in turn, depend on the deformation mechanisms. An understanding of low-temperature creep deformation behavior is thus essential for both the design of new alloys and the optimization of the microstructure for existing alloys. A number of factors like grain size and stress level could affect low-temperature creep resistance in titanium alloys. In this paper the effect of some of the factors and the creep deformation mechanisms of α, β, and α-β Ti-Mn and Ti-V alloys are critically reviewed. Further, ways to improve the low-temperature creep resistance of these alloys are identified.

2. TECHNICAL BACKGROUND

Creep curves for most of the materials can be represented by three stages of creep deformation [1]. These three stages include primary, secondary and tertiary creep. Creep at the low temperatures of interest is generally of the transient type, achieving creep exhaustion during stage 1, primary creep, and never reaching stage 2, or secondary creep. Secondary creep is also called steady state creep because of the dynamic recovery process that maintains a constant strain rate. The thermal energy required for dynamic recovery is not available in the lower temperature range proposed and so the material experiences creep exhaustion or creep saturation. Modes of deformation during creep of titanium alloys at ambient temperatures include twinning [2, 3], interface sliding [4], and slip [2-5]. Some of these modes are more prominent in some alloys than the others. For example, in two-phase α-β alloys there is more grain boundary sliding, in α alloys there is extensive twinning while in the more stable β alloy (Ti-13wt% Mn) slip predominates creep deformation [2-5].

3. DEFORMATION MECHANISMS

Ashby [6] has developed deformation maps for pure single-phase materials. A deformation map has been published for pure titanium. The deformation map shows that the deformation mechanisms depend on the normalized stress, σ/μ, and the homologous temperature T/T_m, where μ is the shear modulus and T_m is the melting temperature, and have a slightly different constitutive relation as described by Ashby. The boundaries between various deformation mechanisms are different for dissimilar materials. There are predominantly two creep mechanisms for polycrystalline single-phase materials for pure titanium. First, grain boundary sliding, which normally occurs at high temperatures and second, twinning, which has been observed at low temperatures.

3.1 α- Titanium Alloys

Creep deformation behavior of commercially pure titanium at low temperatures (below $0.2T_m$) was earlier reported by Adenstat [7] in 1949. Recently, Ankem, Greene and Singh [2] studied the ambient temperature tensile and creep deformation behavior of α Ti-0.4%Mn alloy. They found that these alloys crept significantly in the transient stage exhibiting creep exhaustion with increasing time. In regard to creep, they have found that the major deformation modes are twinning and slip. Further, they have observed a practically important and scientifically interesting phenomenon, namely, time-dependent twinning, in coarse-grained (500μm) material (Fig. 1). In the above investigation, it was also observed that the creep strain increased with grain size, which will be discussed in detail in Section (4.1).

3.2 β-Titanium Alloys

The ambient temperature deformation behavior in β Ti-13%Mn and β Ti-14.8%V alloys were studied by Greene and Ankem [5], Sil, Greene and Ankem [8] and Ramesh and Ankem [9]. When subjected to tensile and creep deformation, the beta Ti-13%Mn deformed by coarse and wavy slip, while the Ti-14.8%V alloy deformed by slip and stress induced plate formation. These plates were identified to be twins. Figures 2 and 3 show the creep curve and the twin

growth as was seen in Ti-14.8wt% V alloy. It is interesting to note that beta Ti-14.8wt% V alloy with a lower stability deforms by both time-dependent twinning (Figure 3) and slip [9]. The observations and explanations in these investigations [5, 8, 9] are consistent with earlier studies by various other investigators on Ti-Mn [10, 11] and Ti-V [12, 13, 14] alloy systems. The presence and absence of athermal ω-phase depends on relative stability. For instance, athermal ω-phase was present in the Ti-14.8wt% V β alloy but only the so-called pre ω-stage formation was observed in the Ti-13wt% Mn β alloy. Therefore, it is difficult to conclude at this point whether the presence of twins in the Ti-14.8wt%V alloy is due to the presence of the athermal ω-phase and/or due to the relatively less stable β phase of the Ti-14.8wt% V Alloy as compared to the β phase of the Ti-13wt% Mn alloy. Nevertheless, these results clearly indicate that the deformation mechanisms in β alloys at the ambient temperatures depend on the amount and type of β stabilizers. The deformation mechanisms, in turn, determine the mechanical properties.

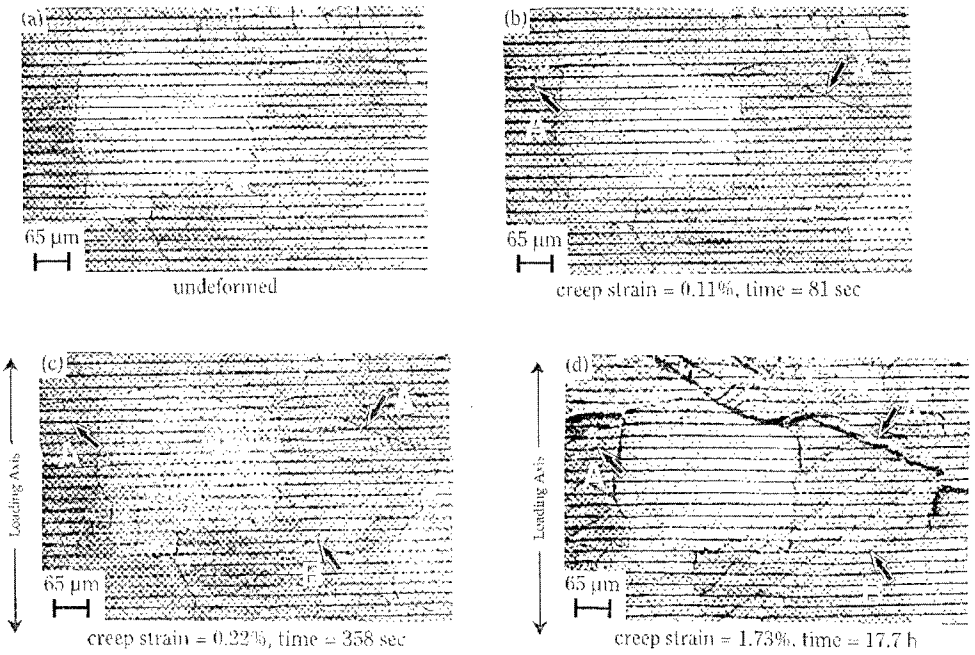

Fig. 1: Optical micrographs of (a) Undeformed and (b), (c), and (d) deformed α Ti-0.4%Mn alloy. Horizontal lines are gold fiducial lines. (b) shows instantaneous twins at "A", (c) shows nucleation of new twins at "B", and (d) shows growth of twins at "A" and "B" and formation of new twins at "C" [2].

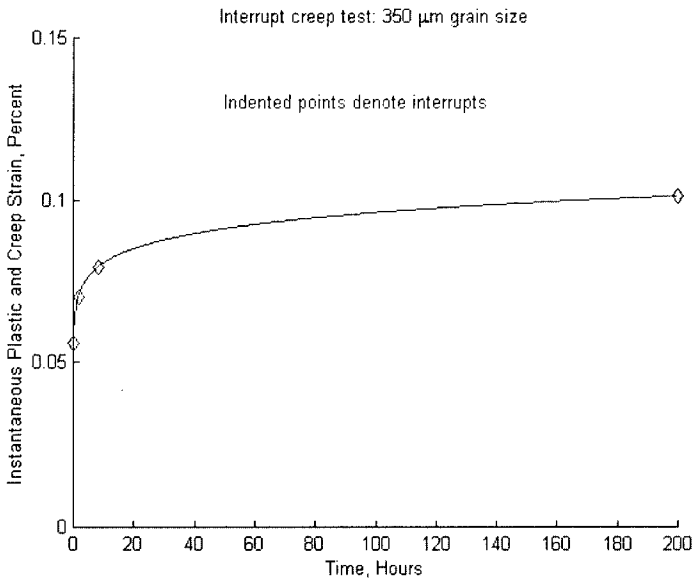

Fig. 2: Ambient temperature interrupted creep curve Ti-14.8V alloy, 350 μm grain size crept at 95% of yield stress. After a total of 200 h of testing, the instantaneous plastic and creep strain was ~ 0.101% [9]

3.3 α-β Titanium Alloys

Ankem *et al* [2] and Greene *et al* [4] studied the tensile and creep deformation behavior of α-β Ti-6.0%Mn alloy and Ti-8.1%V alloy. The volume percent of β phase in the former is about 54%, in the latter, it is about 49%. The microstructure of both these alloys consisted of Widmanstatten (i.e., plate like) α structures and grain boundary α in β matrix. They [4] found that the α-β Ti-Mn alloy deforms by fine as well as coarse slip in α phase and α-β interface sliding during tensile deformation. In contrast, coarse slip lines in both phases, as well as the slip lines crossing the α-β interfaces, were observed in the Ti-V alloy. The reason for this difference is not clear at this time but the difference in the deformation mechanism was attributed to the observed higher creep strain in the Ti-V system when subjected to creep at a stress of 95%YS. Miller, Chen and Starke Jr. [15] studied the creep behavior of near α two-phase titanium alloy, Ti-6Al-2Nb-1Ta-0.8Mo, at temperatures ranging from 298 K to 873 K. These authors suggested that different creep mechanisms including interfacial sliding may be operating depending on the activation energy value, though the actual creep mechanisms were not clearly identified.

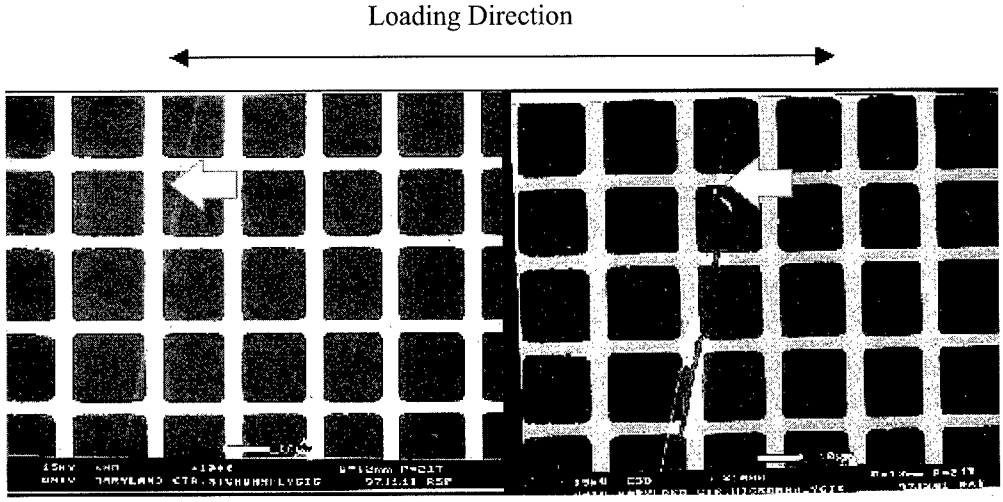

Fig. 3: Interrupt Creep Test, Ti-14.8V, 350 μm grain size.
Arrows indicate presence of SIP. Note growth of plate in (b).
(a) Interrupt I : Time = 3.62 min, Strain = 0.056%
(b) Interrupt II : Time = 1.68 hr, Strain = 0.07 % [9]./

4. FACTORS INFLUENCING LOW-TEMPERATURE CREEP DEFORMATION

4.1 Effect of Grain Size

The effect of grain size has been extensively studied by Anand *et al* [9] and many other investigators [3, 4, 5, 16] in α and β alloys for grain sizes ranging from 18 to 350 μm in β alloys and up to 500 μm grain size in α alloys. Coarse-grained material was found to creep significantly greater than fine-grained ones. In the 350 μm grain size Ti-14.8%V beta alloy, the Stress Induced Plates (SIP) characterized as twins were found to nucleate and grow with time thereby contributing to the ambient temperature creep strains. The extent of SIP formation and growth were found to decrease with decreasing grain size, i.e., creep strain was found to decrease with decreasing grain size. Coarse grained samples showed extensive twinning compared to fine grained ones owing to the fact that critical stresses required for the nucleation and growth of twins are greater in fine grained samples than coarse grained ones. In addition, it could also be explained in terms of the presence of large number of grain boundaries, which prove to be a hindrance for the propagation of the SIP.

4.2 Effect of Stress Level

There have been contrasting results on the effect of stress level on the ambient temperature creep behavior of Ti-6-4 alloy. For example, Wood [17, 18] reported that room temperature creep occurred in Ti-6-4 at torsion shear stresses as low as 10% of the yield stress. However, Riemann [19], who used torsion testing, reported that room temperature creep below yield stress did not occur at all if the stress was unidirectional, but it did occur if the stress was reversed after exceeding the yield stress in the forward direction. Nevertheless, Riemann stated that creep did not occur below 85% yield stress. These results were disputed by Thompson and Odegard [20]. They found that under tensile creep loading conditions at ambient temperature, the Ti-6-4 alloy had significant creep deformation at 60% yield stress after 1000 hours for aged specimens and crept at even lower stresses of 40% yield stress in as-welded specimens. Thompson and Odegaard [21] also conducted studies on the Ti-5Al-2.5Sn alloy at temperatures ranging from 194 to 422 K and stress levels from 40% to 90% yield stress as measured at ambient temperature (299K). Measurable creep strains were recorded at stress levels of 60% yield stress at temperatures ranging from 299 to 422 K. Miller *et al* [15], found similar trends in their studies on the Ti-6211 alloy, an $\alpha+\beta$ alloy, and found that stress levels of 55% and 60% yield stress values were minimum threshold levels for appreciable creep to occur at low temperatures. The tests conducted on Ti-Mn and Ti-V alloys were performed at 95% of their Yield Stress values, which resulted in significant creep strains, consistent with the previous observations. At these low stress levels there is little increase in dislocation density, instead the existing sources are operated and may be "exhausted". This might be responsible for the creep exhaustion observed in the transient stage of titanium alloys.

4.3 Effect of Stability of Beta Phase

Beta stability is defined as the amount of beta stabilizers necessary to retain 100% β on quenching. This is normally defined in terms of Molybdenum Equivalency [28], where at least 10%Mo is required to retain 100% β phase on quenching. Based on this, a Ti-13wt% Mn is a much more stable alloy than Ti-9.4wt% Mn or Ti-14.8wt% V. In the creep studies conducted on Ti-13wt% Mn and Ti-14.8wt% V systems at 298K, it was observed that the former creeps much less than the latter and that the mode of deformation was slip in the former, whereas SIP formation and slip in the latter. Also, a less stable alloy is more prone to ω-phase formation in the β matrix, which was true in the case of Ti-14.8wt% V alloy. In earlier work by Bagaryatskiy *et al* [22], deformation at room temperature resulted in ω-phase formation in a Ti-8wt% Cr alloy. Brozen *et al* [23] found that compressive deformation of a quenched Ti-15wt% V alloy caused an increase in the amount of omega phase. However, Silcock [24] could find no effect of deformation in a Ti-20wt% V or Ti-13wt% Mo alloy. Omega phase transformation causes a misfit in the lattice, producing an internal strain in the material. ω-Phase is stable at higher temperatures and longer times in systems with higher misfits like Ti-V [25]. The ω-phase particles act as pinning agents in the matrix, in turn, affecting the properties of the materials. They cause the hardness values to increase, resulting in a virtual loss of ductility [25]. There have not been detailed studies as to how the ω-phase formation effects the creep behavior.

4.4 Effect of Microstructure

Microstructure plays an important role in the mechanical behavior of bulk materials and the phenomenon of ambient temperature creep is no exception. The role of microstructure has been studied by many investigators [21, 26, 27], although this work has been alloy specific. Odegard and Thompson [21] have compared the aged and as-welded structures in Ti-6-4. As mentioned earlier, the as-welded specimens, which consisted of Widmanstatten α plates in the fusion zone while the HAZ had a mixture of microstructures was found to creep at lower stress levels as compared to the aged specimens which contained fine α' martensite interspersed with α phase. They also found that the creep strains at the same stress levels were larger in the as-welded specimens. Imam and Gilmore [26] have also found that the microstructures not only influence the amount of creep strain at a given stress level but also determine the threshold value of stress below which creep will not occur. As mentioned in the previous section, in metastable β alloys the precipitation of ω phase and martensite effects the creep behavior of these alloys, though the way the mechanical properties are affected are not very clear. As mentioned before, in α-β alloy systems where slip crosses the α-β interfaces, creep strains were found to be higher at ambient temperature.

5. CONCLUSIONS

Titanium alloys exhibit significant creep behavior at low temperatures in the range of 298 to 458 K. The creep occurs in the transient stage with creep exhaustion occurring before the alloy enters the secondary stage. Among the three types of alloys, namely, α, β, α+β alloys, the α alloys creep the most and β alloys creep the least. The modes of creep deformation at low temperatures vary between twinning and slip and sometimes interface-interphase sliding. There are many factors influencing low temperature creep behavior in titanium alloys, including grain size, stress level, and microstructure. In the case of β alloys, the stability of β phase also effects the total creep strain and the extent of creep deformation increases with increasing grain size and increasing stress level. In α+β titanium alloys, the creep-resistance depends on the morphology of microstructure and whether slip cuts through the interfaces or not. Therefore, for applications where low-temperature creep is a critical factor, more stable β titanium alloys with smaller grain sizes are preferred. For higher creep-resistance, small grain sizes are also preferred in α alloys.

ACKNOWLEDGEMENTS

The author thanks Dr. George Yoder for his keen interest and encouragement. This work is being supported by the Office of Naval Research under Grant No. N0001496101819.

REFERENCES

1. E. Dieter: Mechanical Metallurgy, Third Edition, McGraw-Hill Book Company, New York, 1986, p 439.
2. S. Ankem, C. A. Greene and S. Singh, *Scripta Met.*, 1994, V 30, n 6, p 803.
3. C. A. Hultgren, C. A. Greene, and S. Ankem, *Met. Trans.*, 1999, V 30A, p 1675.
4. C. A. Greene, S. Ankem and S. Singh, Proceedings of the Eighth World Conference on Titanium, Birmingham, U.K., Eds. P.A. Blenkinshop, W.J. Evans, and H.M. Flower, 1995, V II, p 1315.
5. C. A. Greene and S. Ankem, Beta Titanium Alloys in the 1990's, Eds. D. Eylon, R. R. Boyer and D. A. Koss, TMS, 1993, p 309.
6. F. Ashby, *Acta Met.* 1972. V 20, p 887.
7. H. Adenstat, *Metal Progress*, 1949, V 56, p 658.
8. D. Sil, C. A. Greene and S. Ankem, *Les Alliages De Titane Beta*, Beta Titanium Alloys, Eds. A. Vassel, D. Eylon, and Y. Combres, 1994, p 173.
9. A. Ramesh and S. Ankem, University of Maryland, College Park, 1998, to be published elsewhere.
10. S. Ankem and H. Margolin, *Met. Trans. A*, 1986, V 17A, p 2209.
11. A. P. Young, R. I. Jaffee and C. M. Schwartz, *Acta Met.*, 1963, V 5A, n 11, 1097.
12. T. S. Kuan, R. R. Ahrens and S. L. Sass, *Met. Trans. A*, 1975, V 6A, p 1767.
13. M. Oka and Y. Tanaguchi, *Met. Trans. A*, 1979, V 10A, p 651.
14. M. K. Koul and J. F. Breedis, *Acta Met.*, 1970, V 18, p 579.
15. H. Miller, R. T. Chen, and A. K. Starke Jr., *Met. Trans.A*, 1987, V 18A, p 1451.
16. S. Ankem, Proceedings of the 2nd Pacific Rim International Conference on Advanced Materials and Processing, Eds. K.S. Shin, J.K. Yoon, and S. J. Kin, The Korean Institute of Metals and Materials, 1995, p 2275.
17. W. A. Wood, *Technical Report no. 45*, Columbia University, April 1967.
18. W. A. Wood, *Technical Report no. 54*, Columbia University, January 1968.
19. W. H. Riemann, *J. Mater.*, 1971, V 6, p 926.
20. B. C. Odegard and A. W. Thompson, *Met. Trans.*, 1974, V 5, p 1207.
21. A. W. Thompson and B. C. Odegard, *Met. Trans.*, 1973, V 4, p 899.
22. Yu. A. Bagaryatskiy, T. V. Tagunova and G. I. Nosova, *Problemy Metallovedenija I Fisiki Metallov*, Moscow, 1958, V 5, p 210.
23. F. R. Brotzen, E. L. Harmon, and A. R. Troiano, *J. Metall.* 1955, V 7, p 413.
24. J. M. Silcock, *Acta Metall.*, 1958, V 6, p 481.
25. B. S. Hickman, *J. Mat.Sci.*, 1969, V 4, p 554.
26. M. A. Imam and C. M. Gilmore, *Met. Trans. A*, 1979, V 10A, p 419.
27. H. P. Chu, *J. Mater., JMLSA*, 1970, V 5, n 3, p 633.
28. Paul J. Bania, **Beta Titanium Alloys in the 1990's**, Eds. D. Eylon, R. R. Boyer and D. A. Koss, TMS, 1993, p 4.

HIGH TEMPERATURE DEFORMATION BEHAVIOR OF Ti40 BURN RESISTANT TITANIUM ALLOY

Y.Q.Zhao, K.Y.Zhu, H.L.Qu, H.Wu, L.Zhou

Northwest Institute for Nonferrous Metal Research
P.O.Box 51 Xi'an, Shaanxi 710016, China

ABSTRACT

Ti40 alloy is a new burn resistant titanium alloy. Its high temperature deformation behavior is studied. The results reveal that dynamic recovery is the main process for Ti40 alloy deformation from 650^0C to 850^0C, and dynamic recrystallization for 950^0C to 1000^0C. The σ-ε flow response of Ti40 is characterized by discontinuous yielding followed by steady state flow. Stacking faults appear in some local zones upon deformation at high temperature. There is not link between stacking fault and twins.

1. INTRODUCTION

The development of advanced aero-engines promotes the seek for high performance materials. Titanium and its alloys are one of the essentially selected metal materials for aero engines because of their excellent comprehensive properties. The consumption of titanium alloys is increasing, for example, the F22 RAPTOR with high performance capabilities requires significant amounts of titanium (42% of all structural materials by weight)[1]. Specifications for the F119 engine in the F22 RAPTOR require the low density of titanium. However, the design demands that the engine nozzle perform additional functions over conventional aircraft, and also specifies the ability to supercruise without the aid of the afterburner. The difficulty is that supercruising produces temperatures and stresses in the exhaust nozzle that exceed the useful strength ranges of conventional titanium alloys such as Ti-6Al-4V. In addition, conventional titanium alloys are susceptible to sustained combustion if ignited at the resulting temperatures and presses [2]. Ignition can be caused by friction arising from the ingestion of foreign objects, or from mechanical failures that results from the contact between moving and stationary titanium components. To eliminate the possibility of sustained combustion under these conditions, the F119 could have chosen a nickel-base super-alloy. However, the heavier alloy would have reduced engine performance. Instead, Pratt & Whitney worked with Teledyne Wah Chang to develop the burn resistant titanium alloy---Alloy C (Ti-35V-15Cr) [3~5]. It has good burn resistance and comprehensive mechanical properties. It has been applied to the F119 engine [3~5]. In China, we began to research burn resistant titanium alloys since 1994. Ti40 (Ti-25V-15Cr-0.2Si), a new burn resistant titanium alloy, was designed and developed in 1996[6~7]. This new alloy possesses good burn resistance and mechanical

properties [8]. It is a stable β titanium alloy, and its hot working is more difficult than that of convention βtitanium alloys [7~8]. Therefore its high temperature deformation behavior is necessary to be studied, and the useful references are required to choose the hot working parameters.

2. EXPERIMENTAL PROCEDURES

5kg Ti40 alloy with diameter of 90mm used in this paper was prepared through double-consumable-vacuum-arc-furnace. The chemical composition was Ti-24.6V-15.2Cr-0.2Si-0.2O. The ingot was isothermally forged and annealed at 910^{0}C for 1h. Its microstructure consisted of equiaxed β grains, 600μm in size, and there are many subgrains within the β grains, 50μm in size. The high temperature true stress-strain response of Ti40 was determined by uniaxial compression utilizing Gleeble-1500 simulator and cylindrical samples (8mm in diameter and 12mm in length). The deformation amount was 60%. The deformation temperatures varied from 650^{0}C to 1000^{0}C, and strain rate from 0.25s^{-1} to 15s^{-1}. After deformation the samples were fast cooled (200^{0}C/s) in order to keep the high temperature microstructures.

3. RESULTS

3.1 True stress-strain (σ-ε) curves

σ-ε curves corrected for different temperatures are shown in Fig.1. At high temperature (>850^{0}C) and the highest strain rates, typically 15s^{-1} and 10s^{-1}, discontinuous yielding follow-

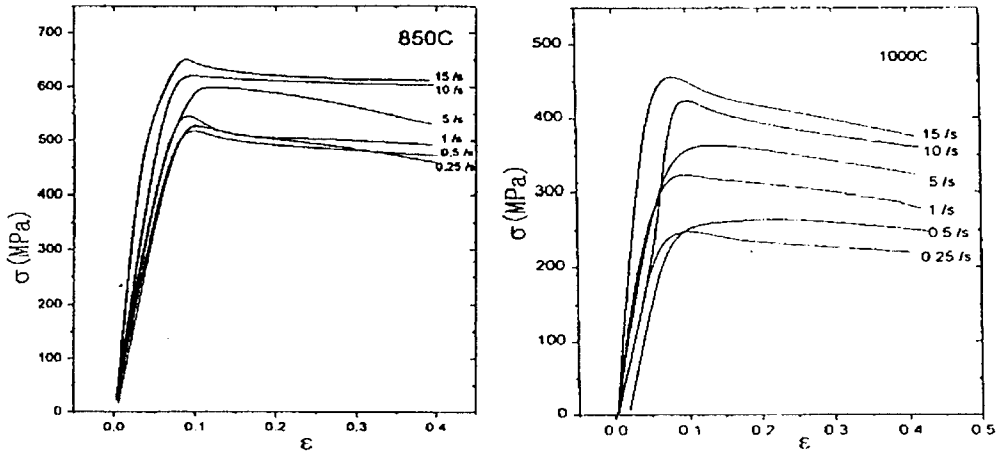

Fig.1 σ-ε curves corrected for different temperatures
a) 850^{0}C b) 1000^{0}C

ed by strain hardening, flow softening, and eventually steady-state flow was observed.

Decreasing the strain rate resulted in elimination of discontinuous yielding and strain hardening, steady state flow ensuing almost immediately upon yielding.

3.2 Optical micrographs (OM)

Fig.2 is the OM images of Ti40 after deformation at 650^0C, 850^0C and 1000^0C with different strain rates. The grains elongate vertically to the direction of applied compressive stress. If the deformation temperature is less than 850^0C, there are not new grains and the grain boundaries are irregular because of the deformation, which reveals that the deformation between 650^0C and 850^0C is controlled by dynamic recovery. There are a lot of deformation twins upon

Fig.2 OM images after Ti40 deformation at 650^0C, 850^0C and 1000^0C with different strain rates
a) 650^0C, $1s^{-1}$ b) 850^0C, $1s^{-1}$ c) 1000^0C, $1s^{-1}$

deformation at 650^0C or 850^0C with high strain rate. The twins in one grain are oriented in the same direction, and the twins run through the grain. There are many new grains selectively formed on β grain boundaries and the triple points when deformation temperature is greater than 850^0C. This result reveals that it is a typical dynamic recrystallization process. The samples break in two upon deformation at low temperatures and high strain rates such as $650^0C/15s^{-1}$,$650^0C/10s^{-1}$ and $850^0C/s^{-1}$, especially for $650^0C/15s^{-1}$. The fracture lies along 45^0 to the direction of applied local stress. The observation of OM and SEM fracture surfaces images after deformation at 650^0C for $15s^{-1}$ reveals there are a lot of deformation twins in the OM, and the different twin directions collide with each other, which may lead to microcracks resulting in laminate brittle fracture. That is to say, twins induce cracks.

3.3 TEM structures

In order to further clarify the high temperature deformation behavior of the Ti40 alloy, the observations of TEM structures were conducted. The results show that complex dislocation networks and dislocation subgrains form during deformation at 650^0C and 850^0C. Density of

dislocations in the subgrains is very low, which is consistent with the tear deformation of twins. The subgrains connect with each other, and the profiles of deformed grains are shown, which reveals that subgrains connecting together come from the sample deformation grains, that is, the deformation is the dynamic recovery process. New equiaxed grains and subgrains emerge along the grain boundary (Fig.3) during deformation at 950^0C and 1000^0C. The very low density of dislocations in the new grains indicates that this deformation is dynamic recovery and dynamic recrystallization, and the latter is the main factor, which is consistent with the results from the deformation activation energy [9]. The results from TEM agree with that from OM.

The changes of microstructures can be demonstrated in Fig.4

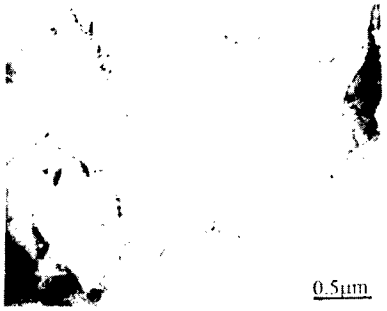

Fig.3 New equiaxed grains and subgrains emerging along the grain boundary during deformation at 950^0C

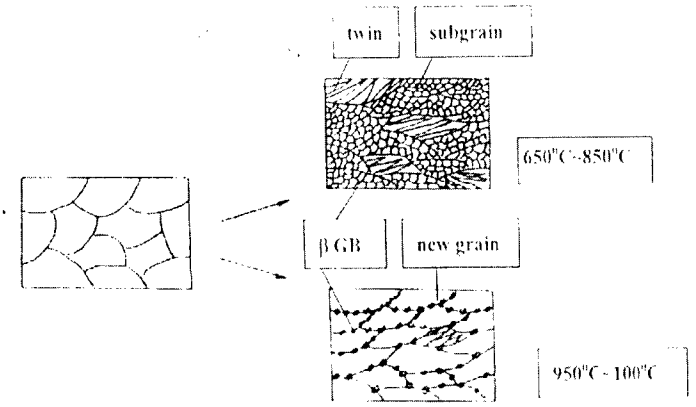

Fig.4 Model of microstructural change

The stacking faults appear in some local regions after the Ti40 alloy deformation at high temperatures, just as shown in Fig.5. However, there are no stacking faults if the deformation temperatures are less than 950^0C. Detailed observations reveal that stacking fault and dislocations coexist, but the dislocation density is very low. This suggests that the appearance of stacking faults has something to do with the interaction of dislocations. The coordination deformation mechanism of stacking faults is related with the angle between the grain and the stress direction. If it is difficult for the coordination mechanism of dislocation and dislocation

loop to start, the stacking fault can coordinate the grain boundary sliding and the total deformation. In the α titanium, stacking faults always accompany with twins, and stacking faults appear in the twins [10~11]. However, the place having stacking faults does not have twins, that is, stacking faults do not have inevitable connection with twins.

Fig.5 Stacking faults appearing in some local regions after deformation at high temperatures

4. Discussion

The influence of temperature, strain rate and strain on the elevated temperature flow behavior of the Ti40 shows good agreement with other studies of near β and metastable β titanium alloys [12~14]. At high strain rates discontinuous yielding followed by softening prior to attainment of steady-state flow corresponds to the rapid generation of dislocations from grain boundary sources [14].

Microstructural observations in the high strain rate regime (as shown in Figs.2 and 3) reveal that stable flow is associated with dynamic recovery and dynamic recrystallization. If temperature is less than 850^{0}C, the grains elongate and no new grains appear. New grains emerge along β grain boundary and triple point when deformation temperatures are greater than 950^{0}C. The changes of microstructures reveal that steady-state flow varies from dynamic recovery to dynamic recrystallization with increasing deformation temperatures.

Dynamic recovery needs the aids of dislocation climbing and cross-slipping. The climbing and cross slipping of dislocations is a non-conservative diffusion process, which requires some time to happen. Thereby, when deformation temperature is higher or strain is lower, atoms diffuse easily, and dynamic recovery takes place easily. When deformation temperature is lower or strain rate is higher, the atom diffusion is difficult, and dislocation pile-up arising from deformation cannot relax in time by dynamic recovery. The dislocation pile-up becomes worse with increasing strain, and twin deformation takes place (Fig.5) in a certain condition. The twins change the grain directions and cause the deformation to continue in some soft direction of grains. In some particular conditions, twins with different directions collide with each other, which leads to micro-cracks at the junctures of twins (Fig.5). The cracks propagate along the twin boundary which causes fracture. This is consistent with the results from Fig.2.

Dynamic recrystallization is the main process if deformation occurs at 950^{0}C and 1000^{0}C. At low strain levels dislocations are emitted from grain boundaries and triple points and travel

towards the grain interior [14]. The new recrystallized grains nucleate and grow on grain boundaries and triple points, which leading to a decrease in the flow stress. However, during this process, twin deformation also appears (as shown in Fig.2 and Fig.5). The interactions among twins do not cause micro-cracks. This is quite different from that of low temperature deformation.

CONCLUSIONS

1. Dynamic recovery is the main process for Ti40 alloy deformation from 650^{0}C to 850^{0}C, whereas dynamic recrystallization occurs between for 950^{0}C and 1000^{0}C.
2. The σ-ε flow response of Ti40 is characterized by discontinuous yielding followed by steady state flow.
3. Stacking faults appear in some local zones during deformation at high temperature. There is not obvious link between stacking fault and twins.

REFERENCES

1. Lockheed Martin, Advanced Materials and Processes, 5(1998), pp.23~26
2. Y.Q.Zhao, X.M.Zhao and K.Y.Zhu, Rare Metal Materials and Engineering, 5(1996),pp.1~5
3. UK Patent Application 2238057, 1987
4. Kneisel Giary, Advanced Materials and Processes, 9(1993), pp.7
5. R.R.Boyer, Mater. Sci.Eng., Vol.A213(1996), pp.103~104
6. Y.Q.Zhao, K.Y.Zhu, X.M.Zhao, Chinese Patent, Application 97 1 12303.9,1997
7. Y.Q.Zhao, Research on Burn Resistant Titanium Alloys---Final Report, NIN, 1996
8. Y.Q.Zhao, L.Zhou and J. Deng, Mater.Sci.Eng. Vol.A267(1999), pp.167~170
9. Y.Q.Zhao, K.Y.Zhu,Q.H.Lei, Mater.Sci.Eng. Vol.A282(2000), pp.253~257
10. H.CH.Gu, Mater.Sci.Eng., Vol.A188(1994), pp.23~26
11. X.L.Tan, H.CH.Gu, Src.Metall.Mater., Vol.33(1995), pp.1977~1980
12. S.Ankem, J,G.Shyue, M.N.Vijayshankar, Mater.Sci.Eng., Vol.A111(1989), pp.51~61
13. R.Srinivasan, I.Weiss, in Beta Titanium Alloys in the 90's, D.Eylon, R.Boyer, D.A.Koss, eds., TMS, Warrendale, PA, (1993), pp.283~290
14. I.Weiss, S.L.Semiatin, Mater.Sci.Eng. Vol.A243(1998), pp.46~65

A STUDY ON THE MACHINING CHARACTERISTICS IN TURNING OF Ti-6Al-4V ALLOY

- TOOL WEAR EXPERIMENT WITH CARBIDE TOOL K10 -

W.P. Hong, H.C. Kim*, D.J. Lee**

Agency for Defense Development, Yusung P.O.Box 35-5, Daejon, Korea
Chungbuk Provincial Univ. of Science & Technology*, 40, Okcheon, Korea
Chungnam National Univ.** 220, Daejon, Korea

ABSTRACT

Ti-6Al-4V alloys have made themselves strong candidate materials for future aerospace or medical use with its material characteristics such as low density, sustained high temperature strength and excellent resistivity to acid. Nowadays the alloy has already been used in everyday's goods such as golf club heads, finger rings and many decorative items. Anticipating the general use of this material and on-going development of the titanium alloys in domestic furnaces, the review and the study of the machining characteristics for those alloys are deemed necessary. The present studies are mainly focused on the machining characteristics of the Ti-6Al-4V alloy because of its dominant position among various titanium alloys. Using the carbide tool K10 as a representative tool material, the flank wear was evaluated and the expected tool life was presented in the form of the Taylor's equation.

1. INTRODUCTION

Titanium alloys are attractive because of their fracture resistant characteristics and high strength to weight ratio. It also has been widely used in Korea due to industrial development specially in aerospace and other similar areas. The methods mainly used for manufacturing titanium alloys are turning, grinding, end milling and drilling. In the last several decades, major advancements have been made in the development of cutting tool materials but have not been found to be much effective in the material removal rate of titanium alloys[1]. Thus it would be much useful to study or evaluate the machining parameters affecting the material removal rate in case of cylindrical turning with the K10 carbide tool most commonly being used for titanium machining. The tool flank wear test was carried out for searching the optimum machining velocity and obtaining the tool life data and thus evaluating the Taylor's constants. Then machining characteristics test was executed for assessing the effects of machining parameters such as the feed, depth of cut on the cutting force and the relationship among the cutting force components, which are tangential, radial, and longitudinal component.

2. EXPERIMENTATION

Ti-6Al-4V alloy and the carbide tool K10 was used for the experiment. The chemical compositions and the mechanical properties of the alloy are shown on Table 1 and 2, respectively. The machine and the cutting tools used for the experiment are presented on Table 3. The tool tip has square configuration with no chip breaker and no cutting fluid was supplied for the test purposes. A cylindrical turning method was used.
First of all, the "cutting tool flank wear tests" were executed in order to investigate the

machinability of the alloy by means of tool wear progress, tool life and Taylor's tool life equation constants. Then, the "machining characteristics tests" were carried out to check the effects of the machining parameters on the cutting forces.

Table 1 Chemical compositions of Ti-6Al-4V alloy used for experiments

Chemical elements	Ti	Al	V	Fe	O2	C	N2	H2	Y	Others
wt %	89.192	6.265	3.77	0.185	0.165	0.01	0.01	0.0015	0.001	0.40

Table 2 Mechanical properties and heat treat condition

Direction	UTS (x 103 psi)	0.2%YS (x 103 psi)	EL(%)	RA(%)	Hardness (HRc)	Heat treatment	
						Temp (°F)	heating time(hr)
Longitudinal	148.7	138.3	12	29.3	34	1300	2
Transverse	144.9	133.5	12	21.6			

Table 3 Machine and cutting tool used for tool wear test

Machine (Lathe)	Manufacturer	GEMA(Germany)
	Type	LZ 200
	Swing over bed	400 mm
Cutting tool	Tool material	Carbide K10
	Geometry	Throw-away type back rake angle: -8° nose radius r = 0.8mm
	Tool holder	CSDNN2525M

2.1 Cutting tool wear test

The specimen shown on Fig. 1 was used for the tool wear test. Low machining velocity of 60 m/min were applied at first trial and then faster velocities were applied gradually up to 110 m/min while feed, depth of cut were set to 0.32mm/rev and 0.75mm, respectively as shown on Table 4. Tool life criterion, V_B = 0.3 mm was applied. The required rpm was calculated and applied to lathe operation so that the peripheral speed should be maintained at the desired one.

After a specified time, the tool tip was taken out of the tool holder and examined to measure the wear width. A specially designed apparatus was used for the tool wear measurement.

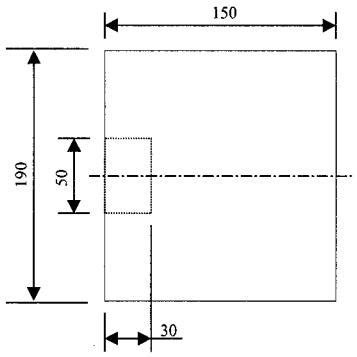

Table 4 Cutting conditions tool for wear test

Cutting conditions	Value
machining velocity (m/min)	60, 70, 80, 90, 110
Feed (mm/rev)	0.3
Depth of cut (mm)	0.75
Lubrication	dry cut

Fig.1 Specimen for tool wear test

2.2 Machining characteristics test

Fig. 2 shows the configuration of cutting specimen and the schematic diagram of machining characteristics test setting. The other cutting conditions are the same as with the tool wear test. Cutting force signals are picked up by a three axes tool dynamometer and amplified through a charge amplifier. The amplified data are converted to digital values through the A/D converter and finally stored on the computer for analysis .

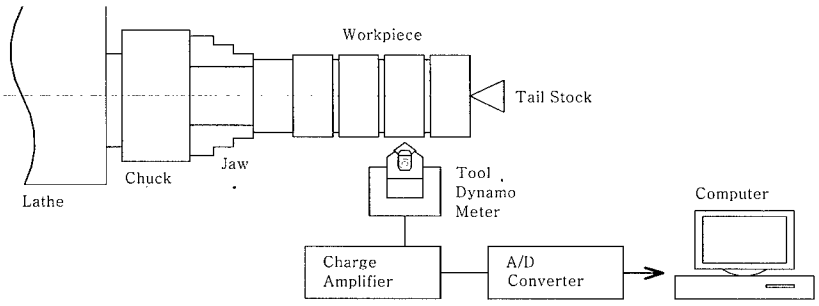

Fig.2 Setup for measuring the 3-component force

3. RESULTS AND DISCUSSION

3.1 Tool wear measurement

Fig.3 shows the measured flank wear progression and hence tool life of carbide tool K10 based on the machining velocities.

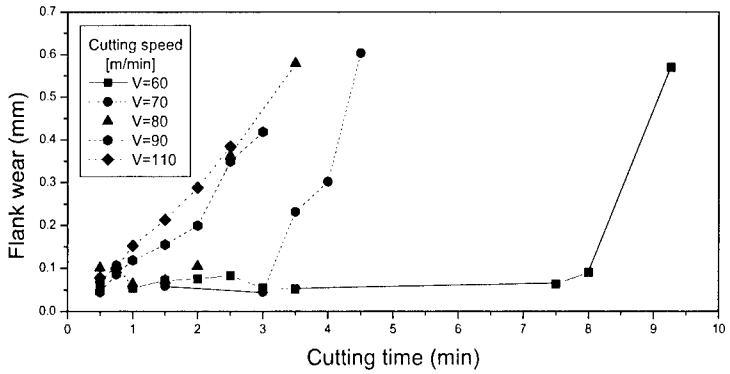

Fig. 3 Wear progression of carbide tool K10 for Ti-6Al-4V titanium alloy

By plotting "tool life" with respect to "machining velocity" and then by fitting the 4 points on the bi-logarithmic axes diagram, a straight line which is expressed as following equation

$$Log\ V = -0.3826\ Log\ T + 130.75$$

could be obtained as shown on Fig. 4. By comparing this equation with the general form of a Taylor's tool life equation $VT^n = C$, the constants $n = 0.3826$, $C = 130.75$ was evaluated.

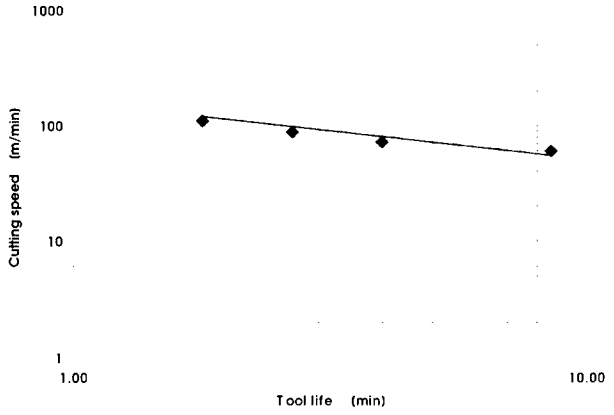

Fig. 4 Tool life diagram using K10 Ti-6Al-4V

With these data compared to those of free-machining steels on Table 5, the tool life sensitivity of the Ti alloy to machining velocity is a little higher(corresponding to "n=0.3826") and the machining velocity of "one minute life"(corresponding to "C=130.75") is much lower than with the free-machining steels thus representing the hard-to-cut characteristics of the Ti-6Al-4V alloy. Cast irons of H_B 200 has the "C" value of

204[2], which represents much easier-to-cut than the Ti-6Al-4V alloy.

Table 5 Taylor's constants for free-machining steels and Ti-6Al-4V alloy with tungsten carbide tools[3]

Workpiece Materials	Sulphur content (wt %)	n	C
Free-machining steels[3]	0.033	0.33	477
	0.11	0.33	549
	0.26	0.33	732
	0.37	0.33	823
Ti-6Al-4V alloy (measured)	-	0.3826	130.75

3.2 Cutting forces vs. cutting depth and feed

Cutting forces acquired through dynamometer are shown on Fig. 5 for an example. The figure shows the each force component in tangential, radial, and longitudinal directions in order of their magnitudes. The tangential force components tend to become smaller while the other two components maintain the magnitudes during cutting time. This fact is likely due to increase of the rake angle during cutting, which may be resulted from developing crater near the principal cutting edge on rake face.

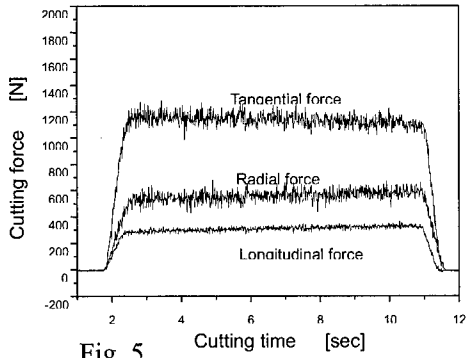

Fig. 5 Cutting force components with respect to cutting time (V=66m/min, f=0.32mm/rev, d=1.0mm)

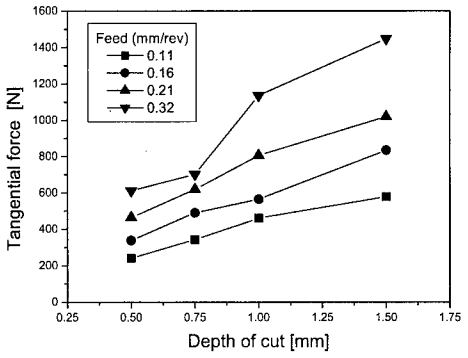

Fig.6 Tangential force component with respect to depth of cut (V=66m/min)

The tangential force components were most dependent to the change of feed and then to depth of cut. Radial components have the similar tendency but in less amount. Longitudinal components get the least effects of them.

4. CONCLUSION

(1) Tool wear test of sintered carbide K10 against Ti-6Al-4V alloy revealed that the wear progression is much slower with low machining velocity of around 60m/min than with higher machining velocities.
(2) The tool life was obtained in the form of Taylor's tool life equation $VT^n = C$, where $n = 0.3826$, $C = 130.75$. With these constants the machinability of the Ti-6Al-4V alloy was evaluated as lowest among the commercially available industrial materials.
(3) The tangential force tends to become smaller while the radial and the longitudinal force maintain the magnitudes. This facts are due to increase of the rake angle during machining, which would be resulted from developing crater near the principal cutting edge on rake face.
(4) The tangential components of the cutting forces were most dependent to the change of feed and then to the change of depth of cut. Radial components show the similar but less tendency. Longitudinal components were the least affected by them.

REFERENCES

1) A. R. Machado, J. Wallbank, "Machining of Titanium and Its Alloys-A Review," *Proceeding of the Institution of Mechanical Engineers*, Vol. 204, No. B1, 1990.
2) *Machinability Data Handbook, Metcut Research Associates*
3) M. C. Shaw, *Metal Cutting Principles*, Clarendon Press, Oxford, pp. 395-399, 510-512, 1986

Session II

MAGNESIUM ALLOYS

NEW MAGNESIUM ALLOYS FOR AUTOMOBILE APPLICATIONS

D. Eliezer[1] E. Aghion[2]

[1] Ben Gurion University of the Negev, Beer Sheva, Israel
[2] Dead Sea Magnesium Ltd. Beer Sheva, Israel

ABSTRACT

The growing use of magnesium for producing automotive drive train components requires the development of new alloys with improved creep properties. This paper discloses the results of a comprehensive study aimed at the development of creep resistance cost-effective die casting alloys with capability of long term operations at temperatures up to 150°C under high loads. The newly developed alloys designated as MRI 15X series exhibit die-castability, corrosion resistance, room temperature strength and short-term elevated temperature strength similar or better than those of AZ91D alloy. However, the most important fact is that the new alloys have creep resistance at temperatures of 130°C-150°C under stress of 50-85MPa significantly better than that of the commercial alloys AZ91D, AE42 and AS21. The principles of alloying and the metallurgical aspects of the new alloys are presented and discussed.

1. INTRODUCTION

Vehicle weight and fuel economy are becoming increasingly important in the automotive industry. The European and North American car producers have committed to reduce the fuel consumption by 25% and thereby to achieve 30% CO_2 emissions reduction by the year 2010 (1). The weight saving has a strong influence on the reduction of fuel consumption, from a fleet economy point of view. It has been calculated that 100 Kg of weight saving allows a fuel consumption reduction of about 0.5 liters every 100 Km covered.

Magnesium alloys are being used in a broad variety of structural applications in the automotive field. The growth of these applications has been driven primarily by weight saving. In fact, with a specific gravity of 1.74 is the world's lightest structural metal. For structural application it is usually alloyed with other metals including aluminum, manganese, zinc, zirconium etc. to obtain a variety of strong, lightweight alloys that lead to the increasing of possible applications giving an available choice of products especially targeted for harsh conditions. Moreover, magnesium alloys are versatile and can be shaped and worked by practically all known methods: casting, extrusion and rolling. In particular, die casting process, allows high production rate of near net shape parts.

Magnesium alloys are the lightest structural material and hence are very suitable for application in the car industry. Particularly it relates to drive train components such as gearbox, intake manifold, crankcase oil pump housing and others. Most of these parts are operating at elevated temperatures. Hence, improved creep resistance and stress relaxation properties are a critical issue for the alloy to be used for manufacturing such components. The

poor creep strength of alloys used for manufacturing various housings can result in a clamping load reduction of bolted joints that causes poor bearing-housing contact, leading to an oil leak and increased noise and vibration. Unfortunately, it should be pointed out that no existing die casting alloy of AZ, AM AS and AE series (2,3) is well suitable for manufacturing drive train parts operating at temperatures higher than 130°C. It appears that most of the drive train components will be produced by high-pressure die-casting – a high volume production technique, which continues to remain the brightest star for magnesium alloys in terms of long-term potential growth. In this case, alloy cost represents a significant proportion of the component cost. Hence, alloy cost becomes a major restriction in the alloy development. It means that new alloys should be cost competitive with existing commercial alloys. This requirement, along with castability problems, reduces possible options to alloy systems containing Al or Zn as principal alloying elements, using Mn, Si, Ce or La-based mish-metal, Ca and Sr as relatively small additions.

Increased activities in the development of creep resistant die casting alloys have been seen during the last decade. Norsk Hydro announced development of a creep-resistant automotive die cast magnesium alloy based on veteran AS21 alloy but with improved corrosion resistance due to a small addition of specific alloying elements (4).

ITM (5) and IMRA (6) American Inc developed new alloys based on the Mg-Al-Mn-Ca system respectively. Both types of alloys exhibited good creep resistance but had susceptibility to hot tearing when die casting real components. Later it was found that these alloys are suitable for thixomolding automotive components (7).

Recently Noranda Inc. developed 3 new alloys with acceptable cost based on Mg-Al-Sr system named Noranda A1, Noranda A2, and Noranda N (8). These alloys exhibit room temperature properties similar to those of AA and Am type commercial alloys but have creep resistance similar or better than that of AE42 alloy at 150°C and 170°C under load of 35 MPa. The results reported so far are related only to separately cast samples. No data was reported regarding industrial die casting trials of real components.

All above-mentioned developments seem to be suitable for gearbox applications at temperatures in the region of 130-150°C. However, in order to expand magnesium application into crankcases and engine blocks operating at temperatures as high as 170-200°C, additional alloying by rare earth element could be required. Two examples of such developments should be pointed out.

Firstly, an alloy designated MEZ and containing typically 2.5% RE. 0.35% Zn and 0.3% Mn was developed by Magnesium Electron Ltd (9). This alloy exhibits creep resistance significantly better than that of AE42 alloy at temperatures in the range of 150-175°C under loads of 45-60Mpa. However, this alloy has very low ductility and maximum strength at room temperature that can restrict its application. Nevertheless MEZ alloy is still being evaluated by some of automotive end users.

Another example is related to alloy ACM522 based on AM50 alloy with addition of 2.5% Ce-based mish-metal and 2% Ca (10). This alloy was developed by Honda R&D Co. and is already in industrial use for production of oil pan for Honda's 1-liter engine for the "Insight" hybrid car with fuel consumption of 35km per liter. It was demonstrated that this

alloy exhibits creep strength in the range of 150-200°C similar to that of aluminum alloy A384. However, the alloy in addition to rather high cost, has very low ductility (2-3%) and impact strength (4-5 J) that can restrict its application. In addition, the presence of 2% Ca in this alloy can lead to hot cracking problems in components with variable wall thickness and more complicated shapes than a specially designed oil pan with wall thickness in the range of 2.5-3 mm.

Summarizing, one can conclude that each car producer usually sets up its specific targets and requirements for certain applications. So in response to the specific requirement defined by Volkswagen for their gearboxes the Magnesium Research Institute (MRI) and Dead Sea Magnesium Ltd and BGU, Undertook, along with other partners, a comprehensive study aiming at the development of a creep resistant die castable alloy with capability of long-term operation at temperatures up to 150°C under high loads. The requirements for the new alloy were as follows:

- Die-castability, corrosion resistance, room temperature strength and short term elevated temperature strength similar to those of AZ91D alloy.
- Creep strength at temperatures 130°C-150°C under increased stresses better than that of AE42 alloy.
- Acceptable cost (maximum by 20% higher than that of AZ91D alloy).

The present paper addresses the principle results obtained in the course of implementing the above project.

2. EXPERIMENTAL

Based on the metallurgical consideration and previous experience various alloys systems were prepared and subjected to detailed examination. Test samples for metallographic examination as well as for tensile and creep testing were produced by direct squeeze casting and high-pressure die casting processes. Mechanical and creep tests were carried out at temperatures of 135°C 150°C and 200°C. The maximum stress was 55 MPa for 200°C and 85 MPa for 135°C-150°C. Taking into consideration die casting properties, creep resistance and mechanical properties, the five most promising alloys designated as MRI 151 – 155 were selected for upscale production and further investigation.

3. RESULTS AND DISCUSSION

When developing Mg alloys for die casting applications it should be taken into consideration that alloying with Al is strongly recommended in order to provide good fluidity properties (castability). Hence, a magnesium alloy should contain a sufficient amount of Al in the liquid state prior to solidification. On the other hand the presence of Al leads to the formation of eutectic $Mg_{17}Al_{12}$ intermetallics, which adversely affect creep resistance. Thus, additional alloying elements that can form specific intermetallics with aluminum should be introduced into a Mg-Al alloy in order to suppress the formation of β-phase ($Mg_{17}Al_{12}$).

Table 1 summarizes ambient temperature mechanical properties and corrosion resistance of new alloys compared to AZ91D and AS21 conventional alloys. It is evident that alloys MRI 151 and MRI 153 exhibit a combination of mechanical properties and corrosion

resistance similar to those of AZ91D alloy. The alloy MRI 155 has ductility and impact strength similar to those of AS21 alloy but exhibits significantly higher strength properties and superior corrosion resistance.

Table 1: Ambient temperature properties of new alloy compared to conventional alloys

Alloy	TYS [Mpa]	UTS [Mpa]	E [%]	Impact* strength [J]	Corrosion rate** $Mg/cm^2/day$
MRI 151	175 ± 4	277 ± 6	7.5 ± 0.5	7 ± 2	0.12
MRI 153	168 ± 6	251 ± 6	5.8 ± 0.9	9 ± 4	0.09
MRI 155	148 ± 3	265 ± 8	12.8 ± 1.6	15 ± 4	0.13
AZ 91D	167 ± 3	277 ± 6	7.0 ± 0.5	8 ± 2	0.11
AS21	126 ± 3	237 ± 3	16 ± 3	14 ± 3	0.34

* unnotched samples
** 100 hr salt spray test according to ASTM Standard B-117

The selective optimization of the materials is particularly striking in connection with their creep characteristics. With a load of 85 MPa at 135°C (Fig.1) the new alloys display a secondary creep rate, which is smaller than the corresponding values of conventional alloys AZ91 and AE42 by more than a power of ten. Fig. 2 and Fig. 3 describe the comparison between the creep properties of MRI alloys and AZ91 alloy at 150°C and 200°C respectively. The improvement of the creep properties of MRI alloys, compared to AZ91, is better in the whole range of temperatures. The MRI-151 and MRI-153 have excellent creep properties as related to the other alloys. The creep properties of MRI-153 alloy are much better that MRI-151 at 200°C. The elevated temperature short-term strength and creep behavior are the most important properties for magnesium alloys designated for gearbox applications. Figure 1 shows that the new alloys exhibit creep strain at 135°C under stress of 85 MPa (typical stress-temperature conditions for gearboxes) significantly less than that of AZ91D alloy (11). Calculations show that the new alloys MRI 151 and MRI 153 exhibit minimum (steady-state) creep rate $E' \sim 10^{-8}\ S^{-1}$ which is by order of magnitude less than that of AZ91D alloy ($E' \sim 10^{-7}\ S^{-1}$). It is evident that under stress of 85 MPa both alloys exhibit similar creep behavior. However, under stress of 90 MPa the creep strain of the alloy MRI 153 is significantly less than that of the alloy AS21. These results are also supported by the data given in Table 2. It is generally accepted to correlate steady-state creep rate to acting stress and testing temperature by the relationship: $E' = A\ \sigma^{n} \exp [-Q/RT]$ where A is a constant, Q is activation energy for creep, n is stress exponent and R is the gas constant.

Table 2 Creep behavior of new alloys

Alloy	Stress exponent 135°C, 85-110 MPa	Activation energy [KJ/mol] 90 MPa, 130-150°C
MRI 151	7	175
MRI 153	7.6	181
MRI 155	8.9	166
AS21	19.5	168

The stress exponent n was calculated for the creep deformation at 135°C under stresses from 85 MPa to 100 MPa. The very high value of the stress component, n=19.5, for AS21 alloy confirms high sensitivity of creep behavior of this alloy to increasing applied stresses, when compared with the new alloys (n=7.9). The activation energy of creep deformation was calculated for the temperature range from 130°C to 150°C under applied stress of 90 MPa. As can be seen from Table 2, the new alloys MRI 151 and particularly, MRI 153 exhibit higher activation energy for creep than that of AS21 alloy. Fig. 4 and Fig. 5 describe the comparison between the tensile strength and the yield strength respectively of MRI-alloys and the AZ91-alloy at 150°C. They show that the tensile strength and the yield strength of the MRI alloys are comparatively similar to the AZ91 alloy. Fig. 6 describes the comparison between the deformation to fracture of MRI alloys and AZ91 at 150°C. Fig. 6 shows that the ductility of the AZ91 alloy is much better than the MRI alloys. The following three major microstructural changes, which were caused by long-term high-temperature mechanical loading, were found in the creep samples (Fig. 7-9). Nucleation, growth and coalescence of voids especially in the vicinity of grain boundaries that are perpendicular to the load axis. These elongated voids were distributed homogeneously in the volume. Micro-cracking in the grain-boundary precipitate phase and adjacent to the grain periphery. Precipitation of numerous spherical particles adjacent to the grain-boundaries, without the dissolving of the primary precipitates.

Summarizing one can conclude that the new alloys MRI 151 and MRI 153 exhibit creep resistance at 135°C under high stresses of 90-110 MPa superior to that of AS21 alloy.
In addition to achieving the best combination of corrosion resistance and mechanical properties at room temperature for these alloys, the other most important factor governing successful commercial application is also castability.

4. SUMMARY

The extensive research program initiated by Volkswagen AG and DSM (MRI) with the aim of developing low cost HPDC magnesium alloys gearbox applications led to the development of new alloys of MRI 15X series. The new alloys exhibit room temperature mechanical properties and corrosion resistance similar or better than those of commercial alloys. However, MRI 15X alloys have a great advantage in creep resistance compared to conventional alloys. The initial die casting trials aimed at the production of real components like gearboxes and clutch housings showed the possibility to produce such components of new alloys with no modification in the gating system and components design. These alloys are being currently evaluated by extensive tests. Additional industrial die casting trials will be

performed in order to produce other components and verify producibility and recycle characteristics of new alloys.

5. ACKNOWLEDGMENT

The authors would like to thank the German Israeli BMBF foundation for their financial support.

6. REFERENCES

1. H. Friedrich and S. Schumann, "The second age of magnesium – research strategies to bring the automotive industry's vision to reality" (paper presented at the second Israeli International Conference on Magnesium Science and Technology, Dead Sea, Israel, 22-24 February, 2000), 9, Editors E. Aghion and D. Eliezer.

2. I.J. Polmear, Metallurgy of Light Alloys, Halstead Press, New York, 1996, 196-247.

3. H. Westengen, "Magnesium alloys for structural applications; recent advances," Journal de Physique IV, (1993), 491-501.

4. K. Pettersen et al. "Creep resistant Mg alloy development" (Paper presented at the International Congress 'Magnesium alloys and their applications,' Munchen, 26-28 September 2000), 29.

5. M.O. Pekguleryuz, A. Luo, "Creep resistant magnesium alloys for die casting," ITM Inc., International Patent Application WO 96/25529, 1996.

6. A. Luo, T.Shinoda, "Magnesium alloy having superior elevated-temperature properties and die castability," Imra America Inc., US Patent 5855697, 1997.

7. E.A. Nyberg et. Al., "High temperature – creep resistant magnesium alloys: Advances in Thixomolding automotive components," SAE Technical Paper 2000-01-1126, Detroit, MI, 2000.

8. M.O. Pekguleryuz, "Development of creep resistant magnesium die casting alloys," Materials Science Forum Vols. 350-351 (2000), 131-140.

9. P. Lyon, J.F. King and K. Nuttal "A new magnesium HPDC alloy for elevated temperature uses" (paper presented at the Third International Magnesium Conference, Manchester, UK, 10-12. April 1996), 99.

10. S. Koike et al. "Development of lightweight oil pans made of a heat-resistant magnesium alloy for hybrid engines," SAE Technical Paper 2000-01-1117, Detroit, MI, 2000.

11. F. v Buch, et al "Development of a low cost, temperature and creep resistant magnesium die cast alloy" (Paper presented at the International Congress 'Magnesium alloys and their applications,' Munchen, 26-28 September 2000), 29.

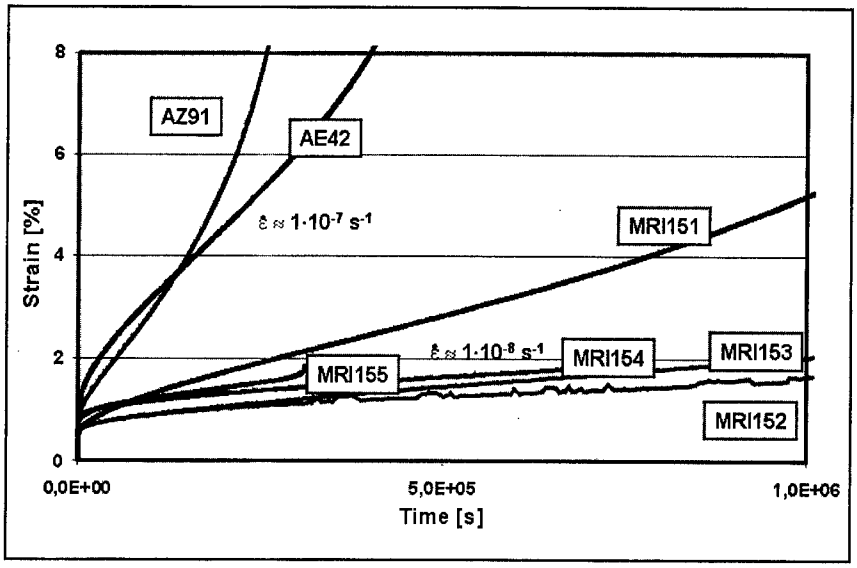

Fig.1: Creep curves of the newly developed alloys MRI 151-155 at 135°C and 85 MPa compared to the conventional alloys AZ91 and AE42

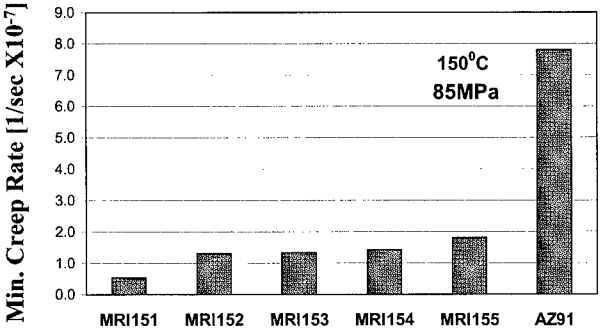

Fig.2: The comparison between the creep properties of MRI alloys and AZ91 alloy at 150°C.

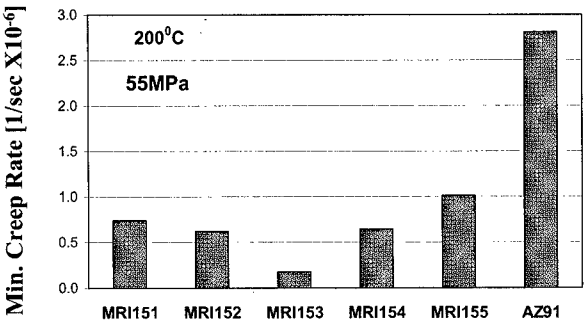

Fig.3: The comparison between the creep properties of MRI alloys and AZ91 alloy at 200°C.

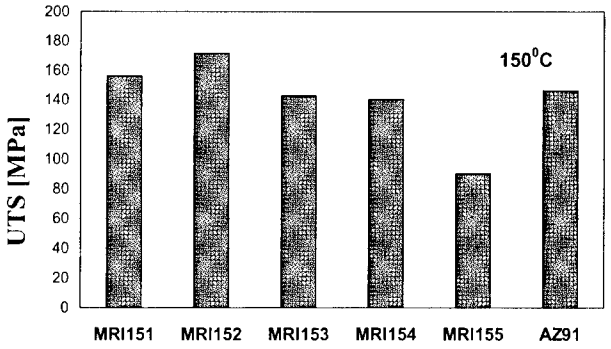

Fig.4: The comparison between the tensile strength of MRI-alloys and the AZ91-alloy at 150°C

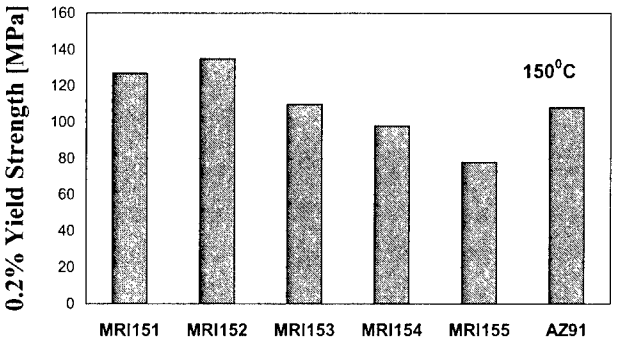

Fig5: The comparison between the yield strength of MRI-alloys and the AZ91-alloy at 150°C

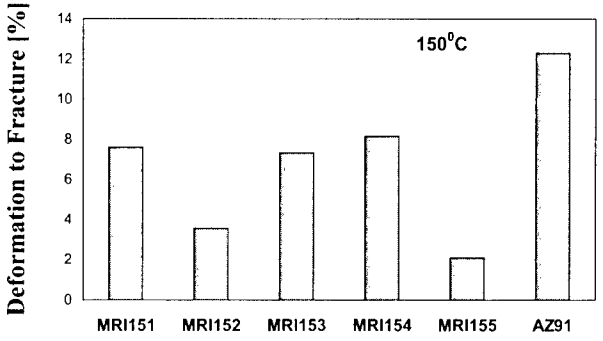

Fig.6: The comparison between the deformation to fracture of MRI alloys and AZ91 at 150°C

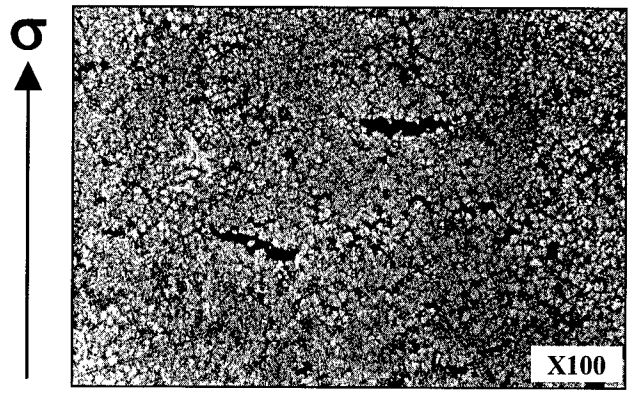

Fig.7: The creep damages that were observed in the MRI-alloys (nucleation, growth and coalescence of voids).

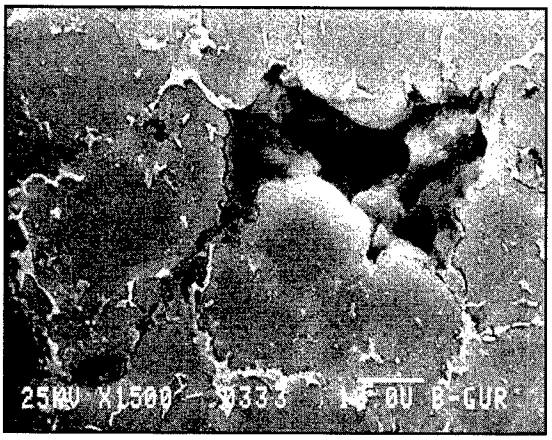

Fig.8: The creep damages that were observed in the MRI-alloys (micro-cracking in and adjacent to grain periphery).

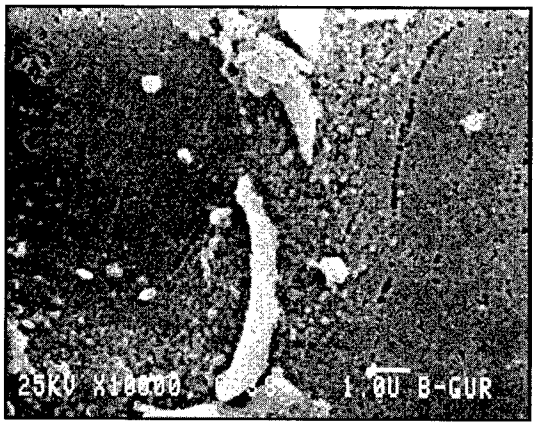

Fig.9: The creep damages that were observed in the MRI-alloys (precipitation of numerous spherical particles adjacent to the grain-boundaries, around the second phase).

NEW SEMISOLID PROCESS OF MAGNESIUM ALLOYS

T. Motegi, E. Yano, and N. Nishikawa

Department of Metallurgical Engineering,
Chiba Institute of Technology, Narashino, Chiba-ken, 275-0016, Japan

ABSTRACT

In order to produce Mg-Al-Zn alloy billets having granular and fine primary Mg crystals in cast structures, the specially designed inclined cooling plate was used. Crystal seeds of primary magnesium were nucleated on the cooling plate. Seeds of primary crystal flowed down with the molten alloy into the mold. The seeds existing in the molten alloy grew to granular grains in the mold. Factors affected the cast structures were the pouring temperature, angle of the inclined cooling plate, and length of the plate. The cast structures without using the cooling plate show that dendrite crystals grew throughout the ingot. The most suitable conditions yielded fine grains of primary crystals in cast structures.

1. INTRODUCTON

The thixocasting process is very useful for producing homogeneously solidified structures in castings. Thixocasting billets used in this process must have globular, fine and homogeneous crystal grains. During heating of the thixocast billets, primary crystals must not remelt, but solid eutectic area must. The molten eutectic areas lubricate as globular and primary crystals move into the mold during the thixocasting. The primary crystals existing globularly in the liquid alloy play an important role in forming the grains that make up the homogeneously cast structures.

In general, semisolid billets were cast by Rheocasting which is stirred by the electro-magnetic or mechanical force during solidification. However, this method needs the huge equipment and the high cost. Ohno and Motegi[1)] have proposed the formation mechanism of globular crystals in ingots and castings; that is, these crystals nucleate on the mold wall and move into the molten alloy by fluid motion. In this investigation, our mechanism is applied to obtain the semisolid state of magnesium alloy. The molten alloy was flowed on an inclined cooling plate where globular crystals generate, and then cast into the mold.

2. EXPERIMRENTAL PROCEDURES

A commercial AZ91E magnesium alloy was used in the whole experiments. Table 1 shows chemical compositions of the alloy. Thermal analysis was performed in order to determine the experimental conditions. The alloy was melted in a stainless steel crucible lined with pure magnesia powder, then a thermocouple was set in the molten alloy and the alloy was cooled slowly to obtain the temperatures of liquidus and solidus lines.

Table 1 Chemical composition of Mg-9%Al-1%Zn alloy. (mass%)

Al	Zn	Mn	Si	C	Ni	Fe	Be	Mg
8.9	0.7	0.25	0.03	0.001	<0.001	0.003	0.0013	Bal.

Figure 1 shows a schematic illustration of the experimental apparatus. This is consisted of an electric furnace, an inclined cooling plate and a permanent mold. Dimensions of stainless steel crucible was 67 mm in outer diameter, 60mm in inner diameter, and 100mm in height, and a 10 mm tap hole was opened in the bottom of the crucible. The tap hole was closed by a stainless steel stopper until the molten alloy was poured. All stainless steel

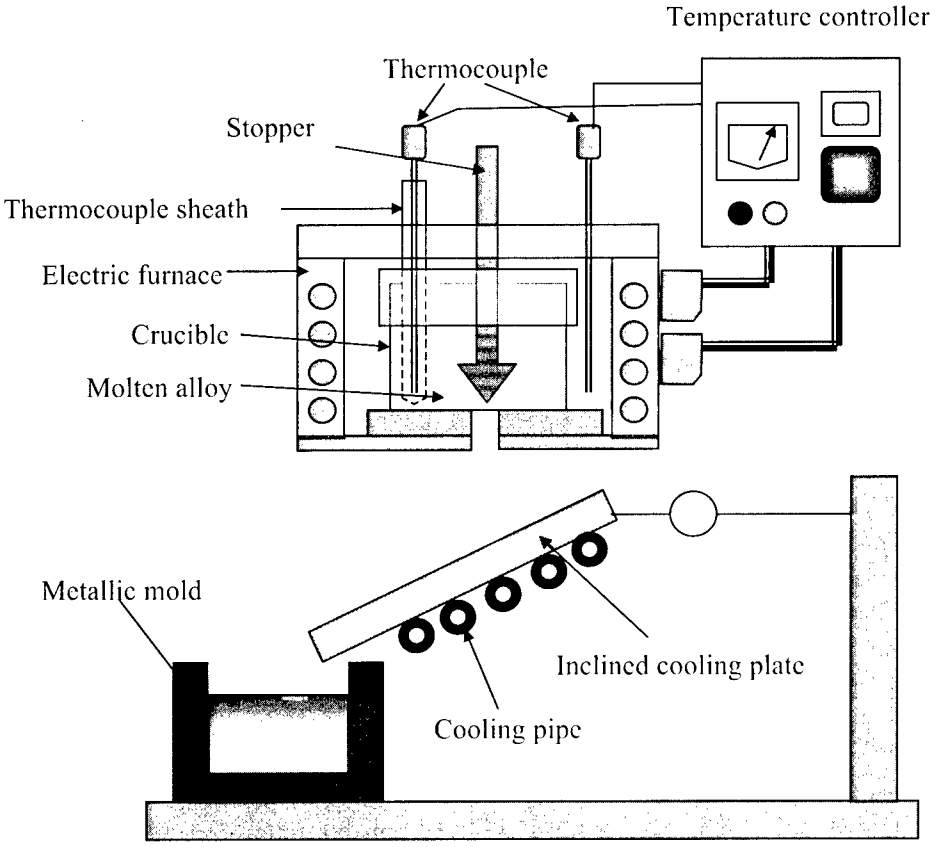

Fig. 1 Schematic illustration of experimental apparatus.

materials used were coated with pure magnesia powder to prevent between active molten magnesium and materials. The inclined cooling plate was made of pure copper and it was kept at the constant temperature by water-cooling pipe set under the plate. The permanent mold which was 53mm in outer diameter and 47 mm in inner diameter and 80 mm in height was placed under the inclined plate. It was held by the insulator to prevent the heat transfer through the mold wall.

A 0.125 kg of the magnesium alloy was melted at 670 ℃. It was covered with flux to prevent burning of the molten alloy. After melting and keeping for desired time, the stopper was pulled out and the molten alloy was poured into the mold through the inclined plate. The mold preheated at 580 ℃ was used and the cast alloy was held for 30 s in the mold, then it was sunk in the water bath.

In order to confirm the influence of holding time of the molten alloy in the mold, the cast structures which were held in the mold or not, and with and without using the cooling plate were compared.

We have estimated on the base of experimental results for semisolid aluminum alloys that the factors influenced on the cast structures were casting temperatures, length and angle of cooling plate.[2] In this experiment, the casting temperature was 615, 635, 645, and 655 ℃, the length of cooling plate was 50, 100, 150, and 200 mm, and the angle was 20, 40 and 60 degrees.

The molten alloy was quenched by chilled copper blocks during pouring just over and under the inclined cooling plate to examine crystallization of the primary crystals on it. Each ingot was observed the microstructures by a scanning electron microscope and an optical ones. It was also measured the grain size by a picture analyzer.

3. RESULTS AND DISCUSSION

The liquidus line temperature of 595 ℃ and solidus line one of 429 ℃ were determined by the thermal analysis. Figure 2 shows the solidified structures of the samples quenched just before touching and just under the cooling plate. Numerous crystals of primary magnesium appeared by flowing on the cooling plate. However, no globular crystals appeared in the sample which was taken just over the cooling plate. It is considered that the cooling plate is greatly influenced the crystallization of globularly primary crystals. Figure 3 shows the solidified structures with and without the isothermal holding of the molten alloy. Only dendrite structures appeared without the holding times. However, grain structures appeared as the molten alloy was held into the mold for 30 s after casting.

On contrast, coarsened dendrite crystals appeared that the molten alloy was cast directly into the mold without using the cooling plate and held for 30 s. This result suggests that the formation of globular crystals in the cast structures were influenced by use of the cooling plate and the isothermal holding.

Figures 4 shows the solidified structures and the average grain size of obtained by various pouring temperatures. The lower the pouring temperature, the finer grain size obtained, because the crystal formation on the cooling plate are little at the high pouring temperatures.

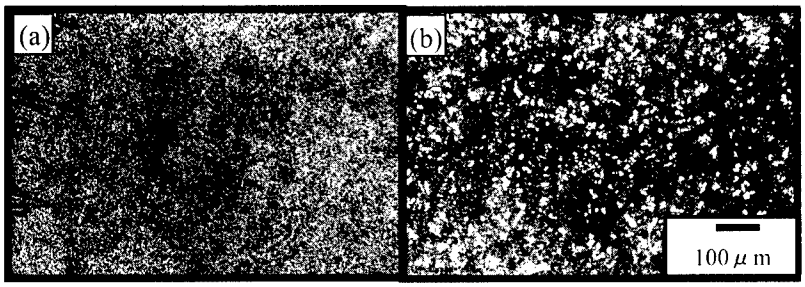

Fig. 2 Solidified structures quenched by copper blocks. (a) Sample taken just over the inclined cooling plate.(b) Sample taken just over the inclined cooling plate.

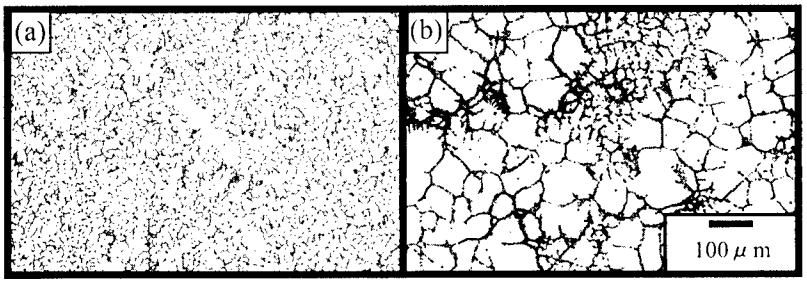

Fig. 3 Influence of holding time in the mold on the solidified structures. (a)Holding time 0s, (b) Holding time 30s

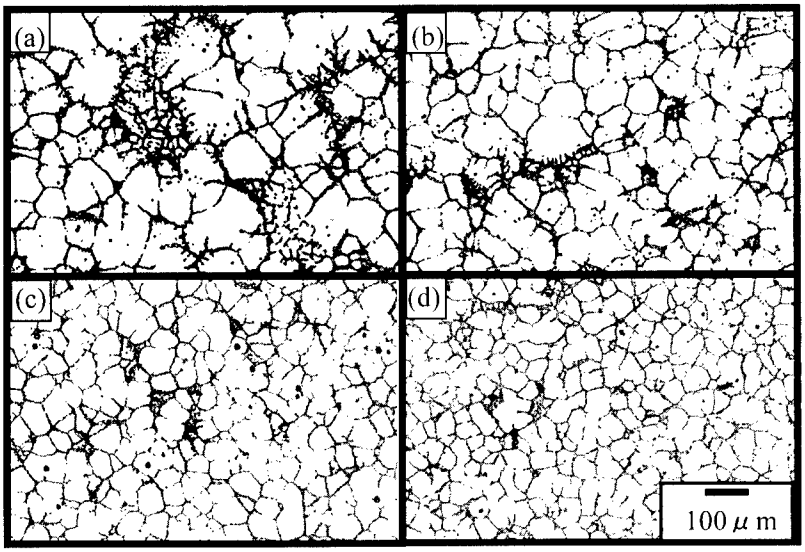

Fig. 4 Influence of pouring temperature on the cast structures. (a) 655 ℃, (b) 645 ℃, (c) 635 ℃, (d) 615 ℃.

As the pouring temperature was 615 ℃ near liquids line temperature, numerous primary crystals generated on the cooling plate and they flowed in the mold with the molten alloy. The finer crystal grains can remain and grow granular grains in the mold. Figures 5 shows the solidified structures and average of grain size of granular crystals obtained by different length of the cooling plate. As the length of the cooling plate is longer, the finer grains are obtained because the longer the cooling plate, the longer the contact time between the molten alloy and cooling plate. In this case numerous seeds of granular crystal can generate.

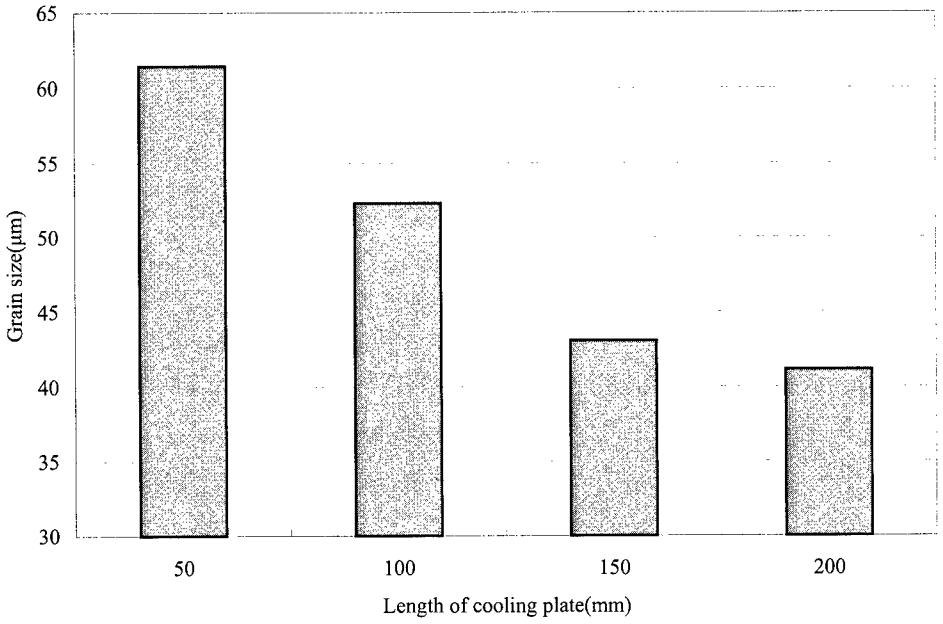

Fig. 5 Relation between the grain size and length of cooling plate.

The smaller grains are obtained by pouring temperature of 615 ℃ and the cooling plate of 200 mm. Using these experimental conditions, the experiments were performed to examine the change of the inclined angle of the cooling plate. Figures 6 shows the solidified structures and the average of the grain size. The result shows that the inclined angle which the smallest grain size was obtained is 40 degree. When the inclined angle of 20 degree was used, the solid shell formed on the cooling plate and no the granular grains appeared, because the flow speed of the molten alloy was slower and the temperature of the molten alloy decreased and formed the solid shell on the plate. On the other hand, when the angle of 60 degree was used, little granular grains generate, because the flow speed was faster than that of 40 degree, little granular grains generated. These results suggest that the balance of the flow speed and cooling ability of the plate needs to obtain numerous granular grains.

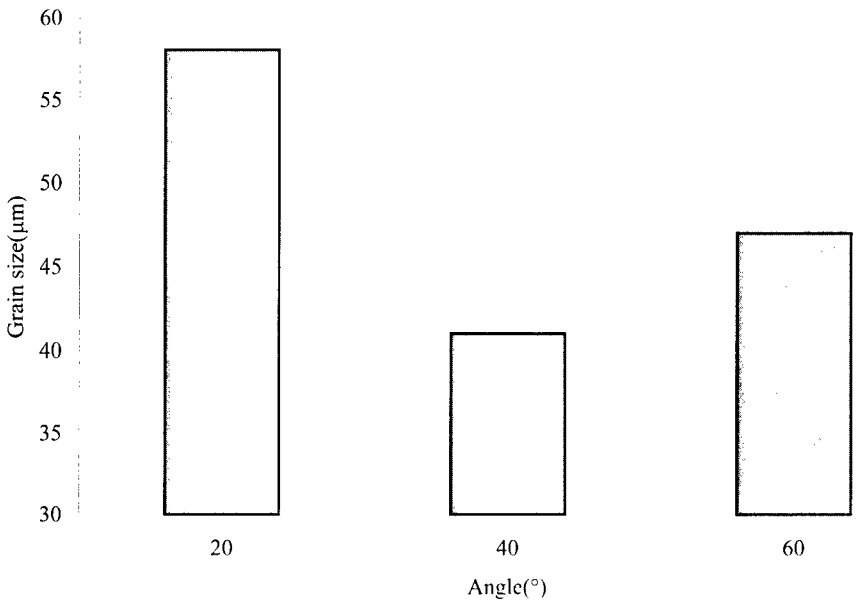

Fig. 6 Relationship between the grain size and inclined angle of cooling plate.

4. CONCLUSIONS

In order to obtain homogeneous and globular crystals in the cast structures of AZ91E magnesium alloy, the special designed inclined cooling plate was used. The results obtained are as follows.

(1) The cooling plate is effective for generating numerously the seeds of granular grains.
(2) Isothermal holding of the molten alloy including the crystal seeds in the mold is effective to grow granular crystal grains.
(3) The best pouring temperature on the cooling plate is 615 ℃ near the liquidus temperature in this alloy.
(4) The best inclined angle and length of the cooling plate are 40 degree and 200 mm.
(5) Heat and mass balances among these three experimental conditions are the most important.

REFERENCES

1. A. Ohno, T. Motegi, and H. Soda, Trans. ISIJ, 18(1978), pp.11-18.
2.T. Motegi, K. Kondo, C. Liu, and S. Aoyama: Proceedings of the 4th Decennial International Conference on Solidification Processing, (1987), pp.14-16.

RHEOLOGICAL AND FLOW BEHAVIOR OF SEMI-SOLID AZ91D MAGNESIUM ALLOY

Chang Dong Yim*, Si Hoon Lee and Kwang Seon Shin**

School of Materials Science and Engineering
DynaMaterials Co., Inc.
*Research Institute of Advanced Materials
Seoul National University, Seoul 151-742, Korea
**Center for Advanced Aerospace Materials
Pohang University of Science and Technology, Pohang 790-784, Korea

ABSTRACT

In the casting processes such as die casting, squeeze casting and semi-solid casting, it is necessary to control the flow behavior of the molten and/or semi-solid alloy properly in order to improve the quality of the cast products. There are a number of parameters that influence the flow behavior of the semi-solid alloy such as the viscosity and velocity of the semi-solid slurry and the shapes of the gate and die cavity. Although the velocity of the semi-solid slurry decreased rapidly after passing through the gate, the viscosity of the slurry maintained the low enough value during the die filling process so that the sound semi-solid pressure die casting could be produced. In the present study, the effects of various thermo-mechanical treatments on the rheological behavior of the semi-solid AZ91D magnesium alloy were investigated by using a concentric cylinder-type viscometer. The effects of the gate thickness and the gate velocity on the die filling behavior of the semi-solid AZ91D magnesium alloy were investigated by using a high-speed camera and a transparent die cover. From the measured viscosity, the die filling behavior of the semi-solid slurry and the microstructures of the pressure die cast products, the semi-solid processing map was constructed for the AZ91D magnesium alloy.

1. INTRODUCTION

The semi-solid metal (SSM) processing is an emerging new technology for near net-shape production of engineering components, in which metal alloys are processed in the temperature range where the liquid and solid phases coexist [1,2]. The semi-solid slurry with a non-dendritic microstructure exhibits distinct rheological behavior, namely, thixotropy and pseudo-plasticity [3]. These rheological properties make the SSM processing as the unique and effective process for near net-shape product and property enhancement. The flow of the semi-solid slurry, however, must be controlled to a laminar flow in order to avoid the gas and oxide entrapments. The flow behavior of the semi-solid slurry is dependent on the various processing parameters such as the viscosity and velocity of the slurry and the shapes of the gate and die cavity. In the present study, the thixotropic behavior of the semi-solid AZ91D magnesium alloy was investigated with the changes of the rest time and the up time. The effects of the gate thickness and velocity on the flow behavior of the slurry during the die filling process were investigated by using a high-speed camera and a transparent die cover.

2. EXPERIMENTAL PROCEDURES

2.1 Thixotropic Behavior of the Semi-solid AZ91D Magnesium Alloy

One hundred and fifty grams of AZ91D magnesium alloy were charged into a low carbon steel crucible attached to a concentric cylinder-type viscometer and heated to 620°C. The molten alloy was cooled from 620°C to 580°C at a cooling rate of 1°C/min. and then held isothermally for 2 hours, while it was continuously stirred at 100rpm. The stirring was temporarily stopped and the semi-solid slurry was held isothermally for a predetermined amount of time (rest time, t_r) without stirring. After the desired amount of rest time, the shear rate imposed on the slurry increased from 0 to 1021 s^{-1} in a given period of time (up time, t_u) and then decreased from 1021 to 0 s^{-1} within the same period of time as the uptime. Table 1 shows the experimental conditions employed for the observation of the thixotropic behavior of the semi-solid AZ91D magnesium alloy.

Table 1. Experimental conditions for the observation of thixotropic behavior.

Stirring Temperature (°C)	Rest Time (sec)	Up Time (sec)
580	0	7
	10	14
	30	28
	60	70
	300	140

The variation of the torque on the stirrer was automatically recorded on a computer during each cycle while varying either the rest time or the up time. The variation of the apparent viscosity of the semi-solid slurry was calculated from the measured torque values.

2.2 Flow Behavior of the Semi-solid AZ91D Magnesium Alloy

The AZ91D magnesium alloy billets of 7 inch diameter were cast in a low carbon steel mold. After homogenization, these billets were subsequently extruded at an extrusion ratio of 22:1 at 350°C. The raw materials for the slugs for the production of the pressure die castings were cut from the extruded bar and compressed by 25% in order to induce strain. The slug was heated to 583°C in order to produce the semi-solid alloy and then inserted into the sleeve of a 75ton horizontal pressure diecasting machine. The flow behavior of the semi-solid slurry during the die filling process was visualized by using a high-speed camera and a transparent die cover, under the various injection conditions by changing either the gate thickness or the gate velocity. The gate thickness was changed from 2 to 8 mm and the gate velocity was varied from 2 to 36 m/s.

3. RESULTS AND DISCUSSION

3.1 Thixotropic Behavior of the Semi-solid AZ91D Magnesium Alloy

Figures 1(a) and (b) show the changes in the apparent viscosities of the semi-solid AZ91D magnesium alloy as a function of the shear rate at various rest times and up times, respectively. As shown in Fig. 1, the apparent viscosity decreased rapidly at the beginning with increasing the shear rate and then decreased slowly with further increase in the shear rate. As the shear rate decreased after its maximum, the apparent viscosity of the slurry further decreased slowly instead of increasing, indicating that the viscosity of the slurry was path(history)-dependent. These results may come from the difference in the rates at which the microstructure of the semi-solid slurry changed with respect to the change in the shear rate. It has been reported that the rate of the de-agglomeration (breakdown) was faster than the rate of the agglomeration between the primary solid particles [4-7]. The apparent viscosity of the semi-solid slurry, therefore, decreased by the de-agglomeration with increasing the shear rate, but it did not change or even slightly decreased further due to little change in the microstructure of the semi-solid slurry with decreasing the shear rate after its maximum in the present study. As shown in Fig. 1(a), the apparent viscosity increased as the rest time increased from 0 to 300sec at a shear rate of $0s^{-1}$. However, the difference between the viscosities after different

rest times decreased rapidly with increasing the shear rate. The up time also affected the rate of change of the apparent viscosity of the slurry as shown in Fig. 1(b). As the up time increased, the slurry would experience a larger number of shearing at a given shear rate and thus the apparent viscosity of the slurry would decrease.

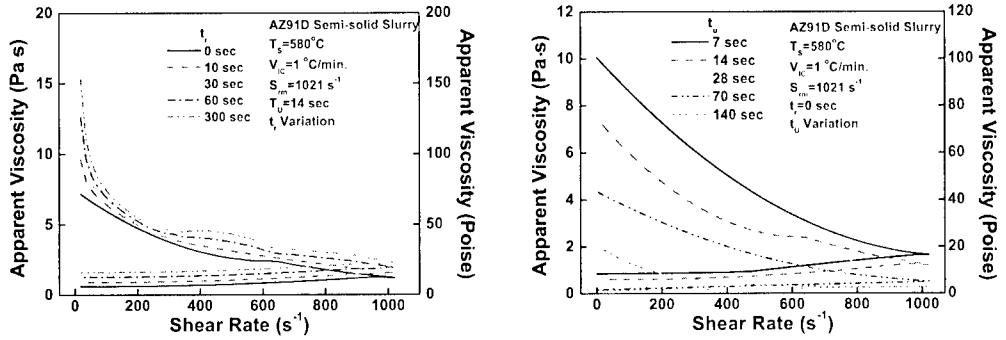

(a) (b)

Fig. 1. Effect of the processing variables on the apparent viscosity during shear rate change cycle; (a) variation of rest time, (b) variation of uptime.

3.2 Flow Behavior of the Semi-solid AZ91D Magnesium Alloy

Figures 2(a) and (b) show the die filling pattern of the semi-solid AZ91D magnesium alloy as a function of time at two different gate velocities of 4 m/s and 8.25 m/s, respectively, when the gate thickness was 8 mm. At the gate velocity of 4 m/s, the front surface of the semi-solid slurry remained rather smooth as shown in Fig. 2(a), indicating a laminar type flow. The front surface of the slurry remained smooth even after the slurry passed by the obstacles. As the gate velocity increased to 8.25 m/s, however, the front surface of the semi-solid slurry was shattered after collision with obstacles and the air pockets were trapped within the cavity as indicated by the arrows in Fig. 2(b). Figure 3(a) and (b) show the optical micrographs obtained from the semi-solid pressure die castings at the gate velocities of 4 m/s and 8.25 m/s, respectively, when the gate thickness was 8 mm. As predicted from the die filling pattern shown in Fig. 2, the sound casting was produced at the gate velocity of 4 m/s. However, micro-pores were observed in the casting produced at the gate velocity of 8.25 m/s. Figure 4 shows the change of the critical velocity at which the flow would transfer from the laminar flow to the turbulent flow as a function of the gate thickness. As the gate thickness increased, the external and internal defects were formed at the lower gate velocity. In general, the Reynolds number (Re) is used to describe the flow behavior of the fluid. The value of Re at which transition from the laminar to the turbulent flow occurs is known to be

approximately 2100 in the usual engineering application of the flow in the pipes [8]. The critical gate velocity, therefore, could be approximately predicted by using the Reynolds number and the equivalent diameter in the case of rectangular gate.

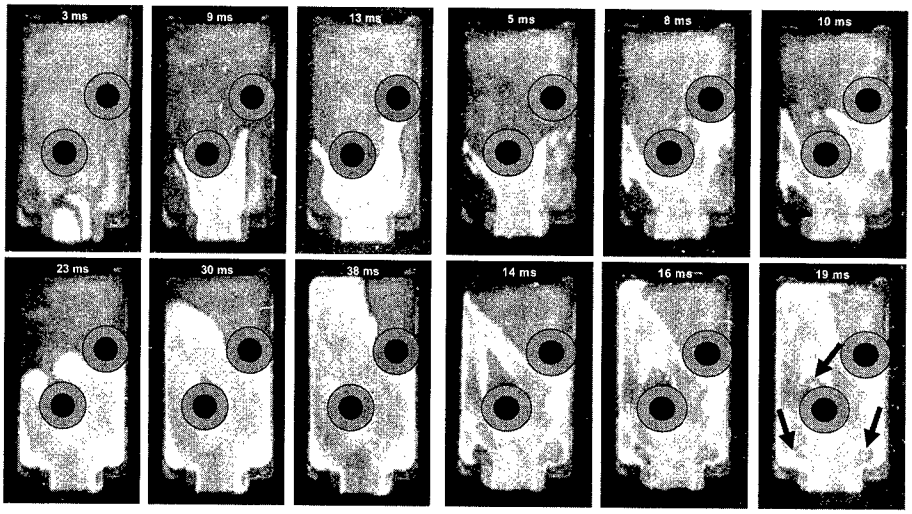

(a) (b)

Fig. 2. Visualization of the die filling pattern of the semi-solid AZ91D magnesium alloy with the gate thickness of 8 mm; (a) V_g = 4 m/s, (b) V_g = 8.25 m/s.

It was reported that the effect of the gate width on the flow behavior could be neglected when the gate width was much larger than the gate thickness and thus the critical velocity could be described as a function of the gate thickness [9]. As shown in Fig. 4, the theoretical value calculated from the Reynolds number and the measured apparent viscosity well predicted the transition from the laminar to the turbulent flow.

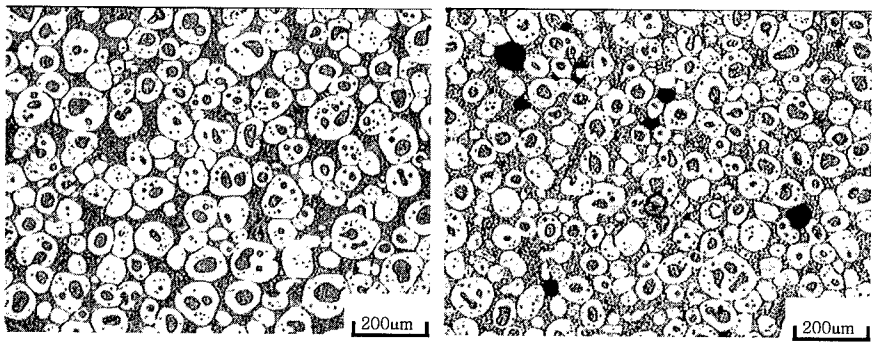

(a) (b)

Fig. 3. Optical micrographs obtained from the semi-solid pressure die castings at different gate velocities with the gate thickness of 8 mm; (a) V_g = 4 m/s, (b) V_g = 8.25 m/s.

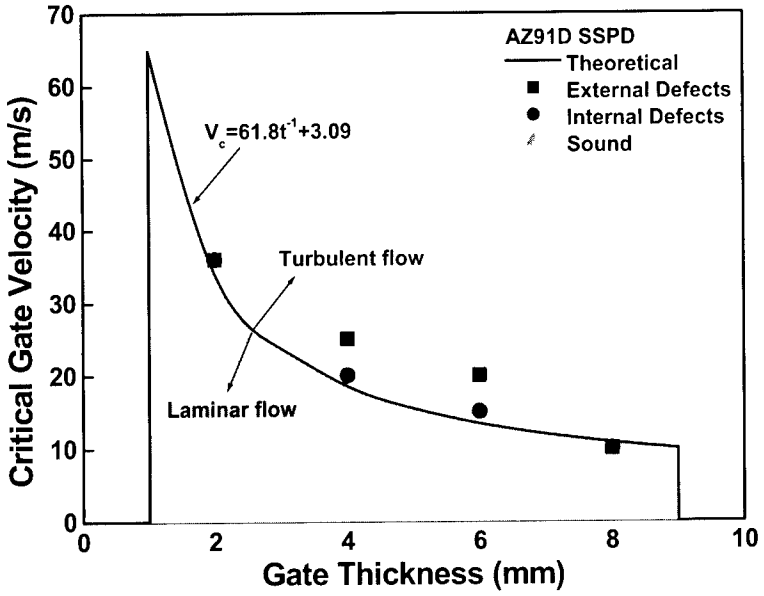

Fig. 4. Comparison between the theoretical and experimental critical gate velocities as a function of gate thickness.

4. CONCLUSION

(1) The apparent viscosity of the semi-solid AZ91D magnesium alloy decreased rapidly at the beginning with increasing the shear rate and then decreased slowly with further increase in the shear rate. As the shear rate decreased after its maximum, the apparent viscosity further decreased slowly, indicating that the viscosity of the slurry was path-dependent. These results come from the difference between the rates of the de-agglomeration and the agglomeration of the primary solid particles at different shear rates.

(2) The flow behavior of the semi-solid slurry during the die filling process was strongly dependent on the gate velocity and the gate thickness. The transition from the laminar flow to the turbulent flow could be well predicted by the theoretical value calculated from the Reynolds number and the measured apparent viscosity.

REFERENCES

1. M. C. Flemings, Metall. Trans. A, Vol. 22A (1991), pp. 957-981.
2. D. H. Kirkwood, Inter. Mater. Rev., Vol. 39 (1994), pp. 173-189.

3. P. A. Joly and R. Mehrabian, J. Mater. Sci., Vol. 11 (1976), pp. 1393-1418.
4. W. Nan, S. Guangji and Y. Hanguo, Mater. Trans. JIM, Vol. 31 (1990), pp. 715-722.
5. P. Kumar, C .L. Martin and S. Brown, in Proc. 2nd Inter. Conf. on Semi-Solid Processing of Alloys and Composites, S. B. Brown and M. C. Flemings, eds., TMS, Warrendale, PA, (1992), pp. 248-262.
6. H. Peng and K. K. Wang, in Proc. 4th Inter. Conf. on Semi-Solid Processing of Alloys and Composites, D. H. Kirkwood and P. Kapranos, eds., The University of Sheffield, Sheffield, U.K., (1996), pp. 2-9.
7. A. R. A. McLelland et al., Mater. Sci. Eng. A, Vol. 232A (1997), pp. 110-118.
8. G. H. Geiger and D. R. Poirier: Transport Phenomena in Metallurgy, Addison-Wesley Publishing Company, Massachusetts, MA(1973), pp. 3-35.
9. J.-C. Lee, C. D. Yim, H.-K. Seok, H.-I. Lee, J. Kor. Inst. Met. & Mater. (submitted).

FABRICATION OF BULK MG-CU-AG-Y GLASSY ALLOY BY SQUEESE CASTING

Eun Soo Park, Hyun Kyu Lim, Won Tae Kim*, Do Hyang Kim

Center for Noncrystalline Materials, Yonsei University, Seoul 120-749, Korea
* Department of Physics, Chongju University, Chongju 360-764. Korea

ABSTRACT

A new $Mg_{65}Cu_{15}Y_{10}Ag_{10}$ alloy having large glass-forming ability has been developed to produce bulk Mg-based glass material. Partial replacement of Ag with Cu in a $Mg_{65}Cu_{25}Ag_{10}$ alloy led to a significant improvement of glass-forming ability. The addition of Ag significantly decreases the melting temperature and also satisfies conditions of a multi-element system with a deep eutectic, large atomic-size difference between its components and a large electronegativity difference between the components for good glass-forming ability. Injection casting produced bulk metallic glass of $Mg_{65}Cu_{15}Y_{10}Ag_{10}$ alloy having a diameter up to 6 mm. Squeeze casting was able to produce larger bulk metallic glass with $Mg_{65}Cu_{15}Y_{10}Ag_{10}$ alloy having diameter of 10 mm, due to the rapid heat extraction and undercooling of the liquid alloy, by applying pressure during solidification.

1. INTRODUCTION

The increased demand for light and strong materials which can withstand severe environmental conditions has stimulated considerable research into metallic glass alloys, due to their significantly improved properties, such as high strength, toughness, hardness, and good corrosion resistance, in contrast to crystalline alloys[1,2]. Much research on Mg-based metallic glass alloys has been carried out since Catka et.al.[3] in 1977 and has shown the possibility of manufacturing $Mg_{70}Zn_{30}$ metallic glass alloy by rapid solidification. However, these metallic glass alloys were produced as ribbon, wire or powder, and were therefore limited in their application.

As for bulk metallic glass materials, extensive research is also being actively carried out to design new alloy systems exhibiting good glass-forming ability and a low critical cooling rate. Among these, Mg-TM-RE (TM=Ni, Cu or Zr) alloy systems exhibit a large undercooled liquid region and high glass-forming ability with critical cooling rates below 10^{-2} K/s[4,5]. In 1991, Inoue and Masumoto[6] were successful in manufacturing bulk $Mg_{65}Cu_{25}Y_{10}$ amorphous alloy having 7 mm in diameter by a high pressure die casting process.

For metallic glasses to be accepted widely as industrial material, demands toward net shape technology, including rapid and simple production techniques, make liquid phase processes attractive for fabricating bulk metallic glass alloys. Considering these factors, squeeze-casting stands out as having high potential for manufacturing bulk metallic glass alloys with an

applied pressure serving to increase the cooling rate and net-shape formation. The squeeze casting process involves the solidification of molten metal under a high pressure within a closed die by utilizing a hydraulic press[7-10]. Solidification under high pressure leads to: i) an increased heat transfer coefficient between the molten metal and die surface; ii) undercooling below the equilibrium solidification temperature; and iii) a complete elimination of shrinkage and/or gas porosity[11-14].

The objective of this work is to examine the possibility of manufacturing new bulk Mg-based glass material with maximum thickness in an Mg-Cu-Y-Ag system by the squeeze casting process.

2. EXPERIMENTAL

$Mg_{65}Cu_{15}Y_{10}Ag_{10}$ alloy was prepared by arc melting Cu(99.9 %) and Y(99.9 %), and then alloyed with Mg(99.9 %) and Ag(99.9 %) using an induction furnace in an Ar atmosphere. Three different liquid processes were used to prepare metallic glass samples, injection casting, squeeze casting, and melt spinning, all of which were in a controlled atmosphere. For injection casting, appropriate amounts of the alloy were induction-remelted in quartz tubes, and then, using Ar pressure, injected into a water-cooled Cu mould, each of which had cavities of 2~7 mm diameters. For squeeze casting, approximately 50 g of the alloy was induction-remelted in a vacuum with a graphite crucible. After completely melting, the liquid alloy was bottom-filled into a water-cooled Cu mould having 10 mm diameter and 75 mm long mould cavity by utilizing a hydraulic press. After a complete filling of the mould with the liquid alloy, the pressure reached 100 MPa and was maintained for 120 s, until the liquid alloy completely solidified. For comparison, ribbon sample having a thickness of approximately 45 μm and a width of approximately 3mm was prepared by melt-spinning. An appropriate amount of the alloy was remelted in a quartz tube and then ejected onto a Cu wheel rotating at a surface velocity of about 36 m/s. The formation of amorphous structure in the as-cast samples was examined by X-ray diffractometry (Rigaku, CN-2301) and optical microscopy (Nikon Epiphot, Leika DMRM). X-ray samples were prepared as powder from the samples. An X-ray diffractometric spectrum was obtained by using monochromatic Cu Kα radiation from 20 to 80 ° with 4 °/min in scanning velocity and 0.02 ° in step-spacing. The glass transition temperature, T_g, and the crystallization temperature, T_x, were measured at a heating rate of 0.667 K/s using DSC (Rheometric scientific DSC) interfaced to a personal computer for data processing and analysis. In order to confirm the homogenity of the entire squeeze-cast sample, X-ray diffraction patterns and DSC traces of the sample were measured separately from the inner and outer regions of the top, middle, and bottom sections of the as-cast sample, respectively.

3. RESULTS

Figure 1 shows the X-ray diffraction patterns of the injection cast $Mg_{65}Cu_{15}Y_{10}Ag_{10}$ alloy with diameters from 2 to 7 mm and melt-spun $Mg_{65}Cu_{15}Y_{10}Ag_{10}$ ribbon for comparison. The melt-spun ribbon and injection-cast samples with diameters up to 6 mm show only a broad peak, indicating the formation of single amorphous phase. However, injection-cast sample 7 mm in diameter shows sharp crystalline peaks within the broad peak, indicating the coexistence of crystalline and amorphous phases.

Figure 2 shows X-ray diffraction patterns of the 10mm-diameter squeeze-cast $Mg_{65}Cu_{15}Y_{10}Ag_{10}$ alloy. The X-ray diffraction patterns were obtained from the inner and outer regions of the top, middle, and bottom sections of the as-cast sample, respectively. All of the X-ray diffraction patterns show only broad peaks, indicating the formation of homogeneous single amorphous phase throughout the sample.

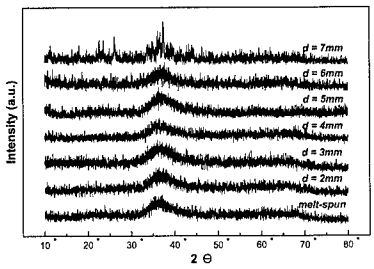

Fig.1. X-ray diffraction patterns of the injection cast $Mg_{65}Cu_{15}Y_{10}Ag_{10}$ alloy with diameters from 2 to 7mm, and the melt-spun $Mg_{65}Cu_{15}Y_{10}Ag_{10}$ ribbon.

Figure 3 shows the surface appearance of the squeeze-cast $Mg_{65}Cu_{15}Y_{10}Ag_{10}$ sample with a diameter of 10 mm and length of 75 mm. The surface of the sample shows good luster and closely mirrors the mould cavity surface having neither holes nor cavities.

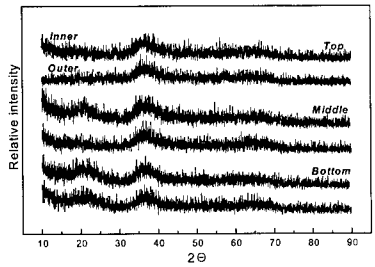

Fig.2. X-ray diffraction patterns of the 10mm-diameter squeeze-cast $Mg_{65}Cu_{15}Y_{10}Ag_{10}$ alloy, obtained from the inner and outer regions of the top, middle, and bottom sections of the as-cast sample, respectively.

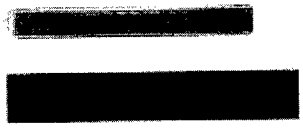

Fig.3. Surface appearance of the 10mm-diameter squeeze-cast $Mg_{65}Cu_{15}Y_{10}Ag_{10}$ alloy.

Figure 4 shows the DSC traces of the 6 mm-diameter injection-cast $Mg_{65}Cu_{15}Y_{10}Ag_{10}$ alloy and the melt-spun $Mg_{65}Cu_{15}Y_{10}Ag_{10}$ ribbon. Both the injection-cast sample and the melt-spun

ribbon show that the identical sequent transition of glass transition, supercooled liquid region, and crystallization occurring are independent of the process. The glass transition temperature T_g is 428 K and the crystallization temperatures T_{x1}, T_{x2}, T_{x3}, and T_{x4} are 469, 496, 539, and 581 K respectively. The integration heats of the first exotherms were 42.3 and 36.7 J/g for melt-spun ribbon and injection-cast 6-mm samples respectively. The total integration heats of the four exothermic peaks were 129.3 J/g and 120.8 J/g for melt-spun ribbon and 6-mm sample respectively. It is expected that the crystallization heat of slowly cooled specimen is lower than that of rapidly solidified specimen, because glass transition temperature decreases with decreasing cooling rate. Therefore, the similar value of T_g, the small difference in the total heat of crystallization, and the absence of distinct crystalline peaks in the XRD trace indicate that the bulk specimen is almost an amorphous structure. The injection-cast samples with diameters smaller than 6 mm also show nearly identical DSC curves, as shown in figure 4.

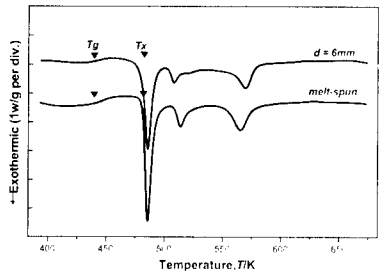

Fig.4. DSC traces of the 6mm-diameter injection-cast $Mg_{65}Cu_{15}Y_{10}Ag_{10}$ alloy and the melt-spun ribbon.

Figure 5 shows the DSC traces of the 10 mm-diameter squeeze-cast $Mg_{65}Cu_{15}Y_{10}Ag_{10}$. The DSC curves were obtained from the inner and outer regions of the top, middle, and bottom sections of the as-cast sample, respectively. As shown, each curve is nearly identical, independent of its position in the squeeze cast samples. The curves again show the sequent transition of glass transition temperature, supercooled liquid region, and crystallization, where

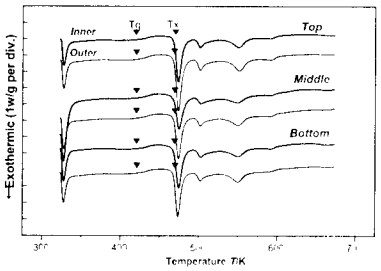

Fig.5. DSC traces of the 10mm-diameter squeeze-cast $Mg_{65}Cu_{15}Y_{10}Ag_{10}$ alloy obtained from the inner and outer regions of the top, middle, and bottom sections of the as-cast sample, respectively

glass transition temperature T_g, is 428 K and the crystallization temperatures T_{x1}, T_{x2}, T_{x3}, and T_{x4} are 469, 496, 539, and 581 K respectively. The temperature interval of supercooled liquid

region, defined by ΔT_x ($=T_x-T_g$), is approximately 41 K, and the reduced glass transition temperature, defined by T_{rg} ($=T_g/T_m$), is approximately 0.62. The integration heat of the first exothermic peak in the squeeze-cast specimen was about 41.5 J/g, which is slightly smaller than the 44.3 J/g result for the melt-spun ribbon shown in figure 4. The total crystallization heat for the squeeze-cast specimen was about 124 J/g, which is again similar to the 129.3 J/g in the melt-spun ribbon specimen. The similar value of crystallization heat between the squeeze-cast specimen and ribbon specimen and the absence of an appearance of distinct crystalline diffraction peaks in XRD trace both indicate that the squeeze-cast bulk specimen with d=10 mm is nearly a single amorphous structure.

4. DISCUSSION

In order to produce bulk metallic glass alloys three criteria must to be satisfied: the existence of (i) an multi-element system with deep eutectic; (ii) a large atomic-size difference between the components; and (iii) a large electronegativity difference between the components[15]. Among the Mg-based alloys, $Mg_{65}Cu_{25}Y_{10}$ is reported to have the largest glass forming ability[6]. Based on this report, the authors attempted to produce a better glass-forming ability Mg-based alloy by partially substituting Cu for Ag. The fourth additional element Ag has an atomic size difference 10 % larger than the other components, namely a 10, 11, and 16.8 % atomic size difference between Mg, Cu and Y respectively. Regarding the electronegativity difference between the components, Cu has –29 and –91 electronegativity differences between Mg and Y, whereas Ag has –47, +5 and –121 electronegativity differences between Mg, Cu, and Y respectively. Also, the partial substitution of Cu for Ag decreases the melting temperature of $Mg_{65}Cu_{25}Y_{10}$, and $Mg_{65}Cu_{15}Y_{10}Ag_{10}$ alloy has an approximately 45 K lower melting temperature than $Mg_{65}Cu_{25}Y_{10}$ does. Therefore, $Mg_{65}Cu_{15}Y_{10}Ag_{10}$ alloy is considered to possess a high glass-forming ability. As can be seen from figures 1 and 4, injection casting was successful in producing bulk metallic glass $Mg_{65}Cu_{15}Y_{10}Ag_{10}$ alloy up to 6 mm in diameter. However, injection-cast samples having a larger diameter than 6 mm show a mixed structure of amorphous and crystalline phases.

Squeeze-casting produced larger bulk metallic glass with $Mg_{65}Cu_{15}Y_{10}Ag_{10}$ alloy up to 10 mm in diameter, as shown in figures 2, 6, and 7. In squeeze casting, The application of high pressure during solidification causes intimate contact between the liquid alloy and the mould wall throughout the solidification period; this leads to the rapid heat extraction of the liquid alloy through the mould wall. Therefore, a higher cooling rate is achieved during solidification. Also, according to the Clausius-Clapeyron equation, the application of pressure causes the melting point of most alloys to increase:[12,16,17]

$$\frac{\Delta T}{\Delta P} = \frac{T_f (V_l - V_s)}{\Delta H_f}$$

where, T_f is the equilibrium freezing temperature, V_l and V_s are the specific volumes of the liquid and solid respectively, and ΔH_f is the latent heat of fusion. Thus, the equilibrium freezing temperature should increase with increasing pressure, leading to an undercooling of the liquid alloy. However, further study is required to calculate how much undercooling is achieved during the pressurization of the liquid $Mg_{65}Cu_{15}Y_{10}Ag_{10}$ alloy.

An additional advantage of squeeze casting arises from the capability of manufacturing net-

shape casting, which closely mirrors the mould surface and has dense, pore-free castings of forging quality, as shown in figure 3. Therefore, considering the rapid heat extraction and undercooling of the liquid alloy by pressurization during solidification, squeeze casting seems to have a high potential for manufacturing net-shape bulk metallic glass components.

5. CONCLUSIONS

$Mg_{65}Cu_{15}Y_{10}Ag_{10}$ alloy has improved glass-forming ability, when Cu is partially substituted for Ag in $Mg_{65}Cu_{25}Y_{10}$ alloy. The addition of Ag significantly decreases the melting temperature and also satisfies conditions of a multi-element system with deep eutectic, large atomic-size difference between its components, and a large electronegativity difference between the components for good glass-forming ability. Therefore, even injection casting can produce bulk metallic glass of $Mg_{65}Cu_{15}Y_{10}Ag_{10}$ alloy having a diameter up to 6-mm. Squeeze casting of the alloy further increased the diameter of bulk metallic glass $Mg_{65}Cu_{15}Y_{10}Ag_{10}$ alloy, since the pressurization of the liquid alloy during solidification leads to a rapid heat extraction and undercooling of the liquid alloy. Also, squeeze casting has the potential for manufacturing sound castings of forging quality, together with net-shape capabilities. Squeeze-casting enabled us to produce bulk metallic glass $Mg_{65}Cu_{15}Y_{10}Ag_{10}$ alloy of 10mm in diameter.

ACKNOWLEDGEMENTS

This work was supported by the Creative Research Initiatives of the Korean Ministry of Science and Technology.

REFERENCES

1. A.Inoue, T.Zhang and T.Matsumoto: Mater. Trans., JIM, 31 (1990), 177-183
2. A.Peker and W.L.Johnson: Appl. Phys. Lett., 63 (1993), 2342-2344
3. A.Catka, M.Madhava, D.E.Polk, B.C.Giessen, H.Matyja and J.B.Vander Sande: Scripta Metall., 11 (1977) 65-72
4. S.G.Kim, A.Inoue and T.Masumoto: Mater. Trans., JIM, 31 (1990), 929-934
5. A.Inoue, T.Zhang, S.G.Kim and T.Masumoto: Mater. Trans., JIM, 32 (1991), 609-616
6. A.Inoue, T.Nakamura, and T.Masumoto: Mater. Trans., JIM, 33 (1992), 937-945
7. R.F.Lynch, R.P.Olley and P.C.J.Gallagher: Trans., AFS, 83 (1975), 569-576
8. R.F.Lynch, R.P.Olley and P.C.J.Gallagher: Trans., AFS, 83 (1975) 561-568
9. J.L.Dorcic and S.K.Verma: Metals Handbook 9th ed., ASM Int., 323-327
10. F.Weinburg: The Metals Society, Solidification Technology in the Foundry and Cast House (1980), 131-136
11. Ph.Jarry, C.Pluchon and G.Regazzoni: Proceeding of the International Conference on Light Metals, Amsterdam, 20-22 June (1990), 643-650
12. G.A.Chadwick and T.M.Yue: Metals and Materials, Jan., (1989), 6-12
13. J.R.Franklin and A.A.Das: Brit. Foundryman, 77 (1984), 150-158
14. G.S.Reddy and J.A.Sekhar: Acta Metall., 37 (1989), 1509-1519
15. A.Inoue: Acta Mater., 48 (2000), 279-306
16. Y.Nishida and H.Matsubara: Z.Metallkde, Bd.71, H.3 (1980), 189-194
17. S.Chaterjee and A.A.Das: Brit. Foundaryman, 66 (1973), 18-24

FATIGUE IN WROUGHT AND CAST MAGNESIUM ALLOYS

Lothar Wagner, Jens Wendt and Matthias Hilpert

Chair of Physical Metallurgy and Materials Technology
Technical University of Brandenburg at Cottbus, 03013 Cottbus, Germany

ABSTRACT

The fatigue behavior of the extruded magnesium alloys AZ31 and AZ80 as well as cast magnesium alloys AM50 and AZ91 was investigated. Owing to marked crystallographic textures in the extrusions, both alloys AZ31 and AZ80 showed pronounced directional mechanical properties in tensile and cyclic loading with strength values in extrusion direction being significantly superior to those perpendicular to the extrusion direction. As a result of weak crystallographic textures, no directionality in mechanical properties was found in the high-pressure die cast alloys. However, cast defects in these alloys lead to fatigue behavior being clearly inferior to those of the extruded alloys. To study potential improvements in fatigue behavior of the various alloys, mechanical surface treatments, i.e., shot peening and roller-burnishing were performed. Both cast and wrought alloys showed marked improvements in fatigue strength, particularly after roller-burnishing.

1. INTRODUCTION

The weight reduction of automobiles is one of the most effective ways in improving fuel consumption since the resistances of a vehicle to rolling, climbing and acceleration are directly dependent on vehicle mass. Therefore, the application of magnesium alloys which density is only roughly 25 % that of steel and 66 % that of aluminum is expected to substantially increase in this decade. While for a limited number of vehicle components cast magnesium alloys are already in production such as materials for transmission gearbox housings, seat frames and steering wheels, both cast and wrought magnesium alloys are potential candidates for many further applications, e.g., as materials for body and suspension components where they can largely substitute steels and even aluminum alloys [1,2].
For these automotive applications, the fatigue performance of both cast and wrought magnesium alloys is of particular importance [3–6]. The aim of this investigation was to outline potential improvements of the fatigue performance of wrought and cast magnesium alloys by mechanical surface treatments.

2. EXPERIMENTAL

The wrought magnesium alloys AZ31 (nominal composition in weight percent: 3Al, 0.8Zn, 0.2Mn, balance: Mg) and AZ80 (8Al, 0.5Zn, 0.2Mn, balance: Mg) were received as extrusions from Otto Fuchs Metallwerke, Meinerzhagen, Germany. The rectangular bars had cross sections of 100 x 20 mm (extrusion ratio, ER: 13) and 110 x 70 mm (ER: 9) for AZ31

and AZ80, respectively. Specimens were machined with the load axis parallel to the extrusion (L) direction as well as in the long transverse (T) direction (Fig. 1a).
The cast magnesium alloys AM50 (5Al, 0.5Mn, balance: Mg) and AZ91 (9Al, 1Zn, 0.2Mn, balance: Mg) were received from Audi AG, Ingolstadt, Germany as high-pressure test bar die castings (Fig. 1b). From these castings, specimens were taken from the round bars with a diameter of 15 mm.
Crystallographic textures were determined by X-ray diffraction using Ni-filtered Cu-K_α radiation and are shown as (0002) pole figures. Tensile tests were performed on threaded cylindrical specimens having gage lengths of 20 mm. The initial strain rate was $8.3 \times 10^{-4} s^{-1}$. For fatigue testing, hourglass shaped round specimens (5 mm gage diameter) were machined. After machining, about 200 µm was removed from the surface of the specimens by electrolytical polishing (EP) to ensure that any machining effect that could mask the results was absent.
Shot peening (SP) was performed with an injector type machine using spherically conditioned cut wire SCCW14 (0.36 mm average shot size). Roller-burnishing (RB) was performed using a conventional lathe and a one-roll hydraulic system. The diameter of the hard metal roll was 6 mm. After mechanical surface treating, the change in surface layer properties was determined by profilometry, microhardness measurements and X-ray measurements and was evaluated by surface roughness profiles and depth profiles of microhardness, half width breadths, and residual macrostresses.
Fatigue tests were performed in rotating beam loading (R = -1) at frequencies of about 60 Hz in ambient air.

3. RESULTS AND DISCUSSION

The microstructures of the various magnesium alloys are shown in Fig. 2. The average α-grain size is roughly 10 µm in AZ31 (Fig. 2a) and about 30 µm in AZ80 (Fig. 2b). For AZ80, a discontinuous precipitation of $Mg_{17}Al_{12}$ is clearly seen by optical microscopy (Fig. 2b). The cast alloys are characterized by massive $Mg_{17}Al_{12}$ compound at the boundaries of small, cored grains (Fig. 2c, d). Presumably, the absence of precipitated discontinuous $Mg_{17}Al_{12}$ is the result of the rapid cooling of the high-pressure die casting process (compare Fig. 2c, d with Fig. 2b).
Typical pole figures of the wrought and cast alloys are illustrated in Fig. 3. Most of the hexagonal magnesium grains in the as-fabricated extrusion of AZ80 (Fig. 3a) are oriented with the basal planes parallel to the extrusion direction and normal to the surface of the extrusion. No significant difference was found for the pole figure of AZ31. As expected, the pole figure of the cast alloy AZ91 (Fig. 3b) is quite different from that of the extruded alloy AZ80. For AZ91 (Fig. 3b), the basal planes are almost randomly oriented. No significant differences were found between the pole figures of the cast alloys AM50 and AZ91.
For both extruded alloys AZ31 and AZ80, the yield stresses $\sigma_{0.2}$ perpendicular to the L-direction are only 60 % of the corresponding values in L-direction (Table 1). Plastic deformation in T-direction occurs more readily than in L-direction since basal planes experience large shear stresses by loading in T-direction, while hardly any shear stresses act on basal planes for loading in L-direction (Fig. 3a). As expected, the values of yield stress, ultimate tensile strength and ductility of the cast alloys are significantly lower than those of the extruded alloys (Table 1). However, due to the random distribution of the basal planes in

the cast alloys (Fig. 3b), no directionality in properties is likely as opposed to the extruded alloys.

Table 1 Tensile properties of the various magnesium alloys

Material	Testing direction	$\sigma_{0.2}$ (MPa)	UTS (MPa)	EL (%)	RA (%)
AZ31	L	210	280	15	26
	T	140	255	11	12
AZ80	L	245	340	12	14
	T	140	200	3	6
AM50		95	165	3	7
AZ91		125	170	2	3.5

Examples of typical fracture surfaces of the various magnesium alloys are illustrated in Fig. 4. By loading in L-direction, the tensile fracture surface of AZ80 appears fairly homogenous (Fig. 4a) while the fracture surface is rough and terraced by loading in T-direction (Fig. 4b). The latter is caused by tension perpendicular to the second phase stringers in the extrusion which also leads to lower ductility values (Table 1). Similar differences in fracture appearance between L- and T- directions were observed in AZ31. The tensile fracture surfaces of the cast alloys are shown in Figs. 4c-4f. At higher magnification, some degree of porosity was observed in both alloys AM50 (Fig. 4c) and AZ91 (Fig. 4f). As will be shown below, these cast defects are potential sites for fatigue crack nucleation during cyclic loading.

The S-N curves of the various alloys in the electropolished reference conditions are given in Fig. 5. As expected, the 10^7 cycles fatigue strength of both extruded alloys AZ31 (Fig. 5a) and AZ80 (Fig. 5b) in L-direction are markedly higher than in T-direction. The scatter in fatigue life of cast alloys AM50 (Fig. 5c) and AZ91 (Fig. 5d) is clearly much higher than in the extruded alloys AZ31 (Fig. 5a) and AZ80 (Fig. 5b).

Typical fatigue crack nucleation sites in the various alloys are shown in Fig. 6. Fatigue cracks in the extruded alloys primarily nucleated within the α–grains along planar slip bands. An example is shown for AZ80 in Fig. 6a. On the contrary, fatigue cracks in the cast alloys often nucleated at cast defects as illustrated for AM50 in Fig. 6b.

In order to improve the fatigue performance of the various alloys, shot peening (Fig. 7a) and roller-burnishing (Fig. 7b) were utilized.

Typical changes in surface layer properties due to these treatments are shown in Fig. 8. Compared to the electropolished reference (EP), shot peening (SP) drastically increases roughness while roller-burnishing (RB) leads to roughness values almost as low as measured for the reference (Fig. 8a).

The depth of plastic deformation as induced by roller-burnishing is much greater than for shot peening while the microhardness at and very close to the surface is somewhat greater in case of shot peening (Fig. 8b). The profiles of the half value breadth of X-ray interference lines as a measure of the total dislocation density exhibit a similar tendency as microhardness, i.e., a gradual decrease from a maximum at the surface to the inner material (Fig. 8c). Compressive residual stresses were measured after mechanical surface treatments with a marked maximum below the surface (Fig. 8d). Again, the penetration depth of residual compressive stresses after roller-burnishing is much greater than after shot peening. Comparing the change in surface layer properties due to mechanical surface treatments among the various alloys, the following can be stated. Roughness values induced by the various treatments are only slightly different among the various alloys, while differences in the magnitude of the residual stresses

are residual stresses was observed with maximum values for the highest strength alloy AZ80 and lowest values for AM50 [10].
The effects of the process parameters in shot peening and roller-burnishing on fatigue life of AZ80 is given in Fig. 9. The fatigue life at a stress amplitude of 175 MPa is shown in Figure 9a as a function of Almen intensity. Starting with the electropolished condition, the fatigue life first dramatically increases by roughly two orders of magnitude irrespective of the particular peening medium and then drops drastically after peening with higher intensities. This strong overpeening effect was also found at stress amplitudes of σ_a = 225 and 200 MPa. Unlike the results after shot peening, the fatigue life of roller-burnished specimens steadily increases with rolling force (Fig. 9b). Since rolling forces higher than 300 N were frequently found to result in surface damage, all further tests were performed with rolling forces of 285 N.
The S-N curves in air of the various magnesium alloys illustrating the effect of mechanical surface treatments on the fatigue performance are shown in Figure 10. Compared to the electropolished reference EP, the 10^7 cycles fatigue strength of AZ31 (Fig. 10a) is increased from 60 MPa to 100 MPa (SP) and 125 MPa (RB), while for AZ80 (Fig. 10b) the corresponding improvement is from 100 MPa (EP) to 140 MPa (SP) and 175 MPa (RB). Although there is more scatter in fatigue life of the cast alloys (compare Fig. 10c, d with Fig. 10a, b) which presumably is caused by pores and other cast defects, the trend again is clear. Compared to the electropolished reference (EP), the 10^7 cycles fatigue strength of AM50 (Fig. 10c) is increased from roughly 50 MPa (EP) to about 60 MPa (SP) and 70 MPa (RB), while for AZ91 (Fig. 10d) the corresponding improvement is from roughly 60 MPa (EP) to 80 MPa (SP) and 85 MPa (RB).
The presented results on the effect of mechanical surface treatments on fatigue in magnesium alloys can be summarized as follows: The change in fatigue performance of magnesium alloys due to mechanical surface treatments depends on the process-induced surface topography, microhardness and residual stress profiles in near-surface regions. The process-induced residual compressive stresses can overcompensate the detrimental effect of surface roughness since the fatigue life of shot peened specimens is higher than that of the electropolished reference. Obviously, fatigue life extension by retardation of microcrack growth owing to the residual compressive stress field is greater than the reduction in fatigue life caused by earlier crack nucleation as a consequence of shot peening-induced higher surface roughness. Best performance was observed for both wrought and cast alloys after roller-burnishing which combines high residual compressive stresses and high degrees of work-hardening in sufficient depths together with low surface roughness.

4. ACKNOWLEDGEMENTS

The authors would like to thank Otto Fuchs Metallwerke, Meinerzhagen, Germany for providing the magnesium extrusions and Audi AG, Ingolstadt, Germany for providing the magnesium castings. Financial support from OSK Kiefer, Oppurg, Germany is gratefully acknowledged.

5. REFERENCES

1. T. K. Aune and H. Westengen, Magnesium Alloys and their Applications (B. L. Mordike, and F. Hehmann, eds.) DGM (1992), 221.
2. H. Friedrich and S. Schuhmann, Magnesium 2000 (E Aghion and D. Eliezer, eds.) MRI (2000), 9.
3. G. L. Song and A. Atrens, Advanced Engineering Materials, Wiley-VCH (1999), 11.
4. M. O. Speidel, M. J. Blackburn, T. R. Weck and J. A. Feeney, in Corrosion Fatigue: Chem., Mech. and Microstructure (ed. O. Devereux), NACE Houston, TX (1986), 331.
5. S. Sannes, H. Westengen, Magnesium Alloys and their Applications (B. L. Mordike and K. U. Kainer, eds.), MAT INFO (1998), 223
6. R. I. Stephens, C. D. Schrader and K. B. Lelase, J. Eng. Mater. Technol. (1995), 293.
7. V. V. Ogarevic, and R. I. Stephens, Ann. Rev., Mater. Sci. (1990), 141.
8. M. Hilpert and L. Wagner, Journal of Materials Engineering and Performance, Vol. 9, No. 4 (2000), 402.
9. M. Hilpert and L. Wagner, Magnesium Alloys and their Applications (B. L. Mordike and K. U. Kainer, eds.), MAT INFO (1998), 271.
10. M. Hilpert and L. Wagner, Surface Treatment IV (C. A. Brebbia and J. M. Kenny, eds.) WIT Press (1999), 331.
11. M. Hilpert, Dr.-Ing. thesis, Techn. Univ. of Brandenburg at Cottbus, Germany (2001).
12. T. Dörr, M. Hilpert, P. Beckmerhagen, A. Kiefer and L. Wagner, Shot Peening, Present & Future (A. Nakonieczny, ed.) IMP (1999), 153.
13. M. Hilpert and L. Wagner, Magnesium Alloys and Their Applications, (K. U. Kainer, ed.), WILEY-VCH-Verlag GmbH, Weinheim (2000), 525.
14. M. Hilpert and L. Wagner, Magnesium Alloys and Their Applications, (K. U. Kainer, ed.), WILEY-VCH-Verlag GmbH, Weinheim (2000), 463.

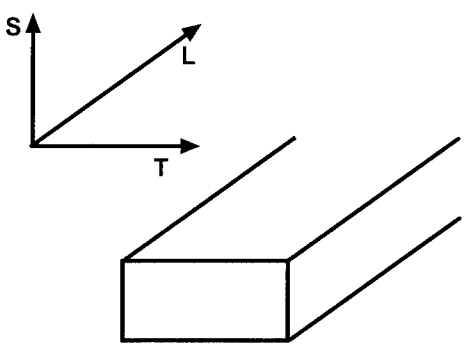

a) Wrought alloys: Extruded rectangular bar stocks

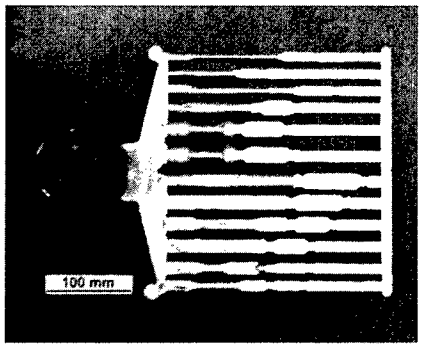

b) Cast alloys: High pressure test bar die castings

Fig. 1: As-received shapes of the various magnesium alloys

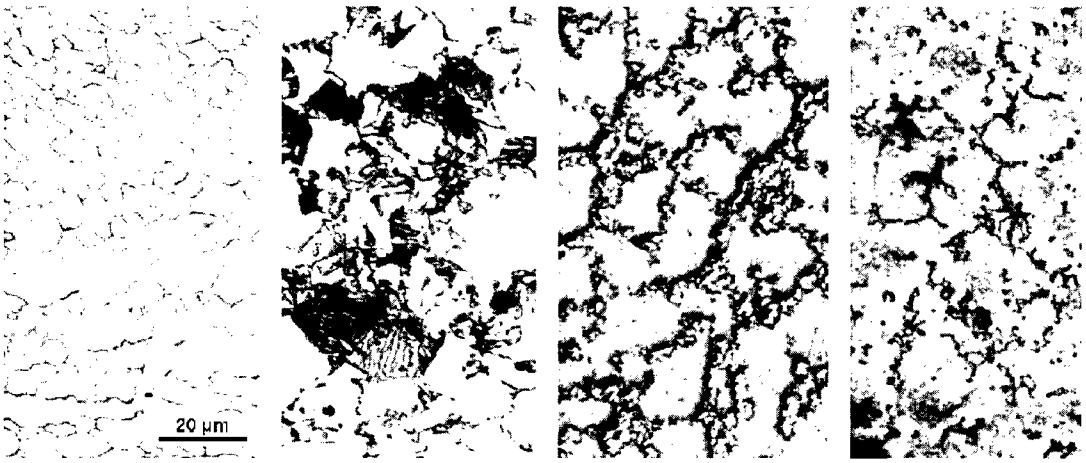

a) AZ31 b) AZ80 c) AM50 d) AZ91

Fig. 2: Microstructures of the various magnesium alloys

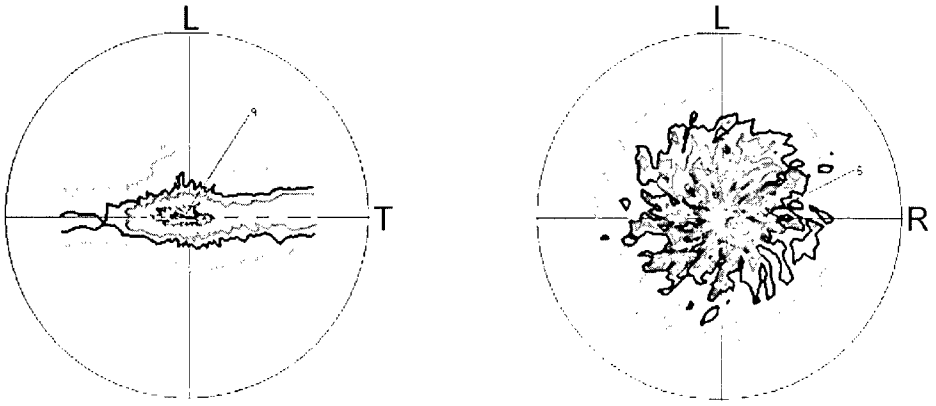

a) AZ80 b) AZ91

Fig. 3: (0002) pole figures of the various magnesium alloys

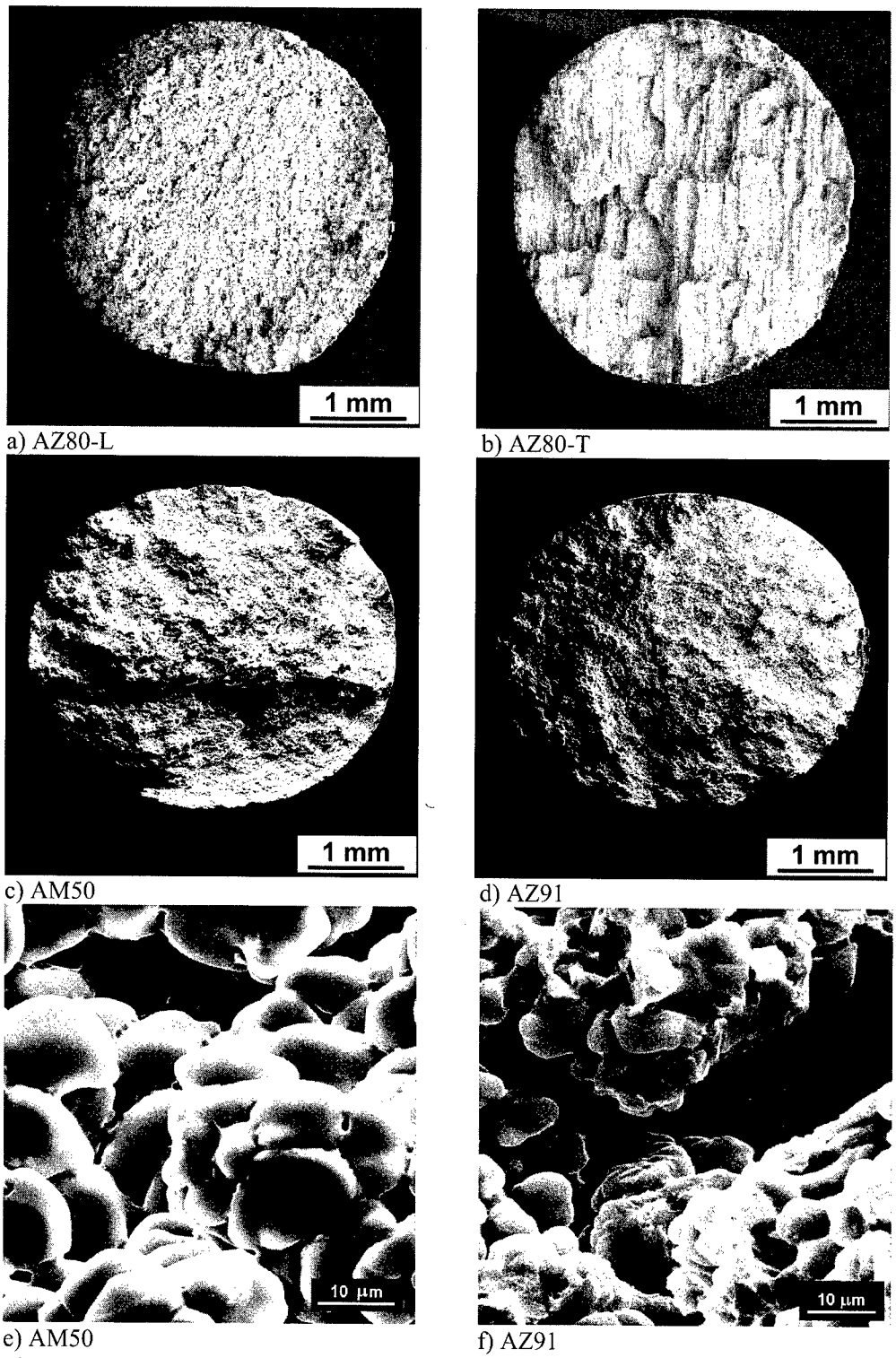

a) AZ80-L b) AZ80-T

c) AM50 d) AZ91

e) AM50 f) AZ91

Fig. 4: Fracture surfaces (SEM) of the various magnesium alloys

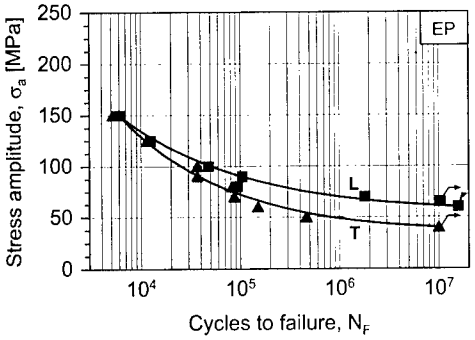

a) AZ31

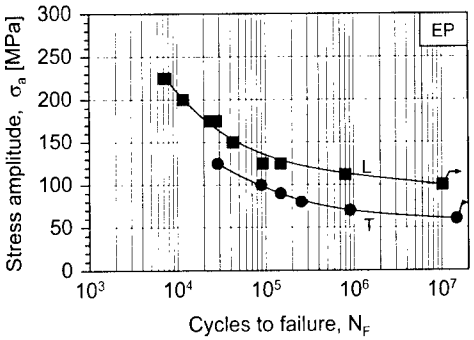

b) AZ80

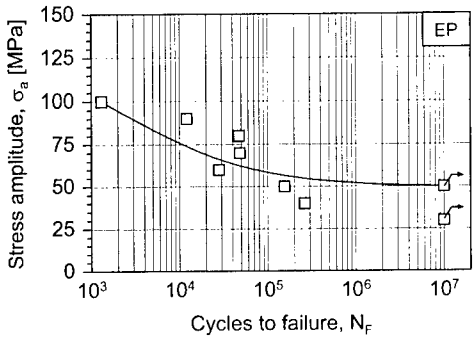

c) AM50

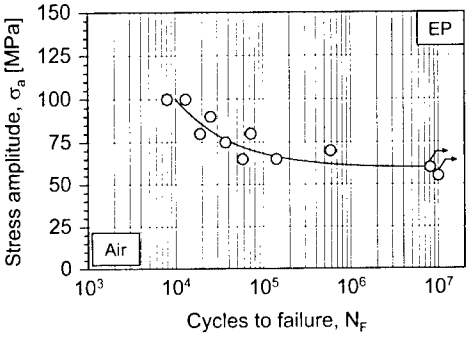

d) AZ91

Fig. 5: S-N curves in rotating beam loading (R = -1)

a) wrought material: AZ80

b) cast material: AZ91

Fig. 6: Fatigue crack nucleation sites

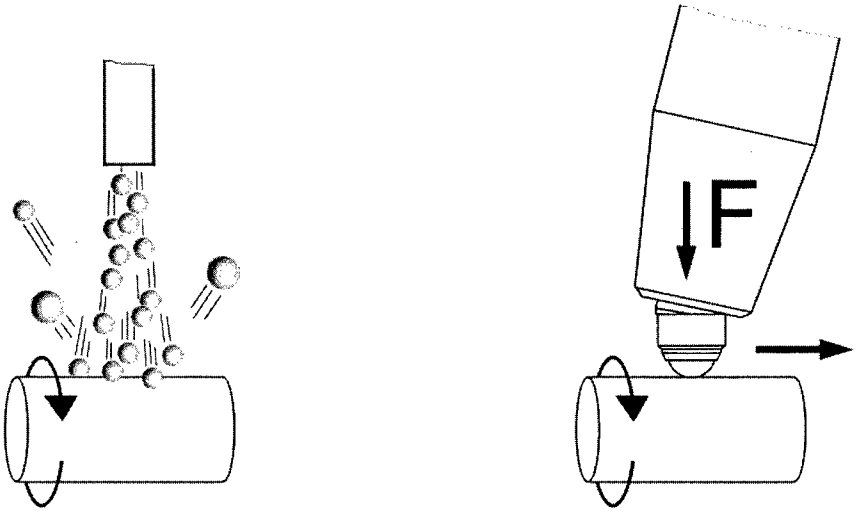

a) Shot peening b) Roller-burnishing

Fig. 7: Mechanical surface treatments (schematic)

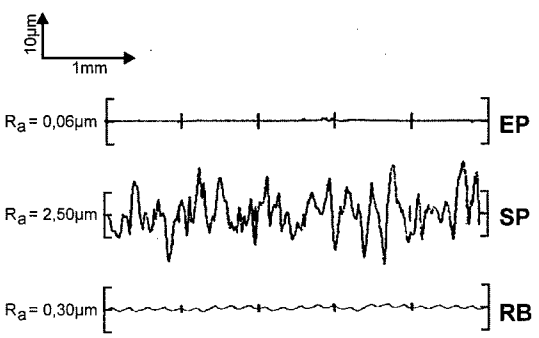

a) Surface roughness (AZ80)

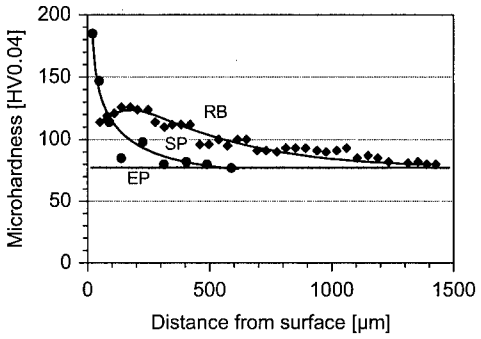

b) Microhardness profiles (AZ80)

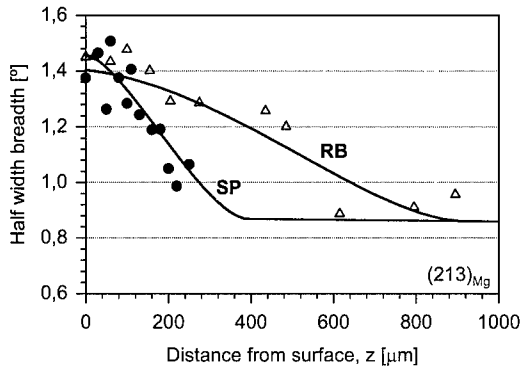

c) Half width breadth profiles (AZ80)

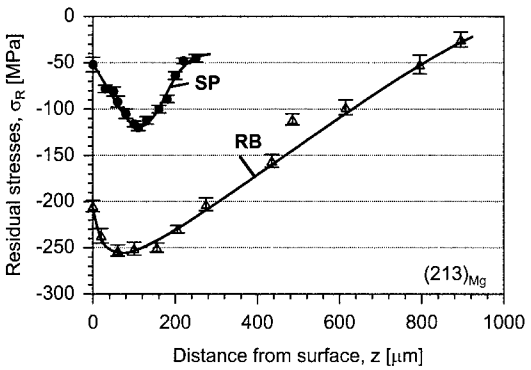

d) Residual stress profiles (AZ80)

Fig. 8: Surface layer properties after various treatments for AZ80

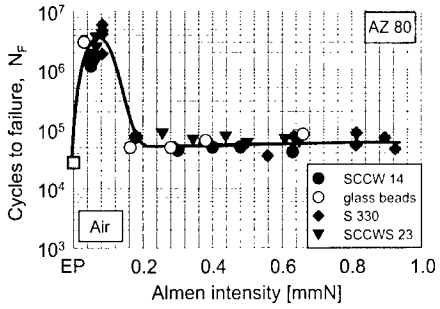

a) Effect of Almen intensity (shot peening), σ_a = 175 MPa

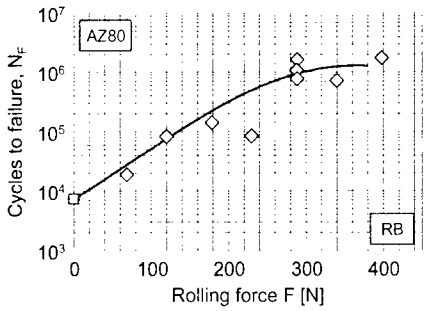

b) Effect of rolling force (roller-burnishing), σ_a = 225 MPa

Fig. 9: Fatigue life vs. process parameters in AZ80 (L-direction)

a) Shot peened (0.05 mmN)

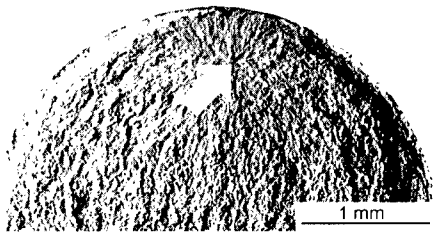

b) Roller-burnished (285N)

Fig. 10: Fatigue crack nucleation sites after mechanical surface treatments (SEM)

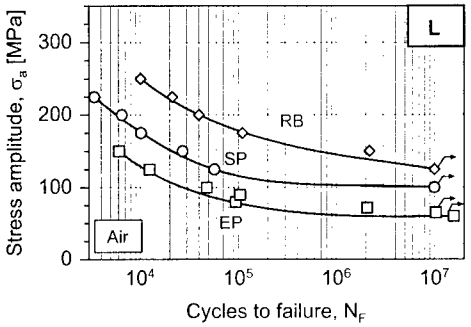

a) AZ31

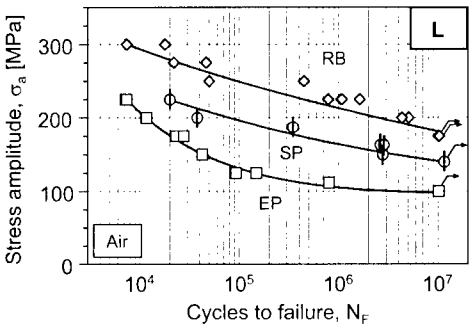

b) AZ80

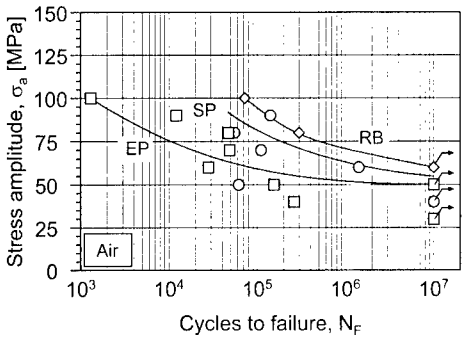

c) AM50

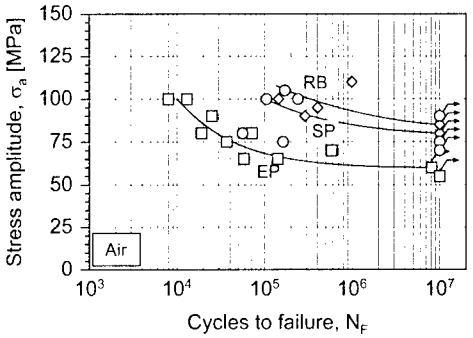

d) AZ91

Fig. 11: S-N curves in rotating beam loading (R = -1)

Effect of Test Environment on Fatigue Crack Propagation Behavior of AZ91D Magnesium Alloy

Hwa Chul Jung and Kwang Seon Shin*

School of Materials Science and Engineering
*Center for Advanced Aerospace Materials
Seoul National University, Seoul 151-742, Korea

ABSTRACT

The effect of test environment on fatigue crack propagation (FCP) behavior of the AZ91D magnesium alloy was investigated in the present study. The fatigue crack propagation tests were carried out under the constant load amplitude in laboratory air and high vacuum at ambient temperature. In order to determine the effect of crack closure on the FCP rates, the crack closure levels were measured using the compliance method. The AZ91D alloy showed the much higher FCP rates in air than in vacuum, particularly in the low and medium ΔK regime. The crack closure measurements showed that the overall closure levels were slightly greater in air than in vacuum. The da/dN vs. ΔK_{eff} curves showed that the FCP rates were much faster in air than in vacuum, possibly caused by the moisture in the laboratory air.

1. INTRODUCTION

Magnesium has the lowest density among the commercially available structural metals and the excellent specific strength and stiffness. Magnesium alloys also have exceptional dimensional stability, high damping capacity and good fatigue resistance. However, magnesium alloys are very reactive with the surrounding environment. In recent years, the demand and usage of magnesium alloys have increased significantly for structural applications, particularly in the automotive industry. For structural applications, the resistance to fatigue crack propagation (FCP) is one of the important design criteria, since the lifetime and the safety of the structure are often determined by the fatigue properties of the materials. Unfortunately, however, there have been very limited studies on FCP behavior of magnesium alloys [1-3]. In the present study, therefore, FCP behavior of AZ91D magnesium alloy was investigated in laboratory air and vacuum with particular attention paid

to the near-threshold region, where FCP behavior is significantly affected by the test environment in Al-Li alloys [4-6]. In the present study, the effect of test environment on FCP behavior was examined in conjunction with crack closure phenomena.

2. EXPERIMENTAL PROCEDURES

The AZ91D magnesium ingots with 180 mm diameter were cast and subsequently extruded to have a cross-section of 80 mm × 12.5 mm. The extruded plates were homogenized and then solution heat treated at 410℃ for 20 hours. The plates were subsequently aged at 160℃ for 60 hours in order to achieve the peak strength. Figure 1 shows the microstructure of the extruded AZ91D Mg alloy, exhibiting highly unrecrystallized grains with pancake shape, elongated along the rolling direction. Cylindrical tensile specimens were prepared from the center portion of the plate and the tensile tests were carried out at a strain rate of 2×10^{-4}/s. The L-T oriented compact tension specimens were also prepared from the plate. A Chevron notch was used in all test specimens.

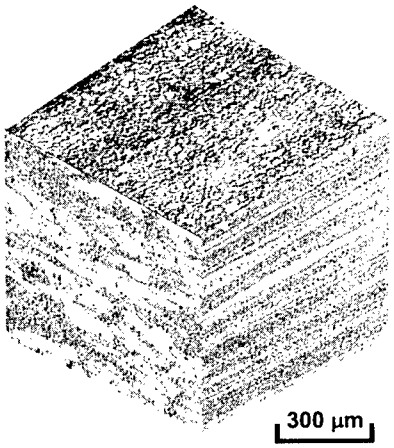

Fig. 1. Microstructure of the extruded AZ91D Mg alloy.

The specimens were fatigue precracked at a constant ΔK to an a/W of 0.25. The FCP experiments were conducted on a servohydraulic machine in laboratory air and high vacuum at ambient temperature. The vacuum system, which is equipped in the dynamic testing machine, consists of rotary pump and turbo-molecular pump. The degree of vacuum of the test chamber was checked by an ion gage and maintained below 10^{-3} Pa. The FCP experiments were conducted principally under the constant-load amplitude with a sinusoidal frequency of 20Hz at a fixed R ratio of 0.1. The FCP rates in the near-threshold regime were obtained by the load-shedding technique in accordance with ASTM E647. Crack closure

loads were determined from a series of load *vs* displacement plots, which were obtained at a reduced frequency of 0.1 Hz, using a global compliance technique with a crack opening displacement gage attached on the face of the crack. The load-displacement data pairs were analyzed to identify the crack-closure load (P_{cl}) corresponding to the first deviation in slope, operationally defined at an offset of 2 pct form the linear-compliance response [7]. The fracture surfaces of the fatigued specimen were examined with a scanning electron microscope (SEM).

3. RESULTS and DISCUSSION

The typical tensile properties of the AZ91D magnesium alloy in the as-extruded condition and after T6 heat treatment were presented in Table 1. The peak-aged alloy showed significantly improved tensile properties compared with the as-extruded counterpart.

Table 1. The mechanical properties of AZ91D magnesium alloy.

	Y. S. (MPa)	U. T. S. (MPa)	Elong. (%)
As-extruded	208.1	314.8	16.4
T6 condition	270.4	392.2	9.4

The FCP rates, da/dN, of the extruded AZ91D Mg alloy obtained in laboratory air and high vacuum are plotted against the stress intensity factor range, Δ K, in Fig. 2. As shown in the figure, in the high Δ K regime, where Δ K is greater than 7MPa$\sqrt{}$ m, the FCP rates obtained from two different test environments appear to show similar values. However, as Δ K decreases and approaches the near-threshold region, the differences between the FCP rates obtained from two different test environments increase significantly. For example, the FCP rates in air were found to be approximately 100 times greater than those in vacuum at a Δ K of 2.2MPa$\sqrt{}$ m, indicating that the significant effect of test environment on FCP behavior in the near-threshold region. The ΔK_{th} values, which were defined as the Δ K at da/dN below 10^{-10} m/cycle in the present study, were found to be 1.1MPa$\sqrt{}$ m and 2.2MPa$\sqrt{}$ m in air and vacuum, respectively. These results indicated that FCP behavior of the AZ91D magnesium alloy was strongly dependent on the test environment. However, the effect of crack closure and/or the possibility of the interaction between the crack closure and the test environment could not be completely excluded. It has been reported in a number of literatures that the crack closure plays an important role in FCP behavior in the near-threshold region. The interaction between the crack closure and the test environment could also

significantly affect FCP behavior in the near-threshold region, as reported for Al-Li alloys [4-6]. The crack closure levels, therefore, were carefully measured in the present study using the compliance technique.

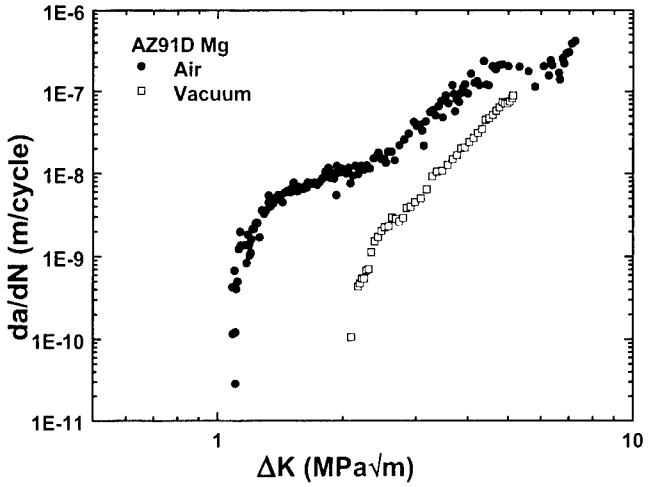

Fig. 2. Fatigue crack propagation rates as a function of Δ K.

The crack closure stress intensity factors were determined during the FCP tests in air and vacuum. The measured crack closure stress intensity factors normalized by the maximum stress intensity factors, K_{cl}/K_{max}, are plotted against Δ K in Fig. 3.

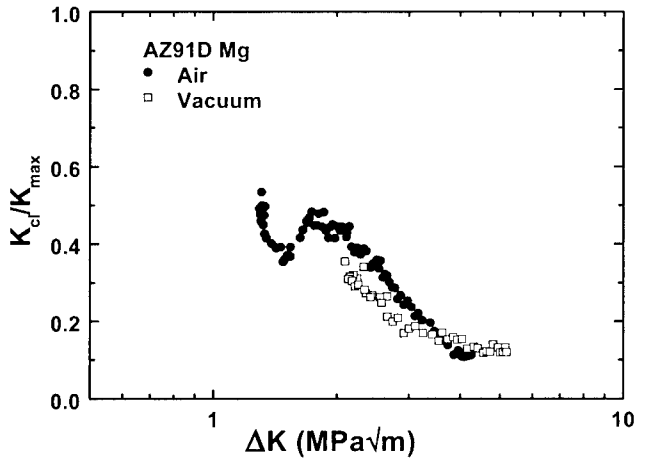

Fig. 3. K_{cl}/K_{max} as a function of Δ K.

As shown in the figure, the normalized crack closure levels generally decreased with increasing ΔK in both test environments. The overall closure levels were found to be slightly higher in air than in vacuum, except at high ΔK above 4MPa$\sqrt{m}$, where the closure levels obtained from two test environments showed the similar values. By combining the results obtained in Figs. 2 and 3, the FCP rates could be plotted against the ΔK_{eff} as shown in Fig. 4, excluding the effect of the crack closure on the FCP rates. From the comparison of the results obtained in air and vacuum, it could be clearly concluded that the FCP rates in air are much faster than those in vacuum in the entire ΔK range examined in the present study. These results indicated that the FCP rates of the AZ91D magnesium alloy could be significantly influenced by even laboratory air, which was generally considered as relatively benign environment for other materials. It was tentatively concluded that the moisture in the laboratory air was largely responsible for the significant difference between the FCP rates obtained in air and vacuum shown in Fig. 4. More detailed study, however, has to be carried out on the effect of various gases including oxygen on the FCP behavior of the magnesium alloys in order to clearly understand the effect of test environment since magnesium alloys are generally very reactive with the surrounding environment.

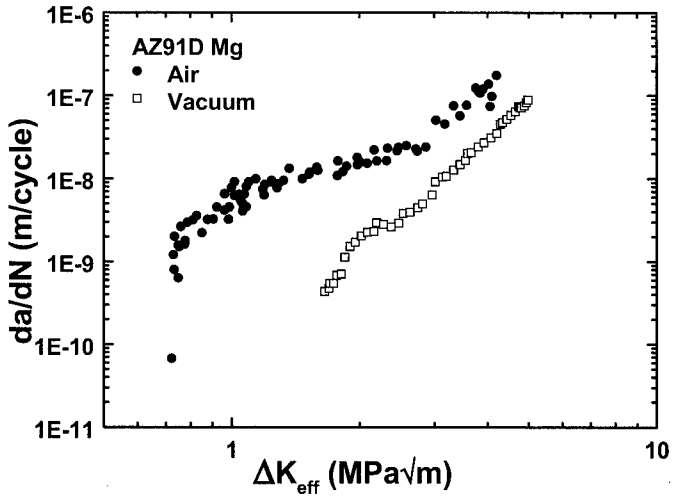

Fig. 4. Fatigue crack propagation rates as a function of ΔK_{eff}.

Figure 5 shows the SEM micrographs of the fatigued fractured specimens obtained in (a) air and (b) vacuum in the near-threshold region. The crack propagation direction was from left to right of the micrographs. The fracture morphology did not show significant difference between the specimens tested in air and vacuum. However, the tendency for intergranular fracture appeared to be greater in the specimen tested in air than that in vacuum.

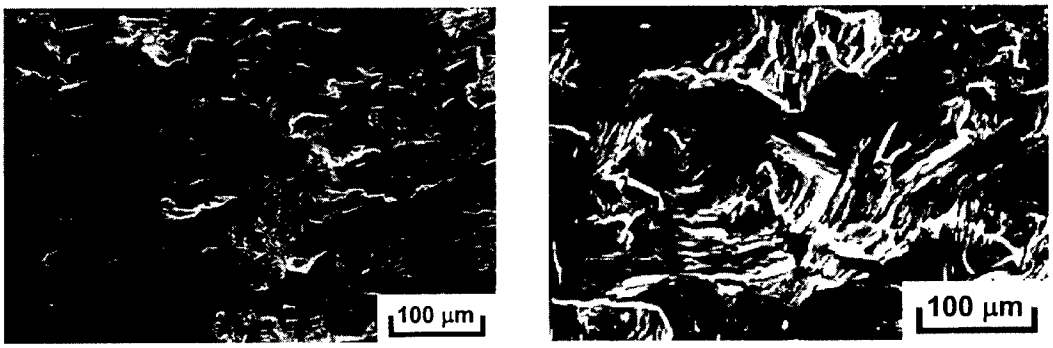

(a) (b)

Fig. 5. SEM fractographs of the fatigue tested AZ91D Mg alloy obtained in the near-threshold region; (a) in air and (b) in vacuum.

4. CONCLUSION

The fatigue crack propagation (FCP) behavior of the AZ91D magnesium alloy was investigated in laboratory air and vauum the present study. In order to determine the effect of crack closure on the FCP rates, the crack closure levels were measured using the compliance method. The AZ91D alloy showed the much higher FCP rates in air than in vacuum, particularly in the low and medium Δ K regime. The crack closure measurements showed that the overall closure levels were slightly greater in air than in vacuum. The da/dN vs. ΔK_{eff} curves showed that the FCP rates were much faster in air than in vacuum, possibly caused by the moisture in the laboratory air.

REFERENCES

1. D. L. Goodenberger and R. I. Stephens, Jour. of Eng. Mater. and Techno., Vol.115(1993), pp. 391-397.
2. Y. Kobayashi, T. Shibusawa and K. Ishikawa, Mater. Sci. and Eng., A234~236(1997), pp. 220-222.
3. T. Shibusawa, Y. Kobayashi and K. Ishikawa, J. Japan Inst. Metals, Vol.61(1997), pp. 1031-1036.
4. C. S. Lee, S. S. Kim and K. S. Shin, Metals and Materials, 3(1) (1997), pp. 51-59.
5. S. S. Kim and K. S. Shin, Metall. and Materials Trans., Vol.29A(10) (1998), pp. 2583-2590.
6. C. H. Yang: Ph.D. Thesis, Seoul National University, (1999).
7. S. S. Kim: Ph.D. thesis, Arizona State University, (1991).

THE EFFECT Of Ca ADDITION ON THE MICROSTRUCTURE, MECHANICAL AND CORROSION PROPERTIES IN Mg-Zn ALLOY

Bo-Young Hur, Jeong-Pil Eom, Su-Guen Lim, Ki-Won Kimm

Dept. of Metallurgical & Materials Eng., Gyeongsang National Univ.
Research Center for Aircraft Parts Technology, ULSFoM Lab- NRL
Chinju, Gyeongnam, 667-701, KOREA

ABSRTACT

Mg-Zn and Mg-Zn-Ca alloys were fabricated under an Ar gas atmosphere. The main interdendritic phase which formed during early solidification of the ternary Mg-Zn-Ca alloys is the Ca2Mg6Zn3 phase. The tensile properties of the as cast Mg-6wt%Zn-Ca magnesium alloys were improved due to grain refinement by addition of Ca. The Ca addition reduced the aging response of the Mg-Zn-Ca alloys compared with Mg-Zn binary alloy, and progressive additions of Ca to alloys decreased the amount of age hardening. The yield strength and ultimate tensile strength of the T6 treated Mg-Zn-Ca ternary alloys decreased with increase of Ca content, due to the brittle fracture arise from Ca2Mg6Zn3 phase formed along the grain boundary. The behaviors of pH change obtained from these tests showed that pitting corrosion proceeded through two steps, namely, pitting initiation and pitting propagation. And also we knew that between these two steps retention period existed. For all Mg alloys tested, corrosion resistance increased by Ca addition.

1. INTRODUCTION

The binary Mg-Zn system was the maximum solid solubility of zinc is 6.2% at 340℃ decreasing to about 1.7% at room temperature. Zinc addition to magnesium was of outstanding interest in promoting strength in castings, due to the solid solution strengthening and precipitation strengthening[1～4]. Effects of Ca addition to Mg-Zn alloy is increase of elevated temperature properties, due to the high melting point compound formation[5], and improvement of workability, grain refinement[6], and improvement the corrosion resistance by the formation of the protective oxide film on the magnesium alloy surface[7].
In this study, the effect of Ca addition on the mechanical properties, aging and corrosion characteristics of the Mg-Zn alloy are presented.

2. EXPERIMENTAL PROCEDURE

Magnesium or its alloys of ingot(rod) was melted in the low carbon steel crucible(coated with boron nitride) by cylindrical electric furnace under an argon atmosphere. The melting and casting apparatus is specially designed for magnesium alloys. The liquid Mg alloys were casted into the metallic mold at 720℃, and cooling part was located at the bottom of mold.
Solution treatment was carried out in air in a cylindrical electric furnace at 425℃ 8hours.

Samples were quenched by allowing them to fall into cold water(0℃ water). Samples that had been water-quenched were rapidly dried with alcohol and cold air, and transferred to the silicon oil baths within a minute.
The tensile specimens, conformed to sub-size. The gauge length of the specimens was 12.6mm with 2mm thickness, 5mm width. To minimize the effects of surface irregularities and finish, the gauge sections were ground using 1200 grit silicon carbide paper in order to remove any and all circumferential scratches and surface machine marks. Specimens of each magnesium alloy were deformed at a constant cross head speed of 1mm/min.
Pitting corrosion proceeds consuming hydrogen ions. The possibility of using the pH change as an indicator for the pitting corrosion resistance properties of Mg alloy was investigated. Mg alloys for test were mounted with epoxy resin for having $0.5mm^2$
Area exposed to solution(5wt% NaCl). Small volume of solution, about $4cm^3$,was used in order to intensify the pH change. During test the pH changes were monitored by pH sensor equipped properly. All tests were produced at room temperature(20℃)

3. RESULTS AND DISCUSSION

Optical micrographs of the as cast Mg-Zn-Ca alloys are shown typical dendritic solidification microstructures with significant amounts of interdendritic phases. The main interdendritic phase which formed during early solidification of the ternary Mg-Zn-Ca alloys is the Ca2Mg6Zn3 phase. The microstructure of Mg-6wt%Zn-0.1～0.3wt%Ca alloys consisted of MgZn precipitates and Ca2Mg6Zn3 phase formed around the grain boundaries. In the alloys with the highest level of Ca(Mg-6wt%Zn-0.5～0.7wt%Ca alloys), the microstructure revealed wholly Ca2Mg6Zn3 phase formed around the grain boundaries. The grain size of Mg-6wt%Zn-Ca alloys decreased significantly with an increase in Ca content and, at 0.5wt% Ca or more, grain size becomes constant at about 60㎛.

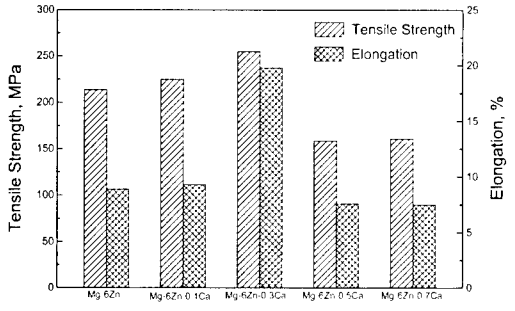

Fig. 1 Effect of Ca on the tensile properties of as cast Mg-Zn-Caternary alloys.

Ultimate tensile strength and ductility, measured by elongation over a 12.6 mm guage length of the specimen, of the Mg-6wt%Zn-Ca alloys increased significantly with an increase in Ca content and, at 0.5wt% Ca or more, ultimate tensile strength and elongation becomes decreased, due to the brittle fracture arise from Ca2Mg6Zn3 phase formed along the grain boundary.

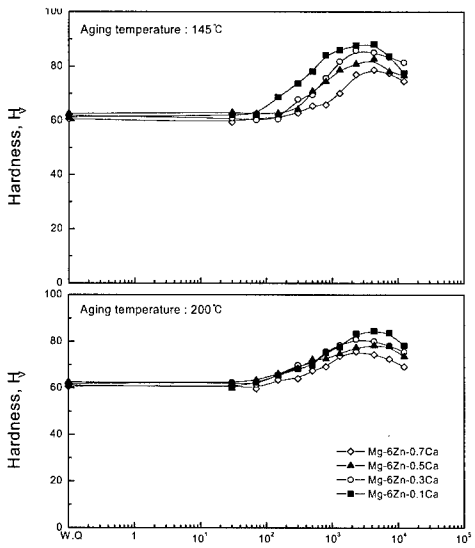

Fig. 2 Age hardening curves of Mg-6wt%Zn-Ca alloys. The samples were solid solution treated at 425℃, and then aged 145℃, 200.

The age hardening curves shown in Figure 2. Samples of the as-cast Mg-Zn-Ca Alloys were heat treated for 8hours at 425℃ and quenched in 0℃ water. These solution treated alloys were then aged 145, 200℃. Aging in the temperature 145℃ and 200℃ produces relatively rapid hardening. The Ca addition reduced the aging response of the Mg-Zn-Ca alloys compared with Mg-Zn binary alloy[8], and progressive additions of Ca to alloys decreased the amount of age hardening. When the tensile properties after T6 treated the Mg-6wt%Zn-0.1～0.3wt%Ca alloys, increase in tensile and yield strength with increasing aging time was observed. As aging progressed, the tensile strength gradually reached 283 and 276MPa, respectively. After aging for 4300min., the change in tensile strength became insensitive to further aging. In the Mg-6wt%Zn-0.5～0.7wt%Ca alloy, on the other hand, the increase in tensile strength with continuing aging for 7200min. was not significant and was gradual.

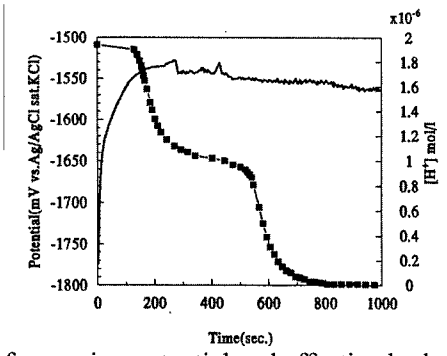

Fig. 3 Changes of corrosion potential and effective hydrogen concentration with time of AZ91Mg alloy in 5wt% NaCl solution of pH6.71

It seemed that the shifting of corrosion potential to lower region was due to pitting propagation. In pitting initiation step dissolved oxygen react consuming hydrogen ions at relatively higher corrosion potential region, but in pitting propagation step hydrogen ions

directly reduce to hydrogen gas at low corrosion potential region because of low dissolved oxygen concentration and high hydrogen concentration of solution in pitting area. It could be thought that the behaviors of both pH and corrosion potential with time during immersion test were necessary to be measured. It is possible to use the pH change with time as a measure for evaluating of pitting corrosion resistance of Mg alloy. As knowing from Fig. 3, in neutral or weak acidic solution, it shows very clear two-steps behavior. Step 1 is pitting initiation period, and step 2 is pitting propagation period. Between these two steps a retention period exists. The longer this period is, the higher the resistance to pitting corrosion is. From the results, we can see that the length of this retention period is shorter when the acidities of solution go to higher level. Other Mg alloys, HK31 and Mg-Zn alloys, were also tested in order to investigated the usefulness of the pH change measurement as a new method for evaluating the pitting corrosion resistance.

4. CONCLUSIONS

Based on a study of the microstructures and mechanical properties of the Mg-Zn-Ca alloys, the following are key observations:

1. The main interdendritic phase which formed during early solidification of the ternary Mg-Zn-Ca alloys is the Ca2Mg6Zn3 phase. The microstructure of Mg-6wt%Zn-0.1～0.3wt%Ca alloys consisted of MgZn precipitates and Ca2Mg6Zn3 phase formed around the grain boundaries.
2. The Ca addition reduced the aging response of the Mg-Zn-Ca alloys, due to presence of undissolvable Ca2Mg6Zn3 compound.
3. In the Mg-6wt%Zn-0.1～0.3wt%Ca alloys, increase in tensile and yield strength with increasing aging time was observed. As aging progressed, the tensile strength gradually reached 283 and 276MPa, respectively.
4. The behavior of effective hydrogen concentration change with time show clearly a consecutive two-step variation in neutral NaCl solution. It was considered that the first step was due to pitting initiation and the second step due to pitting propagation The length of the retention period between those two step was very dependent on pH of solution and the pitting corrosion resistance of Mg alloy.
5. In neutral NaCl 5wt% solution, the evaluation of relative pitting corrosion resistance of different Mg alloys could be done easily by measurement of pH change with time.

5. REFERENCES

[1] W. Unsworth, Light Metal Age, 45 (1987) 10.
[2] E. F. Emely, "Principles of Magnesium Technology", Pergamon Press, (1966) 272.
[3] L. B. Duffy, Foundary Trade J., 3 (1991) 319.
[4] I. J. Polmear, "Light Alloys", 2nd (1989) 169.
[5] T. Horie et al., J. of Japan Inst. of Light Metals, 49 (1999) 272
[6] J. P. Eom, S. G. Lim and B. Y. Hur, J. of Korean Foundrumen's Society, 19 (1999) 7
[7] W. W. Park and B. S. You, J. of Korean Foundrumen's Society, 19 (1999) 377
[8] J. P. Eom, S. G. Lim and B. Y. Hur, J. of Korean Foundrumen's Society, 16 (1996) 352
[9] D.A.Jones. 'Principles and prevention of corrosion' Maxwell Macmillan Int., 1991
[10] K.H. Kim, K.W.Kim, S.G.Lim, H.J.Ahn. B.Y.Hur. J. Korean Inst. of Met&Mater., 1995, 34(2), 109

STRIP CASTING OF Mg ALLOYS

Sung S. Park, Young S. Park and Nack J. Kim
Center for Advanced Aerospace Materials
Pohang Univ. of Science & Technology, Pohang 790-784, KOREA

ABSTRACT

A study has been on the microstructural evolution in strip cast AZ91 Mg alloy. The microstructure of the as-cast alloy is characterized by the equiaxed dendrite structure. There is a variation of secondary dendrite arm spacing through the thickness of strip, showing the smallest value at the wheel surface and the largest value at the center of strip. The distribution of $Mg_{17}Al_{12}$ particles is also not uniform in as-cast strip. The microstructure of solution treated strip consists of fine α-Mg grains and Al-Mn particles in the matrix with no $Mg_{17}Al_{12}$ particles. Aging of the solution treated strip results in the precipitation of $Mg_{17}Al_{12}$ particles. However, the distribution of $Mg_{17}Al_{12}$ particles in T6 treated strip is not uniform through the thickness of strip. The volume fraction of $Mg_{17}Al_{12}$ particles decreases from the wheel side to the center of strip. It shows that the strip cast AZ91 Mg alloy shows the best combination of tensile properties in T4 condition. It is believed that the respectable tensile properties of T4 treated strip is due to the presence of Al-Mn particles, which induces homogeneous deformation.

1. INTRODUCTION

Lightweight alloys have had varying degree of importance in transportation systems. In aerospace industries, for example, the advances made in lightweight alloys have always provided the key to the improvements in performance. Moreover, recent growing demand for weight reduction of the vehicle due to the increasing importance of fuel efficiency and environmental problems has generated a considerable interest for lightweight alloys from the automotive industries. From these respects, Mg alloys, the lightest commercial alloys developed so far, have great potential for high performance aerospace and automotive applications [1-4]. However, the majority of Mg alloys currently in use are cast products. Only a limited number of Mg alloys is available in wrought products. The development of wrought Mg alloys, particularly sheet alloys, would greatly expand the application areas of Mg alloys. It is believed that the strip casting process can be an alternative for the production of Mg alloys sheets. Strip casting process combines casting and hot rolling into a single step, having an advantage of one-step processing of flat rolled products. Besides being such a cost-effective process, strip casting also has beneficial effects on microstructure such as reducing segregation, improving inclusion size distribution and refining microstructural and textural homogeneity. The current interest in strip casting is on the production of steel products such as stainless steels [5-7] and Al alloys with limited alloy contents [8-10]. Recently, attempt has been made to fabricate the highly alloyed Al alloys by strip casting [11,12] and it shows that strip casting can be applied in the production of highly alloyed Al alloys.

In the present study, the strip casting process has been applied for the production of Mg alloy strip. AZ91 alloy was selected for the study since it is the most common Mg alloy and

also has good castability. [13]. The microstructure and mechanical properties of the cast strip have been investigated and compared with those of the conventionally cast ingot.

2. EXPERIMENTAL PROCEDURE

Chemical composition of commercial AZ91 alloy was Mg-8.8% Al-0.67% Zn-0.26t% Mn (wt.%). The alloy was remelted under an inert atmosphere of CO_2 and SF_6 mixture followed by strip casting. The details of strip casting process are described elsewhere [11]. Two different roll temperatures were used to see the effect of cooling rate; 50°C for the strip 1 and 10°C for the strip 2. The strips were solution-treated at 420°C for 1 hour followed by aging treatment at 170°C. The microstructure was examined by optical microscopy, scanning electron microscopy, transmission electron microscopy and X-ray diffractormetry. TEM specimens were prepared by electro-polishing in a solution of 99% ethanol and 1% perchloric acid at -30°C. Tensile properties were measured by using flat tensile specimens of 12.6 mm gage length, 2 mm gage thickness and 5 mm gage width. Strain rate used was 6.4×10^{-4} s^{-1}.

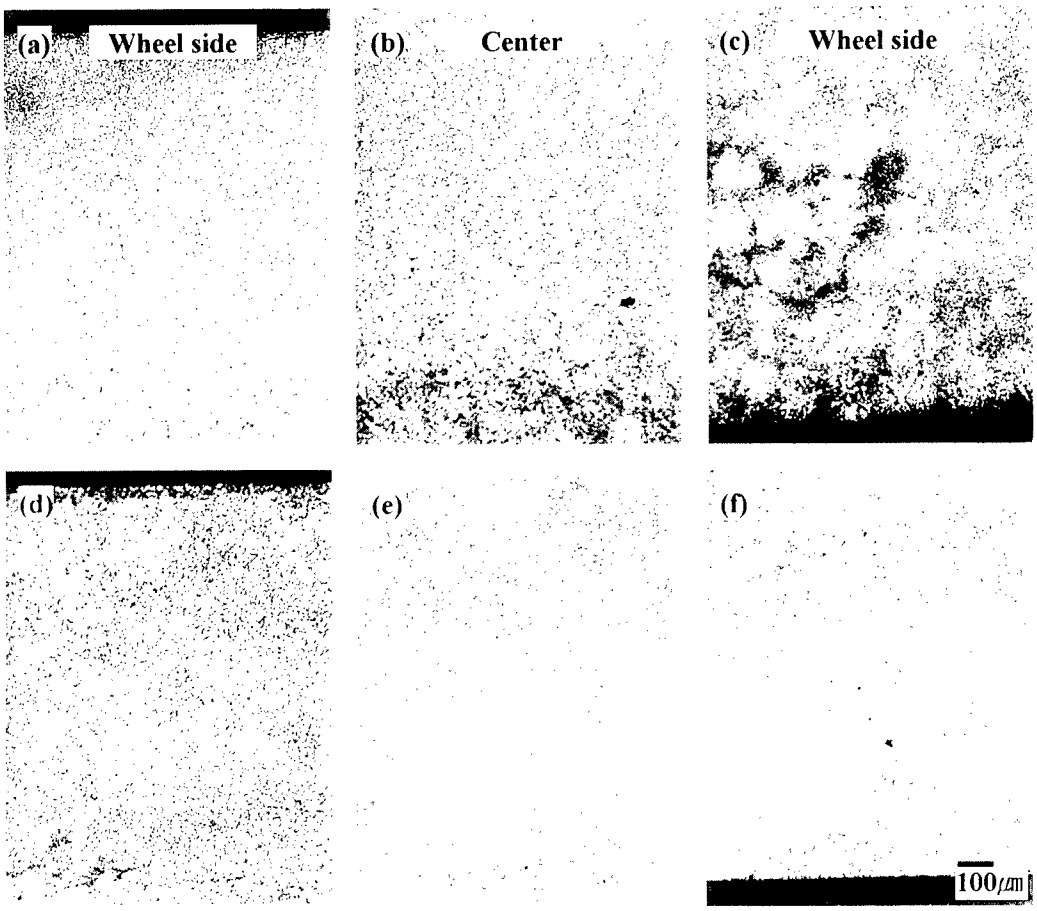

Fig. 1 As-cast microstructure: (a)-(c) strip 1 and (d)-(f) strip 2

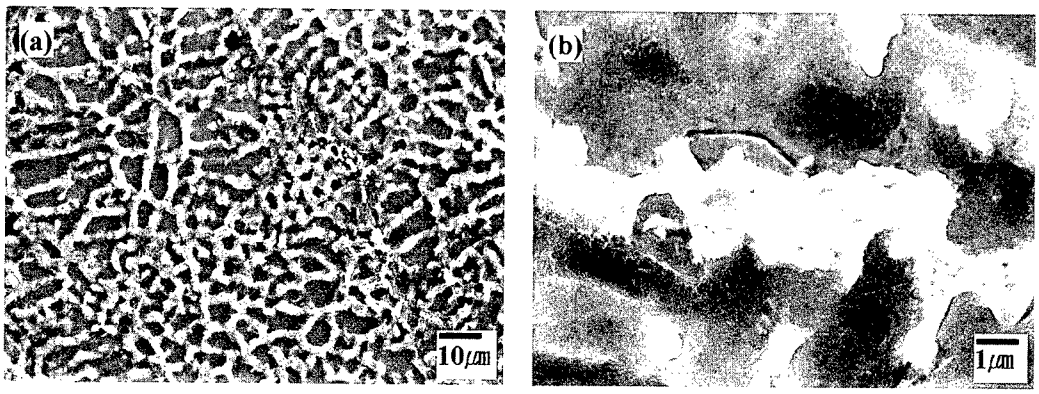

Fig. 2. a) SEM micrograph of as-cast strip and b) magnified view of $Mg_{17}Al_{12}$ phase.

3. RESULTS AND DISCUSSION

3.1 Microstructure

The solidification sequence of AZ91 alloy starts with nucleation of primary α -Mg followed by the formation of Mg-$Mg_{17}Al_{12}$ eutectic at 437℃ [14]. Fig. 1 shows the as-cast microstructures of the strip1 and strip 2. Fine equiaxed dendrites are observed in the strips. It is well known that the formation of equiaxed dendrite can occur under the conditions of high cooling rate, high solute concentration and low melt over-temperature [15]. As shown in Fig. 1, the strip 2 has the relatively finer microstructure than the strip 1 due to the higher cooling rate employed in the former than in the latter. It can also be seen that the strip 1 has a larger degree of macro-segregation than the strip 2. Fig. 2 shows the details of as-cast microstructure. It shows that $Mg_{17}Al_{12}$ particles are present between dendritic regions in network form [13].

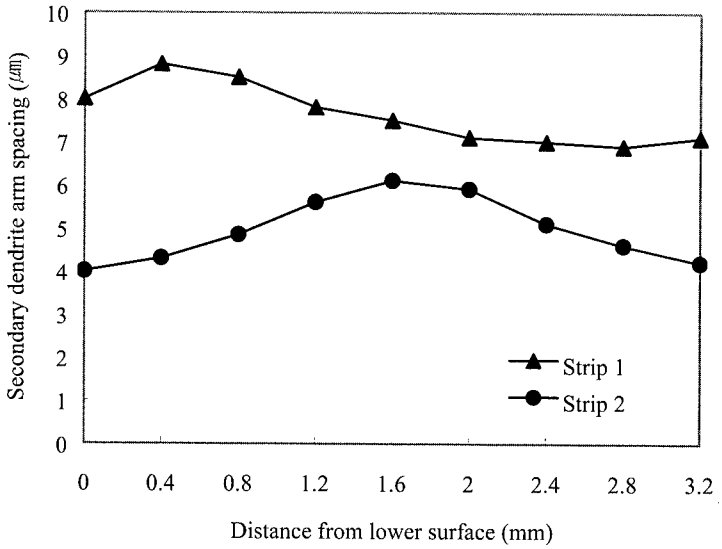

Fig. 3. Variation of secondary dendrite arm spacing through the thickness of strip.

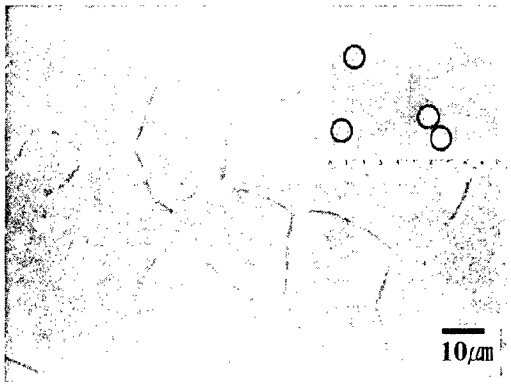

Fig. 4. SEM micrograph of the strip 2 after solution treatment (Insert: EDS spectra of Al-Mn particles).

It shows that there are more $Mg_{17}Al_{12}$ particles at the wheel side than at the center of strip. Secondary dendrite arm spacing (SDAS) has been measured to estimate the cooling rate of strip casting (Fig. 3). It shows that the SDAS of the strip 1 varies from 7 to 9 μm, showing the largest SDAS at near one of the wheel surface. On the other hand, the strip 2 shows the large variation of SDAS through the thickness of strip, showing the smallest value at the wheel surface and the largest value at the center of strip. The cooling rate was estimated from the measured SDAS by using the following relationship [16].

$$SDAS = 5.3 \cdot t_f^{0.43}$$
$$R = \Delta T_s / t_f$$

where the t_f is the local solidification time (s), R is the cooling rate (K/s) and ΔT_s is the nonequilibrium temperature range of solidification which is 171K for the AZ91 alloy. It shows that the strip 1 experiences a more or less uniform cooling rate of 50 – 100K/s through the thickness. The highest cooling rate experienced in the strip 2 is approximately 370K/s at the wheel side, while the lowest one is 120K/s at the center of the strip. These values of cooling rate are much slower than those obtained in the strip casting of Al alloys, which are around 10^3K/s [11].

420°C was chosen for the solution treatment temperature since there can be an occurrence of incipient melting when the solution treatment temperature exceeds 420°C. DTA analysis shows that incipient melting occurs at about 427℃. Fig. 4 shows the SEM micrograph of the strip 2 after solution treatment at 420°C for 1 hour. It shows that the microstructure of the solution treated strip cast AZ91 alloy consists of fine Mg grains with Al-Mn particles within the matrix and at the grain boundaries. As is the case of SDAS, grain size after solution treatment also varies through the thickness of strip. It shows that the grain size of the strip 1 varies from 22 to 30 μm, while that of the strip 2 varies from 12 to 20 μm. Variation of grain size through the thickness after solution treatment follows the same trend observed in the variation of SDAS. Nevertheless, it is worth mentioning that the grain size of the strip cast alloy is much finer than 250 μm which is the typical grain size of ingot cast alloy.

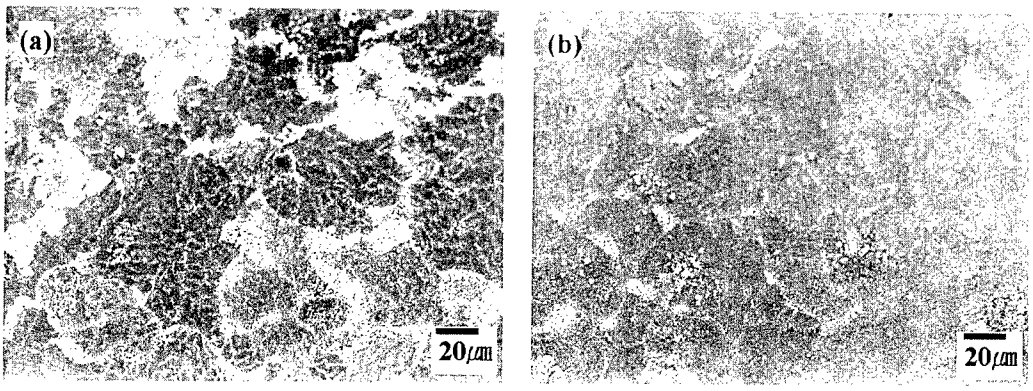

Fig. 5. T6 microstructure showing the inhomogenous distribution of $Mg_{17}Al_{12}$ particles; (a) wheel side and (b) center.

Fig. 5 shows the microstructure after aging treatment for 22 hours. It shows that there is a variation of volume fraction of $Mg_{17}Al_{12}$ particles through the thickness of the strip. Larger volume fraction of $Mg_{17}Al_{12}$ particles is found at the wheel side region than at the center region.

3.2 Mechanical properties

The variation of hardness through the thickness of strips is shown in Fig. 6. The strip 2 shows higher hardness values than the strip 1 at all heat treatment conditions. However, the strip 2 shows a larger variation of hardness through the thickness of the strip than the strip 1. Comparison of the hardness values among the as-cast, T4 treated and T6 treated specimens shows that the difference in the hardness between at the surface and at the center is large in

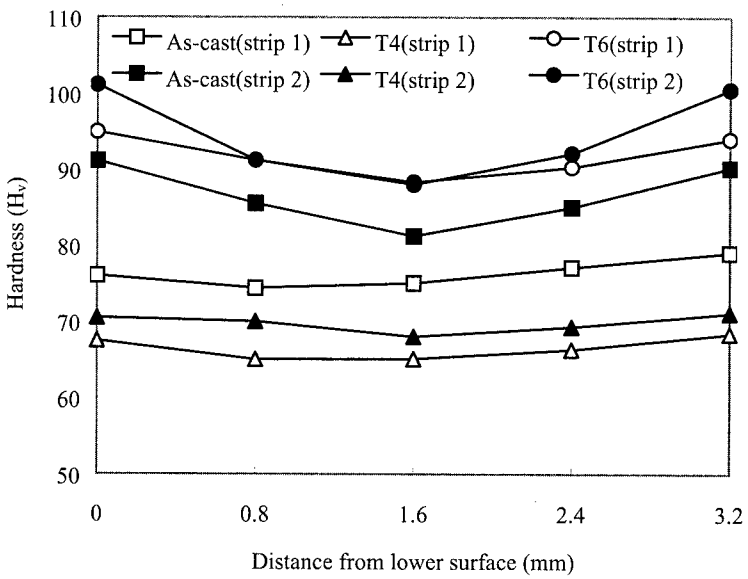

Fig. 6. Variation of hardness through the thickness of strip.

the as-cast and T6 specimens while the T4 specimens show relatively uniform hardness values through the thickness. In the case of T4 specimens, factors affecting the hardness are solid solution hardening and grain size since $Mg_{17}Al_{12}$ precipitates are all dissolved by solution treatment. Although there exists a variation of grain size through the thickness after solution treatment, the variation is too small to result in a large difference in hardness. Same can be said for the effect of solute contents although exact distribution of solute elements is not known. On the other hand, there is another factor which exerts a large effect on hardness in T6 specimens; namely, $Mg_{17}Al_{12}$ precipitates. As shown previously, the volume fraction of $Mg_{17}Al_{12}$ precipitates is not uniform through the thickness of the strip, having the largest value at the surface and the smallest at the center of the strip. Such inhomogeneous distribution of $Mg_{17}Al_{12}$ precipitates results in the variation of hardness through the thickness of the strip in T6 treated and as-cast specimens.

Fig. 7 shows the tensile properties of the strip cast AZ91 alloy. The properties of ingot cast AZ91 alloy are also shown for comparison purposes. It shows that the strip cast AZ91 alloy has much higher yield and tensile strength values than ingot cast AZ91 alloy at all teat treatment conditions. Between two types of strips, the strip 2 has better tensile properties than the strip 1. It is shown that the yield strength of the solution treated specimen is lower than that of the as-cast specimen. In the as-cast specimen, strength is derived mostly from the $Mg_{17}Al_{12}$ precipitates and dislocation substructure formed by hot rolling effect during strip casting. Solution treatment of as-cast specimen dissolves $Mg_{17}Al_{12}$ precipitates and removes the dislocation substructure. Therefore, it might be expected that the yield strength of the T4 treated specimen becomes much lower than that of the as-cast specimen. However, the yield strength of the T4 specimen is high approaching the respectable value of about 150 MPa, which is in fact much higher than that of ingot cast alloy. It is believed that high strength of the T4 treated specimen comes mostly from the uniformly distributed Al-Mn particles.

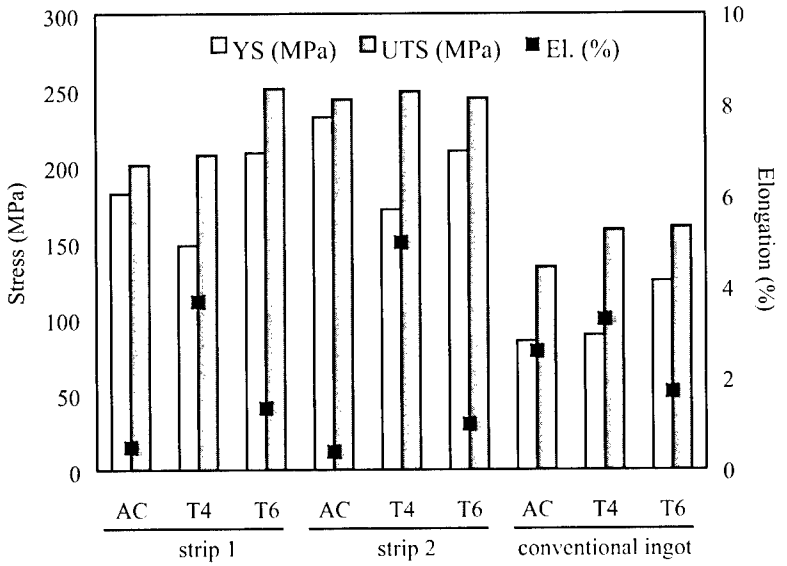

Fig. 7. Tensile properties of strip cast alloy. Properties of ingot cast alloy are also shown for comparison purposes.

The presence of Al-Mn particles enhances homogeneous deformation, thereby increasing strength as well as ductility. One of the main advantages of strip casting is the refinement of intermetallic compounds, which usually exist as harmful coarse particles in conventionally processed alloys. Similar behavior has been found in strip cast Al alloys [11]. T6 treatment promotes the formation of $Mg_{17}Al_{12}$ precipitates, resulting in an increase in yield strength but with a considerable decrease in ductility.

4. CONCLUDING REMARKS

The present study shows that strip casting can be applied for the production of Mg alloy sheet products. However, there are several metallurgical issues which should be resolved before further investigation is being made. It has been shown there is a variation of microstructure through the thickness of strip. The wheel side microstructure has a finer secondary dendrite arm spacing and a larger volume fraction of $Mg_{17}Al_{12}$ particles (i.e., larger amount of Al) than the microstructure at the center. Such inhomogeneity present in as-cast state prevails even after solution treatment. It shows that the variation of grain size is not so critical since the magnitude of variation is not large enough to exert a significant variation in mechanical properties. However, the variation of solute contents through the thickness of strip appears to be the one which should be controlled for the development of high performance Mg alloy sheet by strip casting. When the strip is subjected to aging, the variation of solute content often results in the variation of volume fraction of second phase particles, which have significant effect on mechanical properties. The large variation in the solute content observed in the present Mg alloy is peculiar in that such large variation has not been found in Al alloys. Further study is necessary to understand the cause of large variation in solute content through the thickness of strip.

REFERENCES

1. A. Luo, J. Renaud, I. Nakatsugawa, and J. Plourde, *JOM*, July (1995) 28.
2. D. H. Kim, K. S. Shin, Nack J. Kim, Advanced Performance Materials, 5 (1998) 319.
3. R. S. Busk, Magnesium Products Design, p. 149, Marcel Dekker Inc. (1987).
4. H. Westengen, in Science and Engineering of Light Metals (eds. by K. Hirano, H. Oikawa and K. Ikeda), p. 77, Japan Institute of Light Metals (1991).
5. D. K. Kim, D. H. Kim, D. K. Choo and H. K. Moon, Metals & Materials, 2 (1996) 211.
6. N. Tsuji, K. Tsuzaki, and T. Maki, ISIJ Int., 32 (1992), 1319.
7. H. Yasunaka, ISIJ Int., 35 (1995), 784.
8. C. J. Petry, in Aluminum Alloys – Physical and Mechanical Properties (eds. by E. A. Starke, Jr. and T. H. Sanders, Jr.), p. 111, EMAS, U. K. (1986).
9. E. A. Loria, in Aluminum Alloys – Physical and Mechanical Properties (eds. by E. A. Starke, Jr. and T. H. Sanders, Jr.), p. 133, EMAS, U. K. (1986).
10. Y. Saito, N. Tsuji, Y. Nagai, and T. Sakai, in Thermec '97 (ed. by Chandra, T.), p.2381, TMS, Warrendale, PA (1997).
11. Young S. Park, Sang B. Lee and Nack J. Kim, in this proceedings.
12. Young S. Park, Sang B. Lee and Nack J. Kim, submitted to Acta Materialia.
13. I. J. Polmear, Light Alloys, 3rd ed., Arnold, London, 1995.
14. A. K. Dahle et al, Journal of Light Metals 1 (2001), 61.

15. K. S. Oh and Y. W. Chang, Bull. of the Korean Inst. of Met. & Mater.,. 7 (1994), 268.
16. T. Z. Kattamis, U.T. Holmberg and M.C. Flemings, J. Inst. Met., 95 (1967), 343.

Session III

FUNDAMENTAL ISSUES

COPPER CONCENTRATION INSIDE GUINIER-PRESTON (I) ZONE FORMED IN AN Al-Cu ALLOY

M.Takeda, Y.Nagura and A.Igarashi

Department of Mechanical Engineering and Materials Science (SEISAN),
Yokohama National University, 79-5 Tokiwadai Hodogayaku, Yokohama 240-8501, JAPAN

ABSTRACT

Copper concentration inside Guinier-Preston (I) zone appearing in an Al-Cu alloy was studied by means of the extended Hückel molecular orbital (EHMO) calculation. The present calculation revealed that the copper concentration inside the G.P.(I) zone depends on the size. The G.P.(I) zone is composed not only of copper but also of Aluminum in a small G.P.(I) zone, whereas the copper concentration increases with the zone size. Lattice distortion which is locally associated with the zone increases the stability, but the stabilizing effect of the distortion is estimated not higher than one-tenth of the energy due to copper coalescence for the G.P.(I) zone with 2nm in diameter.

1. INTRODUCTION

Al-Cu alloy is one of the most important precipitation-hardening Aluminum alloys for practical purposes, and a large number of studies have been devoted to clarify the precipitation behavior in the alloy. As far as aging process in the alloy is concerned, an interpretation has been widely accepted, that several metastable and stable phases appear in the following sequence; supersaturated solid solution(ssss)→G.P.(I)→G.P.(II) (or θ'')→ θ' → θ. In most of works, the G.P.(I) zone is interpreted as an solute aggregate initially formed with a monolayer thickness [1,2]. There are, however, disputes on several basic points such as copper concentration and structure inside the zone. These points were discussed in a special issue of Scripta Metallurgica (1988)[3], but no definitive conclusions have been presented there and even in successive works.

As far as the concentration is concerned, Gerold presented a monolayer platelet model comprising only copper atoms as a the G.P.(I), based on X-ray diffraction experiment[4]. But EXAFS [5] and FIM [6] works supporting a model containing Al atoms were also reported. Jouffrey and his co-workers have recently investigated the composition of the zone, by means of high resolution TEM and energy-dispersive X-ray analysis (EDX) and claimed that the G.P. zone is composed of both copper and Aluminum [7,8].

To investigate the copper concentration inside the G.P.(I) from a somewhat different viewpoint, one of the present authors applied an empirical chemical-bond calculation based on the extended Hückel Molecular Orbital (EHMO) theory to estimate the stability of the G.P.(I). Although they published some results in 1992[9], the size dependence of the composition of the G.P.(I) was not examined. The present work aimed at examining the solute composition of the G.P.(I) zone by the EHMO calculation, taking into the zone size account.

2. FUNDAMENTAL ASPECT OF THE EHMO CALCULATION

The present calculation method is based on the extended Hückel Molecular Orbital theory (EHMO) which is categorized as an empirical MO method.
The EHMO calculation is based on the time-independent Schroedinger's equation,

$$H\psi = \varepsilon\ \psi \qquad (1)$$

where H is Hamiltonian, ε the eigenvalue of energy and ψ the eigenfunction. To solve the Schroedinger's equation for a cluster model consisting of many atoms, the linear combination of atomic orbital (LCAO) approximation is introduced for numerical computation. That is,

$$\psi = \sum_{i=1}^{N} C_i \chi_i \qquad (2)$$

where χ i is the atomic orbital of constituent atoms.
The secular equation (3) is obtained by the equations (1) and (2).

$$\text{Det}\,|H - \varepsilon S| = 0 \qquad (3)$$
$$H_{ij} = \langle \chi_i | H | \chi_j \rangle \qquad (4)$$
$$S_{ij} = \langle \chi_i | \chi_j \rangle \qquad (5)$$

Using further approximations; (i) the Slater-type orbitals used as the bases, (ii) the Coulomb and resonance integrals related as $H_{jj}=-I_j$ (ionization potential) and (iii) $H_{ij}=K(H_{ii}+H_{jj})S_{ij}/2$ (K=1.75), the total energy is calculated by

$$^{o}E = \sum n_i \varepsilon_i \qquad (6)$$

The cohesive energy is given by

$$^{c}E = \sum n_i \varepsilon_i - \sum N_j I_j. \qquad (7)$$

In the present study, the difference of the energy (Δ E) between the cluster with and without a G.P.zone, is estimated by the following equation,

$$\Delta E = {}^{c}E_{GP} - {}^{c}E_{disorder} = {}^{o}E_{GP} - {}^{o}E_{disorder} \qquad (8)$$

where ${}^{o}E_{GP}$ is the orbital energy containing a G.P.(I) and ${}^{o}E_{disorder}$ means the energy of the solid solution. I_j, the ionization potential for an electron considered. In this work we calculated $E_{disorder}$ with an assumption that the value is equal to the average determined by an interpolation of a pure Aluminum and a pure copper cluster, based on the concentration. In addition, the difference of the energy ΔE is normalized by dividing with the number of constituent atoms. Thus, $\Delta E/n$ is finally used for the estimation of the stability of the structure.

$$\Delta E/n = ({}^{o}E_{GP} - {}^{o}E_{disorder}) /n \qquad (9)$$

In this work, the 2s, 2p-atomic orbitals (AOs) of Aluminum and the 4s, 4p-AOs of copper were taken into account. Although no lattice distortion was included in the previous EHMO calculation [9], both cluster models with and without local lattice distortions were considered in the present work since the EHMO calculation can, in principle, involve lattice distortion locally associated with the G.P.(I) zone. The lattice parameter of the Al matrix was used for the models (=0.406nm) with no local distortion model. The present calculation considered local lattice distortion up to 10%, taking the difference of lattice constants in pure Aluminum and pure copper bulk crystals into account.

Figure 1 shows an example of cluster models for the present EHMO calculations. Most of the models were constructed with a special attention to avoid an artifact due to the modeling of the structure in this work. Therefore, the models were built up as much symmetric and spherical as possible. With the same reason, the copper atoms were also placed on symmetric sites. Figure 2 shows the atomic arrangements in the copper layer, which have different copper concentrations. The copper concentrations inside the zone are estimated as (a)100%, (b)55.6% and (c)38.5%, respectively. Since the present purpose is to examine the stability depending on the copper concentration inside the monolayer G.P.(I), the center layer containing copper atoms are sandwiched by several pure Aluminum layers on both sides.

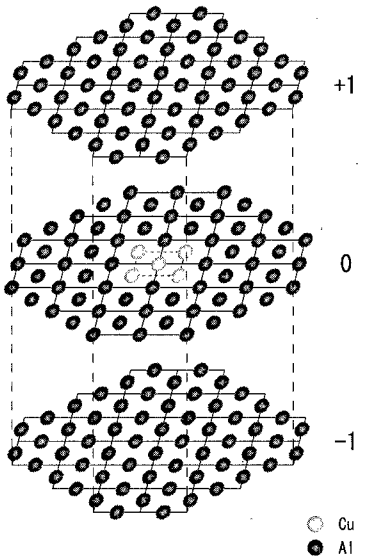

Fig. 1 Al-Cu G.P.(I) zone cluster model for EHMO

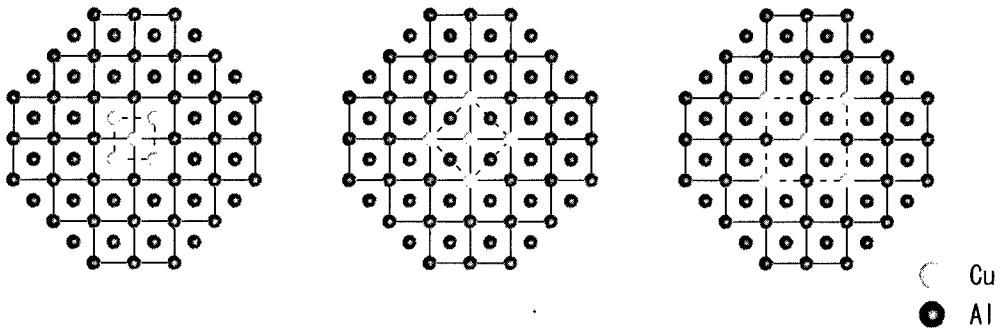

(a) 100% (b) 55.6% (c) 38.5%

Fig. 2 Atomic arrangements of G.P.(I) plane (the zeroth-layer in Fig. 1)

3. RESULTS AND DISCUSSION

Figure 3 shows the result of the present EHMO calculation. The formation energy (ΔE/n) is dependent on the total number of copper atoms, and the energy is negatively increased with the number of copper atoms. It is clearly shown that the formation energy of the G.P.(I) is minimized at a certain copper concentration in each curves. If a small number of copper atoms are involved to form the zone, for example five, the curve of the formation energy (ΔE/n) shows a large plateau. In this case, the stability is almost similar whether copper concentration inside the G.P.(I) zone has 30at% or 100at%. The formation energy, however, tends to have a narrow plateau and to shift the minimum value towards 100% in copper concentration, when larger number of copper atoms commit the G.P. zone formation. Thus, the result shown in Figure 3 strongly suggests that the copper concentration inside the G.P.(I) is gradually changed and approach to 100% with the growth. Converting the number of copper atoms involved in the G.P.(I) into the zone size, we found that the G.P.(I) zone approximately 3.2-4.5nm in diameter has been occupied by copper atoms up to more than seventy percent. Taking the size dependence of the formation energy into account, one can expect that the G.P.(I) zone larger than around 4.0nm in diameter

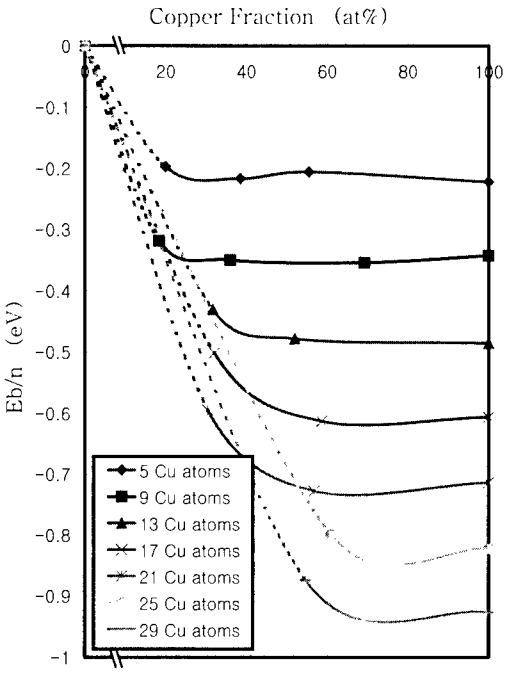

Fig. 3 Formation energy of G.P.(I)

is fully composed of copper atoms, based on the present EHMO calculation.

Since a bight field TEM imaging normally associates a significant strain contrast with the G.P.(I) zone in an Al-Cu alloy the zones, the size of the G.P.(I) estimated from a bright-field TEM image, is sometimes over estimated twice as large as the value obtained from weak-beam TEM image which is much close to the real size[10]. In this sense, G.P.(I) zone 8.0-9.0nm in diameter can be considered to be critical as a fully copper-occupied G.P.(I) zone. Moreover, temperature may give an influence to the critical size since the configurational entropy affects the stability. The present results suggest that G.P.(I) zone size should be taken into account, when a critical examination is intended with an experimental technique.

Figure 4 shows the curves of the formation energy which are obtained with cluster models including the lattice distortion in zone plane. If the G.P.(I) zone is small, the distortion slightly alters the level of the energy. The influence of the lattice distortion becomes clear to the zone with a large diameter. The compressive distortion 10% in ratio reduces the formation energy and makes the zone more stable. But the reduction is approximately

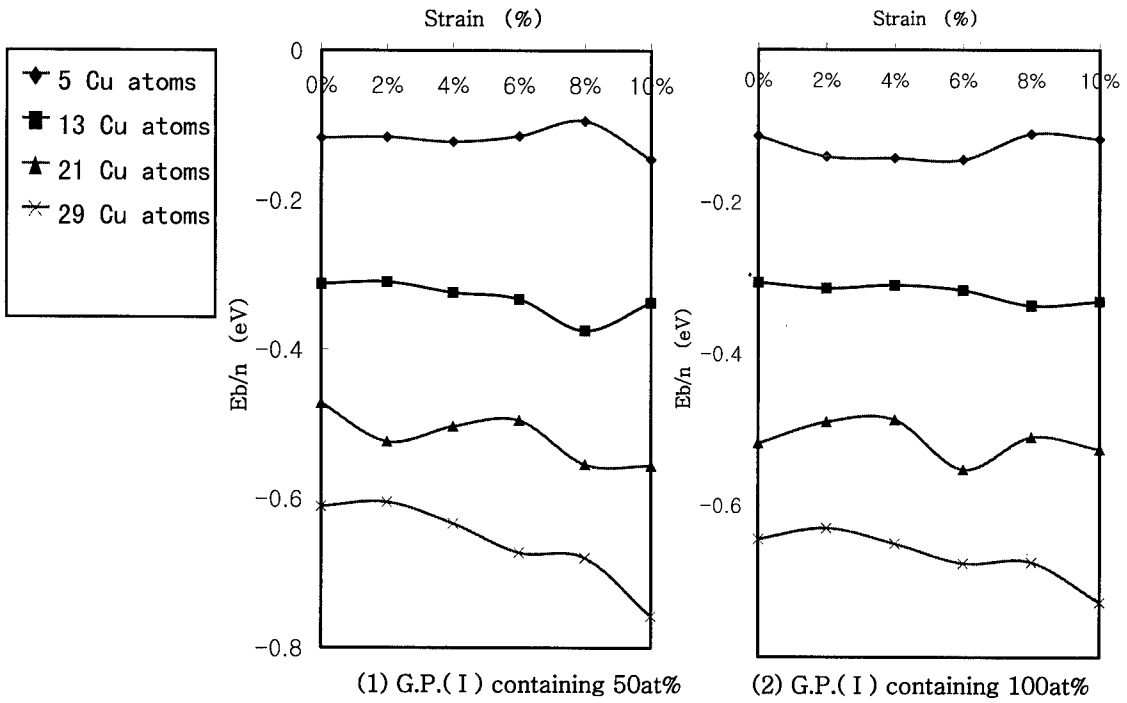

(1) G.P.(I) containing 50at% (2) G.P.(I) containing 100at%

Fig. 4 Influence of lattice distortion inside G.P. (I) to the stability of G.P. (I) zone

10% based on the present EHMO calculations. Thus, the stability of the G.P.(I) zone is mainly due to chemical effect of solute coalescence.

We adopted a measuring scale (i.e., equation (9)) which was also used in the previous study carried out by the present authors. In this context, the EHMO calculation has successfully provided a possible reason to the fact that contradictory conclusions were experimentally presented. There are several possible approaches based on the similar theoretical basis. Further investigation should also be intended to correlate with one another in future.

4. CONCLUSION

The present extended Hückel Molecular Orbital calculation examined the size dependence of copper concentration inside a monolayer G.P.(I) zone formed in an Al-Cu alloy. The formation energy of a G.P.(I) depends on the zone size. When the G.P.(I) zone is small, the curve of the formation energy shows a plateau corresponding to the minimum energy from 35at% to 100% in copper concentration and the stability of the zone is almost similar in the wide concentration range. When the G.P.(I) zone grows, the plateau becomes narrow and is limited near at 100% in copper concentration. It is concluded that size dependence of copper concentration inside the G.P.(I) zone is a possible reason that controversial results were obtained in experiments.

REFERENCES

[1] A.Guinier, Nature (London) 142, 569(1938)
[2] G.D.Preston, Phil.Mag.,26,855(1938)
[3] V.Gerold, Z.Metallkde., 45,593,599(1954)
[4] A.Fontaine, P.Lagarde, A.Naudon, D.Raoux and D.Spanjaard, Phil. Mag., 40, 17(1979)
[5] K.Hono, T.Hashizume, Y.Hasegawa, K.Hirano and t.Sakurai, Scripta Metall., 20, 487(1986)
[6] Scripta Metall., 22(7)(1988)
[7] B.Jouffery and D.Dorignac, J.Phys.I, 2,1067(1992)
[8] B.Jouffery and M.Karlik, Microsc.Microanal.Microstruct., 3, 243(1992)
[9] M.Takeda, H.Oka and I.Onaka, phys.stat.sol.(a) 132,305(1992)
[10]H.Yoshida, "Electron Microscopy (in Japanese) " (Kyoritsu Pub., 1980) (ed. R.Uyeda) pp.227.

Effect of Damage Growth on Sheet Metals Forming

Young Suk Kim and Sung Yeun Won*

School of Mechanical Engineering, Kyungpook National University, Taegu 702-701, Korea
* Graduate School, Kyungpook National University, Taegu 702-701, Korea

ABSTRACT

Most fractures in metal forming processes are mainly occurred due to the results of development of ductile damage. In this paper, anisotropic version of Gurson-Tvergaard's yield function for voided materials is developed to represent the plastic deformation characteristics of anisotropic sheet metals. The associated flow rules are presented and the laws governing void growth with accumulated strain are derived. The work hardening ability, the strain rate sensitivity and the normal anisotropy of the sheet metal are taken into consideration. Using the proposed model the effect of void growth on the deformation characteristic of anisotropic sheet metals is investigated. Also, the flow curves of voided materials of known initial porosities are predicted and compared with experiments.

1. Introduction

In sheet metal forming processes, the formability of sheet metals is limited by the occurrence of localized necking. This is often evaluated using a strain analysis based on the concept of forming limit diagrams (FLD) originally introduced by Keeler [1] and Goodwin [2]. Marciniak and Kuczynski [3] analyzed the causes of necking and subsequent failure under the assumption of the presence of local inhomogeneities in the original sheet metal. Storen *et al.* [4] developed a localized necking model based on bifurcation theory. Zhao *et al.* [5] investigated limit stains using the limit stress concept.

It has also been observed that ductile fractures in sheet metals involve the generation of considerable porosity via the nucleation and growth of voids (Graf [6], Parmar and Mellor [7]). In order to model the plastic flow and fracture of these structural metals, Gurson [8] carried out an upper bound analysis and proposed an approximate yield criterion for perfectly rigid materials where the matrix obeys the von Mises yield criterion, containing two different types of void geometries (i.e. a long circular cylinder and a sphere. Tvergaard [9] suggested a modified version of Gurson's yield criterion by comparing the results of shear band instability based on a finite element model for porous materials with those based on a continuum model using Gurson's yield criterion. Hill's [10] anisotropic yield function and others (Hill [11], Hosford [12], Barlat [13]) were often used to study the forming limit of various kinds of anisotropic sheets. Kim *et al.* [14] investigated that the Gurson's models with the Hosford's anisotropy yield criterion might predict well the effect void volume fraction on the yield loci and the effect of void growth on tensile flow curve.

In the present work, an approximate Gurson-Tvergaard's yield function in cooperating with Hosford's [12] anisotropic yield criterion is applied to describe the plastic deformation of voided materials. These anisotropic yield criteria for voided materials are then used to investigate the yield surface shapes of various void volume fractions and damage evolution of an anisotropic sheet under equibiaxial tensile loading. In addition, the work hardening ability of the metal, the strain rate sensitivity and the normal anisotropy of the sheet metal are taken

into consideration.

2. Theoretical Analysis

2.1 Constitutive model

Theories describing the plastic deformation characteristic for voided materials suggest that the yield criterion is a function of the first invariant of the stress tensor, J_1, and the second invariant of the deviatoric stress tensor, J_2'. Tvergaard modified Gurson's model [8] with a single spherical void. The yield function of Gurson-Tvergaard model is given by:

$$g(\sigma_{ij},\sigma_M,f)=\left(\frac{\bar{\sigma}}{\sigma_M}\right)^2+2fq_1\cosh\left(\frac{q_2\sigma_{kk}}{2\sigma_M}\right)-1-q_1^2f^2=0 \tag{1}$$

Where $\bar{\sigma}$ and σ_M are the effective stresses of the voided material and matrix, respectively and f represents the current void volume fraction. Equation (1) has been widely used to investigate the damage growth effects on the plastic deformation behaviors of voided isotropic sheet metals. In this work, equation (1) can be further combined with Hosford's definition of $\bar{\sigma}$ for describing anisotropic property of normal anisotropic sheet metal as given by:

$$\bar{\sigma}=\left\{\frac{1}{(1+R)}\left[R|\sigma_1-\sigma_2|^a+|\sigma_2-\sigma_3|^a+|\sigma_3-\sigma_1|^a\right]\right\}^{\frac{1}{a}} \tag{2}$$

where R is the mean anisotropy parameter, the averaged anisotropy parameter measured in 0°, 45° and 90° direction tension tests. Hosford [11] proposed the yield functions of equation (2) - based on the Hill-Bishop analysis - for crystallograpic textured fcc and bcc metals. Hosford also suggested that the even integer, a, should be 6 for bcc metals and 8 for fcc metals. According to the normality rule of the plastic strain vector for a yield surface, principal plastic strain increments are derived based on the partial differential of the yield function with respect to the stresses, respectively. Thus,

$$d\varepsilon_1^p=\left\{2\bar{\sigma}^{(2-a)}\frac{1}{(1+R)}\left[R|\sigma_1-\sigma_2|^{a-1}-|\sigma_3-\sigma_1|^{a-1}\right]+\frac{fq_1q_2^2}{2}\sigma_{kk}\right\}d\lambda' \tag{3a}$$

$$d\varepsilon_2^p=\left\{2\bar{\sigma}^{(2-a)}\frac{1}{(1+R)}\left[-R|\sigma_1-\sigma_2|^{a-1}+|\sigma_2-\sigma_3|^{a-1}\right]+\frac{fq_1q_2^2}{2}\sigma_{kk}\right\}d\lambda' \tag{3b}$$

$$d\varepsilon_3^p=\left\{2\bar{\sigma}^{(2-a)}\frac{1}{(1+R)}\left[-|\sigma_2-\sigma_3|^{a-1}+|\sigma_3-\sigma_1|^{a-1}\right]+\frac{fq_1q_2^2}{2}\sigma_{kk}\right\}d\lambda' \tag{3c}$$

Where $d\lambda'=\frac{1}{\bar{\sigma}_M^2}d\lambda$ is a non-negative proportionality factor. As a result, the volumetric plastic strain, $d\varepsilon_v$, can be obtained by summing:

$$d\varepsilon_v=d\varepsilon_1^p+d\varepsilon_2^p+d\varepsilon_3^p=\frac{3fq_1q_2^2}{2}\sigma_{kk}d\lambda'=\frac{3fq_1q_2^2}{2}\sigma_{kk}\frac{d\lambda}{\bar{\sigma}_M^2} \tag{4}$$

The porosity of a material is characterized by the void volume fraction, f, which can be defined by:

$$f=\frac{V_V}{V_T}=\frac{V_T-V_M}{V_T} \tag{5}$$

Where V_V, V_M and V_T designate the void, matrix and total volume, respectively.
From equation (5), $V_M = V_T(1-f)$, which upon differentiation of an incompressible matrix material, $dV_M = 0$, yields:

$$d\varepsilon_v = \frac{dV_T}{V_T} = \frac{dV_V}{V_T} = \frac{df}{1-f} \tag{6}$$

Substituting equation (6) into equation (3) give the plastic strain increment as follows:

$$d\varepsilon_1^p = \left\{2\bar{\sigma}^{(2-a)}\frac{1}{(1+R)}\left[R|\sigma_1-\sigma_2|^{a-1} - |\sigma_3-\sigma_1|^{a-1}\right] + \frac{fq_1q_2^2}{2}\sigma_{kk}\right\}\frac{2}{3q_1q_2^2\sigma_{kk}}\frac{df}{f(1-f)} \tag{7}$$

The yield condition, equation (1), and flow rule in equation (7) can determine the relationships between stress and strain as long as the current volume fraction, f, is known.
At this stage, it is interesting to consider void growth in the case of plane stress, where $\sigma_2 = \alpha\sigma_1$ and $\sigma_3 = 0$ from equation (7). This can be integrated for an initial void volume, f_o, to give:

$$\varepsilon_1^p = \left\{\frac{\left[R(1-\alpha)^a + \alpha^a + 1\right]}{(1+R)}\right\}^{\left(\frac{2}{a}-1\right)}\frac{\left[R(1-\alpha)^{a-1}+1\right]}{(1+R)}\frac{4}{3q_1q_2^2(1+\alpha)}\ln\frac{f(f_o-1)}{f_o(f-1)} + \frac{1}{3}\ln\frac{f_o-1}{f-1} \tag{8}$$

Where f_o is the initial void volume fraction.
Assuming isotropic hardening, the effective stress of the matrix material for equation (1) can be written as:

$$\bar{\sigma}_M = \frac{1}{(1-q_1f)}\left\{\left[\frac{1}{(1+R)}\left(R|\sigma_1-\sigma_2|^a + |\sigma_2-\sigma_3|^a + |\sigma_3-\sigma_1|^a\right)\right]^{\frac{2}{a}} + \frac{fq_1q_2^2}{4}\sigma_{kk}^2\right\}^{\frac{1}{2}} \tag{9}$$

If an effective matrix plastic strain increment is denoted by $d\bar{\varepsilon}_M^p$, then the plastic work done by the unit volume of a porous material is identical to that of a matrix material, which has the volume $(1-f)$. Hence,

$$dw^p = \sigma_{ij}d\varepsilon_{ij}^p = (1-f)\bar{\sigma}_M d\bar{\varepsilon}_M^p \tag{10}$$

By substituting equation (3) and (9) into equation (10), the rearrangement gives:

$$d\lambda = \frac{(1-f)}{2(1-q_1f^2)}\frac{d\bar{\varepsilon}_M}{\bar{\sigma}_M} \tag{11}$$

$$d\bar{\varepsilon}_M^p = \left\{\left[\frac{1}{(1+R)}\left(R|\sigma_1-\sigma_2|^a + |\sigma_2-\sigma_3|^a + |\sigma_3-\sigma_1|^a\right)\right]^{\frac{2}{a}} + \frac{fq_1q_2^2}{4}\sigma_{kk}^2\right\}^{\frac{1}{2}}\frac{4}{3fq_1q_2^2\sigma_{kk}}d\varepsilon_v \tag{12}$$

2.2 Work hardening ability

In the following, the flow curves of voided metals subjected to uniaxial loading are presented according to the yield criteria of Hosford. The simplified version of Gurson's model and its modified form – which are amendable to analytical derivations – are used in the analysis. Since the loading is uniaxial, it is expected to obtain results identical to that when using the original Gurson's models. In these applications the matrix material is assumed to obey the simple power-hardening law:

$$\bar{\sigma}_M = K_M \bar{\varepsilon}_M^{n_M} \dot{\bar{\varepsilon}}^{\gamma_M} \tag{13}$$

Where K_M, n_M and γ_M are the strength coefficient, strain hardening and strain-rate sensitivity exponents of the matrix material, respectively. These parameters are assumed to be initially known as indicated in the relevant figures. Note that in dealing with strain-rate sensitive materials, a viscoplastic potential identical with the yield function is assumed to exist. A surface with a constant rate of dissipation of energy per unit volume thus replaces the yield surface and the components of the strain-rate tensor become normal to it. For uniaxial loading, the effective matrix stress is related to the apparent stress when considering $\sigma_2 = \sigma_3 = 0$ in the previous yield model. The effective matrix strain can be also related to the apparent strain, ε_1, for the model by substituting equation (11) into equation (3a). Hence the apparent flow curve (i.e. that corresponding to the matrix-void aggregate as a whole) is predicted by replacing the matrix effective stress and strain in equation (13). Thus, the apparent flow stress as provided is given by:

$$\bar{\sigma} = K_M \frac{(1-q_1 f)^{n_M+1+\gamma_M}}{(1-f)^{n_M+\gamma_M}} \left[1 + q_1 q_2^2 \frac{f}{4}\right]^{-\frac{(n_M+1+\gamma_M)}{2}} \varepsilon_1^{n_M} \dot{\varepsilon}_1^{\gamma_M} \tag{14}$$

3. Results and discussion

Figure 1 shows the yield surfaces in a normalized principal stress plane calculated from equation (9) for Hosford's and Hill's yield criteria for a void volume fraction with $R = 1.87$. The predicted results are compared with the measured yield surface by Kuwabara [15] for the equibiaxial tensile testing of cold-rolled low-carbon steel sheets.

The shrinkages of the yield surfaces were self-evident as the void volume fraction increased. This shows that the strain softening of the material occurred through damage evolution caused by plastic deformation. Comparing Hosford's yield criterion with Hill's one shows that the shrinkage of the yield surface is lower at the case of Hosford than for Hill's case as increasing void volume fraction. The result of Hill's yield criterion did not agree well with that obtained experimentally by Kuwabara, yet that of Hosford's yield criterion agrees well with the experiment results.

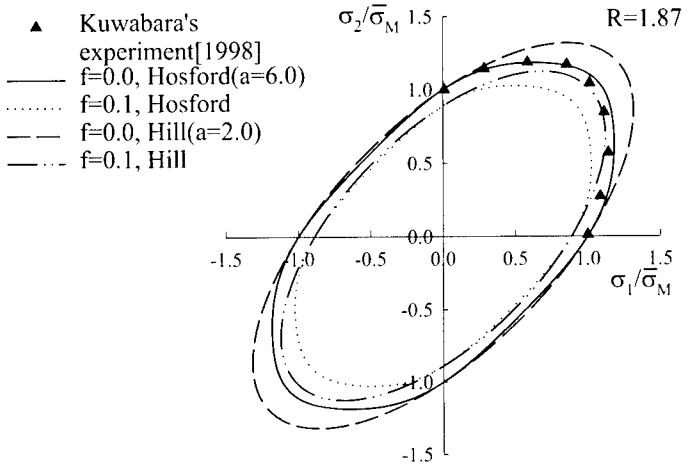

Figure 1 Effect of void fraction on the yield loci

Figure 2 shows the variation of void volume fraction with strain under equibiaxial tension for three alloys tested by Parmar and Mellor [7]. Generally, three zones can be distinguished: nucleation, growth and coalescence of voids (two of them appear only in Figure 2). The initial value of the void volume fraction employed in the analysis was obtained from extrapolation of the curve representing the growth zone to the zero strain (vertical) axis. . The extrapolation of the curve to strain value of $\varepsilon = 0.0$ for steel ($R = 1.68$), 70/30 brass ($R = 1.68$) and soft aluminum ($R = 0.64$) gives the initial void volume fraction values of $f_0 = 7\times10^{-4}, f_0 = 3\times10^{-4}$ and $f_0 = 4\times10^{-5}$, respectively. In the present analytical model, only void growth is considered excluding the initiation phase in the nucleation state

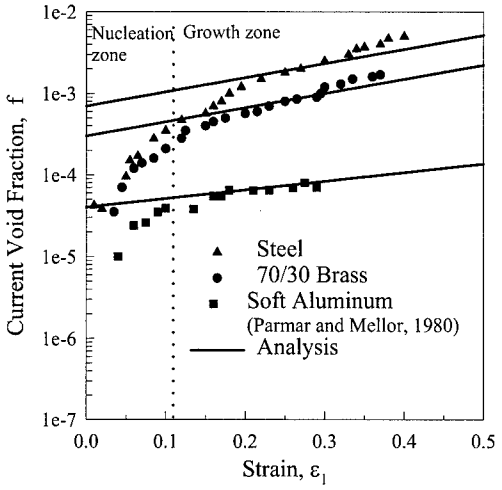

Figure 2 Measured current void fraction with strain under equibiaxial tension for different materials

Figure 3 shows the predicted stress-strain curves at the appropriate void volume fraction, which are also compared with Ragab's [16] analysis using Hill's yield criterion and experimental curves for the sintered Ti which have $K_M = 688MPa$, $n_M = 0.19$ and $\gamma_M = 0.0$. Modification of Gurson-Tvergaard's model in cooperation with Hosford's anisotropic yield criterion for voided sheet metal can deduce closer predictions to the

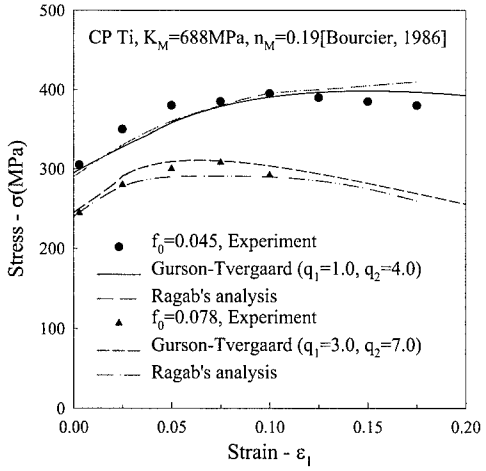

Figure 3 Experimental and analyzed tensile flow curves for CP Ti

experimental results with proper values of fitting parameters. These introduced parameters in Gurson-Tvergaard's models are only fitting parameters where they could not be related to the materials or even the initial porosity level.

4. Conclusion

Gurson-Tvergaard's yield function for voided materials was extended to describe the plastic deforming characteristic of anisotropic sheet metals. The variation of yield surface relative to the void volume fraction and the damage evolution of an anisotropic sheet metals were investigated using the Hosford's anisotropic yield function and corresponding constitutive law for anisotropic voided sheet metals. The anisotropic yield function for voided sheet metals gave an effective representation of the yield behavior of an anisotropic sheet. This result clarified that Gurson-Tvergaard's models with Hosford's criterion could predict well the effect void volume fraction on the yield loci. Gurson-Tvergaard's model with the proper initial volume fraction values determined as a fitting parameters can fit their plastic forming flow behaviors reasonably well. Accordingly, the modification of Gurson-Tvergaard's model with approximate anisotropic yield function of Hosford's criterion for voided anisotropic sheet metals can be successfully used to evaluate the forming limit and damage evolution of voided sheet metals.

Acknowledgement
This work was financially supported by the Brain Korea 21 Project.

References

1. Keeler, S.P. : SAE paper, 1965, No.650535
2. Goodwin, G.M., SAE Paper, 1968, No. 680093
3. Marciniak, Z. and Kuczynski, K, Int. J. Mech. Sci. Vol. 9(1967), pp. 609~620
4. Storen, S. and Rice, J., J. Mech. Phys. Solids, Vol. 23(1975), pp. 421~441
5. Zhao, L., Sowerby, R. and Sklad, M.P., Int. J. Mech. Sci., Vol. 38(1996), pp. 1307~1317
6. Graf, A. and Hosford, W.F., Meta. Trans., Vol. 24A(1993), pp. 2503
7. Parmar, A. and Mellor, P.B., Int. J. Mech. Sci., Vol. 22(1980), pp. 133~150
8. Gurson, A.L., J. Eng. Mater. Tech. ASME, Vol. 99(1977), pp. 2~15
9. Tvergaard, V., Mechanica, Vol. 26(1991), pp. 11~16
10. Hill, R., Oxford University Press, London(1950)
11. Hill, R., Math. Proc. Camb. Phil. Soc., Vol. 85(1979), pp. 179~191
12. Hosford, W.F., Proc. 7th North Am. Metalworking Conf., SME, Dearborn, MI(1979), pp. 191~196
13. Barlat, F. and Lian, J., Int. J. of Plasticity, Vol. 5(1989), pp. 51~66
14. Y.S. Kim, S.Y. Won and H.S. Son, being printed Int. J. of KSME, 2001.
15. Kuwabara, T., IKeda, S. and Kuroda, K., J. Mater. Proc. Tech., Vol. 80(1998), pp. 517~523
16. A.R. Ragab and Ch.A.R. Saleh, Int. J. of Plasticity, Vol. 15(1999), pp. 1041-1065.

ADVANCED INDENTATION APPROACH TO CHARACTERIZE MICRO-MECHANICAL PROPERTIES OF SMALL-VOLUME MATERIALS

Yeol Choi*, Yun-Hee Lee, Jeong-Hoon Ahn and Dongil Kwon

School of Materials Science and Engineering
Seoul National University, Seoul 151-742, KOREA
*R & D Division , Frontics, Inc., Seoul 151-742, KOREA

ABSTRACT

Evaluation of mechanical properties of micro-materials is needed for new development of advanced materials and safe usage of current structural components. But, conventional standard methods for mechanical properties have the problems of bulky specimen, destructive procedure and complex procedure of specimen sampling. Therefore, an advanced indentation technique was proposed for simple and non-destructive testing of in-field structures and for local range testing of micro-materials. This test measures indentation load-depth curve during indentation and analyzes the mechanical properties related to deformation. Hardness and elastic modulus of micro-phase can be estimated by applying small indentation load of mgf order. And, flow properties such as yield strength, tensile strength and work hardening index can be evaluated through the analysis of the deformation behavior beneath the spherical indenter. In this paper, we characterized the micro-mechanical properties of each phases in ultra-fine grained steels. And, work-hardening behaviors including the yield and tensile strengths of various structural steels are evaluated.

1. INTRODUCTION

Large-scaled structures and industrial facilities increase with developments of techniques. And, the operating conditions of these facilities become severe. Especially, the reliabilities of aircraft components are highly reduced under corrosive environment, moisture and temperature. Therefore, a proper diagnosis on the mechanical properties of the components is indispensable for the safe operation and maintenance [1]. This diagnosis technique should have some advantages such as the rapid and easy procedure, repeatability, non-destructiveness,

and in-situ testing of operating components. Mechanical properties of materials have been evaluated by using the uni-axial tensile and fracture mechanics tests. However, it is very difficult to obtain the bulky standard specimens from in-service structural components without strength reduction of the components. Thus, a simple indentation hardness test is proposed as a nearly non-destructive mechanical test. But, the hardness from the observation of indentation mark involves some measuring errors and the effects of surface roughness and friction. Also, the hardness value is just a qualitative estimation of combined mechanical properties.

Therefore, a new indentation technique to evaluate various mechanical properties has been developed by measuring the materials response during indenting cycle and by analyzing the indentation deformation and stress fields beneath the indenter theoretically [2-4]. The deformation behaviors of a specimen by penetration of the indenter are represented as an indentation load-depth curve. This curve consists of the elastic/plastic loading and elastic unloading parts. Various mechanical properties such as work-hardening index, yield and tensile strengths are evaluated by defining the effective stress and strain values from the analysis of load-depth curve and the stress fields modeling beneath the spherical indenter [5]. The nanoindentation technique as a kind of advanced indentation technique can also be used to evaluate the mechanical properties in the sub-micron regime of multiphase materials. Because, a nanoindenter can apply a ultra-low load to each phase using a sharp indenter.

In this study, we evaluated the flow properties including work-hardening index, yield and tensile strengths of various structural steels and aluminum alloy from the advanced indentation technique. The mechanical properties compared with the results from the uni-axial tensile and compression tests. The nanoindentation technique was applied to analyze the strength properties of ultra-fine grained steels. Ultra-fine grained steels are composed of various micro-phases such as ferrite, pearlite and martensite. But, the contributions of micro-phases to the strength have not been studied yet. Thus, we used the nanoindentation combined with atomic-force microscopy to analyze these mechanical properties. The overall strength of ultra-fine grained steels is then analyzed in terms of the volume fractions and strengths of the micro-phases.

2. THEORETICAL ANALYSIS FOR SPHERICAL INDENTATION

Strength properties related to plastic deformation such as yield, tensile strengths and hardness were evaluated by analyzing the unloading curve from the advanced indentation test [5]. For this end, we analyzed the contact radius. Hardness was calculated by dividing indentation load with contact area. Flow stress and effective strain were defined as the terms

of contact radius, mean pressure and indenter radius. And then, these parameters were related with strength properties and the detail researches were summarized below.

2.1 Contact properties between indenter and specimen

The advanced indentation system developed by Frontics and indentation load-depth curve are shown in Fig. 1. The indentation depth consists of plastic contact depth and elastic deflection depth around contact. The separation of plastic contact depth h^*_c from the total indentation depth h is very important, because hardness means the resistance to plastic deformation. The contact depth [3] at maximum indentation load can be evaluated by analyzing the indentation load-depth curve as shown in Eq. (1) and by considering the indenter shape.

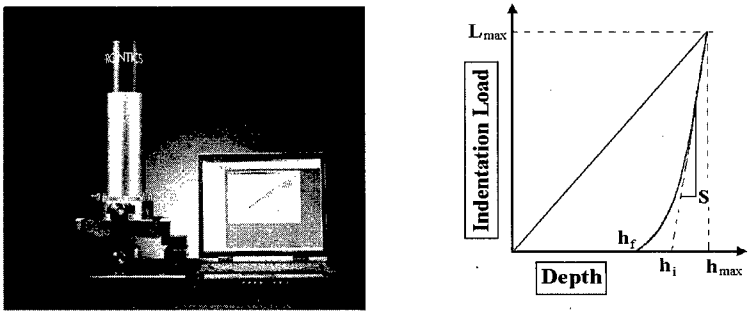

(a) (b)

Fig. 1. (a) advanced indentation system and (b) schematic of indentation load-depth curve.

$$h_c^* = h - \omega(h - h_i), \tag{1}$$

where, h_i is the intercept indentation depth as shown in figure 1 (b) and indenter shape parameter ω is 0.72 for sharp Berkovich and 0.75 for blunt spherical indenters. And then, hardness is calculated using Eq. (2). The relationship between indentation depth and contact area is obtained from the indenter geometry for large indentation. However, it was calibrated as an empirical fitting curve for nanoindentation test.

$$H = \frac{L_{max}}{A_c} = \frac{L_{max}}{f(h_c^*)}. \tag{2}$$

But, in the case of advanced indentation with a 1mm-diametered spherical indenter, the deformation shape is more complex by the effect of material pile-up around the contact [6-7].

The plastic contact radius a with pile-up was expressed as Eq. (3) in the terms of work-hardening index n and the spherical geometry of indenter.

$$a = \frac{5}{2}\frac{2-n}{4+n}\left(2Rh_c^* - h_c^{*2}\right). \tag{3}$$

2.2 Flow properties of plastically hardening materials

Generally, the relationship between true stress and true strain is expressed as Eq. (4) after initial yielding as same as the result from the uniaxial tensile test.

$$\sigma = K\varepsilon^n. \tag{4}$$

The true strain from spherical indentation is defined as Eq. (5) by differentiating the indentation depth with z-directional displacement and multiplying a fitting constant. The fitting constant was generally 0.1 [5].

$$\varepsilon = \frac{\alpha}{\sqrt{1-(a/R)^2}}\frac{a}{R}. \tag{5}$$

Deformation behaviors beneath a spherical indenter divided as 3 steps of elastic, elastic/plastic and plastic deformations [2,4].

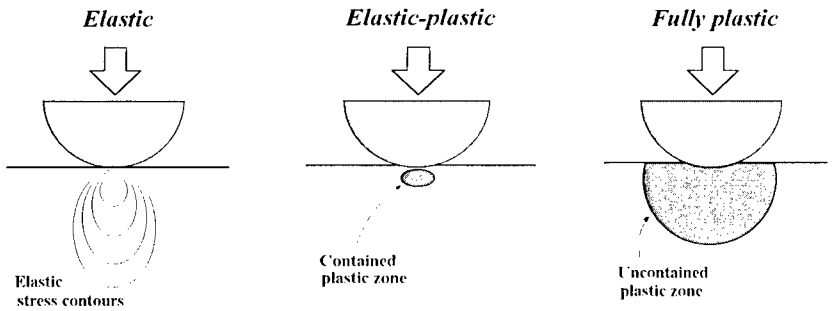

Fig. 2. Schematic of deformation steps during spherical indentation.

Reversible deformation in the elastic step does not leave indentation mark. Local plastic zone forms at 0.5a point along the z-axis and expands to surface. However, the material beneath the contact region generally exists in the plastic step, because the expansion of plastic zone is very fast by the effect of surface friction. The ratio of true stress to mean contact pressure is constant in this step as shown in Eq. (6). And, the value of the ratio was about 3 [5].

$$\frac{P_m}{\sigma} = \Psi . \tag{6}$$

The values of true stress and true strain were evaluated from each unloading curve in multicycle indentation load-depth curve. And, the evaluated values were fitted using the flow curve as shown in Eq. (4). The work-hardening index was the exponent in Eq. (4). The yield and tensile strengths were calculated by extrapolating the curve into initial yielding and maximum tensile regions.

3. EXPERIMENTAL PROCEDURES

3.1 Advanced indentation testing using spherical indenter

Two structural steels of SM50 and SA508 and one Al alloy were used as specimens. 20mm×20mm×10mm sized steel specimens were prepared by surface grinding and polishing. But, 10mm diametered rod specimen was used for advanced indentation in the case of Cr containing Al alloy. Testing machine was AIS2000 made by Frontics, Inc. The maximum capacities of load and displacement sensors were 300kgf and 2mm, respectively. The resolutions of both sensors were 300gf and 0.2μm. The indenter is a tungsten ball of 0.5mm radius. The testing modes for flow properties can be selected as maximum load and maximum depth controlling methods. And, maximum depth controlling mode for same equivalent strain was used in this study. The maximum indentation depth was 250μm, and 15 partial unloadings down to 70% of maximum load at each point were applied. All loading and unloading speed was 0.3mm/min. The distance between indentation marks was 3mm to avoid the superposition of plastic deformation fields. The indentation load-depth curve obtained from the multiple indentation technique was analyzed as flow properties including yield strength, work-hardening exponent and ultimate tensile strength based on the theoretical background. Indentation load-depth curve with slippage at low load region was treated as testing error and excluded from the analysis. And, uniaxial tensile and compression tests were done on 3 specimens for comparison.

3.2 Micro-phase characterization using nanoindentation testing

Ultra-fine-grained steels were fabricated by isothermal multi-pass rolling of API X65 steel above the Ar3 transformation temperature and subsequent cooling steels at Pohang Iron & Steel Co., Ltd. The chemical composition of API X65 steel is 0.1C-0.26Si-1.5Mn-0.016Ti-0.046Nb-0.053V. The specimen formed by hot rolling and water quenching had ferrite and martensite phases. The ferrites are divided by grain size into strain-induced dynamic-transformation ferrite and cooling ferrite.

For the nanoindentation test, 10mm×10mm×1mm specimens were machined from the rolled plate. The specimen surface was mechanically polished and etched in 2% Nital solution. Optimum indenting rate was determined as 100 μN/s up to a maximum indentation load of 1000 μN. Nanoindentation tests were done on the surface of specimen after indenter positioning by AFM. Several indentation mark arrays with sub-micrometer spacing were made. After indenting, the residual indentation, indented grain shape, and size were observed by AFM.

4. RESULTS AND DISCUSSION

4.1 Flow properties of structural steels and aluminum alloy

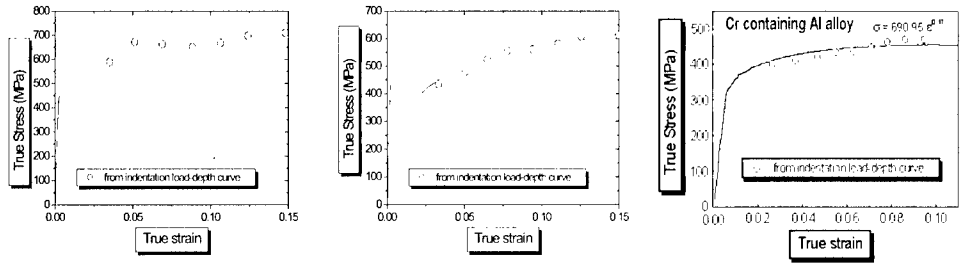

(a) SM 50 (b) SA508 (c) Al alloy

Fig. 3. Comparisons between flow properties calculated from advanced indentation (dotted line) and those from standard tensile and compression tests(solid line).

Flow properties evaluated from uniaxial tensile and compression tests were plotted as solid line in Fig. (3). The dotted lines expressing the flow properties from advanced indentation superposed well with the results from conventional tensile test. In the case of Al alloy, the evaluated flow properties from indentation also agree with the results form uniaxial

compression test. Al alloy has the crystal structure of face centered cubic. Therefore, this alloy has no difference in two deformation results from uniaxial tensile and compression test.

4.2 Characterization of micro-phases in ultra-fine grained steel

An AFM was used for accurate indenter positioning and observation of the ultra-fine ferrite. Hardness values of various ferrite phases differed with grain size and shape. The hardness of the fine grain size of 1~2 μm, classified as strain-induced dynamic-transformation ferrite (SIDTF) [8], was about 3 GPa above the 2 GPa of coarse ferrite transformed during cooling. And, there was the third unidentified phase. The variations of indentation load-depth curves are shown in Fig. 4. The unidentified phase had much lower maximum indentation depth than ferrite. Also, it had very high hardness compared with ferrite values shown in Table 1. This phase had a unique island shape with 4~5 μm grain size (different from ferrite phases in AFM and SEM images). It had the same alloy content as ferrite phase from the EDS test. Consequently, from these results, the unidentified phase was determined to be martensite. The average hardness of martensite was about 5GPa.

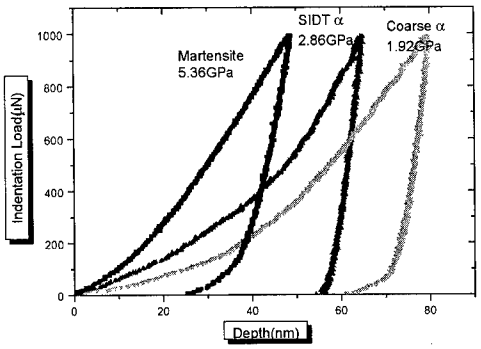

Fig. 4. Load-depth curves of micro-phases in ultra-fine-grained steel.

Table 1. Properties of micro-phases in ultra-fine-grained steels from nanoindentation.

	SIDTF	Coarse Ferrite	Martensite
Hardness	2.92	2.01	5.74

Strain-induced dynamic-transformation ferrite has equiaxed and polygonal grain shape with fine grain size less than 2 μm. The hardness value of SIDTF was 2.6~3.1 GPa higher than 2.01GPa of coarse cooling ferrite. The cooling ferrite has random grain shape and coarse grain size about 5 μm. SIDTF was found to have high strength compared with that of normal

coarse ferrites in this study. The strengthening mechanisms are expected to be the presence of cementite particles in SIDTF grain and dislocation movement.

Hard cementite particles play a role in strengthening SIDTF. There are cementite particles of size 0.1~0.2 μm at grain boundary between individual SIDTF grains and also much smaller cementite particles inside the SIDTF grain. Cementite particles are formed by the precipitation of supersaturated carbon in SIDTF ferrite during cooling [9-10]. The rate of phase transformation of SIDTF is very rapid, and carbon diffusion is not fast enough for para-equilibrium between austenite and ferrite. SIDTF ferrite is thus supersaturated with carbon, and cementite particles formed during cooling that act as a barrier to dislocation movement and consequently strengthen SIDTF.

5. CONCLUSIONS

The stress and strain beneath the spherical indenter were defined in terms of contact radius, mean contact pressure and indenter radius. The flow properties of structural steels and Al alloy were agreed well with the results from uniaxial tensile and compression tests.

The strength characteristics of micro-phases including ferrite and martensite in ultra-fine-grained steels was analyzed using nanoindentation and AFM. Fine ferrite grains (1~2 μm) of equiaxed, polygonal grain shape were formed by strain-induced dynamic transformation. This strain-induced dynamic-transformation ferrite has higher hardness than coarse ferrite. This was explained by the action of fine cementite particle formed during rapid cooling.

REFERENCES

1. D. Kwon: Present Status of Materials Damage Evaluation for Industrial Structure Facilities, Report for Ministry of Science & Technology (1998), pp. 17-69.
2. F.A. Francis, J. Eng. Mater. Tech., Trans. ASME, Vol. 98(1976), pp. 272-281.
3. W.C. Oliver and G.M. Pharr, J. Mater. Res., Vol. 7(1992), pp. 1564-1583.
4. K.L. Johnson: Contact Mechanics, 1st ed., Cambridge Univ. Press, (1985), pp. 170-184.
5. J.H. Ahn, Y. Choi and D. Kwon, J. Korean Inst. Metal Mater., Vol. 38(2000), pp.1606-1611.
6. A.L. Norbury and T. Samuel, J. Iron Steel Inst., Vol. 117(1928), pp. 673-687.
7. R. Hill et al., Proc. Royal. Soc. London A, Vol. 423 (1989), pp. 301-332.
8. P.J. Hurley et al., Scripta Mater., Vol. 40(1999), pp. 433-438.
9. J.K. Choi et al., in Proc. of 3rd Workshop on the Development of High Performance Structural Steels for 21th Century, Pohang, (2000), pp. 17-21.
10. H. Mabuchi et al., ISIJ International, Vol. 39(1999), pp. 477-485.

Ab Initio Study on Generalized Stacking Fault Energy of Basal Plane in Magnesium

Tokuteru Uesugi, Masanori Kohyama, Masahide Kohzu and Kenji Higashi

Department of Metallurgy and Materials Science, Graduate School of Engineering, Osaka Prefecture University, Sakai 599-8531, Japan

ABSTRACT

We calculate the generalized stacking fault (GSF) energies on basal and prismatic plane in magnesium by *ab initio* pseudopotential method with periodic supercell approach. The GSF energy is identified with the energy necessary to ideal slip, and shear strength of real materials should increase as the GSF energy increases. In HCP metals including magnesium, basal slip and prismatic slip with ***a*** dislocations are well known and basal slip is dominant in magnesium. It is also investigated from the GSF energy that the dissociation with stacking fault of ***a*** dislocations on prismatic plane is not so clear. The calculated GSF energy on basal plane is much lower than that on prismatic plane. This result agrees with that the observed main slip system is basal slip in real magnesium.

1. INTRODUCTION

Recently the usage of magnesium alloys are increased as light weight and high specific strength structural materials in automotive and aerospace industries. However, it is large problem that magnesium alloys have low plastic formability because of the HCP structure. The ductility of HCP metals such as magnesium is generally lower than FCC metals. The ductility greatly depends on slip deformations and it is important to understand the deformation mechanism associated with the slip. In magnesium, $\{0001\}<11\bar{2}0>$ basal slip and $\{10\bar{1}0\}<11\bar{2}0>$ prismatic slip with ***a*** dislocation are commonly known. It has been reported that $\{10\bar{1}1\}<11\bar{2}0>$ first order pyramidal slip and $\{11\bar{2}2\}<\bar{1}\,\bar{1}23>$ second order pyramidal slip are also active in magnesium [1,2]. These slip systems are shown in Fig. 1.

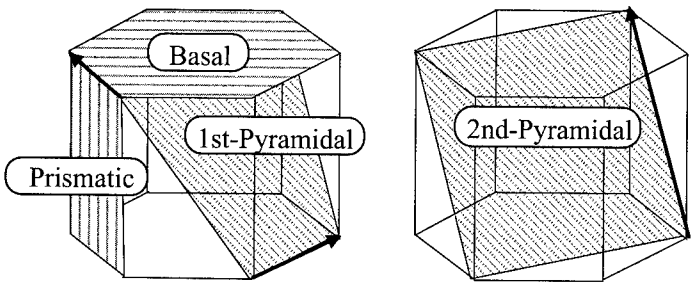

Fig. 1 Slip systems in magnesium.

Despite these many slip systems, magnesium has low ductility at room temperature because the active slip system is mainly only basal slip at room temperature. The temperature dependence of critical resolved shear stress (CRSS) of basal and prismatic slip are shown in Fig. 2. The CRSS of prismatic slip is higher over 60 times than the CRSS of basal slip (~1Mpa) at room temperature. Essentially, this difference of shear strength of slip system should depend on electronic structure. Hence, an *ab initio* calculation, witch is accurate electronic structural calculation, is required.

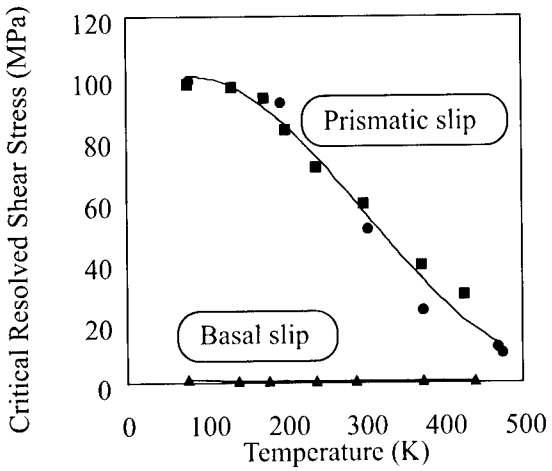

Fig. 2 The CRSS of basal and prismatic slip in magnesium [3-5].

In slip deformations, the generalized stacking fault (GSF) energy is a critical parameter. The GSF energy is defined as follows; a crystal is cut into two halves along the slip plane and one half is displaced relative to the other by the vector **t**. As this vector is varied, the energy changes and traces out the GSF energy $\gamma(\mathbf{t})$, which is defined as energy differences from bulk crystal. If this vector are varied along with Burgers vector, the GSF energy is identified with the potential necessary to ideal slip. Hence, shear strength of real materials should increase as the GSF energy increases. In the present work we employ *ab initio* pseudopotential method for magnesium to study accurate GSF energy on basal and prismatic plane and discuss the dislocation behavior.

2. CALCULATION METHODS

All calculations were performed using Cambridge Serial Total-Energy Package (CASTEP). CASTEP is an *ab initio* pseudopotential method code for the solution of the electronic ground state of periodic systems with the wavefunctions expanded in plane wave basis using a technique based on density functional theory (DFT) [6,7]. The electronic exchange-correlation potential is given by the generalized gradient approximation (GGA) of Perdew and Wang [8]. We use the pseudopotential suggested by Troullier and Martins [9]. The pseudopotential is transformed to a separable form as suggested by Kleinman-Bylander [10]. The electronic ground state is efficiently obtained using the conjugate-gradient technique [11]. The cutoff energy for the plane-wave basis is 4.36×10^{-17} J (272 eV) which is sufficient for all our purposes. The stable atomic configurations are obtained through

relaxation according to the Hellmann-Feynman forces. The periodic supercells containing 10 basal atomic layers and 12 prismatic atomic layers are used for the calculation of the GSF energies on basal and prismatic plane, respectively (see Fig. 3). For basal and prismatic supercells, Brillouin zone integration over k points are performed using 12×12×2 and 11×7×3 regular divisions of each axis in reciprocal space, respectively.

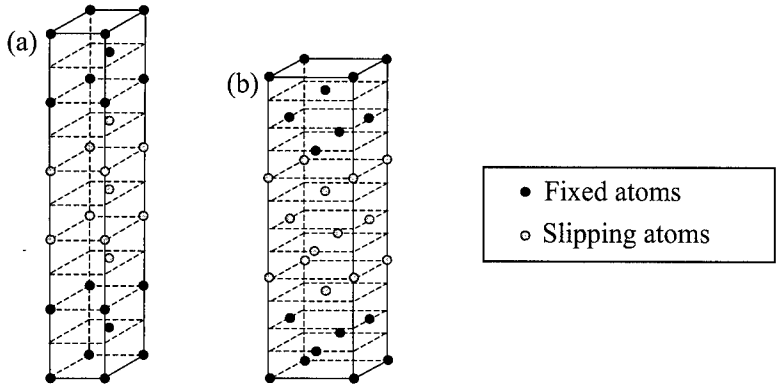

Fig. 3 The periodic supercells (a) for basal slip and (b) for prismatic slip.

The slip deformation occurs with dislocations along Burgers vector, but dislocations are dissociated to partial dislocations with stacking fault. Hence, it is important the GSF energy displaced by dissociated Burgers vector of partial dislocations. We calculate the GSF energies displaced by vector **t** that changes continuously 0 to $\boldsymbol{b}_{\text{patial}}$. The $\boldsymbol{b}_{\text{partial}}$ is dissociated Burgers vector of partial dislocations. The GSF energy $\gamma(\mathbf{t})$ is defined by

$$\gamma(\mathbf{t}) = \frac{E_{\text{fault}}(\mathbf{t}) - E_{\text{bulk}}}{2\mathbf{A}}, \tag{1}$$

where E_{bulk} is the total energy of supercell of magnesium bulk, $E_{\text{fault}}(\mathbf{t})$ is the total energy of supercell containing two generalized stacking faults displaced by vector **t**, and **A** is the area of stacking fault per a supercell.

3. RESULTS

When splitting of $\boldsymbol{a}$ dislocation in HCP metals is considered, the situation is clear on basal plane. The dissociation of $\boldsymbol{a}$ dislocations is the splitting on basal planes according to the reaction

$$\frac{1}{3}<11\bar{2}0>=\frac{1}{3}<10\bar{1}0>+\frac{1}{3}<01\bar{1}0>, \tag{2}$$

with the I_2 stacking fault between the partial dislocations.

However, the dissociation of $\boldsymbol{a}$ dislocations on prismatic plane is not so clear. Using a hard-sphere model, Tyson [12] proposed the splitting

$$\frac{1}{3}<11\bar{2}0>=\frac{1}{6}<11\bar{2}1>+\frac{1}{6}<11\bar{2}\,\bar{1}>. \quad (3)$$

Vitek and Igarashi [13] suggest from the GSF energy by empirical many-body potentials calculation that the same dislocations may also split on prismatic planes according to the reaction

$$\frac{1}{3}<11\bar{2}0>=\frac{1}{6}<11\bar{2}\mathbf{x}>+\frac{1}{6}<11\bar{2}\bar{\mathbf{x}}>, \quad (4)$$

where **x** varies from material to material. Hence, we calculate the GSF energies displaced by the vector $\boldsymbol{b}_{partial}$= 1/6[11$\bar{2}$**x**], **x** is from 0 to 1.2, in order to examine the stacking fault point on prismatic plane. We find lowest energy stable stacking fault point $\boldsymbol{b}_{partial}$=1/6[11$\bar{2}$**x**], **x**=0.76.

We also calculate the GSF energies displaced by **t**=1/6[10$\bar{1}$0]u, with u from 0 to 1 on basal plane, and the GSF energies displaced by **t**=1/6[11$\bar{2}$**x**]u, **x**=0.76, with u from 0 to 1 on prismatic plane. These are calculated by using the three different relaxation methods of atoms. First, the atomic relaxation perpendicular to the slip plane is allowed but parallel is not allowed at all. Second, the atoms of two layers constituting stacking fault are relaxed only perpendicular to the slip plane, while other atoms move freely in all directions. Third, the atoms of two layers constituting stacking fault are relaxed in all directions, while other atoms are relaxed only perpendicular to the slip plane. On both basal and prismatic plane, the GSF energies do not change very much by different three relaxation scheme. The results by third relaxation method are shown in Fig. 4. The calculated GSF energy on basal plane is much lower than that on prismatic plane. Hence, it is explained that shear strength of prismatic slip is much higher than basal slip. This result agrees with that the observed main slip system is basal slip in real magnesium.

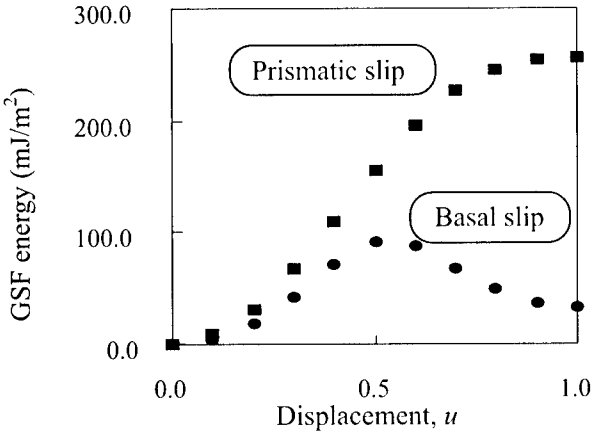

Fig. 4 The GSF energies on basal and prismatic plane.

The stacking fault energy on basal plane, which is the minimum of the GSF energy path, is 32.4 mJ/m^2. The dislocation of basal slip seems to be dissociated with widely extended stacking fault because of this stable and low stacking fault energy. On prismatic plane, it is different from basal plane, and staking fault point is the peak of the GSF energy path, and the

stacking fault energy is 255.1 mJ/m^2. It seems to be difficult that prismatic plane has stacking fault, because the stacking fault energy is not stable.

4. SUMMARY

The GSF energies on basal and prismatic plane in magnesium has been studied by *ab initio* pseudopotential method. It is also investigated that the dissociation with the stable stacking fault of ***a*** dislocations on prismatic plane is not so clear. We find the stacking fault point $1/6[11\bar{2}\mathbf{x}]$, $\mathbf{x}$=0.76. The calculated GSF energy on basal plane is much lower than that on prismatic plane. This result agrees with that the observed main slip system is basal slip in real magnesium. The stacking fault energies are 32.4 mJ/m^2 on basal plane and 255.1 mJ/m^2 on prismatic plane.

ACKNOWLEDGMENTS

We are grateful to the financial support of "the Priority Group of Platform Science and Technology for Advanced Magnesium Alloys, Ministry of Culture, Science and Education" and "The Light Metal Educational Foundation Inc.".

REFERENCES

1. H. Yoshinaga and R. Horiuch, Trans. JIM, Vol.4(1963), pp.134-141.
2. J. F. Stohr and J. Poirer, Phios. Mag., Vol.25(1972), pp.1313-1329.
3. A. Akhtar and E. Teghtsoonian, Acta Metall., Vol.17(1969), pp.1339-1349.
4. P. W. Flynn, J. Mote and J. E. Dorn, Trans. Met. Soc. AIME, Vol.221(1961), pp.1148-1154.
5. A. Akhtar and E. Teghtsoonian, Acta Metall., Vol.17(1969), pp.1351-1356.
6. P. Hohenberg and W. Kohn, Phys. Rev., Vol.136(1964), pp.864-871.
7. W. Kohn and L. J. Sham, Phys. Rev. A, Vol.140(1965), pp.1133-1138.
8. J. P. Perdew and Y. Wang, Phys. Rev. B, Vol.46(1992), pp.6671-6687.
9. N. Troullier and J. L. Martins, Phys. Rev. B, Vol.43(1991), pp.1993-2006.
10. L. Kleinman and D. M. Bylander, Phys. Rev. Lett., Vol.48(1982), pp.1425-1428.
11. M. P. Teter, M. C. Payne, and D. C. Allan, Phys. Rev. B, Vol.40(1982), pp.12255-12263.
12. W. Tyson, Acta Metall., Vol.15(1967), pp.574-577.
13. V. Vitek and M. Igarashi, Philos. Mag. A, Vol.63(1991), pp.1059-1075.

MECHANICALLY ALLOYED MAGNESIUM ALLOYS FOR HYDROGEN STORAGE

C. Suryanarayana*, E. Ivanov**, and I.G. Konstanchuk@

*Department of Mechanical, Materials and Aerospace Engineering
University of Central Florida, Orlando, FL 32816-2450, USA
**Tosoh SMD, Inc., 3600 Gantz Road, Grove City, OH 43123-1895, USA
@Institute of Solid State Chemistry, Siberian Branch of Russian Academy of Sciences,
Kutateladze 18, 630128 Novosibirsk, Russia

ABSTRACT

The synthesis of magnesium-based metal hydrides by mechanical alloying (MA) has been reviewed. MA is capable of synthesizing alloy phases in a nanocrystalline condition directly by milling and further, the hydride phase produced continues to be nanocrystalline. In comparison to conventional alloys, nanocrystalline magnesium alloys have a higher hydrogen storage capacity, do not require any (or very little) activation, and can be hydrided and dehydrided at lower temperatures and pressures. Thus, nanocrystalline magnesium alloys processed by MA seem to have a very good potential as hydrogen-storage materials.

1. INTRODUCTION

Hydrogen storage is an important topic chiefly because of its relevance to the energy economy of the future. This assumes additional significance in view of the recent energy crises and rolling blackouts even in advanced countries. Hydrogen can be stored in the form of either gaseous, liquid or solid states. Gas cylinders are far too heavy and bulky and liquid hydrogen as a fuel is energetically not very efficient. On the other hand, hydrogen stored as a metal hydride is compact, economical, safe, and easy to transport. Therefore, there have been several investigations conducted in recent years on metal hydrides. Metal hydrides have a large range of applications such as purification of hydrogen, hydrogen embrittlement in powder metallurgy, control materials in nuclear reactors, and electrodes for batteries and hydrogen storage materials.

For a material to be seriously considered for hydrogen storage, it should have (a) high hydrogen storage capacity, (b) fast kinetics of storage and removal (reversible hydrogenation and dehydrogenation), (c) low hysteresis, (d) possibility to hydride/dehydride at relatively low temperatures and pressures, preferably at room temperature and atmospheric pressure, (e) long lifetime, (f) high chemical stability and thermally easily decomposable, (g) no or minimal need to activate the material, (h) easy availability, (i) relative immunity to impurities, and (j) low cost (including that of fabrication).

Several alloys based on titanium (TiFe, TiNi, Ti_2RuFe, etc.), lanthanum ($LaNi_5$), zirconium (Zr-Ni), hafnium, vanadium, palladium, and magnesium have been explored as hydrogen storage materials [1]. Amongst these, magnesium has the pronounced advantage because of its highest hydrogen capacity (7.6 wt%) (except lithium), low price, and easy availability. Table I summarizes the characteristics of some of the hydrogen storage systems.

Table I. Hydrogen storage capacity of different hydrides

Medium	Density (g/cm^3)	Hydrogen content		Accumulated energy	
		Wt.%	H atoms/cm^3	kJ/g	kJ/cm^3
H_2, gas at 100 atm	8.2×10^{-5}	100	0.49	142.7	2.13
H_2, Liquid	0.071	100	4.2	142.7	9.96
LiH	0.8	12.7	5.3	-	-
$LiAlH_4$	0.91	10.6	5.74	-	-
MgH_2	1.4	7.6	6.7	10.8	15.64
Mg_2NiH_4	2.6	3.6	5.9	5.1	13.75
$TiFeH_2$	5.47	1.8	6.0	2.7	14.93
$LaNi_5H_6$	8.25	1.5	7.58	2.0	13.04

The conventional practice of obtaining materials for hydrogen storage consists of preparing the mixture, alloying, high-temperature annealing, crushing of alloy ingots to powder, and prolonged activation by hydriding-dehydriding cycles. Magnesium in the form of powder absorbs hydrogen more readily than other forms and 70% of the reaction can be completed within one hour at about 573 K [2]. But, in recent years the technique of mechanical alloying, amongst others, has been extensively employed to produce hydrides of magnesium and its alloys. The present article reviews the status of mechanically alloyed nanocrystalline magnesium alloys processed by MA for hydrogen storage purposes.

2. MECHANICAL ALLOYING

Mechanical alloying (MA) is a solid-state powder processing method that involves repeated welding, fracturing, and rewelding of powder particles in a high-energy ball mill. Because of the repeated fracturing of powder particles, small particles with refined grain sizes and with fresh surfaces are constantly produced. These particles have a large surface area and consequently they possess high reactivity. Generation of a high density of crystalline defects due to the heavy deformation increases the diffusivity of solute elements. The small temperature rise due to the impact of grinding balls amongst themselves, between them and the powder, and between them and the container walls also helps in the alloying behavior. Thus, blended elemental powder mixtures subjected to MA have been shown to exhibit formation of a variety of alloy phases such as supersaturated solid solutions, stable and metastable intermetallics, quasicrystalline phases, amorphous alloys, and composites. Additionally, MA can easily synthesize alloys from immiscible components, and from metal combinations that have widely differing melting points and/or vapor pressures; not easy to produce by other techniques. However, the most important attribute of MA that will be of interest for hydrogen storage materials is its ability to produce the material with nanometer-sized grain structure [3].

3. PROBLEMS IN HYDROGENATION OF MAGNESIUM ALLOYS

Magnesium, being a reactive metal, always contains a thin layer of oxide on the surface. This inhibits the absorption of hydrogen on the surface of pure magnesium in the first hydrogenation cycle [4]. MA can easily break up the surface oxide layer because of the impact forces and therefore efficient hydrogenation can occur even in the first cycle.

Another difficulty in the hydrogenation of Mg alloys is that they normally require activation to break up the surface oxide layer. This is done by annealing the metal at a high temperature of about 573 K under high hydrogen pressure (20 bar); and this needs to be repeated several times to obtain reproducible characteristics [5]. It has been shown that mechanically alloyed magnesium alloys need not be activated for efficient hydrogenation, since the oxide layer breaks down during the impact of the powder particles by the grinding medium [6].

A catalyst is often required to accelerate the kinetics of hydrogenation of Mg alloys. The catalysts investigated include palladium, nickel, and some organic compounds. Surface modification by HCl treatment and fluorination seems to remove the existing oxide layer and prohibit further oxidation by the formation of a special catalytic structure on the surface [7]. Additions of Ag, Al, Cu, In, Li, Ni, rare earths, and their combinations or compounds have been made to improve the performance of magnesium alloys [8]. Sufficient hydrogenation could be achieved in MA magnesium alloys at reasonable rates even without the addition of a catalyst.

4. SYNTHESIS OF MAGNESIUM ALLOYS

Pure magnesium metal and a variety of magnesium-based alloys have been synthesized in the nanocrystalline state by MA starting from blended elemental powder mixtures. Most commonly a SPEX 8000 mixer/mill has been used to produce small quantities of powders.

4.1. Pure Magnesium

Pure Mg powders with different grain sizes have been produced by MA. Because of the ductility of magnesium, the process parameters need to be carefully optimized to produce the metal powder in a nanocrystalline state. By milling for 0.25 h the grain size of Mg was found to be about 1 μm; subsequent milling led to further grain refinement reaching a value of 20-30 nm [8]. On the other hand, Chen and Williams [9] produced the MgH_2 phase by directly milling the Mg powder in a hydrogen atmosphere for 47.5 h in a vertical planetary mill. Huot et al. [10] produced nanocrystalline MgH_2 powder by milling the hydride powder to different times. They also noted that a metastable γ-MgH_2 phase formed after milling the powder for 2 h. Wang et al. [11] noted that milling of Mg under hydrogen atmosphere and in the presence of an additive like $ZrFe_{1.4}Cr_{0.6}$ formed the MgH_2 phase rapidly. X-ray diffraction peaks corresponding to the MgH_2 phase appeared as early as 0.25 h, while the MgH_2 peaks did not appear when the pure Mg powder (without the additive) was milled for 4 h. They had also reported formation of the γ-MgH_2 phase after milling for 1 h. Milling of the hydride phase (instead of milling the pure metal and then hydriding it) has the advantage that the hydride particles do not stick to the surface of the balls or the interior walls of the container. It has been reported that hydrogen desorption is much more rapid (at 573 K) in the milled hydride phase and that subsequent hydrogenation kinetics are also greatly improved [10]. Addition of about 5 at.% V seems to result in hydrogen desorption at even lower temperatures (473 K) [12].

4.2. Mg-Ni Alloys

Probably the most investigated magnesium alloys for hydrogen storage are the Mg-Ni alloys [13-21]. It has been well known that, in comparison with magnesium, Mg_2Ni is more stable in air (and so no activation is required), has a lower hydrogen desorption temperature of 523 K, but with a lower hydrogen capacity of only 3.6 wt% (see Table I). Synthesis of Mg_2Ni by conventional methods is difficult due to the large difference in the melting points (and hence vapor pressures) of Mg and Ni. Further, since Mg_2Ni forms by a peritectic reaction, heavy segregation of the constituents is another serious problem. MA overcomes all these problems. MA of blended elemental powders of Mg and Ni for a short time results in the formation of an intimate mixture of Mg and Ni [13], but milling for longer times produces the Mg_2Ni phase, in a nanocrystalline structure. The typical crystallite (grain) size reported varied between 10 and 30 nm [14,19,20], even though a value as low as 4 nm has also been reported [16]. In addition to the monolithic Mg_2Ni intermetallic, two-phase Mg-Mg_2Ni alloys have also been synthesized by a proper choice of the proportion of Mg and Ni in the initial powder mixture.

The phase formed on hydriding the Mg-Ni alloys has been reported to be Mg_2NiH_4. At low temperatures of hydriding, this phase has an orthorhombic/monoclinic structure but at higher temperatures (>523 K), it undergoes a polymorphic transformation to the cubic structure.

4.3. Other Magnesium Alloys

Some work is also reported on Mg-Fe [22,23], Mg-$MmNi_5$ (Mm = misch metal) [24] and other alloy systems with the hope of obtaining higher storage capacities and/or faster kinetics of hydrogenation/dehydrogenation. Other less extensively investigated systems include magnesium with the additions of metals (Ag, Al, Ce, Co, Cr, Cu, Cu-Ni, In, Li, Mn, Nb, Ti, V, Y, Y-Zn, Zr), non-metals (C and Si), mixtures of a non-metal and a metal (graphite and Pd), transition metal oxides of Ti, V, Sr, Mn, Fe, or Ni, intermetallics of the $CaCu_5$ structure type ($LaNi_5$, $CFMmNi_5$ (CF= cerium-free), MmM'_5 where Mm is misch metal and M' is nickel partly replaced by Al, Co, and Mn), and other intermetallics (FeTi, Mg_2Cu, Mg_2Ni, YNi_2, $ZrFe_{1.4}Cr_{0.6}$, $TiMn_{1.5}$), or mixtures of intermetallics (La_2Mg_{17}-$LaNi_5$, and Mg_2Cu-$Ti_{0.6}Zr_{0.4}Mn_{0.8}CrCu_2$). Some alloys, without disclosing their composition, have also been reported to have the hydrogen storage capacity close to that of pure magnesium [25].

5. HYDROGEN STORAGE CAPACITY AND KINETICS

Hydrogen absorption kinetics are temperature dependent, increase with a decrease in grain size, and with additions of other phases such as $LaNi_5$ (with a consequent decrease in the amount of hydrogen); all of these can be easily achieved by MA. It has been consistently reported by many investigators that the temperatures at which absorption and desorption of hydrogen occur

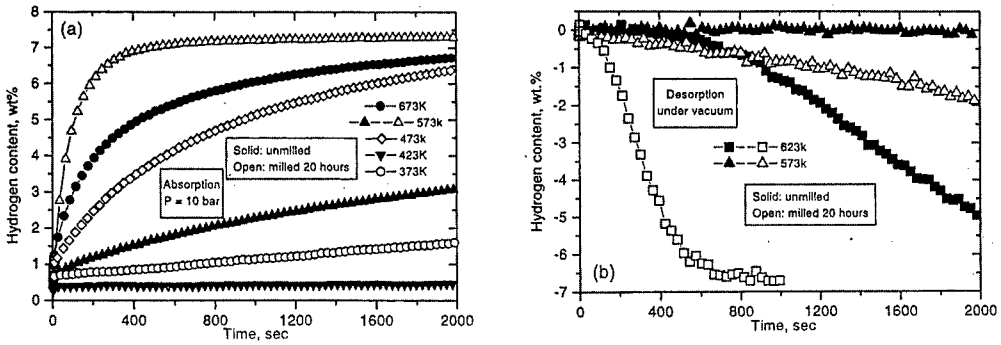

Figure 1. (a) Hydrogen absorption and (b) desorption curves for unmilled (solid symbols) and 20 h milled (open symbols) MgH_2 at various temperatures.

are lower in MA powders. In fact, it has been reported [26] that the unmilled Mg powder does not absorb any hydrogen below 423 K, while the milled powder absorbs a significant amount at 373 K. Further, it takes more than 30 min to store 3 wt.% of hydrogen in the unmilled powder, while it takes only 6.5 min to store 7 wt% hydrogen in the milled powder [26]. A similar behavior was reported for the desorption behavior (Figure 1). In addition to decreasing the absorption temperature, milling of the powders also increases the amount of hydrogen stored in the material. All these beneficial effects have been explained mainly on the basis of the grain size refinement achieved in these alloys by MA. Figures 2 and 3 show that the amount of hydrogen increases as the grain size decreases for pure magnesium and Mg_2Ni, respectively. Figure 2 clearly shows that while the coarse-grained (1 μm) magnesium powder hardly absorbs any hydrogen at 573 K, nanocrystalline magnesium obtained by MA absorbs as much as 6 wt.%

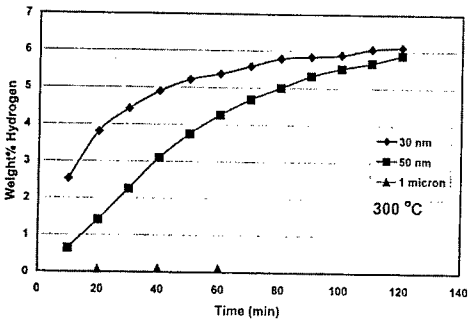

Figure 2. Effect of grain size on hydrogen absorption in MA magnesium powder. Mg_2Ni.

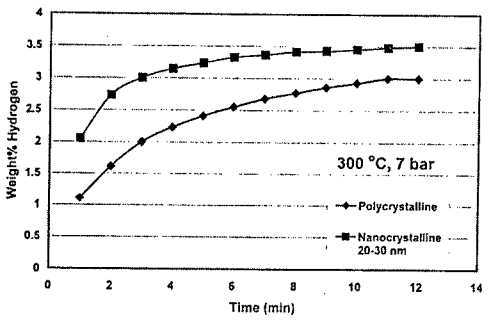

Figure 3. Rate of hydrogen absorption by polycrystalline and nanocrystalline

hydrogen. It has also been noted that the nanocrystalline Mg_2Ni compound synthesized by MA could absorb hydrogen rapidly without activation. The $Mg+Mg_2Ni$ composites need activation; but, once activated they absorb hydrogen more rapidly than Mg_2Ni at low temperatures and with a high capacity [19].

Reasons for the increased hydrogen content and lower absorption/desorption temperatures in MA powders can be traced to three factors. Firstly, MA results in the formation of a variety of crystalline defects (dislocations, grain boundaries, vacancies, stacking faults, and others), which act as heterogeneous sites for the nucleation of the hydride phase. Secondly, the presence of these defects and the creation of fresh surfaces allow the hydrogen atoms to absorb and penetrate the material more easily. Thirdly, the large grain boundary area (due to the small grain size) allows faster diffusion of hydrogen and hence faster growth of the hydride phase.

The nanocrystalline grain sizes in the MA powders have been shown to be quite stable and that grain growth is very limited reaching only 30 nm at 723 K. As expected, milling of two brittle compounds such as MgH_2 and $LaNi_5$ produced a smaller particle size, thus improving the hydrogen absorption kinetics; desorption kinetics were not, however, improved [27]. It has also been reported that addition of titanium to Mg_2Ni increases the thermal stability of the nanostructure, even though it destabilizes the hydride phase slightly [28].

The alloy constitution seems to affect the hydrogen sorption kinetics. For example, addition of Ti and V to Mg_2Ni improved the sorption kinetics. It has also been reported that the sorption kinetics of ternary Mg-La-Ni alloys are better than Mg-La or Mg-Ni binary compositions [27].

6. MECHANISM OF HYDRIDE FORMATION

The formation of hydrides during hydrogenation has been explained [13] by suggesting that MgH_2 is formed around the catalyst particles (Figure 4). Since it is difficult for the hydrogen to diffuse through the hydride layer, the reaction slows down with continued hydriding. With an increase in the catalyst concentration, the thickness of the hydride layer, determined by the catalyst particle spacing, decreases and therefore the amount of hydride formed increases. But, on a weight basis, the amount of hydrogen decreases due to the high atomic weight of the catalyst. Experimentally it was found that the optimum catalyst content is in the range of 2 to 25 wt% [1]. However, in alloys subjected to MA, a high reaction rate and sufficiently high hydrogen capacity are achieved due to the absence or only a small amount of the catalyst [29].

During MA of magnesium powders it has been observed that the hydrogen pressure in the milling chamber decreases [9]. It was explained that hydrogen is first absorbed on new particle surfaces created by fracturing during initial milling. The absorbed hydrogen then reacts with the metal to form the hydride during continued milling. It was also suggested that the hydride embrittlement of the powder particles promotes fracturing and particle size reduction resulting in a large surface area for hydrogen absorption.

Another mechanism that has been proposed is that in the first stages of the interaction of hydrogen with a metal, a solid solution of hydrogen in the metal is formed; nuclei of the hydride phase form with continued hydriding [30].

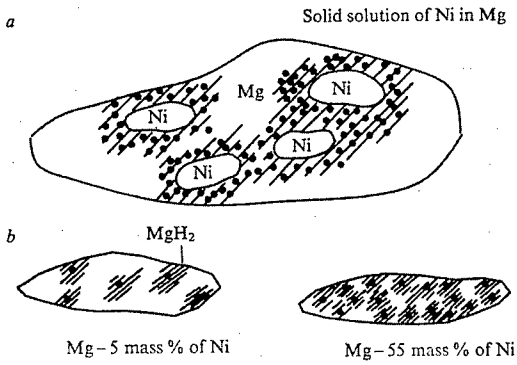

Figure 4. Schematic diagram showing the effect of nickel content (catalyst) on the amount of hydride phase formed.

7. CONCLUDING REMARKS

All the available results indicate that MA is a promising and economical method (consumes much less energy and time than other conventional methods) for the preparation of hydrogen- storage alloys. The main advantage is the ability to synthesize nanocrystalline alloys, which absorb higher amounts of hydrogen and at a rapid rate. Further, these nanocrystalline alloys do not require any activation before hydrogenation. These effects have been attributed to the formation of fresh surfaces and a variety of crystalline defects that enhance the diffusivity of hydrogen into the metal. Still higher values of hydrogen capacity and/or faster rates of hydrogenation could be achieved by adding catalysts. Even though these attributes are applicable to all alloys processed by MA, magnesium hydrides appear to be most promising because of their low cost and easy availability.

The research activity in this area is still in the early stages. A great variety of potential alloys still await investigation and optimization of process parameters is still to be performed to achieve the best combination of highest hydrogen capacity, fast kinetics of hydrogenation/ dehydrogenation, sufficient reactivity at relatively low temperatures and pressures.

REFERENCES

1. I.G. Konstanchuk, E.Yu. Ivanov, and V.V. Boldyrev, Russian Chem. Rev., Vol. 67 (1998), pp. 69-79.
2. B. Vigeholm, K. Jensen, B. Larsen, and A. Schroder-Pedersen, J. Less-Common Metals, Vol. 89 (1983), p. 135.
3. C. Suryanarayana, Prog. Mater. Sci., Vol. 46 (2001), pp. 1-184.
4. F.D. Manchester and D. Khatamian, Mater. Sci. Forum, Vol. 31 (1988), p. 261.
5. J.J. Reilly an R.H. Wiswall, Jr., Inorg. Chem., Vol. 7 (1968), p. 2254.

6. L. Zaluski, A. Zaluska, P. Tessier, J.O. Ström-Olsen, and R. Schulz, J. Alloys & Compounds, Vol. 217 (1995), pp. 295-300.
7. X.L. Wang, N. Haraikawa, and S. Suda, J. Alloys & Compounds, Vol. 231 (1995), pp. 397-402.
8. A. Zaluska, L. Zaluski, and J.O. Ström-Olsen, J. Alloys & Compounds, Vol. 288 (1999), pp. 217-225.
9. Y. Chen and J.S. Williams, J. Alloys & Compounds, Vol. 217 (1995), pp. 181-184.
10. J. Huot, G. Liang, S. Boily, A. Van Neste, and R. Schulz, J. Alloys & Compounds, Vol. 293-295 (1999), pp. 495-500.
11. P. Wang, H.F. Zhang, B.Z. Ding, and Z.Q. Hu, J. Alloys & Compounds, Vol. 313 (2000), pp. 209-213.
12. G. Liang, J. Huot, S. Boily, and R. Schulz, J. Alloys & Compounds, Vol. 305 (2000), pp. 239-245.
13. A. Stepanov, E. Ivanov, I. Konstanchuk, and V. Boldyrev, J. Less-Common Metals, Vol. 131 (1987), pp. 89-97.
14. L. Zaluski, A. Zaluska, and J.O. Ström-Olsen, J. Alloys & Compounds, Vol. 217 (1995), pp. 245-249.
15. H. Aoyagi, K. Aoki, and T. Masumoto, J. Alloys & Compounds, Vol. 231 (1995), pp. 804-809.
16. Arvind Kumar Singh, Ajay Kumar Singh, and O.N. Srivastava, J. Alloys & Compounds, Vol. 227 (1995), pp. 63-68.
17. J. Huot, E. Akiba, and T. Takada, J. Alloys & Compounds, Vol. 231 (1995), pp. 815-819.
18. R.L. Holtz and M.A. Imam, J. Mater. Sci., Vol. 32 (1997), pp. 2267-2274.
19. G. Liang, S. Boily, J. Huot, A. Van Neste, and R. Schulz, J. Alloys & Compounds, Vol. 267 (1998), pp. 302-306.
20. N.H. Goo, J.H. Woo, and K.S. Lee, J. Alloys & Compounds, Vol. 288 (1999), pp. 286-293.
21. Z. Dehouche, R. Djaozandry, J. Goyette, and T.K. Bose, J. Alloys & Compounds, Vol. 288 (1999), pp. 312-318.
22. I.G. Konstanchuk, E. Ivanov, M. Pezat, B. Darriet, V.V. Boldyrev, and P. Hagenmuller, J. Less-Common Metals, Vol. 131 (1987), pp. 181-189.
23. R.L. Holtz and M.A. Imam, J. Mater. Sci., Vol. 34 (1999), pp. 2655-2663.
24. S.S. Sai Raman and O.N. Srivastava, J. Alloys & Compounds, Vol. 241 (1996), pp. 167-174.
25. L. Zaluski, A. Zaluska, P. Tessier, J.O. Ström-Olsen, and R. Schulz, Mater. Sci. Forum, Vol. 225-227 (1996), pp. 853-858.
26. R. Schulz, J. Huot, G. Liang, S. Boily, G. Lalande, M.C. Denis, and J.P. Dodelet, Mater. Sci. & Eng., Vol. A267 (1999), pp. 240-245.
27. G. Liang, J. Huot, S. Boily, A. Van Neste, and R. Schulz, J. Alloys & Compounds, Vol. 297 (2000), pp. 261-265.
28. G. Liang, J. Huot, S. Boily, A. Van Neste, and R. Schulz, J. Alloys & Compounds, Vol. 282 (1999), pp. 286-290.
29. E. Ivanov, I.G. Konstanchuk, A.A. Stepanov, and V.V. Boldyrev, Dokl. Akad. Nauk SSSR, Vol. 286 (1986), pp. 385-388.
30. M. Mintz and J. Bloch, Prog. Solid State Chem., Vol. 16 (1985), p. 163.

A MICROSTRUCTURAL MODEL FOR THE PREDICTION OF HIGH CYCLE FATIGUE LIFE BASED ON THE SMALL CRACK THEORY

J. S. Park, S. H. Park* and C. S. Lee

Center for Advanced Aerospace Materials
Department of Materials Science and Engineering
Pohang University of Science and Technology, Pohang 790-784, KOREA
*POSCO Technical Research Laboratories, Pohang 790-785, KOREA

ABSTRACT

The purpose of the present research is to develop a model predicting the high cycle fatigue life in relation to the microstructural variable, especially, grain size. To achieve this goal, the concept of small crack propagation has been adopted since it is thought that the fatigue crack initiation is similar to the propagation of small crack, which is greatly influenced by the microstructural variables. It is assumed that the whole fatigue crack initiation process can be represented by the microcrack propagation through one grain and one barrier, i.e., consisting of two steps, the propagation through one grain and the arrest at a barrier. For the first step, modification of the small crack growth law suggested by K. J. Miller has been made to consider the influence of grain size on the resolved shear stress, which is the major driving force for the small crack propagation. For the second one, the concept of strain accumulation criterion has been used to calculate the cycles required in overcoming a barrier. Reasonable agreement is found between the experimental data and the predicted curve.

1. INTRODUCTION

High cycle fatigue properties are generally represented by the S-N(stress-life) curves[1]. Since obtaining a S-N curve takes great time and efforts, there have been several attempts to develop the fatigue life prediction model. Although it is well known that the microstructure has great influence on the fatigue life, earlier models did not consider the effects of microstructural variables, but consider only the effects of tensile strength[2].

There have been two main streams for predicting the high cycle fatigue life. The first one is the approach using continuum damage mechanics. Important aspect of this theory is to monitor the accumulation of damage in materials and, in general, the macrovariables such as strain energy, elastic modulus have been used for this purpose. But continuum damage mechanics is not adequate method to develop the microstructural model, because it is difficult to relate the macrovariable to the microstructure. The second approach is based on the small crack theory. The small crack can be distinguished from the long crack by the different growth behavior. It is well known that the microstructure has great influence on the small crack growth and the initial fatigue crack follows the behavior of small crack propagation. However, previous studies on the small crack have been focused on the propagation behavior and there have been no attempts to relate the small crack concept into the HCF prediction model.

Therefore the objective of this study is to construct a microstructural model predicting HCF life using the small crack theory. Particular interests have been given to develop the life prediction model with respect to the grain size.

2. CONSTRUCTION OF HCF LIFE PREDICTION MODEL

2.1 Basic concept for the prediction model

It is well known that the fatigue crack initiation step takes most of the high cycle fatigue life as shown in Fig. 1 [3]. In the small crack theory, the fatigue crack initiation step is thought to be composed of three steps, such as crack nucleation, microcrack propagation and propagation through a barrier[4-6].

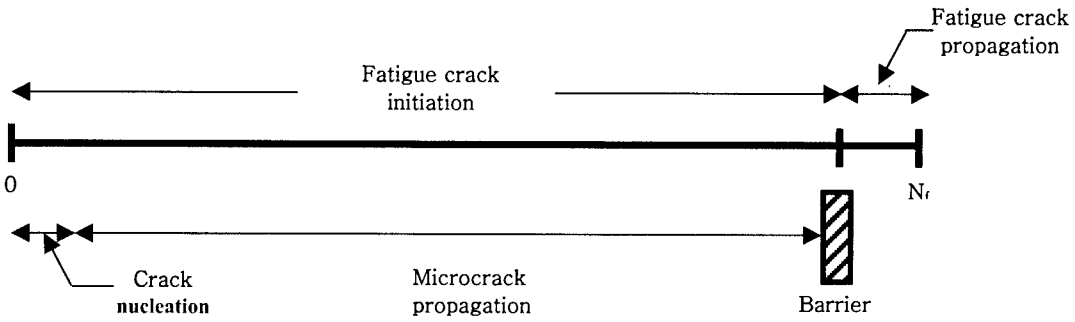

Fig. 1 Schematic diagram of high cycle fatigue life

However, since the crack nucleation step is considered negligible in the entire life, since it has been reported that the crack nucleation occurs in a few cycles[7,8]. Therefore, the fatigue crack initiation step is thought to be the sum of each period for microcrack propagation and propagation through the barrier. To make matters simple, it is assumed that the entire life is proportional to the cycles spent in one grain and one barrier, as shown in Fig. 2.

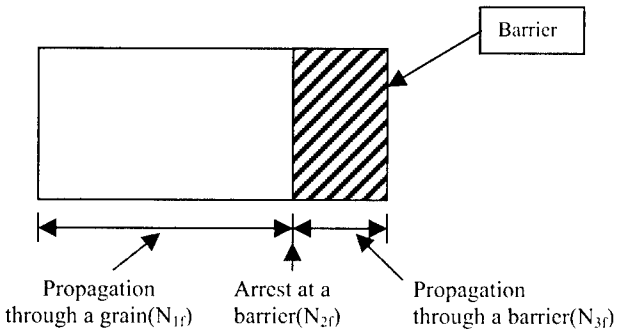

Fig. 2 Schematic diagram showing the concept of modeling : 1grain + 1barrier

If the barrier is a grain boundary, N_{3f} can be neglected, because the width of grain boundary is very small. Since the entire life can be expressed by the sum of N_{1f}, the propagation period through a grain and N_{2f}, the arrest period at grain boundary.

2.2 Modeling for N_{1f} : propagation through the grain

At a first approximation to construct the N_{1f}, the small crack growth law(Eq. 1) suggested by K.J. Miller[8,9] was adopted.

$$da/dN = A(\Delta\tau)^m(d-a) \tag{1}$$

When $\Delta\tau$ is the driving force (the shear stress at the crack tip), d is the grain size and a means the crack length. However, in this study, some modification for $\Delta\tau$ has been made by considering the microstructural effect on the driving force as shown in Eq. 2.

$$\Delta\tau = \Delta\tau_{app} - \Delta\tau_f - \Delta\tau_b \tag{2}$$

where $\Delta\tau_{app}$, $\Delta\tau_f$ and $\Delta\tau_b$ indicate the applied stress, the friction stress due to solute atom and the friction stress due to the back stress resulted from the dislocation pile-up, respectively. The $\Delta\tau_b$ can be expressed by Eq. 3, where d is the grain size and C_b is a constant.

$$\Delta\tau_b = C_b d\Delta\tau_{app} \tag{3}$$

When substituting Eq. 1 and 2 into Eq. 3, the modified small crack growth raw can be obtained by Eq. 4.

$$\frac{da}{dN} = A[\Delta\tau_{app} - \Delta\tau_f - C_b d\Delta\tau_{app}]^m(d-a) \tag{4}$$

Integrating from a=0 to a_{cr} and from N=0 to N_{1f}, the cycles required to propagate through the grain can be obtained in the form of Eq. 5 where a_{cr} is the length of crack when the small crack is arrested in front of barrier.

$$N_{1f} = \frac{\log\left(\frac{d}{d-a_{cr}}\right)}{A\ (\Delta\tau_{app} - \Delta\tau_f - C_b d\Delta\tau_{app})^m} \tag{5}$$

2.3 Modeling for N_{2f} : arrest at a barrier

Cumulative strain criterion has been used to calculate N_{2f}, the cycles spent in the arrest at barrier[10]. When the crack is arrested in front of barrier, the crack does not advance with continued cycles. The strain resulted from the pile-up dislocations will be accumulated during the cyclic loading. With continued cycling, the accumulated strain reaches to a critical value, then the barrier breaks. In general, when τ is applied on the slip band having the length of L, the pile up stress τ_p can be expressed by Eq. 6 where ν is Poisson ratio and μ is the shear modulus[7].

$$\tau_p = \frac{(1-\nu)\pi\tau^2 L}{4\mu} \tag{6}$$

When the crack is arrested at a barrier, the applied stress on the slip band is given by Eq. 7.

$$\tau = \Delta\tau_{min} = \Delta\tau_{app} - \Delta\tau_f - C_b(d-a_{cr})\Delta\tau_{app} \tag{7}$$

Note that $\Delta\tau_{min}$ is the applied stress on the slip band when the crack length is a_{cr}. From Eq. 6 and 7, the pile-up stress on the barrier can be expressed as follows.

$$\tau_p = \frac{(1-\nu)\pi\Delta\tau_{\min}{}^2(d-a_{cr})}{4\mu} \tag{8}$$

Using Eq. 8 and the monotonic stress-strain relation, the strain accumulated on the barrier in a cycle, γ can be obtained. If the γ^* is the critical strain required to overcome the barrier, then N_{2f}, the cycles spent at crack arrest can be expressed as γ^* divided by γ.

$$N_{2f} = \frac{\gamma^*}{\gamma} = f\left[\Delta\tau_{app} - \Delta\tau_f - C_b\Delta\tau_{app}(d-a_{cr})\right]^{-2/n}\left[d-a_{cr}\right]^{-1/n}, \text{ where } f = \frac{\gamma^*}{K}\left[\frac{(1-\nu)\pi}{4\mu}\right]^{-1/n} \tag{9}$$

The total life, the sum of N_{1f} and N_{2f}, can be given by Eq. 10.

$$N_T = \frac{\log\left(\frac{a_{cr}}{d-a_{cr}}\right)}{A\ (\Delta\tau_{app} - \Delta\tau_f - Cd\Delta\tau_{app})^m} + f\left[\Delta\tau_{app} - \Delta\tau_f - C_b\Delta\tau_{app}(d-a_{cr})\right]^{-2/n}\left[d-a_{cr}\right]^{-1/n}$$

$$\text{where} \quad f = \frac{\gamma^*}{K}\left[\frac{(1-\nu)\pi}{4\mu}\right]^{-1/n} \tag{10}$$

3. VERIFICATION OF THE MODEL WITH EXPERIMENTAL RESULTS

To verify the suggested model, S-N test was conducted using steel specimens with various grain sizes. The chemical composition of the tested steel is 0.17wt% C, 0.94wt% Mn and balanced Fe. To obtain the specimens with various grain sizes, as received specimens (average grain size of 4.6 μm) were heat-treated differently, i.e, normalizing at 800 and 1000℃ for 30 minutes followed by air cooling. As shown in fig. 3, the average grain sizes of the steels were measured as 4.6, 9.3 and 13.3μm. To determine the unknown constants in Eq. 10, the iteration method was used. Table 1 shows the variation of the constants with the grain size. The $\Delta\tau_f$ is the friction force resulted from the solute atoms in the grain interior. Therefore, it is assumed to have a fixed value in the steels with the same chemical composition. Also C_b is regarded as a constant, since it is the back stress coefficient related to the nature of grain boundary in a given material. The m value is related to the propagation velocity of small crack thorough the grain interior. Chan has reported that m possesses the value of 2 in a plain carbon steel[11], which shows the good agreement with our result.

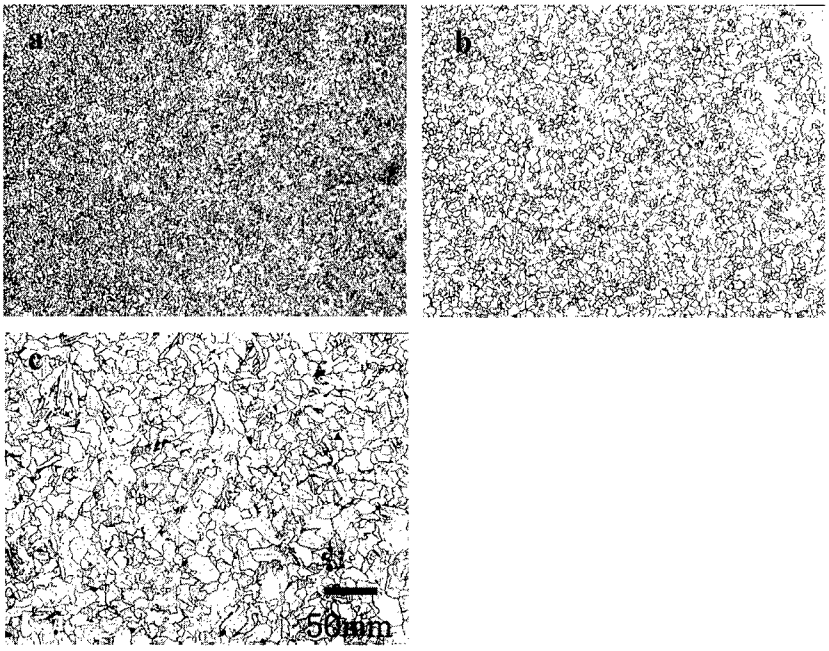

Fig. 3 Microstructures of (a) as received specimen (b) specimen normalized at 800℃ for 30 minutes and (c) specimen normalized 1000℃ for 30 minutes.

Table 1. The values of coefficients with the grain size

	$\Delta\tau_f$	C_b	d	a_{cr}	m	n
As received	175	0.0325	4.57	4.53	2.3	0.182
800℃	175	0.0325	9.30	8.96	2.32	0.235
1000℃	175	0.0325	13.34	12.10	2.37	0.267

Using the constants of steels (in Table 1) with grain sizes of 4.6 and 9.3 μm, the predicted life for specimen with grain size of 13.3 μm was calculated. It was assumed that the grain size and the unknown constants in the given model show the linear relationship. The value of $\Delta\tau_f$ and C_b was fixed due to the same reason mentioned above. As shown in table 2 and fig. 4, reasonable agreement was found between the experimental data and the predicted curve. The deviation found near the short fatigue life region in fig 4 is regarded natural because the concept of small crack is valid in the high cycle fatigue region.

Table 2. Comparison of the expected constants with the measured ones

	d	$\Delta\tau_f$	C_b	a_{cr}	m	n
Expected	13.3	175	0.0325	12.2	2.45	0.269
Measured	13.3	175	0.0325	12.1	2.37	0.267

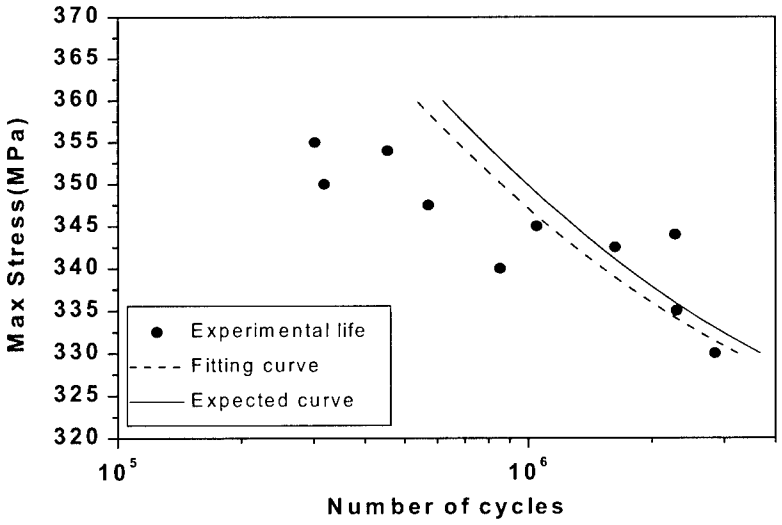

Fig. 4 Plots showing the experimental curve and predicted curve

4. CONCLUSION

In this study, the microstructural model for the prediction of high cycle fatigue life has been suggested on the basis of the small crack theory. As a first approximation, the influence of grain size on the high cycle fatigue life has been considered and incorporated in the model. Our experimental results on steels with different grain size show a good agreement with the predicted curve.

REFERENCES

1. Julie A. Bannatine, Fundamentals of metal fatigue analysis, prentice hall(1990), pp. 2
2. Y. Sakuma, D .K. Matlock, and G. Krauss, Metall. Trans. A , Vol.23(1992), pp. 1221
3. Joon Sik Park, Sung Joon Kim and Chong Soo Lee, Materials Science and Engineering A, A298(2001), pp.127-136
4. Kujawski, D. and Ellyin, F., Short fatigue cracks, Mechanical engineering publications Ltd (1992), pp.3915
5. Hironobu Nisitani and Takayuki Fukuda, JSME International Journal, Vol.35, No.3(1992), pp.354
6. M. R. Mitchell, Fatigue and Microstructure, ASM, Metals Park(1976), pp.175
7. John Price Hirth and Jens Lothe, Theory of dislocations, 2nd edition, Wiley Interscience (1982), pp.775
8. K. J. Miller, Fatigue Fract. Mater. Struct., Vol. 10, No. 2(1987), pp.93
9. Miller K. J., Fatigue Tract. Engng Mater, Vol.10, No.4(1977), pp.253
10. Tomkins, Phil. Mag., Vol.18(1968), pp.1041
11. K. S. Chan, Scripta Metall., Vol.17(1983), pp.529

Trace and Control of Binder Removal Processes from MIM Compacts by Simultaneous Application of Thermogravimetry and Mass Spectrometry

T. Senda*, K. Suzuki ** and Y. Kankawa***

* Rigaku Corporation, Ltd. Matsubaracho 3-9-2, Akishima, Tokyo, 196, Japan
** Pohang University of Science and Technology, San 31, Jigokdong, Nam-ku, Pohang, 790-784, KOREA
***Kyoto Municipal Institute of Industry Research, Minamimachi 17, Shimogyo-ku, Kyoto

ABSTRACT

In order to develop a concept for controlling heat patterns in the dewaxing and binder removal stages of the MIM process, the thermal decomposition of organic substances, often used as a binder for MIM compacts, is traced by a system combining analytical systems, such as thermogravimetry, gas chromatography, and mass spectrometry. These organic substances are divided into two categories: (a) random scission types, such as ethyl vinyl acetate and polypropylene, and (b) random scission and unzipping types, such as polystyrene and polymethyl methacrylate. The decomposition scheme of the type (a) binder does not depend on decomposition conditions such as temperatures at different locations in the MIM compacts. However, type (b) binders decompose depending largely on environmental conditions such as rate of temperature increase and degree of difficulty for decomposed gaseous molecules to escape.

1. INTRODUCTION

The metal Injection Molding process (MIM) has recently been commercialized as one of the net shape technologies of complicated shapes of stainless steel and/or titanium alloys with higher accuracy in product dimensions. In this process MIM compacts consisting of alloy powders, organic binders and wax are slowly heated within a relatively low temperature range (to remove the binder and wax) and are then sintered at a higher temperature. Binder and wax removal greatly influences the quality of the finished products since the amount of binder is usually kept as high as 40~60 volume % to guarantee room temperature strength of the compacts. However, thermal decomposition of the binder has not been systematically studied due to the fact that such a study would include various operating variables, such as size, temperature profile in a MIM compact, and atmosphere. Consequently, in general MIM compacts are heated very slowly (40~80 hours) in order to avoid the rapid evolution of gaseous molecules which cause cracks and the reaction of gaseous molecules with alloy powder. Low productivity, brought about by this heating pattern, is becoming a major bottleneck in the MIM process. In this study, the binder decomposition process was traced by an analytical system consisting of equipment for thermogravimetry (TG), differential thermal analysis (DTA), gas chromatography, and mass spectrometry. A process control model is proposed based on the experimental results, in which the intensity ratio of two ionic species, evolved from the binder and ionized in a mass spectrometer, is used as a parameter for binder decomposition degree.

2. EXPERIMENTS

2.1. AN ANALYTICAL SYSTEM

An analytical system consisting of equipment for TG-DTA (Rigaku Denki, TAS-200 or TG8120), gas chromatography (Hewlett Packard Co. 5800), gas mass spectrometry (Nitiden-Anelva QMS-NAS7000) and a gas inlet system with multi-channel cold traps.

2.2. DECOMPOSITION OF STYRENE IN MIM COMPACTS

Specimens used for analysis were a pulverized mixture of stainless steel powder (SUS 316) and 15 wt. % of binder (polystyrene and a small amount of wax). These specimens were pressed and dewaxed in an Ar atmosphere at 453 K for 2 hrs. The powder specimen was held in a cylindrical Al container (5 mm inside diameter and 2.5 mm in height). Two types of containers were used: (a) lidless, Open Pan (OP) and (b) one having a lid with a pinhole (10~20 μm in diameter) at the center (PH). These containers were used in order to simulate the evolution of gas and/or the decomposition of the binder at a distance not far from the surface and at the center of the MIM compacts, respectively. The operating conditions of the analytical equipment were:

Mass spectrometer:
Ionization voltage: 70 eV,
Range of mass number: 30-300,
Scanning interval: 1.1s
Gas chromatography:
Dimension of quartz capillary column (0.2 mmϕ, 25m long and with a film thickness of 11μm) with methyl Si,
oven temperature: 303 K for 3 mins followed by heating to 543K(15K /min).

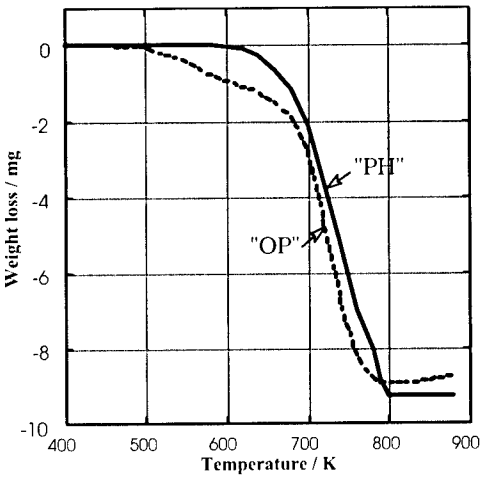

Fig.1 Typical TG curves for "OP" and "PH"

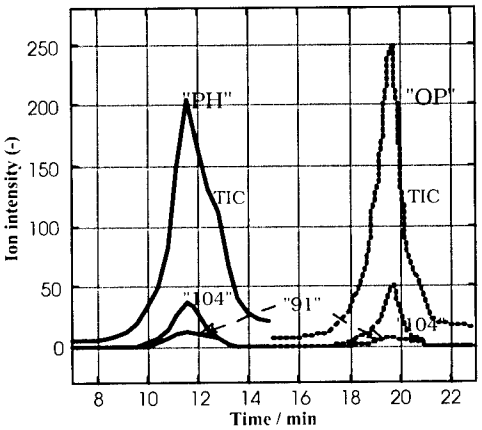

Fig. 2 Typical ion intensity profiles for "OP" and "PH"

Fig. 1 shows typical thermal gravimetry curves for the mixture of polystyrenes. It is noted that decomposition of the binder kept in the OP occurred in three stages with maximum decomposition rates of about 573 K, 713 K, and 753 K.

In the case of PH, decomposition at the first stage (573 K) did not occur, at the second stage (713 K) was suppressed, but at the third stage (753 K) increased markedly with a slight increase in maximum decomposition temperature.

Gas evolved from the MIM compacts was analyzed using a mass spectrometer. The results are shown in Fig. 2, where TIC (Total Ion Chromato) corresponds to the amount of total evolved gas, and 91 and 104 correspond, respectively, to the intensities of decomposed gaseous ions with a M/e of 91 (viz. lacking one H atom from a Toluene molecule) and 104 (Styrene monomer). In comparison with OP, it is also noted that the decomposition range in PH shifted to a higher temperature with a wider range.

Gases evolved at the final stage of decomposition (733 K for OP and 773 K for PH) were introduced into a gas chromatography/mass spectrometer system and analyzed. The results are shown in Table 1. In the case of OP, the intensity of the styrene monomer was superior to others decomposed from polystyrene; besides, peaks caused by wax in the compacts were still

detected which suggests that wax removal is not complete at 453 K.

Table 1 Gaseous components evolved from a MIM compact during the binder removal test

conditions		abundance (-)				
	components	styrene*, monomer	toluene*	benzene	α-methyl styrene	wax
	time/min**	8.94	8.48	7.00	10.2	17.5
OP, 30K/min		10^4	200	560	2000	4150
PH, 30K/min		10^4	1780	3272	4200	7760
PH, 50K/min		10^4	2760	4920	5250	3750

* M/e values for Styrene monomer and toluene are 104 and 91, respectively.
** Time at which the peak appears in GC analysis.

On the contrary, irregular decomposition behavior was observed. Fig. 2 shows that the area fraction of the 104 'PH' peak (styrene monomer) is roughly 20% of the 'PH' TIC's, and that the area fraction of the 104 'OP' peak (styrene monomer) is roughly 15% of the 'OP' TIC's. However, the area fraction of the 91 'PH' peak is 3% which is higher than that of the 91 "OP" peak (2%) (even though 91 is a 104 fragment ion). In an environment where decomposed gases cannot easily escape, polystyrene does not decompose easily. When the heating rate is further increased, the ratio of sub-decomposition products, such as toluene, benzene and α-methyl styrene, also increases (Table 1). The ion intensity ratio of the 91 fragment ion to that of the 104 styrene monomer is influenced by heating rate (Fig. 3), in which the decomposition reaction seems to occur uniformly throughout a specimen in the 'favorable region' (Fig. 3). The maximum heating rate in this area is one in which production efficiency is kept at a maximum without any defects occuring in the compacts.

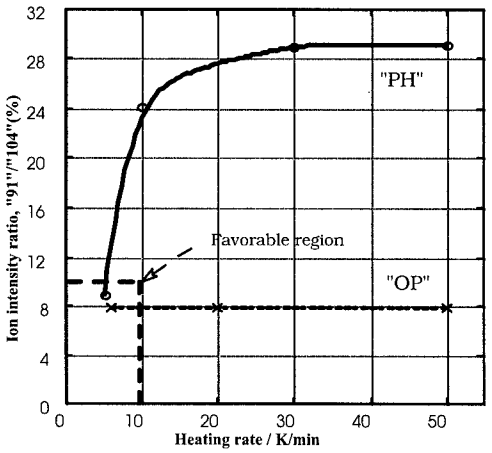

Fig. 3 Relation between ion intensity ratio of "91" to "104" and heating rate

2.3. DECOMPOSITION OF PP(POLYPROPYLENE) and EVA (ETHYLENE VINYL ACETATE)

One of purposes of this study is to clarify the decomposition behaviors of PP (polypropylene) and ethylene-vinyl acetate (EVA - Toyo Soda Co., Type 533 without any additions) which are often used as polymer type organic binders for MIM compacts.
In a typical EVA thermogravimetry (Fig. 4), weight loss appears at 621 K and 662 K which corresponds, respectively, to the evolution of CH_3COOH and to the break-up of the main chains in EVA. Using gas chromatography, it was difficult however, to detect any difference in composition between gases evolved from the compacts kept in the OP and PH containers, regardless of temperature.
In the case of PP, similar results were observed as expected from the theory. For both binders, the gas evolved from the PH container was abundant in components with lower molecular weight than those from OP.

However, gas composition evolved from EVA after rapid heating to the decomposition temperature range depended on temperature; i.e., the number of C (carbon) atoms in the decomposed gas was more than 16 when EVA decomposed just above 662 K (the critical decomposition temperature). With an increase in decomposition temperature the number of C atoms in the evolved gas fell to a range of 10~15.

With a heating rate of 20 K/min, the break up of the main chain in EVA started at 662 K and became very rapid in a temperature range of 750~783 K. It was also found that the composition of the decomposed gases did not change throughout the decomposition period and that the decomposition process did not depend on the type of container used.

In fact, the removal of the binder in a press formed compact (3.5x2.5x4.5 mm), with the composition (stainless steel powder 92.8, PP 1.8, EVA 1.8, and wax 3.6 mass%) finished at 673~683 K in the CR (Controlled Rate) - TG curve, which was identical to that of the powder mixture without press forming. This observation suggests that binder removal processes in the bulk of MIM compacts with random scission type binders take place quite similarly to those at the surface of the compacts. Accordingly, it may be concluded that the control concept which will be proposed for polystyrene (viz. heating rate control by using the ion intensity ratio of decomposed gases) can not be applied to the random scission type polymers, such as PP and EVA.

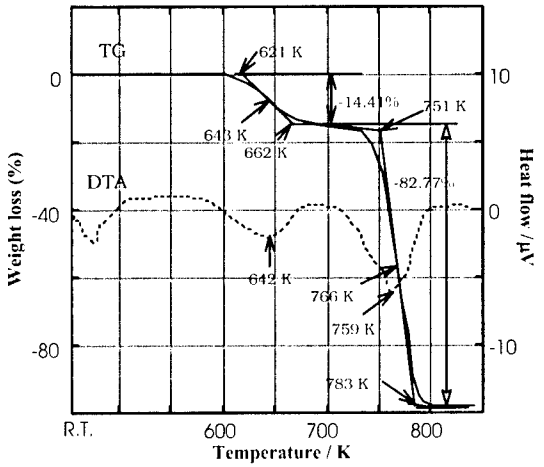

Fig. 4 A typical trace of degradation of EVA by TG and DTA

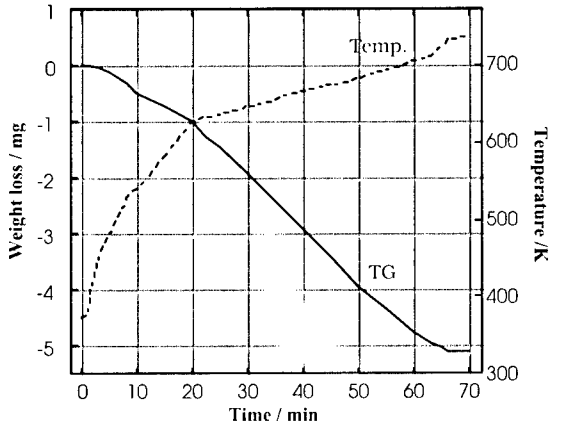

Fig. 5 Change in weight and temperature of a MIM compact

3. A TRIAL TO OPTIMIZE REMOVAL OF STYRENE FROM MIM COMPACTS

One of the aims of this experiment is to ascertain how to control heating rate during the binder removal stage. The specimens used were MIM compacts (30 mg) containing polystyrene as a binder. These specimens were kept in a PH type container. From all the ion intensity output signals from the mass-spectrometer operating in SIM (Single Ion Chromato Mode), those of M/e 104 (styrene monomer) and 41 (ions lacking one H atom from propylene, one of the fragments of a styrene monomer) were used as process controlling parameters. The ion intensity ratio of 41/104 was fed back to the temperature control circuit of the furnace and the temperature was raised so that the ratio would not exceed 0.1 (a typical value for specimens kept in OP containers). When the 104 signal is zero, about 5% of the maximum signal voltage of 104 was added to that of the 104 signal as bias voltage.

Temperature change, MIM compact weight, and the ion intensity ratio of 41/104 are shown in

Figs. 5 and 6 in cases where furnace temperature is controlled by the concept in which the weight of the compacts decreased at a reasonably constant rate during heating as in the constant weight loss control mode in CRTA (Controlled Rate Thermal Analysis) - TG analysis.
As it was not easy to guage the distance from the surface of the MIM compacts simulated in this experiment, cubic MIM compacts (4 x 4 x 4 mm) were heated to 1273 K at a constant rate of 7 K/min, or by applying the control concept. As shown in Fig. 7, many voids (presumably caused by rapid gas evolution) were observed in compacts heated at a constant rate of 7 K/min. However, the microstructure of the MIM compacts, made by applying the control concept, was free of any of the voids or defects usually caused by rapid gas evolution.

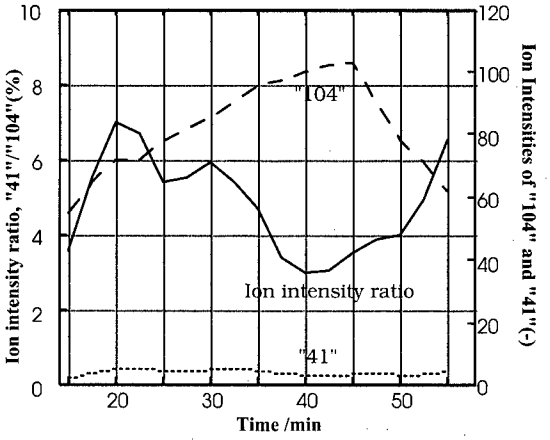

Fig. 6 Results of temperature control during binder removal from a MIM compact

4. DISCUSSIONS ON THE CONCEPT OF HEATING RATE CONTROL FOR MIM COMPACTS

Within high temperature decomposition theory, organic compounds can be divided into three types: a) random scission, b) unzipping and c) mixed[1]. The fact that EVA and PP are type A and polystyrene is type C may well explain the differences observed in the degradation behavior of these compounds. In the case of type C organic material -the concept proposed in the previous section- may be effective. A schematic for the binder removal furnace with a control device is shown in Fig. 8.
It is now evident that random decomposition type organic binders, such as EVA and PP, can be removed at a fixed temperature to obtain a uniform sintered matrix throughout the MIM compacts (the compacts used in this study had a thickness of 2.5mm). In other words, EVA and PP in MIM compacts decomposed similarly throughout the compacts which were 2.5 mm thick.

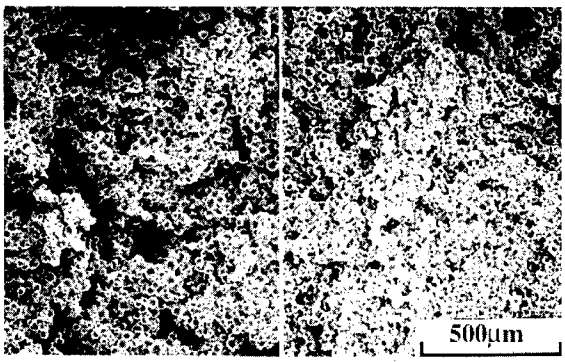

Fig. 7 Comparison of microstructure of MIM compacts after binder removal (Left: Constant heating rate, Right: by the proposed method)

For the purpose of optimizing the heating pattern for MIM compacts, it may be possible to use the ion intensity of hydrocarbon gas with approximately 10 C atoms as a control signal, however, this may not be easy since the M/e number monitored may be duplicated with the M/e value of organic gases with a higher number of C atoms with multi-ionic valences.
In a method to pursue an optimized heat cycle by applying the CR-TG mode of operation, it may be required to adjust the aimed rate of weight loss frequently during the heating cycle.
With commercial production of MIM compacts thicker than 2.5 mm, a steeper temperature gradient in the compacts is expected during heating, in addition to a non-uniform temperature profile throughout the furnace. At about the temperature at which decomposition of an

organic binder starts, gas evolution takes place from the surface of the compacts and the interface of gas evolution gradually moves to the core of the compacts. When non-uniformity of temperature in the heating furnace is taken into account, monitoring the ion intensities of decomposed gases will indicate the binder decomposition of all MIM compacts charged into the furnace.

Even when polystyrene type binders are used in the MIM compacts, the operating conditions are similar to those previously mentioned. It is supposed that the previously proposed concept for controlling furnace temperature is much more effective than that of the random scission type binder. This concept was designed to increase the efficiency of the previously described MIM process. By applying the proposed concept of temperature control, the time required to remove all of the mixed type binders is expected to be reduced to 2/5 of that required in the existing method. In addition, constant monitoring of the evolution of gaseous molecules is essential. These molecules decomposed from the binder may react with the titanium alloy powder in MIM compacts. This is because titanium alloy powder is much more reactive than stainless steel powder.

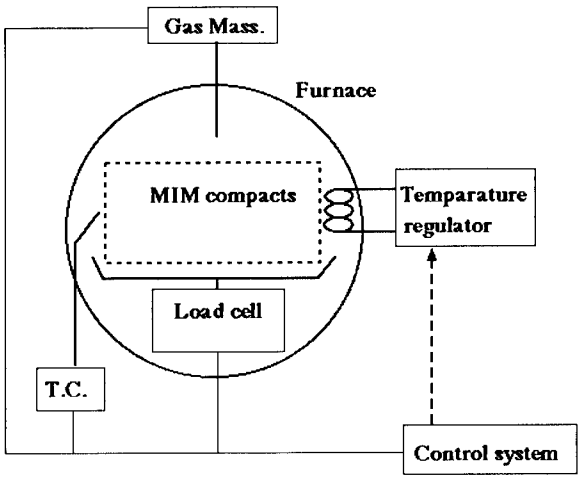

Fig. 8 A schematic diagram for rate control of the binder removal process of MIM compacts

5. CONCLUSION

Thermal decomposition of popular organic substances used as binders for MIM compacts was studied in order to develop a control concept for a heating furnace during the MIM process. Results obtained are as follows:

1) Popular organic substances used as a binder for MIM compacts were divided into two categories: (a) random scission (such as EVA and PP) and (b) mixed (with some random scission, some unzipping as with polystyrene).
2) In the case of the random scission type binder, the decomposition scheme is practically constant and does not depend on decomposition conditions such as temperature or its location in the MIM compacts. Decomposed gas molecules shed carbon atoms only when decomposition is suppressed by rapid heating to decomposition temperatures.
3) Decomposition of a mixed type binder (such as polystyrene) depends largely on surrounding environmental variables such as heating rate and the difficulty with which decomposed gaseous molecules escape.
4) The concept for controlling the binder removal process of MIM compacts with a mixed type binder has been proposed and verified to be effective.
5) When non-uniformity in a heating furnace is taken into account, monitoring of gaseous molecules is recommended for precise control of the binder removal stage.

6. REFERENCES

1. S.A.Liebman and E.J. Levy, Pyrolysis and GC in Polymer Analysis (Chromatographic Science, Vol. 29), Marcel Dekker, Inc., New York, 1985.

ADDRESSING URGENT MASS REDUCTION REQUIREMENTS BY THE USE OF LIGHTWEIGHT COMPONENTS

Martin Leary and Colin Burvill

Department of Mechanical and Manufacturing Engineering
University of Melbourne, Parkville 3010, Australia

In association with National Forge
West Footscray 3012, Australia

ABSTRACT

The substitution of ferrous metal suspension components with lightweight alternates has significant potential for reducing vehicle mass. Unsprung mass reduction has the threefold benefit of improving fuel efficiency, reducing vehicle emissions and improving vehicle handling [1]. Lightweight suspension components have found limited application in passenger vehicles due to the associated cost premium.

The cost constraint associated with material selection may be considered to have a single caveat, being government enforced emissions and fuel economy standards. The structure of these standards may require manufacturers to accommodate incremental mass categories or sales weighted average performance of the product range. This necessitates scenarios where manufacturers need to respond to mass reduction with some degree of urgency. This mass reduction urgency increases the perceived value of mass reduction beyond nominal values, and may negate the cost premium associated with lightweight component substitution.

A case study is presented which compares the mass of sample vehicles with the test requirements of Australian Design Rule 37 (ADR-37) [2]. ADR-37 is an example of tests associated with government standards that lead to testing based on incremental categories of vehicle mass. Vehicles with urgent mass reduction requirements are identified within ADR-37. These target vehicles are subject to a mass reduction urgency, and are therefore excellent candidates for light metal substitution strategies. The mass reduction achievable through light metal substitution is estimated using a feasibility study of forging replacement on sample target vehicles.

1 GOVERNMENT STANDARDS AND MASS REDUCTION OPPERTUNITIES

Existing legislation such as Australian Design Rule 37 (ADR-37) and the United States Corporate Average Fuel Economy (CAFE) [3] creates opportunities for mass reduction by material substitution. This mass reduction is associated with the rapid response by manufacturers necessitated by legislation of this type. Mass reduction urgency introduced by

legislation is associated with incremental mass categories or a sales weighted average performance ceiling.

1.1 Incremental Mass Categories

ADR-37 places limiting values on vehicle emissions and provides the basis for unrestricted (but publicly available) fuel efficiency statistics [2]. Compliance with this standard is determined by testing the vehicle on a dynamometer under simulated driving conditions. Vehicle mass is accounted for by modifying the resistance to wheel rotation. The magnitude of this resistance is based on incremental categories of vehicle mass [4].

If the mass of a vehicle is not in danger of exceeding its current mass category, and is not within the range of a lower category, mass changes will not change the dynamometer resistance and will have little influence on fuel economy or vehicle emissions. In such cases the acceptable price premium of mass reduction is low (corresponding to the troughs in Fig.1.) Conversely, if the vehicle can undergo mass reduction leading to the next lower category the dynamometer resistance can be reduced, leading to improved fuel economy and vehicle emissions. This legislative opportunity for mass reduction can lead to a mass driven need for material substitution. In such cases the acceptable price premium asymptotes toward the of urgent price premium (peaks of Fig.1) and may be high enough to support the cost premium of mass reduction by lightweight material substitution.

This provides opportunities for lightweight component manufacturers to introduce mass reduction strategies that may not be cost effective outside an urgent mass reduction scenario (Fig.1). If a component manufacturer can provide a mass reduction of, say, δ kilograms, the target vehicles for that manufacturer may be defined as vehicles which:

1. are within feasible reach (δ+) of a lower reference mass category,
2. or are close to the upper limit of the current category (δ–) and may require mass reduction strategies to maintain this category in future models (due to added mass from new features – e.g. luxury options),
3. and are produced in sufficient volumes to justify the resources required for the introduction of a design and development programme for material substitution (Fig.1).

1.2 Sales Weighted Average Performance Ceiling

Legislation may lead to an urgent mass reduction scenario by limiting the sales weighted average performance of the vehicles sold by a manufacturer. The US CAFE is an example of federal legislation that limits the sales weighted fuel economy of the vehicles sold by a manufacturer. US CAFE standards require that a vehicle manufacturer's product range meet an average fuel economy of 27.5 miles per gallon (mpg) for cars and 20.7 mpg for light trucks (include vans, minivans and sport-utility vehicles) [3]. Manufacturers are fined if this performance ceiling is exceeded, resulting in urgent mass reduction scenarios. Target vehicles for urgent mass reduction due to a sales weighted average performance ceiling are those with high sales volumes and are therefore significant contributors to the average performance.

Test methods used to determine the efficiency of US vehicles are very similar to ADR-37. Therefore US vehicles may provide mass reduction opportunities in response to urgent mass reduction requirements due to both sales weighted average performance ceiling and testing based on an incremental categories of vehicle mass.

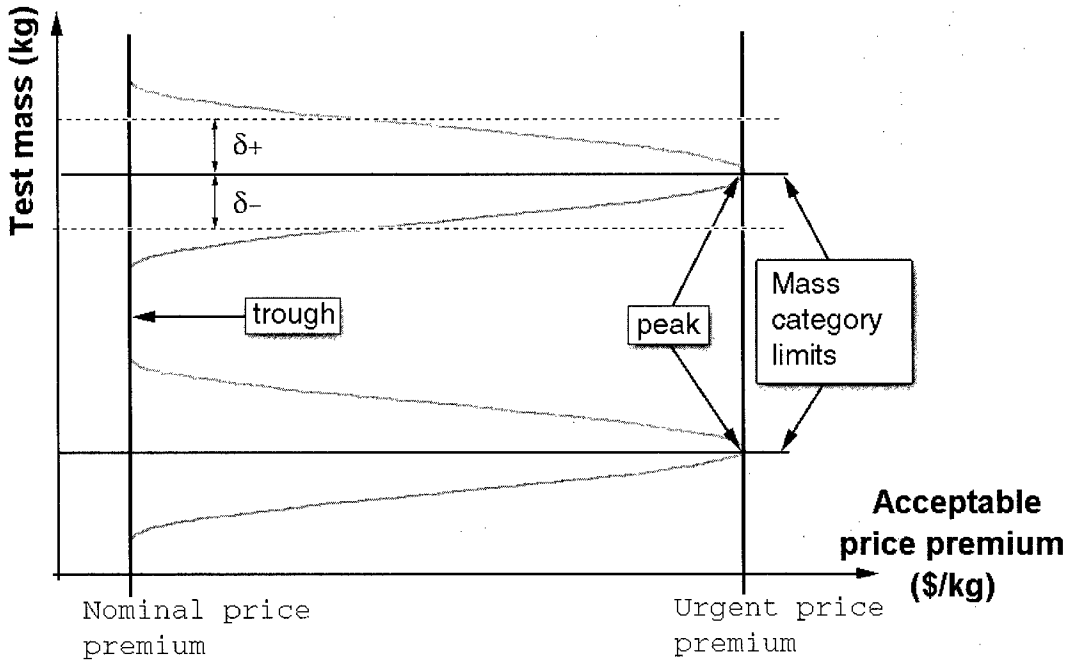

Fig.1. Test Mass versus Acceptable Price Premium

2 MASS REDUCTION FEASIBILITY STUDY

The test mass of a selection of the General Motors Holden's Commodore range (Australia) is plotted against the test mass categories of ADR-37 (Fig.2). The mass reduction urgency of these vehicles is quantified by plotting the mass change required to change the vehicles existing test category (Fig.3). The potential of light metal suspension components to meet urgent mass reduction requirements in these vehicles has been reviewed. The scope of this review is limited to forged steel components in the unsprung mass associated with the Commodore range of vehicles (Fig.4).

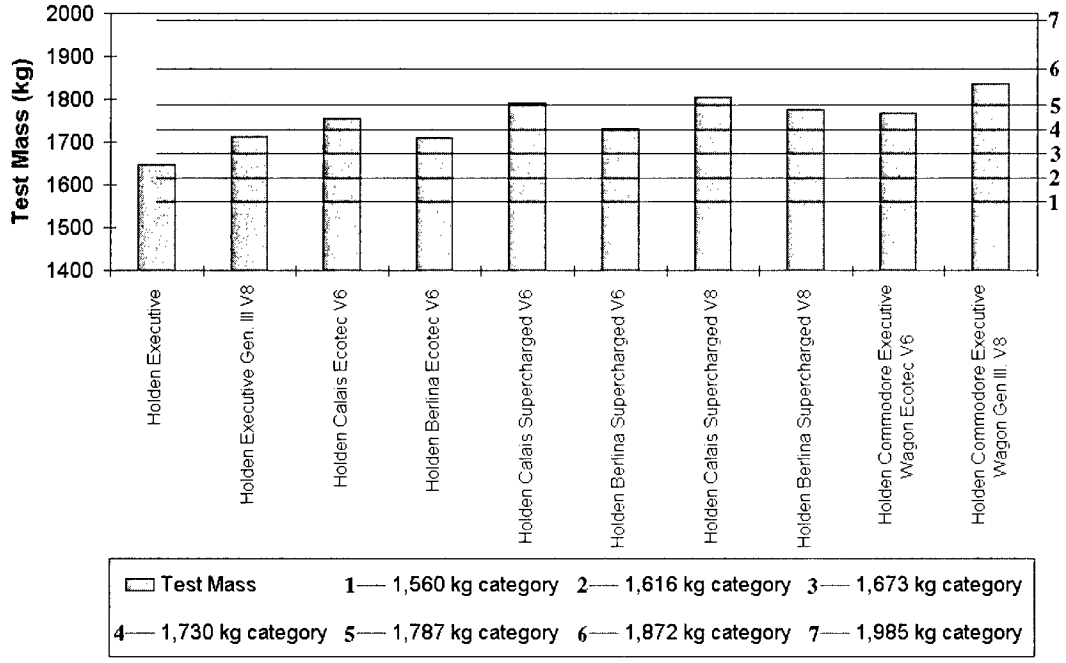

Fig.2. Sample Holden Vehicle Mass versus Mass Categories of ADR 37

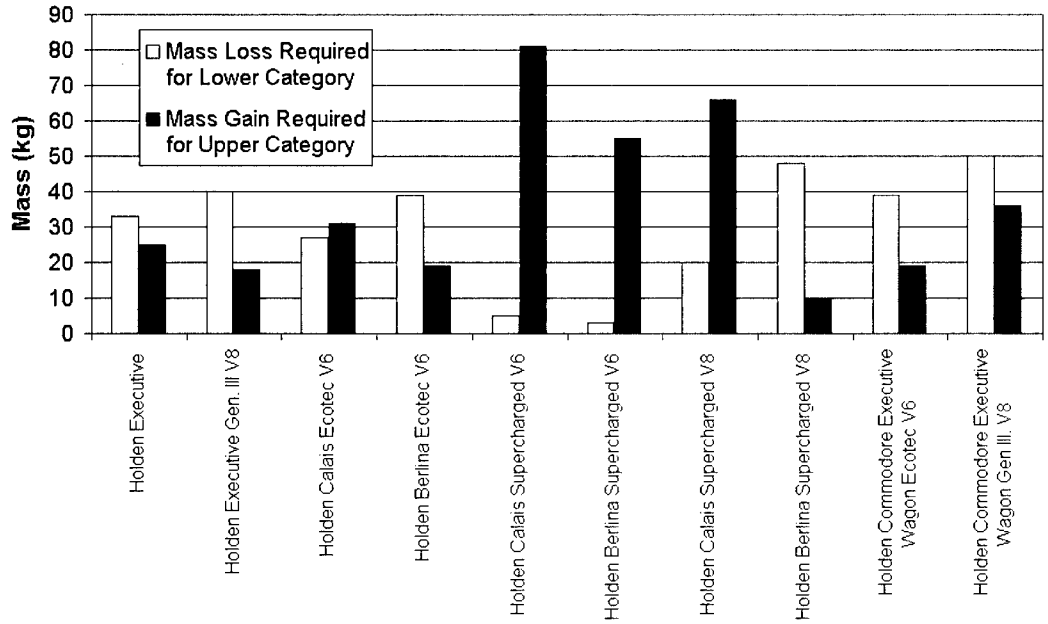

Fig.3. Mass Change Required for New Mass Category

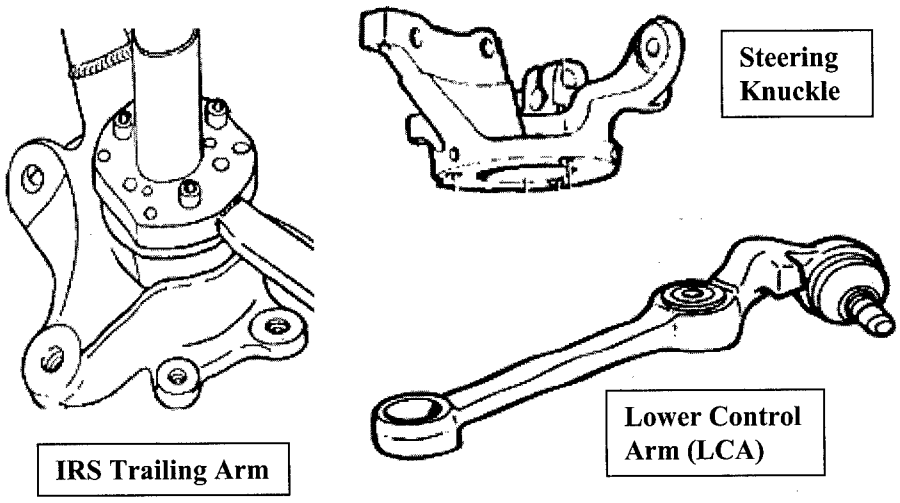

Fig.4. Potential Steel Components for Material Substitution [5]

The potential mass saving by the substitution of these steel components with lightweight forgings has been estimated.

The steering knuckle (two units per vehicle) allows the front wheel to pivot within the suspension assembly and has a mass of approximately 5 kg. A prototype design developed by the authours [6] suggests conversion of the steel knuckle to aluminium would reduce component mass to approximately 2.5 kg.

The function of the lower control arm (two units per vehicle) is to provide lateral constraint to the steering knuckle and has been approximated as a tie. Mass reduction may be estimated via material indices of tie mass [7,8]. Assuming an endurance of 100 million (1E8) cycles the substitution of forged magnesium would reduce component mass from 3.5 kg to approximately 1.75 kg.

The IRS trailing arm (two units per vehicle) provides a housing for the rear wheel bearing and mounting brackets for the brake calipers and shock absorber. An estimate of potential mass reduction has been made based on the mounting brackets. Using material indices for cantilever mass [7,9], and assuming an endurance of 1E8 cycles, aluminium substitution should reduce component mass from 11 kg to approximately 7 kg.

Based on three unsprung forged components this study estimates a total achievable mass reduction of 16.5 kg. Additional reduction may be achieved within a formal strategy where all components are considered (e.g. brake rotors and drive shafts). Setting the feasible mass reduction ($\delta+$ and $\delta-$) to 16.5 kg identifies candidates for urgent mass reduction from those listed in Fig.3. The supercharged Calais V6 (5 kg above existing test category limit) and supercharged Berlina V6 (3 kg above existing test category limit) are within the mass reduction achievable by the proposed material substitution strategy. The supercharged Berlina V8 is currently 10 kilograms below the current test category limit. Material substitution

provides scope for the addition of mass to this vehicle (e.g. luxury options) whilst allowing the vehicle to remain within its existing category.

3 CONCLUDING REMARKS

This paper has identified target vehicles with urgent mass reduction requirements that may be addressed by the use of lightweight components. The target vehicles are niche vehicles and may not meet the necessary sales volume requirements to institute mass reduction. The high sales volume vehicles of the Australian Holden Commodore range (Executive, Calais and Berlina) are not currently subject any mass reduction urgency (Fig.3). The material substitution strategies investigated in the case study may be useful in the design of future vehicles should the added mass of additional features results in an urgent mass reduction scenario.

A method has been proposed that will identify vehicles with urgent mass reduction requirements which arise due to government standards, allowing lightweight component manufacturers to focus design effort where it will best match a need for mass reduction.

REFERENCES

[1] H. Lowak and D. Brandt: Aluminium Materials Technology for Automobile Construction, Expertverlag, (1993), pp. 135.

[2] ADR-37/01 Emission Control for Light Vehicles, Federal Office of Road Safety, Australia, (1995).

[3] EPA CAFE Standards, (2001), available at www.epa.gov.

[4] Australian Standard 2877-1986, Standards Association of Australia, (1986).

[5] Holden VT Series Service Manual Vol. #1, General Motors Holden's Limited, Australia, (1997).

[6] M. Leary and C. Burvill: Internal Report, Feasibility Study of Light Metal Substitution of the Holden Commodore Steering Knuckle, University of Melbourne, (2000).

[7] M. Ashby: Material Selection in Mechanical Design, Butterworth Heinemann, UK, 2000.

[8] M. Leary and C. Burvill, Material Selection Indices for Finite Life Automotive Applications, in Engineering Materials 2001 Conference and Exhibition, Melbourne, Australia, (2001).

[9] M. Leary and C. Burvill, in Light Materials for Transportation Systems, Addressing Urgent Mass Reduction Requirements by the use of Lightweight Components, Pusan, Korea, (2001).

OPTIMAL MATERIAL SELECTION FOR FINITE LIFE AUTOMOTIVE SUSPENSION APPLICATIONS

Martin Leary and Colin Burvill

Department of Mechanical and Manufacturing Engineering
University of Melbourne, Parkville 3010, Australia

In association with National Forge
West Footscray 3012, Australia

ABSTRACT

The traditional approach to automotive suspension design is the infinite life design paradigm [1]. This strategy results in components that will theoretically survive unlimited load cycles without failure, but may lead to overdesign and therefore unnecessarily heavy components. Mass reduction imperatives in the automotive industry are motivating a paradigm shift toward finite life components. Design for finite life has the potential to minimise component mass, but requires detailed understanding of the required endurance to ensure safe application.

A systematic approach has been employed to compare the performance of candidate materials for suspension application of over a range of endurance and design objectives, namely mass, cost or a compromise between the two. Resulting in a family of performance curves for a simplified cantilever element in each scenario. This guides the selection of suspension materials (against selected criteria) for finite life applications. Defining the envelope of conditions for which light metals are optimal for finite life suspension applications, and providing a basis for assessing the relative merit of the candidate materials. Material selection will be achieved within the framework of material selection indices [2].

1 MATERIAL SELECTION INDICES

A structural component may be fully defined by its functional requirements (F), geometry (G), and material properties (M). When these measures are independent, the performance (P) may be expressed as:

$$P = f_1(F)f_2(G)f_3(M) \tag{1}$$

For a given function and geometry, $f_1(F)f_2(G)$, the performance is defined by the material index, M^*, where $M^* = M^{-1}$ [2]. Minimising the material index results in optimal material selection.

Vehicle suspension requirements for constrained motion typically result in a single degree of freedom mechanism, and are dominated by ties, columns and cantilevers. Material indices for simplified tie and cantilever elements for the objectives of minimal mass or cost are defined in Table 1. Where σ_e is the fatigue strength at the intended endurance and C_m is the material cost per unit mass.

Table 1. Material indices for cantilever and tie of minimal mass or cost [2]

Objective	Tie	Cantilever
Minimal mass	$M^*_{tm} = \rho/\sigma_e$	$M^*_{cm} = \rho/\sigma_e^{2/3}$
Minimal cost	$M^*_{tc} = C_m M^*_{tm}$	$M^*_{cc} = C_m M^*_{cm}$

Computing the material indices for a range of endurance values generates a series of curves of material performance as a function of the required endurance. The materials of interest include traditional steel (AISI 1040) which provides a performance baseline for assessing the relative performance of substitute materials. The potential substitute metals include grades of aluminium, magnesium and titanium (Table 2). Unlike ferrous metals, these non-ferrous metals do not display an endurance limit (the fatigue strength consistently decreases with required endurance). Additionally, non-ferrous metals are more expensive (per kilogram) than traditional ferrous metals. To investigate the influence of these properties on the cost and mass of a suspension component the performance curves of a cantilever are provided, (Fig.1). The implications for a tie are discussed in [3].

Table 2. Materials investigated

Material	Type	Common applications	Material cost, C_m $US/kg[1]
2024-T6	Aluminium	Aerospace, transport [4]	3
6061-T6	Aluminium	Architectural, transport [4]	2
7075-T6	Aluminium	Weight critical applications [4]	5
AZ31B-F	Magnesium	Aerospace, racing vehicles [5]	4
ZK60A-T5	Magnesium	Aerospace, transport [5]	4
Ti-6-4	Titanium	Weight critical applications [5]	18
AISI 1040	Steel	Automotive suspension application [6]	0.35

2 VALIDITY OF RESULTS

The scope of this investigation is restricted by the availability of fatigue data, which is severely limited by high testing costs. The data used is a combination of rotating and axially loaded forged specimens with a polished surface, leading to some uncertainty in data comparison [7]. Fatigue data is statistical in nature and it is common to find large spread in reported values. Additionally there is significant difference in the response of actual components to that predicted by experimental results. The estimated material costs (Table 2) are subject to continuous fluctuation and are useful in finding broad trends rather than precise values. These uncertainties must be considered when reviewing the following results, specifically that the values are not absolutes, but subject to considerable variation.

[1] Australian supplier estimates

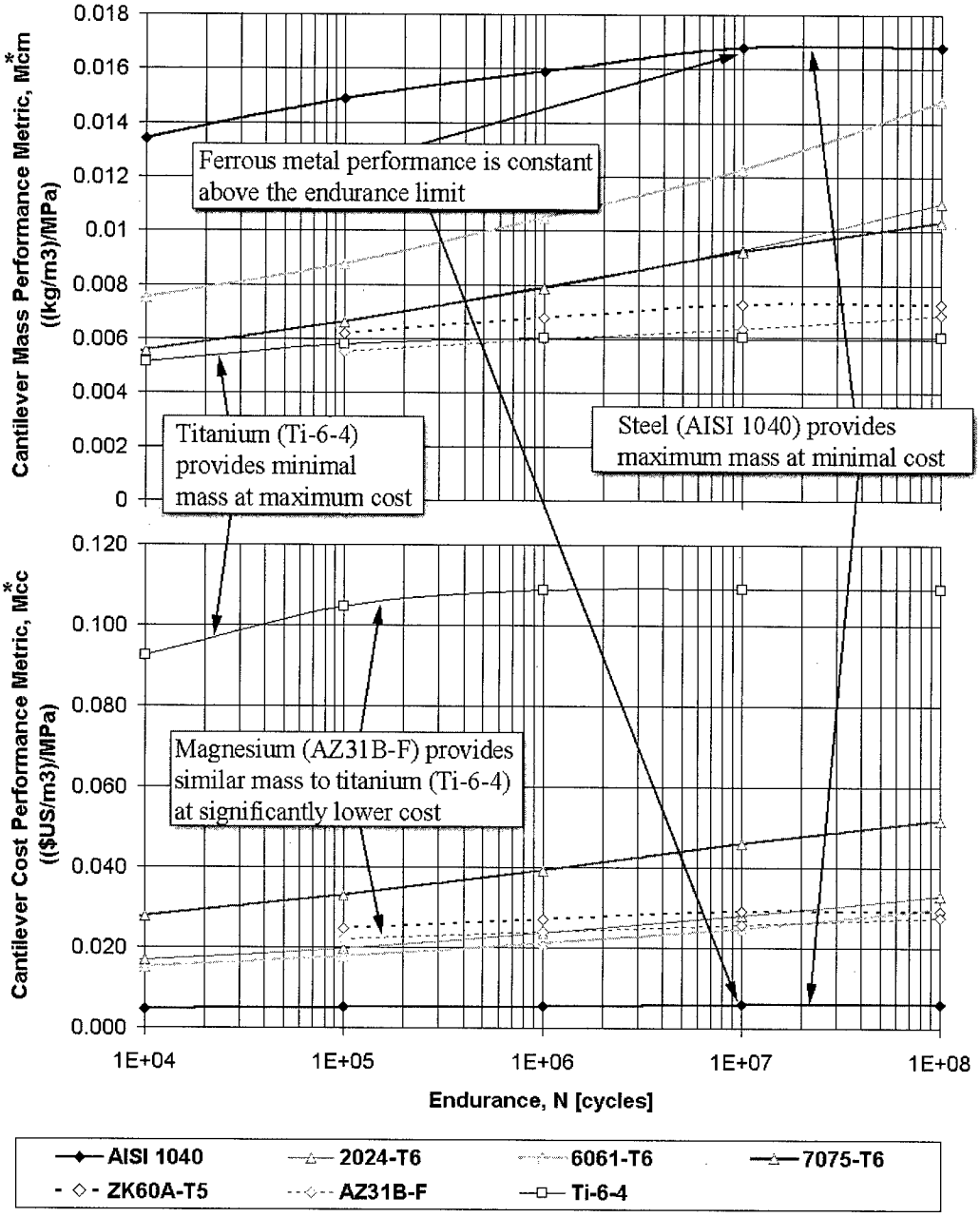

Fig.1. Upper: Performance Curves for a Light, Fatigue Resistant Cantilever Beam (M*cc), Lower: Performance Curves for a Cheap, Fatigue Resistant Cantilever Beam (M*cc)

3 MATERIAL SELECTION FOR MINIMAL MASS OR COST

Of the materials investigated, titanium (Ti-6-4) is the optimal material for a cantilever of minimal mass, conversely it provides the most expensive option (Fig.1). These attributes suit weight critical applications and has found extensive aerospace applications, including the Space Shuttle. Automotive applications include con-rods and valves in racing vehicles [5]. Magnesium (AZ31B-F and ZK60A-T5) provide similar mass to titanium (Ti-6-4) at significantly lower cost (Fig.1), allowing more general automotive application than titanium. Aluminium alloys provide moderate performance in terms of both mass and cost (Fig.1). It is interesting to note the significant cost advantage of the aluminium alloy 2024-T6 over 7075-T6 (Fig.1. Lower), both of which provide similar performance in terms of mass (Fig.1. Upper).

Steel (AISI 1040) is optimal for a low cost cantilever beam, but is the least effective in terms of mass (Fig.1). These qualities suit cost critical applications including passenger vehicle suspension components. The most interesting quality of ferrous metals (including AISI 1040) is the influence of the endurance limit at approximately 1E6 cycles (Fig.1), above which the material displays constant fatigue strength, and hence constant performance. This implies that although the sampled non-ferrous metals provide lower mass than the ferrous metal, this advantage is continuously reduced above the ferrous metal endurance limit.

4 COMPOUND OBJECTIVE MATERIAL SELECTION

Section 1 defines material selection techniques suitable for optimisation against a single objective. These results do not provide design data for the suspension engineer who must compromise between conflicting objectives, such as mass and cost. The selection procedure is further confounded when the performance indices are measured in different units so that direct comparison is not possible. A solution is provided by the use of a value function [2], which in this case defines the value of component mass in financial terms via an exchange constant, $E^{\$}$:

$$V = E^{\$} M^*_{cm} + M^*_{cc} \tag{2}$$

This requires the relative desirability of the performance indices to be defined with respect to cost. Minimising the value function results in optimal material selection. Value functions have been investigated for the scenarios of sections 4.1 to 4.4 and reviewed in section 4.5.

4.1 Holistic Value Function

The holistic value function estimates the contribution of mass to petrol costs over a vehicle life, thereby simulating the total cost of material selection to the consumer. The relationship between vehicle mass and running costs has been based on annual petrol consumption statistics of the Environmental Protection Agency (EPA), Fig.2 [8].

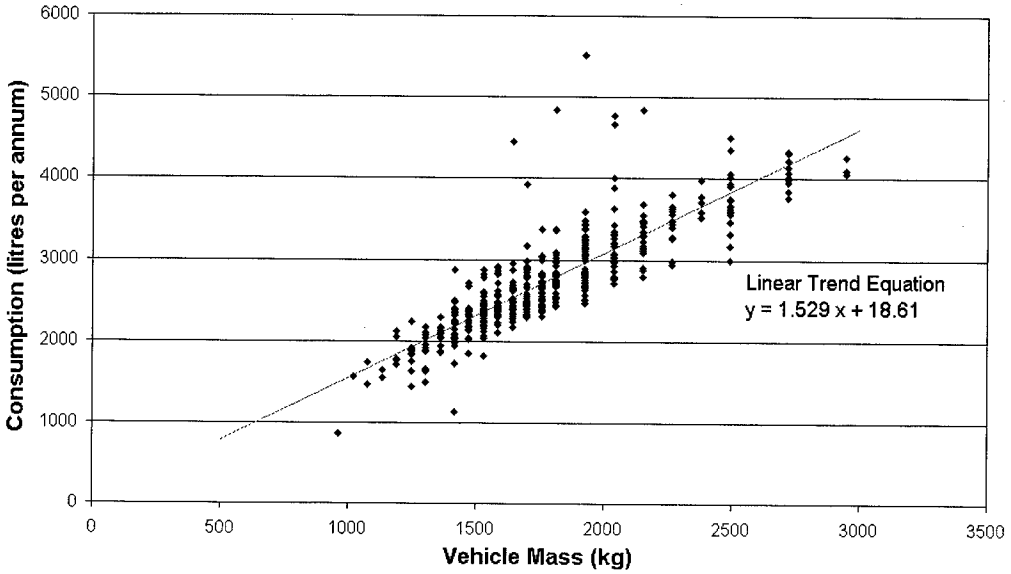

Fig.2. Vehicle Fuel Consumption Per Annum Versus Mass [8]

The linear regression line of annual petrol consumption versus vehicle test mass has a gradient of 1.529 litres per annum per kilogram. Assuming petrol cost of $US 0.43 per litre [8] and a vehicle life of 20 years, each kilogram of vehicle mass contributes $US 13.14 to fuel cost over the vehicle life. The holistic exchange constant ($E^{\$}_{ch}$) and holistic value function (V_{ch}) are therefore (Fig.3. Upper):

$$E^{\$}_{ch} = 13.14 \quad [\$US/kg] \tag{3}$$

$$V_{ch} = M^*_{cc} + 13.14\, M^*_{cm} \quad [\$US] \tag{4}$$

4.2 Present Value Function

Ashby suggests the range of exchange constants representing acceptable cost premiums of mass reduction for passenger vehicle manufacturers are between 0.5 and 1.5 $US/kg [1]. Using the median value of 1.0 $US/kg the present exchange constant ($E^{\$}_{cp}$) and present value function (V_{cp}) of a cantilever (Fig.3. Middle) are:

$$E^{\$}_{cp} = 1 \quad [\$US/kg] \tag{5}$$

$$V_{cp} = M^*_{cc} + M^*_{cm} \quad [\$US] \tag{6}$$

4.3 Convergent Value Function

The convergent value function defines the exchange constant required for non-ferrous metals to be the optimal material selection at an endurance of 1E6 cycles. This provides a limiting value, below which traditional materials are optimal. The convergence exchange constant ($E^{\$}_{cc}$) and convergent value function (V_{cc}) for a cantilever element are approximated as follows (Fig.3. Lower):

$$E^{\$}_{cc} \approx 1.9 \quad [\$US/kg] \tag{7}$$

$$V_{cc} \approx M^*_{cc} + 1.9\, M^*_{cm} \quad [\$US] \tag{8}$$

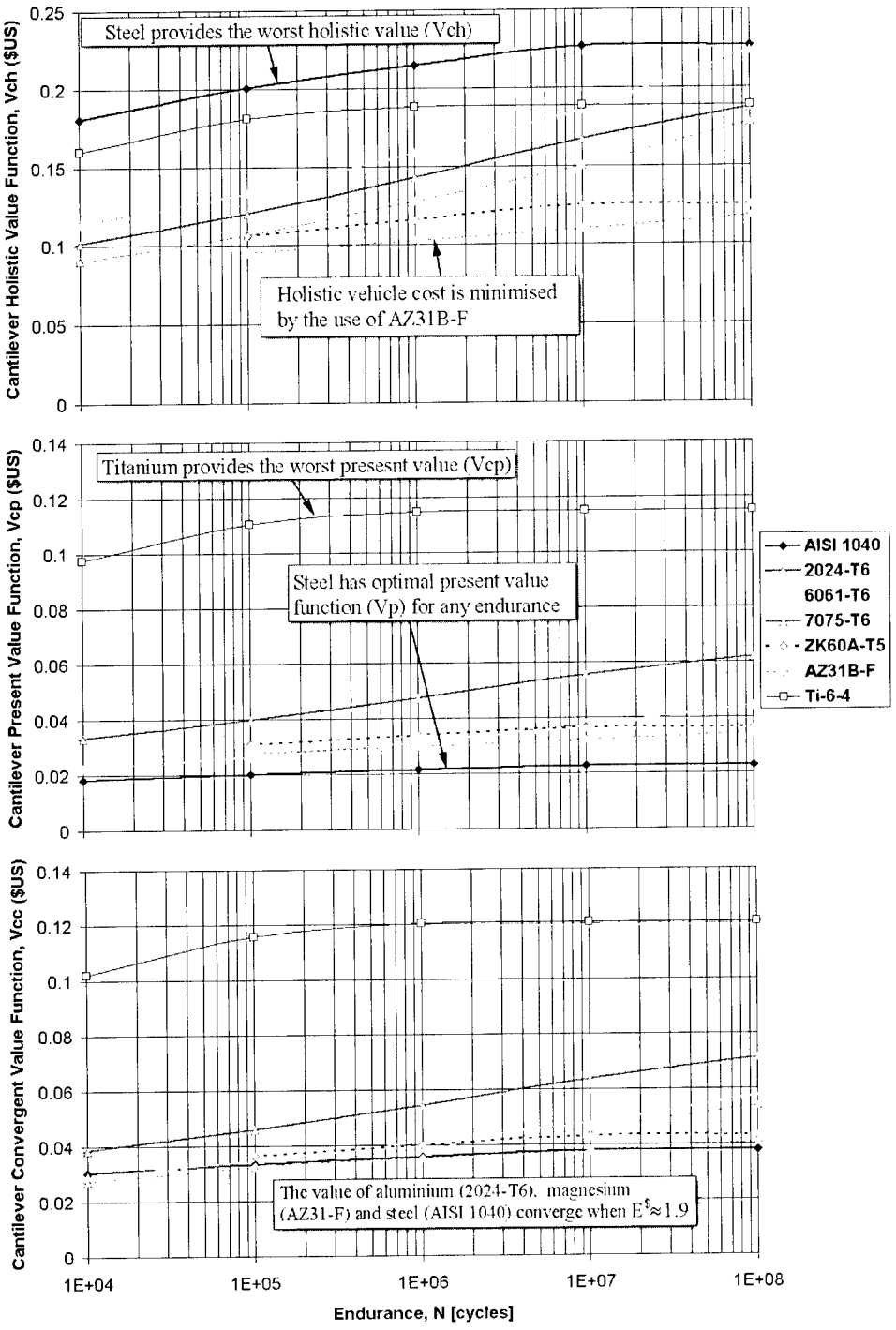

Fig.3. Value Functions Versus Endurance. Upper: Holistic Value Function (Vch), Middle: Present Value Function (Vcp), Lower: Convergent Value Function (Vcc)

4.4 Future Value Function

When the exchange constant for mass is greater than the convergent exchange constant light metals are optimal. The future value function provides an exploratory mechanism to investigate optimal light metals for material substitution strategies when the exchange constant for mass is $1US per kilogram above the convergent case. These results may be applied to vehicles that are subject to urgent mass reduction requirements due to increased emission or economy stringency, or in response to government standards that lead to a mass reduction urgency [10]. The future exchange constant ($E^{\$}_{cf}$) and future value function (V_{cf}) are as follows:

$$E^{\$}_{cf} = E^{\$}_{cc} + 1 = 2.9 \quad [\$US/kg] \quad (9)$$

$$V_{cf} = M_{cc} + 2.9\, M_{cm} \quad [\$US] \quad (10)$$

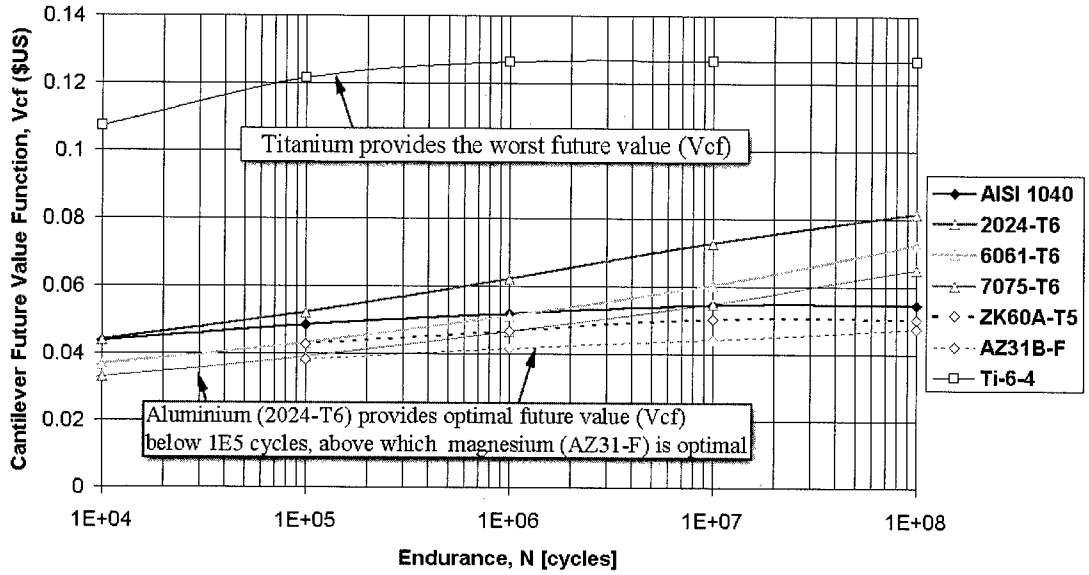

Fig.4. Future Value Function (Vcf)

4.5 Value Function Review

The value functions of figures 3 and 4 represent degrees of compromise between optimal mass and cost, and are bound by the mass and cost performance metrics of shown in Fig.1.

Magnesium (AZ31B-F) provides optimal holistic value (Fig.3. Upper) for component manufacturers interested in minimising both raw material and running costs. Steel (AISI 1040) provides the poorest holistic performance (Fig.3. Upper).

Steel (AISI 1040) has the optimal present value (Fig.3. Middle) for any endurance confirming the extensive use of this material in modern passenger vehicles and validating the preference of the automotive industry for low manufacturing costs at the expense of higher running costs. Aluminium alloys 6061-T6 and 2024-T6 have an almost identical present value and provide the most competitive option to steel for an endurance below 3E5 cycles. Above 3E5 cycles

magnesium (AZ31B-F) becomes the second best option. Light metals are not optimal for passenger vehicles defined by the present value function (Fig.3. Middle). Suitable rationales must be explored that may justify the use of light metal substitution strategies.

The convergent exchange constant for mass is approximately $US 1.9 per kilogram, at this value the performance of magnesium (AZ31-F) and steel (AISI 1040) converge at an endurance of 1E6 cycles (Fig.3. Lower). Light metals are the optimal material selection when the exchange constant for mass is greater than this cutoff value.

The future value function illustrates the relative merit of alternate materials when the exchange constant for mass reduction is increased above the associated cutoff (Fig.4), as may occur in response to urgent requirements for mass reduction [10]. Using this function aluminium (2024-T6) is optimal below approximately 1E5 cycles and is suited to applications with low to moderate endurance requirements (e.g. steering wheel and foot pedals). Magnesium (AZ31B-F) is preferred for applications above 1E5 cycles (e.g. suspension and drive train components). Magnesium has a low strength per unit volume [4], requiring a significant increase in component volume when converting from steel to magnesium. Spatial limitations may exclude the use of magnesium (AZ31B-F) as a lightweight substitute. Metals with higher strength per unit volume ratio (such as aluminium 2024-T6) may be the optimal material selection for high cycle applications.

A method has been proposed to systematically address the issue of optimal material selection for finite life applications and has been illustrated by the generation of performance of a finite life cantilever element. The curves generated guide optimal material selection for a finite life component under a range of scenarios applicable to the automotive industry. The method can assist light metal component manufacturers to define scenarios for which light metals are optimal. The method discussed can be generalised to any application which requires material selection for finite life applications.

REFERENCES

[1] J. N. Devlukia: Ph.D. thesis, Fatigue Studies Relating to the Automotive Industry, Sheffield University, (1994).

[2] M. Ashby: Material Selection in Mechanical Design, Butterworth Heinemann, UK, (2000).

[3] M. Leary and C. Burvill, Material Selection Indices for Finite Life Automotive Applications, in Engineering Materials 2001 Conferenceand Exhibition, Melbourne, Australia, (2001).

[4] Military Handbook-5, Metallic Materials and Elements for Aerospace Vehicle Structures, Batelle, US, (1998).

[5] S. D. Henry et al: Fatigue Data Book Light Structural Alloys, ASM, USA, (1995).

[6] H. Boyer: Atlas of Fatigue Curves, ASM, (1986), pp. 73.

[7] H. A. Rothbart: Mechanical Design Handbook, McGraw Hill, (1996), pp. 7.29.

[8] Model Year 2001 Fuel Economy Guide, EPA, (2001), available atwww.epa.gov.

[9] M. Ashby, Engineering Materials 1, Pergamon Press, (1993).

[10] M. Leary and C. Burvill, Addressing Urgent Mass Reduction Requirements by the use of Lightweight Components, in Light Materials for Transportation Systems, Pusan, Korea, (2001).

Session IV

FORMING

TEXTURES AND STRUCTURES OF ASYMMETRICALLY ROLLED ALUMINUM SHEETS

Dong Nyung Lee, Su-Hyeon Kim* and Keun-Hwan Kim**

School of Materials Science and Engineering, Seoul National University,
Shilim-dong, Kwanak-gu, Seoul 151-742, Korea
*Research Institute of Advanced Materials, Seoul National University,
Shilim-dong, Kwanak-gu, Seoul 151-742, Korea
**Sheet Products & Process Research Group, Technical Research Laboratories,
Pohang Iron & Steel Co., Ltd. Pohang, Gyungbuk 790-785, Korea

ABSTRACT

Asymmetric rolling, in which the circumferential velocities of working rolls are different, is a novel technique that introduces an intense plastic shear strain for the purpose of uniform development of shear texture and grain refinement. A component of ND//<111> in the shear texture can improve the plastic strain ratios and in turn the deep drawability of aluminum sheets. The strain histories and distributions and the texture evolution in 1050 aluminum sheet during asymmetric rolling have been measured and calculated. The shear texture can vary with the ratio of shear to normal deformation gradients. As the ratio increases from zero to infinity, the texture moves from the plane strain compression texture (β fiber) to the ideal shear deformation texture consisting of {001}<110>, {111}<110>, and {111}<112>. When subjected to several passes of asymmetric rolling of aluminum alloy sheets, the shear textures approaching to but deviated from the ideal shear components develop along the thickness. TEM and EBSD analyses show that the asymmetrically rolled sheets comprise fine grain structures with large misorientations, whereas symmetrically rolled sheets have coarse grains with low angle boundaries.

1. INTRODUCTION

Asymmetric rolling, in which the circumferential velocities of working rolls are different, is a novel technique that introduces an intense plastic shear strain for the purpose of uniform development of shear texture and grain refinement of a sheet [1-8]. Unlike conventional or symmetric rolling, which can introduce shear strains only in the surface region of a sheet, asymmetric rolling can give rise to shear strains through the thickness. Recent studies have reported that shear strains can develop shear deformation textures, which in turn improve the plastic strain ratios and in turn deep drawabilities of aluminum sheets [1-12]. The ideal components of shear deformation textures of fcc metals are {001}<110>, {111}<110>, and {111}<112>, in which ND//{111} is the most useful component for the deep drawability [2,3,13]. The cube texture that is observed in the cold rolled and subsequently annealed aluminum alloy sheets is known to give rise to inferior deep drawabilities. The uniform shear texture through the thickness made by asymmetric rolling therefore means a substantial increase in the plastic strain ratio.

In addition to the texture development, a severe plastic deformation by shear has been focused on as an effective method of producing fine-grained materials. Several processes have been proposed for the grain refinement, such as torsion straining [14,15], equal channel angular pressing (ECAP) [16-24], and asymmetric rolling [25]. Among them, asymmetric rolling seems to be the most practical and feasible method for fabrication of large-scale sheets. For the effective grain refinement by asymmetric rolling, the control of rolling conditions is important, because the strain distribution along the thickness is dependent on rolling parameters.

In the present study, the through-thickness distributions of texture and microstructure in asymmetrically rolled aluminum alloy sheets have been investigated.

2. EXPERIMENTAL

The materials used in this study were 6.5mm thick 1050 commercial purity aluminum (99.5% Al-Fe-Si) sheets, which were fully annealed at 400°C for 1h prior to rolling. The average grain size was about 40μm. Asymmetric rolling was carried out under unlubricated condition at room temperature with a mill of which the upper and lower roll diameters were 248mm and 128mm, respectively, at a rotation rate of about 7 rpm. Figure 1 shows a schematic diagram of the asymmetric rolling process. The specimens were rolled in unidirection, in which the rolling direction and the specimen position are kept the same in all rolling passes. The total reduction was about 91% through 12 passes. The rolled specimens were annealed for 1h at 195°C.

The textures were measured with an X-ray diffraction goniometer in the back reflection mode with Fe filtered Co-Kα radiation. The microstructures of specimens were observed under a transmission electron microscope (TEM). To investigate the grain refinement effect, selected area diffraction patterns (SADP) were obtained using a 3μm diameter aperture. For the TEM foil preparation, the specimens were mechanically polished and then electro-polished in a nitric acid solution. The grain boundary structures were investigated using electron back-scattering diffraction (EBSD). The EBSD specimens were electro-polished in a solution consisting of 20% perchloric acid and 80% ethanol. JEOL JSM-6300 SEM equipped with a Link ISIS OPAL system was employed.

The deformation was analyzed by the elasto-plastic FEM. In the analysis, the friction coefficient between rolls and material was assumed to be 0.4, because sticking friction occurred between rolls and material and the flow curve of aluminum was approximated by $\sigma=179\varepsilon^{0.22}$ [26]. The undeformed aluminum was assumed to consist of 978 randomly oriented crystallites in each element. The strain increment history of each element was obtained and used to calculate crystallographic orientations based on the full constraints Taylor theory [27] together with the Renouward-Wintenberger theory [28]. The orientations were expressed as Gaussian peaks with a scattering angle of 10° and superimposed to obtain distributions in pole figures [29].

3. RESULTS AND DISCUSSION

Figure 2 shows the deformed meshes of an aluminum sheet obtained by FEM analysis of

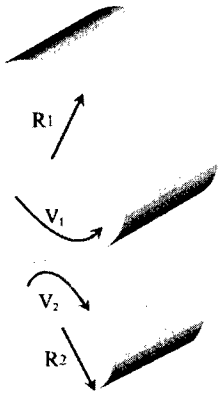

Fig. 1 Schematic drawing of asymmetric rolling process (R_1:R_2=V_1:V_2).

asymmetric rolling by 50% at roll radius ratios of 1.25, 1.5 and 2.0. The deformed meshes show that the shear strain can be increasingly uniform through the thickness with increasing the roll radius ratio. When an aluminum sheet having a random distribution of orientations undergoes deformations in Fig. 2, the textures in Fig. 3 are calculated to form. The textures in Fig. 3 all deviate from the ideal shear deformation textures. It is known that shear deformation textures approach the ideal shear deformation texture with increasing α ($=e_{13}/e_{11}$ with the suffixes 1and 3 indicating the rolling and normal directions, respectively) [1]. As α increases from zero to infinity, the stable texture moves from the plane strain compression texture (β fiber) to the ideal shear deformation texture consisting of {001}<110>, {111}<110>, and {111}<112>.

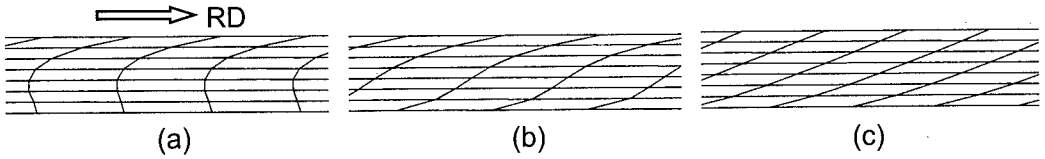

Fig.2 Deformed FEM meshes of aluminum sheets asymmetrically rolled by 50% at roll radius ratio of (a) 1.25, (b) 1,5, and (c) 2.0.

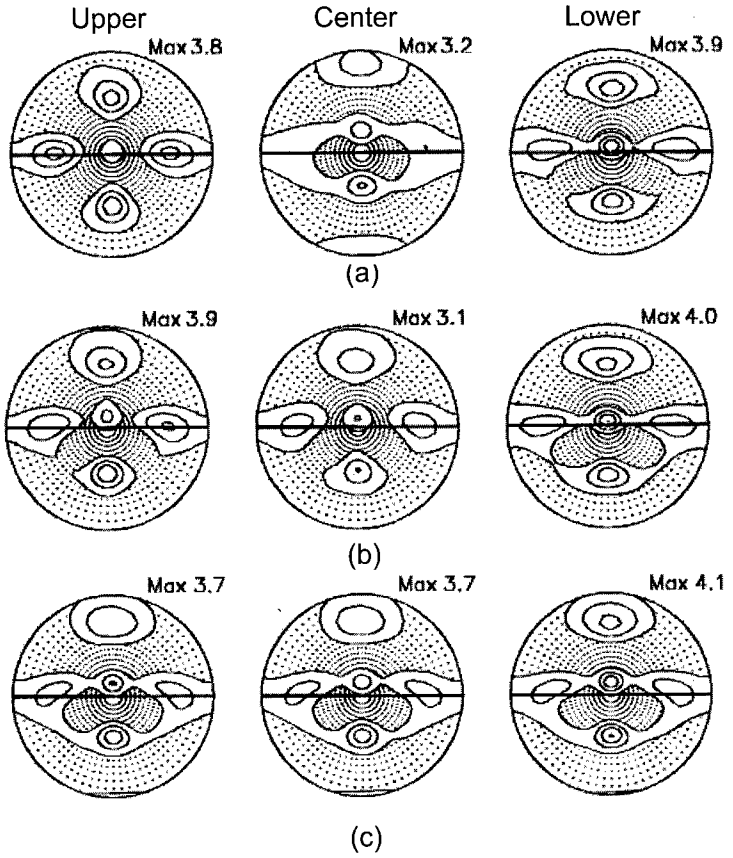

Fig. 3 Calculated (111) pole figures of aluminum sheets asymmetrically rolled by 50% at roll radius ratio of (a) 1.25, (b) 1.5 and (c) 2.0.

Figure 4 shows (111) X-ray pole figures measured at the upper surface, center, and lower surface layers of 1050 aluminum alloy sheet asymmetrically rolled by 91% through 12 passes at a roll radius ratio of 2 and subsequently annealed at 195°C for 1 h. The texture of the rolled sheet approaches to but deviates from the ideal shear deformation texture and its intensity is weak. It is also noted that the texture is not uniform due to non-uniform shear deformation along the thickness. The texture density tends to increase with increasing distance from the upper surface toward the lower surface. This trend is in agreement with the calculated textures in Fig. 3 (c). It can also be seen that the macroscopic textures remain almost unchanged after annealing at 195°C. Kim and Lee [8] reported that well developed shear deformation textures remained unchanged even after annealing at 350°C. They attributed this phenomenon to the loss of the driving force for recrystallization by rapid annihilation of dislocations due to their characteristic array shown schematically in Fig. 5. The array is based on the fact that the slip systems in asymmetric rolling of (001)[110] crystal that is a major component in the ideal shear deformation texture are calculated to be $(\bar{1}\,11)[110]$ and $(1\,\bar{1}\,1)[110]$, which share the same slip direction. When the specimen is annealed, dislocations in the arrays can interact to annihilate rapidly. This was indirectly shown in a hardness test result.

Figure 6 shows TEM bright field (BF) microstructures and selected area diffraction patterns (SADP) of the upper surface, center, and lower surface layers of the rolled and annealed specimens. The TEM samples were thinned parallel to the rolling plane. SADPs were obtained in the center areas of corresponding BF images using 3μm diameter aperture. The microstructures show that the specimens consist of fragmented or refined grains and the numerous spots in the SADPs indicate the presence of high angle grain boundaries. More sharply defined boundaries in the lower surface regions could be due to dynamic recovery during rolling.

After annealing, the recovered or coarsened microstructures developed. The grain sizes and image contrast suggest that the materials have uniformly distributed high angle boundaries through the thickness.

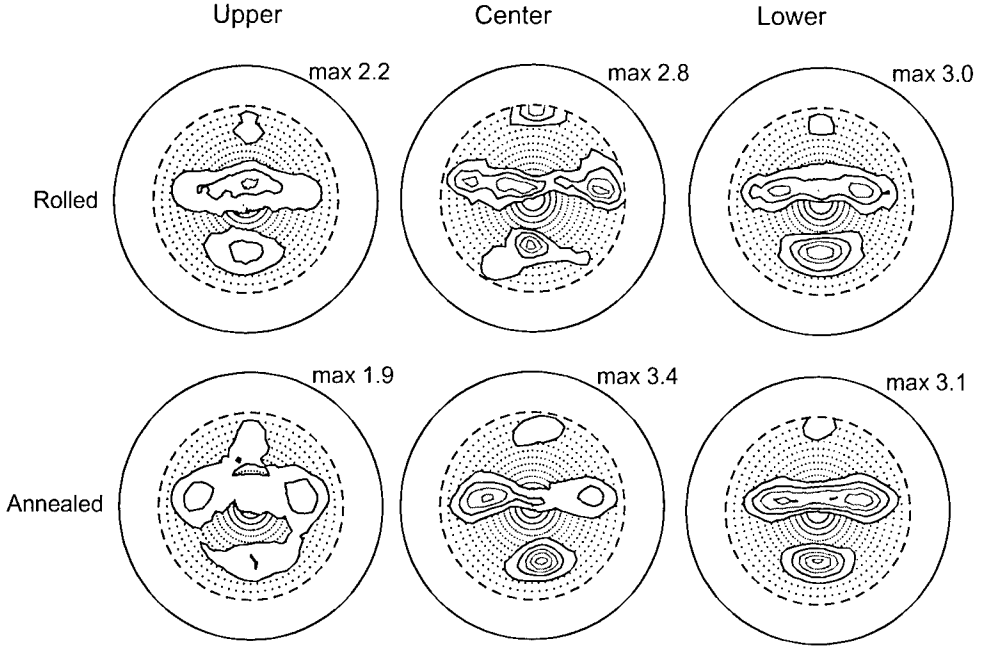

Fig. 4 (111) X-ray pole figures of upper surface, center, and lower surface layers of 1050 aluminum alloy sheet asymmetrically rolled by 91% through 12 passes at roll radius ratio of 2 and annealed at 195°C for 1 h. (Contour levels: 1, 1.5, 2.0, 2.5, 3.0).

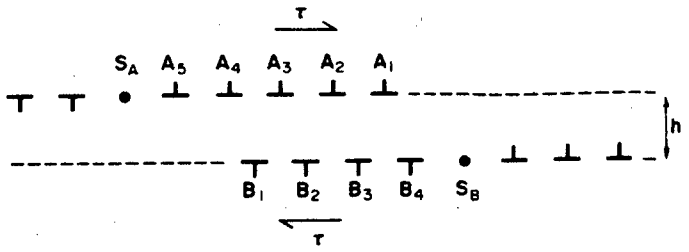

Fig. 5 Dislocation sources S_A and S_B generate dislocations A_1, A_2, A_3.....and B_1, B_2, B_3.....whose Burgers vector is [110].

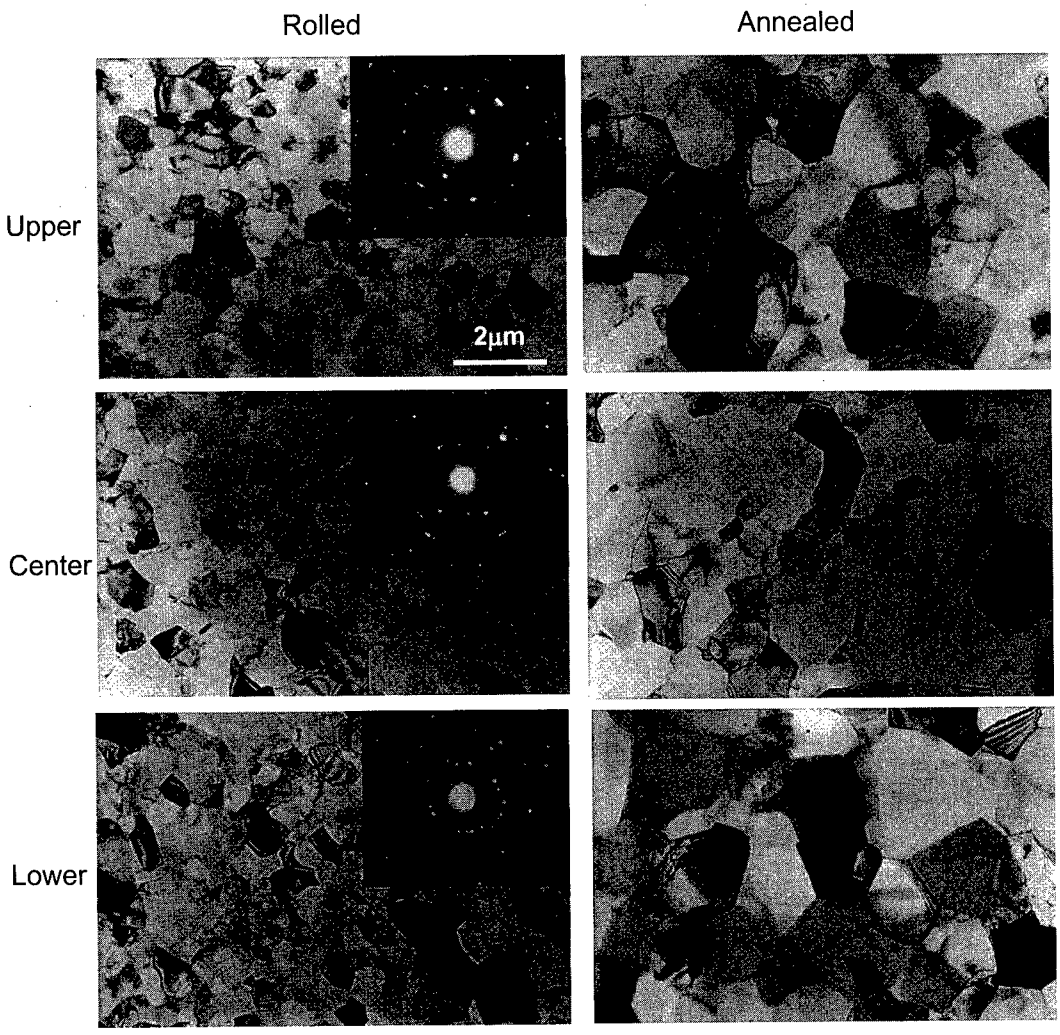

Fig. 6 Bright field TEM micrographs and SADPs of upper surface, center, and lower surface layers of 1050 aluminum alloy sheets asymmetrically rolled by 91% and subsequently annealed at 195°C for 1h.

EBSD mappings of annealed specimens in the rolling plane view are shown in Fig. 7 and the grain size and boundary characteristics are summarized in Table 1. The grain size means an equivalent circle diameter obtained from 3° tolerance grains. It can be seen that uniformly distributed fine grained microstructures develop through the thickness. The grain sizes are under 2μm and the boundary miorientations are high angled, that is, the boundaries are of higher angle boundary character.

In order to compare microstructural evolutions in the asymmetrically rolled sheet and a plane strain rolled sheet, the same initial material was symmetrically rolled by 91% under lubrication and annealed at 195°C for 1h. EBSD map of the plane strain rolled and annealed specimen is shown in Fig. 8, which indicates that grains are coarse compared with ones in asymmetrically rolled specimens and grain boundaries are of low angles.

The shear strain is thus an important factor for developing the shear deformation textures and producing fine-grained materials. Asymmetric rolling makes the shear strain penetrate into the center region of the sheet and the uniformity of the shear strain and texture can be controlled by rolling parameters such as the roll velocity ratio, reduction per pass, etc. [1].

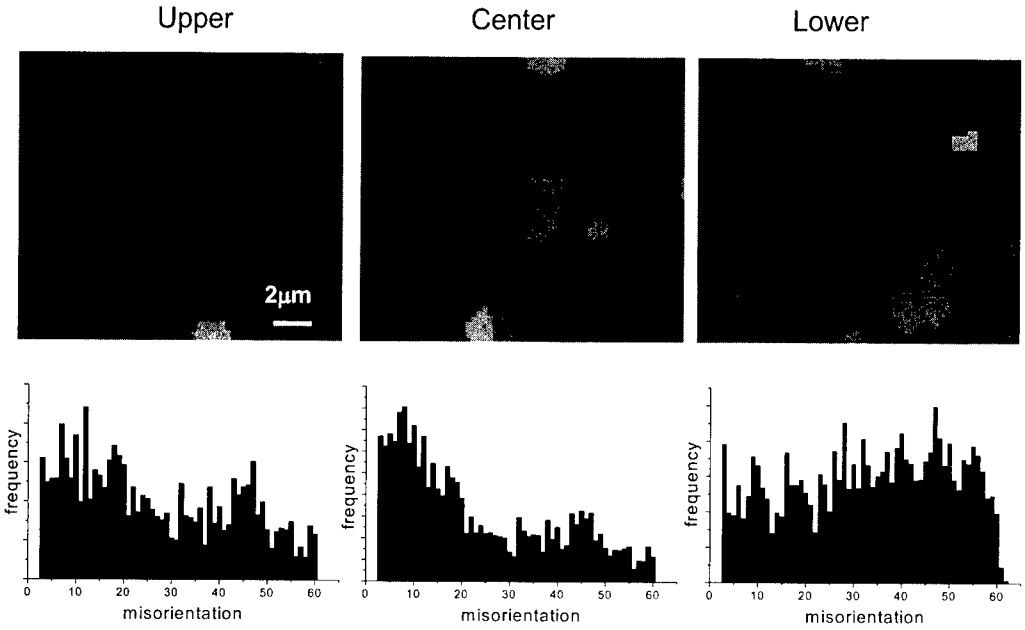

Fig. 7 EBSD analyses of upper surface, center and lower surface layers of 1050 aluminum alloy sheets asymmetrically rolled by 91% and annealed at 195°C for 1h.

Table 1. Grain sizes and grain boundary misorientations of upper surface, center, and lower surface layers of 1050 aluminum alloy sheet asymmetrically rolled by 91% and annealed at 195°C for 1h.

	Upper	Center	Lower
Average grain size, μm	1.57	1.77	1.84
Average boundary misorientation, °	30.1	22.9	33.2
Fraction of high angle boundaries ≥15°	0.67	0.54	0.80

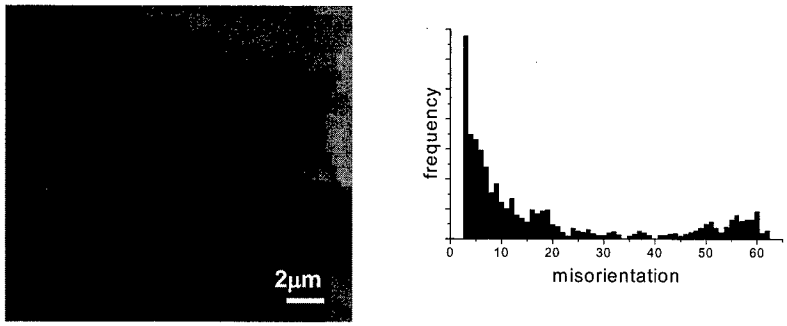

Fig. 8 EBSD analysis of surface layer of 1050 aluminum alloy sheet symmetrically rolled by 91% and annealed at 195°C for 1h

4. CONCLUSIONS

A 1050 aluminum alloy sheet was asymmetrically cold rolled by 91% through 12 passes using a mill whose upper and lower roll diameters are 248 and 128 mm, respectively, and annealed at 195°C for 1hr. The textures of asymmetrically rolled sheets were a little deviated from the ideal shear deformation texture, {001}<110> and ND//{111}, and the texture intensity increased with increasing distance from the upper surface toward the lower surface. The textures remained unchanged after annealing. The rolled and annealed sheets had fine-grained microstructures with high angle grain boundaries. A little non-uniform texture and microstructure distributions along the thickness are due to the non-uniform shear strain distribution along the thickness, which can be controlled by rolling parameters.

ACKNOWLEDGEMENT

Financial support from National Research Laboratory for Texture Control, Seoul National University is gratefully acknowledged.

REFERENCES

1. K.-H. Kim and D.N. Lee, Acta Mater., in press.
2. K.-H. Kim, C.-H. Choi and D. N. Lee, in ICOTOM 12, J.A. Szpunar, eds., NRC-CNRC, Montreal, Canada, (1999), pp. 755-760.
3. C.-H. Choi, K.-H. Kim, S.-Y. Jeong and D.N. Lee, J. Kor. Inst. Met. & Mater., Vol.35(1997), pp. 429-439.
4. C.-H. Choi, K.-H. Kim and D.N. Lee, Mater. Sci. Forum, Vol.273-275(1998), pp. 391-396.
5. C.-H. Choi, K.-H. Kim and D.N. Lee, in Synthesis/Processing of Lightweight Metallic Materials II, C.M. Ward-Close, F.H. Froes, D.J. Chellman and S.S. Cho, eds., TMS, Florida, (1997), pp. 37-48.
6. Dong Nyung Lee, Keun-Hwan Kim, Chang-Hee Choi and Hyung-Gu Kang, in International Conference on Advanced Automobile Materials, W. Xianjin and W. Zubin, eds., The Chinese Soc. for Metals, Beijing, China, (1997), pp. 67-76.
7. D.N. Lee and K.-H. Kim, in Proc. 98 International Symposium of the RCPAM, B.I. Kim, Y.B. Park, and S.S. Kim, eds., Sunchon National University, Sunchon Korea, (1998), pp. 39-49.
8. D.N. Lee and K.-H. Kim, in Proc. The Second Global Symposium on Innovations in Materials Processing and Manufacturing, M.Y. Demery, ed., TMS, Warrendale, Penn.USA,

(2001), pp. 219-235.
9. T. Kamijo and H. Fukutomi, in 16th Riso International Symposium of Materials Science, H. Hansen, D.Juul Jensen, Y.L. Liu and B. Ralph, eds., Riso National Laboratory, Roskilde, Denmark, (1995), pp. 377-382.
10. J. Hu, K. Ikeda and T. Murakami, J. Japan Inst. Met., Vol.60(1996), pp. 1130-1135.
11. N. Tsuji, Y. Nagai, T. Sakai and Y. Saito, Mater. Trans. JIM, Vol.39(1998), pp. 252-261.
12. C.-H. Choi and D.N. Lee, Met. Mater. Trans. A, Vol.28A(1997), pp. 2217-2222.
13. PH. Lequeu and J.J. Jonas, Metall. Trans A., Vol.19A(1988), pp. 105-120.
14. R.Z. Valiev, A.V. Korznikov and R.R. Mulyukov, Mater. Sci. Eng A., Vol.168A(1993), pp. 141-148.
15. Z. Horita, D.J. Smith, M. Furukawa, M. Nemoto, R. Z. Valiev and T. G. Langdon, in Thermac 97, T. Chandra and T. Sakai, eds., TMS, Warrendale, PA, (1997), pp. 1937-1943.
16. V.M. Segal, Mater. Sci. Eng A., Vol.197A(1995), pp. 157-164.
17. S. Ferrasse, V.M. Segal, K.T. Hartwig and R.E. Goforth, Metall. Mater. Trans A., Vol.28A(1997), pp. 1047-1057.
18. Sun-Hwa Jin, Hyoung-Wook Kim and Suk-Bong Kang, J. Kor. Inst. Met. & Mater., Vol.38(2000), pp. 1600-1605.
19. Jae-Chul Lee, Hyun-Kwang Seok, Jin-Yoo Seo, Young-Hoon Jung and Ho-In Lee, J. Kor. Inst. Met. & Mater., Vol.39.(2001), pp. 293-300.
20. Min-Hong Seo and Hyoung Seop Kim, J. Kor. Inst. Met. & Mater., Vol.39(2001), pp. 360-366.
21. A. Gholinia, P. B. Prangnell and M. V. Markushev, Acta Mater., Vol.48(2000), pp. 1115-1130.
22. Y. Iwahashi, Z. Horita, M. Nemoto and T.G. Langdon, Acta Mater., Vol.45(1997), pp. 4733-4741.
23. Y. Iwahashi, Z. Horita, M. Nemoto and T.G. Langdon, Acta Mater., Vol.46(1998), pp. 3317-3331.
24. D.H. Shin, I. Kim, J. Kim and K.-T. Park, Acta Mater., Vol.49(2001), pp. 1285-1292.
25. Q. Cui and K. Ohori, Mater. Sci. Tech., Vol.16(2000), pp. 1095-1101.
26. C.-H. Choi, J.-W. Kwon, K.H. Oh and D.N. Lee, Acta Mater., Vol.42(1997), pp. 5119-5128.
27. G.L. Taylor, J. Inst. Met. Vol.63(1938), pp. 307-324.
28. M. Renouard and M. Wintenberger, C. R. Acad. Sci. Paris Serie B, Vol.292(1981), pp. 385-388.
29. H.-J. Bunge: Texture Analysis in Materials Science, Butterworths, London(1982), pp. 180-183.

EVOLUTION OF ANISOTROPY IN PRECIPITATION HARDENING AL-LI 2090-T8E41 ALLOY

H. Garmestani[1], S. R. Kalidindi[2], C. Fountain, L. Williams, E. W. Lee[3], O. S. Es-Said[4]

[1] FAMU-FSU COE, Tallahassee, FL 32310-6046, (garm@magnet.fsu.edu)
[2]Drexel University, Philadelphia, PA 19104
[3] Naval Air Systems Command, Patuxent River, MD 20670
[4] Loyola Marymount University, Los Angeles, CA 90045-8145

ABSTRACT: This paper presents a crystal plasticity based modeling effort to incorporate the segregation of the contributions to the overall anisotropy from crystallographic texture and precipitation hardening in Al-2195 material. The new model correlates the contribution from precipitate hardening to either co-planar slip activity or the non-coplanar slip activity in the cold-working step prior to the aging heat treatment. A Taylor-type (fully-constrained) crystal plasticity model was formulated to predict the yield strength of the fully processed sheet and its anisotropy, while accounting for the initial texture in the hot-worked sheet, its evolution during the cold-working step prior to aging, and the inhomogeneous nucleation of the T_1 phase platelets (these are known to form on {111} planes, but not usually in equal amounts on the different {111} planes in a given crystal).

INTRODUCTION: T_1 precipitate is recognized as the major source of strengthening in Al-Li-Cu alloys (Lee et al. [1999]). This precipitate has a hexagonal structure, and occurs as thin plates on {111} planes, which also happens to be the slip planes for face-centered cubic alloys. Anisotropy in Al-Li alloys can be attributed to at least two factors: (i) the strong texture in these alloys in the processed condition, and (ii) the inhomogeneous nucleation of T_1 precipitates. The precise contributions from these two factors are not clearly known at the present time. It is the purpose of this paper to assess in particular the contribution to the overall anisotropy from the second factor listed above. Off-axis rolling were applied on the sheet at room temperature prior to the aging treatment, and the mechanical anisotropy in the fully processed sheets was characterized by performing tension tests on coupons cut from the sheet at 0, 30, 45, 60 and 90 degrees to the original rolling direction (RD). Both the initial texture in the sheet and its evolution during the different off-axis stretches were characterized. The alloys processed in this study showed pronounced anisotropy. The application of the methodology developed in this study revealed that much of the observed anisotropy in this particular data set could be explained by accounting for the texture in the sample in the processed condition. A careful set of uniaxial tensile tests provided information on the mechanical strain hardening coefficient evolution during the aging and prior deformation processes. These measurements were necessary to isolate the effect of latent hardening to overall strengthening mechanism. The model simulations show clear correlation of the anisotropy with preferential hardening mechanisms arising from either co-planar or non-coplanar slip activity during the off-axis rolling.

EXPERIMENTAL PROCEDURES AND RESULTS: The effect of the off-axis stretch on the yield strength anisotropy in the sheet is shown in Fig. 1. A similar behavior was discussed by Lee et al. [1999] for 2095 Al-Cu-Li alloy. The minimum strength was obtained at either 45 or 60 degrees to the rolling direction (RD) in all the sheets produced in this study. The lowest overall strength level was obtained in the samples stretched at 45 degrees to RD. There was significant anisotropy in all sheets produced for this study, which ranged from about 15% to 45%. Comparison of the textures indicates that the texture did not change much during the stretching and aging process. The major change appears to be some weakening (or spreading) of the Brass component.

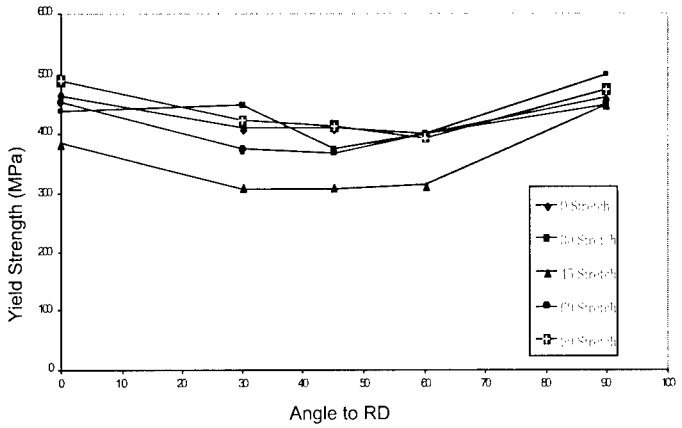

Figure 1. Measured anisotropy of yield strength in 2090 Al-Li Alloy.

Crystallographic texture was measured both in the as-received condition and in the stretched and aged condition. For texture measurements, samples were mechanically polished and etched to remove any residual deformation layers. In all cases, the original rolling direction was used as the pole figure reference direction. The crystallographic texture was measured using the X-ray diffraction technique on a Philips X'Pert PW3040 MRD X-ray diffractometer operating at 40 KV and 50 mA using CuK_a radiation. The diffractometer was equipped with a curve monochromator. Three incomplete pole figures (111), (200), and (220) were obtained using the reflection technique. The resulting data was analyzed using the popLA software package (Kallend et al., 1991) from which the Orientation Distribution Functions (ODFs) were calculated using the spherical harmonic approach.

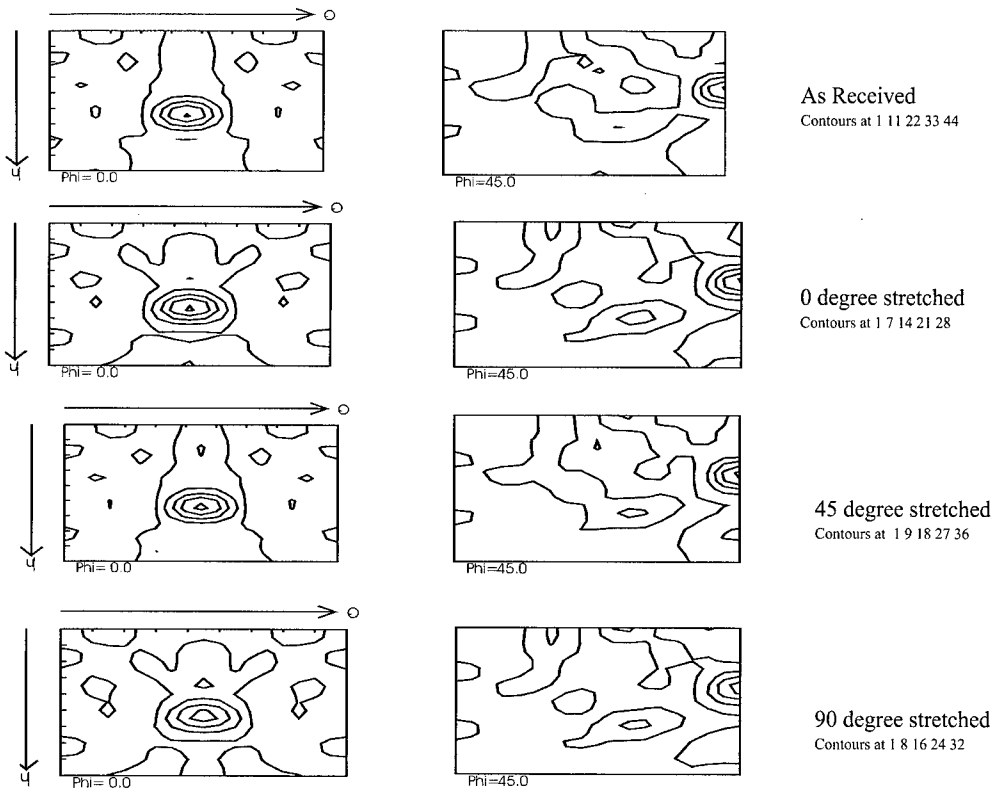

Figure 2. ODF micrographs of the material at different stages of processing

The initial texture in the as-received material is presented in Figure 2 as ODF sections. The results are plotted using three Euler angles (j_1, F, j_2) according to the convention suggested by Bunge (1993). In the as-received state, the material exhibited a very strong Brass component ({110}<112>) and a weak Copper component ({112}<111>) with intensities of about 45X and 2X random, respectively. Brass and Copper components occur at locations (j_1, F, j_2) =(35,45,0), (90,30,45) respectively. The high Brass intensity is common in Al-Li alloys, especially in the Al-Li superplastic materials. Other significant texture components observed in the as-received material included R {124}<211>, P {110}<122>, S {123}<634> and shear {111}<112> orientations, with intensities of about 9 – 11X random.

MODELING AND SIMULATION: An extended Taylor-type model is used to simulate the anisotropy of the yield strength in the rolled plates of the Al-Li alloys described in the previous section. The shearing rate on the slip system is dependent on the resolved shear on the slip system and the slip resistance of that slip system, and can be expressed in a power-law relationship as $\tau^{\alpha} \approx \mathrm{T}^{*} \bullet \mathrm{S}_{o}^{\alpha}$, where $\dot{\gamma}_{o}$ denotes a reference value of the slip rate and m represents the strain rate sensitivity parameter (see e.g. Kalidindi et al., 1992). In general, the evolution of the slip system resistance can be expressed as

$$\dot{s}^{\alpha} = \sum_{\beta} h^{\alpha\beta} \left| \dot{\gamma}^{\beta} \right| \qquad (1)$$

where $h^{\alpha\beta}$ represent the slip hardening rates and s^{α} are taken as constants ($h^{\alpha\beta} = 0$). The effect of slip activity during the cold-working stage on the corresponding slip resistances in the aged condition (through inhomogeneous distribution of T_1 precipitates) can be studied by invoking one of the two following forms:

$$s^{\alpha} = s_o + K^{cp} \sum_{\substack{\beta \in \text{co-planar} \\ \text{slip systems of} \alpha}} \left| \gamma^{\beta} \right| \qquad (2)$$

$$s^{\alpha} = s_o + K^{ncp} \sum_{\substack{\beta \in \text{non-coplanar} \\ \text{slip systems of} \alpha}} \left| \gamma^{\beta} \right| \qquad (3)$$

where s_o represents the initial constant value (before cold-working and/or aging) for all slip systems, and K^{cp} and K^{ncp} represent modeling parameters. As an example, we show in Fig. 3, influence of the parameter K^{cp} on the yield strength anisotropy in the sheet that was stretched at 60 degrees to the rolling direction.

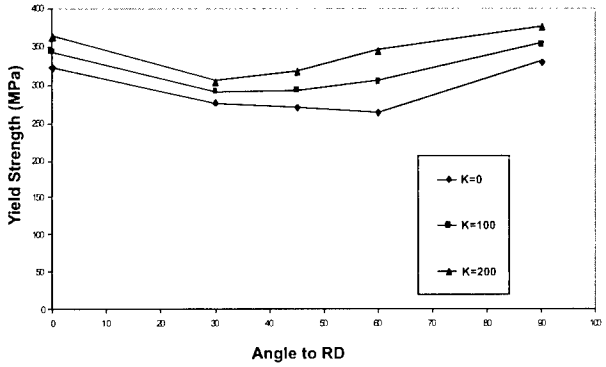

Figure 3. Influence of co-planar slip hardening on the predictions of the yield anisotropy for the sheet stretched at 60 degrees to the rolling direction.

CONCLUSIONS: Yield strength anisotropy in stretched and aged Al-Li sheet alloys was characterized as a function of the angle of the stretch with respect to the rolling direction. A detailed analysis was then conducted using a Taylor-type crystal plasticity model to identify the potential sources of this anisotropy. It is quite clear from the above study that the underlying texture plays a dominant role in anisotropy with a lesser contribution from the inhomogeneous nucleation of the T_1 precipitates..

REFERENCES

Kalidindi, S. R. , Bronkhorst, C. A. and Anand, L. 1992, "Crystallographic Texture Evolution During Bulk Deformation Processing of FCC Metals", Journal of the Mechanics and Physics of Solids, 40, pp. 537-569.

Lee, E. W., Kalu, P. N., Brandao, L., Es-Said, O. S., Foyos, J. and Garmestani, H. 1999, "The effect of off-axis thermomechanical processing on the mechanical behavior of textured 2095 Al-Li alloy, Journal of Materials Science and Engineering, A265, P100-109.

THROUGH-THICKNESS VARIATION OF MICROSTRUCTURE AND TEXTURE IN HIGH SPEED HOT ROLLING OF ALUMINUM AND ALUMINUM ALLOY SHEET

Tetsuo Sakai, Seong Hee Lee and Yoshihiro Saito

Department of Materials Science and Engineering
Graduate School of Engineering
Osaka University
2-1 Yamada-Oka Suita Osaka, 565-0871 Japan

ABSTRACT

Effects of inhomogeneous shear strain on the through-thickness variation of microstructure and texture of hot rolled aluminum and aluminum alloy sheet are investigated. Sheet specimens of 1050 and 5052 aluminum alloys are rolled at temperatures ranging from 410 to 560°C at a rolling speed of 15m/s without lubrication and quenched into water at an interval of 30ms after rolling.

The redundant shear strain induced by high friction increases beneath the surface at a reduction above 50% for 5052 and above 60% for 1050. Recrystallization occurs in the surface region when effective strain exceeds a critical value that depends on rolling temperature, while only recovery occurs in the center region. The critical effective strain for the occurrence of recrystallization in 5052 alloy is lower than that in 1050 alloy. When large shear strain is introduced beneath the surface, the shear texture of which main components are {001}<110> and {111}<110> develops. In the center region, Cu-orientation and cube orientation develop. The shear texture beneath the surface is weak when recrystallization occurs.

1. INTRODUCTION

In hot rolling of metal strips, redundant shear strain is generated by friction between a strip and rolls. The shear strain is inhomogeneous through thickness and has marked effects on the formation of microstructure in the hot rolled strip. In high speed hot rolling, the shear strain tends to accumulate below the surface and forms a severely sheared region; a thin layer of fine recrystallized grains is often observed beneath the surface of the sheet quenched into water shortly after rolling [1-3]. The redundant shear strain is also responsible for the texture variation through the thickness of a hot rolled sheet, because it affects a formation of deformation texture and consequently produces an inhomogeneous recrystallization texture.

In the previous paper [3], we reported the effects of redundant shear strain in high speed hot rolling of austenitic stainless steel sheets on the formation of an inhomogeneous texture through the sheet thickness. The deformation texture became inhomogeneous in higher reductions; <111>//ND axis density increased and <110>//ND axis density decreased with increasing shear strain, and recrystallization after rolling randomized the texture except in the severely sheared region where recrystallization texture with a high <111>//ND axis density developed.

The inhomogeneity of texture due to shear deformation in hot rolled sheets plays sometimes an important role in the manufacture of high quality metal strip. It is well known that the well developed <111>//ND texture is effective for improvement of r-value not only of bcc metals but also of fcc metals [4]. Accordingly, an introduction of shear deformation to an aluminum alloy sheet by rolling is a promising method for improving press formability. The

purpose of the present work is to investigate the effects of rolling condition on inhomogeneous strain distribution of the pure aluminum and Al-Mg alloy sheets in high speed hot rolling. The microstructure and texture variation through the thickness of rolled sheet caused by inhomogeneous strain distribution is also investigated.

2. Materials and Experimental Procedure

Starting materials were cold rolled and annealed 3mm thick sheets of aluminum (AA1050) and Al-2.5%Mg alloy (AA5052). The width of the specimen was 28mm. Rolling temperature was varied from 410 to 560°C. Rolling speed was fixed at 15m/s and reduction was varied from 40 to 60%. The high speed laboratory mill equipped with rolls 530mm in diameter and 120mm in length was used. The rolled specimen was quenched by a water spray with the interval of 30ms after rolling. In order to roll in high friction condition, rolling was conducted without lubrication. Roll surface was degreased by solvent before rolling.

The strain distribution through the thickness was determined by measuring the distortion of a pin of 1050 aluminum or 5052 aluminum alloy with the diameter of 2mm that had been embedded in the sheet before rolling with its axis perpendicular to the sheet plane [5]. After rolling, the specimen was cut in the midplane perpendicular to the rolling plane and parallel to the rolling direction so that the distortion of the pin due to shear deformation can be observed. The shear strain is expressed as follows on the basis of 3 assumptions:

(1) The ratio of incremental shear strain to incremental compressive strain is constant during rolling.

(2) Incremental compressive strain is uniform through the thickness.

(3) Plane strain condition prevails in the deformation zone.

$$\gamma = \frac{2(1-r)^2}{r(1-r)} \tan\theta \cdot \ln\frac{1}{1-r} \tag{1}$$

where r is the reduction in thickness and θ is the slope of the tangent to the distortion line of the pin. Equivalent strain $\bar{\varepsilon}$ that may directly affect the microstructure of rolled sheet is expressed as follows.

$$\bar{\varepsilon} = \frac{2}{\sqrt{3}} \sqrt{\left(\ln\frac{1}{1-r}\right)^2 + \frac{\gamma^2}{4}} \tag{2}$$

The {111} pole figures were measured at the various positions of the thickness of the sheet after rolling and after annealing by Schulz's reflection and transmission method. The contours in pole figures were expressed in the units of the intensity from the randomly oriented standard sample.

3. RESULTS

3.1 Strain Distribution through Thickness

The variation of the shear strain through the thickness of rolled sheet measured from the inclination of the embedded pin is shown in Fig. 1. Shear strain increases with increasing the distance from center. At higher reduction, shear strain accumulates beneath the surface to form a severely sheared region. Figure 2 shows the effects of rolling temperature and reduction on maximum equivalent strain. The equivalent strain for plane strain compression without shear deformation is expressed by thin solid line in Fig. 2. In the range of the present experiment, rolling temperature does not exert a marked effect on the distribution of shear

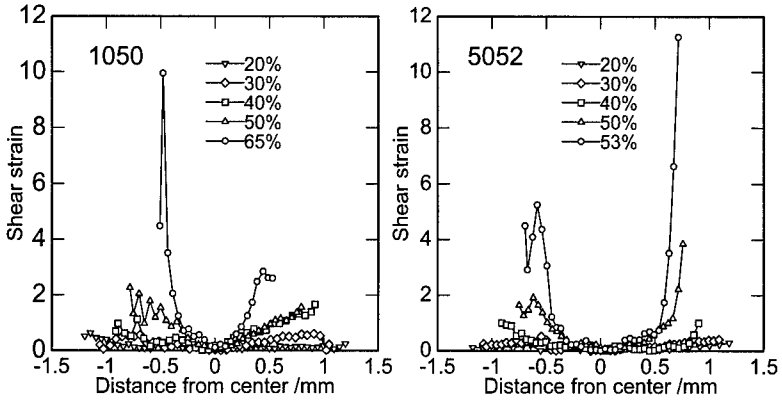

Fig. 1 Variation of shear strain through the thickness of rolled sheet.

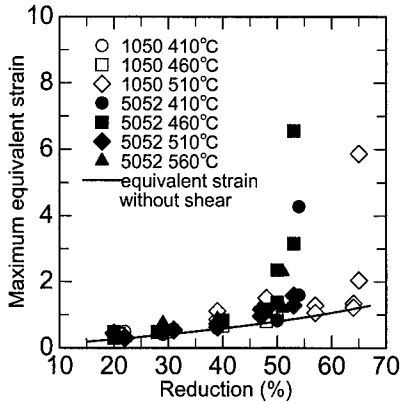

Fig. 2 Effects of reduction and rolling temperature on the maximum equivalent strain.

strain. The maximum equivalent strain steeply increases when reduction exceeds 50%(5052) or 60%(1050). This abrupt increase in shear strain is probably due to large friction force caused by seizure.

3.2 Microstructure

The microstructures observed beneath the surface and at the center of the thickness of the sheets rolled to large reduction are shown in Fig. 3. Equiaxed recrystallized grains appear at the severely sheared region. Large equivalent strain induced by large shear deformation promoted recrystallization. At the midthickness, grains are elongated and recrystallization does not occur. The change of microstructure through the thickness corresponds to the variation of shear strain. Grain boundaries in center region become serrated. Grain boundary serration is observed in aluminum deformed at low Z condition and is induced by dynamic recovery [6]. Serration is more pronounced in 1050 sheet than in 5052 alloy because the stacking fault energy is higher in pure aluminum than in Al-Mg alloy. The effects of rolling temperature and strain on the microstructure of the severely sheared region of the 1050 and 5052 sheet quenched at the interval of 30ms after hot rolling are shown in Fig. 4. In 1050

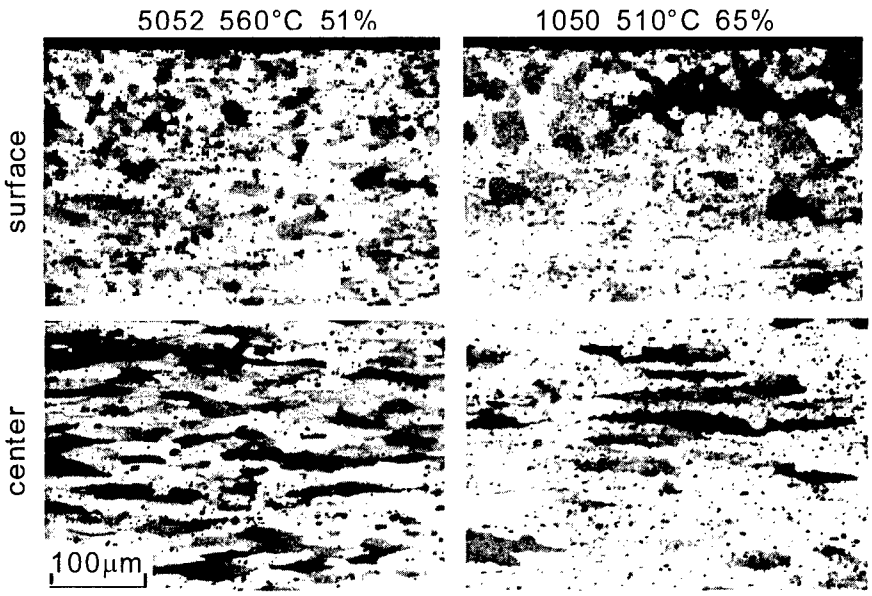

Fig. 3 Microstructures observed at the plane perpendicular to transverse direction.

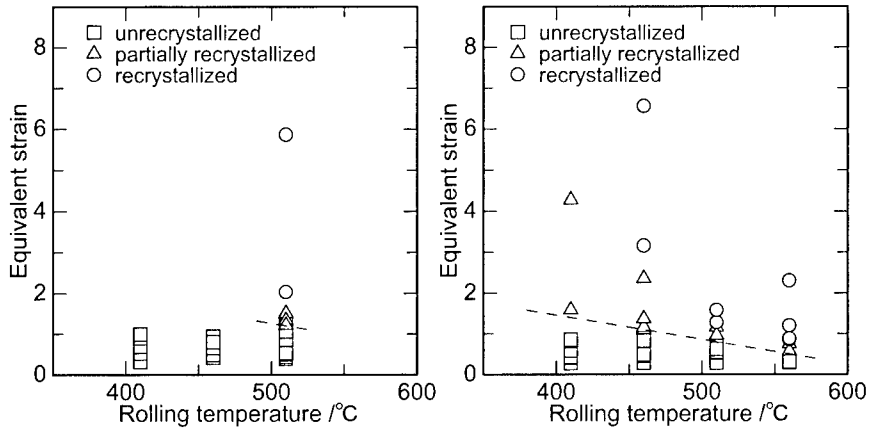

Fig. 4 Effect of rolling temperature and equivalent strain on the microstructure at the severely sheared region of the rolled sheet.

alloy, large shear deformation was introduced only at the rolling temperature of 510°C and recrystallization occurred only in the sheet rolled at 510°C. In 5052 alloy, the critical strain required for the occurrence of recrystallization decreases with increasing rolling temperature. The critical strain for 5052 alloy is smaller than that for 1050. The difference in recrystallization behavior of both alloys reflects the difference in stacking fault energy.

3.3 Texture variation through the thickness

Figure 5 shows {111} pole figures measured at the severely sheared region and at the

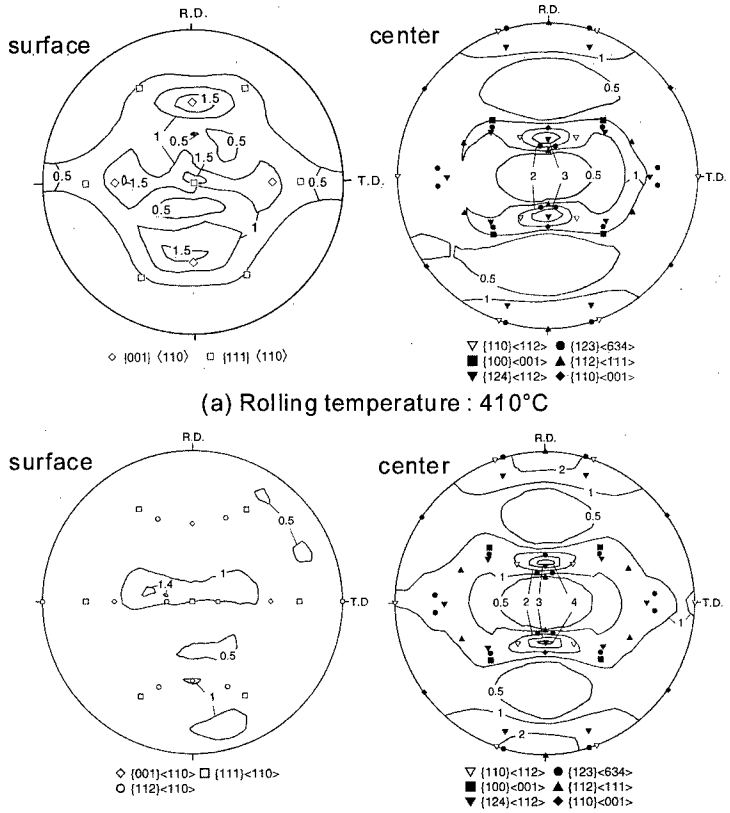

Fig. 5 {111} pole figures measured at the severely sheared region and at the center of the rolled sheet.

midthickness of 5052 alloy sheets rolled 50% at 410°C (Fig. 5(a)) and 510°C (Fig. 5(b)). At the severely sheared region of the sheet rolled at 410°C where partial recrystallization occurs, weak {111}<110> and {001}<110> orientations which are main components of shear texture of fcc metals are formed. When severely sheared region completely recrystallized, almost random texture develops while weak <111>//ND orientation remains (Fig. 5(b)). At the midthickness of both samples where only recovery occurs and shear strain is not introduced, the conventional rolling texture with the orientations of {123}<634>, {112}<111> and {110}<112> develops. The retention of the deformation texture after recrystallization of severely sheared material has been observed in ferritic [7,8] and austenitic steels [3]. In aluminum alloy, retention of <111>//ND orientation is an interesting problem because this orientation increases r-value of aluminum alloy sheets.

4. CONCLUSIONS

The effect of inhomogeneous deformation on the microstructure and texture variation through the thickness of hot rolled aluminum alloy sheet is investigated. The results obtained are summarized as follows.

1) The shear strain beneath the surface of the rolled sheet increases with reduction.

2) Equiaxed recrystallized grains appear in the severely sheared region when the equivalent strain exceeds a critical value which depends on rolling temperature. At the center part of thickness, dynamically recovered structure with serrated grain boundaries develops.
3) The texture with the main components of {001}<110> and {111}<110> orientations develops beneath the surface when a certain amount of shear deformation is induced. Intensity of these components decreases with the progress of recrystallization. At the center part, conventional rolling texture is formed.

REFERENCES

[1] Y. Saito, T. Sakai, F. Maeda and K. Kato: Tetsu-to-Hagané, Vol.72(1986), pp.799-806.
[2] Y. Saito, T. Sakai, K. Takeda and K .Kato: Tetsu-to-Hagané, Vol.73(1987), pp.1146-1153.
[3] T. Sakai, Y. Saito and K. Kato: Trans.ISIJ,Vol.27(1987), pp.520-525.
[4] P H. Lequeu and J. J. Jonas: Met. Trans.A, Vol.19A(1988), pp.105-120
[5] T. Sakai, Y. Saito, K. Hirano and K. Kato: Trans. ISIJ, Vol.28(1988), pp.1028-1035.
[6] F. J. Humphreys and M. Hatherly: Recrystallization and Related Annealing Phenomena, Pergamon, Oxford, (1995), pp. 363-392.
[7] T. Sakai, Y. Saito and K. Kato: Trans. ISIJ, Vol.28(1988), pp.1036-1042.
[8] T. Sakai, Y. Saito, M. Matsuo and K. Kawasaki: ISIJ International, Vol.31(1991), pp.86-94

TEXTURE EVOLUTION OF THE Al SHEET PROCESSED BY CONTINUOUS CONFINED STRIP SHEARING BASED ON EQUAL CHANNEL ANGULAR PRESSING

Jae-Chul Lee, Hyun-Kwang Seok, Jun-Hyun Han, Jin-Yoo Suh, and Ho-In Lee

Div. of Materials Science and Engineering, Korea Institute of Science and Technology (KIST)
P.O.Box 131, Cheongryang, Seoul, 130-136 Korea (jclee@kist.re.kr)

ABSTRACT

A new concept process, a so-called as C2S2 process based on equal channel angular pressing, for fabricating the Al alloy sheets with a high formability is introduced. The C2S2 machine was designed so that it can feed the metal strip in a continuous manner at a relatively high speed in the range of ~20 m/min. A significant amount of the shear deformation could be achieved by passing the sample through the ECAP die with Φ=120°. The pole figures were calculated both to demonstrate the evolution of the textures of the 1050 Al alloy sheets and to elucidate the feasibility of the proposed process as a means for enhancing the formability of the metal strips.

Keywords : Alloys; Structural materials; X-ray diffraction; Crystal structure

1. INTRODUCTION

The formability of metal strips can be judged by such parameters as the average R value($\overline{R}$), $\Delta\overline{R}$, and the limit drawing ratio. High values of $\overline{R}$ are readily measured from BCC metals. For example, interstitial free(IF) steels, which currently are used for the exterior of the commercial vehicles, exhibit $\overline{R}$ greater than 1.8[1]. On the other hand, FCC metals tend to have $\overline{R}$ values less than 1.0. Values of $\overline{R}$ exhibited by most commercial Al alloy strips lies between 0.7 and 0.8 as can be seen in Fig.1[2]. Such a low $\overline{R}$ of most Al alloys acts as one of the major obstacles for the automotive exterior application.

The low $\overline{R}$ exhibited by Al alloy sheets is originated from the metal forming process, which is employed currently to produce various Al sheets. The Al alloy sheets are usually fabricated by consecutive hot rolling and cold rolling of the cast slab followed by heat treatment to control the textures. The dominant texture of the Al alloy sheets produced by this method is the rolling texture with {011}<211> components combined with the cube texture with {100}<001> components, resulting in relatively low $\overline{R}$ as compared to that of the steel.

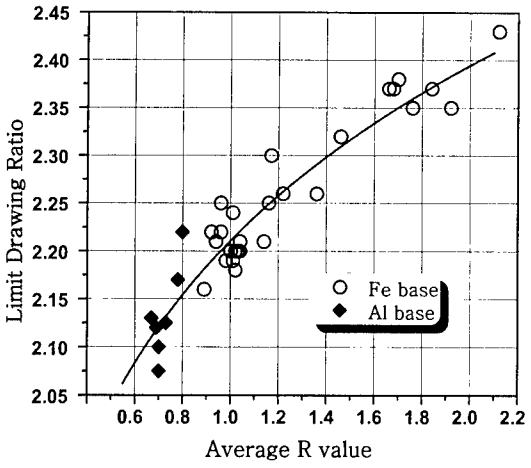

Fig. 1 A plot showing the average R value ($\overline{R}$) and the limit drawing ratio of the Fe-base and the Al-base alloys.

As reported by various researchers[3-5], equal channel angular pressing(ECAP) can induce a significant amount of the simple shear strain into the material. Under the appropriate die geometry, more than 100% of the shear strain can be introduced into the material even at a single pass through the ECAP die[3]. Extensive research works on grain refining of bulk metals as a means for strengthening[3-5] or developing materials with superplasticity[6] have carried out in the past, while relatively little is known on the evolution of the textures[7-10]. However, considering that ECAP introduces the simple shear deformation into the material, it can be used as a new forming technique for developing the shear texture, which, in turn, enhances $\overline{R}$ values of the metal strips.

The purpose of this study is to introduce a new concept process, which is capable of developing the shear textures within the Al alloy strip, and to study the feasibility of the proposed process as a means for producing Al alloy sheets with high formability.

2. THE C2S2 PROCESS

The concept of the developed process, which can impose the simple shear deformation into the metals strip in a continuous manner, is introduced briefly in this section. Shown in Fig.2 is the schematic of the C2S2 machine developed at KIST to apply the simple shear into the metal strips in a continuous mode. A specially designed feeding roll with nulls on its surface was used so that it can deliver the power required to feed the metal strip through the ECAP channel at speeds in the vicinity of 20 m/min. The oblique angle(Φ) of the ECAP channel was set to 120° with the curvature angle(Ψ) of 0°. The use of a twin-roll, instead of using the ram of the hydraulic press, not only makes continuous operation possible but also allows multi-pass operation. The machine was also designed so that it can remove materials affected by the roll surface by scalping with the lower die. Adjusting the position of the cutting edge of the lower die can control the scalping depth.

3. EXPERIMENTAL PROCEDURES

A commercially pure 5mm thick 1050 Al alloy plate was procured and annealed at 500°C for 1.5h before rolling. Unidirectional cold rolling was carried out on the Al alloy sheets to 68% of reduction in thickness to produce a 1.55mm thick sheet. Repeated cold rolling has been conducted without any intermittent annealing process until the final thickness was obtained. A reduction ratio of about 10% per pass was used to obtain homogeneous metal flow while minimizing the formation of edge cracks due to rolling. The rolled sheets were annealed at 350°C for 1.5h to recrystallize the cold rolled structures. The prismatic bars with dimensions of 20(w) x 1.6(t) x 500(l)mm were cut out from the rolled sheet with their long axis parallel to the rolling direction.

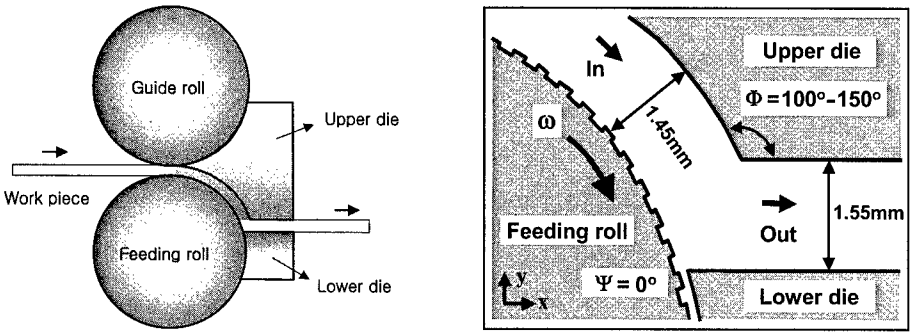

Fig.2 A schematic showing the concept of the C2S2 machine used for continuous confined strip shearing based on ECAP

The samples were fed into the C2S2 machine equipped with an ECAP channel having the oblique angle(Φ) of 120° and the curvature angle(Ψ) of 0° and processed at the approximate speed of 18 m/min. To prepare specimens for optical microscopy, the ECAPed strips were ground mechanically on abrasive papers and etched electro- chemically using the Baker's regent. The voltage and current used for electro-chemical etching were 8 DC volts and 16A, respectively. The electrolyte was maintained at 15-20°C throughout the etching procedure. The microstructures of the specimens were then observed using optical microscopy under the polarized light to reveal individual grain structures.

The textures of the strips were determined by measuring pole figures by means of an automated X-ray texture goniometer. Two different samples, i.e., the annealed raw sample(cold rolled and annealed) and the ECAPed sample, were used to measure the R-values. The samples used for XRD were prepared by thinning into half the thickness in a NaOH solution. {111}, {200}, and {220} pole figures were determined using the Schultz reflection method. From three incomplete pole figures, the orientation distribution functions(ODF) were

calculated according to the series expansion method suggested by Bunge [11] with l_{max}=22. The Lankford parameter(R) along 0-90° at 15° interval with respect to the direction of rolling were calculated using popLA program with the ODF data.

4. RESULTS AND DISCUSSION

Fig.3 is the shear deformation pattern observed from the side surface of the 1050 Al strip that had been pressed through the ECAP channel with Φ=120°. The grids in the figure are the lines drawn on the side surface of the work pieces to provide an insight into the shear deformation patterns as a result of ECAP. . The shear angle measured from the middle surface of the strip was ~47°, which is close to that predicted by Segal[12], i.e., 49°. As cen be seen clearly in this figure, the deformation, which was achieved by a simple shear, was observed to be uniform along the thickness direction except the bottom surface of the strip. In addition, judging from the shape of the deformed grids in Fig.3, the plastic deformation introduced by ECAP was achieved by the simple shear rather than the pure shear.

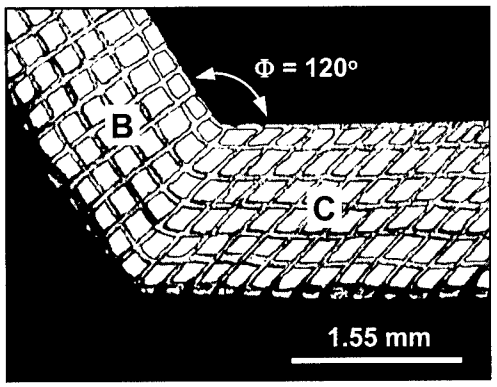

Fig.3 An optical micrograph showing the shear deformation patterns

Fig.4(a) is the optical micrograph recorded from the side surface of the undeformed region, i.e., region B in Fig.3, which is the same microstructure of the cold rolled and annealed specimen showing relatively uniform and equiaxed grain structures. Average grain size measured from this specimen was ~30 μm. Shear deformations as a result of ECAP observed from Fig.3 can cause the rotation of the individual grain as well as the subgrain formation. Figs.4(b) and (c) are the optical micrograph and the TEM micrograph recorded from the side surface of the strips, showing deformed grain structures and the formation of the subgrains as a result of ECAP. As can be seen in Fig.4(c), cell structures with numerous interior dislocations were observed to form by dislocation tangles. The SAD pattern shows a spreading of the diffracted beams, indicating that the subgrains are separated by boundaries having misorientation angles of ~5°.

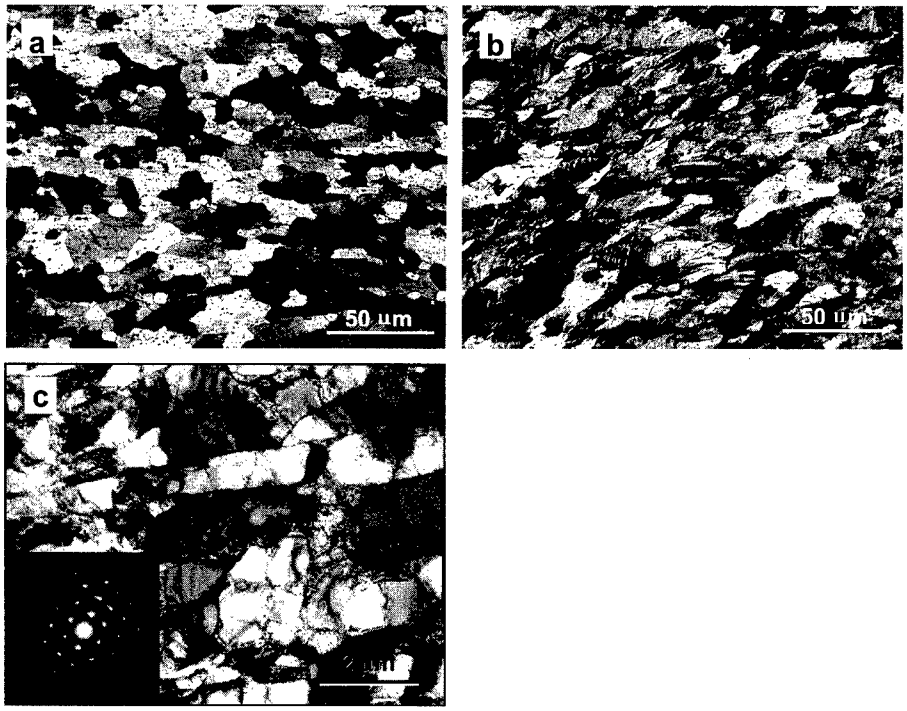

Fig.4 Micrographs recorded form region A and B of Fig.3, showing grain structures (a) before and (b) after ECAP, (c) A TEM bright field image and a SAD pattern showing the formation of the cell structures after ECAP

Fig.5 is the SEM miscrograph recorded from the side surface of the strip, showing significant amounts of slip bands formed within the grains along directions as marked by the brocken lines in the figure. Considering that {111} is the major slip plane of the FCC metals, the experimental observation in Fig.5 is indicative of the possible crystallographic restructuring such that the {111} planes of the individual grains are oriented along a direction parallel to the surface of the strip.

To study the effect of ECAP on the development of the textures in the 1050Al alloy, {220}, {200}, and {111} pole figures were recorded at the middle surface of the specimens. Samples, i.e. the annealed raw(rolled and annealed) and the ECAPed, were prepared for XRD to investigate the evolution of the texture. Fig.6 are the {111} pole figures measured from the middle planes of the annealed raw and the ECAPed samples.

As already expected, in the raw sample, very strong cube texture with the {100}<100> component was developed during annealing after cold rolling as seen in Fig.6(a). After ECAP, however, the presence of the {111}<110> shear texture as well as the {100}<110> rotated cube texture were observed. It is well known that <111>//ND improves the R-value, while

<100>//ND degrades the R-value. Therefore, the R-values of the ECAPed specimen are expected to be improved due to the formation of the {111}<110> shear texture.

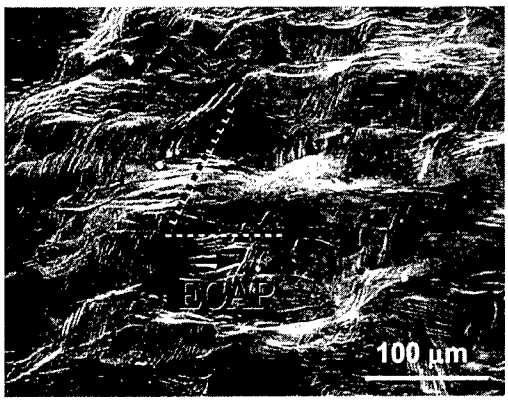

Fig.5 A SEM micrograph showing the slip bands observed from the side surface of the ECAPed strip.

The Lankford parameters(R) along 0-90° at 15° interval with respect to the direction of rolling were calculated using the popLA program. Variations in the R-values measured as a function of the angle to the rolling direction are shown in Fig.6. The average R-value($\overline{R}$) and ΔR were also calculated by incorporating the measured R-values into the relations given in Eqs.1 and 2 and presented in the same graph.

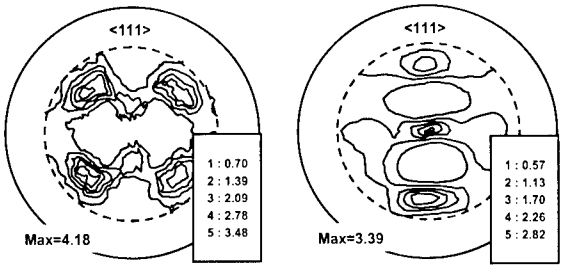

(a) Before DCAP (b) After DCAP

Fig.6 {111} pole figures of (a) the raw and (b) the ECAPed samples recorded from the middle surface of the strips

$$\overline{R} = \frac{R_0 + 2R_{45} + R_{90}}{4} \quad (1)$$

$$\Delta R = \frac{R_0 - 2R_{45} + R_{90}}{2} \quad (2)$$

As seen in this graph, in the case of the raw sample, i.e., the rolled and annealed specimen, the R-values were measured to be relatively low such that they range from 0.3 to 0.7, resulting in $\overline{R}$=0.46 and ΔR=0.38. In the case of the ECAPed specimen, however, the R-values were observed to increase to values ranging from 0.7 to 1.1, resulting in significantly high $\overline{R}$(0.83) with a slightly reduced ΔR(0.27). Saito et al. [8], based on their experiment with the conshearing machine, had also obtained $\overline{R}$(0.86) similar to that obtained from the present study. Although studies on how the textures are evolved under the simple shear deformation is to be carried out further in the future, the experimental results obtained in this study indicates that ECAP can be used as a means for controlling the texture of the Al alloy strips suitable for the sheet forming application.

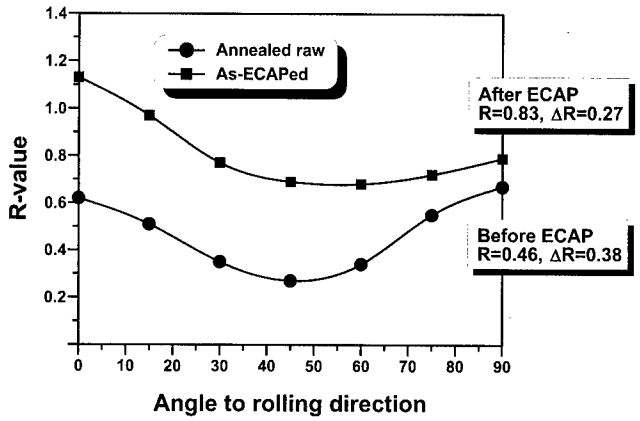

Fig.6 Variations in the R-values calculated as a function of the angle to the rolling direction.

5. CONCLUSIONS

The feasibility study of ECAP as a means for controlling the texture of the Al alloy strip, thereby producing Al alloy sheets with high formability, was conducted using the concept process termed as the continuous confined strip shearing(C2S2) process based on ECAP. The proposed process was effective for introducing a large amount of shear deformation in a single press through the ECAP die. The {111}<110> shear texture was developed even at a single pass through the ECAP die. The $\overline{R}$-values measured from the specimens were observed to increase from the initial value of 0.46 to 0.83 after ECAP, while the crystallographic anisotropy, i.e., ΔR, was slightly reduced from 0.38 to 0.27. Such experimental results indicate that ECAP can be used as a means not only for enhancing the tensile strength but also for controlling the texture of the Al alloy strips suitable for the sheet forming application.

References

1. Mechanical Metallurgy, M.A. Meyers and K.K. Chawla, Prentice-Hall, Inc., New Jersey, (1984) pp.635.
2. G. Jun, J.W. Lee, and D.J. Yoo, Proc. 16th Biennial Congress of IDDRG, June 11-13, Borlange, Sweden (1990) pp.339
3. Y. Iwahashi, Z. Horita, M. Nemoto, and T.G. Langdon, Acta mater., **46**, (1998) 3317-3331
4. K. Nakashima, Z. Horita, M. Nemoto, and T. Langdon, Acta mater., **46**, (1998) 1589-1599
5. Y. Iwahashi, Z. Horita, M. Nemoto, and T. Langdon, Acta mater., **45**, (1997) 4733-4741
6. M. Furukawa, Y. Ma, Z. Horita, M. nemoto, R.Z. Valiev, T.G. Langdon, Mater. Sci. Eng. A., **241**, (1998) 122-128
7. M.A. Gibbs, K.T. Hartwig, L.R. Cornwell, R.E. Goforth, and E.A. Payzant, Scripta. Mater. **39**, (1998) 1699-1704
8. Y. Saito, H. Utsunomiya, H. Suzuki, and T. Sakai, Scripta. Mater. **42**, (2000) 1139-1144
9. O.V. Michin, V.Y. Gertman, R.Z. Valiev, and G. Gottstein, Scripta. Mater. **35**, (1996) 873-878
10. C. Pithan, T. Hashimoto, M. Kawazoe, J. Nagahora, and K. Higashi, Mater. Sci. Eng. A., **280**, (2000) 62-68
11. H.J. Bunge, Mathematishe Mathoden der Texturanalyse, Akademie Verlag, Berlin, (1969)
12. V.M. Segal, V.I. Reznikov, A.E. Drobyshevskiy, and V.I. Kopylov, Russ. Metall. **1,** (1981) 99-105

ELONGATION-CONTROL ROLLING OF WIRES WITH ASYMMETRIC CROSS SECTION

Hiroshi Utsunomiya, Yoshihiro Saito, Munetoshi Ueyama and Ryouichi Souba

Department of Materials Science and Engineering,
Graduate School of Engineering, Osaka University
2-1, Yamada-oka, Suita 565-0871, JAPAN

ABSTRACT

Profiled wires are mainly produced from round circular wires by rolling and drawing. The authors proposed a new size-free rolling method of such profiled wires (elongation-controlled rolling). It is characterized by active use of interstand forces in continuous rolling, which are varied in a wide range being not only tensile but also compressive. In this study, the elongation-control rolling is applied to L-shaped wires. Although asymmetric wires have demands, they are not produced in large quantities. This is because difficulties in rolling operations such as curl, camber or twist are inevitable due to their asymmetry. Compressive interstand forces increase flange height, while tensile interstand forces decrease it. It is concluded that size-free rolling of asymmetric wires are also possible. Camber of wire is observed even in tension-free rolling. Tensile interstand force deteriorates camber of wires. On the other hand, compressive interstand force results in twist as well as camber. It is found that introduction of an edging stand where flange height is reduced slightly, is very effective to suppress not only twist but also camber of wires.

1. INTRODUCTION

Profiled wires have many applications such as electronic parts, springs, piston rings and rails. They are mainly produced from round circular wires by rolling and drawing. The process requires many rolls and dies depending on cross-sectional profiles. These tools must be changed frequently, so the process is neither economical nor productive. The authors recently proposed a new size-free rolling method of such profiled wires (**elongation-controlled rolling** [1-3]). The method is characterized by active use of interstand forces, which are varied in a wide range being not only tensile but also compressive. In conventional rolling, interstand forces has been controlled to be tension-free or slight tension to ensure stable operation and dimensional accuracy. It was found that

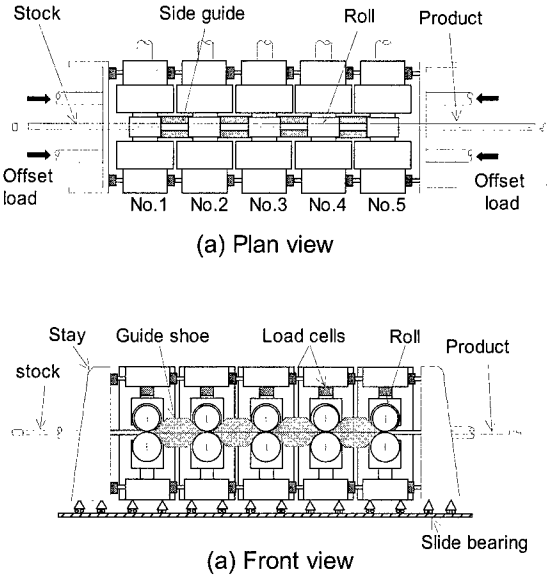

Fig. 1 Schematic illustration of the elongation control mill.

size-free rolling of round-edged flat, square, rectangular, H-shaped and U-shaped wires were feasible by the method [4-7]. In this study, the size-free rolling of wires with asymmetric cross section, e.g. L-shape is investigated. Although asymmetric wires have great demands, they are not produced in large quantities due to the difficulties in rolling operations.

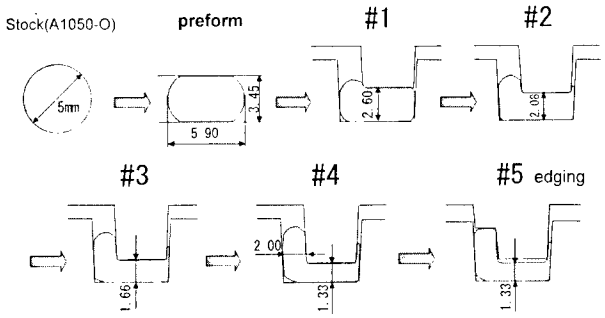

Fig. 2 Schematic illustration of used pass schedule.

Defects in shape such as curl, camber or twist of wires are inevitable due to their asymmetry. Studies on these shape defects in wire rolling have been limited, especially effects of interstand forces are unknown. In this study, the rolling characteristics of L-shaped wires on elongation-control mill are investigated experimentally.

2. EXPERIMENT

2.1 Rolling equipment

A schematic illustration of the used elongation-control mill is shown in **Fig. 1**. Details were provided in the references [1-3]. This mill consisted of five cassette-type rolling stands. Each stand was equipped with two-high 100mm diameter rolls, load cells for roll separating forces, a torque meter, and a tachometer. Each stand was independently driven at a prescribed speed by a servomotor. All stands were mounted on a pair of slide guides (linear guides) and could move smoothly in the rolling direction. Load cells were inserted between the adjacent stands, so that the interstand force was measured directly and precisely [1-3]. The stands were all pushed against each other while affording an adequate pre-load from the entrance and exit stays. The distance between adjacent roll axes was 230mm.

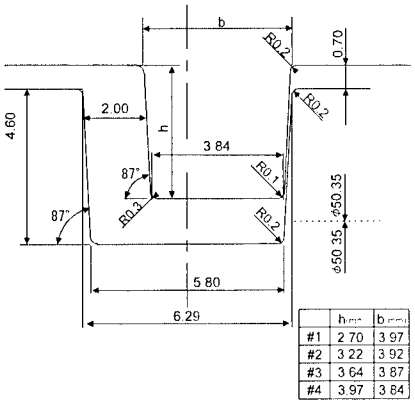

(a) from first to fourth stand

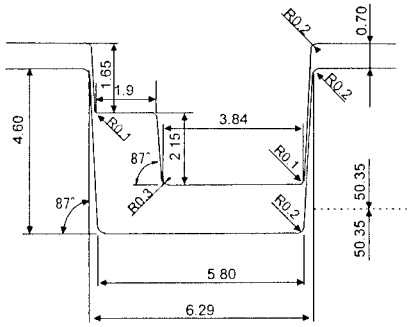

(b) fifth stand (edging stand)

Fig. 3 Roll passes used.

2.2 Rolling procedure

Annealed aluminum JIS A1070-O wires 5mm in diameter and 2m in length were supplied by the Sumitomo Electric Industries, Co. ltd. The used pass schedule is schematically shown in **Fig. 2**. The detailed roll passes are shown in **Fig. 3**. Prior to the elongation-control rolling, the wires were preformed into round-edged flat wires by one-pass flat rolling. The width of preformed wires was controlled to 5.90 mm, to fit the groove on the roll and to prevent meandering. The thickness of the preformed wires was 3.45mm. Closed roll passes were used in the elongation-control mill. The grooves on the bottom rolls were same shape from the first to the fifth stand. The web thickness of the product is 1.33mm. In order to suppress curl of wires, the pitch line and the rolling line were adjusted [8]. The roll diamter was designed so that the peripheral speed of the top roll and that of the bottom rolls are identical at the center of web thickness as shown in **Fig. 3**. In some series of experiments, the fifth stand was used as an edger; the flange height is reduced. The decrease in flange height, i.e., the edging draft was varied from 0mm to 0.4mm. Between adjacent rolling stands, the wires were guided in a closed channel formed by a pair of guide shoes as shown in **Fig. 1**. The channel was L-shaped and the clearance between the wire was 0.1mm. All rolling experiments were conducted at ambient temperature lubricated with mineral oil. In order to investigated the wire deformation in the mill, the rolling operation was interrupted after a sufficient distance of steady state rolling had been performed.

2.3 Roll speed

The interstand forces were generated by prescribing the roll speeds on each stand as follows [1-3]: first, the roll speed at the first stand, v_1^o, was fixed at 1m/min, and the roll speed at i-th stand, v_i^o (i=2,..4) (which established the tension-free rolling), was experimentally determined from upstream stand by stand. The obtained v_i^o is plotted in **Fig. 4** as a=1.00. it increases downstream due to the elongation of wire. For rolling with interstand forces, the roll speed of i-th stand v_i was set as,

$$v_i = a^{i-1} v_i^o \qquad (i=1,\ldots,4) \qquad (1)$$

where the parameter a is an arbitrary constant that indicates the degree of imbalance of roll

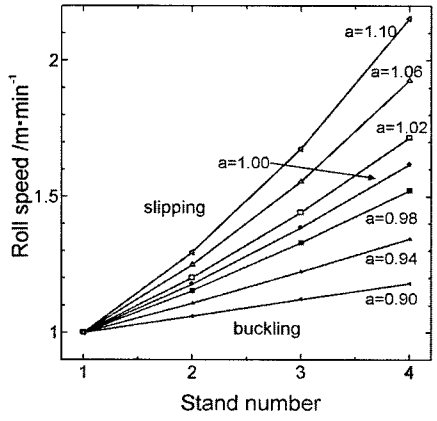

Fig. 4 Roll speeds at each stand.

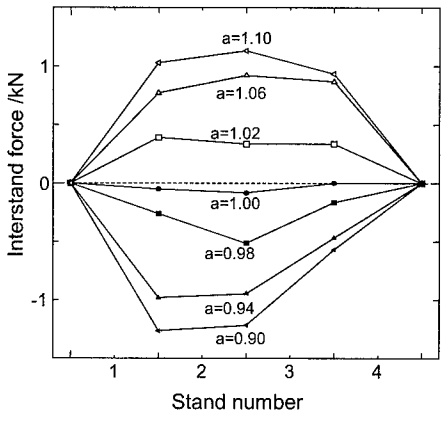

Fig. 5 Distribution of interstand force.

speeds and determines the interstand forces. This parameter will be referred to as **the roll speed parameter**. When a=1, v_i equals v^0_i, and tension-free rolling is achieved. If a>1, v_i/v_{i-1} is larger than v^0_i/v^0_{i-1}, and tensile forces are generated between adjacent stands. Conversely, if a<1, compressive forces are generated. The prescribed speeds are shown in **Fig. 4**.

When the edging drought was applied at the fifth stand, v^o_5 depended on the edging drought and was not known a priori. So v_5 is assumed to be v_4 ($v_4 = v_5$), the compressive force between the fourth and the fifth stands increases with the edging drought.

3. RESULTS

3.1 Interstand forces

The distribution of interstand forces is shown in **Fig. 5**. Interstand tensile forces are generated when a>1; compressive forces are generated when a<1. These forces exhibit a concave distribution. Interstand forces at intermediate stands are sensitive to the roll speed parameter a. Both maximum tensile and compressive interstand forces are greater than 1kN. It means the maximum interstand stress is approximately 100MPa. These trends corresponds with the previous results [1-7].

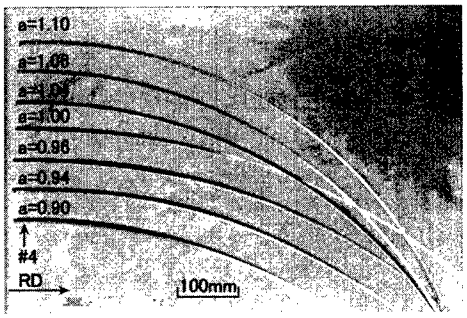

Fig. 6 Appearances of rolled wires.

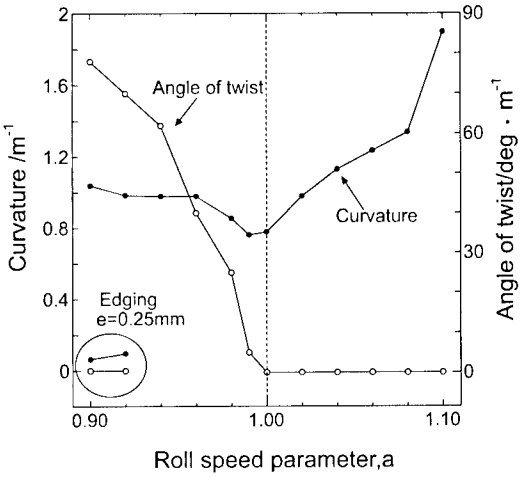

Fig. 7 Curvature and angle of twist as a function of roll speed parameter.

3.2 The rolling limits and shape of wires

It is found that the stable rolling conditions are $0.90 \leqq a \leqq 1.12$ as shown in **Fig. 4**. The upper limit is determined by the slippage between rolls and wires. The lower limit is determined by buckling of wires between stands. It is found that curl, camber, twist of wire between rolling stands are negligible. This is due to the use of the above designed rolls and guide shoes. Appearance of wire after passing the fourth stand is shown in **Fig. 6**. Bend of wires in the rolling plane, i.e., camber (saber) is observed. The wires curve with the flange inside. In the case of compressive interstand force, twist of wire also occurs. The cross-section rotates clockwise on the rolling direction. The curvature of the camber and the angle of twist are plotted in **Fig. 7**. In the figure, the curvature was calculated from the chord length of 500mm long product. The angle of twist is evaluated as the rotation angle in degree per unit product length 1m. In the case of tension-free rolling (a=1.0), no twist occurs, and small camber is detected. Although tensile interstand force does not cause twist, it deteriorates camber. On the other hand, compressive interstand force deteriorates both camber and twist. Curl of wire is negligible under all conditions.

3.3 Cross-sectional profiles

The variations of cross-sections of wires in the cases of a=0.90, 1.00, and 1.10 respectively are compared in **Fig. 8**. The flange grows by passing rolling stands. The smaller a causes higher flange and better filling of the roll grooves. When $a \leq 1$, burr is formed at the opposite side of the flange. Since the burr is formed in the gap caused by the elastic deformation of mill, i.e. the mill jump, it is difficult to be suppressed. However it will be removed easily after rolling. The flange height is controlled between 2.09mm and 4.17mm, where 2.64mm in tension-free rolling. It is notable the flange height increases at downstream stands in the case of a=0.90 so that the obtained flange height is greater than the perform thickness. Greater interstand force also causes higher burr height and cavity at the bottom corner.

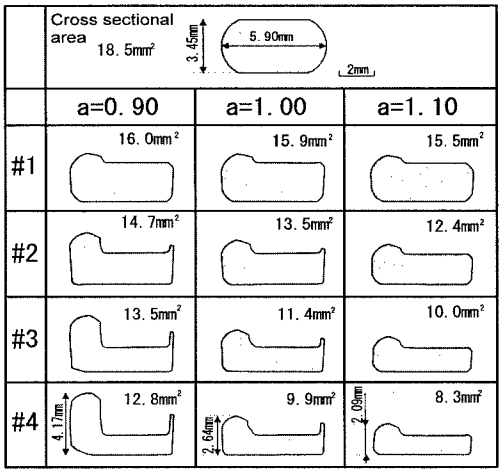

Fig. 8 Changes in cross-sectional profile during rolling.

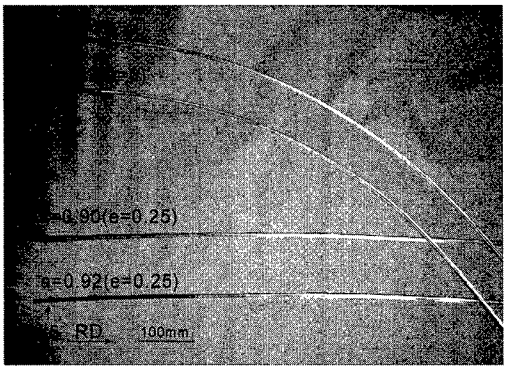

Fig. 9 Effect of edging on apperances of rolled wires.

3.4 Effect of edging

Since the applicable flange height is limited with the edging pass (Fig.3b), the edging was performed in the cases a=0.90 and 0.92. Typical appearances of rolled wires are shown in **Fig. 9**. When the edging of flange height is applied, camber and twist are significantly improved. Results are also imposed in **Fig. 7**. Effects of edging drought on camber and on twist are shown in **Fig. 10**. It is found that small edging drought improves both camber and twist. They are negligible when the edging drought is 0.30mm. Change in cross-section by edging is shown in **Fig. 11**. Dotted lines show the profiles before the edging. It is notable that the cross-sectional area increases with edging drought. This is because the compressive interstand force is generated on wire between the fourth and the fifth stands since the roll speed was set as $v_4 = v_5$. The edging is also effective to improve the shape of flange top and the cavity at the bottom corner.

4. DISCUSSIONS

Observed camber is explained by the difference of the elongation in width direction. The high reduction in web increases the asymmetry and causes the excessive elongation, the wire curves to the flange. Tensile interstand force increases the mean elongation and decreases the cross-sectional area. It decreases the flexural rigidity and deteriorates camber. On the other hand, although the compressive interstand force increases the difference in elongation and also increases the flexural rigidity. Since the torsional rigidity does not increase as much as

the flexural rigidity, the excessive elongation of web is relaxed by twist of wire.

The edging causes the elongation of the flange part and decreases the imbalance of the elongation. It is effective to both camber and twist. Ona et al. reported a similar effect of edging in a roll-forming process of asymmetric profiles [9]. It is found that the edging is very useful for practical operation to avoid camber and twist and to improve the cross-sectional shape.

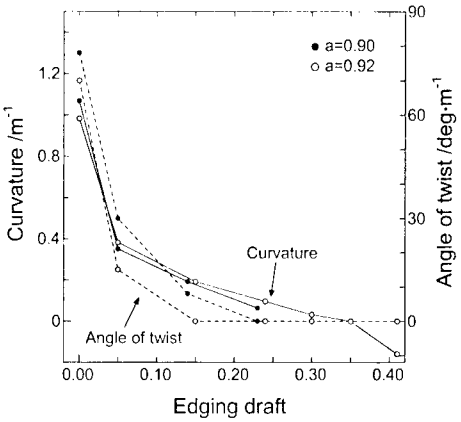

Fig.10 Curvature and angle of twist as a function of edging drought.

5. CONCLUSIONS

In this study, elongation-control rolling has been successfully applied to the size-free rolling of L-shaped aluminum wire. The flange height varied over a wide range, from 2.09mm to 4.17mm. In the case of tension-free rolling (a=1.0), no twist and small camber is detected. Although tensile interstand force does not cause twist, it deteriorates camber. On the other hand, compressive interstand force deteriorates camber and induces twist. The curl of wire is not observed under all conditions. It is found that the edging is very effective to improve curl, twist and shape of products.

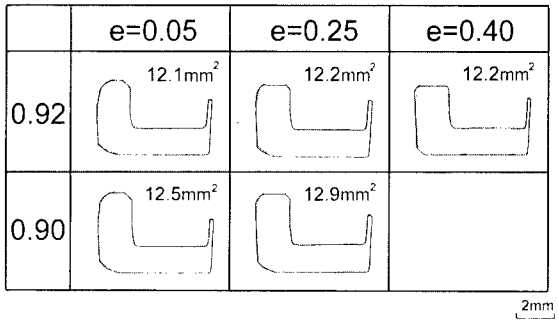

Fig.11 Effect of edging on cross-sectional profiles.

REFERENCES

1. Y. Saito, H. Utsunomiya, M. Shinkawa and F. Shimaya, J. Mat. Proc. Tech., Vol. 80-81(1998), pp. 351-355.
2. Y. Saito, H. Utsunomiya, M. Shinkawa and K. Oka, in Proc. of the 7th Steel Rolling, M. Kiuchi et al. ed., ISIJ, Chiba, Japan, (1998), pp. 811-815.
3. Y.Saito, H. Utsunomiya, M.Shinkawa and K. Oka, J. Jpn. Soc. Tech. Plast., Vol. 40(1999), pp. 966-970.
4. H.Utsunomiya, Y.Saito, M.Shinkawa and F.Shimaya, in Advanced Technology of Plasticity, (1999), pp.1537-1542.
5. Y. Saito, H. Utsunomiya, M. Shinkawa and M. Ueyama, in Proc. 1999 Jpn. Spring Conf. for Tech. Plast., (1999), pp.175-176.
6. H. Utsunomiya, Y. Saito, M. Shinkawa and F. Shimaya, in Proc. of the 2nd Intelligent Processing and Manufacturing of Materials, J. A. Meech et al. ed., Hawaii, USA, (1999), pp. 555-562.
7. Y. Saito, H. Utsunomiya, R. Souba and M.Ueyama. in Proc. 2000 Jpn. Spring Conf. for Tech. Plast., (2000), pp. 225-226.
8. The United Steel Co., ltd., in Roll Pass Design, (1960), pp.29-32.
9. H. Ona, T. Jimma and N.Fukaya: J. Jpn. Soc. Tech. Plast., Vol. 22 (1981), pp.1244-1251.

Effect of Preform Shape on a Surface Grain Coarsening Behavior at the Hammer-Forged Al7050

Youngseon Lee, Junghwan Lee and Youngsun Choi*

Dept. of Material Processing Technology
Korea Institute of Machinery and Materials, Changwon 641-010, Korea
*Hanil Forging Co., Changwon 641-090, Korea

ABSTRACT

Fatigue strength, electrical conductivity and stress-corrosion-cracking resistance are considered as important factors at aircraft Al alloys, therefore Al7050 alloy has been developed to improve such properties. However, hammer-forged Al7050 parts showed the undesirable structures such as severe local grain coarsening and inhomogeneous material flow, resulted in the degraded mechanical properties. In this paper, process conditions are investigated for elimination of the grain coarsening and improved material flow during forging process by both of experiments and FEM analysis. Particular interest has been given to understand role of preform shape on the grain coarsening behavior and magnitude of the hammer forging load.

As the results of FEM simulation by using DEFORM-3D, the simulated forging loads were 2,200ton at machined bar which is machined from 65 mm to 60mm diameter, and below 1,900ton at machined preform, respectively. The use of preform has been beneficial for reduction of the forging load and elimination of the surface grain coarsening. However, in the cases of machined bar, which was skinned off by 2.5mm thick, abnormal surface grain coarsening behavior has been observed. The optimized preform shape could be properly designed by applying the FEM simulation.

1. INTRODUCTION

An abnormal grain coarsening is a defect occurring sometimes during the forging process of aluminum alloy. The undesirable structures such as severe local grain coarsening and inhomogeneous material flow result in the degraded mechanical properties, especially fatigue strength and stress-corrosion-cracking resistance. Fatigue strength, electrical conductivity and stress-corrosion-cracking resistance are considered as important factors at aircraft Al alloys. However, hammer-forged Al7050 parts showed the undesirable structures such as severe local grain coarsening and inhomogeneous material flow. In this paper, process conditions are investigated for elimination of the grain coarsening and improved material flow during forging process by both of experiments and FEM analysis. Particular interest has been given to understand role of preform shape on the grain coarsening behavior and magnitude of the hammer-forging load. Also, investigation has been carried out for effect of the isothermal and non-isothermal conditions by FEM simulation.

2. EXPERIMENTAL DETAILS

There are many causes of the grain-growth phenomenon in forged part. The final structure

of the forged part depends on the structure of the raw material, strain, strain rate and temperature, friction conditions, heat-treatment parameters, heating and cooling rates during hot forming operation, and etc. [1,2,3] To investigate effects of the strain and the temperature among above parameters, model experiments are preformed at various heating temperature for as-received billet, machined bar and machined perform.

2.1 Al7050-T7452

Al7050 is a Al-Zn-Mg-Cu-Zr alloy developed to have a combination of high strength, high resistance to stress-corrosion cracking, and good fracture toughness, particularly in thick sections. The use of zirconium in lieu of chromium provides a low sensitivity to quench, which results in high strengths in thick sections. The chemical compositions and the mechanical properties of the Al7050-T7452-Die-Forging cited in the AMS4333A are shown in Table 1. and 2, respectively. T7452 temper is solution-heat-treated following MIL-H-6088, stress-relieved by compressing for 1 to 5% permanent deformation, and then overaged. Table 3 shows the condition of T7452 temper. Fig.1 shows the microstructure of as extruded Al7050 bar.

Table 1 Chemical compositions of Al7050

Alloy	Zn	Mg	Cu	Zr	Fe	Si	Al
Al7050	5.7~6.7	1.9~2.6	2.0~2.6	0.08~0.15	~ 0.15	~ 0.12	Balance

Table 2 The mechanical properties of Al7050-T7452-die-forging

Direction	Nominal thickness at time of heat treatment (mm)	Tensile strength (Mpa)	Yield Strength at 0.2% offset (Mpa)	Elongation (%)
With grain flow	~ 51	496	414	9
	51 ~ 102	490	407	8
Across grain flow	~ 51	469	379	5
	51 ~ 102	462	365	4

Table 3 The mechanical properties of Al7050-T7452-die-forging

Solid solution treat	Stress-relieving	Overaging
477°C, 2hr (60~70°C water quenching)	Compressing to produce a 1 ~ 5% permanent set	125°C, 2hr & 162°C, 27hr (air cooling)

2.2 Model experiment for selecting the forging temperature

To select forging temperature, the microstructures of specimen in heating, forging, solid solution and over-aging are investigated. The hydraulic press was used and die was heated at 300°C. Fig. 1 represents the specimen and conditions used in experiment. Over the 450°C, the microstructure has been grown from only heating and abnormal surface layer has been generated. As shown in Fig. 2, abnormal layer has not been generated in the case of 430°C, however, the microstructure of forged specimen is not homogeneous. Therefore, we know that the forging temperature needs to be lower than 430°C.

2.3 Hammer-forged Al7050 part

As mentioned above, forging temperature is appropriate under 430°C. Therefore, the prototype is manufactured at 400°C. The used billet is a machined bar which extruded bar of 65mm diameter is machined to 60mm. The extruded bar is machined to eliminate the abnormal surface layer of raw material. Fig.3 shows the section of forged part after solid

solution. The abnormal grain growth was generated in surface from 1mm to 4mm thickness. From the results, we know that hammer forging is more severe than that of hydraulic press with respect to the friction and strain rate. And, strain distribution of forged part is more non-homogeneous in hammer forging. Therefore, the preform is designed to reduce the friction and forging load and to make strain distribution better.

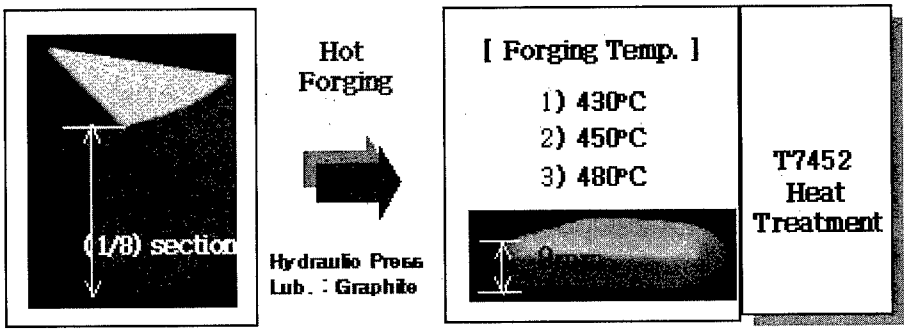

Fig. 1 The diagram of model experiment to select the forging temperature

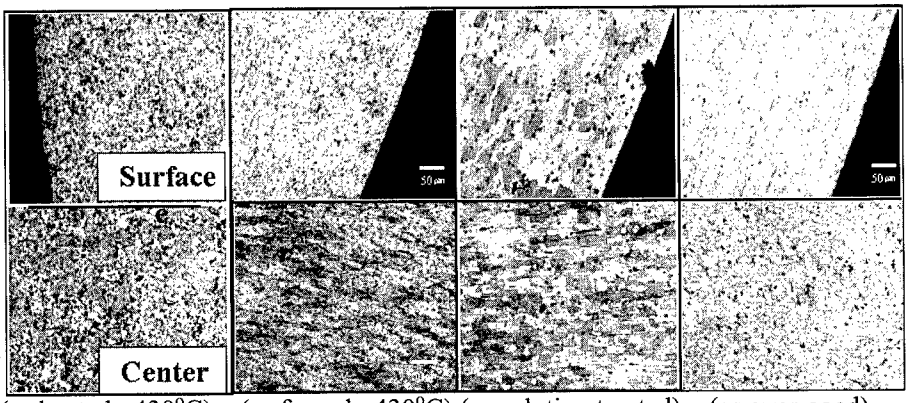

(as heated : 430°C) (as forged : 430°C) (as solution treated) (as over-aged)

Fig. 2 The microstructure of forged specimen at forging temperature 430°C

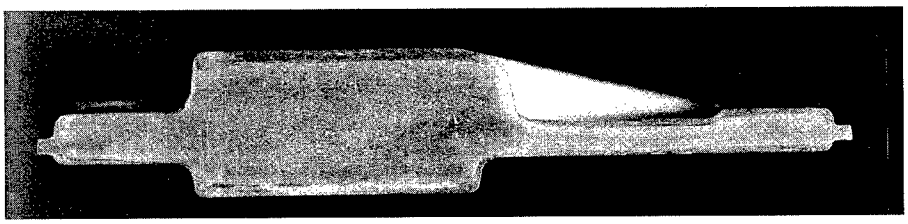

Fig. 3 The abnormal surface layer of hammer-forged Al7050 part

2.4 The effect of preform shape

When preform is used, the friction and deformation-induced heating can be reduced and strain distribution is more uniform. Additionally, it is an effect which non-homogeneous surface layer is eliminated. Fig. 4 shows that the coarsening was not generated in the case of machined preform. On the other hand, when machined bar was used, surface grain coarsening

was generated in all surface. Fig.5 shows the photo of hammer-forged Al7050 part when the machined preform was used.

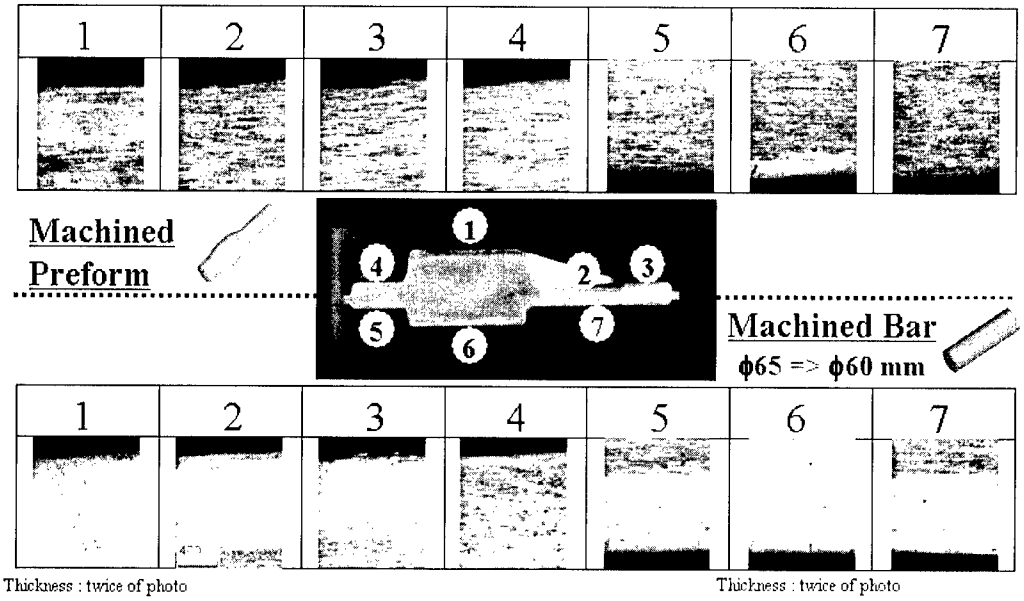

Fig.4 The comparisons of prototype microstructure of machined bar and machined preform (as hot forged-solid solution)

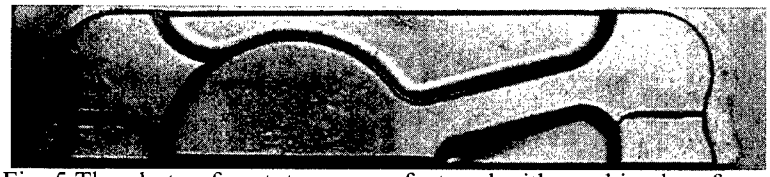

Fig. 5 The photo of prototype manufactured with machined preform

3. The 3-dimensional FEM analysis

The FEM analysis is performed to investigate the effect of parameter in hammer forging. The mesh number is 100,000 and non-isothermal condition is used. Fig.6 shows the 3D model used in simulation. The calculating time is applied 240hr in the case of machined bar and 30hr in the case of machined preform. The difference of calculating time is due to flash amount. When the metal is flowed in flash land, mesh is distorted very much and remeshing is required. Also, when the preform is used, flow of the metal is better.

As the results of FEM simulation by using DEFORM-3D, the simulated forging loads were 2,200ton in the case of machined bar which is machined from 65mm to 60mm diameter, and below 1,900ton in the case of machined preform respectively, due to the friction and strain distribution. Fig.7 shows the deformation patterns and prototype when the machined bar is forged. Fig.8 shows the deformation patterns and prototype when the machined preform is forged. When the preform machined for reduced section area was used, the temperature distribution was decreased to 10°C compared to that machined bar. Fig.9 and Fig.10 shows the effective strain and temperature distribution when the machined bar and machined preform are used, respectively.

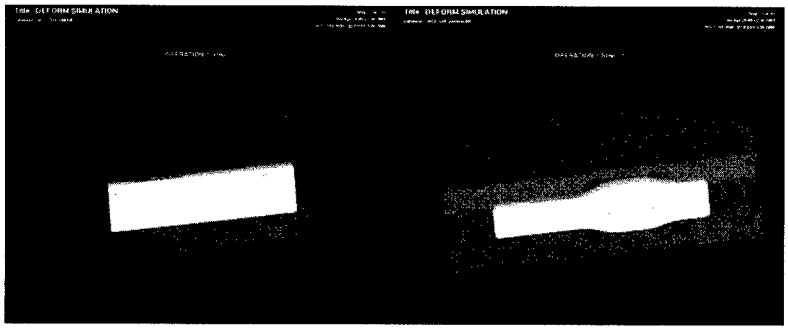

❖ ϕ60mm, Machined Bar ❖ Machined Preform

Fig. 6 The 3D model of machined bar and preform for hammer-forged Al7050 part

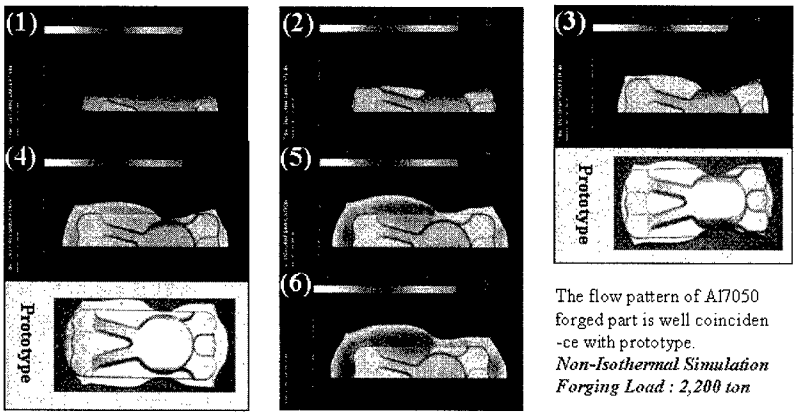

Fig. 7 The deformation patterns and prototype used in machined bar

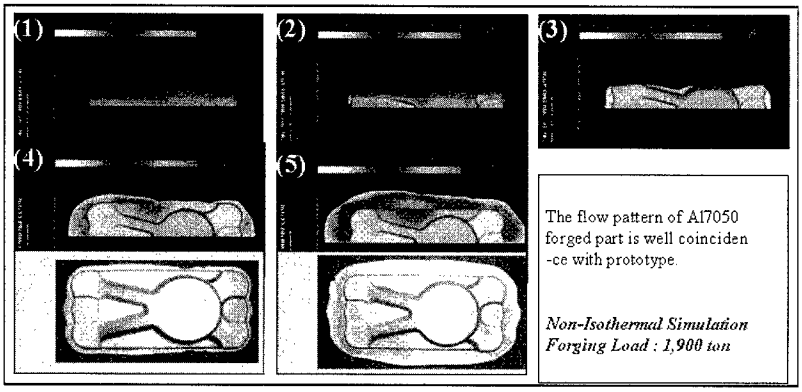

Fig. 8 The deformation patterns and prototype used in machined preform

4. FINALLY

Hammer-forged Al7050 parts showed the undesirable structures such as severe local grain coarsening and inhomogeneous material flow, resulted in the degraded mechanical properties. Therefore, process conditions are investigated for elimination of the grain coarsening and improved material flow during forging process by both of experiments and FEM analysis

[ϕ60mm, Machined Bar] [Machined Preform]

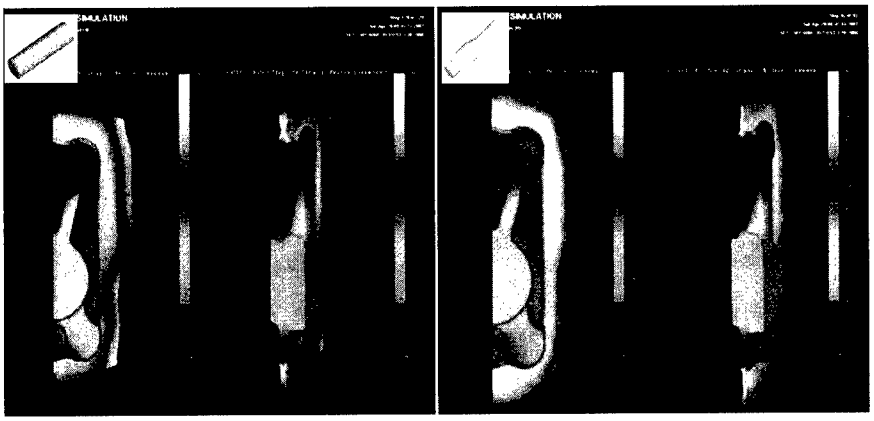

❑ Effective Strain(with Flash) : 0.38 ~ 3.46
❑ Effective Strain(without Flash) : 0.38 ~ 2.12
❑ Effective Strain(with Flash) : 0.42 ~ 3.40
❑ Effective Strain(without Flash) : 0.42 ~ 2.02

Fig. 9 The effective strain of forged part estimated by FEM analysis

❖ ϕ60mm, Machined Bar ❖ Machined Preform

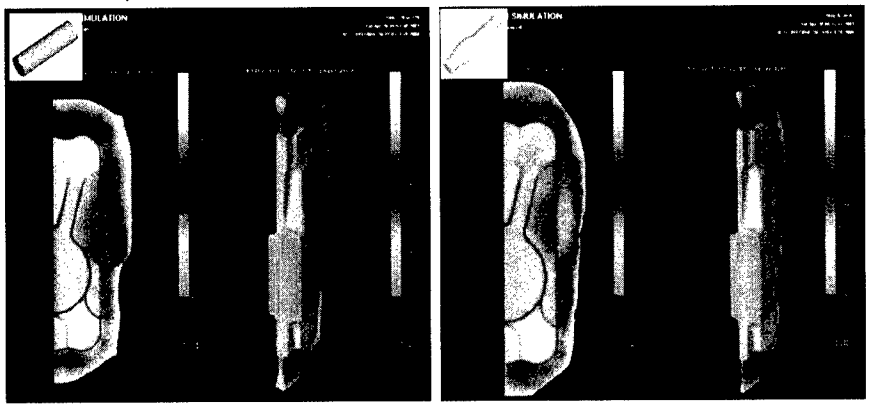

❑ Temperature(with Flash) : 400.8 ~ 472°C
❑ Temperature(without Flash) : 400.8 441°C
❑ Temperature(with Flash) : 401.3 ~ 460°C
❑ Temperature(without Flash) : 401.3 ~ 428°C

Fig. 10 The temperature distribution of forged part estimated by FEM analysis

The microstructural change during the heating, forging, solid solution, and overaging as well as the role of preform shape on the grain coarsening behavior has been investigated.
As the results of FEM simulation by using DEFORM-3D, the simulated forging loads were 2,200ton at machined bar and below 1,900ton at machined perform, respectively. And, when the preform machined for reduced section area was used, the temperature distribution was decreased by 10°C compared to the machined bar. The use of preform has been beneficial for reduction of the forging load and elimination of the surface grain coarsening. However, in the case of machined bar, which was skinned off by 2.5mm thick, abnormal surface grain coarsening behavior has been observed.

REFERENCES

1. K.P. Rao, K. Sivaram, J. Mats. Proc. Technol. 29(1992), p91
2. L.C. Lim, H.S. Fong, J. Mats. Proc. Technol. 23(1990), p211
3. W. Weronski, A. Gontarz, Zb. Pater, J. of Mats. Proc. Technol. 92-93(1999), pp50-53

LIGHT WEIGHT ALUMINUM FORGED SUSPENSION PARTS FOR AUTOMOBILE

Yoshiya INAGAKI

KOBE STEEL,LTD.,MIE 511-0284 JAPAN

ABSTRACT

Weight saving of suspension is very effective for fuel economy, environmental conservation and improve driving faculty.

We developed light weight aluminum forged suspension arms using our original alloy which has 20% higher strength than 6061 alloy. It was converted from steel to aluminum forging and we got more than 40% weight saving.

Although light weight, this arm satisfied lord requirements and has high deformability, and durability. (Average yield strength was 340 MPA and elongation was 15%) These performance means safety and reliability.

For production, we use large capacity mechanical press and automatic production line. These facilities have high productivity and stability.

1.Preface

Until recently,most of the automobiles had pressed iron or forged iron suspension. But usage of aluminum supension is increasing for the improvement of fuel efficiency and environmental protection. 6061 aluminum alloy for forging and A356 for casting are commonly used for automobile supension.But car makers are requiring further weight reduction.We use KS651 aluminum alloy which has higher tensile strength and fatigue strength for the suspension designed by using FEM analysis.And we check the sterngth of products as soon as we made them. By these things , we can supply the products which meet the car makers needs for weight reduction in a short manufacuturing period.Now I explain more details of this.

2.Alloy for automobile suspension

We recommend car makers to use KS651 alloy which has higher strength and durability.

I show chemical composition of KS651,6061 and A356 aluminum alloys on Table1.In order to get the higer strength, we changed the proportion of Si and Mg at KS651 alloy.(Fig1)KS651 has 0.85-1.00% Si.That is because more than 1.1% of Si does not improve strength and decrease the elongation and corrosion resistance.6061 alloy has 0.1-0.4% Cu.But we changed the proportion of Cu to 0.25-0.4% at KS651 alloy to get the higher strength. And we use transition metals such as Mn,Cr and Zr to stabilize the tissue and minimize the crystal.I show the results of tensile strength test and fatigue test on Table2 and Fig2. This shows KS651 has 20% higher tensile strength than 6061 and 50% higher than A356. As for fatigue stregth, KS651 is 10% higher than 6061 and 60% higher than A356.As shown at Table3,by changing the alloy of products from 6061 to KS651 we can get about 10% weight reduction and by changing A356 to KS651, we can get about 40% weight reduction.

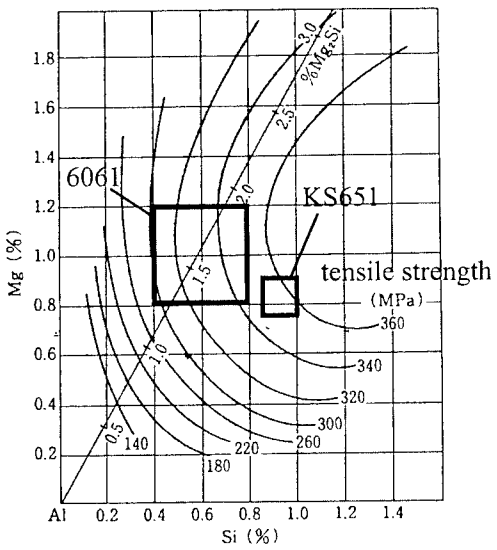

Fig.1 The relation between tensile strength and proportion of Si and Mg

Table.1 Chemical composition (KS651,6061,A356)

Alloy		Typical Chemical Composition (mass %)								
		Si	Fe	Cu	Mn	Mg	Cr	Zn	Ti	Zr
KS651	Forged	0.95	<0.35	0.35	0.30	0.75	0.15	<0.25	<0.10	0.10
6061	Forged	0.60	<0.70	0.30	<0.15	1.0	0.20	<0.25	<0.15	-
A356	Cast	7.0	<0.20	<0.20	<0.10	0.35	-	<0.10	<0.20	-

Table.2 Mechanical properties

Alloy	Tensile Strength (MPa)		Yield Strength (MPa)		Elongation (%)	
	Typical	Guaranteed	Typical	Guaranteed	Typical	Guaranteed
KS651-T6	360	345	340	315	15	10
6061-T6	290	265	260	245	15	10
A356-T6	280	240	240	200	8	2

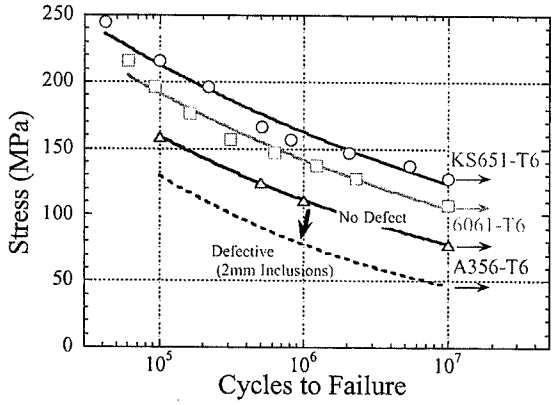

Fig.2 Fatigue strength

Table.3 Mass comparison

Mass comparison		
KOBE's Forging (KS651)	Usual Forging (6061)	Casting (A356)
60 (-40%)	67 (-33%)	100

3.Product design

To make the product with required strength in a short period,product design, product making, strength test and feedback of the test must be done quickly.So we have been designing the products and testing the strength of them ,not only making the products.Fig3 shows flow-chart from product design to completion of products.At first, we decide manfacturing process and kind of aluminum alloy based on the customer's requrement about strength and price of products.Then we design 3D model of product and do the FEM analysis.(Table4,Fig4,Fig5) When we design the product,we try to make them easy-to-forging (or casting) shape and we also do plastic flow analysys for forgings and solidification analysis and melt flow analysis for castings to make the most suitable shape.We use many of the softwares our company developed for these analysis.(Fig6) We decide the shape of prototype from the result of analysis and make some samples.We test the strength of the sample and feedback the result of the test to revise the shape if necessary.After these procedure,we decide the final shape of theproduct and make the products.

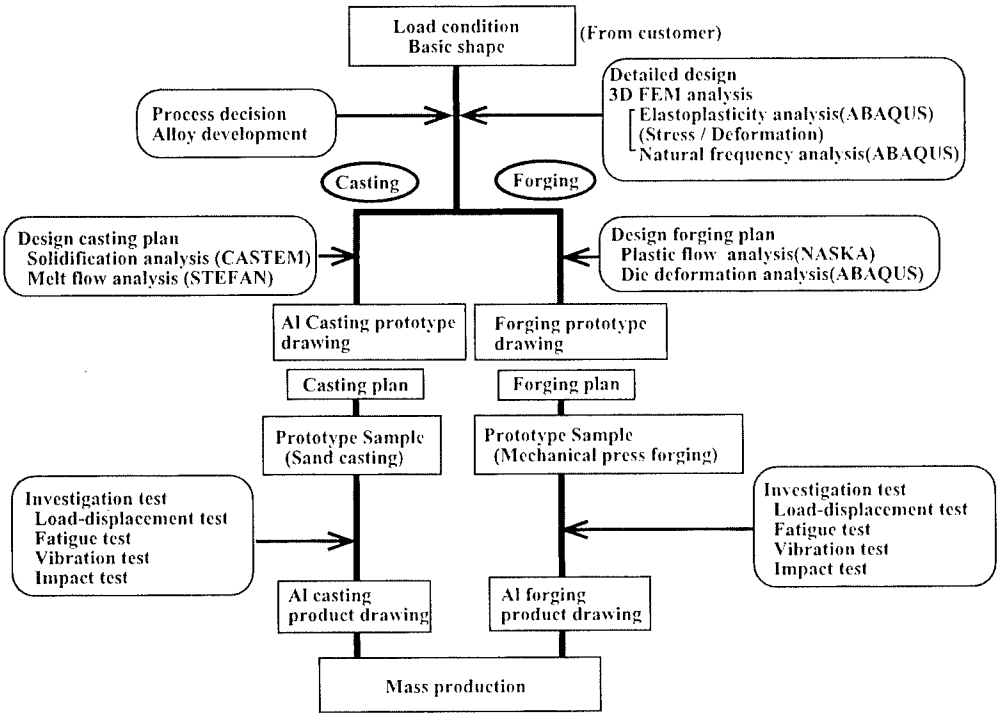

Fig.3 Flow-Chart from product design to completion of products

Table.4 Analysis result (process and mass)

Process	Mass kg
Forging	1.7
Casting 1 (normal)	2.1
Casting 2 (defect tolerant)	2.8

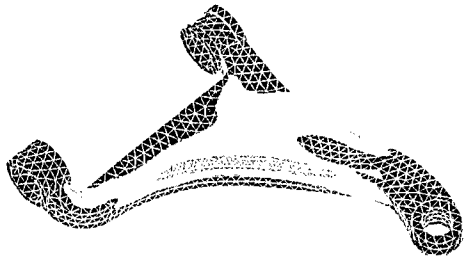

Fig.4 Equivalent stress distribution

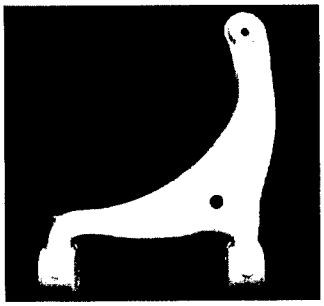

Forging

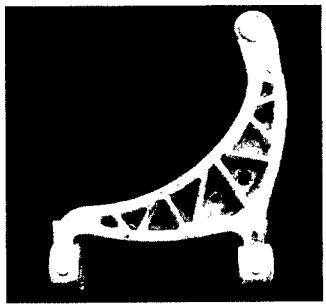

Casting

Fig.5 Differense of shape between Forging and Casting

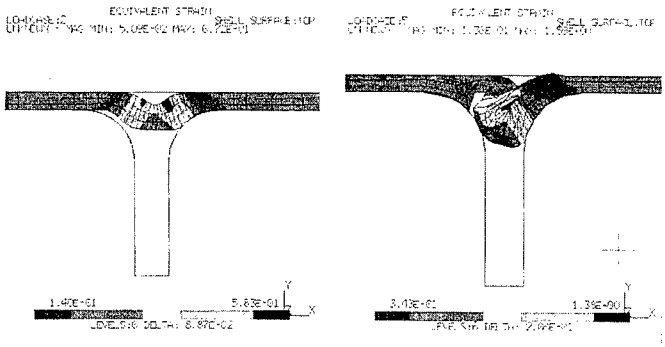

Plastic flow analysis (NASKA)

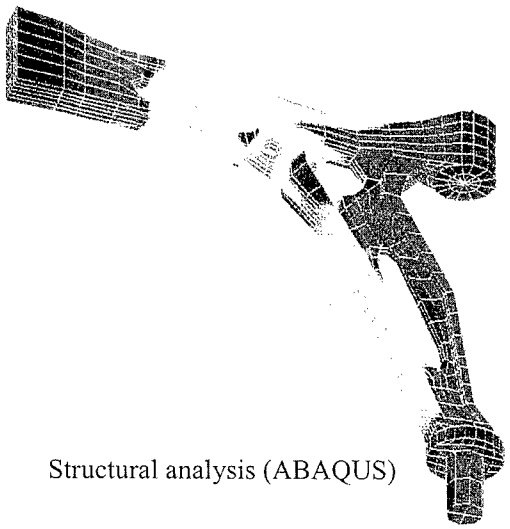

Structural analysis (ABAQUS)

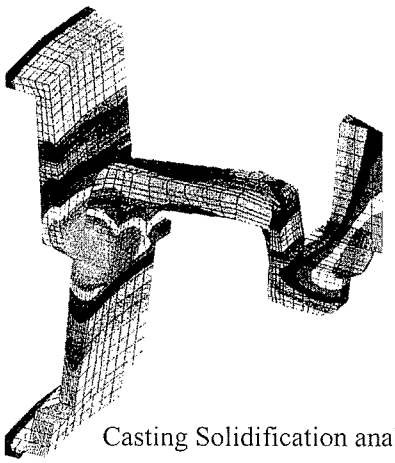

Casting Solidification analysis (CASTEM)

Fig.6 Computer simulation of Casting and Forging process

4.Finally

As I said, we could accomplish the manufacturing of high strength products in a short period by developing aluminum alloy and designing products in our own company.But car makers are requiring the supply of products with higher strength in a shorter manufacturing period.To meet this requiremnet, we are now developing new alloy based on KS651 which has higher strength and toughness than KS651 and we make the accuracy of analysis higher by the feedback of strength test of products.

Characteristics of Strain Profile at Hydroformed Al Tubes

Sang Yong Lee, Ywan Je Jo**, Sung Man Sohn*, Mun Yong Lee* and Young Suk Kim**

Dept. of Material Processing Technology
Korea Institute of Machinery and Materials, Changwon 641-010, Korea
*Technical Institute
Sung Woo Hitech Co. Ltd., Pusan 940-15, Korea
**Dept. of Mechanical Engineering
Kyungpook National University, Taegu 702-701, Korea

ABSTRACT

The strain characteristics of aluminum hydroforming have been phenomenologically investigated. Annealed Al6063 seamless tube was used for hydroforming of automotive bumper rail. Hydroformed bumper rail showed the complexity of the shape, which resulted in non-uniform distribution of deformation at overall cross-section of the product. Strain profiles of both along the length and at the circumference of the tube presented the existence of locations of lacallized thinning, of which strain values were 2 or 3 times greater than the average. Design consideration for the shape of sharp curved area of the product and the formability of tube materials were very important factors for hydroforming.

1. Introduction

Tube hydroforming has been extensively developed for the application in automotive industry. By using the hydroforming process, complex near net-shape components can be formed out of extruded or welded tubes. Most of the current components by tube hydroforming are made of steels due to the better elongation values. Aluminum showing good strength-to-weight ratio, corrosion resistance, and recyclability is a competent material to possibly replace steel for the production of hydroformed parts in future cars [1-3]. But, up to now the depth of knowledge on tube hydroforming of aluminum has been relatively insufficient[4]. The major research target in tube hydroforming is to control the strain distribution in tube hydroforming of complicate shaped components[5-6]. It is very difficult to take countermeasures against tube wall thinning because it is a combined process of bending, stretching and press working. This paper presents the analyzed results of strain profiles at hydroformed aluminum bumper rail. Some factors affecting the characteristics of strain distribution of hydroformed product such as formability of materials, friction, tooling and processing parameters will be phenomenologically discussed

2. Experimental Procedure

2.1 Tube material and analysis of strain profiles

Extruded Al6063 seamless tube, followed by T6 heat treatment, was used for the hydroforming of bumper rail. Table 1 shows the chemical composition of the tube materials.

Table 1 Chemical composition of A6063 tube

Element	Mg	Si	Fe	Mn	Cr	Cu, Zn, Ti	Al
Wt, %	0.5	0.44	0.09	0.025	0.032	≤0.01	REM.

The 100mm outer diameter and 5mm thick tube was cut by 1795 mm in length, and annealed before hydroforming of the automotive bumper rail. Typical annealing condition of Al6063 (415 °C/2 hr, furnace cooling to 300 °C at the cooling rate of 30 °C/hr, then air-cooled) was applied to ensure the enough elongation property for forming the complicated shape without defects. Mechanical properties of tube materials in as-received and post-annealed conditions were presented in Table 2.

Table 2 Mechanical properties of Al6063 tube

Material Condition	Y.S.[MPa]	T.S.[MPa]	El. [%]
As-Received(T6)	199	243	12
Fully Annealed(O)	50	97	32

Characteristics of strain profiles were analyzed through measurements of wall thickness in the hydroformed bumper rail product. The bumper rail did not show the uniform deformation contour in any section of the hydroformed part. Thickness measurements were performed for the longitudinal cross section normally in a given distance (4mm). For the position of heavy deformation, it was measured in 2mm distance. The circumferential strain measurement was made in 2mm distance in 5 characteristic cross sections of hydroformed part. Mechanical properties were analyzed using specimen cuts in 5 different positions of not only hydroformed part but also hydroformed and T6 treated part. Tensile tests were performed at room temperature.

2.2. Hydroforming equipment and procedure

Fig. 1 presents schematically the hydroforming equipment used for the experiment. The maximum capacity of equipment was 25000kN in closing force and 4000bar in internal pressure. Important process parameters were pre-set and on-line controlled by servo-hydraulic units. Hydroforming of bumper rail was processed by the procedure shown in Fig. 2. It was characteristic in the present tube hydroforming process that bending and bulging of aluminum tube were performed consecutively in a single operation by use of one set of tool system.

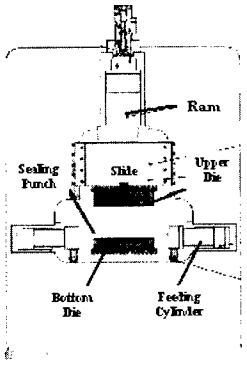

Fig. 1 Hydroforming system(Kang Eng.)

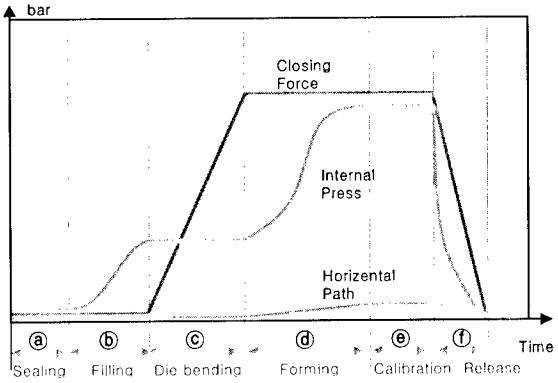

Fig. 2 Hydroforming process

3. Results and discussion

3.1 Hydroforming process and products

Fig. 3 shows the appearance of a successfully hydroformed bumper rail made with Al6063 material. Pressure and time curves that make hydroforming without significant defects are presented as shown in Fig. 4. Initial pressure of about 100 bar was applied for bending operation after sealing and feeding of tube. Maximum pressure required for main bulging process with present tube materials was between 400 and 500 bar. Typical failures have been bursting and incomplete deformation in the area of small radii. Wrinkling was not produced in any case due to the thickness effects. It was, however, expected that more critical design consideration of the local shape of curves and the adequate lubrication between tool and tube were necessary to prevent defects for forming higher strength materials.

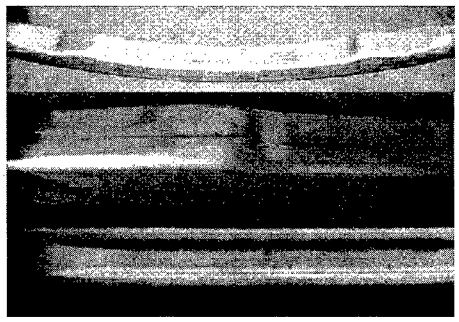

Fig. 3 Hydroformed bumper rail

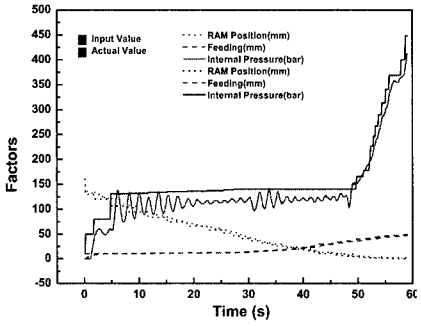

Fig. 4 Typical pressure and time curves

3.2 Strain profiles in the longitudinal cross section of tube

Characteristics of strain distribution of hydroformed bumper rail was analyzed by measurements of wall thickness in a given distance at both longitudinal and circumferential cross sections. Apparent strain could be calculated from the thickness measurements at each point. Fig. 5 (a) shows the longitudinal cross-section of a hydroformed aluminium product and traces of thickness measurements for both sides (A, B) of cross section. Fig. 5 (b) is the results of steel hydroforming that was produced with the same tool for comparison with aluminum hydroforming. The tube in thickness of 1.4mm that was manufactured by welding of plates out of AISI 1008 was used in case of steel hydroforming.

Due to symmetry relative to center, only the half of bumper rail was measured. The right side in the figure is the end part of bumper rail that was sealed, the left is the center part that was set as "0" point.

Both aluminum and steel show similar strain profiles along the longitudinal direction of products. It is clear that the sharp curved area (nose) presents locally severe thinning effects. The thickness change in most area is below 10%. But the location of 'nose' shows a strain of nearly 30% for aluminum and about 20% for steel. These results mean that the position of strongly thinning is mainly determined by the shape of product, and the amount of the strain depends mostly on the material properties

3.3 Strain profiles in the circumference of tube

It is more difficult to analyze the characteristics of strain profiles in the circumference of hydroformed product. 5 positions of bumper rail that could show most of different deformation shapes were selected for the measurement of wall thickness as shown in Fig. 6.

The half shape and the thickness distribution for each section were presented. There are more than one "nose' in each section, which could be a source of defects during hydroforming by

inadequate processing and material parameters. The maximum strain is about 25%, the average strain is lower than 10%.

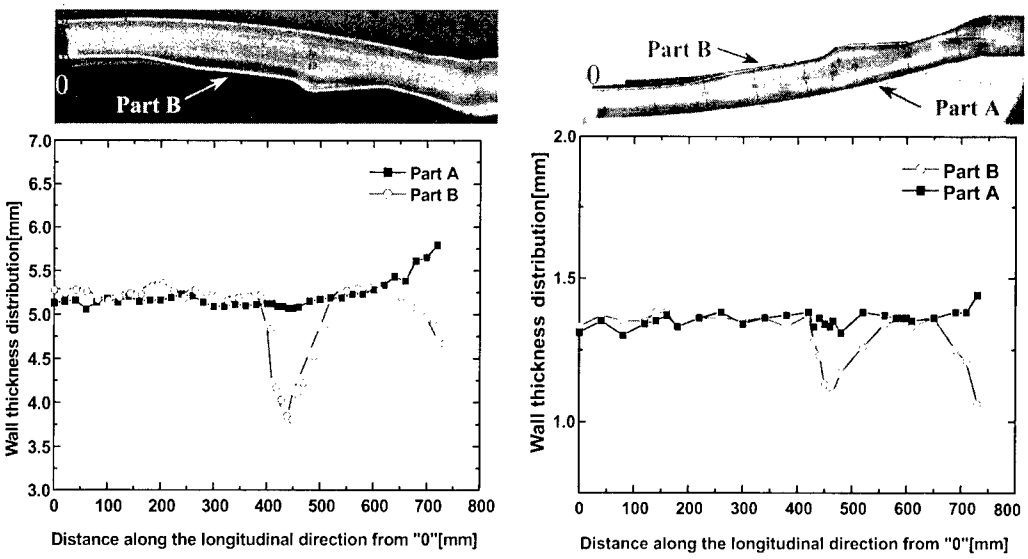

(a) Al bumper rail (b) steel bumper rail

Fig. 5 Longitudinal cross section and thickness profiles in hydroformed Al and steel bumper Rail

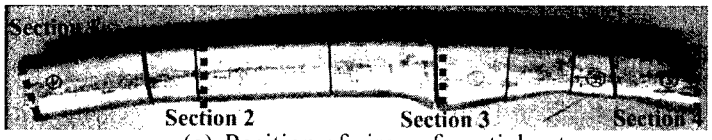

(a) Position of circumferential cuts

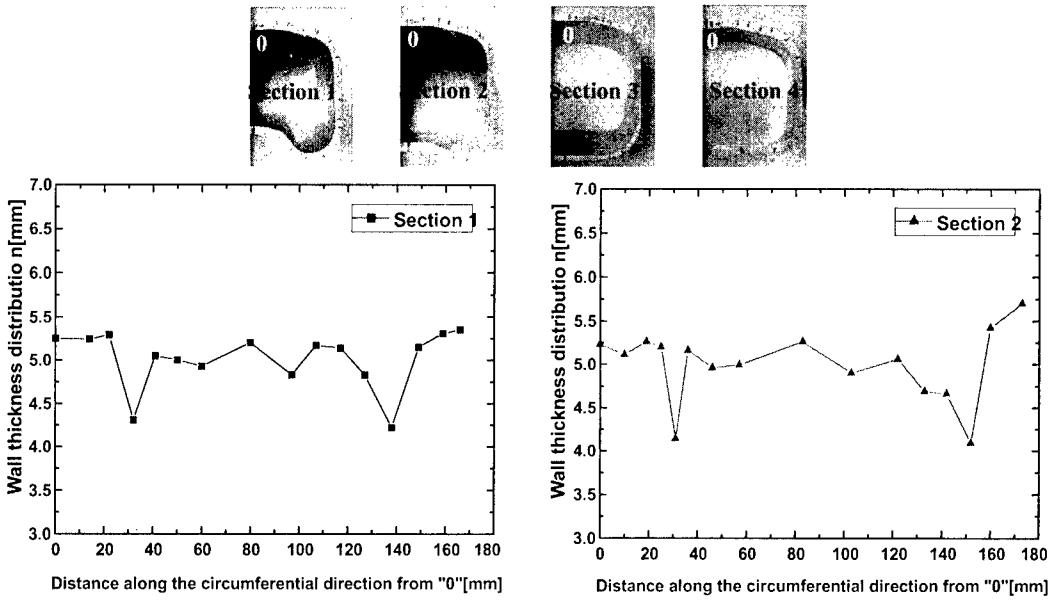

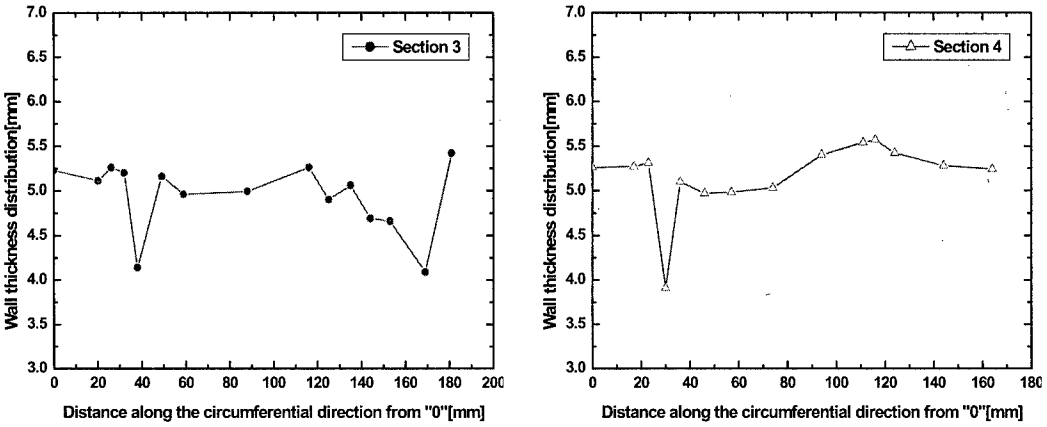

(b) Appearances and thickness profiles in the circumferential cuts

Fig. 6 Appearances and thickness profiles in the circumferential cuts of hydroformed Al bumper rail

3.4 Tensile properties

Fig. 7 shows the change of mechanical properties for hydroforming of Al6063 tubes. Hydroforming resulted in the about 25% increase of tensile strength. It could mean that the increase of strength was strongly related to the strain by hydroforming. Elongation value decreased after hydroforming.

As the bumper rail showed not the same amount of deformation in any location, mechanical properties according to the location of a deformed tube has been investigated. Fig. 8 presents tensile strengths according to the locations of a tube at each step of hydroforming. Tensile strengths of a annealed tube should be same in any location before hydroforming. It is, however, characteristic that specimens of the hydroformed tube and the T6 treated tube after hydroforming showed slightly increased strength values in the direction center. It was assumed that the difference in strength according to location in a tube resulted mainly not from hydroforming but from bending operation before hydroforming

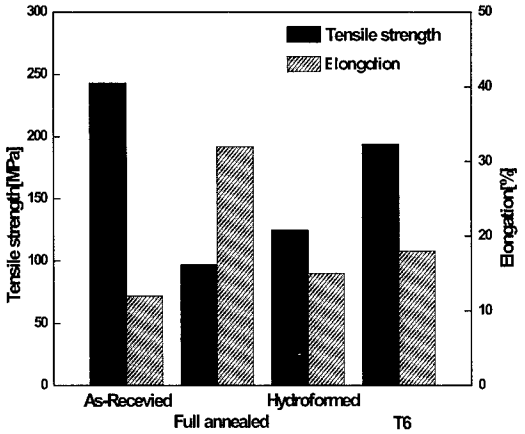

Fig. 7 Tensile properties at each step of hydroforming

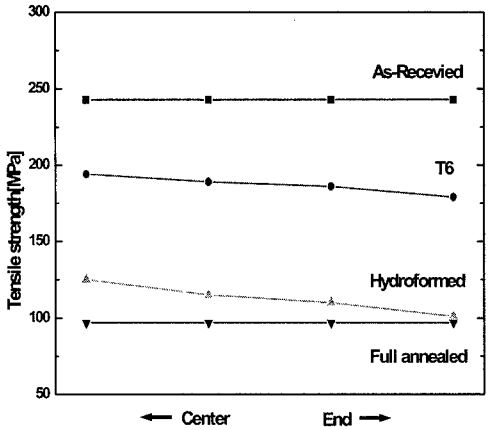

Fig. 8 Tensile strengths in different longi -tudinal positions of Al bumper rail

4. Conclusion

Phenomenological strain characteristics of hydroformed Al6063 tubes have been investigated. Bumper rail showed the complexity of the shape, which resulted in non-uniform distribution of deformation at overall cross-section of the product. Strain profiles of both along the length and at the circumference of the tube presented the existence of locations of locallalized thinning, of which strain values were 2 or 3 times greater than the average. It turned out that design consideration for the shape of sharp curved area of the product and the consideration of formability of tube materials were of the great importance.

REFERENCES

1. F. Vollertsen, T. Prange and M. Sander, Proc. of 6th ICTP, Vol. II(1999), pp. 1197-1210.
2. W. Leitermann, K.-H. von Zengen and P. Dick, Proc. of 6th ICTP, Vol. II(1999), pp. 1165-1170.
3. C. Kunz, R. Maechler, P.-J. Uggowitzer and M. Speidel, Proc. of NNS 97, (1997), pp. 121-128.
4. A. Shirayori, S. Fuchizawa and M. Nazaraki, Proc. of 6th ICTP, Vol. II(1999), pp. 1223-1228.
5. S.-M. Sohn, M.-Y. Lee and S.-Y. Lee, Trans. Mat. Proc., Vol. 9, No.6 (2000), pp.561-566.

THE HEMMING PROCESS FOR ALUMINUM BODY SHEET

K. Noda, Y. Takaki and H. Konishi*

Aluminum & Copper Company, KOBE STEEL, LTD.
15 Kinugaoka, Moka-city, TOCHIGI 321-4367, JAPAN
*Aluminum & Copper Company, KOBE STEEL, LTD.
5-5 Takatsukadai 1-chome, Nishi-ku, Kobe, HYOGO 651-2271, JAPAN

ABSTRACT

The effect of tool design on hemming test was investigated using 6xxx series aluminum alloys. The crack of surface after hemming by down-flange method was larger than that by V-block bend method in same specimens. The maximum strain of bending point by down-flange was larger than that by V-block bend from the results of FEM simulation. The specimens bended by down-flange caused shear deformation only on flange side, which relieved maximum strain, but the specimens bended by V-block bend caused shear deformation on both sides of bending point.

Hem formability should be evaluated in much the same way as practical hemming process for outer panel since the results of bending test are different by bending method. In the future, bending test method for aluminum body sheet should be specified.

1. INTRODUCTION

It is important to evaluate hem formability correctly for increasing application with aluminum alloy to auto body sheet for outer panel. V-block bend method and pressing bend method, which are standardized by Japanese Industrial Standards, are generally used for bending test. But these methods are different from practical hemming process.

In this study, the effect of bending method was investigated on the results of bending test using 6xxx series aluminum alloy.

2. EXPERIMENTAL METHOD

2.1 Specimens

The specimens used in this study were 6xxx series alloy (1.0mm thickness), which contained 1.0% silicon and 0.6% magnesium, and the strength was changed by heat treatment (100℃ × 10hr). Table 1 shows the mechanical properties of specimens.

Table 1 Mechanical properties of specimens

Materials (Al-1.0%Si-0.6%Mg)	Thickness mm	Test direction	TS N/mm^2	YS N/mm^2	El %
6000-A (T4)	1.0t	L	264	145	29.0
		LT	252	140	30.1
6000-B (100℃ × 10hr)		L	273	160	29.2
		LT	259	155	30.4

2.2 Bending method

The specimens were pre-stretched (5～10%) on the assumption of press forming before bending test. The bending test were consisted of three step process in much the same way as practical hemming process for outer panel, 90° , 135° (pre-hemming) and 180° bend (flat hemming, inner thickness=1.0mm). The effect of tool design of 90° bend on hem formability, V-block bend type and down-flange type (bend radius=1.0mm), were investigated. Fig.1 shows the schematic drawing of the 90° bend method. Hem formability was rated five levels from visual observation (good 1>2>3>4>5 poor) after flat hem.

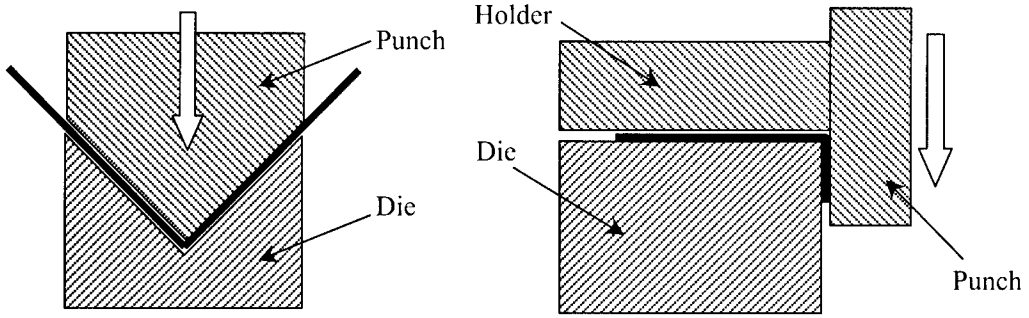

V-block bend (bend radius=1.0mm) Down-flange (bend radius=1.0mm)

Fig.1 Schematic drawing of 90° bend method

2.3 FEM simulation

Each hemming process was simulated by FEM analysis (ABAQUS Implicit). The stress-strain curve of 5% pre-stretched typical 6xxx series alloy was used for calculation. It was assumed that all bending tools were rigid body and friction coefficient between materials and tools were 0.15.

3. RESULTS

3.1 The effect of 90° bend method

Fig. 2 shows the appearance of bending specimens after hemming by V-block bend and

down-flange. This figure shows that the crack of surface after hemming by down-flange was larger than that by V-block bend in same specimens. The bending condition of down-flange was stricter than V-block bend. In the case of 6000-B (high strength), such tendency was remarkable.

5% pre-stretch, inner thickness=1.0mm

Materials	90° bend method	Evaluation of hem formability (Attached number is hem level)
6000-A	V-block bend	// 2 ⊥ 1.5
	Down-flange	// 2.5 ⊥ 2
6000-B	V-block bend	// 4 ⊥ 2.5
	Down-flange	// 5 ⊥ 3

Fig. 2 Appearance of specimens after flat hem
(Bending direction : upper L, lower LT)

3.2 FEM simulation

Fig. 3 show the maximum strain of bending point after 90° and 180° bend by down-flange and V-block bend from the results of FEM simulation. The maximum strain of bending point by down-flange was larger than that by V-block bend. The specimens bended by down-flange caused shear deformation only on flange side, which relieved maximum strain, because die and holder fixed the opposite side of flange side. But the specimens bended by V-block bend caused shear deformation on both sides of bending point. These results agreed well with the experiments, and it is considered that the bending deformation by down-flange was stricter than V-block bend.

Fig. 4 shows the strain distribution on the outside of bending part after 90° bend. V-block bend showed approximately symmetrical strain distribution. But down-flange showed the strain distribution which strain concentrated on bending point, because bending deformation on the opposite side of flange side became small.

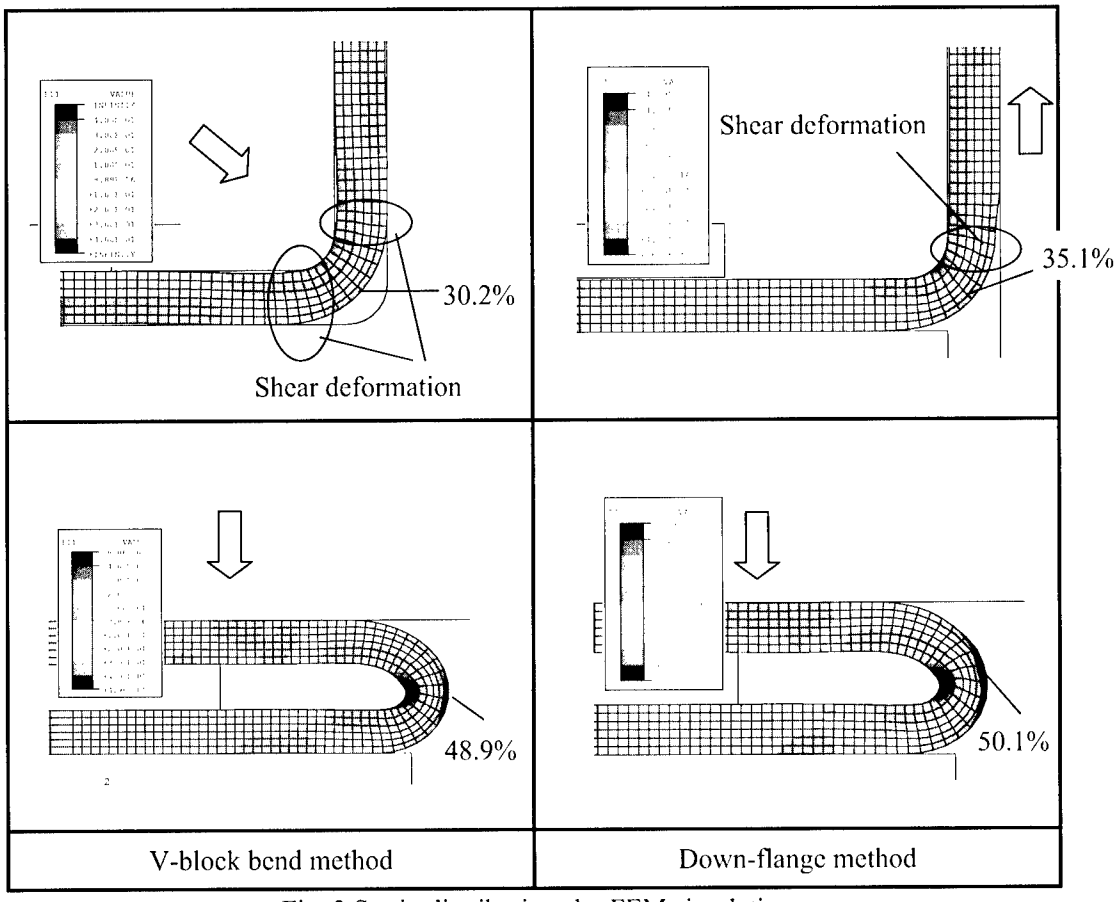

Fig. 3 Strain distributions by FEM simulation

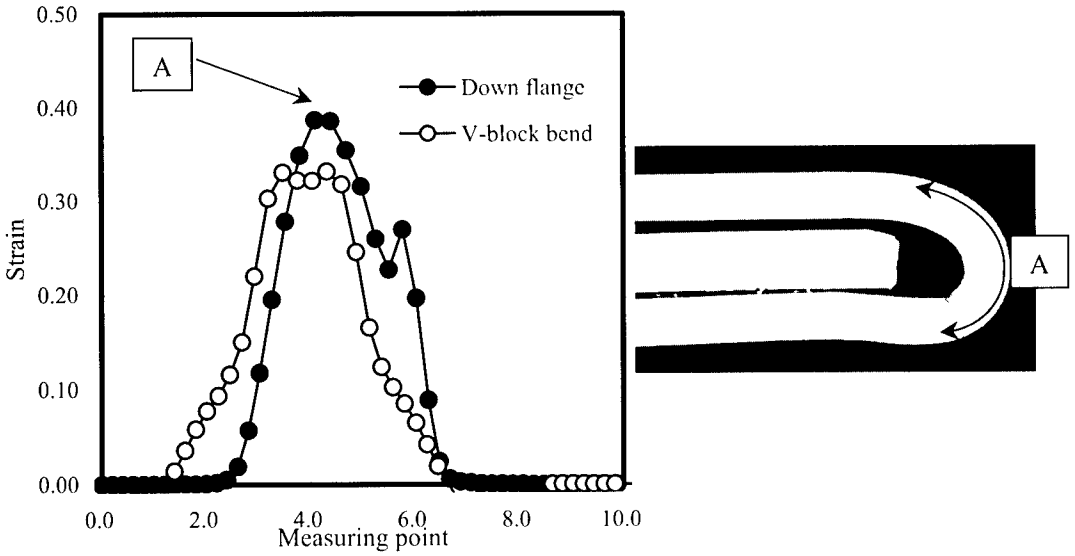

Fig. 4 Strain distribution on the outside of bending part after 90° bend (FEM simulation)

3.3 Vickers hardness distribution of bending point

Fig. 5 shows the Vickers hardness distribution of the section after 90° bend in the practical bending test. The specimens bended by down-flange showed unsymmetrical hardness distribution, which bending point had highest hardness, but the specimens bended by V-block bend showed the gentle hardness distribution. These results agreed well with the FEM simulation shown in Fig. 3 and 4.

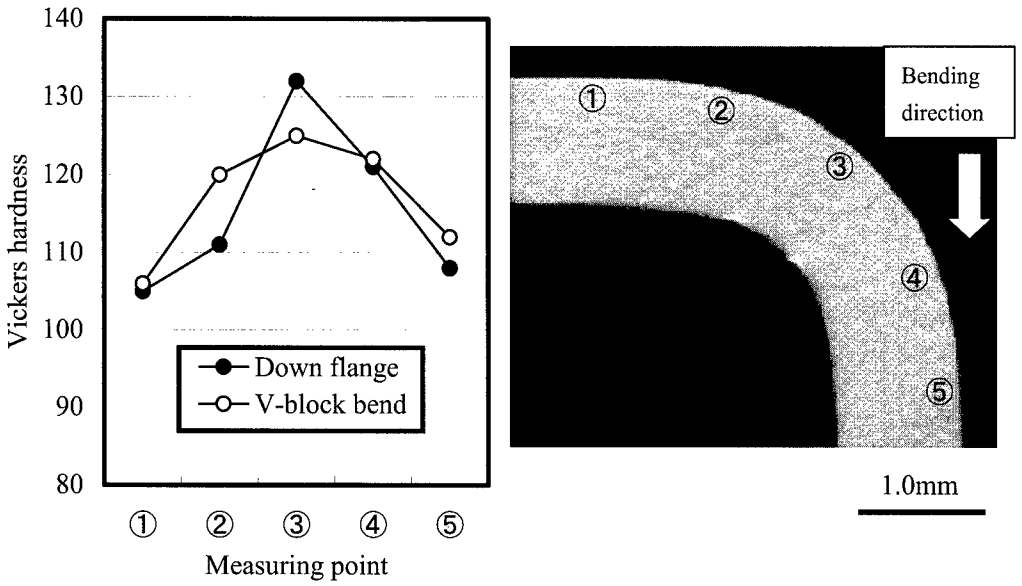

Fig. 5 Vickers hardness distribution after 90° bend

4. CONCLUSION

In this study the effect of bending method was investigated on results of bending test with 6xxx series aluminum alloy.

(1) Hem formability of aluminum body sheets should be evaluated in much the same way as practical hemming process for outer panel, since the results of bending test are different by bending method.

(2) In the future, bending test method for aluminum body sheet should be specified.

(3) Bending deformation by down-flange method is stricter than V-block bend method, because the specimens bended by down-flange cause shear deformation only on flange side, which relieve the maximum strain, but the specimens bended by V-block bend cause shear deformation on both sides of bending point.

INHOMOGENEOUS DEFORMATION BEHAVIOUR DURING EQUAL CHANNEL MULTI-ANGULAR PRESSING

Hyoung Seop Kim and Min Hong Seo

Department of Metallurgical Engineering, Chungnam National University
Taejon, 305-764, KOREA, hskim@cnu.ac.kr

ABSTRACT

The properties of the materials are strongly dependent on the shear plastic deformation behaviour during equal channel angular pressing (ECAP), which is controlled mainly by die geometry, material properties, and process conditions. In the present paper, we studied the plastic deformation behaviour of specimens during equal channel multi-angular pressing (ECMAP) which gave a total strain of approximately 2 on a single pass through the die, using the two dimensional rigid-plastic finite element method. The ECMAP process is explained in terms of two stages based on the corner filling procedure. Numerical simulations on annealed pure copper show that the first corner gap which occurs during stage I doesn't occur during stage II due to the back pressure effect developed by the second corner deformation. This back pressure effect results in the local severe shear at the bottom of the ECAP samples of the routes A and C. It would be possible to obtain homogeneous deformation and isotropic samples by controlling the deforming route and processing conditions.

1. INTRODUCTION

The severe plastic deformation (SPD) process has been the subject of intensive investigations in recent years due to the unique physical and mechanical properties inherent in various ultrafine-grained materials [1]. Also SPD-produced materials have a number of advantages over nanostructured materials manufactured by other methods through powder processing. Among various SPD methods, such as multiple forging, torsion straining, accumulative roll bonding and equal channel angular pressing (ECAP), the ECAP process is a most promising and interesting method. ECAP process involves large simple shear plastic deformation within a thin layer of a workpiece pressed through a die containing two intersecting channels of identical cross-sections that meet a predetermined angle. This process, invented by Segal *et al.* [2] in the beginning of the 1980s, has been the subject of intensive study in recent years due to its capability of producing large full dense samples containing an ultrafine (or nanometer scale) grain size by repeating the process while maintaining the original cross-section of the workpiece.

Figure 1 shows the principle of ECAP, where two channels of equal cross-section intersect at an oblique angle (or channel angle) Φ. With reference to the workpiece, three perpendicular directions denoted as pressing direction, width direction and thickness direction, respectively, are introduced. In order to account for the difference in the local deformation in the workpiece, the workpiece parts that flow near the inside corner (point A) and the outside corner (arc BC) of the die will be referred to as the inside part and the outside part, respectively. The

deformation mode in ECAP under ideal condition in Fig. 1 is 'simple shear' as the case of torsion. The major difference of ECAP with torsion or other plastic deformation processes, which is unique in ECAP, is that deformation occurs in the immediate vicinity of the plane, i.e. the shear plane, lying at the intersection of the two channels. Therefore, the deformation in the ECAP sample is very homogeneous. In a rectangular workpiece, the thickness direction is perpendicular to the width and length directions, so that the strain along the thickness direction is zero, i.e. plane strain condition prevails. Therefore, the deformation during the ECAP process of rectangular specimens becomes two-dimensional.

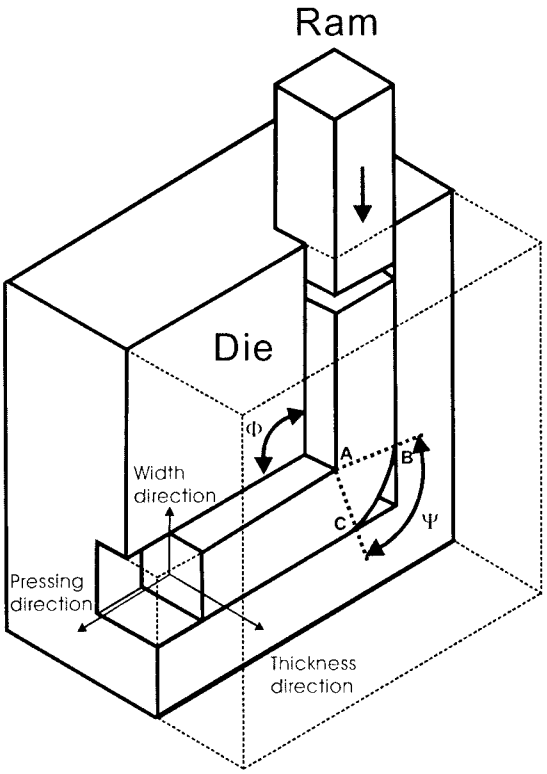

Fig. 1. Schematic representation of the ECAP process, illustrating the channel angle Φ and the corner angle Ψ.

Segal [1,3] has demonstrated that, providing the workpiece is constrained to fully-fill the die channel and the die corner is sharp, on travelling through the die an element will be sheared abruptly on crossing the join line between the two channels by an amount dependent on the die channel angle. Under these conditions, the magnitude of the shear strain γ during ECAP for N passes can be obtained as:

$$\gamma = 2N \cot\left(\frac{\Phi}{2}\right) . \tag{1}$$

However, unlike the idealized case, the real deformation characteristics is inhomogeneous

due to the effects of friction, a curved die corner or incomplete filling of the die. The die corner angle Ψ is defined as the angle subtended by the arc curvature and lies between $\Psi=0$ and $\Psi=\pi-\Phi$. Kim [4,5] has demonstrated that the lesser shear zone in the outer part of the workpiece occurs because of the faster flow, that is shorter travel path, of the outer part compared to the inner part within deformation zone (area ABC in Fig. 1) when the corner angle of the die is not zero. According to Iwahashi *et al.*'s analysis [6] using the analytical methods. a general equation for the shear strain γ generated in the workpiece after N passes of ECAP is given by the following relation:

$$\gamma = N\left[2\cot\left(\frac{\Psi}{2}+\frac{\Phi}{2}\right)+\Psi\ \mathrm{cosec}\left(\frac{\Psi}{2}+\frac{\Phi}{2}\right)\right] . \qquad (2)$$

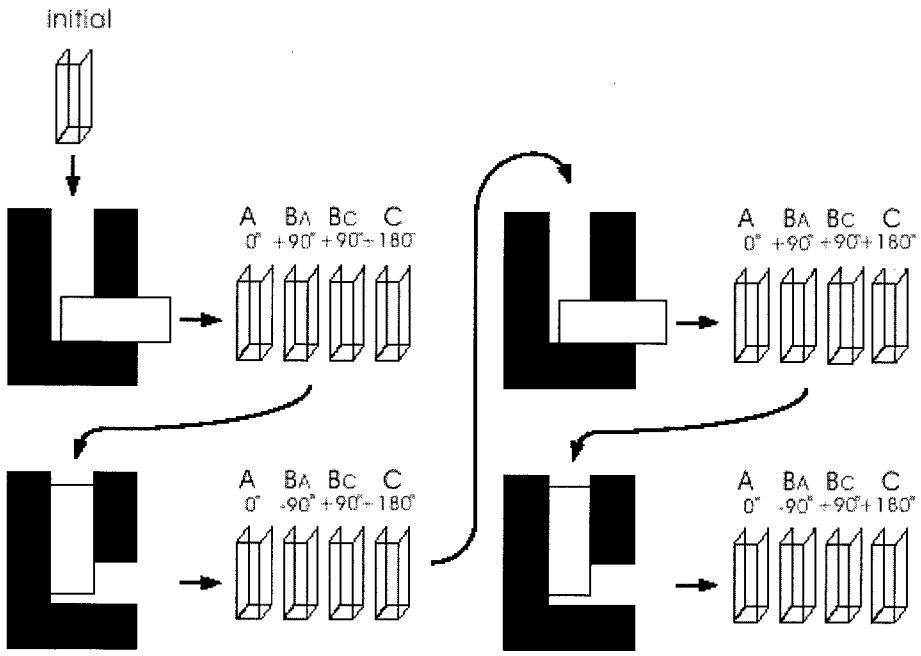

Fig. 2. Schematic diagram of the four fundamental strain routes for multi-pass ECAP.

The distinguished merit of ECAP is that repetitive pressings may be conducted to achieve very high total strains since the cross-sectional dimensions of the workpiece remain unchanged. By changing pressing directions in conducting the repetitive pressings, various microstructures and properties of the workpiece can be obtained. The direction and number of billet passes through the channels during ECAP are very important for microstructure refinement. It is possible to define four fundamental processing routes in ECAP. These routes are illustrated schematically in Fig. 2 where route A involves no rotation of the sample between repetitive pressings, route C involves a rotation of 180 °, and route B involves a rotation of 90 ° where route B_A denotes alternate rotations of 90 ° and route B_C denotes a rotation of 90 ° in the same direction between each pressing, respectively. The shearing

characteristics associated with these different routes are described in detail elsewhere [7] and experiments have shown that route B_C is the optimum processing condition for attaining a homogeneous microstructure of equiaxed grains separated by high angle grain boundaries [8]. Although it is useful to conduct the repetitive ECAP process where samples are pressed through a die, removed and rotated, and then re-inserted into the die for additional pressings for a homogeneous and equiaxed microstructure, productivity of the batch type process is low. Hence, to develop the continuous ECAP process which can produce several shear deformation at one stroke by passing the sample through a multi-angular channel die is necessary for the industrial application of the ECAP process.

Recently, equal channel multi-angular pressing (ECMAP) has been proposed for improving the efficiency of the processing. Liu *et al.* [9] used the die with the channel angle of 160 ° and the final effective strain developed is so low (about 0.4) that it cannot allow large strain even if multi-channel is used. Nakashima *et al.* [10] fabricated a multi-pass facility for ECAP which gave a total strain of approximately 5 on a single passage through the die and showed from the experiments on high purity aluminium that, when comparisons are made at the same total strains, both the hardness and the evolution of the microstructure are identical when using the multi-pass facility or when repetitively pressing samples through a standard die containing a single shearing plane. As the ECMAP process is feasible for high productivity, it is meaningful to investigate the deformation behaviour of materials during the process. In the present study, plastic deformation behaviour of materials during the ECMAP process is analysed using FEM. The work focuses on the inhomogeneity and flow behaviour of materials during ECMAP.

2. FINITE ELEMENT ANALYSIS

Isothermal two-dimensional plane-strain FEM simulations of the ECMAP process have been carried out using the commercial rigid-plastic finite element code, DEFORM2D [11]. Figure 3 shows the ECMAP dies and workpieces used in this investigation. The second channels with opposite directions in Figs. 3(a) and 3(b) were designed after the first channels for the consecutive process. Since the second shearings of the samples in Figs. 3(a) and 3(b) follow effective rotations of 0 ° and 180 °, the configuration of Figs. 3(a) and 3(b) correspond to processing route A and route C as illustrated in Fig. 2., respectively. In the simulations, the simple model die with the prototype geometry of $6 \times 6 \times 60$ mm^3, Φ=90 ° and Ψ=0 ° was used.

The workpiece material used in the calculations was annealed copper, of which the flow curve was calculated up to large strain range based on the dislocation cell evolution model [12]. Constant ram speeds of 1 mm·s^{-1} were employed. All simulations used automatic remeshing to accommodate large strains and the occurrence of flow localization during the simulation. The coefficient of friction between the die channel inside and the specimen was assumed to be zero, implying frictionless condition. The time of a calculation was less than 5 h on an alpha workstation.

3. RESULTS AND DISCUSSION

Figure 3 shows the deformed geometries of the workpieces during the ECMAP process. We distinguished the deforming process as two stages according to the passing step of the

samples through the first intersection (stage I, Figs. 3(a) and 3(c)) and the second intersection (stage II, Figs. 3(b) and 3(d)). Since the deforming conditions are the same until the workpiece reaches the second intersection in both route A and route C, the deformed geometries in Figs. 3(a) and 3(c) are identical. It can be found that the corner gap between the die and the workpiece develops. This corner gap formation due to the hardening characteristics of materials and the resultant inhomogeneous deformation have been reported [4]. The annealed copper used for the calculation satisfies the corner gap formation condition of the distinct strain hardening behaviour. That is, the high strain hardening exponent n value of 0.335 is obtained from the flow curve of the reference [12]. The reason for the formation of die corner gap can be explained using the stress distribution developed in the workpiece. For the strain hardening materials, the inner part of the workpiece within the deforming zone, which receives more severe deformation, is much harder than the outer part of the deforming zone because of the large hardening exponent. The outer part of the workpiece, which receives lower deformation and therefore softer than the inner part within the deforming zone, can flow faster to the exit channel and the corner gap is formed. The corner gap (or round shaped die corner) results in the lesser sheared zone at the bottom region.

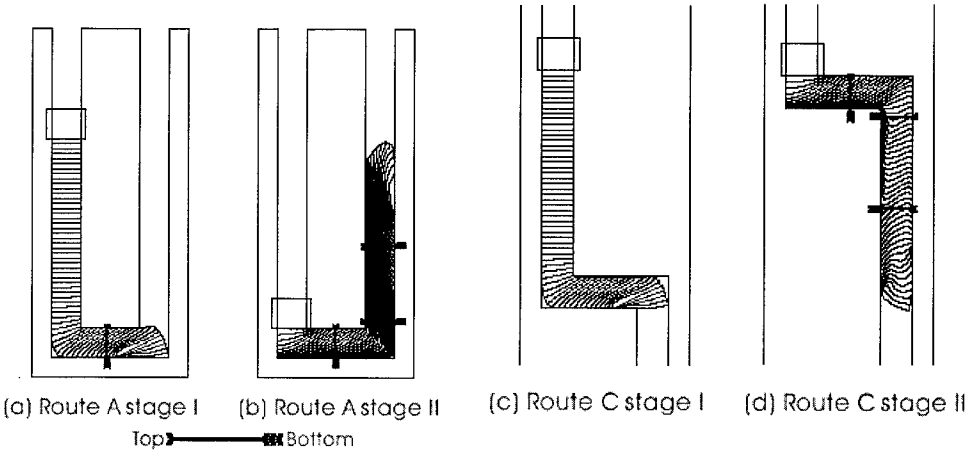

Fig. 3. FEM predictions of deformation geometry changes during ECMAP.

From the stage II of the route A and the route C in Figs. 3(b) and 3(d), the difference in the deforming characteristics between the two routes is explicit, in that the shear deformation at stage II is more intensive due to the same shear direction of the second shear in the route A sample than that of the stage I. On the other hand, at stage II of the route C sample the shear line is in the reverse direction and the shear deformation is much lessened due to the reverse shear direction of the second shear compared to the first one. It should be noted that even though the shear deformation is quite different, the effective strain values between the samples of the route A and C are not so different. Interestingly, the corner gaps occurred at stage I disappeared at stage II. It should also be noted that the lesser sheared zone found at stage I disappeared, instead that positions turned to more sheared states. The fact that corner gap disappeared and the bottom region was more sheared than the other region is attributed to the effect of the back pressure which comes from the second intersection zone on the deformation at the first intersection zone. The back pressure effect which diminished the

lesser sheared zone was reported by Bowen *et al.* [13]. By controlling the deforming route and processing conditions, it would be possible to obtain homogeneous deformation and isotropic samples.

4. CONCLUSIONS

Finite element analysis using the rigid-plastic DEFORM2D code was carried out in order to investigate the plastic deformation behaviour of the workpiece during the ECMAP process with two intersecting zones.

The shear deformation at stage II is more intensive in the routes A sample and is lessened in the reverse direction in the route C sample due to the difference in the shear direction of the first and the second shear.

The corner gaps occurred at stage I disappeared at stage II in both the routes A and C processes, which is attributed to the effect of the back pressure which comes from the second intersection zone on the deformation at the first intersection zone.

ACKNOWLEDGEMENTS

This work was supported by the Korea Research Foundation Grant (KRF-2000-042-E00095).

REFERENCES

1. R.Z. Valiev, R.K. Islamgaliev and I.V. Alexandrov, Prog. Mater. Sci., 45(2000) 103.
2. V.M. Segal, V.I. Reznikov, A.E. Drobyshevskiy and V.I. Kopylov, Russian Metallurgy (Metally), 1(1981) 99.
3. V.M. Segal, Mater. Sci. Eng., A197 1995) 157.
4. H.S. Kim, M.H. Seo and S.I. Hong, Mater. Sci. Eng., 291A(2000) 86.
5. H.S. Kim, Mater. Sci. Eng., A(2001) in press.
6. Y. Iwahashi, J. Wang, Z. Horita, M. Nemoto and T.G. Langdon, Scripta Mater., 35(1996) 143.
7. M. Furukawa, Y. Iwahashi, Z. Horita, M. Nemoto and T.G. Langdon, Mater. Sci. Eng., A257(1998) 328.
8. Y. Iwahashi, Z. Horita, M. Nemoto and T.G. Langdon, Acta Mater., 46(1998) 3317.
9. Z.Y. Liu, G.X. Liang, E.D. Wang and Z.R. Wang, Mater. Sci. Eng., A242(1998) 137.
10. K. Nakashima, Z. Horita, M. Nemoto and T.G. Langdon, Mater. Sci. Eng. A281(2000) 82.
11. SFTC: DEFORM ver. 5.2.
12. Y. Estrin, L.S. Toth, A. Molinari and Y. Brechet, Acta Mater., 46(1998) 5509.
13. J.R. Bowen, A. Golinia, S.M. Roberts and P.B. Prangnell, Mater. Sci. Eng. A287(2000) 87.

PLASTIC AND SUPERPLASTIC FORMING OF ALUMINIUM BASED METAL MATRIX COMPOSITES FOR TRANSPORT APPLICATIONS

F.Bardi*, P. Cavaliere*, L. Ceschini**, A. Morri**, S. Spigarelli*, E. Evangelista*

*Dipartimento di Meccanica, Università di Ancona, I-60131 Ancona, Italia
** Istituto di Metallurgia, Università di Bologna, I-40100 Bologna, Italia

ABSTRACT

Hot formability of two aluminium alloys of 6000 series reinforced with ceramic particles has been studied with the aim to optimize the parameters for produce prototypes in net-shape by means isothermal forging and superplastic forming. The plastic behaviour of 6061/Al_2O_3/20p was investigated through hot-torsion and hot-compression tests in the range of temperature and strain rate of 350-500°C and 10^{-3}-0.1 s^{-1} respectively and the results were utilised to produce processing and stability maps. Superplastic tensile tests were carried out on 6013/SiC/20p reinforced with ultrafine particles and manufactured by powder metallurgy, at strain rates ranging from 10^{-4} s^{-1} to $10^{-1}s^{-1}$ and temperatures from 450°C to 550°C. The evaluation of damage occurring during deformation, in term of particles' fracture and void formed at particle-matrix interfaces, has been related to the "safe" and "unsafe" regions in processing and stability maps. Processing maps data and constitutive equations of hot deformation have been used as input in simulation in a FEM code to model hot forging trials of some prototypes. Preliminary results on the isothermal forging of a simulacrum are discussed.

1. Introduction

Over the last two decades aluminium alloys reinforced with ceramic particles have been studied as potential structural materials for transportation systems since their attractive mechanical properties such as low density and high strength. In spite of numerous researches performed, up to the present a use of MMCs in production of low-cost automotive components is inhibited by ineffective manufacturing techniques, high cost of raw material and machining. Net-shape production processes via casting, isothermal forging and superplastic forming are expected to shoot down the large cost of final machining [1-3]. Moreover, as far as the reduction of composite cost is concerned, promising results have been achieved by a new stirring method allowing complete mixing of SiC (up to 30 vol%) in aluminium alloys in a few minutes [4]; the molten composite can be cast using net shape technologies such as sand, permanent moulds or investment casting. Superior mechanical properties close to the ones of wrought product are obtained by means of squeeze casting, high pressure die casting and thixocast technologies that reduce the formation of porosity and particle agglomeration during slow solidification [5]. For net-shape fabrication of MMCs components, isothermal forging and superplastic forming of cast or extruded billet are also

claimed but their use in the automotive industries is not considered since the high manufacturing cost depending from low productivity of the processes.
A brake drum produced with 359/Sic/20p by means of hydraulic press with the temperature of 360°C the upper and 320°C the lower die, showed very low damage levels, in terms of particle cracking and matrix-particle debonding, but the machining critical regions dramatically increased the manufacturing cost [1]. To produce sound brake drum, analysis by FEM predicted typical conditions of isothermal forging, with temperatures above 430°C [6].
In addition to isothermal forging, superplastic forming appears a promising technology to produce net shape components. The superplastic behaviour of MMCs has been studied extensively studied [2,3,7]. Moreover, several studies recently demonstrated that various aluminium based composites exhibit superplasticity at relatively high strain rates (10^{-2} s^{-1}). These strain rates are considerably higher than the ones used for conventional superplastic materials and rather close to commercial hot working rates. High strain rate superplasticity (HSRS) is therefore very attractive for commercial applications, mainly in the case of materials difficult to shape or machine with conventional techniques, permitting the production of net-shape components, with a significant reduction of the production costs[8].
In metal forming processes, a useful tool for the selection of the parameter allowing production of high quality components are becoming processing and stability maps [9].
The study aims to investigate the mechanical conditions for producing sound simple-shape items by means of isothermal and superplastic forming. To this end, extensive mechanical tests are carried out in order to collect reproducible data available to create processing and stability maps that are useful for defining proper forming conditions.

2. Experimental Procedure

The composites studied have the matrix of 6000 series alloys, namely 6061 and 6013.
The composite 6061/Al_2O_3/20p, produced by stir casting, was supplied by Duralcan in billets pre-homogenized 4 hours at 570°C, cooled to room temperature at 200°C/h and then extruded (extrusion ratio 1:13) into rods 80 mm in diameter. The composite was studied for the isothermal forging. The composite 6013/SiC/20p, PM, studied for superplastic forming, was produced by means of proprietary high-energy mixing process by Aerospace Metal Composite (UK) and supplied as extruded billet, 100 mm in diameter.
The chemical composition of the alloys is reported in Table 1.

Table 1 Chemical composition of composites.

Alloy	Mg*	Mn*	Si*	Cu*	Fe*	Cr*	Ti*	Zn*	Al*	Particulate
6013	0.8-1.2	0.2-0.8	0.6-1	0.6-1.1	0.5 max	0.1 max	0.1 max	0.25 max	bal	SiC, 20vol%
6061	1	0.15	0.6	0.28	0.3	0.2	0.15	0.25	bal	Al_2O_3, 20vol%

*wt%

Microstructural characterisation was carried out by means of optical and scanning electron microscopy.

The 6061/Al_2O_3/20p hot deformation behaviour was investigated by compression and torsion tests carried out at temperatures and strain rate in the range of 350-500°C and 10^{-3}-1.0 s^{-1}

respectively. Cylindrical specimens, 12 mm in diameter and 18 mm in length, were used for compression; before testing specimens were heated in a resistance furnace for 90 min before test. Specimens for torsion test, were machined from the extruded bar with the gauge dimension of 10mm in length and in diameter.
Equivalent stress and equivalent strain were calculated by the conventional equations for torsion tests [10]. In the compression the load-stroke data were converted into true stress-true strain after making corrections for the friction.
The 6013/SiC/20p was preheated at 475°C and then rolled, 10% per pass, to final thickness of 3mm. Specimens of 10mm gauge length and 5 mm width, were machined from the hot-rolled sheet with the tensile axis parallel to the rolling direction. The superplastic tensile tests were performed in air at temperatures from 520 to 590°C and with initial strain rates between $1 \cdot 10^{-2}$ and $3.8 \cdot 10^{-1}$ s^{-1}. Specimens of 10 mm gauge length and 5 mm width, were machined from the hot rolled sheet with tensile axis parallel to the rolling direction. Prior to testing, the specimens were held at the test temperature for 15 min.
Microstructural analyses on the PM 6013/SiC_p composite, in the hot-rolled conditions, carried out by OM and SEM, evidenced the presence of very fine (< 3 μm) and homogeneously distributed SiC particles. The average grain size of the aluminium alloy matrix ranged between 1 to 3 μm.

3. EXPERIMENTAL RESULTS AND DISCUSSION

3.1 Preliminary study of forging.

Fig.1 shows typical stress-strain curves obtained in torsion. The curves show peak stress (σ_p) followed by a moderate softening. The ductility, expressed as ε_f, was find to increase monotonically with T at lower strain rates, above 450°C tends to reverse. The correlation between $\dot{\varepsilon}$ and σ_p can be presented by the equation:

$$A\sinh(\alpha\sigma_p)^n = \dot{\varepsilon} \exp(Q/RT) \quad (1)$$

where A, α, and n are constants, R is the universal gas constant, Q is the apparent activation energy of the deformation. The activation energy was calculated as Q = 2.3 n R S, where n and S were the average slope of the curves $\dot{\varepsilon}$ vs. $\sinh(\alpha\sigma_p)$, Fig.2a, and $\sinh(\alpha\sigma_p)$ vs.1000/T, Fig.2b, respectively. The resulting activation energy was 150 kJ/mol. This value matches the one for self-diffusion in aluminium alloys and shows that the deformation process is mainly controlled by the matrix.

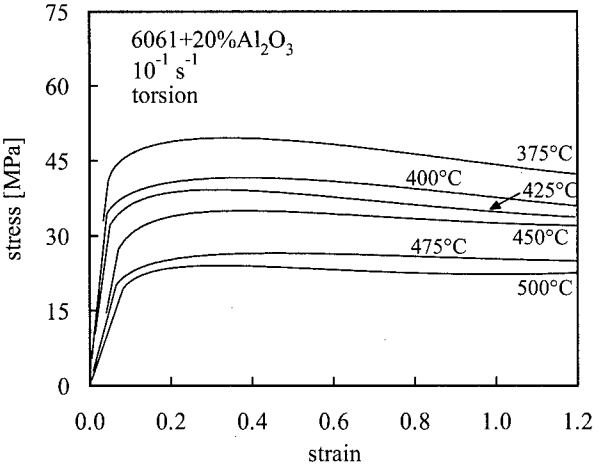

Fig. 1 Typical equivalent stress- equivalent strain torsion curves.

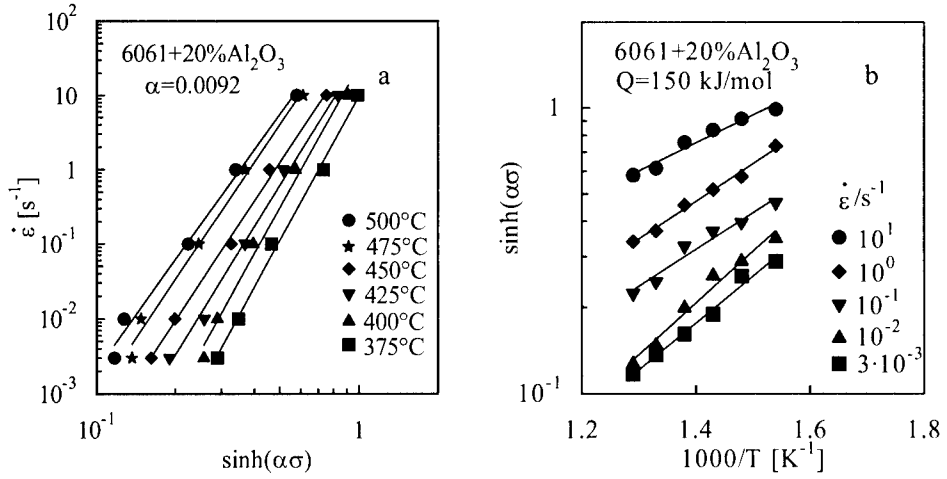

Fig. 2: (a) $\dot{\varepsilon}$ vs. $\sinh(\alpha\sigma_p)$ and (b) $\sinh(\alpha\sigma_p)$ vs.1000/T for the torsion tests

3.2 Processing and stability maps.

In metal forming the selection of the parameters to obtain high quality component production is successfully done by means of the processing and stability maps based on the Dynamic Material Model that considers the metal-forming systems as energy manipulators. The power generated by a source is transmitted by the dies to the workpiece under deformation. The deformation of workpiece dissipates the power into metallurgical dynamic processes [9,11,12] both of restoration (recovery and/or recrystallization, superplastic flow, phase transformation) and of damage (plastic instability, cracks). The power dissipated is defined as $J = \sigma\dot{\varepsilon}\ m/(m+1)$, where m is the strain rate sensitivity:

$$m = \partial \log\sigma / \partial \log\dot{\varepsilon}\big|_{T,\varepsilon} \qquad (2)$$

When m=1 (the workpiece behaves as a linear dissipator), J is at maximum $J_{max}= \sigma\dot{\varepsilon}/2$; but m<1 and so efficiency η of power dissipation is defined as:

$$\eta = J/J_{max}= 2m/m+1 \qquad (3)$$

High η values are indicative of effective processes in dissipating power.
Based on these premises, processing maps are generated as a plot of the iso-efficiency curves of power dissipation η in function of strain rate and temperature. Since damage processes also contribute to the efficiency η, it is imperative to identify in processing map the safe region of forging in terms of temperature and strain rate producing stable plastic flow.
The stability criterion, as formulated by Prasad [13], is based on the dimensionless parameter ξ

$$\xi(\dot{\varepsilon}) = \frac{\partial \ln(m/m+1)}{\partial \ln\dot{\varepsilon}} + m \qquad (4)$$

Prerequisite for stable flow is $\xi > 0$. If this criterion is satisfied, more uniform deformation occurs across the workpiece without dynamic strain ageing, propagation of pre-existing or formed microcracks, strain localisation producing failure at high strain rate and localised adiabatic heating producing adiabatic shear bands.
The equation 4 provides the necessary, but not sufficient, condition for stability and is probabilistic indicator of the hot forming behaviour exhibited by a material.
In the figure 3 the superimposition of processing and stability map for the composite investigated is shown. The highest values of efficiency were observed in the regions characterised by high temperature (475-500°C) and high strain rate (0.1 s^{-1}). The unstable region is represented by a large region in correspondence of high strain rate and all the temperatures investigated and in particular in the temperature range 400-450°C. A second unstable region is present at lower strain rates for all the temperature investigated in particular in correspondence of the range 350-400°C.

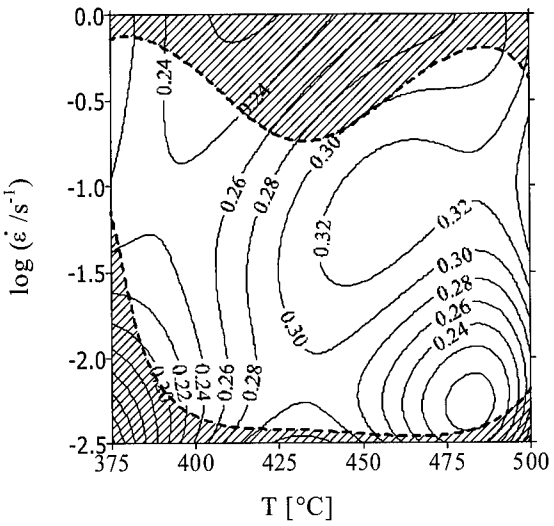

Fig. 3: Power efficiency dissipation map at ε=0.5, obtained from torsion tests, the shaded area represent the zone of unstable flow as predicted by Eqn. 4.

3.3 Isothermal Forging Trials

The results obtained from the analysis of power efficiency dissipation map were validated by carrying out isothermal forging experiments on small samples, with the shape illustrated in Fig.4. One test was carried out at a strain rate corresponding to the maximum in efficiency (475°C, tool rate of 16 mm/s); a further experiment was carried out at the same strain rate, but at lower temperature (375°C). The microstructure at the six different locations reported in Fig. 4 was investigated by means of light microscopy. Fig.5

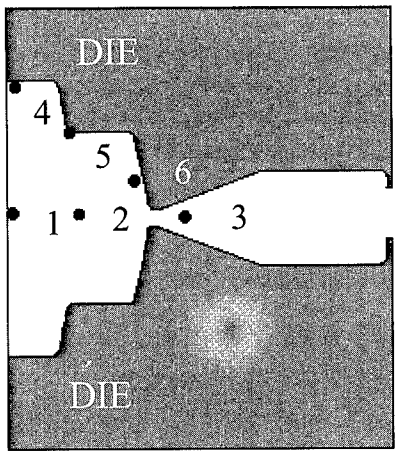

Fig.4. Schematic representation of the die geometry selected for isothermal forging experiments; the microstructure of the deformed samples was investigated in 6 different locations.

shows a typical example of the microstructure of the two samples; in particular, in both cases the high strain experienced in that region of the sample results in de-cohesion at the particle-matrix interface and in reinforcement fracture. Comparison between Fig.5a and b, however, confirms that fracture of reinforcing particles is more extensive in the sample deformed at low temperature.

3.4 Superplastic forming

The superplastic behaviour of the alloy was investigated out by means of uniaxial tensile tests. Fig.6 shows the effect of temperature on elongation-to-failure of the present composite, at an initial strain rate of $1 \cdot 10^{-1}$ s^{-1}. The elongations to failure were equal to or greater than about 200% in the temperature range between 550 and 580 °C, while decreased both at lower and higher temperatures, reaching a minimum value of about 130 % at 590 °C. At this strain rate, the composite exhibited a maximum elongation to failure of 370% at a temperature of 560 °C.

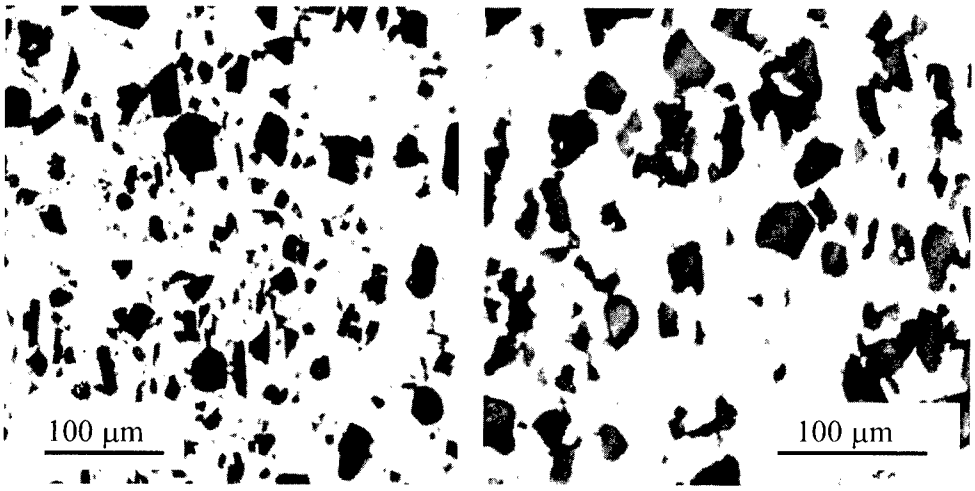

a) b)

Fig.5 Microstructure of the isothermally forged samples (location 3); a) 375°C, 16 mm/s; b) 450°C, 16 mm/s.

It should be noted that this temperature is very close to the temperature value at which the melting of the composite starts, as shown by DTA analyses.
The effect of temperature on elongation-to-failure at the initial strain rate of $1 \cdot 10^{-1}$ s^{-1} is shown in the Fig.6 a), while the effect of the initial strain rate in elongation to failure at the optimum superplastic temperature of 560 °C, is shown in Fig.6 b). It can be seen that also strain rate, as temperature, significantly influences the superplastic behaviour of the composite. The maximum elongation to failure, at the optimum superplastic temperature of 560°C, was measured in the specimen tested at $1 \cdot 10^{-1}$ s^{-1}. Lower elongations to failure, instead, were measured both at lower and higher strain rates, equal to 130 % at $5 \cdot 10^{-2}$ s^{-1} and 250% at $3.8 \cdot 10^{-1}$, respectively. These strain rate values are significantly higher than those generally observed in superplastic materials (ranging from 10^{-3} to 10^{-4} s^{-1}), and they indicate that the PM 6013/SiC/20_p composite exhibits high strain rate superplasticity. This optimum

superplastic strain-rate range may be attributed both to the fine grain size of the composite and, as reported in other studies, to the small amount of liquid phase existing at the interfaces, at the optimum superplastic temperature. As previously mentioned, in fact, this temperature is very close to the temperature at which melting begins; over this temperature, instead, superplastic flow gradually disappears, due to an increased amount of liquid phase, that favours an intergranular fracture.

A typical SEM micrograph of the fracture surface of specimen tested at the optimum superplastic conditions (560 °C, $1 \cdot 10^{-1} s^{-1}$) is shown in Fig.7. Typical filaments (that were also called "whiskers" or "fibres") can be clearly seen; they are, generally, as fine as 1 μm and more than 20 μm long.

Their formation in superplastic materials is frequently reported and it is generally thought as the evidence of the existence of a liquid phase, present at the grain boundaries or at the matrix/reinforcement interfaces, during the deformation [14,15]. This suggests that, also for the PM 6013/SiC_p composite used in this study, the presence of a liquid phase could play an important role as an accommodation helper mechanism for superplasticity.

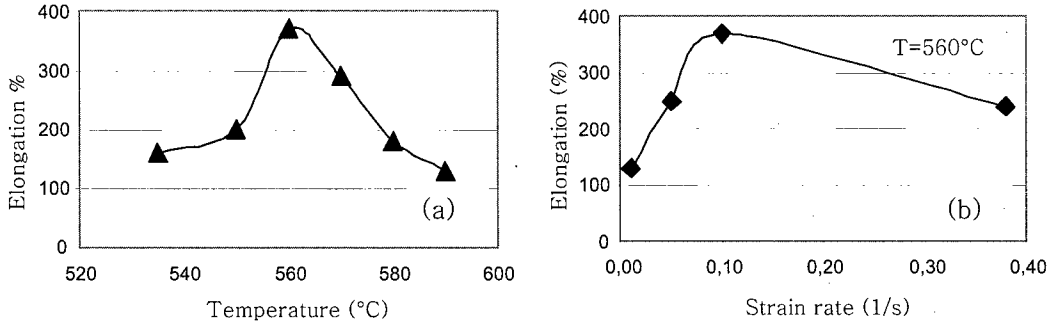

Fig. 6. The elongation to failure as a function of : (a) testing temperature, initial strain rate of $1 \cdot 10^{-1}$ s^{-1}, (b) initial strain rates at optimum superplastic temperature of 560°C.

Fig. 7 – SEM micrograph of the fracture surface of the PM 6013/SiC_p composite tested at 560 °C with an initial strain rate of $1 \cdot 10^{-1} s^{-1}$.

4. CONCLUSIONS

The aim of the present research was to evaluate the use of net-shape, hot forming technologies for production of low cost component in MMCs to be used in transportation systems. The plastic behaviour of 6061/Al_2O_3/20p has been studied in a large range of strain rates and temperatures in order to define the constitutive parameters and create the processing and stability maps. Forging trials have been performed in working conditions included in the safe region of the map; the forged parts have shown no macro or micro scale defects. The superplastic behaviour of PM 6013/SiC/20p has been investigated and the proper temperatures and strain rates that gave the maximum elongation to fracture, have been assessed. The maximum elongation of 375% resulted at 560°C, when the composite started to melt, and at strain rate of 0.1/s that was the same used for industrial forging. Such results are considered the starting point for a motorcycle brake drum production in MMCs via isothermal forging and superplastic forming.

AKNOWLEDGEMENTS

The research was supported by CNR, Progetto Finalizzato Materiali Avanzati / Materiali Compositi per applicazioni Strutturali and Ministry of University and Scientific research.

REFERENCES

1. A.M.DeSanctis, E.Evangelista, A.Forcellese, A.Fuganti, Metallurgical Sci. Techn. Vol.14 (1996), pp.13-19.
2. M.Mabuchi. K.Higashi, Key Eng.Mat. Vols 104-107 (1995), pp 225-240
3. M.Mabuchi, H.Iwasaki, K.Higashi, Acta Mat. Vol.46(1998), pp.5335-5343.
4. G.L. McWay, E.L.Countright, R.H,Jones and M.T,Smith, Light Metal Age, October 1998, pp.6-11.
5. D. J. Lloyd, Int.Mat.Rew, Vol.39(1994), pp.1-23.
6. S.M.Roberts, P.J.Withers, S.I.Barnes, P.B.Pragnell, in Numerical Predictions of Deformation Processes and the Behaviour of Real Materials. S.I.Andersen et al. eds. Riso National laboratory, Roskilde, Dk, 1994, pp. 505-510.
7. W.J.Kim, S.H.Hong, J.H.Lee, Mat. Sci. & Eng. Vol. A298 (2001), pp.166-173.
8. K.Higashi, Mat. Sci & Techn., Vol.16, (2000),pp.1320-1329.
9. Hot Working Guide, Y.V.R.K.Prasad and S.Sasidhara editors. ASM International, 1999.
10. G.E.Dieter, in Metals Handbook, ASM, Metals Park, Ohio, Vol.14, 1988.
11. J.C.Malas, V.Seetharaman, JOM, June 1992, pp.8-13.
12. S.V.S.Narayana Murthy, B.Nageswara Rao, Metall.Trans.Vol.28A (1977) pp.2170-2183.
13. Y.V.R.K.Prasad, Indian Jour.Tech. Vol.28,(1990), pp.435-445.
14. W.D.Cao, X.P.Lu, H.Conrad, Acta Mat., Vol.44 (1996), p.697-706.
15. M.G.Zelin, Acta Mat., Vol.45 (1997), p.3533-3542.

AN ANLAYSIS OF GAS PRESSURE FORMING OF SUPERPLASTIC AL 5083 ALLOY

C.K. Syn, M.J. O'Brien*, D.R. Lesuer, and O.D. Sherby**

Lawrence Livermore National Laboratory, Livermore, CA 94551, USA
* Now at The Aerospace Corp., Los Angeles CA 90009, USA
** Stanford University, Dep't of Mat'ls Science and Eng., Stanford CA 94305, USA

ABSTRACT

Al 5083 disks of superplastic forming grade were gas-pressure formed into hemispheres and cones at constant forming pressures with and without back pressure. The forming operation was performed using an in-house designed and built biaxial forming apparatus. The temporal change of dome heights of the hemispheres and cones were measured for the different forming and back pressures applied. The flow stresses and strain rates developed at the top of the dome during the forming step were shown to closely follow the flow stress – strain rate relationship obtained from the strain rate change tests performed at the same temperature using uniaxial tensile samples.

1. INTRODUCTION

Recent interest in lightweight and inexpensive alloys for transportation sytems has attracted attention to aluminum - magnesium alloys. Al 5083 alloy, because of its good weldability, reasonably high corrosion resistance and high strength with reasonable ductility, has been an alloy of choice for these applications. The large ductility required in forming engineering parts with contoured geometry has led to the development of a superplastic grade of the alloy [1-4]. Deformation behavior and microstructural evolution of superplastic Al 5083 has been extensively investigated for tensile deformation [1-8] and the deformation behavior has been modeled for uniaxial tension tests [6, 8] and biaxial forming of rectangular pans [7, 8]. The purpose of the present study is to investigate the deformation behavior during equi-biaxial forming of a commercial superplastic Al 5083 alloy using hemispherical and conical dies.

2. EXPERIMENTAL AND ANALYSIS PROCEDURES

2.1 Material

High-purity superplastic forming (SPF) grade Al 5083-O alloy (Sky Aluminum's Alnovi-1) sheets of nominal 2.5 mm thickness were used in this study. The supplier's composition is compared in Table 1 with that of standard non-SPF grade. The room temperature tensile properties of 297 MPa tensile strength, 145 MPa yield strength, and 20% elongation were claimed by the supplier of the SPF grade material.

Table 1. Composition (in wt. %) of the SPF 5083 alloy used and the standard 5083 alloy

	Si	Fe	Cu	Mn	Mg	Cr	Zn	Ti	Al
Std 5083	0.4 Max	0.4 Max	0.1 Max	0.4-1.0	4.0-4.9	0.05-0.2	0.25Max	0.15 Max	Bal.
Alnovi-1 SPF 5083	0.05	0.05	Tr.	0.69	4.58	0.12	Tr.	0.01	Bal.

2.2 Uniaxial Tensile Tests

The SPF grade material was characterized first with uniaxial tensile tests at elevated temperatures in argon gas atmosphere by strain rate jump tests and constant strain-rate tests to failure. A typical strain-rate change test employed nine different true strain rates from the lowest strain rate of $1x10^{-4}$ s^{-1} through $3x10^{-4}$, $5x10^{-4}$, $1x10^{-3}$, $2x10^{-3}$, $3.5x10^{-3}$, $6x10^{-3}$, $1x10^{-2}$ s^{-1} to the highest strain rate of $2x10^{-2}$ s^{-1}. If the specimen did not fail at the highest strain-rate, several cycles of the nine strain rates were repeated until it failed as shown in Fig. 1. The strain rate jump tests used were also described elsewhere [9].

2.3 Biaxial Gas-Pressure Forming Tests

The forming apparatus for these tests mainly consisted [10], of i) forming die assembly, see Fig. 2, ii) loading mechanism to provide the support for the die assembly and the compressive force to keep the dies closed, iii) heating furnace around the die assembly, iv) pressure control panel which delivers argon gas to the die assembly, and v) data acqusition system for recording forming pressure, back pressure, dome height of the specimen being formed, and temperature history.

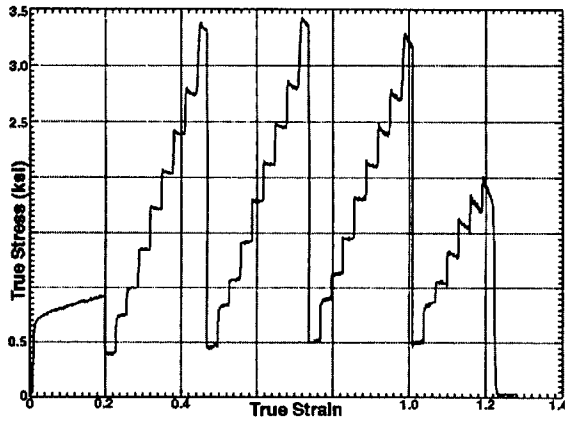

Fig. 1. Example of strain rate change tests. After the initial strain of 0.2 at $5x10^{-4}$ s^{-1}, the strain rate was changed step by step from $1x10^{-4}$ s^{-1} to $2x10^{-2}$ s^{-1}, and the cycle was repeated until the specimen failed.

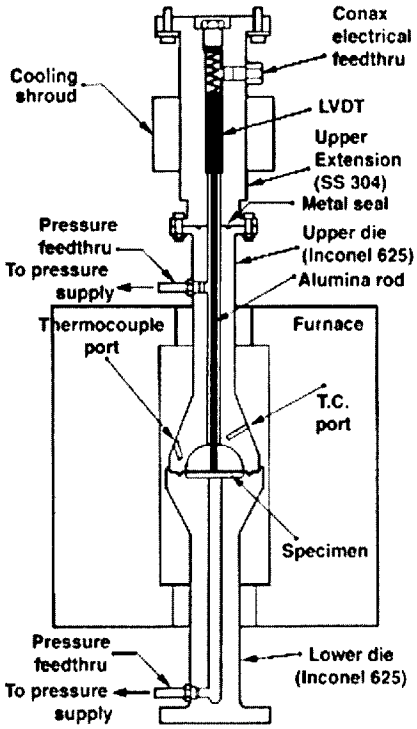

Fig. 2. Die assembly of the superplastic forming apparatus using gas pressure

The die assembly shown in Fig. 2 comprised of three major components: upper die, lower die, and upper extension. The upper and lower dies were made of Inconel 625 alloy. The upper extension componen, made of stainless steel 304, houses a linear voltage displacement transducer (LVDT). The tip of the LVDT is connected to a thin hollow alumina rod that is in contact with the test specimen. When the specimen bulges up, the alumina rod is pushed up and its displacement is mesaured by the LVDT. The specimen temperature is monitored through two thermocouples placed in the upper die T.C. ports. Forming pressure is provided by pressurizing the lower die below the specimen. The upper extension is pressurized when back pressure is used. The upper die cavity determines the shape of the formed parts. Two cavity designs, hemisperical and conical, were used. The diameter of the hemispherical and conical dies was 50 mm. The apex angle, α, of the conical die was 42.46•.

Some of the specimens were gridded with a square array of touching circles of 2.5 mm diameter. Prior to forming, both sides of the specimen were sprayed with boron nitride powder as a releasing compound. The dies were preheated to the forming temperature. Once the die temperature equilibrated, the furnace was opened and the specimen was inserted in the lower die. This procedure minimized possible static grain growth in the material. The specimen dimensions were 78.7 mm diameter and 2.5 mm thick. When the specimen stabilized at the forming temperature, usually within 5 minutes, a clamping force up to 1360 kg was applied at about 225 kg/min to form the pressure seal. When back pressure was used, argon gas was admitted into both the upper and lower dies and an equal gas pressure was initially applied. The specimen started to form once the gas pressure began to increase in the lower die. A forming operation was terminated either when the predetermined dome height was reached or when the forming pressure started to drop rapidly because of gas leak through tears developed in the specimen.

2.4 Data Analysis

For analysis of the superplastic forming behavior, the disk specimens were assumed to bulge to spherical membranes of uniform thickness. An applied pressure, P, in a hemispherical die of radius R_o would deform a disk specimen of the initial thickness t_o into a spherical membrane of radius, ρ. The membrane would thin to a uniform thickness, t, as shown schematically in Fig. 3. By measuring the dome height H_D of the membrane, and assuming the volume constancy of the material, one can calculate the radius ρ, thickness t, strain ε, strain rate $\dot{\varepsilon}$, and shell stress σ, of the membrane at the pole using the following equations.

$$\rho = (R_o^2 + H_D^2)/2H_D \quad (1), \qquad t = R_o^2 \cdot t_o/(2\rho \cdot H_D) \quad (2),$$

$$\varepsilon = \ln (t / t_o) \quad (3), \qquad \dot{\varepsilon} = - \dot{H}_D/\rho \quad (4),$$

$$\sigma = P \cdot \rho/2t \quad (5),$$

where $\dot{H}_D$ is the temporal change rate of the dome height.

For the analysis of forming behavior in the conical die, as shown in Fig. 4, Eqs. (1) to (5) can be used until the membrane touches the internal surface of the cone. Once the bulging membrane contacts the cone internal surface, the material in contact was assumed to stick to the die, but in the crown (uncontacted) region it was assumed to continue bulging spherically and thinning uniformly, as proposed by Ghosh and Hamilton [11]. Adopting the relationship between the thickness and meridional strain derived by Ghosh and Hamilton to the present cone geometry with the apex angle $\alpha = 42.46°$, the radius and thickness of the crown region were found given by the following equations.

$$\rho = 1.1538 - 0.5479 \cdot H_D \quad (6), \qquad t = t_c \cdot (\rho/\rho_c)^{1.8250} \quad (7),$$

where H_D is the dome height of the crown region measured from the surface of initial unbulged specimen, while t_c and ρ_c are the thickness and radius of the membrane at the initial contact. Once the radius and thickness of the crown region are determined, the strain, strain rate, and stress can be calculated using Eqs. (3) to (5).

3. RESULTS AND DISCUSSIONS

The results of forming tests using hemisperical and conical dies run at 520°C and the uniaxial tensile tests performed at the same temperature are described in this report.

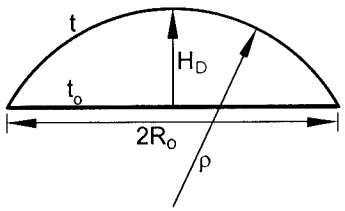

Fig. 3. Spherical membrane geometry assumed in stress analysis of the gas-pressure formed in hemispherical die.

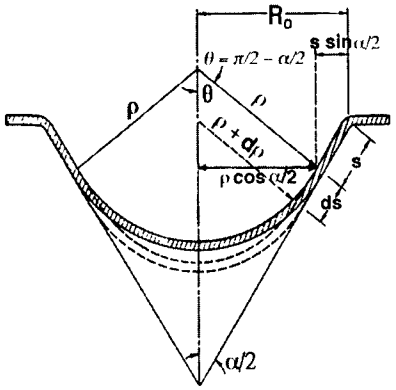

Fig. 4. Stress analysis for the gas-pressure forming in conical die. Spherical membrane geometry assumed after the membrane touches the inner wall of the conical die.

3.1 Uniaxial Tensile Stress - Strain-Rate Relationship

The uniaxial tensile strain-rate jump tests were performed at 520°C. Fig. 5 shows the tensile flow stress - strain-rate curves for the first and third cycles of strain-rates used in the test. At strain rates less than 5 x 10^{-4} s^{-1}, the material shows a strain-rate sensitivity of m=0.5 indicating deformation by a grain boundary sliding mechanism. At higher strain rates, the sensitivity decreases indicating a gradual transition to different deformation mechanisms.

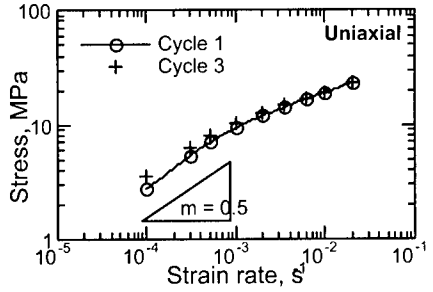

Fig. 5 Stress - strain-rate curve obtained from uniaxial tensile strain-rate jump tests

3.2 Gas-Pressure Forming Behavior

Forming tests with the dies were also performed at 520°C. Each specimen was formed at a constant pressure by rapidly increasing the pressure to a prescribed level. At low pressures, deformation of the specimen during the pressure rise was negligible, while for high forming pressures, it was not negligible. Fig. 6 illustrates examples of forming pressure profiles used in hemisperical die forming. Fig.7 illustrates examples of conical die forming with application of back pressure where P_F and P_B represent the pressures in the lower and upper die respectively, and ΔP represents the net forming pressure. Figs. 8 and 9 show the corresponding dome height profiles measured under the applied forming pressures shown in in Figs. 6 and 7 respectively. Fig. 9 also includes the dome height profiles of three other specimens (#11, #14, and #15) which were formed at 0.86, 1.6, and 0.58 MPa respectively in addition to the specimens represented in Fig. 7. One can see from Figs. 8 and 9 that the level of dome height achieved is higher for the specimens formed in the conical die and highest in the specimens formed with back pressure. It can be seen also that the rates of dome height change (dH_D/dt) are faster for specimens formed at higher pressure levels. Figs. 10 and 11 show the calculated shell stresses using Eq. (5) plotted against the dome heights measured for both sets of specimens formed in hemispherical and conical dies. Both in hemispherical and conical die forming, specimens seem to have formed at rather stable or

roughly constant stress levels for the dome height range of 8 mm to 22 mm, although the stress increases gradually as the dome height increases. The stress rises faster and higher under the higher forming pressure.

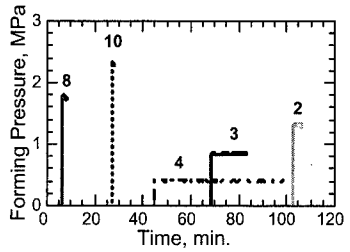

Fig. 6. Pressure profiles used in hemispherical die forming. Labels on the curves represent specimen numbers

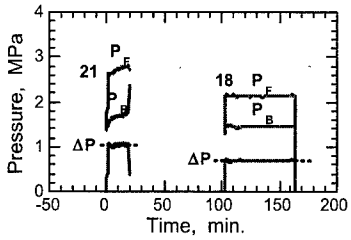

Fig. 7. Pressure profiles used in conical die forming with back pressure. P_F, P_B and ΔP represent the forming, back, and net pressures.

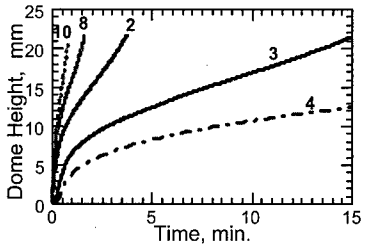

Fig. 8. Dome height profiles for hemispherical-die formed specimens using pressure profiles shown in Fig. 6.

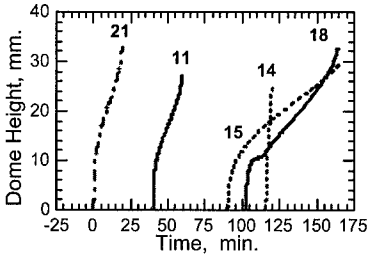

Fig. 9. Dome height measured for specimens represented in Fig. 7 and other specimens formed without back pressure.

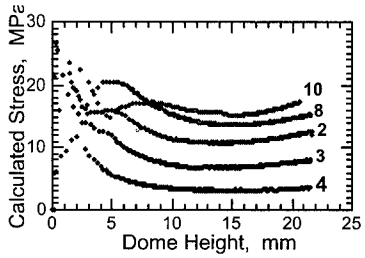

Fig. 10. Calculated shell stress - dome height curves for hemispherical die formed specimens shown in Fig. 8.

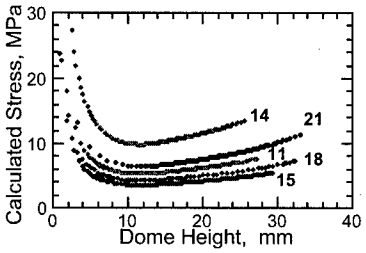

Fig. 11. Calculated shell stress - dome height curves for conical die formed specimens represented in Fig. 9.

Figs. 12 and 13 illustrate the effective stress - effective strain-rate relationships obtained in both sets of forming tests. The stresses and strain rates calculated for the dome heights greater than 5 mm were plotted and compared with the results of the uniaxial tensile tests shown in Fig. 5. The calculated stresses are shown as blobs of datapoints in Figs. 12 and 13. For specimens (# 4, 3, 2 and 15) formed at low forming pressures, the forming characteristics coincide with the uniaxial tensile plastic behavior, while at the higher forming pressure, specimens (#10, 8, and 14) exhibit lower stresses than the uniaxial tensile stresses.

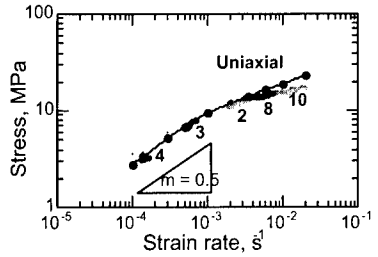

Fig. 12. Stress - strain-rate relationships for specimens formed in the hemispherical die compared with the uniaxial test results

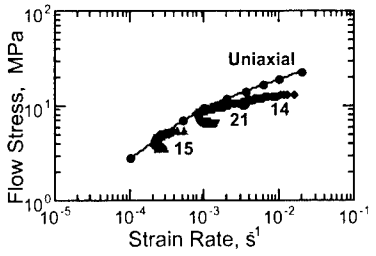

Fig. 13. Stress - strain-rate relationships for specimens formed in the conical die compared with the uniaxial test results

4. CONCLUDING REMARKS

Gas pressure forming of SPF grade Al 5083 into hemi-spherical and conical dies was performed at 520°C and variable or constant gas pressures with or without back pressure. The effective stress – effective strain-rate relationship was close to the uniaxial tensile stress – strain-rate relation. Additional metallographic investigations of the tested specimens and modeling by finite element method (FEM) were performed. Findings include: (i) high volume fractions of cavitation measured in the dome areas; (ii) the thickness at the peak of dome predicted from Eq. (2) or (7) is close to the measured thickness; (iii) FEM modeling using the NIKE 2D code closely simulates the thinning behavior of the material during forming. The additional findings will be examined further in a future report.

ACKNOWLEDGEMENT

This work was performed under the auspices of the United States Department of Energy by the Lawrence Livermore National laboratory under Contract No. W-7405-ENG-48.

REFERENCES

1. H. Iwasaki et al., in Superplasticity in Advanced Materials, S. Hori, M. Tokizane and N. Furushiro, eds., Japan Society for Research on Superplasticity (1991), pp. 447-452.
2. H. Imamura and N. Ridley, ibid, pp. 453-458.
3. J.S. Vetrano et al., in "Superplastic Behavior in a Commercial 5083 Aluminum Alloy", Scripta Metall. Mater., 30 (1994), pp. 565-570.
4. R. Verma, A.K. Ghosh, S. Kim and C. Kim, Mat. Sci. Eng. A191 (1995), pp. 143-150.
5. R. Verma et al, Metall. Mater Trans. A, 27A (1996), pp. 1889-1898.
6. P.A. Friedman and A.K. Ghosh, ibid, pp. 3827-3839.
7. R. Verma et al., J. Mat'ls Eng. Performance, 4 (1995), pp. 543-550.
8. M.A. Khaleel et al., Int'l J. Plasticity, 14 (1998), pp. 1133-1154.
9. Lesuer et al,. in Superplasticity in Advanced Materials, S. Hori, M. Tokizane and N. Furushiro, eds., Japan Society for Research on Superplasticity (1991), pp. 139-144.
10. S.L. Stoner et al., LLNL Report UCRL-JC-118229 (1994).
11. A.K. Ghosh and C.H. Hamilton, Metall. Trans. A, 11A (1980), pp. 1915-1918.

HOT FORMING RELATED PROPERTIES OF Al 6061/Al_2O_3 AND Al 2618/Al_2O_3 COMPOSITES

M. Vedani, E. Gariboldi

Politecnico di Milano, Dipartimento di Meccanica
Piazza Leonardo da Vinci 32, I-20133 Milano, Italy

ABSTRACT

The hot tensile deformation behaviour of the 6061/Al_2O_3, 2618/Al_2O_3 and 2618/SiC particulate reinforced composites was investigated over a range of temperatures and strain rates. A unreinforced 6061 monolithic alloy was also considered for comparison purposes. The composite materials exhibited a similar hot working behaviour with anticipated onset of matrix restoration mechanisms as a function of temperature with respect to the unreinforced alloy. Microstructural analyses on broken specimens allowed to observe reinforcement damage and matrix evolution during hot deformation.

1. INTRODUCTION

Discontinuously reinforced metal matrix composites (MMC's), especially aluminium based particulate reinforced composites, have emerged as a new class of advanced materials having attractive combination of mechanical properties (enhanced stiffness, isotropic behaviour), physical properties (low coefficient of thermal expansion, low density) and wear resistance.
Their isotropic properties make them amenable to most conventional metalworking processes such as rolling, extrusion, forging [1]. Owing to limited plasticity at room temperature, particulate reinforced MMC's are more suited to processing at elevated temperature. In such condition the enhanced matrix plasticity prevents localisation of stresses around particles to build up, thus reducing the extent of particle damage by cracking or interface decohesion.
Despite the similarities to unreinforced monolithic alloys, standard processing parameters of the matrix cannot be directly adopted for the corresponding particulate reinforced composite and hence, the forming temperatures and strain rates have to be optimised for each specific composite system. Research in this field is indeed very active as demonstrated by the number of papers recently published on hot deformation behaviour [2-5], efficiency and instability maps [6-11], microstructure and microstructural damage [12-17] during elevated temperature plastic strain of Al-based MMC's.
The present investigation is aimed at focussing on hot deformation under tensile conditions of three particulate reinforced composites and a monolithic unreinforced alloy. Analysis of data obtained at four different testing temperatures and three strain rates allowed to state general trends for high temperature mechanical behaviour of composites and to comment on variations existing amongst materials differing in their reinforcement type or matrix composition.

2. MATERIALS AND EXPERIMENTAL PROCEDURES

Four different materials were considered to investigate hot formability of MMC's. A 6061/20%Al_2O_3 particulate reinforced composite and the corresponding monolithic unreinforced 6061 alloy were selected to evaluate the effect reinforcement addition on high temperature behaviour of the matrix alloy. Further testing on a 2618/20%Al_2O_3 and a 2618/20%SiC particulate reinforced composite allowed to assess the effect of reinforcement type. Both materials were manufactured by the producer through a proprietary molten metal mixing process and supplied as extruded bars having a diameter of 80 mm.

After material heat treatment to T6 temper, cylindrical tensile specimens with a gauge length of 30 mm and a diameter of 6 mm were machined. Tensile tests were carried at 350, 400, 450 and 500°C at strain rates of $1 \cdot 10^{-3}$, $1 \cdot 10^{-2}$, $1 \cdot 10^{-1}$ s^{-1}. A soaking time of 30 minutes at testing temperature was maintained before pulling to fracture the specimens. From recorded data, true stress vs. true plastic strain plots were obtained and analysed to draw information on evolution of strength, flow stress, ductility and strain rate sensitivity of the different materials. In addition, microstructural analyses were performed by SEM and optical microscopy on longitudinally sectioned fractured specimens.

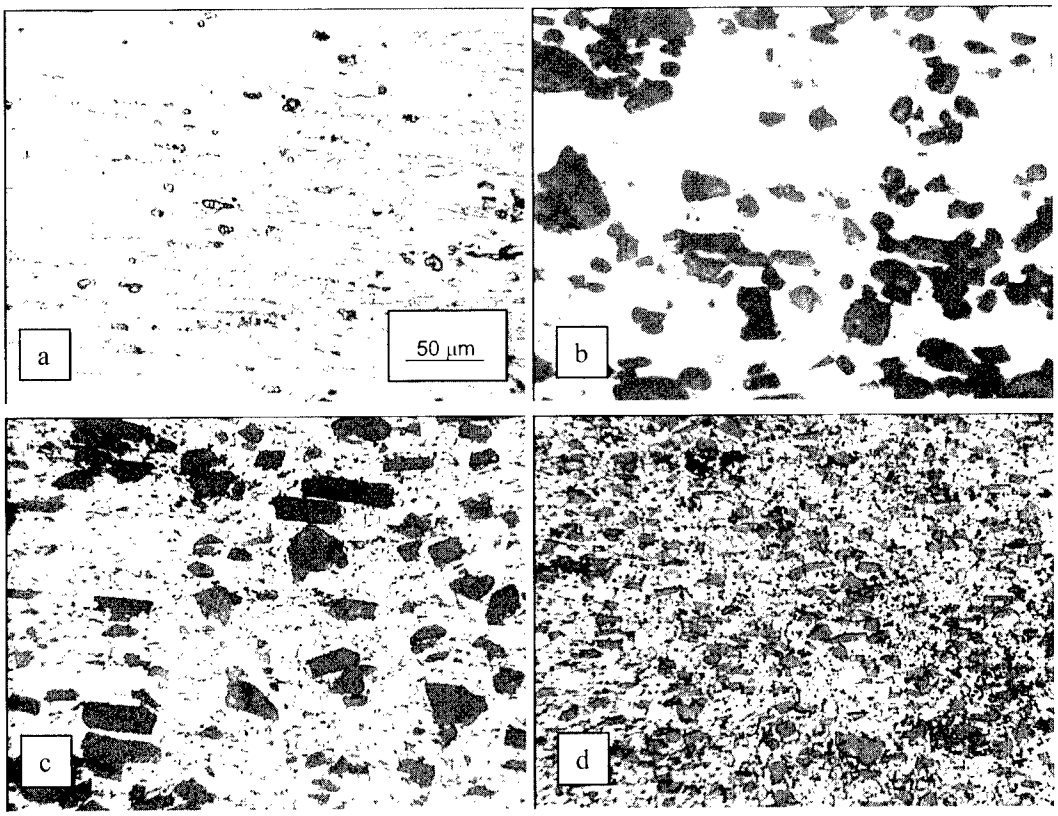

Fig.1. Representative optical micrographs of the materials investigated. (a) 6061 monolithic alloy, (b) 6061/20%Al_2O_3 composite, (c) 2618/20%Al_2O_3 composite, (d) 2618/20%SiC composite.

3. RESULTS AND DISCUSSION

Figure 1 summarises the materials microstructure after T6 heat treatment. In the unreinforced 6061 alloy, a fine structure of both equiaxed and elongated grains was observed. On the contrary, in the corresponding 6061/20%Al_2O_3 composite, the structure was made up of larger fully equiaxed grains. A much finer matrix grain structure was noticed in the 2618-alloy based composites. In these materials a fairly copious precipitation of phases rich in Fe-Ni-Cu-Si (as detected by EDS microanalyses) was noticed in the matrix.
The micrographs in figure 1 also demonstrate that the reinforcement size was larger for the Al_2O_3- than for the SiC-reinforced composites. The average particle size, measured along the major axis, was estimated to be 35 μm in the former case and 15 μm in the latter.

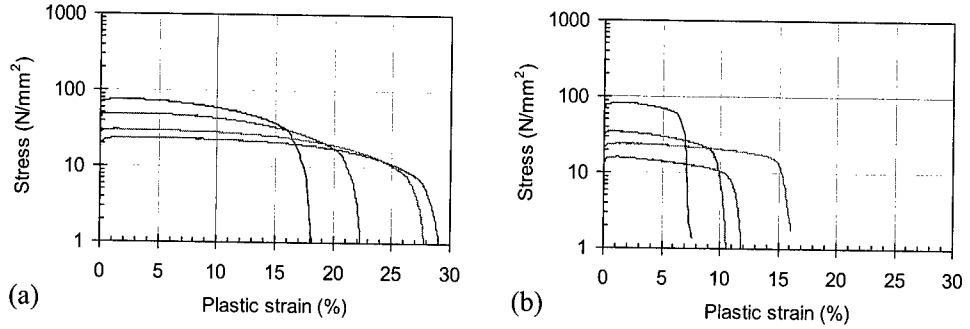

Fig.2. True stress vs. true plastic strain curves of the 6061 alloy (a) and of the 6061/20%Al_2O_3 composite (b) at a strain rate of $1 \cdot 10^{-2} s^{-1}$

The high-temperature stress-strain curves of the 6061 alloy and of the 6061/20%Al_2O_3 composite are depicted in figure 2 to discuss on the general behaviour of the materials under tensile strain condition. The curves refer to tests performed at decreasing temperatures, from the top to bottom: 350-400-450-500°C. In literature, data on hot forming behaviour are usually generated under compression or torsion testing in order to better simulate common hot working condition and retard material instability. Elongations greater than 50% are readily achieved also in MMC's and an almost constant flow stress regime is generally reached after a peak stress [8,12,14,15]. On the contrary, in tensile testing, necking soon occurs and composite damage is reported to develop more easily by ceramic particle cracking [16,18-20]. However, it must be considered that stress conditions having a tensile component during metalworking are often produced in shaping complex geometries. Therefore, apart from the fundamental research interest, investigations on high temperature tensile behaviour of MMC's are of great practical importance.
Despite the onset of necking in the specimens, the unreinforced 6061 alloy featured a fairly high ductility. On the contrary, for all the investigated composites, fracture occurred at relatively low plastic strain values. Data on tensile strength of the materials investigated are better visualised in figure 3, where the profiles of UTS are given as a function of test temperature and strain rate. In the examined temperature range, the unreinforced alloy showed a continuous and decreasing trend of UTS with increasing temperature. In the composites, at temperatures exceeding 400°C, a substantial plateau of the UTS values was noticed for the slowest strain rate investigated. Such trend was supposed to be related to the anticipated activation of restoration mechanisms in the composite matrices during hot deformation. In literature, depending on composite and testing conditions investigated and authors

interpretation, either dynamic recrystallisation (DRX) or dynamic recovery were proposed as active mechanisms. It is also well established that reinforcement addition decreases the critical strain for DRX due to increased dislocation generation during hot deformation, thus anticipating the onset of dynamic restoration regime with respect to the unreinforced monolithic alloy [14].

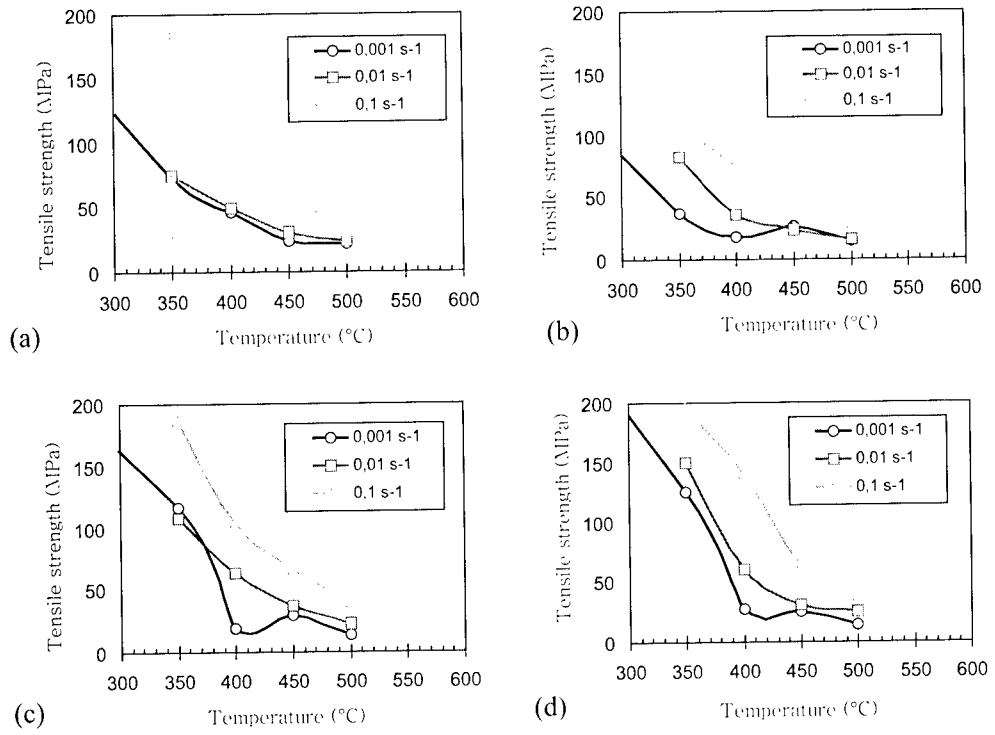

Fig.3. Evolution of ultimate tensile strength as a function of temperature and strain rate for the materials investigated. (a) 6061 monolithic alloy, (b) 6061/20%Al_2O_3 composite, (c) 2618/20%Al_2O_3 composite, (d) 2618/20%SiC composite

As expected, a increase in strain rate produced a shift toward higher stress values of the curves and reduced possibility of structure restoration. The above mentioned plateau at temperatures higher than 400°C became less evident at the strain rate of $1 \cdot 10^{-2}$ s^{-1} and completely absent at the highest strain rate level.

Finally, it is worth emphasising that, apart from slight differences probably related to experimental data scatter, the two 2618 alloy based composites had a substantially identical tensile behaviour thus confirming that, at high temperatures, the reinforcement strengthening effects are of little significance and even lower importance can be addressed to small differences in reinforcement distribution and size.

In figure 4, data on tensile ductility of the 2618/20%SiC and 2618/20%Al_2O_3 composites are given as a function of temperature and strain rate. The comparison is proposed to discuss on the effects of reinforcement type and size. It can be observed that the composite with finer particles (SiC) experienced a clear improvement in tensile ductility with increased testing temperatures. On the contrary, in the Al_2O_3 reinforced material, the ductility remained at low levels even at the highest temperature investigated.

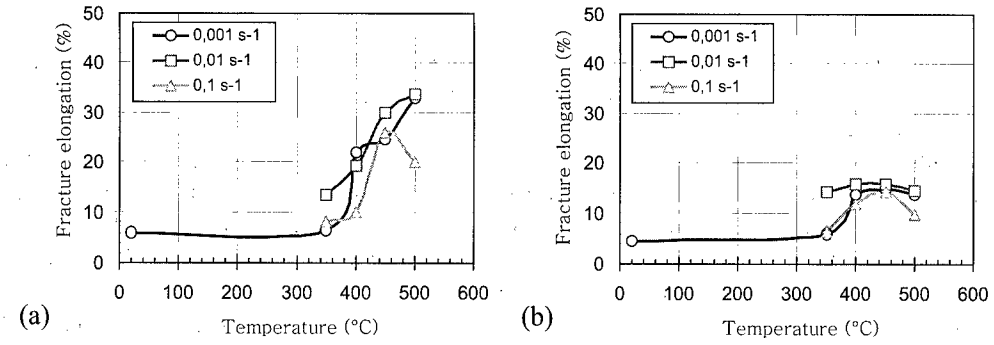

Fig.4. Evolution of tensile ductility as a function of temperature and of strain rate for the (a) 2618/20%SiC and (b) 2618/20%Al_2O_3 composites

Interpretation of the above data were supported by microstructural observations carried out on longitudinally sectioned broken specimens. Figure 5 shows typical micrographs taken close to fracture surface of the 2618/SiC composite. Limited damage associated to ceramic particles is visible in figure 5a, referring to an as polished sample observed by SEM. Ductile voids originated either by decohesion of particle-matrix interfaces or by fracture of the coarser and more elongated particles. No predominant failure mechanism as a function of material or testing conditions was identified from micrographs and analyses of the fracture surfaces. Figure 5b is an optical micrograph of an etched samples showing that the deformed structure featured well recrystallised fine equiaxed grains. Again, this behaviour was observed in all of the composites investigated at the testing temperature of 500°C. Further work is currently in progress to elucidate the grain structure modification at lower deformation temperatures..

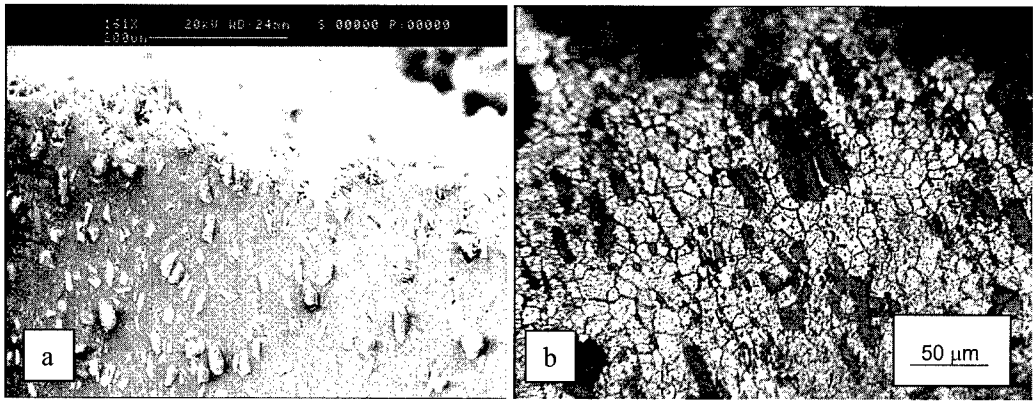

Fig. 5. Micrographs of sectioned specimens of the 2618/SiC composite strained at 350°C, $1 \cdot 10^{-3} s^{-1}$ (a) and of the 2618/Al_2O_3 composite strained at 500°C, $1 \cdot 10^{-3} s^{-1}$ (b)

4. CONCLUSIONS

The hot tensile deformation behaviour of the 6061/Al_2O_3, 2618/Al_2O_3 and 2618/SiC particulate reinforced composites and of the unreinforced 6061 monolithic alloy was investigated over a range of temperatures and strain rates.

The data allowed to state differences with the unreinforced alloy and similarities amongst the hot deformation behaviour of the three composites. In the composites, the action of dynamic recrystallisation mechanisms inducing an abrupt decrease of the flow stress was observed, at the lowest strain rate, at temperatures exceeding 400°C whereas the monolithic alloy featured a significantly higher strength at this testing temperature.

The high temperature strength of the composites was ruled by matrix properties, the 6061 alloy matrix being softer than the 2618 one, as expected. The two 2618-based composites showed a substantially identical behaviour as a function of temperature and strain rate. The only difference was observed in tensile ductility whereby the composite reinforced with the coarser Al_2O_3 particles revealed to be more brittle than the 2618/SiC material, especially at the highest testing temperatures.

REFERENCES

1. T.F. Klimowicz. J.O.M., 46, 11 (1994) pp.49-53
2. M. Ferry, P.R. Munroe. Mater. Sci. Techn., 11, 7 (1995) pp.633-640
3. M.S. Yeh, W.P. Weng, S.C. Wang, T.H. Chuang. Metall. Mater. Trans., 31A, 4 (2000) pp.1310- 1313
4. B.L. Zhang, M.S. Maclean, T.N. Baker. Mater. Sci. Techn., 16, 7-8 (2000) pp.897-902
5. W.J. Kim, Y.S. Lee, S.J. Moon, S.H. Hong. Mater. Sci. Techn., 16, 6 (2000) pp.675-680
6. B.V. Radhakrishna Bhat, Y.R. Mahajan, H. Md. Roshan, Y.V.R.K. Prasad. Mater. Sci. Techn., 11, 2 (1995) pp.167-172
7. S.V.S. Narayana Murty, B. Nageswara Rao. J. Phys. D: Appl. Phys., 31 (1998) pp.3306-3311
8. B.V. Radhakrishna Bhat, Y.R. Mahajan, Y.V.R.K. Prasad. Matell. Mater. Trans., 31A, 3 (2000) pp.629-639
9. S.V.S. Narayana Murty, B. Nageswara Rao, B.P. Kashyap. Adv. Composites Lett., 9, 2 (2000) pp.147-151
10. Y.V.R.K. Prasad, S. Sasidhara. Hot Working Guide – A Compendium of Processing Maps, ASM Int. Publ. (1997)
11. E. Evangelista, S. Spigarelli, P. Cavaliere. Proc. Nat. Conf. AIM, Milan (2000) pp. 935-943
12. M. Ferry, P.R. Munroe. Mater. Sci. Techn., 11, 8 (1995) pp.734-740
13. X. Xia, P. Sakaris, H.J. McQueen. Mater. Sci. Techn., 10, 6 (1994) pp.487-496
14. B.-C. Ko, G.-S. Prk, Y.-C. Yoo. J. Mater. Proc. Techn., 95 (1999) pp.210-215
15. H. Xu, E.J. Palmiere. Mater. Sci. Forum, vols. 217-222, 2 (1996) pp.1091-1096
16. B.Y. Zong, B. Derby. J. Mater. Sci., 31 (1996) pp.297-303
17. C.M. Styles, I. Sinclair, P.J. Gregson, S.M. Flitcroft. Mater. Sci. Techn., 10, 6 (1994) pp.475-480
18. J.R. Brockenbrough, F.W. Zok. Acta Metall. Mater., 43, 1 (1995) pp.11-20
19. M.T. Kiser, F.W. Zok, D.S. Wilkinson. Acta Mater., 9 (1996) pp.3465-3476
20. J. Llorca, P. Poza. Mater. Sci. Engng., A185 (1994) pp.25-37

PARTICLE WEAKENGING IN HIGH-STRAIN-RATE SUPERPLASTIC POWDER-METALLURGY PROCESSED 2124 AND 6061 ALUMINUM COMPOSITES

W. J. Kim* and K. B. Kim**

*Dept. of Metallurgy and Materials Science Eng. Hong-ik University
72-1 Mapo-ku, Sangsu-dong 121-791, Korea
**Dept. of materials Eng. Hang-kong University
200-1 kyunggi-do, koyang-shi, hwajon-dong 421-791, Korea

ABSTRACT

High-strain-rate superplastic behaviors of powder-metallurgy processed 2124 and 6061 Al alloys, and SiC/2124 Al and SiC/6061 Al composites reinforced by SiC particulate were studied over a wide temperature and strain rate ranges. The matrix alloys and composites showed large tensile elongations above $10^{-2}s^{-1}$. The strengths of both composites are unexpectedly lower than that of the Al matrix alloys in the temperature range where grain boundary sliding dominates the plastic flow. Their difference in strength is also temperature dependent, increasing with increase in temperature. Abnormally high activation energy for plastic flow, being considerably higher than those for the matrix alloys, is another important feature of the composites. High-resolution transmission electron microscopy indicates that solutes such as Mg and Si strongly segregate at interfaces between SiC and Al matrix. Particle weakening, possibly with some liquid formation at the interfaces, is discussed qualitatively and partially quantitatively by adapting the concept of effective diffusivity considering mass flow through liquid phase formed at interfaces between reinforcement and Al matrix.

1. Introduction

A number of experimental data for high-strain-rate superplastic (HSRS) aluminum matrix composites reinforced by Si_3N_4 particulates or whiskers fabricated through either powder-metallurgy (PM) or mechanical alloying process are now available [1-11]. As the HSRS behavior of these composites has been often observed near the onset temperature for partial melting, it is believed that a proper amount of liquid phase is needed for superplasticity in aluminum matrix composites [12,13]. Microstructures of aluminum composites reinforced with Si_3N_4 whiskers or particles have been studied by using transmission electron micrography (TEM) and high resolution TEM (HRTEM) [14-16], and the melting of solute-rich reaction phases at interfaces between Si_3N_4 and Al matrix was claimed to cause the partial melting.

The relationship between partial melting and HSRS behavior, the effect of reinforcement on the superplastic-flow, and interface microstructure and solute segregation behavior in the HSRS SiC reinforced aluminum composite, on the other hand, have never been studied in detail. It is the purpose of the present study to investigate these in the SiC/2124 Al and SiC/6061 Al composites.

2. Experimental procedures

The materials in the present investigation were fabricated by powder-metallurgy processing. Commercial 2124 Al and 6061 Al powders with an average diameter less than 20μm, and α-SiC particulates having a diameter of 3μm was used. The aluminum and SiC powders were mechanically stirred, ultrasonically mixed in an alcoholic solvent and then dried in air. The mixed powders were consolidated at 570°C in a vacuum hot press with a pressure of 90MPa for 0.2 hour. The consolidated billet was then extruded by 70:1 or 85:1 at elevated temperatures. A series of SiC_p/Al composites (p denotes particulate) were prepared with the content of silicon carbide systematically varied from 0 to 30 vol. %. High resolution TEM (HRTEM) observations were performed to investigate interface structure using a 400kV electron microscope with a resolution of 0.17nm. Chemical analyses of precipitates, grain boundaries and interfacial regions were conducted with a 300kV electron microscope equipped with energy-dispersive X-ray spectroscopy (EDS). The probe size used for the EDS analysis was 5nm. Differential scanning calorimetry (DSC) was utilized to find any evidence for partial melting.

3. Results and discussion

3.1 Particle weakening

Figure 1(a) and (b) show the grain size compensated strain rate vs. flow stress for the 2124 and 6061 Al materials at given temperatures, respectively. Here, the grain size exponent, p, is assumed to be 2 based on the phenomenological relation developed to describe a number of D_L controlled superplastic metallic alloys[17]. As can be seen, "particle weakening" occurs in both material systems. Particle weakening means that strength of a reinforced composite is lower than that of the unreinforced matrix alloy.

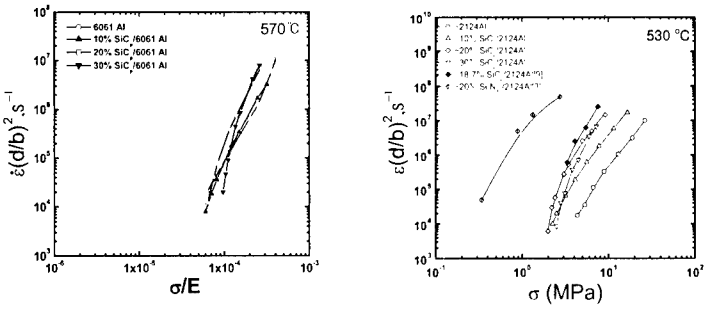

(a) (b)

Figure 1. $\dot{\varepsilon}\,(d/b)^2$ Vs. σ : (a) 6061 Al and (b) 2124 Al composites

The stengths of 2124 and 6061 Al materials are compared as a function of temperature in Fig. 2 (a) and (b) as $(\sigma-\sigma_o)/E$ vs. 1/T plot, respectively. The plot in Fig. 2 was constructed first by plotting $\dot{\varepsilon}\,(d/b)^2$ vs. $(\sigma-\sigma_o)/E$ and then plotting the values of $(\sigma-\sigma_o)/E$ as a function of 1/T at a given $\dot{\varepsilon}\,(d/b)^2$ of 10^6 s^{-1}. The data from other materials [3, 18] were also plotted for comparison. Three important features in Fig. 2 are discussed. (i) The value of $(\sigma-\sigma_o)/E$ at a

given temperature decreases with increase in the amount of SiC. (ii) At a given volume fraction of reinforcement, the strength decreases with decrease in the size of reinforcement. (iii) The strength difference between the materials decreases with decrease in the temperature. Extrapolation of the data to lower temperatures predicts that the composites would have the same strength as the matrix alloy at about 460°C in the 2124 Al system and 480°C in the 6061 Al system, if GBS continues to be retained as the rate controlling process. This temperature is 20°C higher than that of the 2124 Al composites [1], where similar strength convergence was observed.

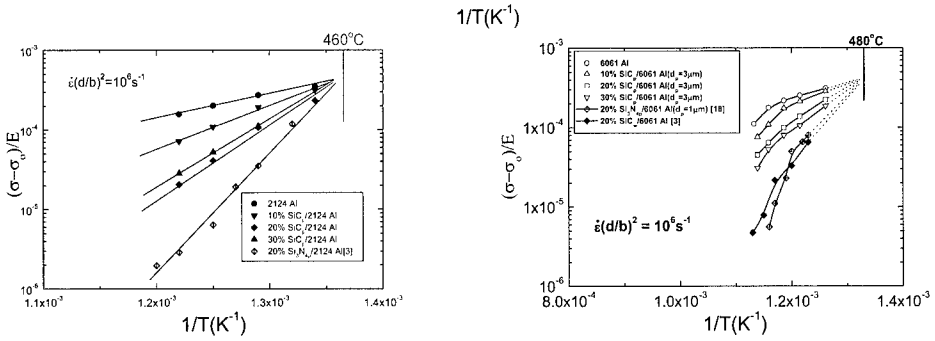

(a) (b)

Figure 2. $(\sigma-\sigma_o)/E$ Vs. 1/T : (a) 2124 and (b) 6061Al composites

3.2 Interface structure and solute segregation behavior

Fig. 3 (a) and (b) show the typical lattice images at SiC/Al interfaces in the SiC/2124 and SiC/6061 Al composites, respectively. It is apparent from the HRTEM image that the interface is smooth and straight, and no reaction has occurred. This interface structure is different from a similar micrograph in the Si_3N_4reinforced Al composites, where curved surfaces of Si_3N_4 crystals and strong reaction at interfaces were observed [12]. The EDS investigation indicates that Mg strongly and preferentially segregates at the SiC/Al interface. Mg is almost undetectable in the regions other than interfaces. If the particle weakening observed in the current composites is a consequence of the partial melting at Mg-rich region confined near SiC interfaces, the region should begin to melt at 460°. It is interesting to note that this temperature is close to the temperature for eutectic reaction in Al-Mg alloy system (450°) [19].

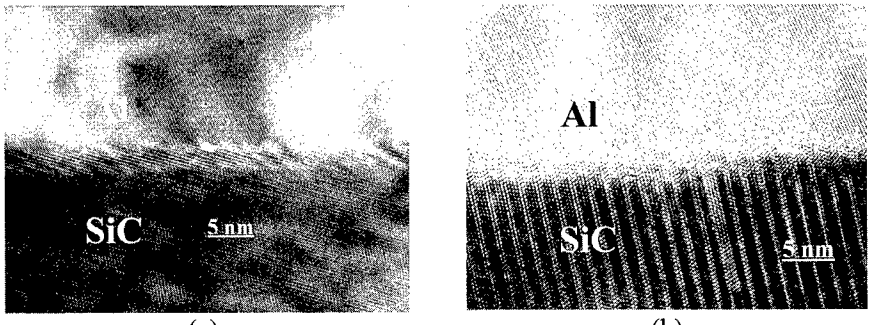

(a) (b)

Figure 3. HRTEM image : (a) 20 % SiC/2124 Al and (b) 20 % SiC/6061 Al composites

3.3 **Influence of interface area on strength of composite**

If the presence of liquid phase at SiC/Al interfaces causes the particles weakening in the current composites, it can be speculated that the behavior would become more pronounced as the SiC/Al interfacial area increases since more boundary area containing liquid phase is available.

Fig. 4 illustrates the relationship between $(\sigma-\sigma_0)/E$ and the interfacial area for the 2124 and 6061 Al composites at a given $\dot{\varepsilon}(d/b)^2$ and T. The interfacial area was calculated as a ratio of the area for the 20% SiC/Al composite with particle size (d_p) of 8μm[20], which is taken as 1. The systematic decrease in $(\sigma-\sigma_0)/E$ is observed in 2124 and 6061 Al composites with increase in the interface area. This result clearly displays that particle weakening is enhanced in the 2124 and 6061 Al composites as the interface area increases.

It needs to be noted that there exists a large strength difference between the 2124 and 6061 Al composites, while the difference between the 2124 Al and 6061 Al matrix alloys is small. This result indicates that the addition of reinforcement results in further difference in strength between the two alloy systems. The strength differential between the two composites may be attributed to the amount of liquid phase accumulated at interfaces. Since the 2124 Al alloy contains higher Mg and Cu content than the 6061 Al alloy, it is likely that solute concentration at the vicinity of interfaces in the 2124 Al composite is higher than that in the 6061 Al composite. Therefore, liquid phase could start to form at lower temperature in the 2124 Al composites than in the 6061 Al composites, and the accumulated amount at a given temperature would be larger.

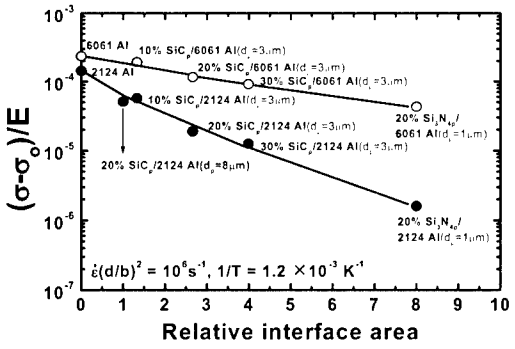

Figure 4. $(\sigma-\sigma_0)/E$ vs. interfacial area

3.4 **Difference in partial melting and superplastic behaviors between Si_3N_4 and SiC reinforced composites**

Data for various 2124 and 6061 Al composites are in Table 1, where the temperatures and strain rates for optimum HSRS, the incipient melting temperature determined by DSC test and the presence or absence of partial melting in the DSC curve are listed. A few differences between the Si_3N_4 reinforced and SiC reinforced Al composites are discussed. First, a small endothermic peak representing partial melting appears in the Si_3N_4 reinforced composite, while it is absent in the SiC reinforced composite. Second, the optimum superplastic

temperature of the SiC reinforced composite is generally higher than that of the Si_3N_4 reinforced composite. These two differences are probably related to the way how Mg solute is distributed at interface areas. If Mg concentration in the reaction phases in the Si_3N_4 reinforced composites varies within a narrow range, partial melting would occur rather at a discrete temperature and the volume of liquid phase would increase rapidly in a short temperature interval. Consequently, a small endothermic peak is visible in the DSC curve and HSRS is obtained near the melting temperature of reaction phase. On the other hand, if Mg concentration at interfaces in the SiC reinforced composites, where reaction phase does not form, varies gradually within a wide range, melting would be initiated from a region where Mg content is high and proceed progressively with increasing temperature. In this case, melting behavior may not be conspicuously detected by a DSC accuracy and higher temperature than the melting temperature of reaction phase is required to accumulate the sufficient amount of liquid phase for HSRS.

Acknowledgement

This work was supported by the Korea Science and Engineering foundation (KOSEF 2000).

Reference

1. T. G. Nieh, C. A. Henshall and J. Wadsworth, Scripta metall. **18**, 1405 (1984).
2. M. Mabuchi, K. Higashi and T. G. Langdon, Acta metall. mater. **42**, 1739 (1994).
3. B. Q. Han and K. C.Chan, Scripta mater. **36**, 593 (1997).
4. M. Mabuchi, K. Higashi, Y. Okada, S. Tanimura, T. Imai and K. Kubo, Scripta. metall. mater. **25**, 2517 (1991).
5. T. R. Bieler and A. K. Mukherjee, *Mater. Sci. Eng. A***128**, 171 (1990).
6. M. Mabuchi, K. Higashi, K. Inoue, S. Tanimura, T. Imai and K. Kubo, Mater. Sci. Eng. A**156**, L9 (1992).
7. K. Higashi, T. Okada, T. Mukai and S. Tanimura, Mater. Sci. Eng. A**195**, L1 (1992).
8. G. H. Zahid, R. I. Todd and P. B. Prangnell, *Mat. Sci. & Tech.* **14**, 901 (1998).
9. W. J. Kim, J. H. Yeon, D. H. Shin and S. H. Hong, Mat. Sci. Eng. A**269**, 142 (1999).
10. W. J. Kim, Y. S.Lee, S. J. Moon, and S. H. Hong, Mat. Sci. & Tech. **16**, 675 (2000).
11. W. J. Kim and O. D. Sherby, Acta mater. **48**, 1763 (2000).
12. M. Mabuchi, H. Iwasaki, H. G. Jeong, K. Hiraga and K. Higashi, J. Mater. Res., **12**, 2332 (1997).
13. K. Higashi, T. G. Nieh, M. Mabuchi and J. Wadsworth, Scripta metall. **32**, 1079 (1995).
14. H. G. Jeong, K. Hiraga, M. Mabuchi and K. Higashi, Acta metall. mater. **46**, 6009 (1998).
15. H. G. Jeong, K. Hiraga, M. Mabuchi and K. Higashi, Phil. Mag. Lett. **74**, 73 (1996).
16. J. Koike, M. Mabuchi and K. Higashi, Acta metall mater. **43**, 199 (1995).
17. O. A. Ruano and O. D. Sherby, *Mater. Sci. Eng.* A. **39**, 211 (1979).
18. M. Mabuchi, H. Iwasaki, and K. Higashi, *Acta mater.* **46**, 5335 (1998).
19. T. B. Massalski, H. Okamato, H. Subramanian, and L. Kacprzak, *Binary Alloy Phase Diagrams (*vol. **1**), 2nd ed. (ASM international, Materials Park, Ohio, 1990), pp. 170.
20. W. J. Kim, Scripta mater, 1999, **41**, 1131.
21. M. Mabuchi and K. Higashi, Mater. Trans. JIM. **35**, 399 (1994).

Table 1. The various superplastic Al composites

Materials (d_p denotes the diameter of reinforcement)	Strain rate (s^{-1})	%	Extrusion ratio	Optimum superplastic temp. (°C)	Incipient melting temperature determined by DSC(°C)	Presence of small endothermic peak for partial melting
10%SiC_p(d_p=3μm)/ 2124 Al composite[11]	$1x10^{-1}$	550	70:1	550	599	No
20%SiC_p(d_p=3μm)/ 2124 Al composite[11]	$1x10^{-1}$	400	70:1	535	620	No
18%SiCp(d_p=3μm)/ 2124 Al composite[8]	$1x10^{-1}$	500	Rolled	500	604	No
20%Si_3N_{4p}(d_p=0.2μm)/ 2124 Al composite[2]	$3x10^{-1}$	280	100:1	500	543	Yes
20%Si_3N_{4p}(d_p=1μm)/ 2124 Al composite[2]	$4x10^{-2}$	840	100:1	515	511	Yes
20%Si_3N_{4w} / 2124 Al composite[2]	$4x10^{-2}$	280	100:1	545	576	Yes
20%SiC_p (d_p=8μm)/ 6061 Al composite[10]	$1x10^{-2}$	350	85:1	600	631	No
20%SiC_p (d_p=3μm)/ 6061 Al composite	$5x10^{-2}$	350	85:1	590-600	632	No
20%SiC_w / 6061 Al composite[3]	$2x10^{-1}$	440	Rolled	600	584	No
20%Si_3N_{4p}(d_p=0.2μm)/ 6061 Al composite[21]	2	620	100:1	560	557	Yes
20%Si_3N_{4p}(d_p=0.5μm)/ 6061 Al composite[21]	1	350	100:1	560	556	Yes
20%Si_3N_{4p}(d_p=1μm)/ 6061 Al composite[21]	$1x10^{-1}$	450	100:1	545	549	Yes

Determination of Superplastic Properties of AlCuAgMgZr Alloys Prepared from Various Techniques

J. Dutkiewicz*, **, P. Malczewski** J. Kuśnierz* and T.G. Nieh ***

*Institute of Metallurgy and Materials Science of the Polish Academy of Sciences 30-059 Kraków ul. Reymonta 25, Poland

**Pedagogical Academy, Institute of Technique, ul. Podchorążych 2, 30-084 Kraków, Poland

*** Lawrence Livermore National Laboratory, L350. P.O. Box 808, L-350 Livermore, CA 94551-9900, USA

ABSTRACT

Two aluminium alloys containing 5 – 6% Cu, 0.4- 0.8 % Ag, 0.4 – 0.6 % Mg and 0.3 – 0.4 % Zr were cast using either continuous casting with "hot top" crystallizer or using static casting to a cold copper mould. Grain refinement was subsequently carried out using hot deformation, quenching, aging, warm rolling and annealing. Depending upon the casting procedure, a grain size in the range of 10 – 20 μm was obtained. The processed alloys were superplastically deformed either by uniaxial tensile tests in the temperature interval 623 – 773K or biaxial tensile tests using gas pressure forming in the temperature range 723-773K. Tensile elongation up to 300% was obtained for the continuously cast alloys below 673K, and at 773K for the copper mould cast alloys. This difference was resulted from the fact that a finer Al_3Zr distribution in copper mould cast and aged samples, which caused effective grain boundary pinning during high-temperature tests. The strain rate sensitivity coefficient **m** was higher for the continuously cast alloys, $\cong 0.7$ for temperatures below 673K, but less than 0.3 for the fast cooled alloys deformed in this temperature range. Preliminary gas forming experiments demonstrated the ability of alloys to deform superplastically, especially for the copper mould cast alloy, which showed a lower flow stress at high temperatures.

1. INTRODUCTION

Currently, there is an increased commercial interest in superplastic forming (SPF) in automotive, aerospace and aircraft industries [1,2]. AlCuZr alloys were one of the first dveloped for SPF many years ago [1-5]. The first reported large elongation in Al6Cu0.5Zr alloy was due to a relatively high level of zirconium in the form of extremely fine Al_3Zr precipitates [4]. These alloys, later known as SUPRAL, were heavily cold worked, then recrystalized to a small grain size. Whereas zirconium is an effective grain refiner, it has disadvantages such as high casting temperature, requiring high casting temperature to retain Zr in the solid solution, and accelerated cavity nucleation and growth during superplastic deformation caused by the presence of Zr rich particles [3].

Limited works on the effect of alloying additions on the superplastic behaviour of AlCu alloys have been carried out. For example, a Al4%Cu2.2%Mg0.6%Mn0.1%Ti alloy

exhibited a strain rate sensitivity coefficient of 0.6 what allowed 600% of elongation after thermo-mechanical treatment [6]. This alloy shows precipitation of S phase instead of Θ'. S phase did not affect superplastic properties. There are also several papers on the superplasticity of AlCuLiMgZr alloys [7,8] which showed **m** values close to 0.6 and large (>1200%) elongations. Our previous results obtained from AlCuAgMgZr alloys [9] demonstrated the alloys have good superplastic properties at temperatures below 450^{0}C. However, the alloys degrade at a higher temperature because a drastic grain growth. The grain growth was caused by the segregation of Zr in large particles and the ineffective grain boundary pinning of Ω and Θ' phases.
In the present paper different casting technology was used to retain zirconium in the solid solution in order to obtain fine Al_3Zr precipitates [4]. Gas pressure forming experiments [1-3], was performed with the present alloys. Comparison was also made between the results from gas pressure forming and the results from the uniaxial tensile tests. The ability of gas forming of aluminum alloys show dependence on **m** values [10,11] influencing thickness variation of gas blown samples and giving rise to a conical shapes at low **m** values.

2. EXPERIMENTAL PROCEDURE

Two aluminium alloys containing: 5% Cu, 0.2% Mn, 0.75% Mg, 0.65% Ag, 0.4% Zr (AG1) and 5.6% Cu, 0.16%Mn, 0.44%Mg, 0.43% Ag, 0.4% Zr (AG2), were either continuously or conventionally cast to a copper mould of thick walls allowing initial thickness of the ingot 20 mm (alloy marked AG1A). Then the alloy AG1A was aged at 653K and both alloys were hot rolled down to 10 mm. The alloys were then solutionized at 800K, water quenched, rolled at 573K to the final thickness of 2 mm.

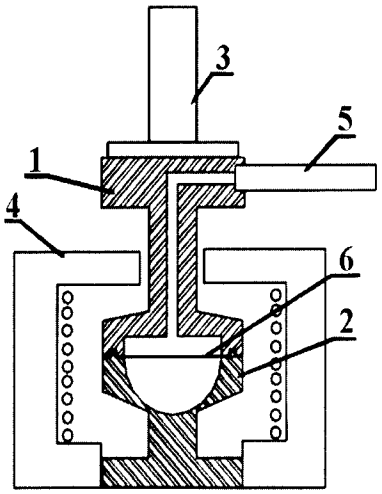

Fig.1 Scheme of the equipment used for gas blowing experiments.

1. stainless steel upper clamp
2. inverted hemisphere shape die and clamp
3. hydraulic piston rod
4. furnace
5. gas inlet
6. sample

The microstructure of the alloys was studied using optical, scanning microscope Philips XL30 and transmission electron microscope (TEM) Philips CM20 operating at 200 kV. Thin foils were obtained by jet electropolishing at subzero temperatures in electrolyte consisting of methanol – 6 % perchloric acid. Tensile tests were performed using Instron 6025 tensile machine equipped with a high temperature furnace. The estimation of the **m** value i.e. strain rate sensitivity, was performed by step strain - rate change tensile tests. The tests were conducted with a slow initial strain rate which increased stepwise to a high constant strain

rates, when the stress was measured. They were performed under air or inert gas atmosphere at temperature range 623-823K. The gas blow deformation was performed using self built equipment of scheme presented in Fig.1. The deformation temperature was in the range of 773-813K and the pressure range 0.2-1 MPa at the sample thickness 1.5-1.8 mm.

3. RESULTS AND DISCUSSION

Fig.2 shows the set of optical microstructures of samples AG2 and AG2A prepared at different technological conditions, i.e. continuously cast and then hot rolled Fig.1(a) and cast to a copper mould (Fig.1b). One can readily see a similar grain size, but finer second phase particles in the case of alloy AG2A

a) b)

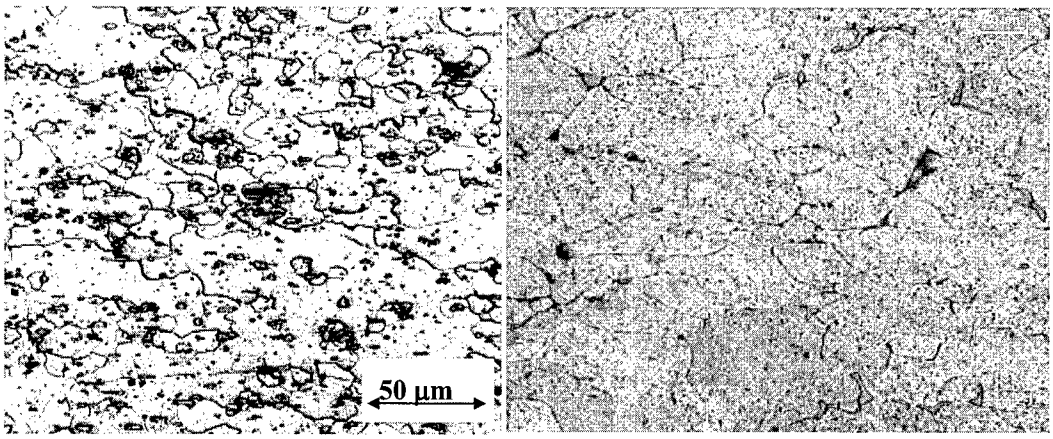

Fig.2 Optical microstructures of alloy AG2 continuously cast and hot rolled at 673K (a) and the same alloy cast to a copper mould AG2A (b)

Although the grain sizes in two thermomechanically-processed alloys are similar, their tensile behaviour was different. Fig.3 shows the results from tensile testing of alloys AG1 (a) and AG1A (b) performed at the temperature range 623-773K and presented as a $\lg\sigma = f(\lg \dot{\varepsilon})$ plot. The tensile stress σ is related to the strain rate $\dot{\varepsilon}$ through the equation:

$$\sigma = \mathbf{k}\dot{\varepsilon}^{\,\mathbf{m}} \qquad (1)$$

where $\mathbf{m} = d(\ln \sigma)/d(\ln \dot{\varepsilon})$ is the strain rate sensitivity and **k** is a material constant. The **m** value was determined by step strain - rate change tests and the results are presented in Fig.3 It can be seen that the highest **m** value for the alloy AG1 approaches 0.7 at the lowest testing temperature of 623K and the strain rates of $\dot{\varepsilon} = 10^{-3} - 10^{-4}\ s^{-1}$. A value close to 0.5 was observed for temperatures of 623 –673K and strain rates $10^{-3} - 10^{-4}\ s^{-1}$. The lowest **m** value occurs at T>673 and the strain rates $> 10^{-3}$. It is noted that the flow stresses of AG1 and AG2 are much more sensitive to the applied strain rate, as compared to other superplastic aluminium alloys [1-4]. It is probably because zirconium rich precipitates have the form of large particles 1 – 5 µm and are not effective inhibitors for grain growth. The existing precipitate phases (Al-Cu based) do not prevent grain boundaries migration.

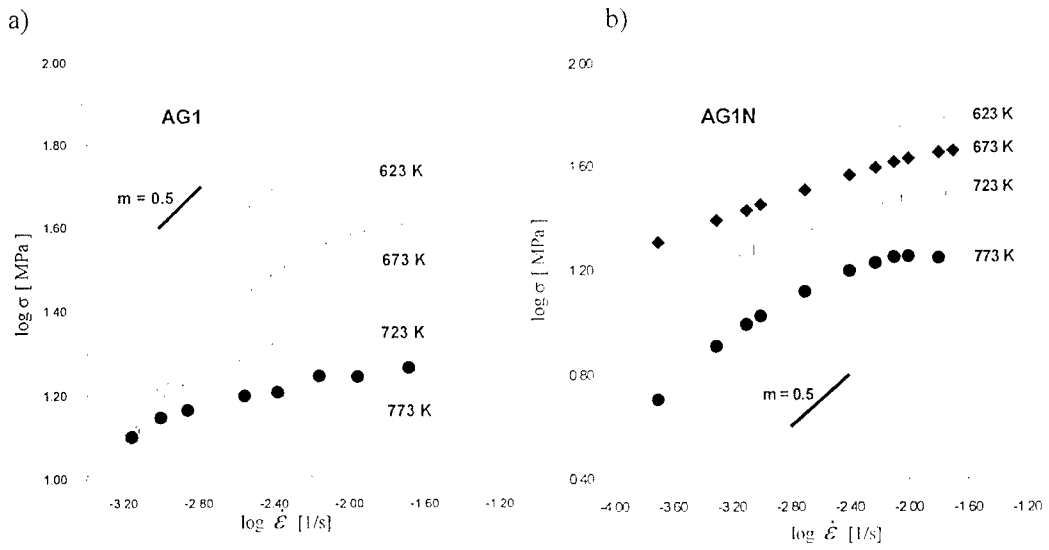

Fig.3 Relationship of tensile stress versus strain rate $\dot{\varepsilon}$ at temperatures 623K, 673K, 723K and 773 K obtained for the alloy AG1 (a) and AG2 (b).

Alloy AG1A cast at the higher rate the highest values of **m** close to 0.6. This was obtained at 773K and the lowest tensile rate, as shown in Fig.3b. At a higher tensile rate and lower temperature the **m** value is significantly lower. This is probably caused by a much finer Al_3Zr particles in alloys type A, which prevents grain growth at higher temperatures [4]. Similar $lg\sigma = f(lg\,\dot{\varepsilon})$ plots were obtained for the alloy 2A.
The microstructures of alloy AG1A deformed 100% at 773K are shown in Figs.5a and 5b. The SEM micrograph taken from the sample etched and tensile tested at 723K shows a grain growth and significant grain boundary sliding similarly as in 7000 series alloys [12]. The TEM micrograph shows a relatively high dislocation density also in the form of dislocation loops, suggesting vacancies play some roles during SPD.

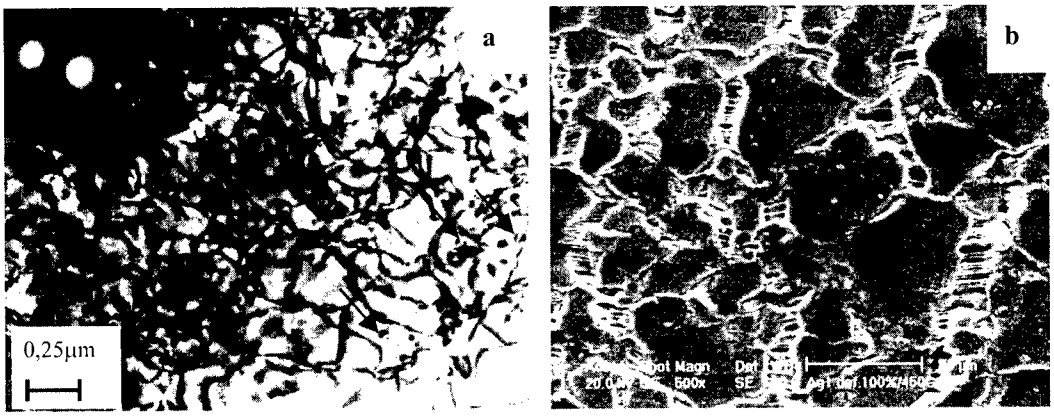

Fig.4 Alloy AG1A deformed at 773K up to 100% elongation. (a) TEM micrograph. (b) SEM micrograph of the sample surface

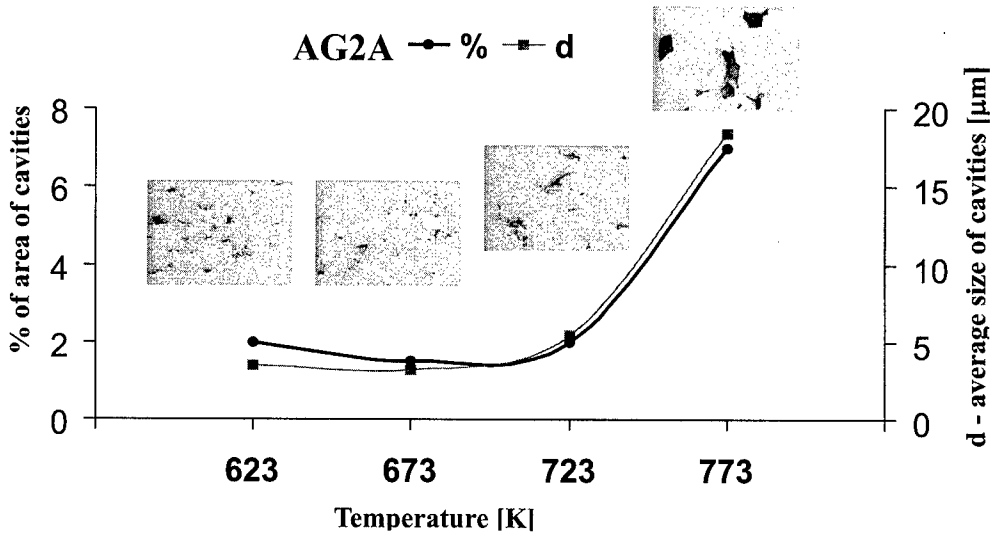

Fig.5 Change of the size and area of cavities of the sample AG2A deformed 100% at various temperatures

Fig.5 shows that the area and size of cavities vary in in a similar manner during deformation at various temperatures. They change little at T<723K, but grow rapidly at 773K. The insets show changes of the microstructure. The area of cavities has been reported to increase with deformation and decrease with deformation rate [5], i.e. it occurs at a favorable deformation conditions.

Fig.6 shows a photograph of gas pressure formed hemisphere shaped samples from alloys AG1A and AG2A formed at 773K withgas pressure increasing continuously from 0.2-0.8 MPa. They were formed in one operation corresponding to 82% of deformation strain. The microstructures of these samples show much less cavities and moderate grain growth indicating a deformation condition which is different from that in uniaxial test. The continuously cast alloys subjected to gas forming fractured earlier than the others.

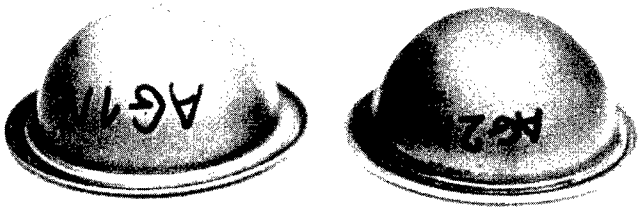

Fig.6 The photograph of gas formed hemisphere like shapes from alloy AG1A (left) and AG2A (right)

4. CONCLUSIONS

1. The Al-Cu-Ag-Mg-Zr alloys continuously cast contain large Zr rich precipitates which are not effective to prevent grain growth. However, they show good superplastic properties with an **m** value exceeds 0.6 at temperatures below 723K. The superplastic properties degrade at higher temperatures
2. The fast cooled (cast to a copper mould) and aged alloys a fines Al_3Zr particles. These particles effectively prevent grain growth at high temperatures. The alloys show good superplastic properties with **m** = 0.5 at temperatures above 773K.
3. The alloys cast at a higher cooling rate show increasing area of cavities with increasing temperatures. For the alloy deformed to a 100% elongation the area increases from 2% to 8% at 773K and average cavity size from 5μm to 18 μm.
4. The alloy cast at a higher cooling rate with fine zirconium particles show better properties for gas forming technology than continuously cast materials. The latter has a high tendency of grain growth, especially during a slow strain rate tests.

REFERENCES

1. A.J. Barnes, Materials Science Forum 170-172 (1994) pp. 701-714
2. T.G. Nieh, J. Wadsworth and O.D. Sherby, Superplasticity in Metals and Ceramics, Cambridge University Press, Cambridge, (1997) pp. 58-68
3. D.J. Lloyd and D.M. Moore, Superplastic Forming of Structural Alloys, N.E. Paton and C.H. Hamilton eds., The Metallurgical Society of AIME, (1982) pp.147-172
4. B.M. Watts, M.J. Stowell, B.L. Baikie and D.G.E. Owen, Metal Science 10 (1976) 189-206
5. Xiaoyu Zhao and T.G. Langdon, . Superplasticity in Metals, Ceramics and Intermetalics Mat. Res. Soc. Symp, Proc. Vol.196 (1990) pp.215-220
6. V.S. Levchenko, O.V. Solovyeva, V.K. Portnoi and Yu. V. Shevnuk, Materials Science Forum, 170-172, (1994) 261-266
7. D.N. Sergeeva, A.O. Nikiforov, I.I. Novikov and V.S. Levchenko, Materials Science Forum, 170-172 (1994) 240-254
8. I.G. Moon, J.W. Park and J.E. Yoo, , Materials Science Forum, 170-172 (1994) 255-260
9. J. Dutkiewicz, J. Kuśnierz, and T.G. Nieh, Proceedings of ICSAM 2000, in press
10. H.S. Yang and a.K. Mukherjee, Superplasticity in Aerospace II, ed. T.R. McNelley and H. C. Heikkenen, Minerals, Metals & Materials Soc. (1990) pp.103-119
11. D.B. Laycock, Superplastic Forming of Structural alloys, N.E. Paton and C.H. Hamilton eds., The Metallurgical Society of AIME, (1982) pp.257-272
12. M.G. Zelin, W.L. Moore, P.H. Caudhury, Superplasticity and Superplastic Forming, ed. A.K. Ghosh and T.B. Bieler, The Minerals & Materials Soc. 1995, pp.67-74

ACKNOWLEDGEMENTS

This work was supported by the Maria-Curie Skłodowska Fund (Contract PAN/NSF -98-331) and the Project supported by the State Committee for Scientific Research No PBZ-12-15.
This work was, in part, performed under the auspices of the U.S. Department of Energy by Lawrence Livermore National Laboratory under contract No. W-7405-Eng-48

FRACTURE AND SUPERPLASTICITY IN HYPER-EUTECTIC AL-20SI ALLOY WITH COARSE PRIMARY SILICON PHASE

Aidang Shan[1] In-Ge Moon[2], Jong-Woo Park[2], and Yong-Ho Park[1]

[1] Materials System Section, Tohoku National Industrial Research Institute, 983-8551, Sendai, Japan

[2] Materials Science and Technology Division, Korea Institute of Science and Technology, P. O. Box 131, Seoul Korea

ABSTRACT

A hyper-eutectic Al-20Si alloy was subjected to one pass ECA pressing. After pressing, cavities were observed around coarse primary silicon particles while the adjacent area of fine eutectic silicon particles is free from cavity. Superplasticity was found in the ECA pressed alloy. Highest elongation is 254% and maximum m value is 0.4. Fracture took place in a neck free mode. Microscopic observation reveals that fracture was resulted from interlinkage and coalescence of cavities.

Key words: superplasticity, hyper-eutectic, Al-Si alloy, ECA pressing

1. INTRODUCTION

Al-Si alloy is one of the most widely used industrial aluminum alloys. With excellent fluidability during solidification, Al-Si alloys are mainly used as castings. These years demand for wrought Al-Si alloys are increasing. Attention has been paid to superplastic forming of hypo-eutectic or eutectic Al-Si alloys. These alloys generally have silicon content below 13%. To exploit the merits of high modules, low thermal expansion coefficient and high wear resistance with increasing silicon content, hyper-eutectic alloy's superplasticity has been studied in those alloys prepared with powder metallurgy[1-2] as well as processed by spray forming [3]. In the viewpoint of industrial application, conventional ingot metallurgy is more preferable for its low cost. However, hyper-eutectic Al-Si alloys prepared by I/M method contain coarse primary silicon phase. To get fine microstructure in the matrix, which is a pre-requisite for superplasticity, cold or warm rolling is commonly performed on Al-Si alloys. During deformation, coarse primary silicon particles will introduce cavities. These cavities will decrease the ductility of the alloys. The other draw back of the rolling method is that it can only supply materials with plate form. However, in many typical applications of Al-Si alloys, like engine blocks and machinery components, bulk materials will be preferable.

Recently a new innovation known as ECA pressing for processing materials with untrafine microstructure appeared. Invented by Segal et al [4], this method has been proved to be very effective in producing untrafine grain size in polycrystal materials through intensive plastic deformation by simple shear [5, 6]. These ultrafine grain sizes impart high strength and low temperature and/or high strain rate superplasticity to the materials. Another merit of ECA pressing is that it will introduce no cavities to the materials so that a dense bulk material could be obtained [6].

Present research aimed at the feasibility of applying ECA pressing to an I/M prepared Al-20%Si hyper-eutectic alloy and the microstructure as well as superplastic properties of the ECA pressed alloy.

2. EXPERIMENTAL PROCEDURE

Alloy with a composition of Al-20%Si was prepared by permanent mold casting with commercial pure aluminum and silicon. Ingot size is about 75×75×120mm. Phosphorus was used to refine the primary silicon phase. After homogenizing at 500℃ for five hours the ingot was cut into 12×12×60mm billet for ECA pressing. Billets were polished to 800 grit SiC paper before ECA pressing.

ECA pressing was performed with a 90 degree sharp angle die. That is, according to Iwahashi et al's[8] nomenclature: $\Phi=90^\circ$, $\Psi=0^\circ$. Graphite was used as lubricant. Pressing was performed at about 200℃ for one pass. Billets broke in the second pass. Effort to press the billet at room temperature was also made but the billets are fractured after the first pass. For superplasticity test, samples were taken after the first pass ECA pressing at 200℃.

Tensile specimens were taken from the pressed billet along the longitudinal direction, parallel to the plane defined by the axis of the two channels which was called Y plane in literature [7]. ECA pressed specimens was sliced by a diamond saw along the Y plane into 1.2mm sheets, Tensile specimens with a gauge size of 1.2×5×14m were machined from these sheets, the surface of the tensile specimens were finished at 1000 grit SiC paper. Thickness error range was kept within ±0.02mm.

Tensile test was performed at 450, 500 and 550℃ on a Shimazu Autograph-10 tensile test machine in constant cross head speed mode. Three initial strain rates were used: 2.4×10^{-4}/s; 6×10^{-4}/s ; 1×10^{-3}/s.

Microstructure was examined under an optical microscope and the fracture surface was examined under a scanning electronic microscope (Hitachi-S-520).

For comparison, one part of the ingot was hot extruded to rods with reduction ratio of 9:1 and a plate with thickness of 2mm was sliced from the extruded rod. The plate was cold rolled to 40% reduction and then tensile specimens with same geometry as that in ECA pressing route were prepared from the rolled plate.

3. RESULTS AND DISCUSSIONS

3.1 Tensile properties

Tensile properties of the "ECA pressed" and "extrusion + cold rolling" samples were presented in table I. From this table it can be seen that superplasticity appears readily in ECA pressed samples. Maximum elongation reached 254% at 550° C under an initial strain rate of 2.4×10^{-4}/s. The morphology of the specimens before and after superplastic deformation was shown in Fig. 1. All fracture took place in a neck free mode. This mode is a typical inner cavity controlled fracture mode. In the "extrusion +cold rolling" route processed sample, a very limited elongation was observed. Maximum elongation is about 100%. However the maximum strain rate sensitivity index, *m* value, is almost the same for the samples processed from different routes.

Table 2. Experimental results of superplasticity test in hyper-eutectic Al-Si alloy

Processing route	Test temperature (°C)	Strain rate	Flow stress	Elongation	Maximum *m* value	Necking
Cast+homo+ extruding+ cold rolling (40%)	550°C	$2.4X10^{-4}$/s	2.0MPa	100%	0.4	free
		$6x10^{-4}$/s	4MPa	54%		free
Cast+homo+ hot ECAP (1pass)	450°C	$2.4X10^{-4}$/s	7MPa	108%	0.38	free
	500°C	$2.4x10^{-4}$/s	3.4MPa	164%	0.4	free
	550°C	$2.4x10^{-4}$/s	1.74MPa	254%	0.38	free
		$6x10^{-4}$/s	2.13MPa	218%		free
		$1.2x10^{-3}$/s	3MPa	189%		free

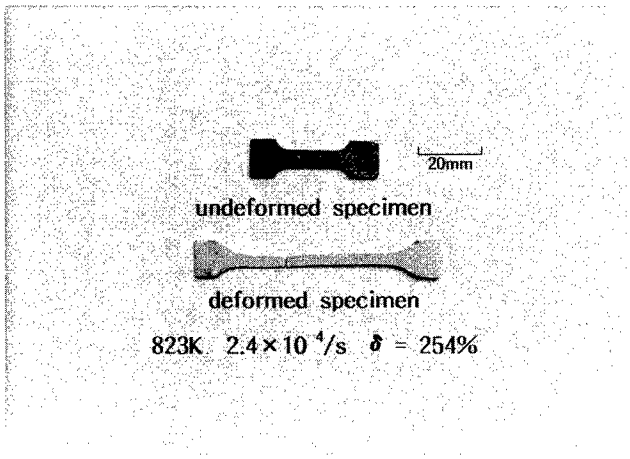

Fig.1. The morphology of the specimen before and after superplastic deformation.

3.2 Microstructures

Fig. 2(a) shows the typical microstructure of the specimen in the as cast and homogenized state. The microstructure is consisted of coarse primary silicon phase and the eutectic matrix. Size of the primary silicon phase is about 20-30 μm and the size of the eutectic silicon phase is about 2-4 μm. After one pass ECA pressing at 200° C, cavities were observed around the coarse silicon particles but not around the fine silicon particles. This was shown in Fig. 2(b). It has been suggested that ECA pressing will not introduce cavities to the billet and ECA pressing method had been performed to many kinds of alloys where no cavities were ever observed [6]. In this case when the particle size is small, that is 2-4 micrometer, no cavities were introduced to the material. But when the particles size is larger, here 20-30 micrometer, cavities were introduced to the alloy. Such cavities is a result of non-uniform deformation in the adjacent area the coarse particles. We failed to process the Al-20Si at room temperature and succeeded to process it at 200℃. That is, the billet was fractured after ECA pressing at room temperature. This should be an indication that the deformation near coarse particles at 200℃ become much uniform compared to that at room temperature.

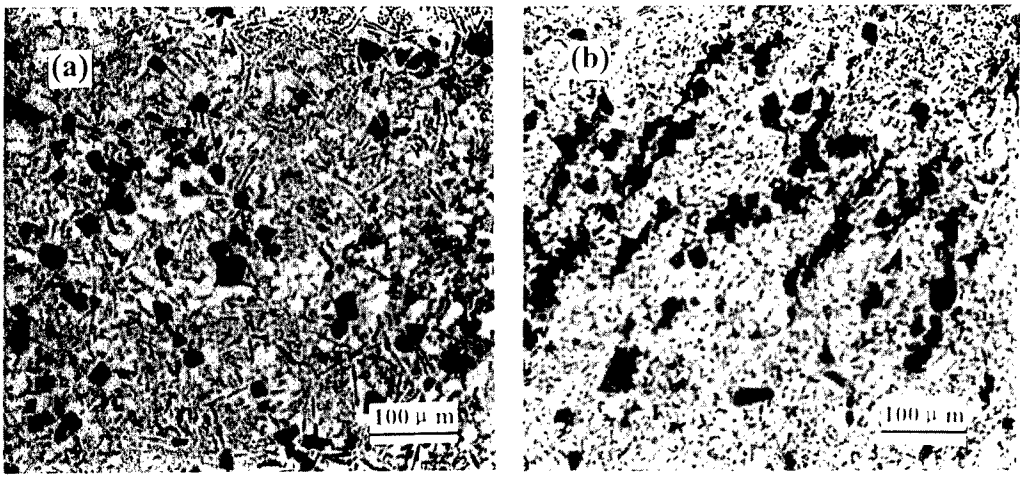

Fig.2. Microstructure of the Al-20Si alloy before and after one pass ECA pressing.

After superplastic deformation, the original cavities introduced through ECA pressing coalescence and interlink together. Larger size cavities were observed all around the coarse paricles and these cavities are generally some elongated along the tensile direction. As shown in Fig. 3 which was taken from the microstructure of the specimen deformed to 254%, the cavities occupied high volume fraction. Apart from large cavities, small cavities were also observed around fine particles. Such large and small cavities were also observed in the fractured surface as shown in Fig. 4. Even though many small cavitites introduced by eutectic silicon particles were observed in the fracture surface, in the microscopic observation there are not so many cavitites around the eutectic particles. It is suggested that upon the time that the fracture is about to take place the small cavitites around the eutectic silicon particles are not catastrophic. There are report [7] that the silicon particles may grow during deformation however In present study after deformation either the primary or the eutectic silicon particle size did not changed. Fibrous morphology as that observed by W-J Kim et al [3] at the fracture surface in Al-25Si alloy prepared by spray forming was not observed in present study. This observation suggested that superplastic deformation proceeded in solid state.

In eutectic Al-Si alloys, where eutectic silicon particles are fine, superplastic deformation was found to be controlled by neck developing [7]. The percentage cavitation is primarily controlled by the level of strain [8]. In the present research, superplasticty was readily observed in Al-20Si binary alloy, this alloy contains coarse primary silicon particle which has a size ranged from 20 to 30 micrometers. These particles introduced cavities during ECA pressing. Since the strain rate sensitivity index, m value, is some high than those observed in eutectic alloys (0.22 for Al-13Si alloy [7], grain size: 18 micrometer), it is reasonable to suggest that in the beginning of the deformation the grain size might be finer than 18 micrometer. Since the matrix is a eutectic structure deformation process in the matrix can be considered to be similar as that in the eutectic alloy. And those coarse primary silicon particles as well as the cavities introduced by ECA processing are detrimental to the final deformation extent. As a result total Elongation of around 250% was observed in the present alloy. This value is similar to that obtained in eutectic Al-13Si alloys. Much high elongation of 520% has been observed in a hyper-eutectic Al-15Si alloy with a fine microstructure prepared with rapid solidification and powder metallurgy [9]. If the primary silicon particle size can be further modified and the cavities can be eliminated during ECA pressing further high elongation can be expected.

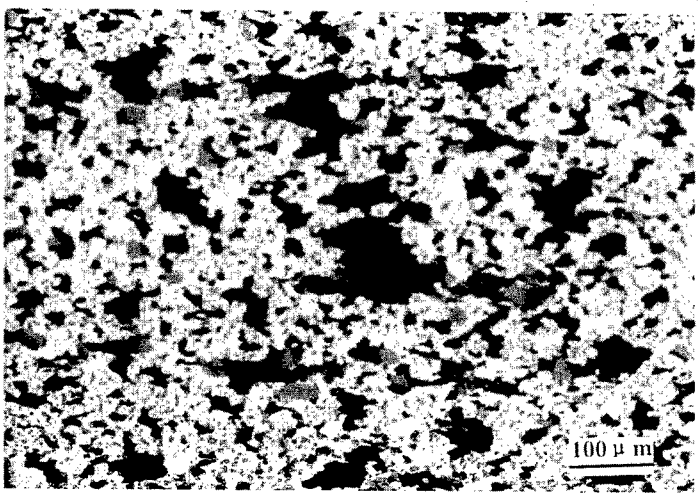

Fig.3. Microstructure of the Al-20Si alloy after superplastic 254% deformation at 550° C and $2.4x10^{-4}$/s

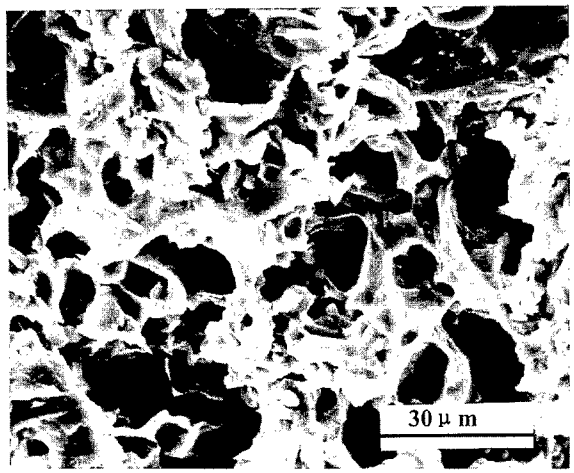

Fig.4. Fracture surface of the Al-20Si specimen tensiled at 550° C and $2.4x10^{-4}$/s

4. CONCLUSIONS

1, In Al-20Si alloy with a hyper-eutectic microstructure, ECA pressing introduced a microstructure with fewer cavities compared to traditional rolling method. Cavities appeared around the coarse primary silicon phase but did not appear around the fine eutectic silicon phase.

2, Hyper-eutectic Al-20Si alloy prepared by ingot metallurgy and one pass ECA pressing shows superplasticity in a temperature range of 450 to 550°C and a strain rate range of 2.4×10^{-4}/s to 1×10^{-3}/s. Maximum elongation reached 254%. The same alloy processed by extrusion and cold rolling shows very limited superplastic deformation degree before

fracture.

3, Fracture in the hyper-eutectic Al-20Si alloy prepared by ingot metallurgy and one pass ECA pressing took place mainly in a cavity coalescence and interlinkage mode. These cavitites are originated around the coarse primary silicon particles during ECA pressing. Nucleation and growth of cavities around eutectic particles was also observed, however these cavitites were not catastrophic up the time before the fracture took place.

REFERENCES

1. T. Satoh, K. Okimoto, S. Nishida and K. Matsuki, *Scripta Metal. Mater.* Vol. 33 (1995), pp. 819-824.
2. S. Fujino, N. Kuroishi, M. Yoshino, T. Mukai, Y. Okanda and K. Higashi, Scripta Materialia, Vol. 37 (1997), pp. 673-678.
3. W-J. Kim J. H. Yeon and J. C. Lee, J. Alloy and Compounds, Vol. 308 (2000), pp. 237-243.
4. V. M. Segal, V. I. Reznikov, A.E. Drobyshevskiy, and V.I. Kopylov, Russ. Metall. (Metally), Vol.**1** (1981), pp.99-105.
5. R.Z. Valiev, N.A. Krasilnikov, and N.K. Tsenev, Mater. Sci. & Eng. A, Vol.35 (1991), pp35-40.
6. V.M.Segal: Mater. Sci. Eng.A, Vol.197A (1995), pp.157-164.
7. R. K. Mahidhara, Mater. Sci. & Eng. A, Vol. 197A, (1995), pp. 15-18.
8. R.K. Mahidhara, A.K. Mukherjee, Mater.Trans., JIM Vol. 36(1995) pp.570-572.
9. T. Satoh, K. Okimoto K, S. Nishida L.Y.T. Choi, and W.W. Park, Met.& Mater. Korea Vol.5(1999), pp. 157-162.

IMPROVING THE SUPERPLASTIC PROPERTIES OF AN ALUMINUM ALLOY USING EQUAL-CHANNEL ANGULAR PRESSING

Sungwon Lee, Minoru Furukawa*, Zenji Horita** and Terence G. Langdon***

Plate Rolling Department, Pohang Iron & Steel Co., Ltd.
P.O. Box 35, Nam-ku, Pohang 790-360, Korea
*Department of Technology, Fukuoka University of Education
Munakata, Fukuoka 811-4192, Japan
**Department of Materials Science and Engineering, Faculty of Engineering
Kyushu University, Fukuoka 812-8581, Japan
***Departments of Aerospace & Mechanical Engineering and Materials Science
University of Southern California, Los Angeles, CA 90089-1453, U.S.A.

ABSTRACT

Processing by Equal-Channel Angular Pressing (ECAP) leads to grain refinement, typically to the submicrometer range, and consequent changes in the mechanical properties of metals including a potential for attaining superplastic ductilities at very rapid strain rates. This paper describes the application of ECAP to the Supral 100 alloy: this is an aluminum Al-2004 alloy containing 6% Cu and 0.4% Zr and having wide applications in the superplastic forming industry. The initial grain size of the as-received material was ~100 μm. It is shown that processing by ECAP refines the grain size to ≤2 μm and introduces a significant improvement in the superplastic ductilities achieved in the alloy at elevated temperatures. By comparison with the conventional unpressed commercial alloy, these results demonstrate that ECAP leads to the occurrence of optimum superplasticity at faster strain rates and at a lower testing temperature. Both of these trends are beneficial for making use of the ECAP process in superplastic forming applications.

1. INTRODUCTION

Superplastic forming is now well established as a processing tool for the fabrication of relatively complex parts from sheet metals and the process is used extensively for the forming of various aluminum-based alloys [1,2]. In practice, the application of the superplastic forming technology is limited because the strain rates associated with optimum forming tend to be fairly slow: for example, typical forming rates are generally of the order of $\sim 10^{-3}$ - 10^{-2} s^{-1} so that the forming times are ~20 - 30 minutes for each individual component. These long forming times necessarily preclude the application of this technology to mass production in the automotive and home product industries. Thus, as a consequence of these long forming times, a major interest has developed in producing alloys where superplastic forming may be undertaken at high strain rates in the range of $\sim 10^{-1}$ - 1 s^{-1}. Under these conditions, it is reasonable to anticipate that the forming times will be reduced to <60 s for each separate component.

Superplastic deformation occurs through the process of grain boundary sliding with a strain rate varying inversely with the grain size raised to a power of ~2 [3]. This suggests that the

optimum strain rate associated with superplastic flow will be displaced to faster strain rates when the grain size of the material is reduced. In practice, this trend is confirmed by experiments showing that a reduction in grain size leads to higher elongations to failure and the occurrence of these high elongations at faster strain rates [4]. Experimental observations of this type led to the suggestion that it may be feasible to achieve a superplastic forming capability at relatively high strain rates by reducing the grain size below the conventional range of ~1 - 5 μm [5]. Thus, it is necessary to examine procedures for grain refinement to the submicrometer level.

Several procedures are available for producing materials with extremely small grain sizes but generally these processes are not suitable for the production of materials for superplastic forming operations because the samples are too small, the process cannot be scaled up for the production of large bulk samples and/or the fabricated samples contain some residual porosity. A possible procedure to overcome these difficulties is through the use of Equal-Channel Angular Pressing (ECAP) where a sample is pressed through a die contained within a channel bent into an L-shaped configuration. The process of ECAP was developed about two decades ago [6] and it is a process in which a metal is deformed in simple shear without any concomitant change in the cross-sectional dimensions of the sample [7]. This paper describes the application of ECAP to a conventional aluminum-based superplastic alloy and the results obtained in the subsequent mechanical testing of the pressed samples.

2. EXPERIMENTAL MATERIAL AND PROCEDURES

The experiments were conducted using an Al-2004 alloy known commercially as Supral 100 and containing, in wt. %, 6% Cu and 0.4% Zr. This is a conventional alloy used extensively in commercial superplastic forming operations [1] and the alloy contains a very fine dispersion of Al_3Zr particles which serve to inhibit grain growth and an array of coarse Al_2Cu precipitates [8,9]. In this investigation, the alloy was supplied after casting, homogenizing at 648 K for 5 hours and then hot rolling into a plate. In this condition, the initial unpressed grain size was measured as ~100 μm.

All of the ECAP was conducted using a solid die containing a channel having a circular cross-section with a diameter of 9.3 mm, The channel was bent through an angle of 90° within the die and there was also an arc of curvature of approximately 45° at the outer point of intersection of the two separate parts of the channel. It can be shown that these two angles lead to an imposed strain of ~1 on each passage of the sample through the die [10]. Repetitive pressings were conducted to attain high strains, with the sample rotated by 90° in the same sense between each pass in the processing route designated B_C [11]. This route was selected because in pure Al it leads most expeditiously to an array of equiaxed grains separated by high-angle grain boundaries [12] and this processing route is optimum for the production of samples exhibiting high superplastic ductilities [13]. The pressings were conducted at temperatures from 298 to 673 K and up to 12 passes through the die, equivalent to a total strain of ~12. Each sample was lubricated prior to pressing. After ECAP, tensile specimens were machined parallel to the pressing direction and pulled in a machine operating at a constant rate of cross-head displacement. The microstructures were also examined using transmission electron microscopy.

(a)

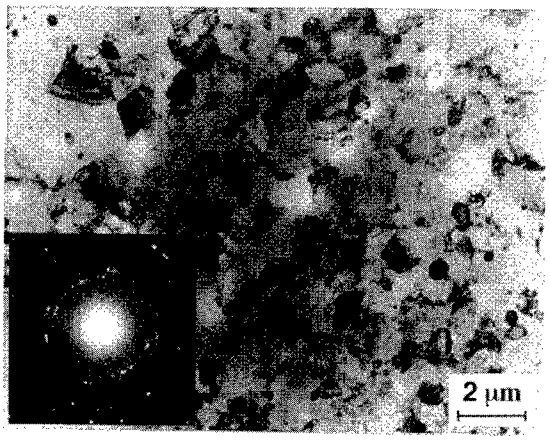

(b)

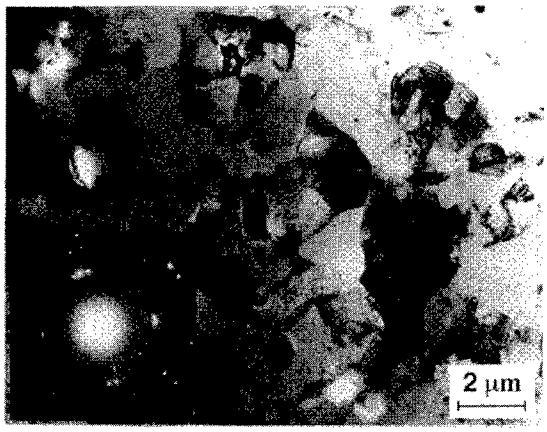

Fig. 1 Microstructures after ECAP (a) at 573 K for 12 passes and (b) at 673 K for 6 passes: selected area electron diffraction patterns taken from an area of 12.3 μm.

3. EXPERIMENTAL RESULTS

Earlier experiments revealed that it was difficult to press this alloy at 298 K because the samples tended to break after ~8 passes through the die. Accordingly, attention was devoted primarily to samples pressed at temperatures from 373 to 673 K. Figure 1 shows representative microstructures in the alloy after pressing using route B_C through (a) 12 passes at 573 K and (b) 6 passes at 673 K: the selected area electron diffraction patterns were taken with an aperture size of 12.3 μm. It is apparent that the grains are reasonably uniform and equiaxed in both of these pressing conditions and the grain sizes were measured as ~0.9 and ~2.0 μm after pressing at 573 and 673 K, respectively. Although the ECAP was conducted at a relatively high temperature, it is apparent from Fig. 1 that there are many dislocations within the grains and along the grain boundaries. This may be due to the pinning effect of the fine Al_3Zr precipitates. Nevertheless, ECAP is clearly very effective in refining the grain size of this alloy and the presence of rings in the diffraction patterns indicates that many of these grain boundaries have high angles of misorientation.

Samples were pulled in tension at elevated temperatures after processing by ECAP and Fig. 2 shows a representative set of curves of stress, σ, versus strain, ε, obtained on samples pressed at 573 K for 12 passes: these curves were obtained at testing temperatures of 623 and 673 K and with initial strain rates from 1.0×10^{-3} to 1.0×10^{-1} s^{-1}. It is apparent from these plots that there is a potential for achieving very high tensile ductilities in this alloy after ECAP and this is demonstrated in Figs 3 and 4 where samples are shown after pulling to failure at testing temperatures of 673 and 723 K: in Fig. 3 the samples were prepared by ECAP for 12 passes at 573 K and in Fig. 4 the samples were prepared by ECAP for 6 passes at 673 K. All of the samples in Figs 3 and 4 have initial gauge lengths of 4 mm and untested samples are shown at the top. It is apparent that these specimens pull out to very high tensile ductilities (>1000% elongation) at both testing temperatures when using an initial strain rate of 1.0×10^{-2} s^{-1} and the elongations are >300% even at a strain rate of 1.0×10^{-1} s^{-1}. Furthermore, no visible necking develops within the gauge lengths in the samples deforming to elongations of >1000% and the specimens pull out and ultimately fail as in conventional superplasticity.

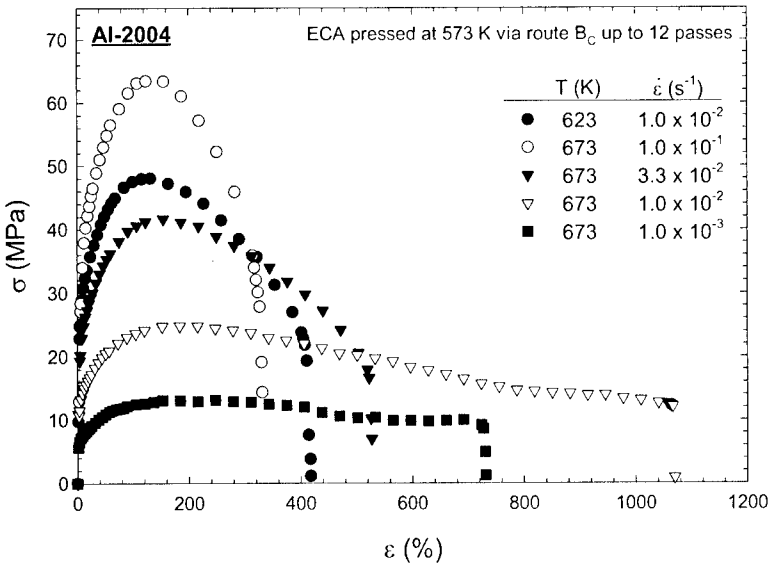

Fig. 2 Stress-strain curves after ECAP for 12 passes at 573 K and subsequent testing in tension at 623 and 573 K.

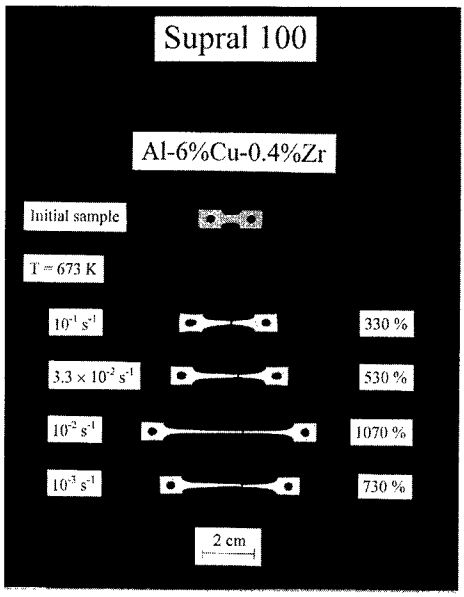

Fig. 3 Examples of tensile ductility in samples after ECAP at 573 K for 12 passes and tensile testing at 673 K.

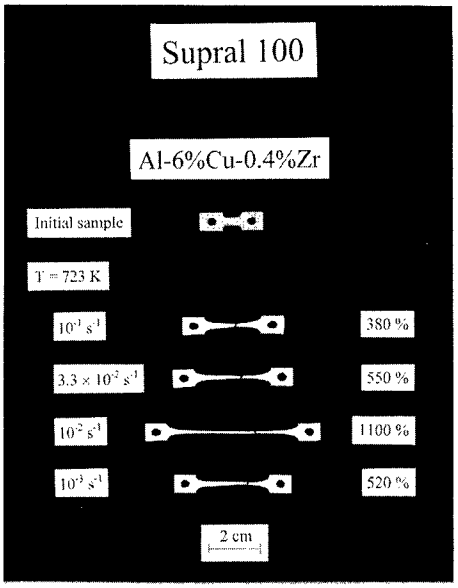

Fig. 4 Examples of tensile ductility in samples after ECAP at 673 K for 6 passes and tensile testing at 723 K.

The maximum elongation achieved in the unpressed alloy was ~450% at a temperature of 773 K with an initial strain rate of 3.3×10^{-4} s^{-1}. Thus, the specimens shown in Figs 3 and 4 have a potential for exhibiting substantially higher elongations by comparison with the unpressed

material and, in addition, these very high elongations occur at faster strain rates. Furthermore, it is possible to achieve these high elongations at lower temperatures than in the conventional unpressed alloy. A similar trend whereby the optimum superplasticity occurred at faster strain rates and a lower temperature after ECAP was also reported earlier for an Al-2024 alloy [14].

4. SUMMARY AND CONCLUSIONS

Equal-channel angular pressing (ECAP) is effective in reducing the grain size of the Supral 100 alloy (Al-2004) from ~100 μm to ≤2 μm. After ECAP, tensile specimens exhibit optimum superplasticity at faster strain rates and at a lower testing temperature.

ACKNOWLEDGEMENTS

This work was supported in part by the Light Metals Educational Foundation of Japan and in part by the U.S. Army Research Office under Grant No. DAAD19-00-1-0488.

REFERENCES

1. A.J. Barnes, Mater. Sci. Forum, Vol. 170-172 (1994), pp. 701-714.
2. A.J. Barnes, Mater. Sci. Forum, Vol. 304-306 (1999), pp. 785-796.
3. T.G. Langdon, Acta Metall. Mater., Vol. 42 (1994), pp. 2437-2443.
4. F.A. Mohamed, M.M.I. Ahmed and T.G. Langdon, Metall. Trans., Vol. 8A (1977), pp. 933-938.
5. Y. Ma, M. Furukawa, Z. Horita, M. Nemoto, R.Z. Valiev and T.G. Langdon, Mater. Trans. JIM, Vo. 37 (1996), pp. 336-339.
6. V.M. Segal, V.I. Reznikov, A.E. Drobyshevskiy and V.I. Kopylov, Russian Metall., Vol. 1 (1981), pp. 99-105.
7. V.M. Segal, Mater. Sci. Eng., Vol. A197 (1995), pp. 157-164.
8. B.M. Watts, M.J. Stowell, B.L. Baikie and D.G.E. Owen, Metal Sci., Vol. 10 (1976), pp. 189-197.
9. B.M. Watts, M.J. Stowell, B.L. Baikie and D.G.E. Owen, Metal Sci., Vol. 10 (1976), pp. 198-206.
10. Y. Iwahashi, J. Wang, Z. Horita, M. Nemoto and T.G. Langdon, Scripta Mater., Vol. 35 (1996), pp. 143-146.
11. M. Furukawa, Y. Iwahashi, Z. Horita, M. Nemoto and T.G. Langdon, Mater. Sci. Eng., Vol. A257 (1998), pp. 328-332.
12. K. Oh-ishi, Z. Horita, M. Furukawa, M. Nemoto and T.G. Langdon, Metall. Mater. Trans., Vol. 29A (1998), pp. 2011-2013.
13. S. Komura, M. Furukawa, Z. Horita, M. Nemoto and T.G. Langdon, Mater. Sci. Eng., Vol. A297 (2001), pp. 111-118.
14. S. Lee and T.G. Langdon, Mater. Res. Soc. Symp. Proc., Vol. 601 (2000), pp. 359-364.

HIGH STRAIN RATE SUPERPLASTICITY (HSRS) IN ALUMINUM BASED ALLOYS AND COMPOSITES FOR AUTOMOTIVE AND AIRCRAFT APPLICATIONS

Young Hwan Han*, Rajiv S. Mishra[+] and Amiya K. Mukherjee

**Department of Chemical Engineering and Materials Science,
University of California, Davis, CA 95616-5294, USA**

*Presently at School of Metallurgical and
Materials Engineering,
Sung Kyun Kwan University, Suwon Kyunggi-do 440-746, KOREA

[+] Presently at Department of Metallurgical Engineering,
University of Missouri-Rolla, MO 65409-1060, USA

High strain rate superplasticity (HSRS, minimum elongation of 200 to 300% and minimum strain rate of 5×10^{-2} s^{-1}) has been observed in Al based alloys and composites. The mechanism and the parametric dependencies of HSRS are matter of some debate and not well understood. The understanding of the microstructural parameters in HSRS is developed for Al alloys and composites. An analysis of HSRS data shows a change in activation energy with particle size. The result is explained on the basis of change of rate controlling mechanism with second phase particles. The prediction of diffusional relaxation models agrees well with the experimental results. Diffusional relaxation models can also predict the temperature for onset of HSRS in mechanically alloyed Al. These concepts can be used to construct a "superplastic mechanism map" for Al alloys and composites, that have significant potential for application in future light automobiles and aircrafts.

1. Introduction

The elevated temperature crystalline plasticity had been given by the Mukherjee-Bird-Dorn (MBD) correlation [1,2] in 1968 and 1969. This correlation has been validated in the context of superplasticity for metals, intermetallics, and ceramic materials [3,4]. High strain rate superplasticity (HSRS) was first introduced by Singer and Gessinger [5] in 1981 on an ultra fine MA6000 oxide dispersion strengthened alloy. HSRS (minimum elongation of 200 to 300% and minimum strain rate of 5×10^{-2} s^{-1}) has revitalized the area of superplasticity with its potential for industrial application of superplastic forming.

HSRS in whisker or second phase reinforced aluminum alloy and composites has been observed, and has provided an efficient near-net shape forming technique to the automobile and aerospace industries, since the HSRS composites usually exhibit a total elongation of 250-600% at a high strain rate of 10^{-1}-10 s^{-1} [6]. HSRS has been reported in a number of dispersion strengthened materials and composites including aluminum based alloys and composites, titanium alloys, Duplex stainless steel, nickel based alloys and magnesium-based composites [3,7].

The general features of HSRS are the following:

1. The parametric dependencies tend to depend on the reinforcement size and grain size,
2. the optimum superplastic temperature changes with the matrix material and
3. the optimum superplastic conditions can be significantly altered by prior thermomechanical processing.

By relating the rate controlling mechanism to HSRS in all the materials it is evident that the size of second phase particle influences the parametric dependencies, particularly the activation energy for HSRS.

In this study, the industrially attractive area of HSRS for various microcrystalline PM and mechanically alloyed aluminum and aluminum composites are explained on the basis of a change in rate controlling mechanism with particle size. The role of diffusional relaxation around second phase particles on the temperature for onset of HSRS is reviewed with a superplastic mechanism map for dispersion strengthened aluminum alloys. The role of a liquid phase on superplasticity is also briefly explained.

2. Analysis and Discussion

2.1. Effect of thermomechanical processing

The thermomechanical processing changes the grain size of material and the nature of grain boundaries. Mishra et al. [10] have reported the effect of rolling on flow behavior and elongation of 2009 Al-15 vol. % SiC_w composite as shown in Figure 1. It can be noted that the flow stresses for the cross-rolled specimens are much lower and elongation are higher. This can be correlated with the reduction in grain size that results from cross rolling. This is a clear indication of the role of microstructure on elongation and strain rate sensitivity. The modified expression, Equation (1), of the presence of a threshold stress by Mukherjee et al. [9,10] is used for the analysis for

$$\dot{\varepsilon}_s = A\frac{DGb}{kT}\left(\frac{b}{d}\right)^p\left(\frac{\sigma-\sigma_o}{E}\right)^n \qquad (1)$$

elevated temperature deformation mechanism.

Where $\dot{\varepsilon}_s$ is the stead state strain rate, A is the constant, D is the appropriate diffusivity, G is the shear modulus, b is the Burger's vector, k is the Boltzman constant, T is the test temperature, d is the grain size, p is the grain size exponent, σ is the applied stress, σ_o is the threshold stress, E is Young's modulus and n is the stress-sensitivity.

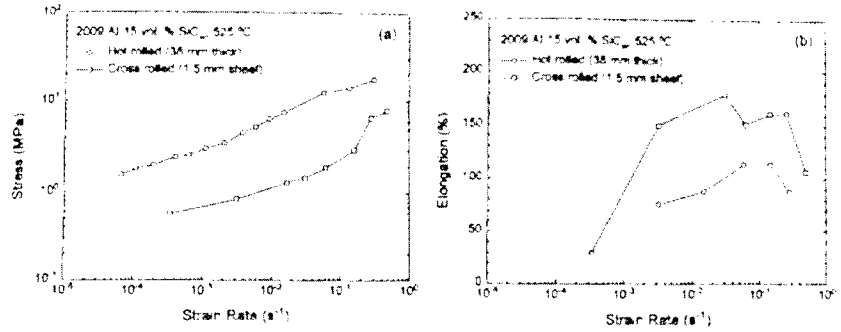

Figure 1. The variation of flow stress and elongation with strain rate for two processing conditions. Note the lower flow stresses and larger elongation after laboratory cross rolling.

2.2. Effect of particle size on micromechanism during grain boundary sliding

Grain boundary sliding is the dominant mechanism for superplasticity. The classic models for grain boundary sliding deal with single-phase materials. The HSRS, however, is mostly observed in two-phase materials where one of the phase is non

deformable at superplastic stress levels. It is very important to discuss the possible effect of second phase particles by considering realistic microstructures. For example, the particles can be as fine as 10-50 nm in mechanically alloyed alloys and it can be 10-30 μm long in the case of whisker reinforced metal matrix composites.

As investigated by Mukherjee et al. [7], a temperature dependent threshold stress exits for high strain rate superplasticity of dispersion strengthened materials. The variation of true activation energy (calculated after taking into account the presence of a temperature dependent threshold stress) with particle size is plotted in Figure 2 for a number of mechanically alloyed aluminum alloys and aluminum matrix composites. An important observation that is apparent from the Figure 2 is the change in activation energy for alloys with higher particle sizes. Equation (2) is based on the correlation of Equation (1) for superplastic flow in aluminum matrix composites [9], which can be

$$\dot{\varepsilon} = 3.6 \times 10^{18} \frac{D_i G b}{kT} \left(\frac{b^2}{d_g d_p} \right) \left(\frac{\sigma - \sigma_o}{E} \right)^2 \qquad (2)$$

written as

where D_i is the interfacial diffusion coefficient, d_g the grain size, d_p the particle size.

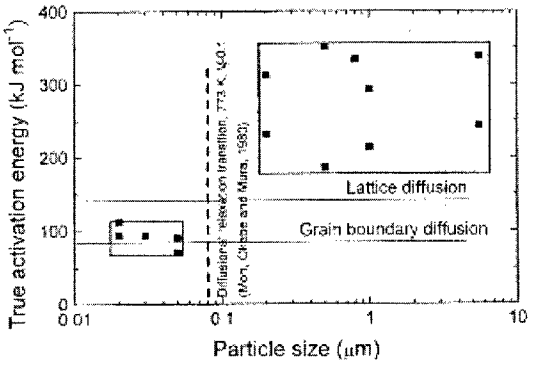

Figure 2. The variation of true activation energy with particle size for a number of mechanically alloyed aluminum alloys and aluminum matrix composites. Note that the change can be predicted by diffusional relaxation models.

At this stage, we examine the role of particle size on the accommodation process during superplasticity. Figure 3(a) shows the classical concept of slip accommodation during grain boundary sliding. This has been shown to be applicable for a number of materials [3]. The second phase particles at grain boundaries (e.g. particle marked p_{gb} in Figure 3(b)) impede the grain boundary sliding and lead to stress concentration. This stress concentration must be lowered for continuous sliding and to avoid cavity nucleation. The stress relaxation can occur by diffusional flow of atoms around the particles as depicted in Figure 3(b). If the rate diffusion relaxation is fast enough to remove the stress build-up, the overall grain boundary sliding would not be influenced parametrically. The presence of large ceramic phase like whisker in composites would mean that certain boundary sliding cannot be accommodated by slip as described in Figure 3(c), which is very similar to the microstructure of 2009 Al-SiC_w composite reported by Mishra et al. [11].

In the case of MMC the microstructure is quite different. The most important feature is the size and morphology of the second phase reinforcement particles. The whisker-

reinforced composites have matrix grains that are significantly finer than the length of the whisker. Figure 3(c) shows a schematic illustration of the microstructure of such composite. It is well known that grain boundary sliding and rotation are essential for superplasticity. It is interesting to consider some of interfaces in Figure 3(c). The grain boundary between grain "D" and grain "E" will be referred as GB_{DE} and interphase interface between grain "D" and whisker will be referred as IDW. The sliding of GB_{DE} cannot be accommodated by slip at point "w". The only option is diffusional accommodation. Also, for a sustained deformation there has to be interfacial sliding at IDW. This raises a question about the activation energy for the overall flow behavior. If the diffusional accommodation at metal/ceramic interface and metal/ceramic interfacial diffusion is rate controlling, the activation energy for superplasticity should be that of interfacial diffusion.

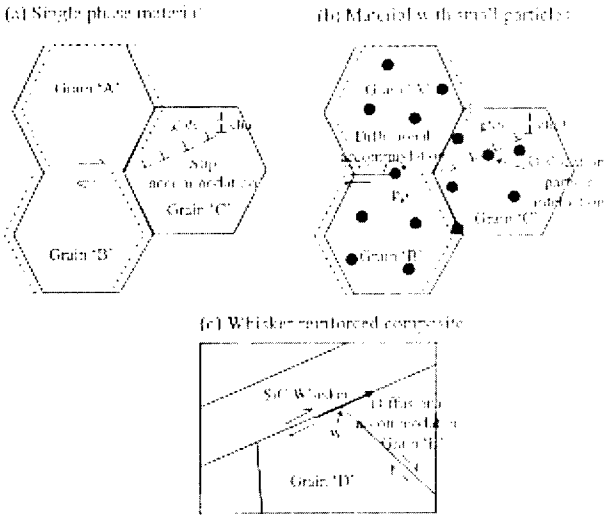

Figure 3. The effect of second phase particles on the slip accommodation during grain boundary sliding.

2.3. Superplastic mechanism map

Mishra et al. [9] have suggested that the interfacial activation energy for Al-SiC composites might be higher than the lattice self-diffusion of Al. Intuitively, it appears that the interfacial diffusion rate would depend on the nature of interfacial bonding. The Al-SiC interfacial bonding has been reported to be excellent and in such a case one can expect slower diffusivity at the interface. Therefore, a transition in rate controlling mechanism is expected. This is a plausible explanation for the observed change in activation energy in Figure 2.

Mishra et al. [11,12] have proposed a "superplastic mechanism map" for dispersion-strengthened materials to depict such transition as shown in Figure 4. It can be noted that the data for mechanically alloyed aluminum alloys and aluminum matrix composites tend to fall in the expected domain.

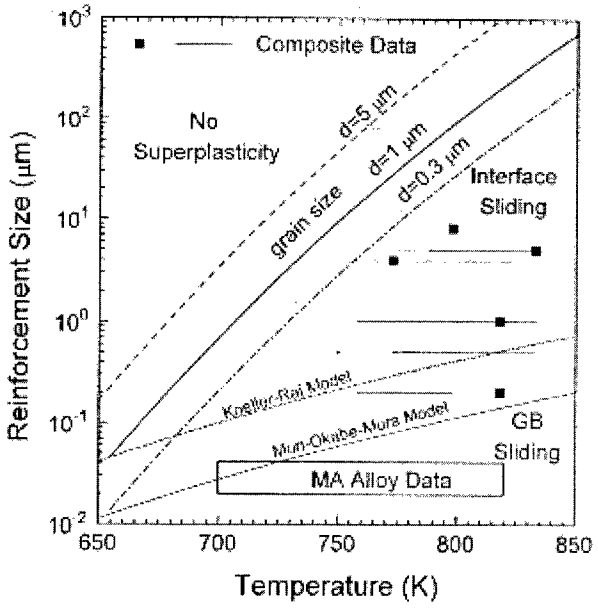

Figure 4. A "superplastic mechanism map" for dispersion strengthened aluminum alloys.

2.4. The role of liquid phase for superplasticity

The role of a liquid phase at or near the optimum temperature for superplasticity has stimulated much research during the past few years. Analyzing a large number of experimental results on mechanically alloyed as well as composite materials Mukherjee et al. [7] concluded that *"incipient melting may occur in a way beneficial to superplastic deformation at sufficiently high temperatures, but it is not necessary in order to account for superplastic elongations observed in the aluminum matrix composites.."*

Mukherjee et al. have found the above quoted statement to be preeminently valid. It is important not to associate the rate controlling deformation mechanism in superplasticity only with the point of maximum ductility. Early literature shows many examples [3,13] where the maximum attainable ductility was influenced by various factors including cavitations. However, the fundamental rate controlling deformation mechanism involving grain boundary sliding and the associated accommodation process were unchanged. This is a very large amount of experimental data on various systems where the tensile ductility is 200-300% or higher and the strain rate is 5×10^{-2} s^{-1} or higher. Thus, they qualify for the HSRS regime. However, these systems simply do not have any liquid phase at the superplastic test temperatures. A compilation of such materials systems exhibiting HSRS with no liquid phase in the matrix under the test conditions is shown in Table 1.

Table 1. Systems demonstrating HSRS with no liquid phase at test temperatures.

Material and [Ref]	Temp K	Grain Size	Optimum $\dot{\varepsilon}$	Optimum Elongation	Investigators (Year)
Al/Pure Al composite [42]	913 K	~ 2 μm	0.1 to 0.3 s^{-1}	200%	Imai et al (1997)
Mg-Y_2Nd-Zn [43]	713K	~ 1 μm	10^{-1} s^{-1}	200%	Mahoney et al (1994)
Al-Ni-Mm-Mg [44]	873K	70 nm	7×10^{-1} s^{-1}	540%	Higashi et al (1993)
UHCS-10Al Steel [45]	1193 K	~ 0.5 μm	10^{-1} s^{-1}	350%	Takeuchi et al (1995)
Mg-Mg$_2$Si Composite [46]	723K	~ 1 μm	10^{-1} - 1 s^{-1}	344%	Mabuchi et al (1995)
β-Si_3N_4/Pure Al Composite [47]	903K	< 2 μm	0.1 s^{-1}	200%	Imai et al (1995)
Al 10wt%-Ti Alloy [48]	873K	2 μm	0.2 s^{-1}	200%	Kum et al (1994)
α-Ti-Intermetallic Ti-(25-50) Al [49]	923 K	0.5 μm	3×10^{-1} s^{-1}	200%	Liu et al (1994)
25Cr-7Ni-3Mo Duplex Stainless [50]	1223 K	~ 1 μm	1.7×10^{-1} s^{-1}	100%	Tsuzaki et al (1995)
Al 10wt%-Ti [51]	923 K	~ 2.8 μm	10^{-1} s^{-1}	497%	Kum et al (1995)
Fe-Cr-Ni Duplex Stainless [52]	1273 K	Dynamic Recrystallized	10^{-1} s^{-1}	1000%	Mabuchi (1995)
α-Ti/Intermetallic Ti-Cr [53]	1023 K	0.3 to 0.6 μm	5×10^{-1} s^{-1}	250%	Fukuyo et al (1995)
Ti-40Cr-4Al-4Mo [54]	973 K	0.4 μm	5×10^{-1} s^{-1}	600%	Fujiwara et al (1995)
MA6000 [3]	1273 K	0.2 μm	10^{-1} s^{-1}	150%	Gregson et al (1995)

3. Conclusions

The parametric dependencies for HSRS change with particle size. Diffusional relaxation models can be used to explain this change as well as for predicting the temperature for onset of HSRS in mechanically alloyed aluminum. A *"superplastic mechanism map"* can be constructed using these concepts. As for the role of a liquid phase, the incipient melting may be beneficial for superplastic deformation at sufficiently high temperatures, but it is not necessary for the manifestation of HSRS in the aluminum matrix composites.

4. References

1. A.K. Mukherjee, J.E. Bird, and J.E. Dorn, The Role of Climb in Creep Processes in Proceedings of Symposium "The Interaction Between Dislocations and Point Defects," vol.II, part III, ed. By B.L. Eyre, United Kingdom Atomic Energy Authority, Harwell, Berkshire, UK, 1968, pp.422-495.
2. J.E. Bird, A.K. Mukherjee, and J.E. Dorn, Int. Conf. Quantitative Relation Between Properties and Microstructure, ed. A. Rosen et al., Haifa, Israel, 1969, pp.255-342.
3. A.K. Mukherjee, in: Superplasticity in Metals, Ceramics and intermetallics, in Plastic Deformation and Fracture of Materials, vol.6, ed. H. Mughrabi, VCH Publishers, Weinheim, Germany, 1993, pp.407-460.
4. T.G. Nieh, J. Wadsworth, and O.D. Sherby, in: Superplasticity in Metals and Ceramics, Cambridge University Press, Cambridge, UK, 1997.
5. R.F. Singer and G.H. Gessinger in Deformation of Polycrystals: Mechanisms and Microstructures, 2nd RISO International Symposium, ed. N. Hansen et al., (Publishers, RISO National Laboratory, Roksilde, Denmark (1981), p.385.
6. T. Imai, S. Kojima, and D. Jiang, "High strain rate superplasticity of SiC_p/1100 and SiC_p/1N90 P/M pure aluminum composites," Mater. Sci. Engin., A225 (1997) pp.184-187.
7. A.K. Mukherjee, R.S. Mishra, and T.R. Bieler, Mater. Sci. Forum 217 (1997) 233-234.
8. R.S. Mishra, C. Echer, C.C. Bampton, T.R. Bieler and A.K. Mukherjee, Scripta Mater., 35, 247 (1996).
9. R.S. Mishra and A.K. Mukherjee, Scripta Mater. 25, 271 (1991).
10. R.S. Mishra, T.R. Bieler, and A.K. Mukherjee, Acta Matall. Mater. 43 877.
11. R.S. Mishra, T.R. Bieler, and A.K. Mukherjee, Acta Mater. 45 (1997) 561.
12. R.S. Mishra and A.K. Mukherjee, in: M. Phillips, J. Porter (Eds.), Advances in Powder Metallurgy and Particulate Materials- 1995, MPIF/APMI, Princeton, 1995, pp. 155-165.
13. A. Chokshi and T.G. Langdon, in Superplasticity, ed. B. Baudelet et al., (Paris, Edition du CNRS, 1985), pp. 2.1- 2.1.5.

HIGH STRAIN RATE SUPERPLASTICITY OF MG-Li- ZN ALLOY

Suk-Won Lim, Tsunemichi Imai*, JianFu Mao**, Takao Choh* and Yoshinori Nishida*

Yeong Dong College, 11 GeumSan-Ri, KangWon-Do, 210-840, Korea,
* National Institute of Advanced Science ant Industrial Technology, AIST Chubu,
1-1 Hirate-cho, Kita-ku, Nagoya 462-8510, Japan
** Harbin Institute of Technology, Harbin, 150001, China

ABSTRACT

Mg-Li alloys are expected to make weight of automobile and aerospace components reduce significantly. Mg-8.5Li, Mg-8.5-Li-1Zn and Mg-8.5Li-3Zn alloys made by stirring method were extruded at 623K with the extrusion ratio of 64, and then the superplastic characteristics were investigated. Microstructure of Mg-8.5Li alloy consists of $\alpha+\beta$ phases and m value, strain rate sensitivity of the flow stress, is less than 0.3 and total elongation obtained is about 500% at the strain rate of $10^{-2}s^{-1}$ and at 623K. In the case of Mg-8.5Li-1Zn alloy, the microstructure were less fine than those of Mg-8.5Li alloys and although the m vale becomes about 0.3, the total elongation became about 500% at the strain rate of $10^{-2}s^{-1}$ and at 623K. Mg-8.5Li-3Zn alloy exhibits m value of 0.3 and the total elongation of about 550% at the strain rate of $10^{-1}s^{-1}$ and at 673K. Therefore, it is clarified that Mg-8.5Li and Mg-8.5Li-3Zn made by casting before extrusion could produce High strain rate superplasticity and it is thought that hot extrusion at 623K is available to build fine grain size in Mg-8.5Li and Mg-8.5 Li-Zn alloys.

1. INTRODUCTION

Magnesium(Mg) alloys and the composites have a great potential to apply to automobile, aerospace industries and even to information technology field since the density of magnesium is low as compared with other metal alloys and the composite is expected to achieve excellent mechanical, physical and thermal properties [1~3]. And lithium(Li) is available to make the density of Mg alloys lower extremely. High Strain Rate Superplasticity (HSRS) is expected to offer the efficiently near-net shape forming method for magnesium alloys and the composites, since the HSRS materials usually exhibit an elongation of 250~600% at a high strain rate of about $0.1\sim10s^{-1}$[4~14]. However, superplastic magnesium alloys and magnesium matrix composites developed up to date were Mg-8.5wt%Li-1wt%Y, ZK60A and AZ61A which indicate the total elongation of 460~700 % at a lower strain rate of $3\sim4x10^{-3}$ s^{-1} and at 453~623K because of their relatively larger grain size of about 35μm[15~17]and Mg-9wt%Li-5wt%BC with a fine-grain of 2μm prepared by a foil metallurgy can produce superplastic behavior at 423~473K[18]. These Mg alloys and the composite are conventional superplastic materials. On the other hand, it was found that a SiC/ZK60 composite made by P/M methods shows an m value of 0.5 and the total elongation of 350% at very high strain rate of about $1.0s^{-1}$[19] and that a TiC/Mg-5wt%Zn composite fabricated by

a stirring method can produce an m value of about 0.3 and the total elongation of 350% at the strain rate of $10^{-1}s^{-1}$ [20]. It was reported that Mg-8.5Li-3Y alloys exhibits m value of about 0.3 and the total elongation of about 400% at the strain rate of $10^{-2}s^{-1}$ due to an effect of 3Y to maintain fine grain size although Mg-8.5Li alloy was still a conventional superplastic material[21].
The purpose of this study is to reveal the HSRS in Mg-Li and Mg-Li-Zn alloys made by a stirring method before extrusion. In addition, the superplastic deformation mechanism of the Mg-Li-Zn alloys will be discussed.

2. EXPERIMENTAL PROCEDURES

Mg-8.5Li alloy, Mg-8.5Li-1Zn and Mg-8.5 Li-3Zn were fabricated in Ar Gass atomosphere by a stirring method. Hot extrusion was conducted at 623K to build fine microstructure of these materials. Round tensile specimens with a 2.5mm diameter and a 15mm gage length were made. Specimens were deformed at 573, 623, 675, and 698K and at strain rates ranging from $1x10^{-4}$ to $1.5s^{-1}$. Microstructure of the samples was examined by SEM and TEM.

3. EXPERIMENTAL RESULTS AND DISCUSSION

The flow stress, σ, relates to true strain rate $\dot{\varepsilon}$, via the equation $\sigma=K\dot{\varepsilon}^m$ In the equation, the strain rate sensitivity exponent, m, is the slope of the curve ($\ln\sigma/\ln\dot{\varepsilon}$), where σ is the flow stress, $\dot{\varepsilon}$ is the strain rate, k is a constant incorporating structure and temperature dependencies. Normally, the m value must be larger than 0.3 in order to observe superplasticity in a material. A high m value material can suppress the development of necking and leads to a high total elongation.

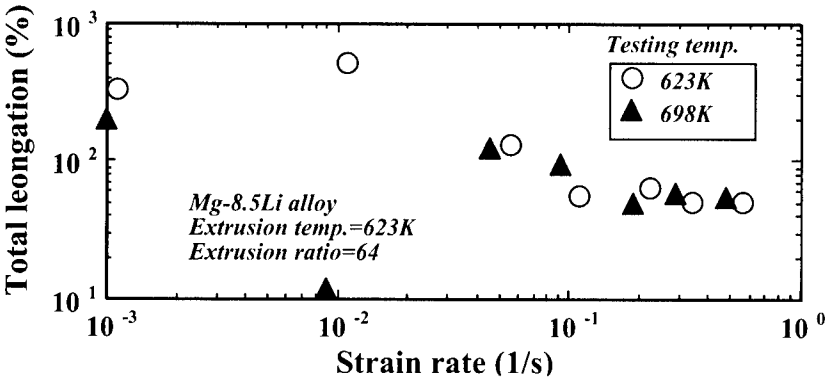

Fig.1 Superplastic characteristics of Mg-8.5Li alloy

3.1 HSRS of Mg-8.5Li alloy

The logarithmic flow stress of the Mg-8.5Li alloy increases approximately with increasing logarithmic strain rate and decreasing temperature. The strain rate sensitivity value of

Mg-8.5Li alloy is about 0.30 at 623, 693K at strain rates ranging from $2.0x10^{-4}$ to $0.6s^{-1}$. And the Mg-8.5Li alloy has threshold stress in strain rate range from $2.0x10^{-2}$ to $1.5s^{-1}$.

Total elongation of the Mg-8.5Li alloy is shown in Fig1 as a function of temperature. The total elongation at 623K becomes more than 100% in the strain rate range from 10^{-3} s^{-1} to $5x10^{-2}$ s^{-1}. Maximum total elongation of before extruding more than 500% in the Mg-8.5Li alloy is obtained at the strain rate of $1x10^{-2}s^{-1}$ and at 623K. Therefore, the results indicate that the Mg-8.5Li alloy could produce High Strain rate Superplasticity(HSRS).

3.2 HSRS of Mg-8.5Li-1Zn

Relationship between flow stress and strain rate of Mg-8.5Li-1Zn after extrusion is shown in Fig.2(a) as a function of temperature. The flow stress of the composite increases with increasing strain rate and decreasing temperature. The m value of the Mg-8.5Li-1Zn becomes less 0.1 in strain rate range less than 10^{-2} s^{-1}, which means that the composite has a threshold stress in the relatively lower strain rate range. However, the m value of the Mg-8.5Li-1Zn increases to 0.30 in the strain rate more than 10^{-2} s^{-1} and at 623~698K. These high m values

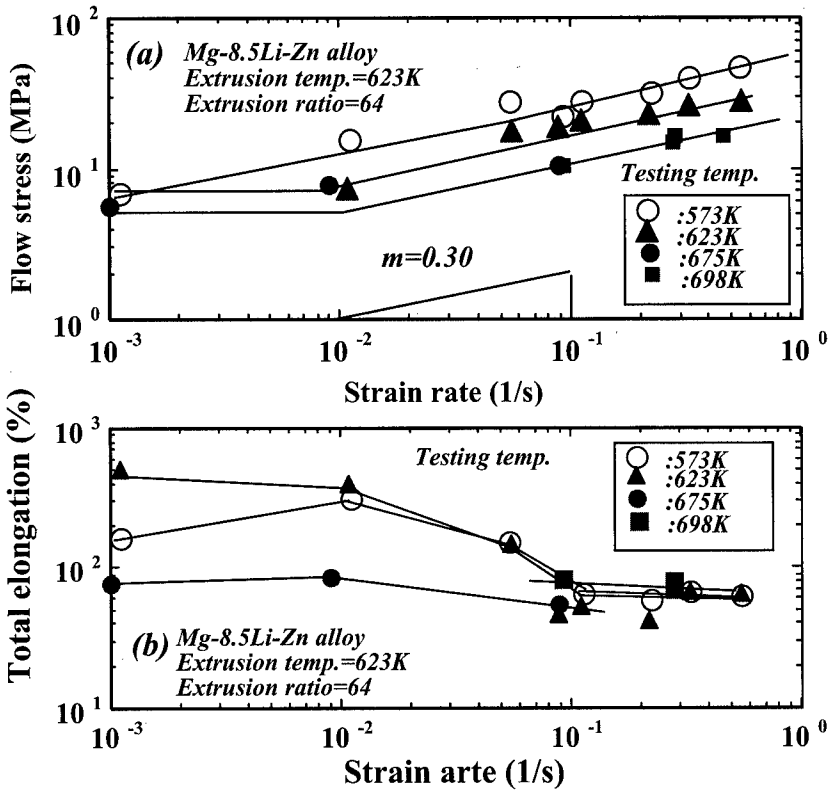

Fig. 2 Superplastic characteristics of the Mg-8.5Li-Zn alloys

reveals that the Mg-8.5Li-1Zn can produce the HSRS in the higher strain rate range, but the m value of the Mg-8.5Li-1Zn deformed at 573K might be less than 0.3 in the same strain rate range.

Relationship between total elongation and strain ate of Mg-8.5Li-Zn alloy is shown in Fig.2 (b) as a function of temperature. Total elongation of the Mg-8.5Li-Zn alloy indicates less than 100% in the strain rate range higher than $10^{-2}s^{-1}$ but in the temperature of 623K, maximum total elongation of about 500% is obtained at the strain rate of $10^{-3}s^{-1}$ which means that the Mg-8.5Li-Zn alloy is a conventional superplasticity. However, at the temperature of 673K, optimum strain rate at which maximum total elongation of 300% is obtained is $10^{-2}s^{-1}$. Therefore, the Mg-8.5Li-Zn alloy produces the HSRS.

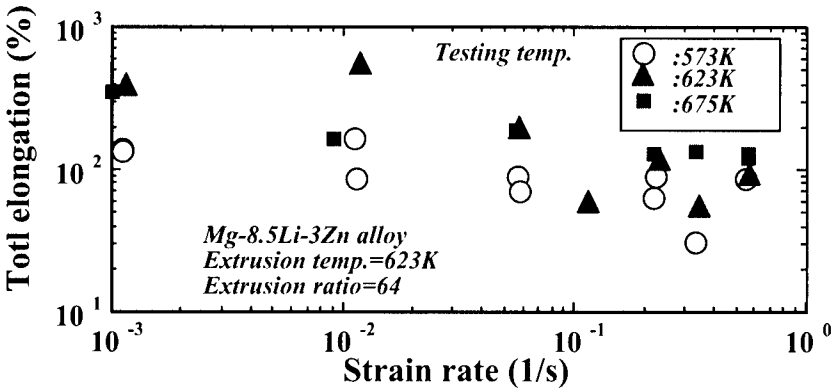

Fig.3 Superplastic characteristics of the Mg-8.5Li-3Zn alloys.

3.3 HSRS of Mg-8.5Li-3Zn alloy

Fig.3 show superplastic characteristics of Mg-8.5Li-3Zn alloy extruded as a function of temperature. m value of the Mg-8.5Li-3Zn alloy indicates more than 0.3 in the strain rate range more than $10^{-2}s^{-1}$ and at 623-675K.

Total elongation of the Mg-8.5Li-3Zn alloy exhibits about 500% at the strain rate of $10^{-2}s^{-1}$ and at 623K, although the Mg-8.5Li-3Zn alloy shows about 200% total elongation at the strain rate of $10^{-2}s^{-1}$ and at 573K and 675K. Therefore, 623K is optimum temperature at which maximum total elongation of 500% is obtained. The Mg-8.5Li-3Zn alloy could produce the HSRS.

3.4 Microstructure and deformation mechanism of HSRS for Mg-Li -Zn alloys

Fig.4 shows SEM microstructures of Mg-8.5Li-Zn alloy (a)before and (b) after superplastic deformation. The grain size of Mg-8.5Li-Zn and Mg-8.5Li-3Zn alloys are fine as compared with that of the Mg-8.5Li alloy because Zn is an effect to maintain fine grain during high temperature deformation. And also it was observed that the grain size of these Mg-Li alloys after superplastic deformation were not so different from ones of as-extruded materials. True stress-true strain curves of Mg-Li alloys indicates that maximum flow stress appears at the beginning of true stress-true strain curves which are typical stress-strain curves observed in materials by which dynamic recrystallization occurs.

Fig.5 shows TEM microstructure of Mg-8.5Li alloy just after extrusion. The grains in the

Mg-8.5Li alloy which include grain with high angle grain boundary or subgrain with low angle grain boundary is about 2μm~3μm. Although it was reported that Mg-8.5Li is still a conventional suprtplastic materials, in Fig.1 it is shown that the Mg-8.5Li alloy produces the HSRS. The fragments of Mg-8.5Li, Mg-8.5Li–Zn and Mg-8.5Li-3Zn were melted so that oxide layers on surfaces of small pieces in Mg-Li alloys might be dispersed in the Mg-Li alloys so as oxide particles to retain fine grain size of these Mg-Li alloys. Therefore, it is thought that primarily deformation mechanism of Mg-Li alloys is grain boundary sliding.

4. CONCLUSIONS

The superplasticity was observed in Mg-8.5Li, Mg-8.5Li–Zn and Mg-8.5Li-3Zn, fabricated by a stirring method and extrusion. The following results were obtained

(1) Mg-8.5Li alloy indicates an m value of about 0.3 and the total elongation of about 500% was obtained at low strain rate of $10^{-2}s^{-1}$ and 623K.
(2) Mg-8.5Li alloy had a threshold stress in strain rate range lower than $10^{-2}s^{-1}$, although the flow stress of the Mg-8.5Li alloy decreased simply with decreasing strain rate.
(3) The strain rate sensitivity (m value) of the Mg-8.5Li –Zn alloys is about 0.30 in the strain rate range higher than $10^{-1}s^{-1}$ at 673~698K.
(4) The Mg-8.5Li–Zn and Mg-8.5Li-3Zn alloys after extrusion exhibited a total elongation of about 500% at a strain rate of $10^{-2}s^{-1}$ at 623K.
(5) The Mg-Li alloys have a fine grain size of about 2~3μm since oxide particles were dispersed so as to avoid grain growth during superplastic deformation.

REFERENCES

1. B.A.Mikucki, Fundamental Relationship Between Microstructure & Mechanical Properties of Metal-Matrix Composites, Edited by P.K.Liaw and M.N.Gunger (1990)715/726
2. B.A.Mikucki, W.E.Mercer 2 and W.G.Green, SAE Technical Paper 906533, Internal Congress and Exposition, Detroit, Michigan, (February 26-March 2, 1990)1/9
3. V.Laurent, P.Jarry, G.Regazzon and D.Apelian, J.Mater.Sci., 27(1992) 447/459
4. T.G. Nieh, C.A. Henshall and J. Wadsworth, Scr. Metall., 18-12(1984) 1405/1408
5. T. Imai, M.Mabuchi, Y. Tozawa and M. Yamada, J.Mater.Sci.Lett., 9 (1990) 255/257
6. M. Mabuchi, T. Imai, K. Kubo, H. Higashi, Y. Okada and T. Tanimura, Mater.Lett., 10 (1991) 339/342

4 T.Imai, G.L'Esperance & B.D.Hong, Scripta Metall. et Mat., 31-3(1994) 321/326

5 T. Imai, G.L'Esperance, B.D.Hong & J.Kusui, in Proceedings of ECCM-6, Edited by A.R.Bunsell, A.K.Kelly & A.Massianh, (Woodhead Publishing Limited 1993) P.533

6 T.G.Nieh, T.Imai, J.Wadsworth and S.Kojima, Scripta Metall. et Mat., 31-12 (1994)1685/1690

7 T.Imai, G.L'Esperance, B.D.Hong and S.Kojima, Scripta Metall. et Mat., 31-3 (1995) 1333/1338

11. H.Xiaoxu, L.Qing, Ciki Yao and Y.Mei, J.Mat. Scie. Letters, 10(1991) 964/966
12. M.Kon, J.Kaneko and M.Sugmata, J.Japan STP, 35(1994) 823/828
13. J.Pilling, Scripta Metall.,13(1989) 1375
14. T.Hikosaka, T.Imai, T.G.Hieh and J.Wadsworth, Scripta Metall. et Mat., 31-9 (1994) 1181/1186

15. M.M.Tilman, R.L.Crosby and L.A.Neumeier, Bureau of Mines Report of Investigations 8382(1979)
16. K.Higashi and J.Wolfenstine, Mat.Letters, 10-7,8(1991)329/332
17. J.Wolfenstine, G.Gonzalez-Doncel and O.D.Sherby, Mat.Letters, 15(1992)305/308
18. P.Metenier, G.Gonzalez-Doncel, O.A.Ruano, J.Wolfenstine and O.D.Sherby, Mat.Sci.Eng., A125(1990) 195/202.
19. T.G.Nieh, A.J.Schwartz and J.Wadsworth, Mat.Eng.Sci., A208(1996) 30/36
20. S.K.Lim, T.Imai and Y.Nishida, Scrip. Metall.et Mat., 32-11(1995) 1713/1717
21. K.Kubota, M.Mabuchi, H.Higashi, J.Materials Science 34(1999)2255-2262

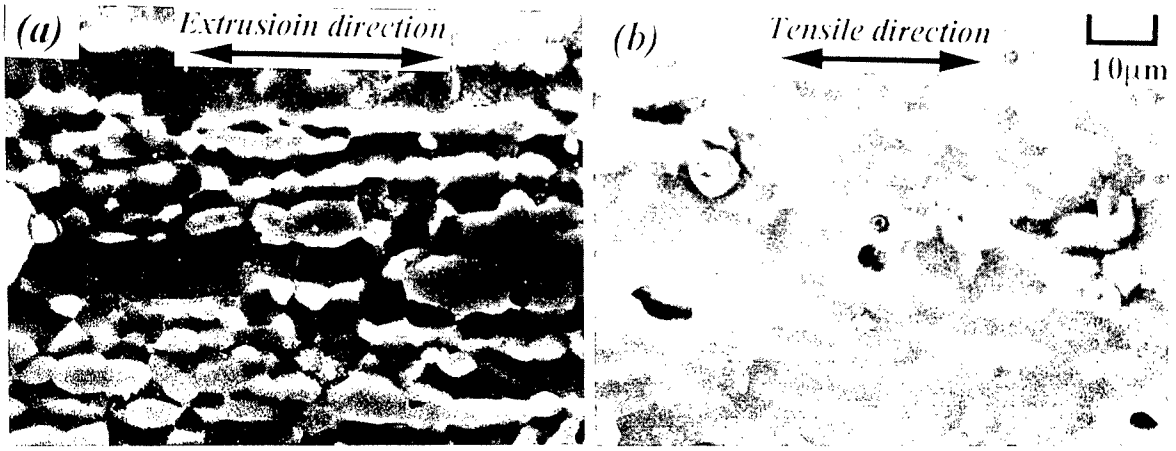

Fig.4 SEM microstructures of Mg-8.5Li –Zn alloys (a) before and (b)after superplastic deformation

Fig.5 TEM microstructure of as-extruded Mg-8.5Li alloy

SUPERPLASTIC FORMABILITY OF FINE-GRAINED AZ61 AND AZ31 MAGNESIUM ALLOY SHEETS AND DEFORMATION MECHANISM MAPS FOR MAGNESIUM ALLOYS

S. W. Chung and W. J. Kim

Dept. of Metallurgy and Materials Science, Hong-ik University
72-1, Sangsu-Dong, Mapo-Ku, Seoul, 121-791, Korea

ABSTRACT

Rolling processes of fabricating thin AZ61 and AZ31 alloy sheets adequate for superplastic forming have been developed. Superplastic behavior of the sheets was evaluated in the temperature range of 573K-693K and compared with the initial materials with relatively coarse grains. Existing deformation mechanism maps for f.c.c. and b.c.c. metals were reviewed and found to be deficient in predicting the deformation behavior of Mg alloys with h.c.p crystal structure. Using the experimental data for a number of Mg alloys, which are associated with various deformation mechanisms competing at elevated temperatures, deformation mechanism maps for Mg alloys could be constructed. Excellent prediction capability of the maps was verified at temperatures of 573K-673K. Superplastic formability of the rolled AZ61 alloy was demonstrated by forming a sheet into a hemi-spherical dome using N_2 gas pressure and into an indented plate using mechanical pressure by hot press.

1. INTRODUCTION

Magnesium is the lightest structural material, and its low density allows thick sections to be used, such that the need for a large amount of stiffening can be eliminated [1]. Besides, magnesium has high specific strength, high corrosion resistance and good damping capacity [2, 3]. Unlike aluminum alloys, however, magnesium alloys are hard to be thermo-mechanically workable since limited number of active slip systems is available in hcp crystal structure. To enhance formability of Mg alloys, application of superplasticity at high temperatures has been proposed as one of methods to form the magnesium alloys into complex near-net shaped components. Another advantage of the SPF technique is that the mechanical properties of the finished parts are superior to those of parts processed by die-casting. This research is to examine the possibility of fabricating a thin Mg alloy sheet adequate for superplastic gas-pressure forming and to evaluate the high-temperature mechanical properties of the sheet. Another objective of this study is to construct deformation mechanism maps (DMM) for Mg alloys at elevated temperatures. DMM can help a designer

to predict the dominant deformation mechanism at a questioned deformation conditions: temperature, stress and grain size.

2. EXPERIMENTAL PROCEDURES

The mean grain sizes (d=1.74×L, where L is the linear intercept grain size determined by optical micrography) of the as-received AZ61 and AZ31 alloys were 16μm and 150μm, respectively. The microstructure of the AZ61 alloy was refined by hot rolling at 648K after preheating for 0.5hr. The initial thickness (2.15mm) was reduced to 0.5mm after nine passes. The material was held in the heated furnace for 3~4 min. between the passes. The final grain size of the rolled AZ61 alloy was measured to be 8.7μm. In case of the AZ31 alloy, the grain size has been reduced to 11.5μm after rolling at 553K.

Elongation-to-failure tests were carried out at 623 K, 648 K and 673 K in the strain-rate range from 1×10^{-4} to 1×10^{-2} s^{-1}. The strain rate change (SRC) tests in the strain-rate range between 2×10^{-4} and 1×10^{-1} s^{-1} were performed to analyze the mechanisms of deformation at the temperature range between 598K and 673K.

Rolled AZ61 alloy sheet (thickness of 0.8 mm) was prepared into a disc (radius of 50 mm) for superplastic gas-pressure forming experiment. The forming temperature was 673 K and the applied gas-pressure was 0.46, 0.65, 0.8 and 1.20 MPa.

3. RESULTS AND DISCUSSION

3.1 Superplastic behavior in fine grained Mg alloy

The strain rate vs. stress relations established by the SRC tests for the rolled AZ61 and AZ31 alloys are presented in figure 1 (a) and (b). Deformation behaviors are divided into two regions: low stress exponent (n) region (n = 2-3) and high stress exponent region (n=5-7). The results of elongation-to-failure tests for the rolled AZ 61, and as-received and rolled AZ31 alloys are provided in figure 2.

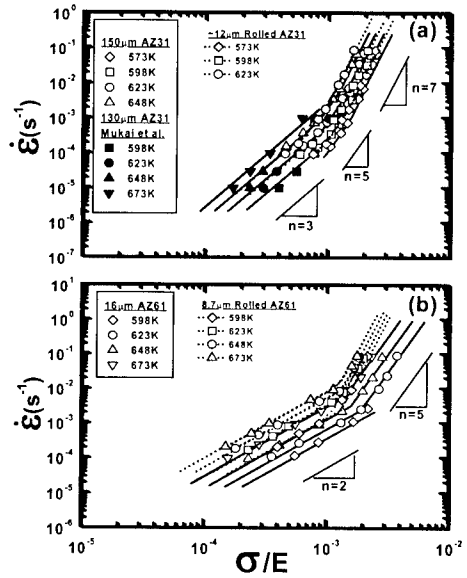

Figure 1. SRC tests for the rolled (a) AZ61 and (b) AZ31 alloys

The tensile elongation data of the AZ61 alloy obtained by Watanabe et al. [4] whose grain

size is very similar to that of the as-received AZ61 alloy in the current investigation, are also included in figure 1 (a) and figure 2 for comparison. In the rolled AZ 61 alloy, the largest tensile elongation of 580% was achieved at $2\times10^{-4}s^{-1}$ and at 673K. When strain rate was further increased, tensile elongation decreased monotonically.

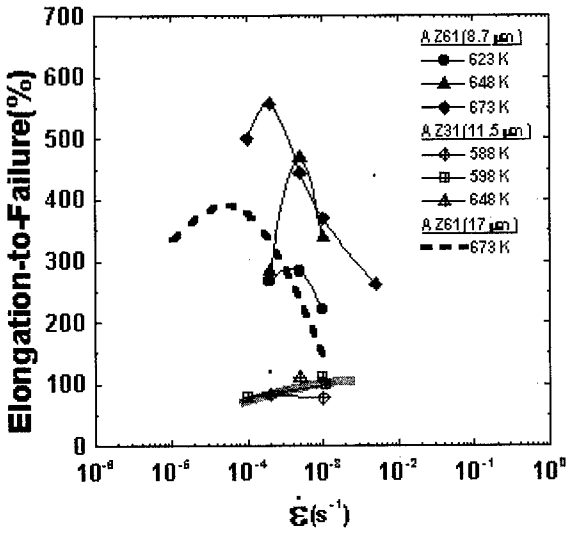

Figure 2. Elongation-to-failure results for the rolled AZ 61, and as-received and rolled AZ31 alloys

Creep process	Equations	k values	
		Sherby et al. [6]	This work for Mg
Nabarro-Herring Creep [7],[8]	(1) $\dot{\varepsilon} = k_1(D_L/d^2)(Eb^3/kT)(\sigma/E)$	14	14
Coble Creep [9]	(2) $\dot{\varepsilon} = k_2(D_{gb}b/d^3)(Eb^3/kT)(\sigma/E)$	50	50
D_L controlled GBS [10]	(3) $\dot{\varepsilon} = k_3(D_L/d^2)(\sigma/E)^2$	6.4×10^{9}	7.59×10^{8}
D_P controlled GBS [11]	(4) $\dot{\varepsilon} = k_4\alpha(D_P/d^2)(\sigma/E)^4$	3.2×10^{11}	3.81×10^{10}
D_{gb} controlled GBS [10]	(5) $\dot{\varepsilon} = k_5(D_{gb}b/d^3)(\sigma/E)^2$	5.6×10^{8}	7.04×10^{7}
Haper-Dorn Creep [12]	(6) $\dot{\varepsilon} = k_6(D_L/b^2)(Eb^3/kT)(\sigma/E)$	7×10^{-11}	7×10^{-11}
D_L controlled Slip [13]	(7) $\dot{\varepsilon} = k_7(D_L/b^2)(\sigma/E)^5$	1×10^{11}	6.67×10^{8}
D_P controlled Slip [13]	(8) $\dot{\varepsilon} = k_8(D_P/b^2)(\sigma/E)^7$	5×10^{12}	5.38×10^{8}
Solute drag creep	(9) $\dot{\varepsilon} = k_9D_S(\sigma/E)^3$	-	4.4×10^{20}
The material constants used for construction of the deformation mechanism map at T= 0.67Tm in **figure 5** are as follows.			
Pure Al	$E = 3.7\times10^{4}$MPa, $b = 3.21\times10^{-10}$m, $\alpha = 4$, $k = 1.38\times10^{-23}$JK^{-1} $D_L = 4.8\times10^{-16}$m^{2}sec^{-1}, $D_{gb} = D_p = 1.5\times10^{-10}$m^{2}sec^{-1}, $D_S = 1.2\times10^{-15}$m^{2}sec^{-1}		
Pure Mg	$E = 6.3\times10^{4}$MPa, $b = 2.86\times10^{-10}$m, $\alpha = 4$, $k = 1.38\times10^{-23}$JK^{-1} $D_L = 2.1\times10^{-16}$m^{2}sec^{-1}, $D_{gb} = D_p = 7.9\times10^{-12}$m^{2}sec^{-1}, $D_S = 1.4\times10^{-15}$m^{2}sec^{-1}		

Table 1. Constitutive equations used for the construction of the deformation mechanism maps.

However, it needs to be emphasized that a high tensile elongation of 375% was obtained at $10^{-3}s^{-1}$. Note that the coarse grained AZ61 alloy (d=17μm) exhibited a tensile elongation less

than 200% at the same temperature [4,5]. This increase in tensile ductility and superplastic strain rate in the rolled AZ61 alloy can be directly attributed to the decrease in grain size. No improvement in tensile ductility was, on the other hand, observed in the rolled AZ31 alloy. This is because of the rapid grain growth during deformation. The grain sizes measured after the elongation-to-failure test were often above 100μm.

This microstructural instability of the fine-grained AZ31 alloy can be attributed to the presence of a small amount of second particles at the testing temperatures based on a Mg-Al binary phase diagram indicating that all of $Mg_{17}Al_{12}$ phase particles dissolve into Mg matrix above 473K.

3.2 Deformation mechanism map(DMM) constructed for Mg alloy

In order to build a proper DMM for Mg alloys, k values in the constitutive equations in **Table 1** need to be evaluated using the experimental data obtained at various test conditions. The effort is summarized in **figure 3**. In **figure 3(a)**, the plots for dislocation climb creep controlled by D_L (n=5) and D_p (n=7) are exhibited. In **figure 3(b) and 3(c)**, the plot for GBS controlled by DL (n=2) and Dgb (n=2) are presented. Finally, solute drag creep associated with n=3 was evaluated in **figure 3(d)**.

The DMM in **figure 4** is the one constructed at 623 K using the k values analyzed based on **figure 3**, which is listed in **Table 1**. Data points in **figure 4** refer to Mg alloys reported by various investigators (**Table 2**) and they clearly demonstrate the prediction capability of the newly constructed DMMs for Mg alloys.

Differences between **figure 4** and **figure 5** are now discussed in detail. **Figure 5** is a DMM for magnesium constructed using the constitutive equations developed by Ruano et al. [6] (**Table 1**) based upon a number of close packed metals with high stacking fault energy. First, the D_p controlled GBS region in **figure 5** is completely replaced by the D_{gb} controlled GBS mechanism in **figure 4**. As the result, the revised DDM predicts the deformation behavior of the fine-grained Mg alloys correctly.

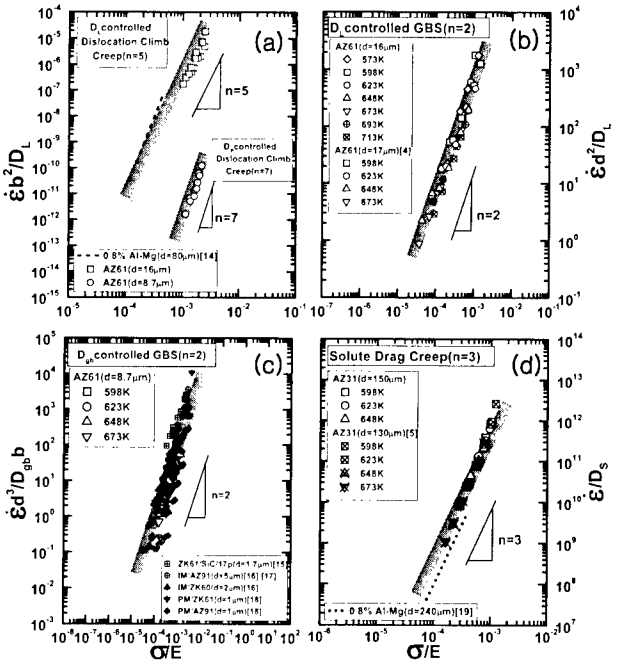

Figure 3. Diffusion coefficient compensated strain rate vs. elastic-modulus compensated flow stress, showing the presence of various deformation mechanisms in Mg alloys; (a) D_L and D_p controlled dislocation climb creeps, (b) D_L controlled GBS, (c) D_{gb} controlled GBS and (d) solute drag creep

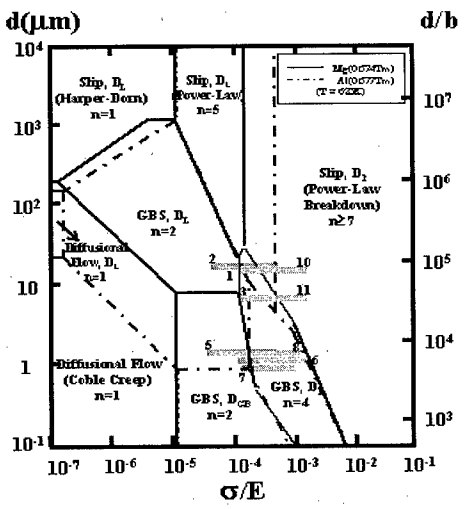

Figure 4. Modified deformation map const -ructed for magnesium alloys at 623K.

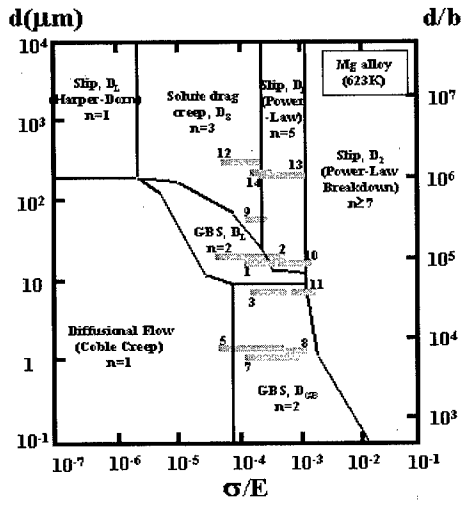

Figure 5. Deformation map constructed for pure Mg and pure Al at 623K.

	Alloys	d (μm)	Temp.(K)	ε (s^{-1})	,n	Q (kJ/mol)
1	AZ61[This work]	16	573~693	10^{-4}~$3x10^{-3}$	2	124
2	AZ61	17	598~673	10^{-5}~10^{-3}	2	143
3	AZ61	8.7	598~673	$2x10^{-4}$~10^{-2}	2	91
4-1	IM/AZ91	5	573	$3x10^{-4}$~$1.5x10^{-1}$	2	121
4-2	IM/AZ91	9	573	$3x10^{-4}$~$1.5x10^{-1}$	2	-
4-3	IM/AZ91	16	573	$3x10^{-4}$~$1.5x10^{-1}$	2	-
5	IM/ZK60	~2	523~773	$2x10^{-4}$~10^{-1}	2	118
6	PM/ZK61	~1	523~623	10^{-3}~10^{1}	2	118
7	PM/AZ91	~1	543~673	10^{-3}~10^{0}	2	121
8	ZK61/SiC/17p	~1.7	598~773	10^{-1}~10^{1}	2	81
9	0.8% Al-Mg	80	473~623	$5x10^{-8}$~$3x10^{-5}$	5	135±10
10	AZ61 [This work]	16	598~693	$1x10^{-3}$~$3.5x10^{-3}$	5	159
11	AZ61[This work]	8.7	598~673	$5x10^{-3}$~10^{-1}	7	80
12	0.8%Al-Mg [11]	240	523~623	$5x10^{-8}$~$6x10^{-6}$	3	140±10
13	AZ31[This work]	~150	573~648	$2x10^{-4}$~$7x10^{-2}$	3	122
14	AZ31[6]	~130	598~673	10^{-5}~10^{-3}	3	127

Table 2. Experimental data of various Mg alloys.

Second, the coble creep region has extended to higher σ/E coordinate by an order of magnitude in all three temperatures, and thus reduced the D_L-controlled GBS region. The third difference is that solute drag creep appears in **figure 5** between Harper-Dorn creep and D_L-controlled dislocation climb creep. Again, experimental data associated with n=3 and $Q \approx Q_s$ (=143kJ/mole),

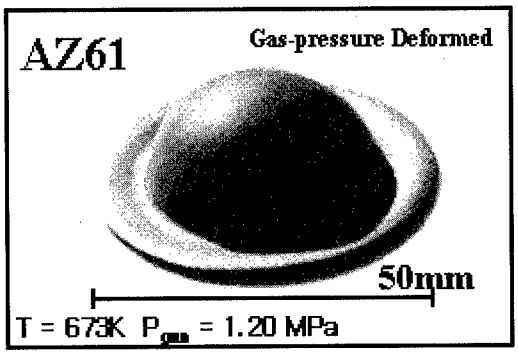

Figure 6. Hemi-spherical AZ61 dome fabricated by gas-pressure deformation.

where Q_s is the activation energy for D_s, are in good agreement with the modified map.

3.3 Superplastic formability of the AZ61 alloy

Superplastic formability of the rolled AZ61 alloy was demonstrated by forming the sheet prepared by using the present thermomechanical treatment into a shape of a hemi-spherical dome. Three different gas pressure conditions were used (P_{gas} = 0.46, 0.65 and 1.20 MPa). In all the three cases, sound dome shape could be successfully obtained. A dome shaped at the highest gas pressure (apex strain rate =~$5x10^{-3}s^{-1}$) is shown in **figure 6**. No visible surface cracking or cavitation was observed. It was taken about 4 minutes for the forming. This result indicates that conventional gas pressure forming techniques that have been used for aluminum alloys can be also well applicable to Mg alloys at reasonably high forming rates.

4. SUMMARY

Thin Mg alloy sheets with microstructures suitable for superplasticity could be fabricated by hot-rolling process. Deformation mechanisms of Mg alloys at elevated temperatures were constructed using the experimental data of a variety of Mg alloys with different grain sizes, stress exponent and activation energies for plastic flow. Excellent correlation between the experimental data for Mg alloys and the map prediction confirms the usefulness of the current deformation mechanism maps. Superplastic Gas-pressure forming technique was found to be applicable to Mg alloys at reasonably high forming speed.

Acknowledgement
This work was supported by KOSEF 2000.

REFERENCES

1. M. M. Avedesian and H. Baker, ASM Specialty Handbook. American Society for Metals, Materials Park, OH (1999), p.5.
2. J. Davis, SAE Technical Paper #850419, SAE International, Detroit, Michigan (1985), USA.
3. J. Davis, SAE Technical Paper #910551, SAE International, Detroit, Michigan (1991), USA.
4. H. Watanabe, T. Mukai, M. Kohzu, S. Tanabe, and K. Higashi, Acta. Mater., **47**(1999), p.3753.
5. T. Mukai, H. Tsutsui, H. Watanabe, K. Ishikawa, Y. Okanda, M. Kohzu, S. Tanabe and K. Higashi, The 8th International Conference on Creep and Fracture of Engineering Materials and Structures, T. Sakuma and K. Yagi, eds., Key Engineering Materials, Trans Tech Publications, Tsukuba, Japan, Vols.171-174 (2000), p.337.
A. Ruano, J. Wadsworth and O. D. Sherby, J. of Mater. Sci., **20** (1985), p.3735.
6. C. Herring, J. Appl. Phys., **21** (1950), p.437.
7. F. R. N. Nabarro, in Report of the Conference on the Strength of solids, The Physical Society, London, England (1948), p.75.
8. R. L. Coble, J. Appl. Phys., **34** (1963), p.1679.
9. H. Luthy, R. A. White, and O. D. Sherby, Mater. Sci. Eng., **39** (1979), p.211.
A. Ruano, and O. D. Sherby, Mater. Sci. Eng., **51** (1981), p.9.
10. J. Harper and J. E. Dorn, Acta Metall., **5** (1957), p.564.
11. S. L. Robinson and O. D. Sherby, Acta Metall., **17** (1969), p.109.
12. S. S. Vagarali and T. G. Landon, Acta Metall., **29** (1981), p.1969.
13. . T. Mukai, T. G. Nieh, H. Iwasaki and K. Higashi, Mater. Sci. and Tech., **14** (1998), p.32.
14. M. Mabuchi, T. Asahina, H. Iwasaki, and K. Higashi, Mater. Sci. and Tech., **13** (1997), p.825.
15. K. Kubota, M. Mabuchi and K. Higashi, J. of Mater. Sci., **34** (1999), p.2255.
16. M. Mabuchi, T. Mohri, N. Saito, M. Nakamura, H. Iwasaki, and K. Higashi, The 3rd Pacific Rim International Conference on Advanced Materials and Processing (PRICM3), M.A. Imam, R. DeNale, S. Hanada, Z. Zhong and D.N. Lee, eds., The Minerals, Metals & Materials Society, Honolulu, USA, (1998), p.1813.
17. S. S. Vagarali and T. G. Landon, Acta Metall., **30** (1982), p.1157.
18. M. Mabuchi, K. Ameyama, H. Iwasaki, and K. Higashi, Acta. Mater., **47**(1999), p. 2047.

SUPERPLASTIC DEFORMATION BEHAVIOR OF Fe-Al INTERMETALLIC ALLOYS

Jin-Hwa Song, Tae Kwon Ha*, Hyun Tae Lim*, and Young Won Chang*

Research Institute of Industrial Science & Technology, Pohang 790-600, Korea
*Center for Advanced Aerospace Materials (CAAM)
Pohang University of Science and Technology, Pohang 790-784, Korea

ABSTRACT

Superplastic deformation behavior of large-grained iron aluminides of the composition of Fe-28 at.% Al has been investigated. The average grain size used in this study was about 500 μm. A series of load relaxation and tensile tests have been conducted at temperatures ranging from 600 to 850°C. The flow curves obtained from load relaxation tests were found to have a sigmoidal shape and to exhibit stress vs. strain rate data in a very wide strain rate range from 10^{-7}/s to 10^{-2}/s. Tensile tests have been conducted at various initial strain rates ranging from 3×10^{-5}/s to 1×10^{-2}/s. Maximum elongation of ~500 % was obtained at the initial strain rate of 3×10^{-5}/s and the maximum strain rate sensitivity was found to be 0.68 at 850°C. Microstructure observation through the optical microscopy (OM) and the electron back-scattered diffraction (EBSD) technique has been carried out on the deformed specimens and the evidences for grain boundary migration and grain refinement during superplastic deformation have been revealed, suggesting the dynamic recrystallization mechanism. The addition of Cr by the amount of 5 at.% appeared to increase the high temperature strength but decrease the elongation.

1. INTRODUCTION

Structural superplasticity (SSP) has been usually exhibited in fine-grained materials (~10 μm) under the optimum conditions of strain rate and test temperature [1-3]. Some fine-grained intermetallic compounds, such as Ni_3Al, Ni_3Si, Ti_3Al, and TiAl, have been reported to show an excellent structural superplasticity [4]. Interestingly, the coarse-grained superplasticity has also been reported in Fe-Al based alloys with a grain size of 100~350 μm [5, 6] or even 700~800 μm [7, 8]. All the deformation characteristics such as a large value of strain rate sensitivity, a low flow stresses independent of strain, and high ductility have been exhibited in large-grained Fe-Al based alloys. The mechanism of large-grained superplasticity has, however, been reported and thought to be different from that of the conventional fine-grained superplasticity.

To understand the exact mechanism of a high temperature deformation behavior such as creep and superplasticity, wide range of flow data is necessary. It is well known that load relaxation test can provide a much wider range of strain rates, applying only a little amount of plastic strain to the specimen without an appreciable change in microstructures [9]. It has been attempted, in this study, to establish a better understanding of the mechanism for the large-grained superplasticity and the effect of Cr-addition in Fe-Al based alloys, by

employing the high temperature load relaxation test and by applying the recently proposed internal variable theory of inelastic deformation [10].

2. EXPERIMENTAL PROCEDURE

Iron aluminides with compositions of Fe-28at.%Al and Fe-28at.%Al-5at.%Cr, hereafter denoted by binary alloy and ternary alloy, respectively were prepared by vacuum induction melting using the 99.99% purity electrolytic Iron, 99.99% purity Aluminum, and 99.9% purity Chromium. The ingots were homogenized at 1000°C for 5 hrs and then rolled from 30 mm to 9 mm in thickness, starting at 1000°C and finishing at 800°C. Rod type specimens with the gauge dimensions of 6 mm in diameter and 27 mm in length for load relaxation tests and plate type specimens with 5 mm in length and 3 mm in thickness for tensile tests, respectively, were machined from the hot rolled plates. These specimens were then recrystallized at 857°C for 1 hr followed by an oil quenching.

Load relaxation tests were then carried out at the temperatures from 600 to 850°C by using a computer controlled electro-mechanical testing machine (Instron 1361 model) attached with a furnace capable of maintaining the temperature fluctuation within ± 1°C. It is well known that load relaxation test can provide a much wider range of strain rates, applying a little amount of plastic strain, 1.5 % in this study, to the specimen without an appreciable change in microstructures [9]. Loading strain rate was 5×10^{-2}/s in all cases. The flow stresses as a function of the inelastic strain rate were determined by following the usual procedure described in the literature [11]. A series of tensile tests were also carried out under the various strain rates ranging from 3×10^{-5}/s to 10^{-2}/s to examine superplastic deformation behavior. Deformed microstructure was observed using the conventional optical microscopy (OM) and the electron back-scattered diffraction (EBSD) technique.

3. RESULTS AND DISCUSSION

3.1. Grain size

The grain sizes of the thermomechanically-processed materials were very large around 500 μm for binary and about 700 μm for ternary alloys, respectively. Each grain appeared to be equiaxed in both alloys.

3.2. Superplastic deformation behavior of the binary alloy

The flow curves obtained from load relaxation tests conducted on the binary alloy at temperatures ranging from 600 to 850°C are summarized in Fig. 1. It is noted that flow data obtained are ranging from near 10^{-7}/s to 10^{-2}/s in strain rate. The flow curves are of the sigmoidal shape with maximum strain rate sensitivity, m, in the intermediate strain rate range, which appeared to shift into faster region with increase in testing temperature. Depending on test temperatures, m values varied from 0.28 to 0.68 in lower strain rate range ($\dot{\varepsilon} \leq 10^{-4}$/s) and from 0.16 to 0.22 in higher strain rate range ($\dot{\varepsilon} \geq 10^{-4}$/s). The m value in higher strain rate range obtained in this study is somewhat lower than that ($m \approx 0.3$) obtained by Chu et al. in Fe-27at.% Al at 800°C [7]. The difference in m value is thought to be attributed to the

difference in grain size and the test method. Maximum value of m has been obtained as 0.68 in the binary alloy, which is the largest ever reported for binary Fe-Al alloys. Close examination of the flow curves reveals that there exist rate-insensitive portions in flow curves except at 850°C, at very low strain rate region around 10^{-7}/s. From the viewpoint of the internal variable theory of inelastic deformation [10], frictional resistance to dislocation motion due to lattices is considered to be predominant mechanism in this strain rate region. Tensile test results of the binary alloy conducted at 850°C under the initial strain rates from 3×10^{-5}/s to 10^{-2}/s are summarized in Fig. 2 as engineering stress vs. engineering strain curves. With decrease in the initial strain rate, elongation to failure increased up to ~500 %, which is also the largest elongation ever reported for binary Fe-Al alloys. The whole gauge section of specimens appeared to be stretched and necking was developed severely.

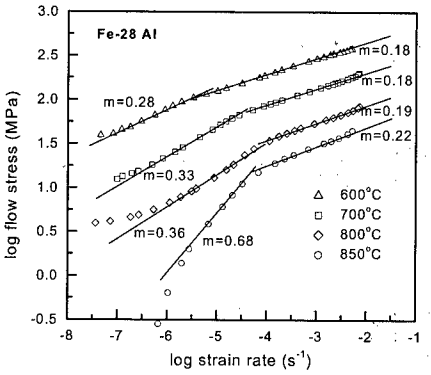

Fig. 1. Flow curves obtained from load relaxation tests on Fe-28 at.% Al alloy conducted at various temperatures.

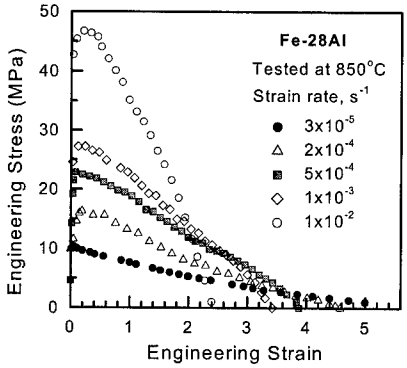

Fig. 2. Tensile test results of Fe-28 at.% Al alloy obtained at 850°C given as engineering stress vs. engineering strain curves.

3.3. Microstructure evolution

In order to examine the microstructure evolution, longitudinal optical micrographs were taken from fractured specimens along the gauge section and they are shown in Fig. 3. Some grain boundary cavities were found in the specimen tested at the initial strain rate of 10^{-2}/s. Despite large elongations to failure, elongated grain structure is not prominent but irregularly curved

grain boundaries, evidence for possible grain boundary migration, were observed at the strain rates of 10^{-2}/s and 10^{-3}/s. Partially and fully recrystallized structures can be noted in the specimens deformed at 10^{-3}/s and 10^{-4}/s, respectively. Grain refinement can be observed in all cases at the tip region of fractured specimens. As the strain rate decreased, grain refinement appeared more severe over the whole gauge region. The aspects of grain boundary migration and dynamic recrystallization during superplastic deformation in iron aluminides are exactly consistent with other researchers' observations [5, 6]. Recently, for example, Chu et al. [8] have summarized the microstructure evolution during superplastic deformation of coarse-grained iron aluminides as the sequence of three stages, i.e. subgrain-boundary formation, grain-boundary migration, and formation of recrystallized grains. From the electron back-scattered diffraction (EBSD) investigation as shown in Fig. 4, a large number of small-angle boundaries near a grain boundary of the gauge region have been observed.

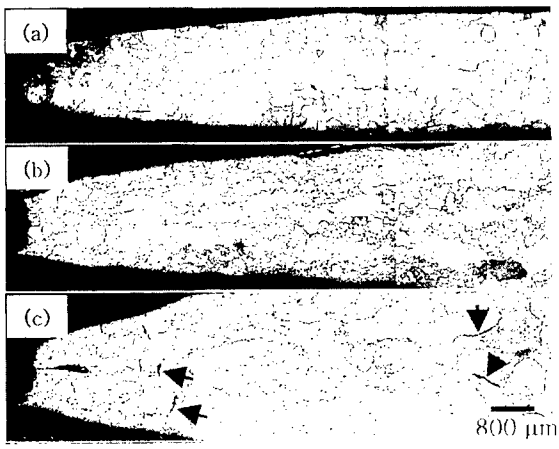

Fig. 3. Optical micrographs taken from surfaces of specimens fractured at 850°C under the strain rate of (a) 2×10^{-4}/s, (b) 1×10^{-3}/s, and (c) 1×10^{-2}/s, respectively.

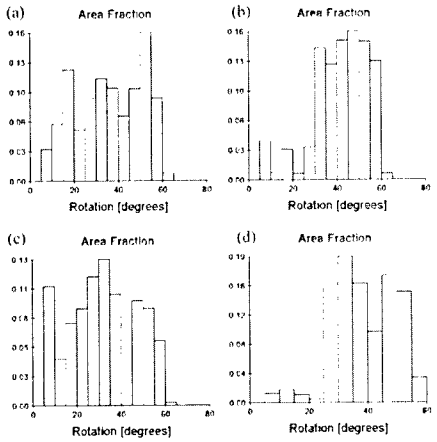

Fig. 4. Frequency histograms of grain or subgrain misorientation taken from the specimens deformed at 850°C under the strain rate of 1×10^{-3}/s, (a) gauge and (b) grip parts, and that of 3×10^{-5}/s, (c) gauge and (d) grip parts, respectively.

3.4. Activation energy

From the flow data given in Fig. 2, activation energy Q can be calculated by plotting the ln σ against 1/T at a given strain rate [6]. The strain rate of 10^{-3}/s was chosen and the Q value was obtained as 387 kJ/mol in this study as illustrated in Fig. 5. It is interesting to note that the activation energy obtained in the present study is very similar to that for creep deformation of Fe-27at.%Al alloy [12], suggesting that the mechanism operating during the superplastic deformation of the binary alloy in the strain rate range higher than 10^{-4}/s is likely controlled by the lattice diffusion.

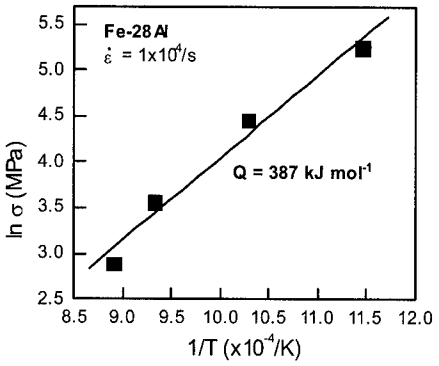

Fig. 5. The plot of ln σ vs. 1/T at the initial strain rate of $\dot{\varepsilon} = 1\times10^{-3}$/s, providing a means to determine the activation energy.

3.5. Effect of Cr-addition

The deformation behavior and the microstructure evolution of the ternary alloy were very similar to those of the binary alloy. The flow curves obtained at the temperature range from 600 to 850 °C are shown in Fig. 6(a) and the maximum value of strain rate sensitivity was evaluated as 0.40, which is somewhat lower than that of the binary alloy. Elongation to failure was also found to be comparable to but slightly lower than the binary alloy. The maximum elongation of the ternary alloy was obtained as about 400 % at 850°C as shown in Fig. 6(b). It is, also, noted from this figure that the peak stress of the ternary alloy is higher than that of the binary alloy. This implies that the ternary alloy is expected to show higher resistance to high temperature creep deformation than the binary alloy.

The activation energy of the ternary alloy was calculated from Fig. 6(a) and obtained as 414 kJ/mol, somewhat higher but very close to that of the binary alloy. Surface observation of deformed specimens revealed that the dynamic recrystallization appeared to be retarded in the ternary alloy. The reduced elongation of the ternary alloy, compared with the binary alloy, seems to be mainly attributed to the less active dynamic recrystallization.

4. SUMMARY

The flow curves of Fe_3Al based alloys were sigmoidal shape and the strain rate range of maximum m value, appeared to shift into faster region with increase in testing temperature. A large elongation of about 500 % was obtained in the binary alloy with the maximum m value

of about 0.68, which is the largest ever reported for binary Fe-Al alloys. Microstructure observation revealed the evidences for the strain-induced grain boundary migration and dynamic recrystallization during the deformation at 850°C. The addition of Cr seemingly retarded the dynamic recrystallization. The activation energy Q of 387 kJ/mol for binary and 414 kJ/mol for ternary alloy suggested that the mechanism operating during the superplastic deformation in the strain rate range higher than 10^{-4}/s is likely controlled by the lattice diffusion. The addition of Cr to the binary alloy appeared to increase the high temperature strength but decrease the elongation.

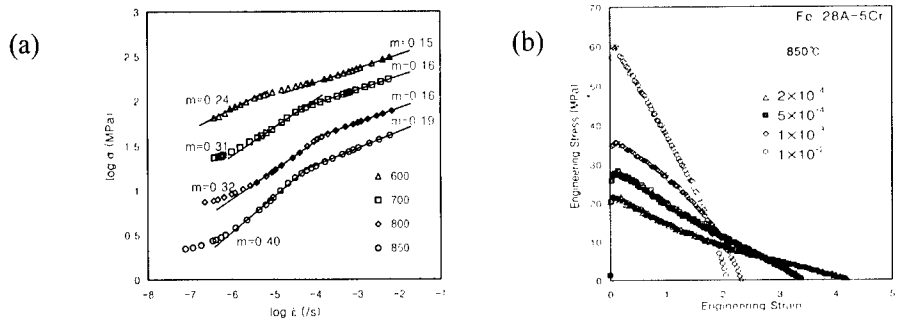

Fig. 6. (a) The flow curves obtained at the various temperatures and (b) tensile elongations at 850°C of the ternary alloy.

REFERENCES

1. A. H. Chokshi, A. K. Mukherjee, and T. G. Langdon, Mater. Sci. Eng. R10 (1993), p. 237.
2. O. D. Sherby, and J. Wadsworth, Prog. Mater. Sci., 33 (1989), p. 169.
3. K. A. Padmanabhan, and G. J. Davis, "*Superplasticity*", Springer-Verlag, New York, NY (1980) p. 11.
4. T. G. Nieh, J. Wadsworth, and O. D. Sherby, "*Superplasticity in Metals and Ceramics*", Cambridge Univ. Press, Cambridge, (1997), p. 125.
5. D. Lin, T. L. Lin, A. Shan and M. Chen, Intermetallics 4 (1996) p. 489.
6. D. Lin, D. Li, and Y. Liu, Intermetallics 6 (1998) , p. 243.
7. J. P. Chu, I. M. Liu, J. H. Wu, W. Kai, J. Y. Wang, and K. Inoue, Mater. Sci. Eng. A258 (1998) p. 236.
8. J. P. Chu, H. Y. Yasda, Y. Umakoshi, and K. Inoue, Intermetallics 8 (2000) p. 39.
9. E. W. Hart, "*Stress Relaxation Testing*", A. Fox ed., ASTM, Baltimore, Md. (1979), p. 5.
10. T. K. Ha, and Y. W. Chang, Acta Mater. 46 (1998), p. 2741.
11. D. Lee, and E. W. Hart, Metall. Trans., 2A (1971), p. 1245.
12. C. G. McKamey, P. J. Masiasz, J. W. Jones, J. Mater. Res. 7 (1992), p. 2089.

Session V

JOINING

DEVELOPMENT OF HIGH DEPOSITION RATE DOUBLE WIRE MIG WELDING PROCESS FOR ALUMINUM ALLOY

BY Takeshi Shinoda, Jitsuo Nakata* and Hideki Miyauchi*

Nagoya University, Materials Processing Department, Nagoya, 464-8603 JAPAN

*Technical Development Department, Air Water Inc., Wakayama, 640-8404 JAPAN

ABSTRACT

An improved MIG welding process has been developed as double wire gas metal arc (DW MIG) welding in which a cold filler wire (called filler wire hereafter) is fed into the molten pool behind the main electrode wire. It is possible to increase the threshold welding current at which puckering occurs to higher values. The formation of puckered beads at high welding currents is a well known phenomenon that occurs in MIG welding of aluminum alloys. The foremost features of DW MIG welding is increased deposition rates and increased welding speed up to 200 cm/min and decreased molten pool temperature up to 200 K. This temperature descend makes positive effects such as preventing formation of puckered bead, stable formation of root bead to square butt welding, decreasing angular distortion and prevention of solidification cracking.

1. DEVELOPMENT OF THE DW MIG WELDING PROCESS

The development of a high efficiency welding process for welding aluminum alloys is considered to be quite important. There are already several practical examples of feeding a second wire into the molten pool (cold or hot wire welding) in order to achieve high deposition rates in gas tungsten arc (GTA) and MIG welding [1]. Recently, double wire MIG welding process for aluminum has been proposed using parallel arcs from independent two power sources [2,3]. These methods are mainly used for welding steels. Hot wire welding appears not to have been applied to welding aluminum alloys. One of the reasons for this is the low electrical resistance of aluminum. Although the melting temperature of aluminum is around 933 K, the temperature of the molten pool in MIG welding of aluminum alloys is higher than 1500 K.

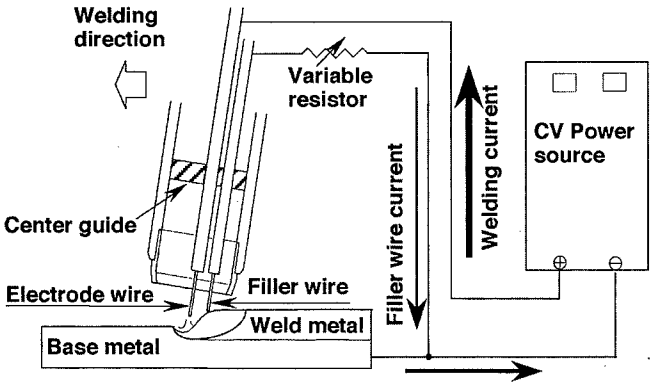

Fig.1 Principal set up of DW MIG welding process

Therefore, it can be considered that feeding of a filler wire into a molten pool with surplus heat would make it possible to increase the deposition rate and improve welding productivities. In the DW MIG process, the filler wire which is positioned behind and parallel to the electrode wire within the a nozzle is fed into and melts in the molten pool produced by the leading electrode wire as shown in Fig. 1.

Because of this arrangement, the torch can be designed to be compact, having a nozzle inner diameter of only 19 mm which is the same as that of conventional MIG welding torches. During welding, a part of the welding current flowing from the base metal to the earth terminal of the welding power source is drawn through the filler wire. For this purpose a splitting circuit was incorporated in a 500 A capacity inverter controlled welding power source with constant voltage characteristics.

Since the direction of the current flow in the electrode wire is opposite to that in the filler wire, the resultant repulsive force deflects the arc in the forward direction. This means that even if the filler wire is positioned close to the electrode wire, it can be fed into the molten pool smoothly. If the current drawn through the filler wire is too high, the arc gets deflected too much and affects welding stability. For this reason, a variable resistor was included in the splitting circuit in order to adjust the split current to a suitable value.Welding current is supplied from one constant voltage power source. Usually, the latter is fed into the molten pool 4 to 5 mm behind the former. When no filler wire is fed, the welding is conventional MIG welding.

2. PROCEDURE TOLERANCE OF DW MIG WELDING PROCESS

The foremost feature of DW MIG welding improves process tolerances. Figure 2 shows a comparative example of stable full penetration ranges for tapered plate thickness without backing support between conventional MIG and DW MIG welding processes. The critical plate thickness to burn-through of DW MIG welding was much wider than that of conventional MIG process illustrated by arrows where burn-through was occurred and lines meant stable root bead formation ranges.

It reveals that DW MIG welding had much wider process tolerance and full penetration can be achieved from 4.7 mm to 2.2 mm plate thickness under 470 A of welding current. Deposition rates obtained in DW MIG welding is more than twice that of conventional MIG welding. The bead width of DW MIG welds is almost unaffected by the increased deposition rate, but the height of reinforcement increases and the penetration depth decreases slightly.

Procedure tolerance is also examined using 4mm thickness 5083 plate. Welding were performed by conventional single wire MIG welding process and developed Double Wire MIG welding. The conditions of the critical burn through penetration is compared MIG and DW MIG under several travel speed and current combinations.

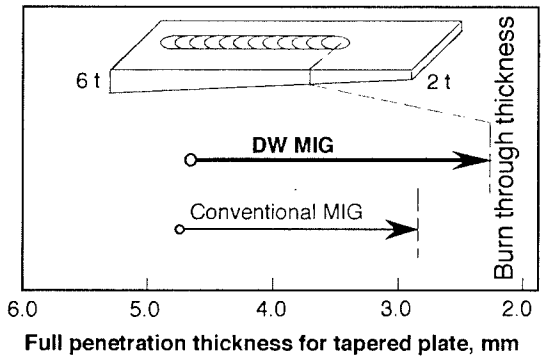

Fig. 2 Comparison of full penetration thickness using tapered plate without backing suport

The results are shown in Fig. 3 where conventional MIG process gave small full penetration zone, almost line area. DW MIG shows relatively higher welding current in case of the same welding speed, and much wider tolerance parameters.

3. DETERMINATION OF THE CRITICAL PUCKERING WELDING CURRENT

Bead on plate welds were made in the down hand position on aluminum alloy plates (400 mm x 73 mm 5083-O alloy), of 10, 12 and 15 mm in thickness. As electrode and filler wires, 5183 alloy wires were used for welding trials. In the case of DW MIG welding, the diameter of main electrode wire was 2.4 mm and that of the cold filler wire 1.6 mm. Experiments by conventional MIG welding performed for comparison the diameter of the electrode wire was 2.4 mm.

The welding conditions which were maintained constant were, welding speed (100 cm/min), wire extension (20 mm) and nozzle to base metal distance (13 mm). The deposition rate of the electrode wire was 1.03 g/s at 400 A, and 1.28 g/s at 500 A, respectively. In the DW MIG welding experiments, the range of deposition rates of the filler wire was controlled so that at the maximum, the deposition rate of filler wire matched that of electrode wire.

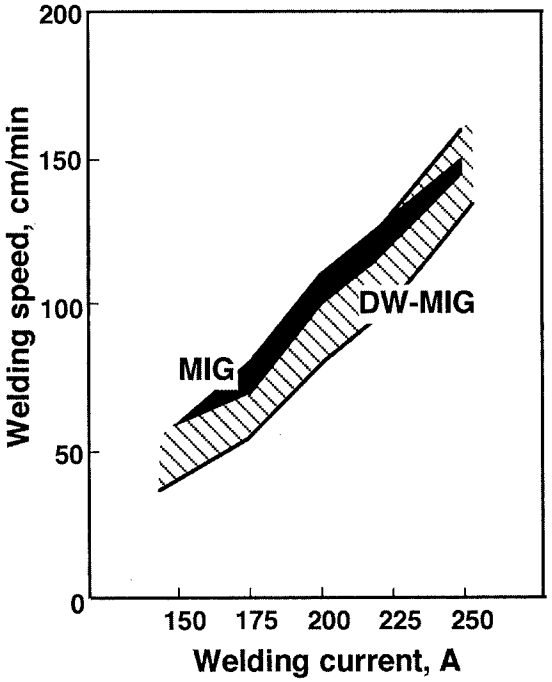

Fig. 3 Comparison of the critical burn through current for conventional MIG welding ang DW MIG welding process

Plate thickness: 4mm, without bucking materials

Bead on plate welds were made by MIG and by DW MIG welding and the threshold welding current at which puckering appeared was determined. During DW MIG welding, the welding current was gradually increased from a low initial current value up to the threshold welding current in order to determine the relation between the deposition rate of the filler wire and the threshold welding current.

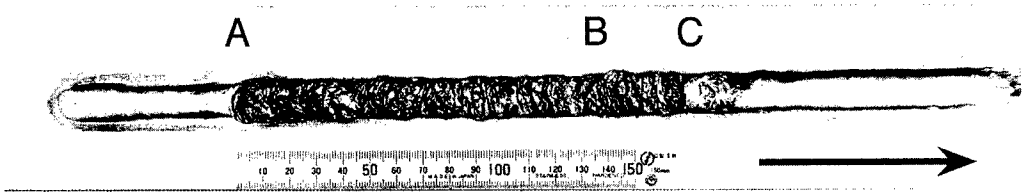

Fig. 4 Appearance of puckered bead in conventional MIG welding and arrest of puckering by DW MIG welding process

Figure 4 shows the appearance of a bead on plate weld first made by MIG welding, followed by DW MIG mode. The welding current in this case was 470 A which was higher than the threshold value for MIG welding. On the beginning of MIG welding, the bead was initially sound but puckering suddenly appeared at point A. At point B the welding mode was changed to DW MIG with filler wire addition of 0.58 g/s, and it could be observed that puckering disappeared from point C onwards

4. THE THRESHOLD WELDING CURRENT TO PUCKERING

Bead on plate welds and fillet welds were made in the down hand position under various combinations of welding current, arc voltage and torch inclination in order to confirm the effectiveness of DW MIG welding on arresting puckering.

Figure 5 collates the results obtained from the bead on plate welding experiments on 12 mm thick plates, and this figure shows the effect of welding current and filler wire deposition rate on the occurrence of puckering. In the MIG welding mode, the threshold welding current was about 440 A. In the DW MIG mode, however, the threshold current shifted towards progressively higher values with increasing filler wire feed. With a filler wire deposition rate of more than 0.4 g/s which was about 40% of the wire deposition rate (about 1.1 g/s) in MIG welding, the threshold current was increased by about 20 A.

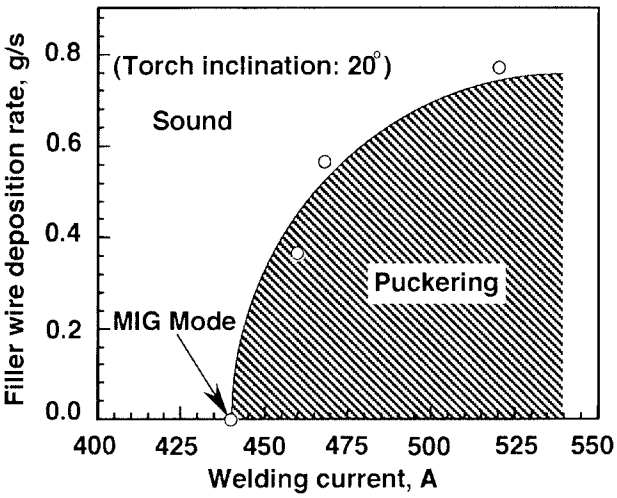

Fig.5 Effect of welding current and filler wire addition on puckering phenomenon for bead on plate experiments

Results of the above experiments confirmed that by using DW MIG welding, the threshold welding current is increased. When puckering occurs, it was observed that the molten metal tends to spout from the molten pool due to the arc force. This suggests that one of the reasons for DW MIG being effective for arresting puckering is that feeding of the 'cold' filler wire decreases the temperature of the molten pool which results in increased viscosity of the molten metal.

The temperature of the molten pool in MIG and DW MIG welding was measured in order to confirm this point. A CA-thermocouple of 1 mm in diameter was attached to the stationary welding nozzle via the guide under the specimen traveling so that the tip of the thermocouple entered the molten pool at a location approximately 1 mm behind the filler wire. With this arrangement, the molten pool temperature could be measured continuously during welding. After welding initially in the DW MIG mode with a filler wire deposition rate of 0.58 g/s, the welding was changed to the MIG mode by stopping the filler wire feed. The temperature in DW MIG is around 1000 K and is about 200 K lower than that measured in MIG welding. It can be inferred from this that in DW MIG welding, because of the lowering of temperature caused by 'cold' wire feeding, the viscosity of the molten metal is increased [4] and that the lower temperature and higher viscosity help to restrain the spout of the molten metal caused by arc force, thus preventing puckering.

5. OBSERVATION OF MOLTEN POOL BEHAVIOR AT PUCKERING

Figure 6 shows typical high speed video photographs of the arc and molten pool taken before, during and after the occurrence of puckering. The welding conditions were, welding current, 470 A, arc voltage, 29 V and filler wire deposition rate, 0.58 g/s. The time elapsed after commencing welding is shown at the top of each frame. The four frames, from 4.808 seconds up to 16.838 seconds after commencing welding are illustrated in the figure.

Figure 6-A (4.808 seconds after commencing welding) shows the condition in 'single electrode wire' MIG welding with spray transfer. The molten pool is stable and its surface is stationary. After 7.132 seconds (Fig. 6-B), the rear wall of the molten pool is seen to rise up and the molten pool has become sharply depressed directly under the electrode wire. After this moment, the arc is observed to have been blown slightly toward the front of the molten pool and at the same time, the rear wall of the molten pool is beginning to fall down. Hereafter, puckering appears 0.020 seconds later and Fig. 6-C (7.152 seconds) shows the state of the arc and molten pool at this instant.

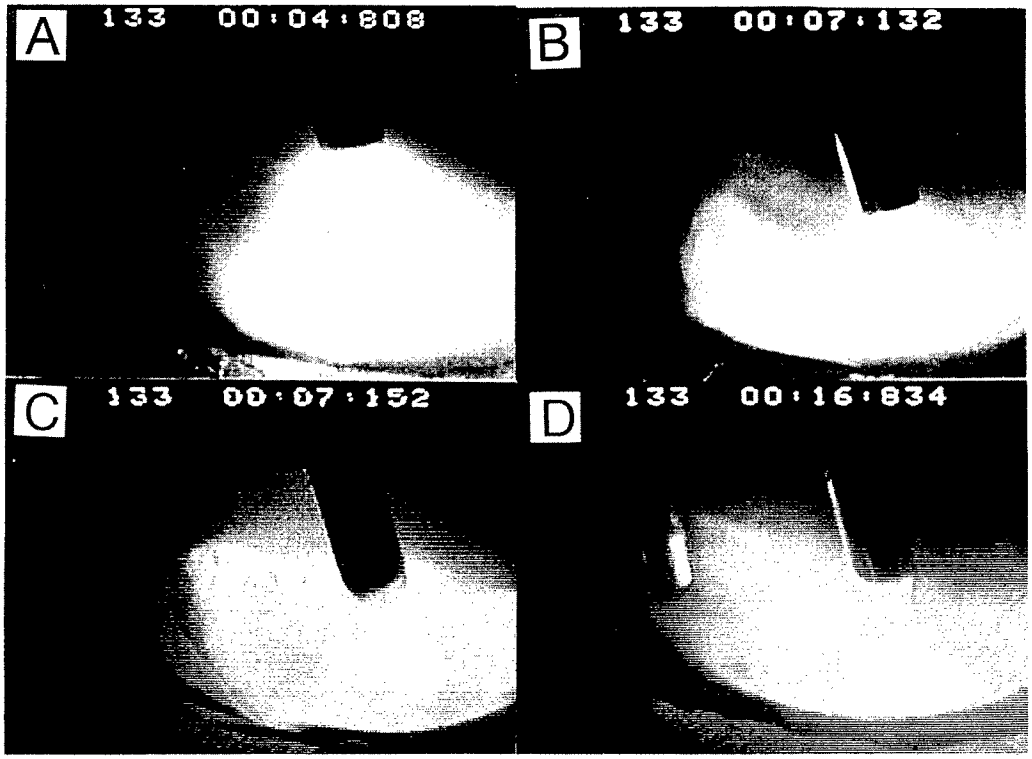

Fig. 6 High speed video photographs of the arc and weld pool during recovery from puckering by filler wire feed by DW MIG welding mode

The surface of the molten pool has sunken sharply and cathode spots are recognized to have formed at the rear wall of the molten pool. This is believed to happen due to breakdown of the gas shielding [5]. As a result, the tip of the electrode wire which was sharply pointed in the spray transfer mode in Fig. 6-A, has become rounded and the arc has become narrower. After 7.152 seconds (Fig. 6-C), the condition is not altered much, but the arc is being blown toward the rear of the molten pool and the liquid surface at the rear of the molten pool is collapsing.

The welding was changed to the DW MIG mode by feeding the filler wire while puckering was taking place. In Fig. 6-D (16.834 seconds), puckering has been arrested by the cold filler wire feed and the tip of the electrode wire has returned to the original pointed state in the spray transfer mode. The rear wall of the molten pool has become smooth and its height has decreased. Almost immediately after this, a wall with a small height difference can be noticed at the rear of the molten pool. The crater into which the filler wire is being fed is very smooth and stable. The bead has become smooth without any sign of wrinkles which are typical of puckering.

The above observations suggest that sequence of events leading to puckering is as follows:

Under high currents where the arc force is large, the molten metal is pushed up toward the rear of the molten pool. This upward force is opposed by gravitational force and as a result, the liquid surface starts to oscillate, which in turn causes the arc to oscillate back and forth. When the arc moves forward, the arc length becomes shorter and immediately after this the molten metal spouts toward the rear of the molten pool in an explosive manner, causing puckering.

6. THE MECHANISM OF PUCKERING AND ITS ARREST

Considering the experimental observations made above, the phenomenon of puckering and its arrest by DW MIG welding can be explained as follows:

The results of the observation on occurrence and arrest of puckering are illustrated in Fig. 7. In conventional MIG welding viscosity of the molten pool is lowered due to its comparatively high temperature [3] and the 'digging effect' of the arc is pronounced. As a result, penetration becomes large, the height of the rear wall of the crater increases and its inclination becomes sharper as shown schematically by arrow in Fig. 7A.

Puckering is believed to be caused by air entrainment brought about by the explosive spout of the molten metal, and/or by the molten pool being pushed behind the arc to form an unstable wall of liquid which results in a breakdown of the gas shield, and consequently, air entrainment. In any event, once air entrainment occurs, oscillation of the arc and air entrainment are repeated as chain reactions resulting in puckering.

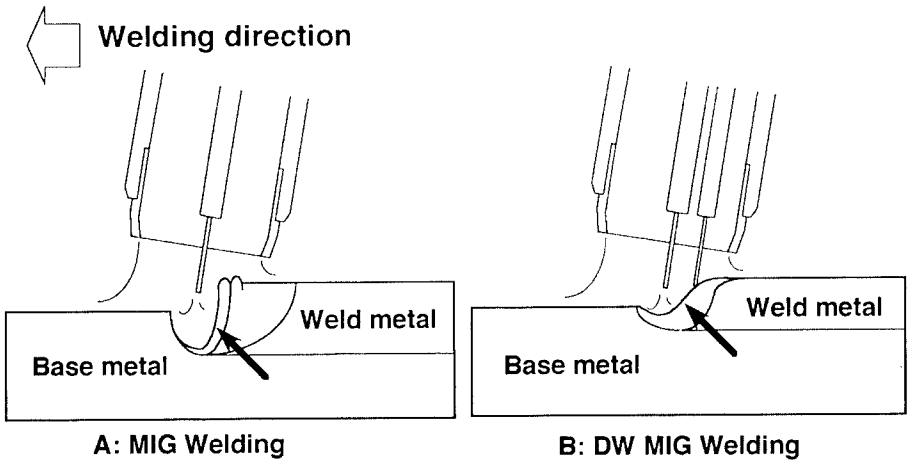

Fig. 7 Schematic comparison of puckering phenomenon in DW MIG and conventional MIG welding process

When welding is performed at currents higher than the threshold value, puckering occurs a few seconds after arc start. If the welding current is still higher, puckering will occur immediately after arc start. The time lag between arc start and initiation of puckering is believed to be dependent on the increasing rate of the molten pool temperature.

DW MIG welding is illustrated schematically in Fig. 7B. The following reasons can be adduced for the increase in the value of the threshold current in the case of DW MIG welding compared to MIG welding.

1) Feeding of filler wire behind the electrode wire impedes the tendency for the molten metal to spout toward the rear of the molten pool and helps to maintain a sufficient amount of liquid directly under the arc.

2) Cold filler wire feeding reduces the temperature of the molten pool and increases its viscosity. This restrains the spout of the molten metal.

In the case of puckering that has occurred at higher welding currents, the arc force is stronger and the molten pool temperature is higher. Therefore, unless a larger amount of filler wire is added, the temperature of the molten pool cannot be decreased sufficiently to arrest puckering.

7. SOLIDIFICATION CRACKING DURING DW MIG WELDING

Aluminium alloy welds sometimes suffer from solidification cracking. This DW MIG welding process depresses the temperature in molten pool fed 'cold' filler wire which was already shown in Fig. 3. This temperature drop may improve the resistance of solidification cracking of aluminum alloy welds.

A series of experiments were carried out to assess the solidification cracking tendencies in case of the conventional MIG and developed DW MIG welding process using modified Houldcraft cracking test.

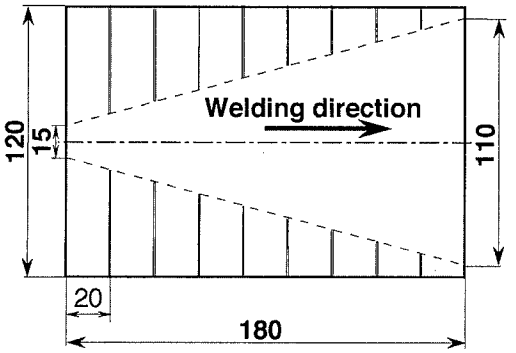

Fig. 8 Specimen dimensions of the modified Houldcraft solidification crack test

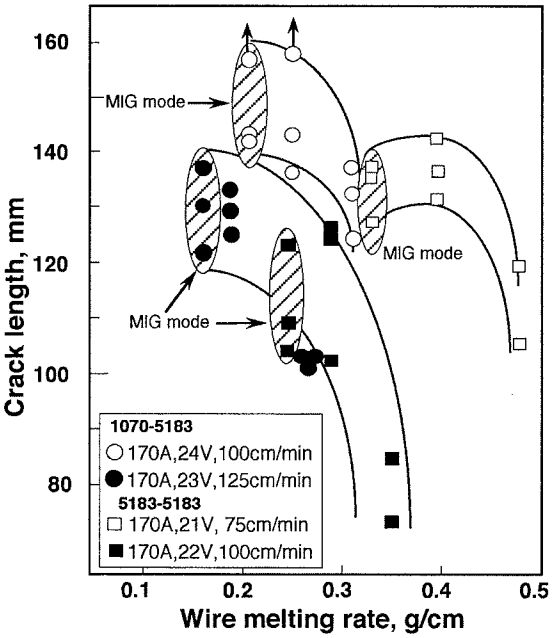

Fig. 9 Results of solidification cracking test for DW-MIG welding procerss

Table 1 Cooling time of weld metals from 873K to 673K

Welding conditions	Wire melting rate, g/cm	Cooling time, sec
5183(1.2ϕ) +5183(1.0ϕ) 170 A 22 V 100 cm/min	0.25	1.00
	0.29	1.44
	0.35	1.17

Test plates were prepared the specified dimensions shown in Fig. 7 and welding trials were performed in bead on plate condition from deeper slot to shallower slot, which was opposite direction proposed by Houldcraft [5]. This welding direction was based on thermal conduction theory [6] and resulted much sensitive for evaluating crack test under higher welding speed more than 100 cm/min.

Figure 8 summarizes the the results of solidification cracking tests. Solidification cracking length decreases with increasing 'cold' filler wire additions which means DW MIG process improves the resistance of solidification cracking. The main reason is considered that temperature in molten pool decreased by DW MIG process and this temperature drop makes less evaporation losses of Mg from molten pool.

This means that DW MIG weld metal has higher Mg contents than that of conventional MIG weld metal.

The peek temperature drop by DW MIG resulted higher cooling rate than that of MIG welding process which is tabulated in Table 1. Increasing wire feeding rate from 0.25 to 0.35 g/cm, cooling time from 873K to 673K decreases. In Fig. 9, crack length at 025 g/cm wire melting rate is about 100mm length and 0.35 g/cm wire melting rate decreases the crack length to 80 mm.

8. CONCLUSIONS

Improved MIG welding process has been developed as double wire gas metal arc (DW MIG) welding in which a cold filler wire is fed into the molten pool behind the main electrode wire. The foremost features of DW MIG welding is increased deposition rates and increased welding speed up to 200 cm/min and decreased molten pool temperature up to 200K. This temperature descend makes positive effects such as preventing formation of puckered bead, stable formation of root bead to square butt welding, decreasing angular distortion and prevention of solidification cracking.

Experimental investigations carried out to clarify these phenomena led to the following conclusions:

1) It reveals that DW MIG welding had much wider process tolerance. Deposition rates obtained in DW MIG welding is more than twice that of conventional MIG welding.

2) DW MIG is effective in increasing the level of threshold current at which puckering occurs in conventional MIG welding. The reasons for the effectiveness of DW MIG welding are believed to be the filler wire reduces the temperature of the molten metal and increases its viscosity, thus restraining the tendency for the molten metal to spout.

3) DW MIG process improves the resistance of solidification cracking for aluminum welding. The main reason is considered that temperature in molten pool decreases and Mg loss is prevented.

REFERENCES

1) Welding Handbook, 8th Edition. 1991. American Welding Society, Miami, Fla.:pp.83
2) H.Hackl,IIW-Doc XII-1439-96
3) U.Dilthey ey al. ,IIW-Doc XII-1548-98
4) W.R.D.Jones, and W.L.Bartlett, J.Inst.Metals, Vol. 81(1952-53), pp.145-152
5) P.T.Houldcraft, British Welding Journal, Vol.2(1955), No. 10 pp.471-475
6) K.Ando, S.Nakata et al, J. of Japan Welding Society, Vol.42(1973), No. 9 pp.879-889

EFFECT OF ALLOY ELEMENTS ON SOLIDIFICATION DISCONTINUITIES OF EB WELDED HIGH TENSILE ALUMINUM ALLOYS

Sung Wook Kim and Chang Hee Lee

Research Institute of Steel Processes & Applications
Division of Materials Science & Engineering
Hanyang University , Seoul 133-791, Korea

ABSTRACT

This study was performed to evaluate basic characteristics of electron beam weldability for high strength Al alloys for express train applications. The Al alloys tested were non-heat treatable A5083-O and heat treatable A6061-T6, and A7075-T6. The principal welding process parameters, such as accelerating voltage, beam current, welding speed and chamber pressure were investigated. The dimension and microstructure of welds were evaluated with OLM, and SEM (EDAX). In addition, weldability variation (cracking and porosity formation) due to process parameters was also evaluated.

EB welds had several discontinuities such as crack, cold shut, porosity and spike. The tendency to form weld discontinuities was strongly dependent upon the EB process parameters and chemistry. Although three Al alloys were welded with the same conditions, alloying elements had an important effect on the dimension of the weld and thus weldability. A6061 showed lower depth than the others. The variation of the weld depth was found to be sensitive to the vaporization tendency of the alloying elements. Si, which is a major element of A6061, is more difficult to vaporize than other elements (such as Al, Mg and Zn). The degree of cracking in the EB fusion zone appears to be affected mainly by D/W, such that as D/W increases the cracking tendency also increases.

The alloying element itself may also affect the hot cracking resistance, but its role is considered to be indirect effect such that the relatively higher vaporization pressure elements of Zn and Mg give deeper weld penetration and thus results in greater cracking tendency.

1. INTRODUCTION

Al and Al alloys, which have excellent corrosion resistance and workability with low density and high elastic modulus, have been applied as structural materials for aircraft, automobiles, high-speed railways and high speed ships. Furthermore, they show excellent characteristics from the viewpoint of economic efficiency and recycling of resources compared to other metals and non-metallic materials. Therefore, rapid growth of Al usage now and in the future is attributed to a unique combination of properties, which makes it one of the most versatile of engineering and structural materials.

The application of high density energy heat sources of laser and electron beams for welding Al alloys has been spotlighted [1-4]. However, application of these techniques in actual manufacturing is seldom found, because the high energy density beam weldability of Al alloys has not been ensured yet. Therefore, the weight reduction by aluminization of transportations and development of new alloys without weldability ensurance appear to be meaningless.

In the applications of the high energy beam welding to high strength Al alloys, serious problems such as cracking and large-elongated pores by gas contamination and evaporation of specific elements in the fusion zone may occur [4].

Consequently, solving these problems may be the key to the application of high strength Al

alloys in transportation systems.

The main objective of this study was the clarification of the phenomena of the formation of discontinuities under rapid thermal excursion of high density electron beam, in the fusion zone and HAZ of the several Al alloys through metallurgical examinations.

2. EXPERIMENTAL PROCEDURES

The EBW used for the welding has a maximum operating voltage of 150kV with a beam current of 100mA, giving a maximum output power of 15kW. The materials tested in this study are the non-heat treatable alloy, A5083-O (Al-Mg), and heat treatable alloys such as A6061-T6 (Al-Mg-Si) and A7075-T6 (Al-Zn-Mg). The chemical compositions of the alloys used in this experiment are listed in Table 1.

The test piece was successively set in line and welded in bead-on-plate, autogeneous, and partial penetration. The thickness of the materials was 17mm. For the welding experiment, bars, 36mm wide and 100mm long were machined. The surfaces were prepared by brushing them with a stainless steel wire to remove oxides and dirt, and were cleaned with acetone just before welding. Because hydrogen is the primary cause of porosity, its entry into the weld pool must be minimized.

Specimens for metallographic examination were extracted from the beginning, middle and ending parts of the weldment to ensure a true representation of the welding characteristics. The transverse section of the specimens was prepared by standard metallographic techniques and etched in Keller's Reagent (HF 1ml, HCl 1.5ml, HNO_3 2.5ml and water 50ml) to reveal the microstructures.

The porosity content of the welds, revealed as dark spots on the polished and unetched longitudinal section (8mm long) of the weld, was measured with an optical microscope. The length of each solidification cracks in the fusion zone and liquation cracks in the heat affected zone (HAZ) on the cross-section of the weld were also measured with a low magnification microscope. The total crack length (TCL) and maximum crack length (MCL) were used as a relative crack sensitivity of alloys, such that an alloy having higher TCL/MCL is more susceptible to weld hot cracking.

The weld shape / dimension, microstructural characteristics, porosity formation tendencies, and hardness and hot cracking resistance of three commercial aluminum alloys were compared.

Table 1 Chemical composition of materials used. (wt.%)

Material	Si	Fe	Cu	Mn	Mg	Cr	Ni	Zn	Ti	Al
5083- O	0.082	0.167	0.019	0.631	4.472	0.121	0.022	0.037	0.017	bal.
6061-T6	0.615	0.189	0.277	0.022	1.021	0.259	-	0.034	0.022	bal.
7075-T6	0.032	0.084	1.608	0.004	2.667	0.246	-	5.414	0.020	bal.

3. RESULTS AND DISCUSSION

3.1 Penetration

The aspect ratio (depth/width) of aluminum alloys with the variation of travel speed and accelerating voltage are shown in Fig.1, from which it is evident that there are considerable differences among the materials. As travel speed is increased, in general, D/W is decreased. For the depth of penetration, A7075 and A5083 are especially narrow and deep,

approximately twice the depth of A6061. In Fig.1, as accelerating voltage is increased, higher heat input makes a deeper penetration.
High vapor pressure elements, Zn and Mg, which are the principal alloying elements in A7075 and A5083, are known to make a deep penetration during welding.

(a) (b)

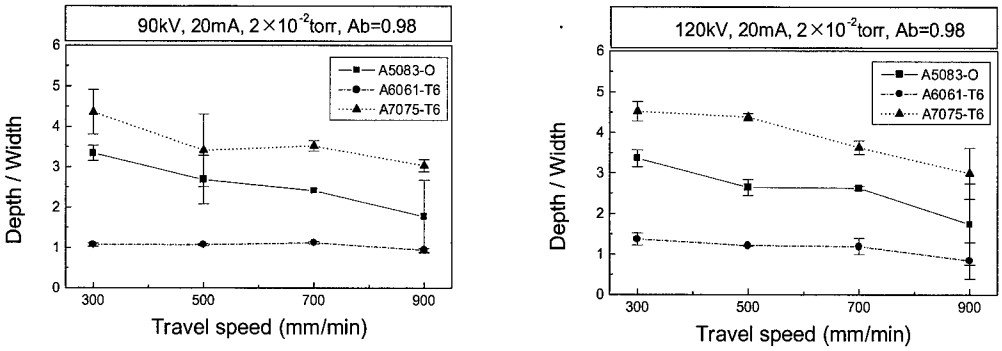

Fig.1 Aspect ratio (D/W) of various materials with heat input. (a) 90kV (b) 120kV

Vapor pressures calculated from equations given in reference [5] as a function of temperature for individual alloying elements are shown in Fig.2. For the simple comparison of vapor pressure of elements, Raoult's law [2] is not considered. As shown in Fig.2, the vapor pressure of Zn and Mg are about 10^2 and 10 torr, respectively at 1000k, but in the case of Si, the principal alloying element of A6061, it is extraordinary lower.
To identify the reduction of alloying elements in the fusion zone, wet-element analysis was conducted and is shown in Table 2. In Table 2, B.M. is base metal, F.Z. is fusion zone, L.V. is low vacuum (2×10^{-2}torr) and H.V. is high vacuum (2×10^{-4}torr). There is a reduction of all alloying elements in all three alloys after welding. In the case of A6061, because the content of Mg, which is a relatively high vapor pressure element, is small and Si, which is a low vapor pressure element, is included, penetration is lower than the other two alloys

Table 2 The Result of wet-element analysis (wt.%)

element / condition	Mg	Si	Zn
A5083-O (B.M.)	4.47	-	-
L.V. (F.Z.)	3.61	-	-
H.V. (F.Z.)	3.74	-	-
A6061-T6 (B.M.)	1.02	0.62	-
L.V. (F.Z.)	0.78	0.32	-
H.V. (F.Z.)	0.72	0.29	-
A7075-T6 (B.M.)	2.67	-	5.41
L.V. (F.Z.)	2.41	-	5.04
H.V. (F.Z.)	2.35	-	4.94

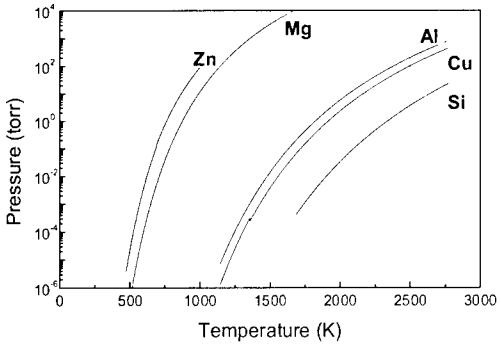

Fig.2 Vapor Pressure vs. temperature diagram

3.2 Porosity

There are several undesirable discontinuities that are associated with electron beam welding. These include porosities [6-11], cold shuts (incomplete fusion), crack and spike [12-21].
Fig.3(a) shows spikes and large root porosity typical in the aluminum EB weld metal. Spiking is the non-uniform and sudden increase in penetration beyond what might be called the average penetration. It is an inherent defect penetrated electron beam welds. Many spikes normally have large cavities (or pores) in their lower portions because molten metal does not fill in completely. A7075 and A5083, which have deep penetration welds, were always accompanied by the root porosity (or cavity) and cold shuts at almost all of the spike areas. The root cavity, compared to other types of porosity, has considerably large size (over than 100㎛) and has dendritic structures inside. (Fig.3(b)). The high vaporization of Mg and Zn led to degasification of the elements during the welding process. The degasification of elements is known to result in a turbulent melting pool and increased porosity of the weld [3].

(a) (b)

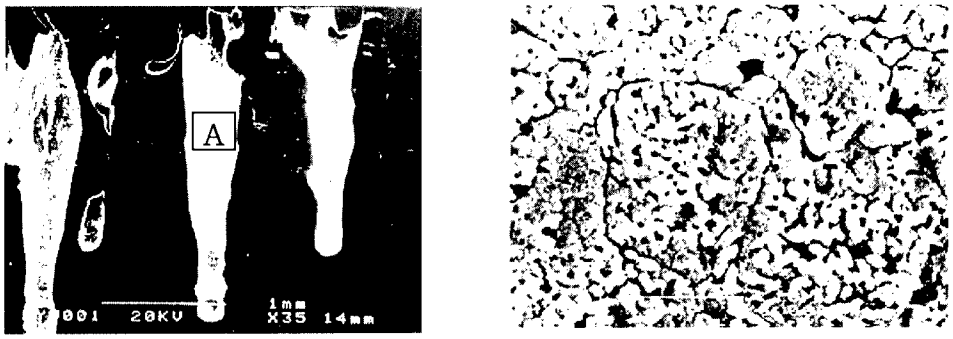

Fig.3 The shape of porosity
(a) Root cavity in the spike (b) Magnified of A in fig.3

3.3 Cracking

It is well known that aluminum alloys are sensitive to solidification cracking in the weld metal and liquation cracking in the heat affected zone(HAZ) [4]. Fig.4 shows hot cracks at the root side of a weld, typical to three alloys. The cracks in the fusion zone formed along the columnar grain boundaries toward the centerline of the fusion zone.

Fig.5 shows the effects of travel speed, accelerating voltage, current and degree of vacuum on TCL and MCL of A5083 in the fusion zone. In general, as the travel speed increases, TCL gradually decreases but MCL is almost constant, showing that the increase in D/W due to the decreased travel speed (i.e., increased energy input) results in the increased number of crack instead of increasing crack length. For a given travel speed, the increase in the energy input by increasing accelerating voltage or current makes the fusion zone more susceptible to hot cracking.

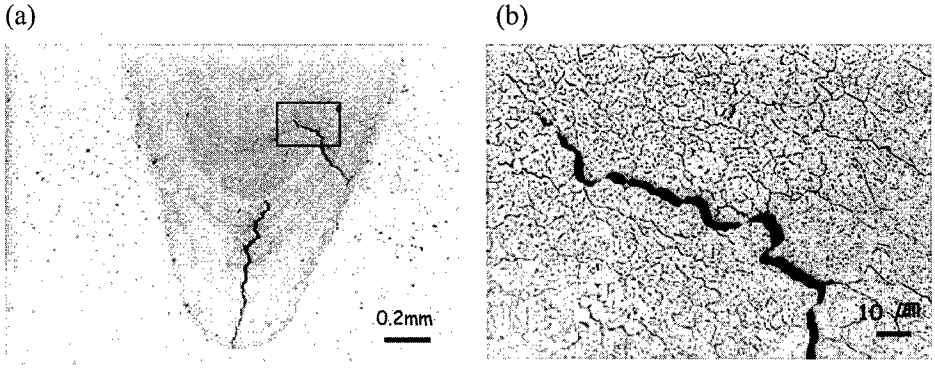

Fig.4 Hot cracks at the root side of a weld.

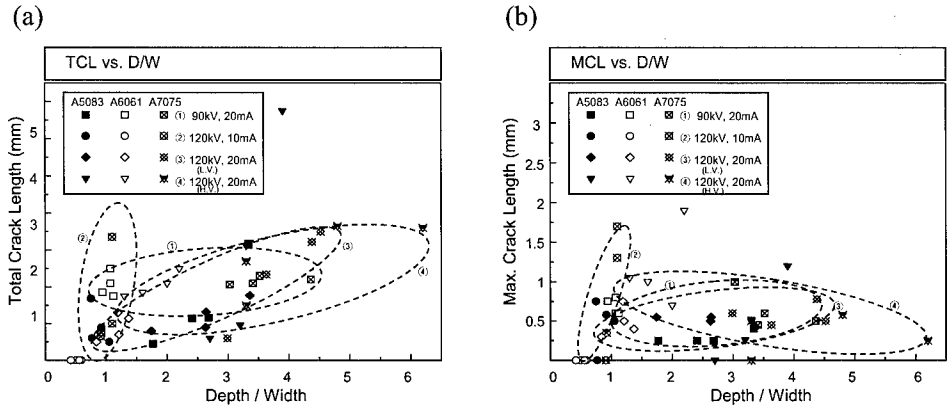

Fig.5 Effect of weld penetration on cracking tendency (a) TCL (b) MCL

4. CONCLUSIONS

The weld penetration characteristics of aluminum alloys are sensitive to the vaporization tendency of alloying elements.

Porosity was found in all weld fusion zones regardless of welding conditions. The porosity formation tendency decreased in the order of A7075 > A5083 >A6061, which is the order of deeper weld penetration.

Because most large pores and cold shuts exist in the bottom root of the fusion zone, especially in the spike, more caution is needed when a partial penetration weld is made.

The degree of cracking in the EB fusion zone appears to be affected mainly by D/W, such that as D/W increases the cracking tendency also increases.

The alloying element itself may also affect the hot cracking resistance, but its role is considered to be indirect effect such that the relatively higher vaporization pressure elements of Zn and Mg give deeper weld penetration and thus results in greater cracking tendency.

Acknowledgements

This study was conducted by the support of specific foundation research (project number: 96-0300-08-01-3) of Korea Science and Engineering Foundation (KOSEF).

REFERENCES

1. M.Kutsuna et al., Weld. World, 31(2) (1993), pp.126.
2. Yoshiaki Arata, Plasma, Electron & Laser beam Technology, ASM, (1986), pp.441.
3. H.D.Steffens, et al, Int. J. for the Joining of Materials, 8(2) (1996), pp.45.
4. A.Sanderson et al., British Welding Journal, 7 (1972), pp.54.
5. E.A.Brandes et al. Smithells Metals Reference Book, Butterworth-Heinemann,(1992) chp.8
6. A.T.D'annessa, W.J, 47(10), (1968), pp.462s.
7. W.Tuttle, W.J, 70(2), (1991), pp.43.
8. D.G.Howden, W.J, 50(2), (1971), pp.112.
9. R.J.Shore et al., W.J, 49(7).(1970) 311s.
10. R.F.Ashton et al., W.J, 54(3), (1975) 95s.
11. R.A.Woods, W.J, 53(3), (1974) 97s.
12. J.L.Murphy et al., W.J, 67(9), (1988) 187s.
13. G.L.Mara et al., W.J, 53(6), (1974) 246s.
14. T.P.O'Brien, W.J, 53(8), (1974) 332s.
15. D.A.Schauer et al., W.J, 57(7), (1978) 189s.
16. R.J.Brungraber et al., W.J, 52(3), (1973), pp.97s.
17. C.H.Lee et al., J. of KWS, 14(3) (1996) 192.
18. G.E.Metzger, W.J, 46(10), (1967), pp.457s.
19. H.M.Hussain et al., Int. J. for the Joining of Materials, 9(2), (1997), pp.74.
20. V.Malin, W.J, 74(9), (1995) , pp.305s.
21. T.Ma et al., Int. J. for the Joining of Materials, 8(3),(1996), pp.105.

UNDERWATER FRICTION WELDING OF A6061 ALUMINUM ALLOY

Kazuyoshi KATOH and Hiroshi TOKISUE

Department of Mechanical Engineering
College of Industrial Technology, Nihon University
2-1, Izumi-cho 1 chome, Narashino-shi, Chiba 275-8575 JAPAN

ABSTRACT

Friction welding of A6061 aluminum alloy was performed underwater, and some characteristics of a joint which were made by using a brake type friction welding machine, has been investigated. That maximum temperature on underwater friction welding considerably lowered in comparison with friction welding in atmosphere. The total loss of welded joints made underwater became short as compared with the welded joints made atmospheric. The width in softened area of welded joints made underwater was narrower than the conventional welded joints, and the hardness of softened area of welded joint made underwater showed higher value than welded joint made atmospheric. The maximum joint efficiency of the welded joint made underwater which was 86% showed higher value than the welded joint made atmospheric which was 82%. The elongation of welded joint made underwater was showing lower value compared with the welded joint made atmospheric. Fracture position of the welded joints made underwater on tensile tests was in the softened area of atmospheric joints as same as conventional welded joints.

1. INTRODUCTION

It is increasing that several products are combined by welding, because the products become high efficiency. And, the aluminum alloys which is used very frequently with lightening considering global environmental problems, etc.. But, in case of welding of aluminum alloy, the strength of welded joint which has good weld part decrease by softening of heat affected zone [1]. The softened area occurs in the heat affected zone, even if friction welding which is the low-temperature welding in comparison with fusion welding is also similar, and even if the friction welding is carried out under the appropriate welding condition [2],[3]. And, there is no the strength degradation by the softening, if the welding is carried out in the soft state by annealing. However, wrought aluminum alloy is generally improved tensile strength by raising hardness according to cold working or heat treatment. Therefore, the generation in softened area in the joint by the thermal effect affects the lowering of joint strength.

Consequently, it is necessary to make width of the softened area of a joint narrow even to the grade which does not affect the tensile strength of joint, and to make a softening rate small. However, no-heatable type alloy and A6061 aluminum alloy which is heat treatment type alloy degreases the strength of the joint, because it is not recovery the hardness of softened area in room temperature. The research on the relationship between softening phenomenon by heat affected and strength of the friction welded joint is remarkably little, while friction heat affects strength of joint.

In this study, friction welding in underwater was tried as one method for reducing the effect of softened area on tensile strength of the joint using A6061 aluminum alloy in which the hardness of softened area does not change almost, even if it is left in friction welding post-room temperature, and some characteristics of the joint were examined.

2. MATERIALS AND EXPERIMENTAL PROCEDURE

For the work piece, the commercial A6061-T6 aluminum alloy(Al-0.59Si-0.91Mg, σ_B = 347MPa, ε =17.3%, 121HV)bar of 20 mm in diameter was used after machining it down to 80 mm in length and degreasing its welding surface with acetone. The welding conditions are given in Table 1. Friction welding was performed by using a brake type friction welding machine. Underwater welding was performed in chamber made from polyethylene which attend between the rotational side chuck and the fixed side clump. Inside the chamber, it designed so that 274K water might always circulate. It is located drill holes (1.2 mm dia.)from weld interface as fixed side to position of 1, 5, 10 mm with center of bar into which the thermocouple (C.A., 0.3 mm dia.) were inserted and thermal cycles were measured. A cross section of the welded joints was observed with optical microscope and hardness test by micro-Vickers hardness tester. And, JIS No.4 specimens were used for the tensile test. All the tests operated in room temperature.

Table 1 Friction welding conditions.

Rotational speed	n (s^{-1})	58
Friction pressure	P_1 (MPa)	15, 30, 45
Friction time	t_1 (s)	0.5, 1.5, 3.0, 4.5
Upset pressure	P_2 (MPa)	30, 60, 90, 120, 150
Upset time	t_2 (s)	5

3. EXPERIMENTAL RESULTS AND DISCUSSIONS

The macrostructures of the friction welded joints are shown in Fig.1. Atmospheric joints clearly show burr as same as generally aluminum alloy friction welded joints and the heat affected zone in seen taking the shape of a concave lens, enveloping the welding part. The joint which carried out the underwater friction welding also has few amounts of burr, and the height is also low. It is observed that heat affected zone of underwater joint is parallel to the weld interface.

(a)atmospheric (b)underwater

Fig.1 Macrostructures of friction welded joints. (P_1=45MPa,t_1=4.5s)

An example of the microstructure of joints is shown in Fig.2. On the welding layer of atmospheric joint, a fibrous structure, which was, observed on the base metal disappears and non-directional fine grain structure appears where a deposit layer is observed along the boundary layer. Microstructure on the welding layer of underwater joint showed same tendency of atmospheric joint, but underwater joint showed finer structure a little as compared with the atmospheric joint. The outside of underwater joints showed finer structure than atmospheric joint as same as center of joint.

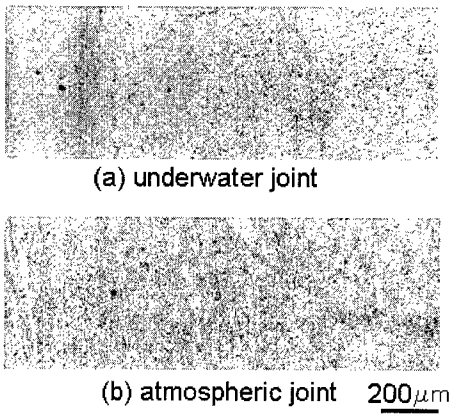

Fig.2 Microstructures of center of welded joints. (P_1=45MPa, t_1=4.5s)

The total loss which is the relation with formation of the burr and it is say that total loss is relation with strength of the friction welded joints. The measuring results of total loss are shown in Fig.3. Regardless the atmosphere of friction welding, the total loss increased almost lineally with increasing of both friction time and friction pressure. The effect of friction time on total loss is more remarkable than friction pressure, regardless the atmosphere of friction welding. The total loss of underwater joint are smaller than that of the atmospheric joint and total loss of underwater joints show 20%～30% of the atmospheric joint. In this result, underwater welding is an effective method by total loss is short.

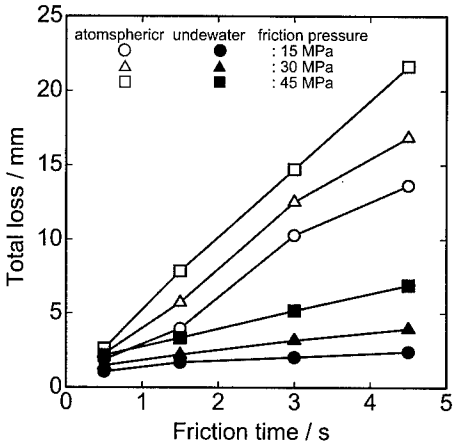

Fig.3 Relation between friction time and total loss.

There are more heat dissipation on underwater welding than atmospheric welding. Therefore, the thing considered that there is also little quantity which the frictional heat generated in base metal. Then, temperature measurement of each part of a joint in friction welding was performed. Measuring results are shown in Fig.4. The temperature- time history in the atmospheric welding process displays the same tendency that the friction welding of the other aluminum alloys [1]. The temperature rise suddenly just after the start of the welding. The speed at which the temperature rise in the position which as 1 mm from weld interface reaches the highest value immediately after it stop rotation. Since, the temperature comparatively lowered. The temperature - time history in the underwater welding show same tendency of atmospheric welding. But the speed at which the temperature rise on underwater welding was more slow than atmospheric welding and maximum temperature was lower than atmospheric welding, furthermore cooling speed just after the friction process of underwater welding was very fast than atmospheric welding. The temperature of the position of 5 mm and 10 mm from weld interface show a similar tendency of position of 1 mm from weld interface. It was clearly that the maximum temperature of

each position in underwater welding showed low value as compared with atmospheric welding. Maximum temperature of atmospheric and underwater welding are increased with the increasing both friction pressure and friction time, and the effect of friction time was bigger than the effect of friction pressure. And, maximum temperature in underwater welding considerably lowered in comparison with atmospheric welding and the effect of both friction time and friction pressure tended to also decrease. It is thought that this is compared with the atmospheric welding and the emission of the friction heat to the outside is due to increase. And it is considered that they are effective measures which can reduce the width and the softening rate of the softened area accepted in a hardness distribution of the joint which is for the amount of discharge to the exterior of frictional heat to increase in underwater welding, and is mentioned later can be reduced as compared with the atmospheric welding.

The hardness distribution of the center of the welded joints in axial direction are shown in Fig.5. Regardless both the atmosphere of the friction welding and welding condition, the softened area is found in heat affected zone. Width of softened area of atmospheric joint is become narrow in case of friction pressure is low, friction time is short and upset pressure is high. But the softened area not observed difference of the lowest hardness. The hardness distribution of underwater joint was also similar tendency that of the atmospheric joint. But, regardless welding conditions, width of softened area of underwater joint was narrower than atmospheric joint and softening rate is smaller than atmospheric joint. In underwater friction welding of the carbon steel, it is reported that hardness of heat affected zone on the atmospheric joint become large by the quenching effect, and the width of heat affected zone become narrow [5]. The result of this experiment was agreement with this.

An example of the relation between maximum temperature in the welding process and hardness of

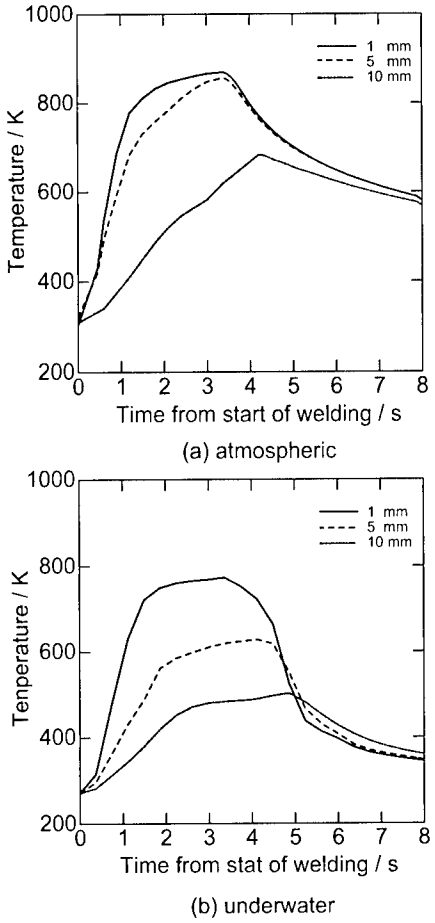

Fig.4 Temperature - time histories of friction welding process. (P_1 = 30 MPa, t_1 = 3 s)

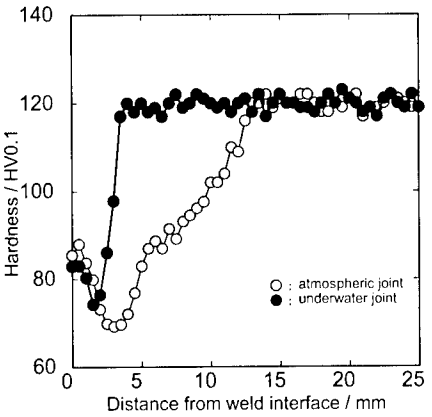

Fig.5 Hardness distributions of friction welded joints. (P_1 = 30 MPa, t_1 = 3 s)

the most softening division of the joint is shown in Fig.6. The hardness of the most softening division of the joint showed good correlation maximum temperature. The hardness in the most softening division show high value by maximum temperature is low. And it is clearly that the softening proportion could be also decreased.

Results of tensile test of welded joint were shown in Fig.7. The value in the figures showed joints efficiency of tensile strength of base metal. The figure showed results of tensile tests of joint which are upset pressure of 150 MPa constant, and exchange of both friction pressure and friction time. It is no effect of friction pressure on tensile strength of the atmospheric joint and the joint efficiency decreased with increasing with friction time. Maximum joint efficiency of atmospheric joint is 82% that of the base metal. And elongation of atmospheric joint is shown low value in case of friction time is the most short in this examination as 0.5 second, but the other welding conditions, the elongation are shown constant value as 71% of base metal. It is considered that width of softened area is change by friction time, but the hardness in the most softening division showed no change. Underwater joint is not recognized the joint efficiency as same as atmospheric joint. The joint efficiency is degreased with increasing the friction time. However, the lowering proportion was smaller than the atmospheric joint, and the effect of the welding conditions was also little. The maximum joint efficiency of underwater joint is 86% that of the base metal, and it is slightly higher comparison with atmospheric joint. The elongation showed the tendency which slightly increased with the increasing in friction time, when friction pressure is 45 MPa. In case of the other welding conditions, the elongation showed the constant value, and the value was lower than the atmospheric joint, and it is decreased about 50% of the base metal. Both atmospheric joints and underwater joints were fractured at softened areas of the joint.

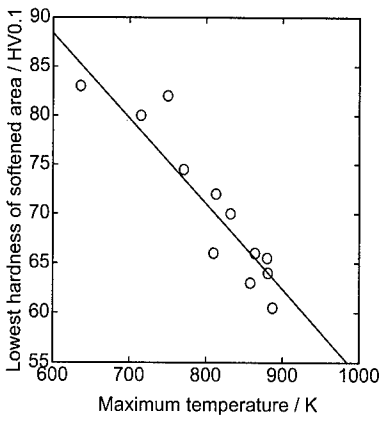

Fig.6 Relation between maximum temperature and lowest hardness of the softened area.

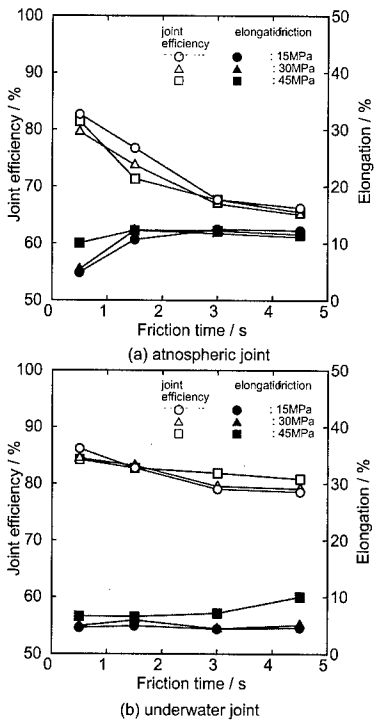

Fig.7 Relation between friction time and joint efficiency and elongation.

The relationship between hardness and joint efficiency in the most softening division is shown in Fig.8. Regardless atmosphere of welding, the fracture position of joints are most softening division of joint of softened area. Between hardness of the most softening division and joint efficiency are recognized good correlated. Joint efficiency is increased with

increasing the hardness the most softening division. It is make a decision according to the result and Fig.8 which is the result of measured maximum temperature, hardness of softening division approaches hardness of base metal by maximum temperature is low and it is possible improved the joint efficiency.

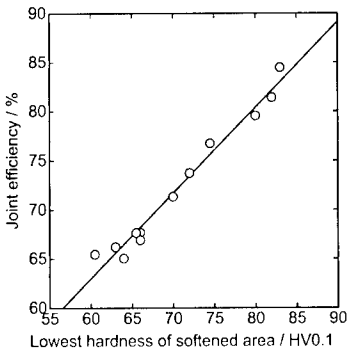

Fig.8 Relation between lowest hardness of the softened area and joint efficiency.

4. CONCLUSIONS

Authors try underwater friction welding which is one method reduce the effect of softening of heat affected zone on joint efficiency of friction welded joint. The following results were obtained;

1) The speed at which the temperature rise on underwater welding was more slow than atmospheric welding and maximum temperature was lower than atmospheric welding, furthermore cooling speed of joint after friction process on underwater welding is very fast which is compared with atmospheric welding.

2) The total loss of underwater joint show 20% ~30% of the atmospheric joint.

3) Regardless both the atmosphere of the friction welding and welding conditions, the softened area is found in heat affected zone. Width of softened area of underwater joint was narrower than atmospheric joint and softening rate is smaller than atmospheric joint.

4) The hardness of the most softening division of the joint showed good correlation maximum temperature. The hardness in the most softening division show high value by maximum temperature is low. And it is clearly that the softening proportion could be also decreased.

5) Joint efficiency of underwater joint such as 86% of base metal was slightly higher than atmospheric joint such as 82% of base metal. Elongation of underwater joint shows the low value such as 50% of base metal of that of the atmospheric joint. Both underwater joints and atmospheric joints are fractured at softened area of joint.

6) The joint efficiency are improved with increasing hardness of softened area.

ACKNOWLEDGMENT

The financial support of the Light Metals Educational Foundation is gratefully appreciated.

REFERENCES

1) S.SATO, J.MATSUMOTO and H.KOBAYASHI, J. of Light Metal Welding & Construction, 18(1980), pp.533-539.
2) K.KATOH and H.TOKISUE, J. of Japan Institute of Light metal, 34(1984), pp.325-330.
3) K.KATOH and H.TOKISUE, J. of Japan Institute of Light metal, 40(1990), pp.351-355.
4) K.KATOH and H.TOKISUE, J. of Light Metal Welding & Construction, 32(1994), pp.203-209.
5) Y.TAZAKI, N.NAKAYAMA and H.KAJIWARA, Reports of The national Industrial Research Institute of Nagoya, 25(1976), pp.183-187.

DIFFUSION BONDING IN PURE MAGNESIUM

H. Somekawa[1], M. Kohzu[2] and K. Higashi[2]

[1] *Graduate Student of Engineering, Department of Metallurgy and Materials Science, Osaka Prefecture University, 1-1 Gakuen-cho, Sakai 599-8531, Japan*
[2]*Department of Metallurgy and Materials Science, Osaka Prefecture University, 1-1 Gakuen-cho, Sakai 599-8531, Japan*

ABSTRACT

Recently, magnesium is paid attention to the inherent advantage of being light. They are lighter than fiberglass and just over half as dense as aluminum. Magnesium is also abundant resource. Thus, there are many potential opportunities for the use of magnesium in automotive drive train components. But, magnesium system alloys normally exhibit limited ductility at room temperature because of h.c.p. structure. Therefore, recent fabrications of magnesium based materials are mainly performed by die casing with hot- or cold- chamber, or semi-solid processing of thixotropic molding, is not performed diffusion bonding processing. However the possibility of diffusion bonding in magnesium have never been investigated. Therefore, diffusion bonding is carried out several temperatures, pressures, and times in air. Diffusion bonding quality is assessed on the lap shear strength and the observation of metallography. The material after diffusion bonding could obtain high strength about 85MPa.

1. INTRODUCTION

Recently, there has been a significant increasing in the use of magnesium as structural materials. There are many potential opportunities for the use of magnesium-based materials in motor vehicle components. This is not only a result of the relatively low density of magnesium, which can directly and substantially reduce the vehicle weight, but is also a result of its good damping characteristics, dimensional stability, machinability, and low casting cost. These attributes enable magnesium to economically replace many zinc and aluminum die-castings, as well as cast iron and steel components, and assemblies in motor vehicles [1]. However, magnesium normally exhibits low ductility near the room temperature, because of the h.c.p. structure. Therefore, recent fabrications of magnesium-based materials are mainly performed by die casing with hot- or cold- chamber, or semi-solid processing of thixotropic molding. Recently, since the combination of cast and wrought materials is also expected to fabricate structural components, there is a strong need to develop joining technique [2-4].

Diffusion bonding is one of the joining techniques and it is a solid state joining process in which two clean metallic surfaces are brought into contact under a low pressure at elevated temperatures of $\leq 0.7\ T_m$, where T_m is the absolute melting point of the material. Diffusion bonding process permits the production of high quality joints with a little or need for post-weld machining [5-6]. However, it is important to consider the optimal conditions for diffusion bonding in order to achieve high quality joints, because there are many factors i.e. temperature, pressure, time and so on [7]. It has been reported that many materials could be obtained successfully diffusion bonded conditions; such as titanium alloys, aluminum alloys

and steels [8-19]. For example, superplastic titanium alloys, mainly Ti-6Al-4V, have come to be widely produced, especially, in the aerospace industry by using superplastic forming and diffusion bonding technology (SPF/DB) [8]. Aluminum alloys and steels have already obtained the optimal conditions to produce high quality in diffusion bonding [13-18].

To data, the possibility of diffusion bonding has not been examined in magnesium-based materials. Therefore, in the present study, diffusion bonding tests were carried out in the wide range of bonding pressures and bonding times to investigate its optimal conditions in pure magnesium. And, the relationship between bonding pressure and bonding time to form sound bonded specimens was also clarified.

2. EXPERIMENTAL PROCEDURES

Pure magnesium was used in order to investigate the diffusion bonding. Pure magnesium of 99.95 % purity was supplied by Osaka Fuji Corp. as a rolled sheet with a thickness of 2.3 mm. The microstructures of the specimens were examined by optical microscopy. The average grain size, d, was estimated using the equation, d=1.74L; L is the linear intercept size. The grain size of the as-received sheet was about 85 μm.

The specimens to be diffusion bonded were cut directly from the rolled sheet. The length and width were 30 mm and 20 mm, respectively. Before diffusion bonding tests, the bonding surfaces were blasted using 20 μm diameter alumina grit for 60 seconds and at a blasting pressure of 3 MPa. After grit blasting treatment, the specimens were cleaned in ethanol using ultrasonic vibration cleaner to remove the alumina particles. The surface roughnesses of as-received and grit blasted materials are listed in Table 1. By using the grit blasting treatment, the surface became more rugged than that of as-received condition. It was found that the surface roughness was nearly equal to the alumina particle size used for grit blasting.

Table 1 Roughness dimensions of as-received and grit blasting treated surfaces.
Rmax; The maximum roughness. Rz; The average roughness.

Surface	Rmax, μ m	Rz, μ m
As-received	10.2	0.35
Grit blasting	35.5	29.7

Diffusion bonding tests were carried out in air on the pressure range from 2 to 20 MPa, the bonding temperature at 673 K and for the times up to 72 hours. The testing temperature is equivalent to the absolute temperature 0.73 T_m, where T_m is 924 K for pure magnesium [20]. The overlap length was taken to be 1.5 t, where t is the thickness of the sheet.

Diffusion bonding quality was assessed by the microstructural observations and the compressive lap shear tests. For the microstructural observations by optical microscopy, the diffusion bonded specimens were polished and then etched in 10%-acetic for 30 seconds. Compression lap shear tests were carried out with an overlap of 1.5 t at cross head speeds of 5 mm/min at room temperature.

3. RESULTS AND DISSCUSIONS

3.1. Compression Lap Shear Tests

The absolute bond strength could not be used to evaluate the extent of bonding, because specimens having different bonding conditions would have different mechanical properties. The shear fracture strengths of the bonds were assessed by comparison with experimentally measured value for the parent metal, i.e. τ_b/τ_p, where τ_b and τ_p are the compression lap shear strength of the bond and the compression shear strength of the parent metal, respectively. For compression lap shear tests, a sound bond was defined as the bond which exhibited a lap shear strength ratio $\tau_b/\tau_p \geq 0.80$. The result of sound bonded conditions, $\tau_b/\tau_p \geq 0.80$, are listed in Table 2. The maximum ratio of lap shear strength was 0.888 when specimen was bonded at 20 MPa for 1 hour. The results of all compression lap shear tests are also shown in Fig. 1. The symbols of ○, △ and × in Fig. 1 show $\tau_b/\tau_p \geq 0.80$, $0.80 > \tau_b/\tau_p \geq 0.60$ and $\tau_b/\tau_p < 0.60$, respectively. It is apparent that the bonding strength depends on the bonding pressure and time, i.e., bonding time decreases with increasing pressure. It is easy to predict the bonding times to obtain a sound diffusion bonded specimen.

Table 2 The results of a sound bonded conditions.

Bonding Condition		Lap Shear Strength, MPa			τ_b/τ_p, %
Pressure, MPa	Time, h				
3	24	97.0	87.4	85.2	0.840
5	12	95.3	94.7	90.5	0.874
10	3	92.3	87.9	81.6	0.816
20	1	109.4	106.8	95.7	0.888

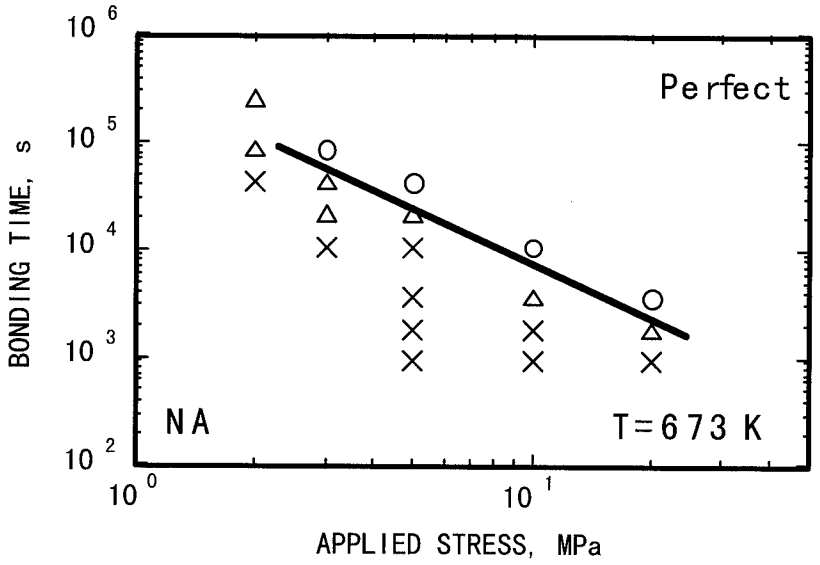

Fig. 1 The summary of lap shear tests of diffusion bonding specimens.
○: $\tau_b/\tau_p \geq 0.80$, △: $0.80 > \tau_b/\tau_p \geq 0.60$ and ×: $\tau_b/\tau_p < 0.60$.

3.2. Microstructural Observations

For the microstructural observations, the optical microstructure of diffusion bonding specimens are shown in Fig. 2. The diffusion bonding tests were carried out at a bonding pressure of 10 MPa. The white arrows in Fig. 2 show the original surface. Figure 2(a) shows the microstructure of the specimen that was bonded for 3 hours. This specimen obtained the high lap shear strength of 0.816 τ_b/τ_p by compression lap shear tests. Figure 2(b) shows the microstructure of the specimen that was bonded for 1 hour. When the lap shear strength was high, $0.8 \geq \tau_b/\tau_p$, the bonding line was not observed. On the other hand, the lap shear strength was low; the visual bonding line was observed. It apparent that original separate surface forms voids, and the voids gradually vanished during diffusion bonding process. It is suggested that low bonding strength is associated with the presence of voids. In order to obtain high ratio of lap shear strengths, the visible bond lines should be disappeared from section. It is noted that more bonding time or bonding pressure are required to enhance the bonding qualities.

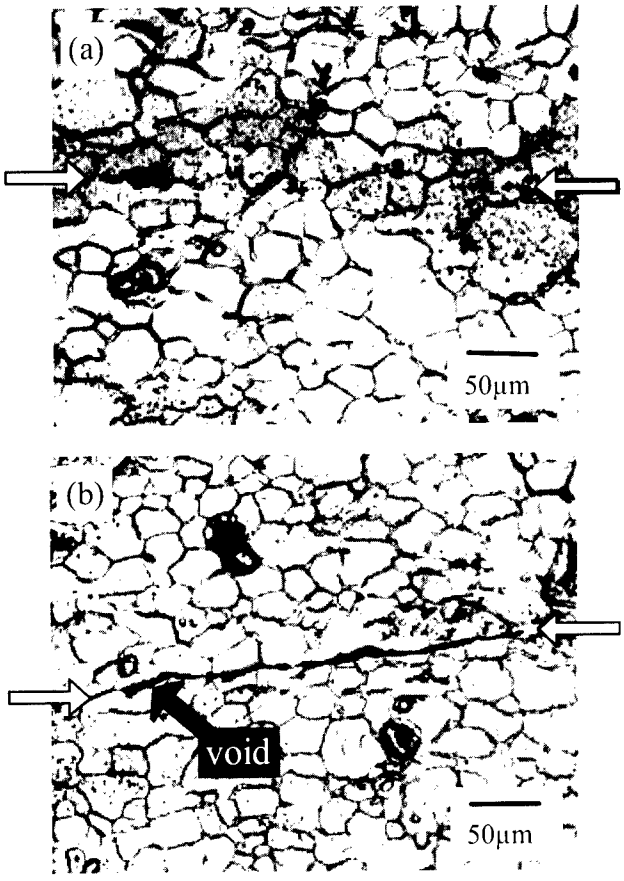

Fig. 2 Cross –sections through bonded specimens at bonding pressure of 3.0 MPa for (a) 3.0 hours and (b) 1.0 hour. The white allows show the bond lines.

4. SUMMARY

Diffusion bonding behavior was investigated by using pure magnesium. The grain sizes were about 85 μm. From the microstructural observations and compressive lap shear test, the several optimal diffusion bonding conditions were obtained at 673 K to be 20 MPa and 1 hour, 10 MPa and 3 hours, 5 MPa and 12 hours, 3 MPa and 24 hours. The specimens bonded under these conditions exhibited high ratio of lap shear strength, $\tau_b/\tau_p \geq 0.80$, and the bond line could not be also observed. From the present results, the time to form sound bonded specimens could be predicted. The relationship between bonding pressure and bonding time to form sound bonded specimens was also clarified.

ACKNOWLEDGMENT

The authors are grateful to Dr. H. Watanabe and Dr. T. Mukai (Osaka Municipal Technical Research Institute) and Dr. H. Hosokawa (National Institute of Advanced Industrial Sciencel and Technology) for their helpful comments. This work was supported by the Light Metal Educational Foundation Inc. and the Priority Group of Platform Science and Technology for Advanced Magnesium Alloys, Ministry of Culture, Science and Education under grant No. 11225209.

REFERENCES

[1] J. Davis: Magnesium in drive train compenents, SAE Tech. Paper Series, SAE-850419, 8: 1985, Warrendale, PA, SAE.
[2] M. Mabuchi, K. Kubota and K. Higashi: Mater. Trans., JIM. **36** (1995) pp.1249-1254.
[3] T. Mukai, H. Watanabe and K. Higashi: Mater. Sci. Technol. **16** (2000) pp.1314-1319.
[4] F. H. Froes, D. Eliezer and E. Aghion: The Science, Thechnology and Applications of Magnesium. JOM **50** (1998) pp.30-34.
[5] K. E. Easterling and A. R. Tholen: Acta Metall. **20** (1972) pp.1001-1008.
[6] J. Pilling: Mater. Sci. Eng. **A100** (1988) pp.137-144.
[7] J. Pilling and N. Ridley: Superplasticity in crystalline solid, The Institute of Metals, London, (1989) pp.175.
[8] J. Pilling, D. W. Livesey, J. B. Hawkyard, and N. Ridley: Metal. Sci. **18** (1984) pp.117-122.
[9] M. T. Salehi, J. Pilling, N. Ridley and D. L. Hamilton: Mater. Sci. Eng. **A150** (1992) pp.1-6.
[10] M. F. Islam, J. Pilling and N. Ridley: Mater. Sci. Technol. **13** (1997) pp.1045-1050.
[11] A. Wisbey, B. Geary, D. P. Davies and C. M. Ward-Close: Mater. Sci. Forum. **170-172** (1994) pp.293-298.
[12] G. Cam, H. Clemens, R. Gerling and M. Kocak: Z. Metallked. **90** (1999) pp.284-288.
[13] J. Pilling and N. Ridley: Mater. Sci. Technol. **3** (1987) pp.353-359.
[14] Y. Huang, F. J. Humphreys, N. Ridley, and Z. C. Wang: Mater. Sci. Technol. **14** (1998) pp.405-410.

[15] J. Harvey, P. G. Partiridge and A. M. Lurshay: Mater. Sci. Eng. **A79** (1986) pp.191-.
[16] N. Ridley, J. Pilling, A. Tekin and Z. W. Guo: Diffusion Bonding, ed by R. Pearce (Cranfield School of Industrial Science, 1987) pp.129-142.
[17] T. D. Byun and R. B. Vastava: Welding, Bonding and Fastening, ed by J. D. Buckley and B. A. Stein, (NASA Langley Research Center, Hampton Va, 1984) pp.231-245.
[18] T. D. Byun and P. Yavari: Superplasticity in Aerospace-Aluminium, ed by R. Pearce and L. Kelly, (Cranfield, 1985) pp.285-294.
[19] N. Ridley, M. T. Salehi and J. Pilling: Mater. Sci. Technol. **8** (1992) pp.791-795.
[20] H. J. Frost and M. F. Ashby: Deformation-mechanism Maps, (Pergamon Press, Oxford, 1982) pp.44.

Corresponding author : Hidetoshi Somekawa

E-mail : cz203@mtl.osakafu-u.ac.jp

Effect of the pulse frequency on solidification crack sensitivity of TIG welded AZ31 magnesium alloy

Toshikatsu ASAHINA, Hiroshi TOKISUE and Kazuyoshi KATOH

Department of Mechanical Engineering,
College of Industrial Technology Nihon University Chiba, JAPAN

ABSTRACT

AZ31 magnesium alloy plates, which set up a Local Tensile Strain cracking tester, were welded using AC pulsed TIG welding machine. Effect of pulse frequency on crack sensitivity of welded AZ31 magnesium alloy was investigated. The longitudinal cracks appeared on center of the bead, which became clear, the solidification crack after observation of fractured surface using SEM. Regardless of the welding conditions, appearances of the solidification crack have a tendency to depend on the pulse frequency, and it is recognized that the solidification crack sensitivity decreases with the frequency of 30 Hz. The lengths of solidification cracks have a tendency to depend on the grain size on the fusion zone. This phenomenon is possibly explained by the fact that cracks did not easily propagated on the fusion zone because the applied stress is dispersed in fine grain. The solidification cracks of TIG welded AZ31 magnesium alloy were occurred by restraint stress due to the deformation during welding process and could not recognized the influence of the segregation of compounds on the fusion zone.

1. INTRODUCTION

The welding heat input to magnesium alloy welding can be small because the alloy's melting point is relatively low. However, its thermal conductivity and thermal expansion ratio are high, so the welding stress apt to be high and welding cracks are easy to occur. Therefore, the control of the heat input is important to obtain a favorable welding joint. The conventional TIG welding controls the heat input only by controlling welding current and welding speed, so controlling heat input in the working process was relatively difficult. In the report of the TIG welding in which pulse are added to the welding current, the pulse were made fine structure, increase joint efficiency, and suppress welding cracks [1].

Furthermore, if magnesium alloy is restricted at welding process, welding cracks can occur. These kinds of welding cracks found in the alloys are high-temperature cracking, in which the ratio of solidification cracks is extremely high. Therefore, any evaluation of the weldability of these alloys will require a research of solidification cracking. There is

no investigation about the extruded magnesium alloy plate for the welding cracks, however, though there are reports on repair welding of cast magnesium alloys [2].

Solidification cracks are considered to occur when the liquid remaining on the boundary surface of dendritic structures that have been developed in the solidification process cannot stand shrinking pressure and opens right before welding metal solidifies [3]. This suggests that suppressing the growth of dendritic grains will prevent the formation of solidification cracks to some extent.

In this research, AZ31 magnesium alloy plate set up an experimental cracking tester and bead welded by pulse TIG welding to investigate the effects of pulse frequency on crack sensitivity.

2. MATERIALS AND EXPERIMENTAL PROCEDURE

AZ31 magnesium alloy plates (6mm in thickness) were machined into the shape and size as shown in **Fig. 1**. The chemical composition and mechanical properties of base metal are given in **Table 1**. Before welding, the specimens were degreased using a wire brush and acetone.

By considering the previous experimental data for TIG welded joints of AZ31 magnesium alloy [4], AC welding current was employed.

The pulse frequencies were 0, 10, 20, and 30Hz. Argon gas was applied to the surface and penetration sides of specimens for shielding to prevent the oxidization of welds. The welding conditions were listed in **Table 2** so as to suppress cracks under the no restraint condition.

The welding starting point was set to the point 10mm from the edge of the test specimen A in Fig. 1, and the centerline of the test specimen was bead welded.

The experimental crack tester designed and created for this study is based on the Local Tensile Strain crack method of Shinoda et al. [5], in which a local tensile load is applied vertically against the welding direction. **Fig. 2** shows the

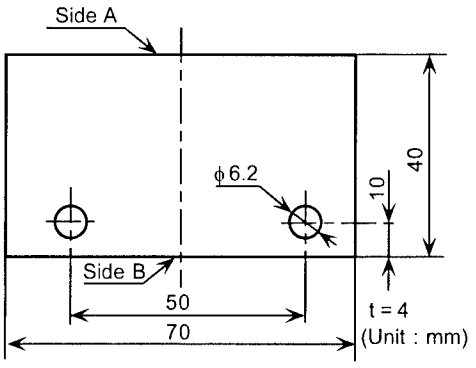

Fig. 1 Size and shape of specimen for Local Tensile Strain cracking test.

Table 1 Chemical compositions and mechanical properties of base metal.

Chemical compositions (mass%)					Mechanical properties		
					Tensile strength	Elongation	Hardness
Al	Zn	Mn	Si	Mg	(MPa)	(%)	(HV0.5)
3.00	0.90	0.31	0.02	bal.	246.5	24.1	55

structure of the tester. One end of the specimen was secured on a bench and the other end was secured on a carriage on a rail. The axis attached to the carriage was loaded by spring. The applied load was adjusted by adjusting the position of the spring with a loading bolt. The degree of load was calculated from the spring displacement, as calculated from differential amplifier output and the spring constant.

Under different welding conditions, the depth of penetration and the bead width slightly change. In this experiment, the pulse frequency and the applied load were varied. The longest crack and the total length of all cracks in the surface and penetration beads were recorded, and crack sensitivity was evaluated in terms of this data. The cracking sensitivity was evaluated based on the maximum crack length and the total crack length.

Table 2 TIG welding conditions.

Pulse frequency	(Hz)	0	10, 20, 30
Welding current	(A)	110	-
Base current	(A)	-	90
Pulse current	(A)	-	150
Arc voltage	(V)	13	
Welding speed	(mm/min)	200	
Gas flow rate	Surface	20	
(ℓ/min)	Backing	15	

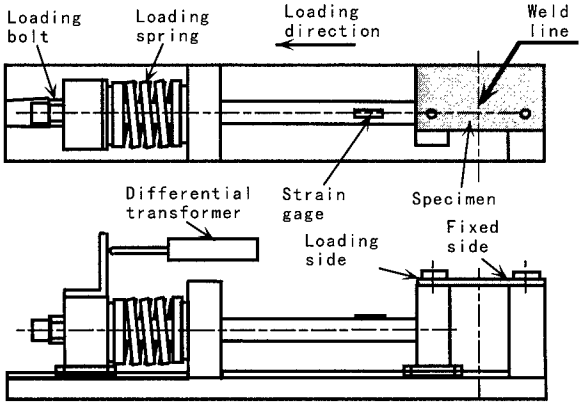

Fig. 2 Principle of Local Tensile Strain Cracking test equipment.

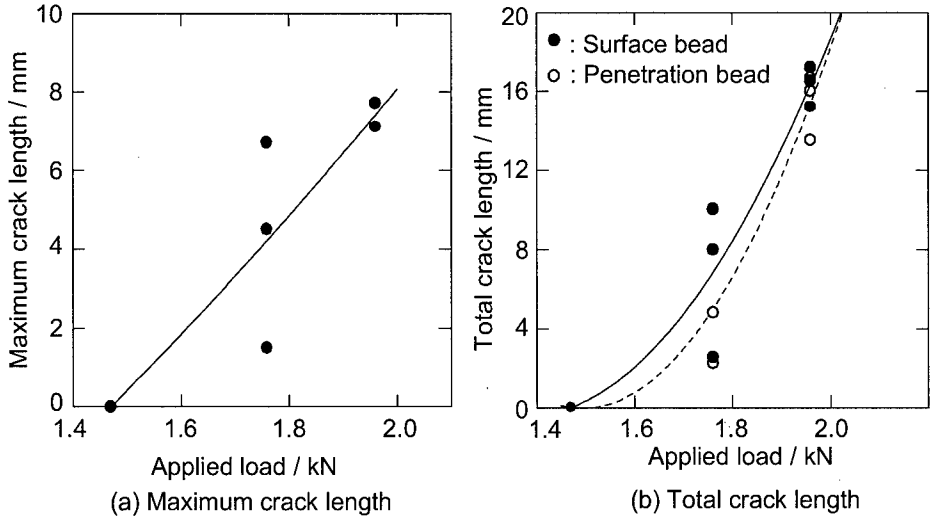

Fig. 3 Effects of applied load on maximum crack and total crack length. (Pulse frequency : 0 Hz)

3. RESULTS AND DISCUSSIONS

3.1 Selection of Applied Load

The effect of the applied load on the maximum crack length and the total crack length without pulse is shown in **Fig. 3**. No cracking was observed under the load lower than 1.47kN, but after the load excesses 1.47kN, the maximum crack length increased as the load becomes larger.

Furthermore, under the load of larger than 1.96kN, the specimen fractured and the measurement became impossible. The total crack length of both the surface and penetration bead showed almost the same tendency that the total crack length increases as the applied load becomes larger. The cracking of heat affected zone was not found under any welding conditions.

Considering the issues described above, in this experiment, the applied load was set to 1.96kN for AC welding.

3.2 Effects of Pulse frequency on Crack length

The effect of pulse frequency on the maximum crack length and the total crack length that occurred is shown in **Fig. 4**. The maximum crack length was found on the surface bead. The length was almost the same with pulse frequency of 0, 10, or 20Hz, but it decreased with the frequency of 30Hz.

The total crack length of both the surface and penetration beads was the greatest with the pulse frequency of 0Hz, and decreased in the order of 20, 10, and 30Hz. Namely, reduction of the cracking sensitivity was recognized with the pulse frequency of 30Hz in the total crack length, as with the maximum crack length. It is assumed that this reduction of solidification cracks comes largely from the shrinking stress with the granular crystal field in the solid-liquid co-existence area added by the refinement of granular crystals of solidification compound, the decrease of the brittle temperature area and the amount of solidification shrinkage by the delay of the gathering of dendrite [6].

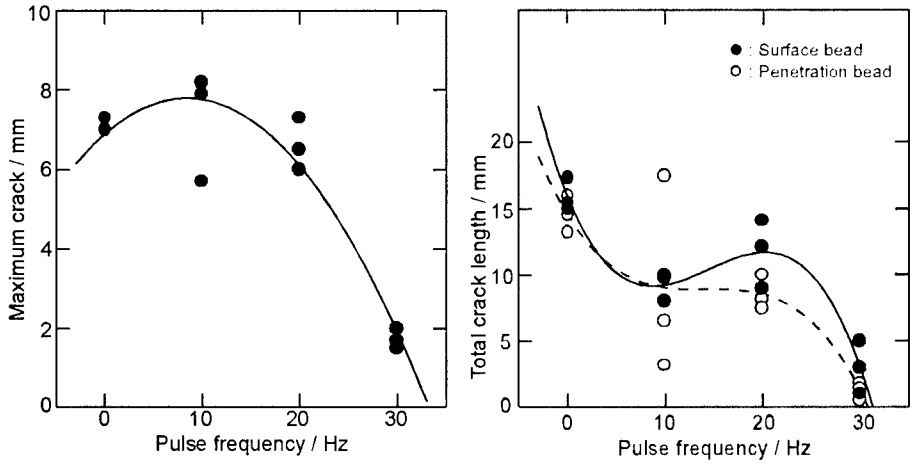

Fig. 4 Effect of pulse frequency on maximum crack length and total crack length.

3.3 Configuration of Crack

An example of the cracking forms is shown in **Fig. 5**. The cracks that occurred were vertical cracks perpendicular to the direction of the applied load, regardless of the pulse frequency. These vertical cracks occurred with the starting point set to the center part of the bead, which is the last solidification part. Although the cracks on the specimen without pulse were continuous, on the specimen with pulse, many relatively small cracks occurred with minute vertical cracks. As described above, we assume this is because the granular crystal is fragmented and the applied load was also fragmented, and the continuous minute cracks that occurred form the major crack.

The horizontal cracks parallel with the direction of the applied load were not found under any welding conditions.

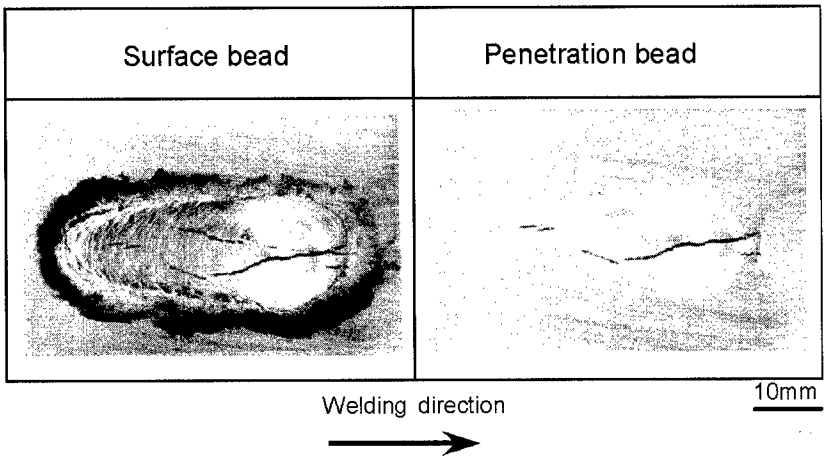

Fig. 5 Bead appearance of AC TIG welded AZ31 magnesium alloy after cracking test. (Pulse frequency : 10 Hz)

3.4 Grain Size of Fusion Zone

The relation between the pulse frequency and the average grain size in the center part of the fusion zone after the cracking test is shown in **Fig. 6**. The grain sizes on the surface and the cross section with pulse showed smaller value than that of without pulse, and showed the tendency of further fragmenting along with the increase of the pulse frequency. The grain size on the surface was slightly greater than that on the cross section. While the grain size on the cross section without pulse was 66.4 mm, with the pulse frequency of 30Hz, it showed the minimum value of 35.5 mm. For this reason, it is considered that the reduction of the cracking sensitivity occurred because granular crystals in the fusion zone were fragmented and consequently the stress was also fragmented, increasing the resistance to the cracking occurrence. It is reported that also in the pulse MIG welding of aluminum alloys, granular crystals were refined and the solidification cracking sensitivity was improved with the frequency of 30Hz [7].

The resonance frequency of the molten pool depends on the base metal and the size of

the molten pool. It is reported that the larger the molten pool is, the lower the resonance frequency becomes [1].

4. CONCLUSIONS

From the investigation on solidification crack sensitivity of AZ31 magnesium alloy plate using Local Tensile Strain cracking tester, the following results were obtained :

1) Most cracks were vertical and classified as solidification cracks from an observation of fractured surfaces.
2) Cracking depends on the pulse frequency and the lowest crack sensitivity occurring at 30 Hz.

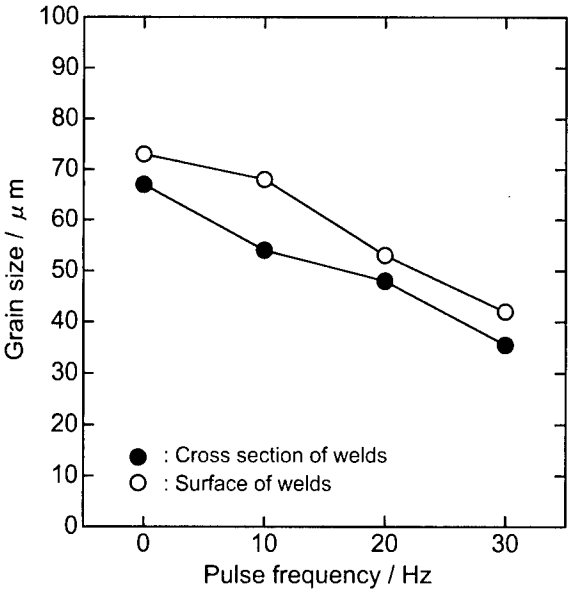

Fig. 6 Relation between pulse frequency and grain size on fusion zone.

3) Solidification cracking depends on grain size in the fusion zone.
4) Pulse TIG welding causes solidification cracks in AZ31 magnesium alloy only under external load, and is not influenced by the behavior of eutectic compounds or inclusions.

REFERENCES

1. T.Watanabe and H.Nakamura, Journal of the Japan Welding Society, Vol.56(1987), pp.16-20.
2. K.Tanaka and K.Furukane, Journal of Light Metal Welding & Construction, Vol.22(1984), pp.539-547.
3. H.Honma, Journal of the Japan Welding Society, Vol.57(1988), pp.26-30.
4. T.Asahina and H.Tokisue, Journal of Japan Inst. Light Metal, Vol.45(1995), pp.70-75.
5. T.Shinoda, Journal of Light Metal Welding & Construction, Vol.26(1988), pp.365-369.
6. F.Matsuda, K.Tanaka, K.Tskamoto and S.Jogan, Journal of the Japan Welding Society, Vol.55(1986), pp.120-124.
7. H.Yamamoto, S.Harada, T.Ueda, S.Ogawa and F.Matsuda, Journal of Light Metal Welding & Construction, Vol.31(1993), pp.64-70.

Mechanical Properties and Interface Reaction in Brazed Joint of Titanium and Stainless Steel

S. C. Kwon, H. J. Yim, S. H. Kim and Y. Y. Kim

System-Integrated Advanced Reactor Project
Korea Atomic Energy Research Institute
150, Duckjin-dong, Yusong-gu, Taejon 305-600, KOREA

ABSTRACT

Direct welding has been known as an unacceptable method for joining titanium to stainless steel, because brittle intermetallic phases are formed in the weld metal. To obtain sound joints, brazing technology was applied with silver-base filler metals in this study.

Optimal brazing conditions were established through evaluation of bonding strength, interface microstructure and fractured surface analysis. The major parameters of processes were the kinds of filler metal, brazing temperature, brazing time and heating rate. Brazed joints using BAg-19(Ag-7.5Cu-0.2Li) filler metal showed higher tensile strength(>250 MPa) than the joints prepared with BVAg-30(Ag-27Cu-5Pd) filler metal did.

According to SEM/EDAX analysis, titanium dissolution to the melted filler metal, Ti-Cu intermetallic compound at the side of titanium, and Ti-Fe intermetallic compounds at the side of stainless steel were observed. Ti and Cu were distributed at both sides of joint.

Although the melting temperature of BVAg-30 was lower, the lower bonding strength was due to poor wetting to stainless steel. To increase the wetting of filler metal and to decrease the formation of brittle intermetallic compound, the effect of Ni plating before brazing was investigated.

To minimize the formation of intermetallic compounds, the brazing time was decreased. As the result, higher bonding strength could be obtained.

1. INTRODUCTION

Brazing titanium to stainless steel has been examined for chemical tanks, space satellites, submarines and ice-breakers. When the joint of such dissimilar metals is fusion-welded, it is difficult to obtain sound welded joint because a brittle intermetallic phase forms at the interface[1].

For a new type of steam generator, brazing method for titanium alloy/stainless steel dissimilar joint has been studied. At the steam outlet, titanium alloy Gr. 9 tubes are connected to AISI 321 stainless steel tubes of secondary cooling system. Generally the brazed joint cannot get the strength of base metals because of the formation of Ti-Fe intermetallics at the interface. Therefore, the connection was designed as a threaded joint to get enough joint strength. And the thread gap is filled with a filler metal for the protection of steam leakage.

There are a few of reports about the brazing technology of titanium alloys to stainless steel. Even though they tried with many kinds of filler metals, they did not attain the joint strength over 300 MPa[2-6].

In this study, the effects of brazing temperature are evaluated with two kinds of filler metals. The clearance of joint cannot meet the value of AWS guide, 0.05-0.13 mm. Ni coating on the stainless steel was tried not only to improve wetting of filler metal, but also to protect the formation of Ti-Fe intermetalic phase. The results demonstrate that joint strength was maximum at 940°C and the keeping time at brazing temperature should be short when BAg-19 filler metal was used.

2. EXPERIMENTAL PROCEDURE

The geometry of real connection sample(Sample A) was as shown in Fig. 1. The length of thread was 38 mm. At the upper of female part, a funnel shape was welded to contain the molten filler metal(Fig. 1(b)). Out diameter/thickness of female part and male part was 50/6 mm and 38/5.5 mm at the position of brazing, respectively. The compositions of base materials used in this study are shown in Table 1. Titanium alloy Gr. 2 was used for tensile test specimen(Sample B) instead of Gr. 9 because applicable size of rod could not be got. The tensile strength was affected by the formation of intermetallic phase (Ti-Fe) at the surface of stainless steel. Therefore, Gr. 2 can be expected not to show large difference of joint strength from that of Gr. 9. The tensile test specimen dimensions were 6 mm diameter x 32 mm long (Fig. 2).

BAg-19 and BVAg-30 were used as filler metals. Chemical compositions and melting temperatures are given in Table 2. BAg-19 contains lithium that helps wettability on stainless steel but its melting temperature is higher than that of BVAg-30. For Sample A, rings of were made with filler metal wire of 1 mm in diameter. The rings were inserted in the container. For Sample B, filler metals were in the form of foils with thickness of 50 μm.

The surface of Sample A was as machined, without additional polishing. But bonding surfaces of Sample B were ground to a 600-grit finish. Stainless steel and filler metal were degreased with acetone. Ti alloys were pickled in solution of 40% HNO_3 + 2% HF + 58% H_2O and cleaned with water and acetone. Ni plating on stainless steel was carried out in Watts type electrolytes. Thickness of Ni layer was 25 μm.

For Sample B, a stainless steel jig was used as shown in Fig. 3. Ti alloy was fixed on stainless steel, after filler metal was placed. Brazing was performed in a vacuum electric furnace equipped with a diffusion pump. The pressure inside a vacuum chamber was held at 1.3×10^{-3} Pa.

Samples were brought to the brazing temperature with 10°C/min heating rate and then held at that temperature for various lengths of time, from 0 to 10 min. The cooling was controlled with Ar gas. The rate was 18°C/min to 400°C and then 7°C/min to room temperature. Brazing temperature was chosen in 20°C increments from 850°C to 910°C for BVAg-30 filler metal and from 880°C to 960°C for BAg-19 filler metal.

Specimen temperature was monitored with K-type thermocouples attached to the specimen surface near the joining area.

Joint tensile strength was measured using INSTRON 8561 at a crosshead speed of 0.5 mm/min.

Joint interface region of Sample A and fracture surface of Sample were examined using

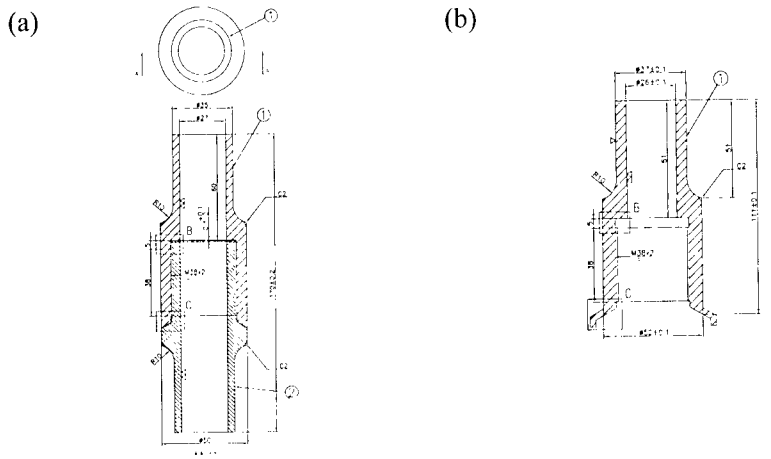

Fig. 1. Geometry of real connection sample: (a) Assembled sample; (b) Female part attached with a container. Male part: Ti alloy; Female part: stainless steel.

Table 1. Compositions of base metals

(a) Stainless steel AISI 321 (wt %)

C	Mn	Si	Cu	Ni	Cr	Mo	V	Ti	Fe
0.05	1.57	0.56	0.33	9.28	17.19	0.37	0.10	0.45	Balance

(b) Ti alloys (wt %)

Material	Composition							
	Al	V	Fe	O	H	N	C	Ti
Gr.2	-	-	0.06	0.12	0.0004	0.03	0.01	Balance
Gr.9	3.5	2.5	0.25	0.15	0.008	0.03	0.08	Balance

Table 2. Compositions and melting temperatures of filler metals

Material	Composition(wt %)					Solidus	Liquidus
	Ag	Cu	Pd	Li	Others	°C	°C
BAg-19	92.69	7.06	-	0.24	0.01	760	891
BVAg-30	67.16	27.93	4.90	-	0.01	807	810

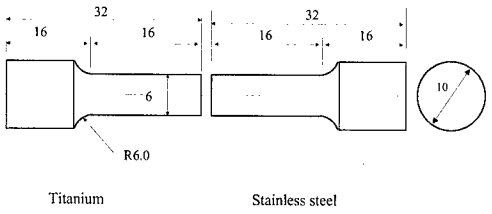

Fig. 2. Tensile test specimen dimension.

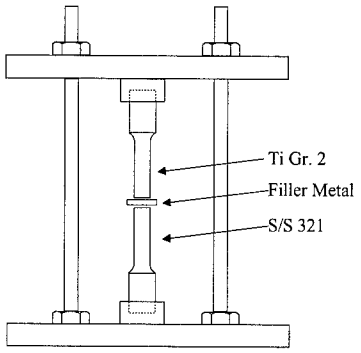

Fig. 3. Brazing jig.

scanning electron microscopy(SEM) equipped with energy dispersive X-ray analyser attachment (EDAX).

3. RESULTS AND DISCUSSIONS

3.1 Joint tensile strength

An effort was made to investigate how brazing temperature, holding time and filler metal affect the joint strength. Fig. 4(a) shows the effect of brazing temperature when holding time at brazing temperature was 4 min. Brazed joint using filler metal BAg-19 showed relatively higher tensile strength as compared with brazed joint with BVAg-30. Maximum was 274 MPa at 944°C. On the other hand, brazed joint using filler metal BVAg-30 showed 199 MPa at 868°C.

In the case of the brazed joint using BAg-19, the tensile strength increased slowly from 877°C to 944°C and decreased rapidly. However, the brazed joint using BVAg-30 showed rapid increase of strength from 852°C to 868°C and then decreased slowly to 910°C.

Fig 4(b) shows joint strength as a function of holding time when Sample B was brazed with BAg-19 at 940°C. It can be seen that the joint strength decreased with increasing holding time. At zero holding time, The joint strength was 311 MPa. The decreasing rate is small to 4 min of holding time. This fact might be due to the difference of temperature between the surface and the center of samples. Though the surface temperature was 940°C, it needed time until the

temperature of sample was homogenized from the surface to the center.

Ni plated sample showed the increase of tensile strength to 337 MPa. This indicates Ni plated layer on the stainless steel could protect the formation of Ti-Fe intermetallic phase. And the melt of filler metal flew down along the surface of lower stainless steel, though it rose along the surface of upper Ti alloy of not-plated sample. This shows that Ni plating helped the wetting on stainless steel.

Accordingly, the optimal condition of brazing can be suggested as 940°C of brazing temperature, no holding time and Ni plating on stainless steel. However, Sample A was not plated with Ni, because it was hard to make uniform thickness on the thread of stainless steel.

3.2 Fracture surface analysis

Fig. 5 shows the fracture surfaces of stainless steel side of joints. There were denser tear ridges at region A than at region B. Brazed joint using BAg-19 showed more tear ridges than the joint using BVAg-30 did. EDAX analysis showed that there is a difference of composition between region A and region B(Table 3). Roughly, region A retained more Ni and Ti and at the same time, less Fe, Ni and Cr than region B did. And region A of brazed joint using BVAg-30 showed some amount of Cu.

Considering the relationship of the chemical composition and joint strength, it is reasonable to propose the following. Region B is near the stainless steel side of interface, brittle Ti-Fe intermetallic layer. Region A is near the center of joint.

3.3 Brazing of real connection sample (Sample A)

After joining, samples were cut vertically into half. The cross section of brazed area was investigated. Even though there were small shrinkage holes near the titanium side, they were acceptable defects.

When Sample A was heated to 940°C, the melt of filler metal leaked from the joint gap of bottom. To fill the joint gap of inlet, the quantity of filler metal was needed 1.5 times more than the calculated one. For the protection of leakage, heating rate should be fast and the brazing time should be short.

3.3 Evaluation of the joint interface region

The cross-section of brazed joint in Sample A was examined. The microstructure and the chemical distribution are shown in Fig. 6. Six regions were observed. In convenience, each region is numbered in the order along the direction from Ti alloy to stainless steel

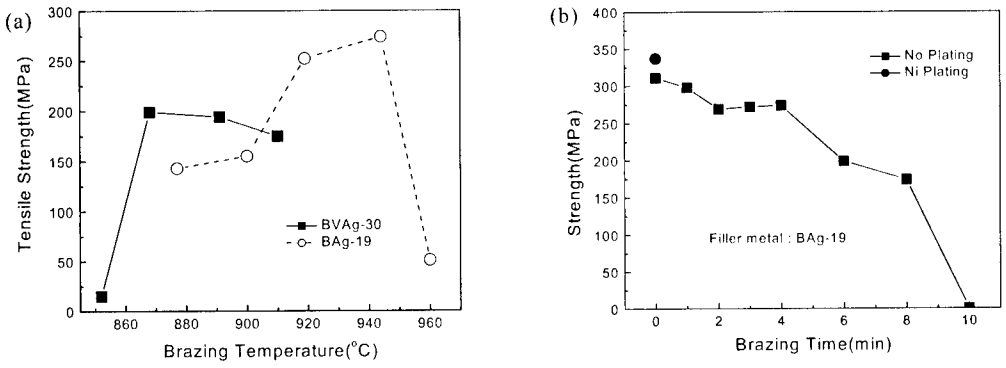

Fig. 4. Joint tensile strength: (a) effect of brazing temperature for 4 min holding time and (b) effect of holding time at 940°C.

Table 3. Chemical composition of the joint area

Sample	Region	Composition (wt. %)						
		Fe	Ni	Cr	Ti	Ag	Cu	Pd
BVAg-30, 868°C	A	26.2	6.6	1.7	43.3	-	20.2	2.0
	B	61.3	3.2	31.3	4.2	-	-	-
BAg-19, 944°C	A	43.9	2.9	9.7	28.8	13.6	1.1	-
	B	55.0	4.0	14.6	24.0	0.7	1.7	-

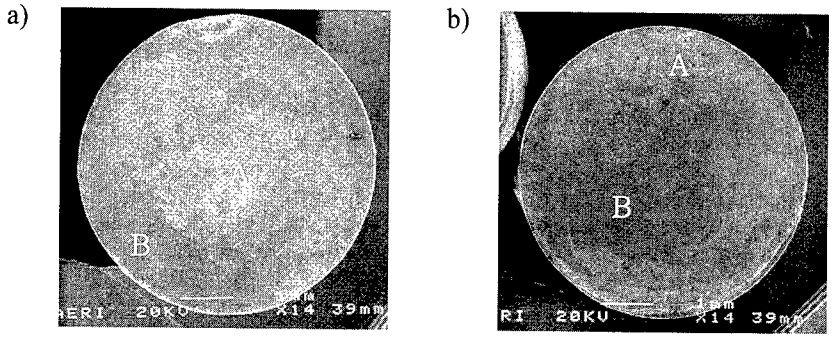

Fig. 5. Fracture surface of samples brazed: (a) With BAg-19 at 944°C, 4 min; (b) with BVAg-30 at 868°C, 4 min.

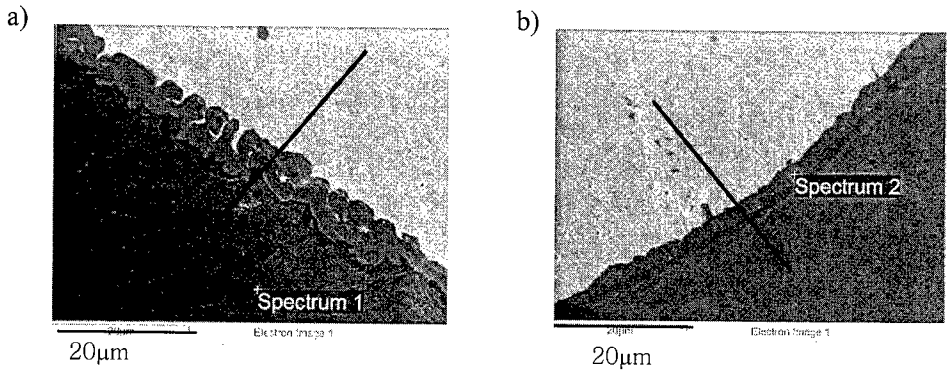

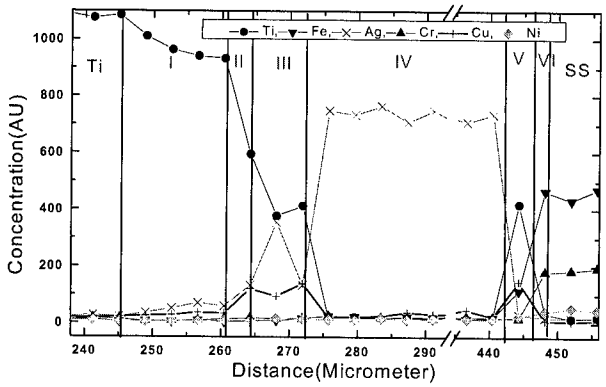

Fig. 6. Microstructure and chemical composition at joint interfaces: (a) Ti alloy side, (b) stainless steel side, and (c) EDAX microanalysis of elements.

In region I, the α-Ti and the Ti_2Cu intermetallic phase formed a lamellar structure. The width of this region was approximately 15 μm. The intermetallic phase grew along the grain boundary of Ti alloy. The microstructure seems to suggest that Cu of filler metal formed β-Ti phase, diffused into titanium alloy, and then formed intermetallics through eutectoid decomposition into α-Ti and Ti_2Cu during cooling.

The width of region II is about 1.5 μm. More Ag and Cu exist than those in region I. This indicates that copper diffuses toward Ti from filler metal and stabilizes β-Ti at the brazing temperature. The β-Ti didn't decompose and remained as a metastable phase.

Region III is composed of Ti, Cu and Ag. The thickness is approximately 5 μm. This layer seems to be formed with $Ti_2(Cu,Ag)$. Even though Camargo et al.[4] suggested the formation of Ti_2Cu, the layer contains relatively high content of Ag. It needs more investigation for the identification of the phase.

Region IV is composed mainly Ag. Ti and Cu are not shown. The distribution of Cu suggests the segregation to both interfaces. Because the gap clearance of Sample A was large, this region was very thick and occupied nearly all of the gap area.

Region V formed due to the interaction between segregated Ti and Cu. This is a result of reactive diffusion of the two elements. The thickness of is about 2.5 μm. Based on the result of chemical analysis, TiCu intermetallic compound seems to be formed.

Region VI is very thin, below 1 μm. Fe, Ni and Cr diffused into this layer from stainless steel. This region seems to contain Ti-Fe, Ti-Ni and Ti-Cr intermetallic phases.

The result of chemical analysis reveals that the region A of fracture surface was formed at the region V and the region B of fracture surface was formed at the region VI. Though the result of Ni plated specimens are not shown in this paper, the microstructure of them did not show the formation of the brittle Ti-Fe intermetallic phases.

4. CONCLUSIONS

Joining of Ti alloy to stainless steel has been studied to find optimal conditions of brazing for a new type of steam generator. Results obtained in this study are as followings.

(1) Brazed joint using BAg-19 filler metal showed better tensile strength than the one using filler metal BVAg-30.

(2) Maximum joint tensile strength was obtained over 250 MPa when processed at 940°C brazing temperature and zero holding time with BAg-19 filler metal.

(3) To limit the formation of brittle intermetallic phases and to increase joint tensile strength, Ni plating on stainless steel is effective.

(4) Brittle layer of Ti-Fe intermetallic phase was formed at the stainless steel side of interface through the reactive diffusion of Ti.

Acknowledgements

This work has been carried out as a part of the Nuclear R&D program funded by Ministry of Science and Technology, South Korea.

REFERENCES

1. M. Futamata and A. Fuji, Q. J. Jpn. Weld. Soc., Vol.7, No.4(1989), pp. 10-16.
2. J. F. Rudy, R. M. Necheles and H. Schwarzbart, Weld. J., Vol.38(1959), pp. 202s-208s.
3. M. M. Schwarz, Welding Research Council Bulletin No. 244(1978).
4. P. R. C. Camargo, R. E. Trevisan and S. Liu, Weld. J., Vol.72, No.12(1993), pp. 537s-544s.
5. R. L. Peaslee, Weld. J., Vol.71, No.5(1992), p. 112.
6. ---, Ind. Heat., Vol.48, No.3(1981), pp. 31-33.

BRAZAING PROCESS AND MICROSTRUCTURES OF Al/Ti BRAZED JOINT

Woong H. Sohn, Seung I. Cha, Ha H. Bong and Soon H. Hong

Dept. of Materials Science and Engineering,
Korea Advanced Institute of Science and Technology,
373-1 Kusong-dong, Yusong-gu, Taejon 305-701, Korea

ABSTRACT

This paper investigates the brazing process for Al and Ti. The joining mechanism between Al and Ti sheets was observed and the microstructures at Al/Ti interface were characterized. 1050Al and cp-Ti were used as base metals, and Al-10Si-1Mg alloy foil of 100 μm in thickness was used as a filler metal. The brazing process of Al/Ti was performed at temperature of 620°C from 5.5 minutes to 2 hours in vacuum. The interfacial bond strengths of Al/Ti brazed joints were assessed by the adhesive shear test. The surface oxide on Al created by Mg element in filler metal was removed within 6 minutes after the brazing process initiated. The bonding at Al/filler interface proceeded by wetting the molten filler metal with Al after brazing time of 6 minutes. The Al/filler interface was moved during the isothermal solidification of filler metal by the diffusion of Si from filler metal into Al layer. The Al/filler interface became curved in shape with increasing the brazing time due to a dragging force by grain boundary. The brazing process at Ti/filler interface proceeded by the formation of two different intermetallic layers, identified as $Al_5Si_{12}Ti_7$ and $Al_{12}Si_3Ti_5$, and followed by the growth of intermetallic layers through the diffusion of solute atoms into Ti sheet. The result showed that the bonding strength at Al/Ti brazing joint increased as the brazing time increased up to 30 minutes at 620°C. However, the bonding strength of Al/Ti brazed joint decreased after the brazing time of 30 minutes at 620°C because of the cavities produced at Al/filler interface.

1. INTRODUCTION

Aluminum and titanium alloys have been regarded as the most suitable materials in aerospace (such as T-45 cone) and automobile industries due to light and high specific strength. Being a new kind of structural material, the successful application of this alloy material must be owing to the joining technology.

Generally the joining process between Al and Ti has been performed by diffusion bonding under high temperature and pressure conditions [1]. However, in the real case, the part that should be bonded is so complex in shape, and thus, the application of pressure is quite difficult. Therefore, bonding between part without pressure needs to be done.

Brazing is a classical joining technique [2] that a metal placed between the two parts to be joined is heated up to its melting points. This leads to the formation of a metallurgical bond between the brazing alloy and the respective parts. The brazing filler alloys are of eutectic in their composition. T. Takemoto [3] tested some Al base alloys with a filler metal in Al-Ti bonding. As such, the brazing of aluminum alloys is usually performed with filler metal based on the Al-Si eutectic at an eutectic temperature of 577°C. Sometimes other elements are added to the Ag-Cu eutectic for reactive or wetting purpose, e.g. Ti or Zr.

This study aims to characterize the bonding mechanism in each separate interface -Al/filler and Ti/filler – and to estimate bonding strength by employing a shear test method. In addition, the microstructure of cavities in interface region that are always produced in pressureless bonding process was observed by using an optical micropscope.

2. EXPERIMENTAL PROCEDURES

1050 Al alloy and cp Ti-alloys with the size of 15mm x 10mm x 5mm were used as base materials. The 1050 Al includes 0.25wt% Si and 0.4wt% Fe as alloying elements and, cp Ti alloy includes 0.2wt%Fe and 0.15wt%O. Because the amount of alloying elements within the base metal was very small, the base metal could be regarded as pure metal under the assumption that small amount of alloying elements do not affect the bonding process. The brazing filler metal used in this test is an Al-Si-Mg foil with the thickness of 100 μm and the composition of 10.0%Si, 1.0%Si and 89%Al. Before brazing, Al-Si-Mg foil, all specimens were cleaned carefully using aceton solution and were finally fixed in a specific fixture. The brazing tests of specimens were performed within the quartz tube that was sealed to produce vacuum with maintaining a pressure of 1mtorr. The brazing is normally carried out at the temperature that is 30 to 50°C above the liquidus temperature of the filler metals. Therefore, the brazing temperature of filler metal with a eutectic temperature of 577°C is set at 620°C. The microstructures and compositions of specimens were analyzed by scanning electron microscopy (SEM), optical microscopy (OM) and EPMA. Especially, in the case of EPMA method, we utilized WDS by ZAF calibrating with standard samples and maintaining take-off angle with 35°. The interfacial bond strengths of Al/Ti brazed joints were evaluated by the adhesive shear test.

3. RESULTS AND DISCUSSIONS

3.1. Microstructures of Interface and Bonding Process

Fig. 1 shows the microstructures of interface between Al and Ti base metal during brazing process at 620°C. The Ti/filler interface was bonded after heating of 5.5min. However, the bonding between Al/filler interface began after 7min heating. By heating for the first 6min, the filler metal became liquid because the melting temperature of Al-10Si-1Mg alloy is about 577°C. The time gap between bonding and melting of filler existed due to the formation of the oxide on the surface of Al base metal. The oxide on the surface of Al base metal was removed after 7min heating, as shown in Fig. 2. At this time, the bonding between molten filler metal and Al base metal took place by wetting molten filler metal while the bonding between filler metal and Ti base metal proceeded by the formation of intermetallic compound at the interface.

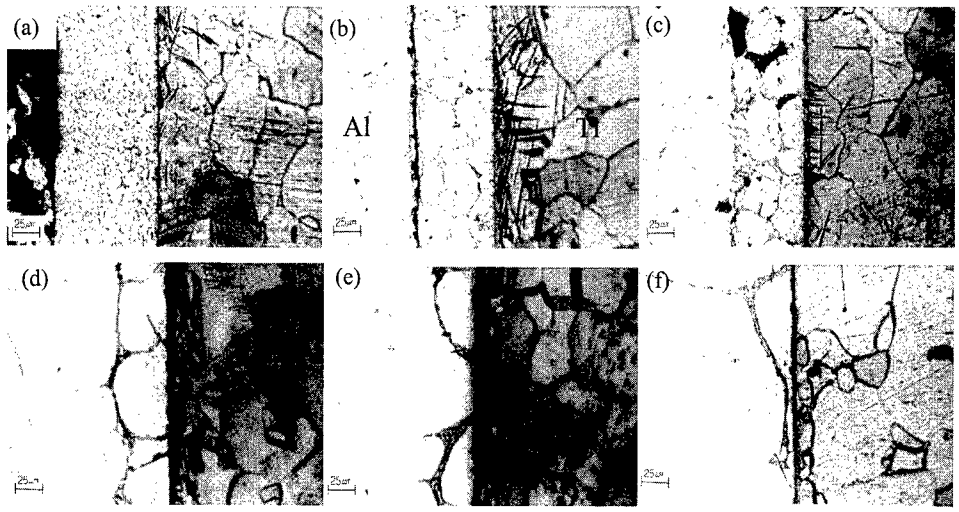

Fig. 1. The microsturctures of Al/Ti specimen bonded at 620°C with increasing heating time. (a) 5.5min, (b) 6min, (c) 7min, (d) 9min, (e) 13min, (f) 30min.

After wetting between Al and filler metal was completed, the Al/filler interface moved into the filler direction. The interface was initially flat, and yet, became wave shape with increasing process time. The interface movement was quite similar to that in the transient liquid phase bonding process. The concentration of Si on filler metal decreased by diffusion of Si that lowers the melting temperature. Therefore, by decreasing Si concentration near the Al-filler interface, the melting temperature of filler near the interface increased. As a result, the isothermal solidification process occurred [4-6]. The Si concentration in the Al base metal was measured by WDX in line scan method as shown Fig. 3. The Si concentration in Al base metal can be calculated as follows;

$$C_{Si} = C_0\left(1 - \mathrm{erf}\left(\frac{x}{2\sqrt{Dt}}\right)\right) \qquad (1)$$

where, C_{Si} is composition of Si in Al base metal, C_o is solution limit of Si and D is 19.5×10^{-13} (m^2/s) at 620°C. The Si concentration in Al base metal was quite fitted with error function

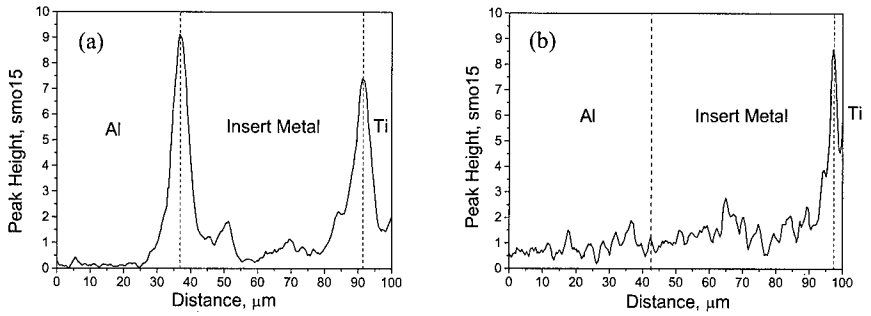

Fig. 2. Oxygen contents of bonding interface measured by Auger electron spectroscopy. (a) bonding for 6min and (b) bonding for 7min.

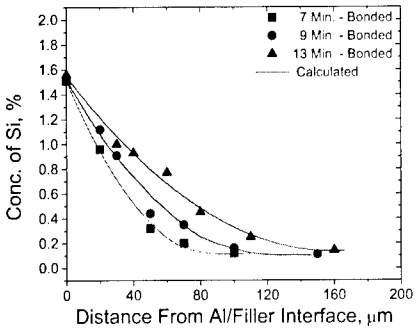

Fig. 3. The Si concentration profile in the Al base metal near the interface. The solid line indicates the theoretically calculated values.

such as eq. (1). However, the Si concentration profile in Al base metal did not severely change during bonding process. Therefore, it is reasonable to mention that the Si concentration in the Al base metal was in steady state and the transfer rate of Al solute into the base metal was consistent. As shown in Fig. 2, the grain of Al base metal grew into the filler layer and at the same time the Al grain was nucleated and grew into the liquid filler layer from intermetallic layer that was formed on the Ti base metal.

The intermetallic compounds at interface between Ti and filler metal consisted of two layers, as shown in Fig. 4. One intermetallic layer located on the Ti surface was continuous while intermetallic layer at outer side was discontinuous with needle-like shape. In order to identify the intermetallic phase, the XRD and EDAX analyses were utilized. It is found from the EDAX study that the continuous intermetallic phase has 17wt%Al-50wt%Si-33wt%Ti composition and the discontinuous phase has 58wt%Al-13wt%Si-27wt%Ti composition. The XRD experiment was performed after removing Al layer by NaOH solution, and it shows that the material gained the diffraction signals from intermetallic layers. As shown in Fig. 5, the diffraction peaks from intermetallic layer were well indexed as $Al_5Si_{12}Ti_7$ for continuous layer and $Al_{12}Si_3Ti_5$ for discontinuous layer, respectively. These XRD results agreed well with the EDAX results in identifying composition of intermetallic layers. The thickness of continuous intermetallic layer increased with increasing brazing time. These results showed that intermetallic layer was formed by diffusion process. In the case of Al-Ti bonding, the cavity could be formed in Al-Al interfaces because, on the Ti-filler interface, the Al grains were nucleated and grew in the direction of base Al metal by Si diffusion into the intermetallic phases.

3.2. Interface Bonding Strength

The interfacial bond strengths of Al/Ti brazed joints were evaluated by the adhesive shear test. The variation of bonding strengths of Al/Ti brazed joints according to the bonding time at the temperature of 620°C was shown in Fig. 6. The maximum bonding strength was 84Mpa at the bonding time of 30min. The bonding strength behavior of Al/Ti brazed joints was divided into 3 stages in terms of the brazing time. In the first stage, from 1min to 7 min, thebonding strength rapidly increased as the bonding time increases. In this stage, as shown in

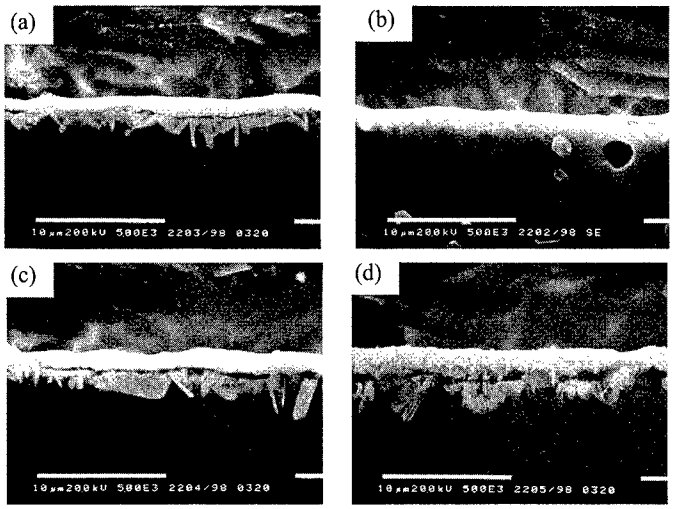

Fig. 4. SEM micrographs of intermetallic compound at Ti/filler interface bonded at 620°C. (a) 5.5min, (b) 6min, (c) 7min, (d) 9min.

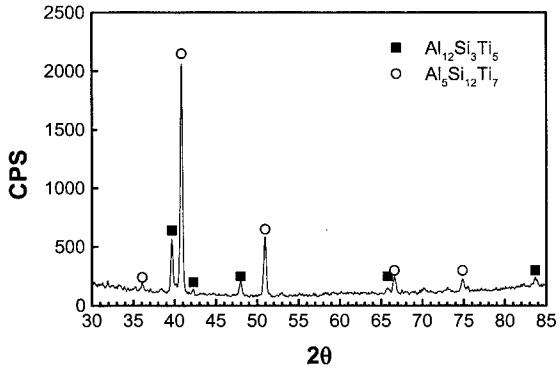

Fig. 6. X-ray diffraction patterns of intermetallic layers on Ti side after removing Al by NaOH solution.

Fig. 2, the bonding was not completed in the Al-filler interface and the oxide of Al surface was fully removed at the bonding time of 7 min. Therefore, the bonding strength increased with the increasing bonding time because bonding area between Al-filler increased with the increasing bonding time and was completely wetted by liquid metal at the 7 min bonding. In the second stage, from 7min bonding to 30min bonding, the shear strength increased slightly with the increasing bonding time. In this stage, the interface of Al base metal moved into the liquid filler metal, and the thickness of eutectic layer of filler was reduced. In the case of filler eutectic phase, the strength was higher than that of Al base metal and, therefore, the stress concentrated in filler eutectic layer. As a result, with the decreasing filler layer, the whole specimen became more homogeneous, and these effects contribute to the slight increase of the

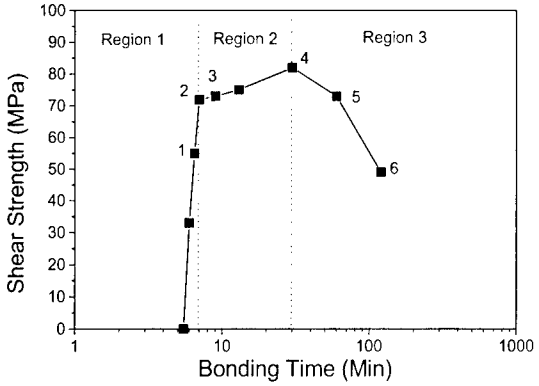

Fig. 6. The bonding strength of Al/Ti brazed joints as increasing bonding time at 620°C.

bonding strength. However, when the bonding time exceeded 30min, the bonding strength of Al/Ti brazed joint decreased after brazing time of 30 minutes at 620°C due to the cavities formed at Al/filler interface.

4. CONCLUSIONS

From the micrography and the bonding strength measurement for Al/Ti brazed joints, we could conclude that:

1. The bonding between Al and filler was performed by removing oxide layer and wetting of liquid filler metal on the Al base metal surface and subsequence isothermal solidification.
2. The bonding between filler and Ti was performed by growth of intermetallic phase that was generated by Si diffusion into the Ti base metal.
3. The bonding strength of Al/Ti bonding increased as the bonding time increases up to 30min because bonding formation between filler and base metals and subsequence homogenization process accompanied. However, after the bonding time of 30 min, the bonding strength decreased due to interfacial cavity.

REFERENCES

1. N. F. Kazakov, Diffusion Bonding of Materials, Pergamon press (1985).
2. M. Schwartz, Brazing for the Engineering Technologist, Chapman & Hall, London, 1995.
3. T. Takemoto and I. Okamoto, *J. Mater. Sci.*, Vol.23 (1988) pp.1301.
4. I. Tua-Poku, M. Dollar and T. B. Massalski, *Metall. Trans. A*, Vol.19A (1988) pp.675.
5. D. R. H. Jones, *Acta Metall.*, Vol.26 (1978) pp. 689.
6. W. D. MacDonald and T. W. Eagar, *Metall. Trans. A*, Vol.29A (1998) pp. 315-325.

Session VI

SPECIAL SESSION ON JAPAN'S NEDO

NEDO's R&D Program on Key Technology for Innovative Low-Cost and Lightweight Structures

Yukio Ito

New Energy and Industrial Technology Development Organization(NEDO), Tokyo, Japan

Abstract

Innovations for low-cost and light structures are required for new-generation, high-speed transport (aircraft, trains, ships) and other structures (bridges, etc.) to conserve resources and energy and protect the environment. Current structures are assemblies that have a high part count. Application of conventional technologies will have little effect for future light weight structures. Recent technological developments have given us hints for near-term future structures. This program covers three areas:
(i) New design and manufacturing technologies for co-cured CFRP structures;
(ii) New precision casting and welding technologies for large-size metal structures;
(iii) Integration technologies for innovative light structures.
The goal is to drastically and cost-effectively save weight and reduce the part count of cockpit and wing structures for civil aircraft. Advanced CFRP manufacturing technologies will be developed for parts having complicated forms, large-size structures, and new-type sandwich panels. In addition, advanced technologies such as thin, large-size precision casting, friction stir welding and super-plastic forming will be developed. Integration technologies for fastening technology between CFRP parts and metal alloy parts, 3-dimensional CAD and a structural work station will also be developed. This will contribute to the verification process of the above work for a commercial aircraft. This program commenced in summer 1999 as a five-year program.

1. Introduction

Global economic growth and a high quality of life demands high-speed transportation. On the other hand, calls to save energy and resources and protect the environment are increasing year by year. For these reasons, low cost and lightweight vehicles are urgently required. Nowadays vehicles are complex and have a large part count due to a design consistent with strength and lightweight. Application of conventional design methods yields little effects. However, recent advanced manufacturing technology developments such as composite materials, aluminum casting, alloy welding and structural design technologies implies the possibility of innovative design and manufacturing technologies for lightweight and an extremely small number of parts. Under these circumstances, NEDO started a R&D program in 1999 entitled "Key Technology for Innovative Low-cost and Light Structures" as a five year program. This program is aimed at design and manufacturing technology development for innovative light aircraft structures using CFRP (carbon fiber reinforced plastic) and aluminum alloy as excellent materials with specific strength. The experience and achievements of this program will be used for high-speed trains, ships and other structures that can conserve resources and energy, and for creating simple, reliable and lightweight structures which will induce and create new industrial fields.

2. Outline of the R&D Program

The program is covers the following three areas:
① Design and manufacturing technologies for co-cured CFRP structures
② Precision casting and welding technologies for large-size metal structures
③ Integration technologies for innovative light structures

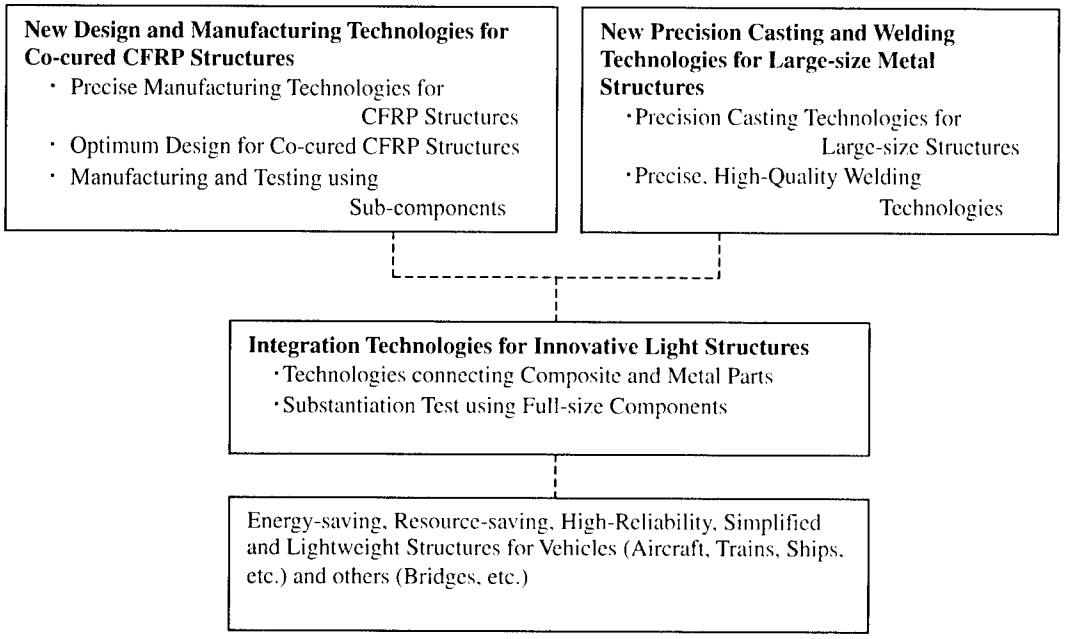

Figure 1. Outline of the R&D Program

2-1 Design and Manufacturing Technologies for Co-cured CFRP Structures

Structures made of metal have been refined and cultivated for lightweight and high strength properties by the "built-up method" (fastening frames, thin skins, etc.). Efforts for lightweight have been made by replacing the metal with an aluminum alloy with high specific strength or a composite material but keeping the conventional built-up method. However, there are limitations with that method. By making the best use of the co-curing characteristic of advanced composite material, a new concept for making structure components and assembling them can be introduced. It will then be possible to reduce part count and weight. For this, the following will be carried out:

(1) Development of precise manufacturing technologies for CFRP structures;
(2) Development of an optimum design for co-cured CFRP structures;
(3) Manufacturing and testing using sub-components.

2-2 Precision Casting, Friction Stir Welding and Super Plastic Forming for Large-size Metal Structures

Conventional large-size metal structures have the disadvantages of a complicated manufacturing process due to a high part count, reliability levels, weight increases from rivet fastening, and a corrosion tendency at the contact surfaces of two materials. For those reasons, it is necessary to develop :

(1) Precision casting technology for large-size and complex figure parts, and

(2) Friction stir welding technology for 2024 and 7075 aluminum alloy parts
(3) Super plastic forming technology for 5083 aluminum alloy parts

2-3 Integration Technology for Innovative Light Structures

In order to optimize strength, cost, etc. for a whole structure, it is necessary to develop technology connecting different materials, design technology including apparatus and devices, evaluation know-how for strength and reliability of a whole structure. The following is being examined in this program :

(1) Technology for connecting composite and metal structure
(2) Efficient integration technology using digital mock-ups, etc.

3. Verification by Design, Fabrication, Testing for Full-scale Component

By incorporating innovative key technologies, cockpit and wing structures equivalent to a small civil transport will be trial fabricated, strength tests will be performed and design and fabrication issues will be identified and solved. Figure 2 shows the actual full-scale components of this project. The first is the cockpit structure, and second is the wing box structure.

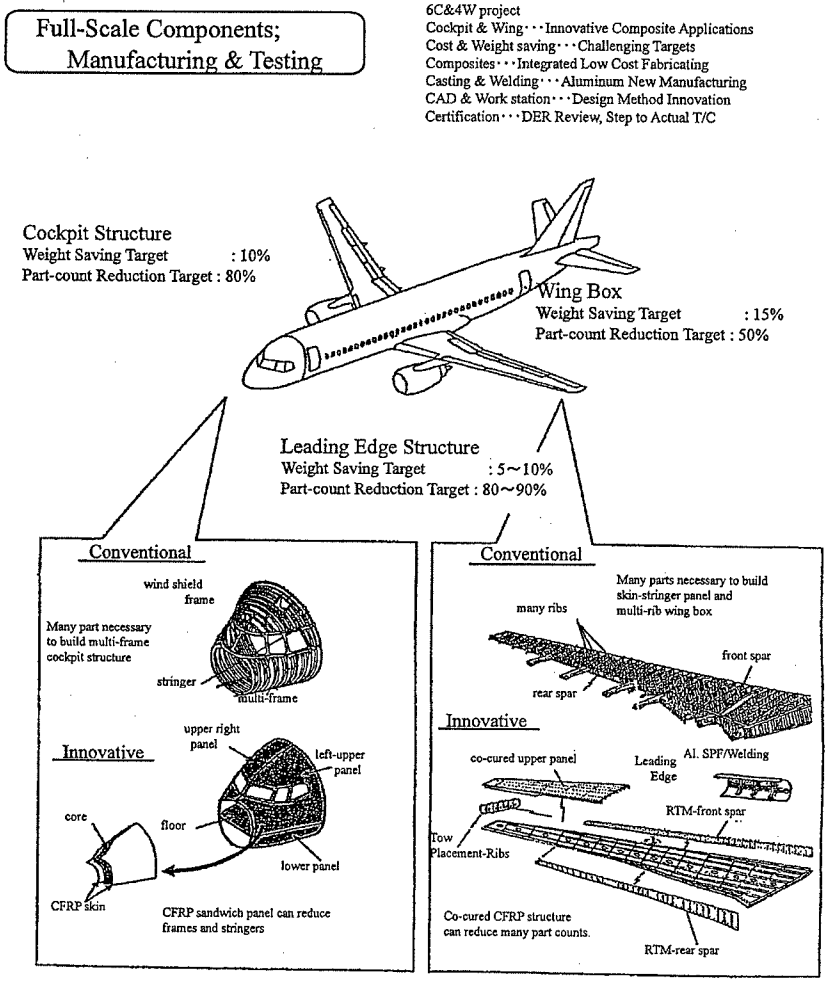

Figure 2 R&D Program of Key Technology for Innovative Structures

Design and manufacturing technologies which conform to airworthiness standards set by airworthiness bureaus, such as the FAA, will be established.

As for cockpit structures, many parts are necessary to build up a multi-frame structure with the conventional method. Using the innovative method, a CFRP sandwich panel can reduce frames and stringers, and new casting and welding techniques can also reduce part count. For example, the pressurized bulkhead is made by friction stir welding. In the case of cockpit structures, the objectives are a 10% weight saving and an 80% part count reduction compared with conventional structures.

In the case of wing structures, many parts are necessary to construct a skin-stringer panel and multi-rib wing box. A new concept for making structure composites and assembling them will be introduced by making the best use of the co-curing characteristic of advanced composite material. Some integrated pieces using advanced composite materials can reduce part count. In this case, the objectives are a 15% weight saving and 50% part count reduction compared with conventional structures.

4. Organization of the Project

The New Energy and Industrial Technology Development Organization (NEDO) solicited proposals for participation in on an R&D program entitled "Key Technology for Innovative Low-cost and Lightweight Structures" in FY1999. Following a strict and fair assessment of all submitted proposals, NEDO selected Japan Aircraft Development Corporation (JADC) as the contractor. The program commenced in summer 1999 as a five-year program. NEDO's policy is to promote the R&D program efficiently with the participation and cooperation of researchers from industrial, academic and governmental fields. An assessment committee composed of NEDO representatives, researchers in these fields, and knowledgeable academic experts was established to promote the project. Assessments are conducted in a timely and proper way.

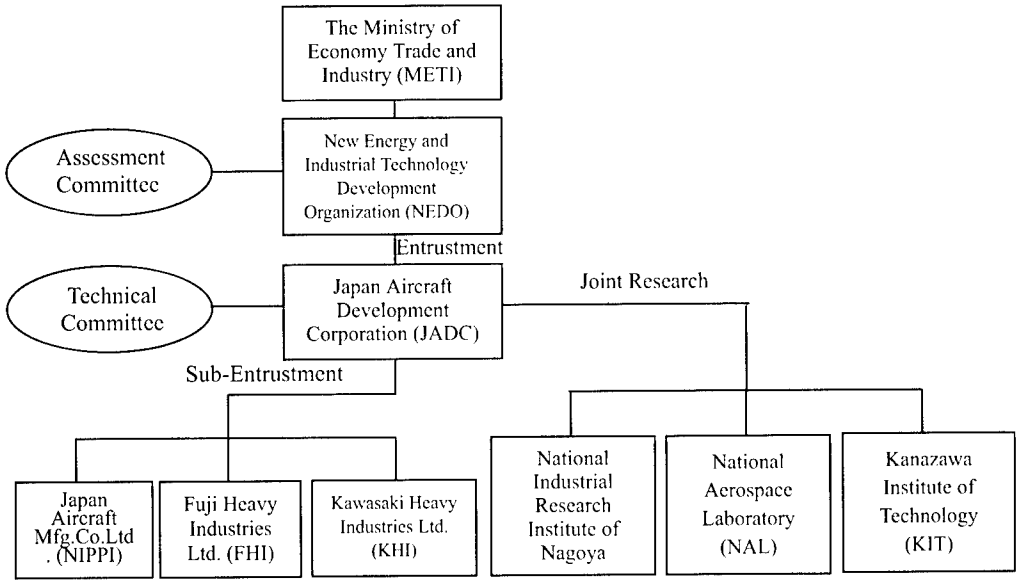

Figure 3 Organization Chart of the R&D Project (FY2001)

5. Eight Key Technologies and Applications

The eight key technologies outlined below are to be developed in the technology development phase (FY1999-FY2001). They are innovative, essential technologies for reaching the weight reduction and part count reduction goals noted earlier.
For composite structures: (1) resin transfer molding (RTM); (2) tow placement; (3) sandwich skin panels using new core materials
For aluminum alloy structures: (4) thin, large-size precision casting using new aluminum alloy D357, (5) friction stir welding applied to aluminum alloys 2024 and 7075, (6) super plastic forming using new aluminum alloy 5083
For design methods: (7) 3D-CAD digital mock-ups, (8) structural workstations

In addition, it will be possible to utilize some technologies for a supersonic transport, trains, ships and bridges as shown in Figure 4, as well as a small airplane.

(1) Co-cured CFRP structures

By making the best use of the co-curing characteristic of advanced composite material, it was found that this method can reduce part count drastically from 50% to 90%. This method will be applied to the wing-box, but it is also possible to apply it to the next-generation supersonic transport shown in Figure 4-(a), where energy-saving and environmental compatibility will be principal objectives.

(2) Sandwich skin panel using new core material

A sandwich skin panel using porous plastic as the core material will be applied to the cockpit structure. Such a panel has already been applied to the nose structure of the super express train shown in Figure 4-(b). It is possible to replace the plastic core with metal core like a magnesium or titanium alloy if greater strength is required.

(3) Large-size precision casting

Efforts will be made to cast a 1850 × 1550 × 2 mm structure using the sand casting method. It is believed that this is the first time this has been done for a structure this size. This size structure requires considerable know-how in the design and heat treatment process. However, if the difficulties are solved, it will be possible to apply large-size casting structures to many parts of ships and bridges as shown in Figure 4-(c,d), as well as airplanes.

(4) Friction stir welding

The principal characteristic of this method is that welding is done at a temperature of about 400℃, which is lower than the conventional welding method temperature of about 660℃. This method is already being used for welding train body structures of 25m length. In this program, this method will be used in order to weld 7075 and 2025 aluminum alloys which are believed to be impossible to weld. The application of this method to airplanes, trains and ships has been confirmed.

(5) Super plastic forming

Super plastic forming was applied to the bulging process and it was successful. Magnesium alloys which have superplastic characteristics at temperatures below 400℃ are now being considered. Because an autoclave is large enough to accommodate a 4000 × 10000 mm panel and can heat it to 400℃, this method makes possible the production of wide-size panels like the inner panels such as airplanes, trains and ships which can have various patterns printed on them.

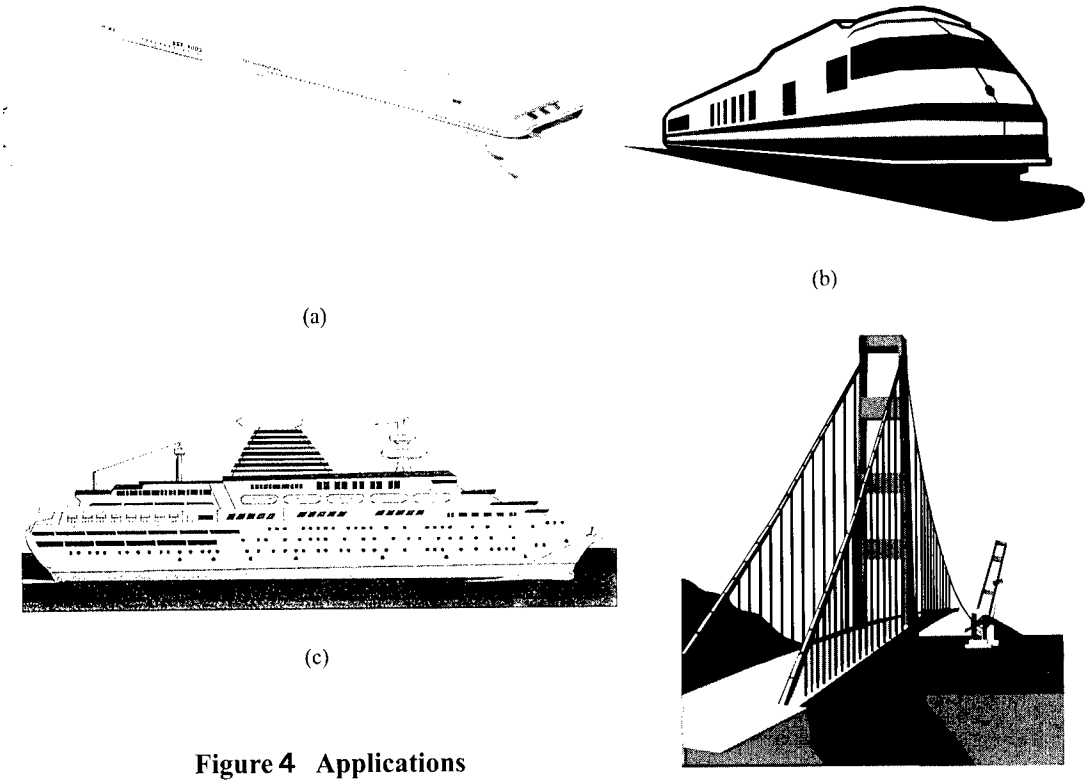

(a) (b) (c) (d)

Figure 4 Applications

6. Conclusion

The targets of this project can be summarized as follows: (1) Wing structures and a cockpit will be fabricated incorporating innovative key technologies and assessment tests equivalent to those in actual aircraft development. Design and manufacturing technologies conforming to airworthiness standards established by airworthiness bureaus, such as the FAA, will be established. (2) As for wing structures, the objectives are a 15% weight saving and 50% part count reduction compared with conventional structures. (3) As for cockpit structures, the objectives are a 10% weight saving and 80% part count reduction compared with conventional structures.

The reason an airframe was adapted as an example of energy conservation research is that it is the most effective field from which technology can be expanded to other fields that require safety, reliability and so on. In aircraft development, the introduction of new and innovative structures will not be easily adopted due to the many risks in verification of airworthiness, safety, reliability and so on. It is hoped that this program conducted during FY1999 to FY2003 will raise key technologies from a research level to an application level, and contribute to removing hesitation about their application, and to stimulate aircraft development. Furthermore, it is believed that these efforts and resulting achievements will be of use not only for aircraft but also high-speed trains, ships and other resource-saving, energy-saving, simple, reliable and lightweight structures, which will induce and create new industrial fields.

R&D SCHEME AND OBJECTIVES FOR INNOVATIVE AIRCRAFT STRUCTURES

A.Yahata, M.Kadoya and H.Kikukawa

Japan Aircraft Development Corporation (JADC), Tokyo 105-0001, Japan

ABSTRACT

Demands for lighter structures are intense for transport vehicles, especially civil aircraft in economical-growth, energy saving, environmental and customer-satisfaction aspects. If we can solve weight-reduction and cost-reduction demands, civil aircraft development would be more activated and accelerated. Recent technology developments have given us hints for near-term future structures. Eventually a R&D plan was presented for "key technology for innovative low cost and light structures", approved and commenced in 1999 as a 5-year program. The first 3 years are "technology establishment phase" and the latter 2 years are "technology verification phase". Part count reduction yields part-fabrication /assembly man-hour reduction directly. The wing and nose structures have numerous part count in an aircraft. So the target is determined 50% and 80% part-count-reduction for the wing and nose structures respectively. The approach to reduce weight is by applying composite material. The target is determined 15% and 10% weight-reduction for the wing and nose structures respectively. Based on a "Building Block Approach" method, simulated certification process for the wing and nose structures will be performed through DER (Designated Engineering Representative) evaluation.

1. INTRODUCTION

Demands for aircraft transportation systems will steadily increase to more than 200% in the next 20 years according to the forecast of passengers (unit : man-miles). In such circumstances, demands will grow for light and low-cost airframes that are not only cost-effective but also conserve energy. So, development of advanced technology for light structures is continuously necessary in the future. But adopting advanced technologies yields a sharp rise of capital cost for developing a new aircraft with high-performances the airlines demand. On the other hand, discount pressure for aircraft prices by the airlines due to market competition remains as intense as before. As a result, the gap between development cost and the aircraft price becomes gradually bigger. Already new aircraft development using conventional methods is not feasible and the aircraft business became very difficult. In order to overcome the situation, drastic light structure design is needed. The technology to achieve both light-weight and low-cost is needed. If we can find a solution, new development for civil transport will be accelerated. Moreover it is desirable to perform an R&D program so that actual development of a new aircraft does not cost so much. For those reasons, NEDO(New Energy and Industrial Technology Development Organization)'s open-bidding program "R&D of Key Technologies of Design and Manufacturing for Innovative Light Structures" was planned. JADC applied for the program with a proposal document and was nominated as a contractor.

2. OUTLINE

The structures of an aircraft are dominantly made by the built-up method in which many parts are assembled by rivets and fasteners, so the part count is an extraordinarily a large number. Reducing part-count is the most effective way to reduce costs because it reduces working time for fabrication, assembling and processing. In the program, we selected the wing structure and the cockpit structure as representative portions since they have a large number of parts and complicated figures. The wing structure is sensitive to strength and has the fuel tank. The nose structure has the pressurized space. The part-count reduction targets are set at 50% and 80%, respectively. The targets and the illustrative summary are shown in Figure 1.

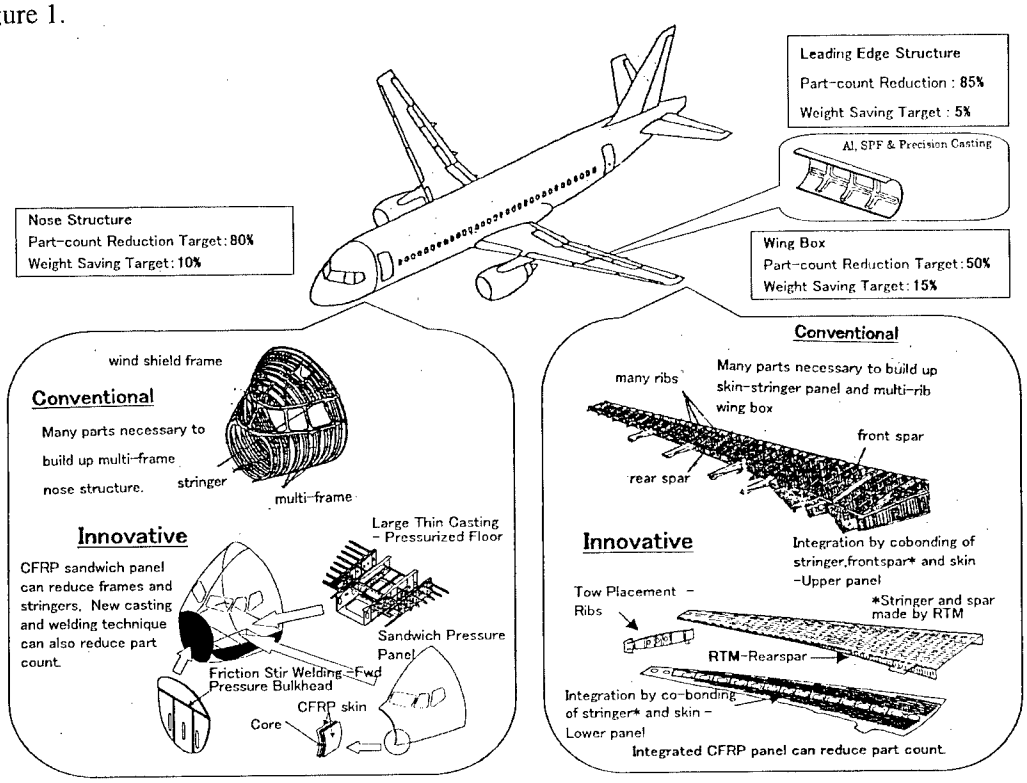

Fig. 1 R&D Program of Key Technology for Innovative Structures

3. THE CLUE TO INNOVATIVE STRUCTURE

For part-count-reduction and weight reduction, we are trying to get innovative structures. The positions or clue of the target are described below.

3.1 Nose structure

Fig. 2 shows the spacing of frames and stringers which are main parts of the fuselage. Part-count can be reduced when the spacing becomes wide. The historical data show that the spacing of frames and stringers remains constant from B707 (First flight: 1954) to B777 (First flight: 1994). The reasons for constant spacing are because the same material, i.e. aluminum

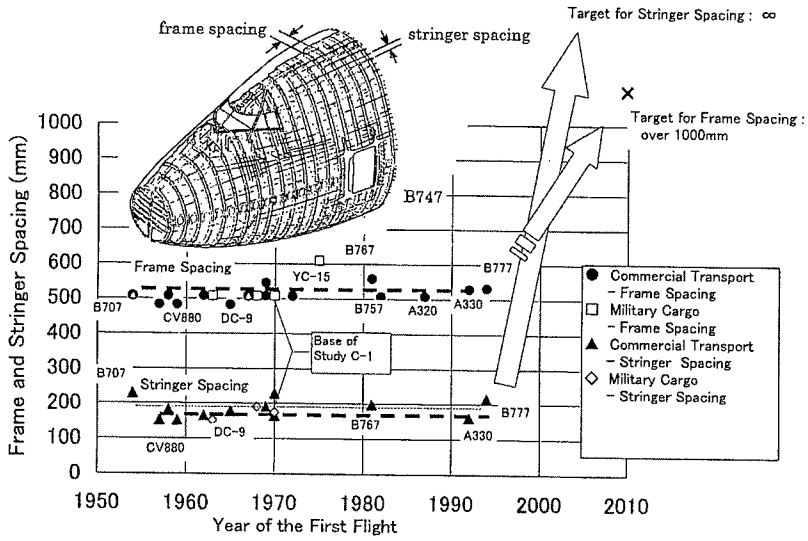

Fig.2 Target of Frame and Stringer Spacing for Nose/Fuselage Structure

alloys, were used. The most lightweight structure for the nose section is the sandwich panel structure. In the program the target of the frame spacing is more than 1000mm, two times the conventional one of 480 to 530mm. Large-size CFRP sandwich panels using unique composite manufacturing techniques could allow stringers to be omitted. Part-count is reduced for not only the skin but also the inner parts by using one-piece-oriented aluminum technologies such as thin, large-size precision casting and friction stir welding (FSW). .

3.2 Wing structure

Fig. 3 shows rib spacing in a wing box. The historical data show that the spacing is scattered 450 to 800mm, but the average is approx. 650mm. The rib spacing has remained nearly constant for forty years as well as the spacing of frames and stringers in the fuselage skin. Our efforts were focused on how to combine ribs and stringers directly without numerous clips or

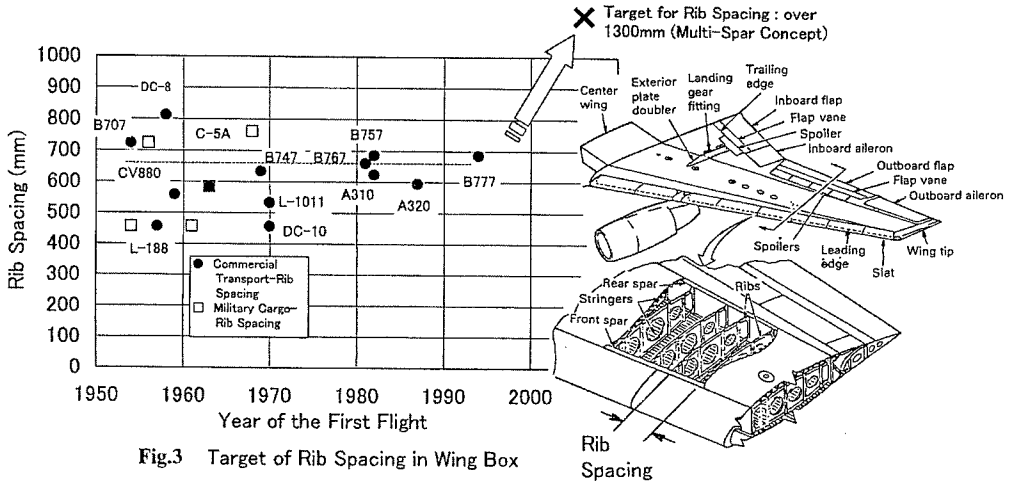

Fig.3 Target of Rib Spacing in Wing Box

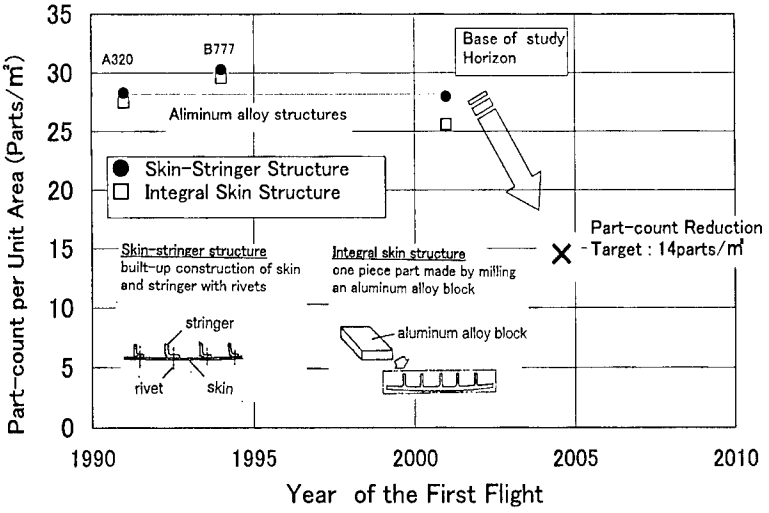

Fig.4 Target of Part-count per Unit Area in Wing Box

other parts stiffening ribs and stringers. Fig. 4 shows part-count per unit area in a wing box. Here, the part-count for an integrally stiffened panel is defined as the number of stringers subtracted from the part-count of a skin-stringer riveted structure. The historical data show that the average part-count per unit area is 29 parts/m^2 for skin-stringer riveted structures. The average for an integrally stiffened panel is 28 parts/m^2. In the program, part-count for a wing box will be reduced by using one-piece-oriented composite technologies such as the unique co-bonding process. The targets are weights of 15% less and part-count of 50% less than those of current civil aircraft.

3.3 Leading edge structure

Fig.5 shows part-count per unit length in a leading edge structure. The historical data show

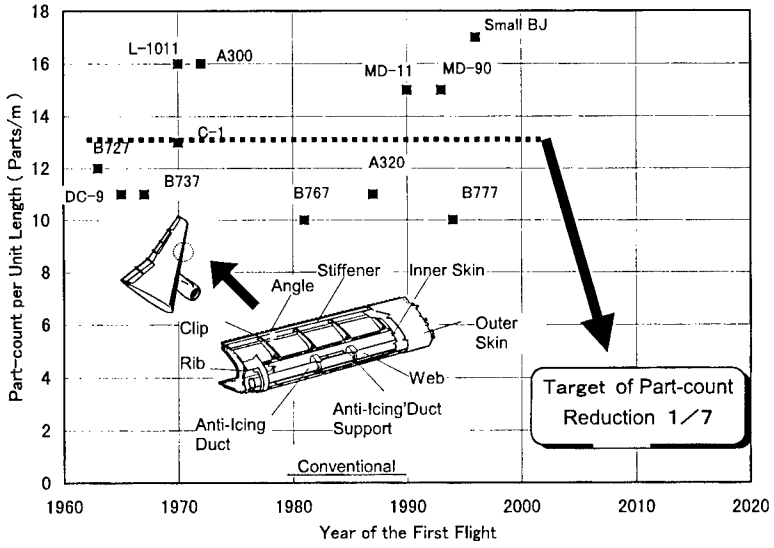

Fig.5 Target of Part-count for Leading Edge

the average of the numbers is 13 parts/m and has not changed for forty years. Composite material is not good for absorption of discrete damage such as a bird strike, compared with aluminum alloy, so we cannot hope for a part-count reduction attained by composite technology. We adopted one-piece-oriented structure combining super-plastic forming, precision casting and welding for aluminum alloy. The target for the leading edge is to reduce the part count to 1/7 of the average in conventional aircraft of 13 parts/m.

3.4 Composite application to innovative structure

The rate of composite material in current aircraft structure occupies about 15% in weight percentage. Applying composite material to nose and wing structures in the program, the rate will increase from about 15% up to about 45% as shown in Fig. 6.

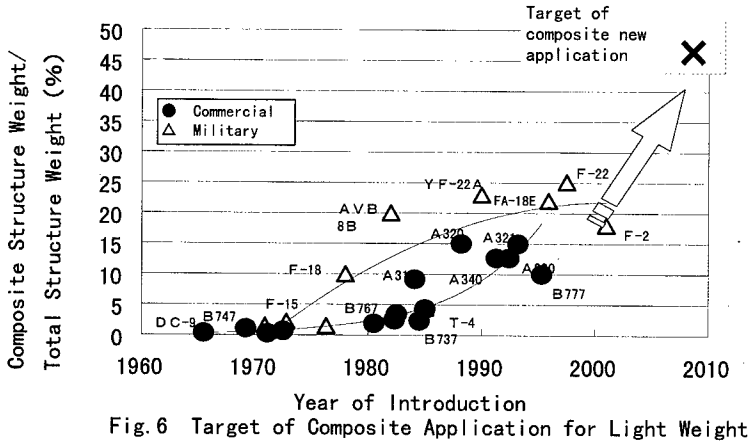

Fig. 6 Target of Composite Application for Light Weight

4. APPROACHING METHODS

The project is a five-year program begun in FY1999. We determined yearly targets, called "Exit Criteria", for the nose, wing, and leading-edge structures. We adopted a method to step up to the next year's entrance through assessing whether the year's target is accomplished or not. Consequently the five-year R&D program schedule was determined. Furthermore we adopted a "Building Block Approach" method. The method is often used for innovative R&D programs in which optimum solution on means, effects etc. are unknown. We expect a steady technological approach to the goal by using the method. In the beginning of the program, we concentrated on steady steps. We intended to perform the same procedures as in the actual development of a new aircraft. We made an execution plan, and considered these important items: (a) a design based on firm procedures, specifications etc.; (b) technical assessment; (c) assessment of a substantiation test by a DER. To assess the design and its validity, we examined the design standards and adopted Japanese Airworthiness Standards Chap. III (Transport Category), FAR Part 25 (the latest revision), Advisory Circulars (AC) and supplemented documents as design rule for a commercial airplane.

5. ENERGY-SAVING EFFECTS

Here is an estimate of how much energy consumption could be saved if the innovative technologies were developed and the substantiation tests were executed successfully. As a result, 2% of the total energy consumption used for transportation in Japan could be saved 20 years from now as shown on Table 1. We forecast that the needs to adopt such light-structure technologies would surge in high-speed vehicles, especially super-express railway vehicles, and so on.

Table 1. Estimated Effect of Energy-Saving (unit : crude oil $\times 10^4$ kilo liter)

		FY 2000	FY 2005	FY 2010	FY 2020
Aircraft		0.0	2.7	6.9	22.7
Ship		0.0	1.2	2.4	3.6
Train		0.0	3.2	6.3	8.4
Motor Vehicles	For Passengers	0.0	4.2	9.2	16.4
	For Cargo	0.0	3.4	6.9	10.3
Sum		0.0	14.7	31.7	61.4

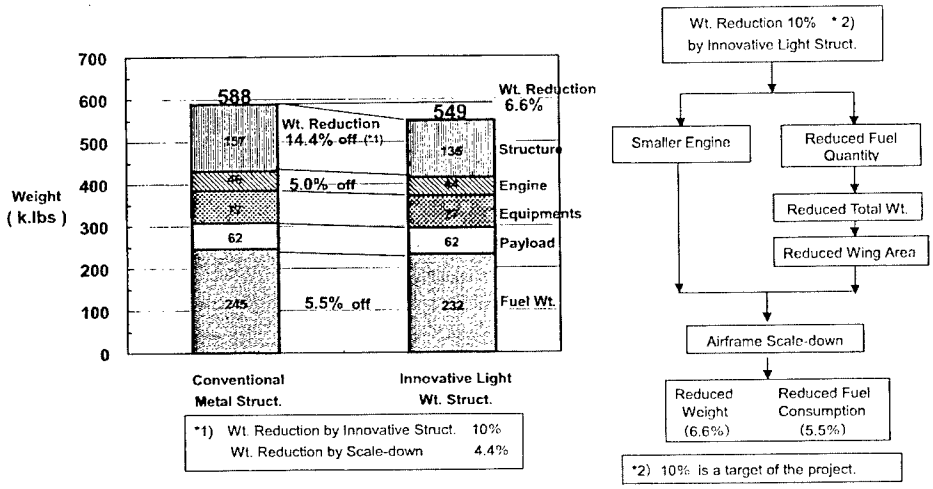

Figure 7. Estimated Effect on Transportation System's Energy Consumption by the attainment of the Project

6. CONCLUSION

The program is aimed at light-structures for energy and cost savings. We will promote key technologies cultivated for a long time to the level where they can be applied to an actual vehicle approximately five years from the start. Furthermore, we are trying to apply the technologies to an airplane in which the requirements for safety, reliability, airworthiness, maintenance are the most rigorous. The introduction of an innovative structural method involves risks for its substantiation. In order to get substantiation, we have made a plan based on legal standards, accumulated characteristic data, full-scale components fabrication and tests. In the future we hope to present these technologies as substantiated and globally competitive. This report is a summary of our two year's result. The authors wish to thank METI and NEDO representatives for their advice, help and suggestions. We also should like to thank all persons concerned for their contributions and promotion to the program.

REFERENCES

[1] A.Yahata, M.Kadoya, T.Kaijima and H.Kikukawa "Innovative Structural Development for Civil Transport", THERMEC 2000, Las Vegas, Dec. 6, 2000

INNOVATIVE NOSE SECTION OF FUSELAGE STRUCTURES APPLIED BY FRICTION STIR WELDING (FSW) OF THE ALUMINUM ALLOY AND LARGE THIN CASTING OF IMPROVED ALUMINUM ALLOY

Y.Hirose*, T.Tsujimoto*, K.Kosugi*, M.Imuta*, H.Fukagawa*

*Aerospace Company, Kawasaki Heavy Industries, LTD.
1.kawasaki-Cho, Kakamigahara City, Gifu-Pref., 504-8710

ABSTRACT

Five-year research activities have started in 1999 sponsored by the New Energy and Industrial Technology Development Organization (NEDO) and Japan Aircraft Development Corporation (JADC).
This paper describes the research plan and results obtained during the last two years. The objective of this research is to apply new technologies to a transport aircraft structures. The nose structure of an existing twin turbojet was selected as a baseline model. It is expected that the application of the new technologies will lead to a considerable reduction in weight and in parts count.
The application of the new technologies is presented as follows:

① Large size precision casting technology
② Friction stir welding technology

In 1999 and 2000, a preliminary design and FEM analysis of the nose structure were carried out including coupon tests, structural element tests and subcomponents test. The results of these activities enabled us for a sound technological assessment in the following areas:

- Appropriate welding conditions for FSW
- Mechanical properties of welded joints
- Fabrication and Evaluation of subcomponent article of forward pressure bulkhead with FSW
- Fabrication and Evaluation of large pressure floor support structure with sand casting method
- Mechanical properties of improved casting material named D357

These activities have clearly shown the viability of the engineering application of the new technologies into the aviation industry.

1. INTRODUCTION

The nose of commercial transports is a tri-dimensional complicated built-up structure. Although there is a need to reduce weight and fabrication cost, few efforts have been conducted towards this goal. In view of this, a five year research program has been sponsored by the NEDO in order to apply the innovative structural approaches including following two technologies, with an ultimate goal to achieve a 10% weight reduction and an 80% parts

count reduction.

① Large Size Precision Casting Technology

It is a large dispersion of material properties, one of the factors that has prevented the application of casting technologies from wide application to the aircraft structures. In this research the improved material named D357 aluminum alloy has been selected to estimate its material characteristics and assess applicability in the manufacturing of a thin large structures. The results shown are very encouraging.

② Friction Stir Welding (FSW) Technology

Most of the 2000 series and 7000 series aluminum alloys cannot be welded with conventional welding technologies. Friction stir welding technology enables these alloys to be welded by joining two materials at the temperature under their melting point. Through this research, FSW equipment was introduced and appropriate welding conditions and mechanical properties of the welded joints were evaluated.

2. DEVELOPMENT PLAN

The development plan is divided into two phases: (1) basic technology establishment phase and (2) structure engineering verification phase.

In the basic technology establishment phase, material characterization tests and process verification tests will be conducted in order to obtain the prospective of the engineering feasibility.

In the structure engineering verification phase, design and verification tests of a full-scale nose structure will be performed in order to show compliance with FAR Part 25.

For this purpose, certification procedures will be simulated and the type design data and substantiation documents will be reviewed by DERs (Designated Engineering Representative) to ensure that the activities meet the regulatory requirements, thus making research efforts readily applicable to the aircraft industry.

3. CONCEPT FOR THE INNOVATIVE COCKPIT STRUCTURE

3.1 Conceptual Design [1],[2]

Considering the conventional structures and the characteristics of the above-mentioned new technologies, the following structures were selected as candidates (see Fig3-1)

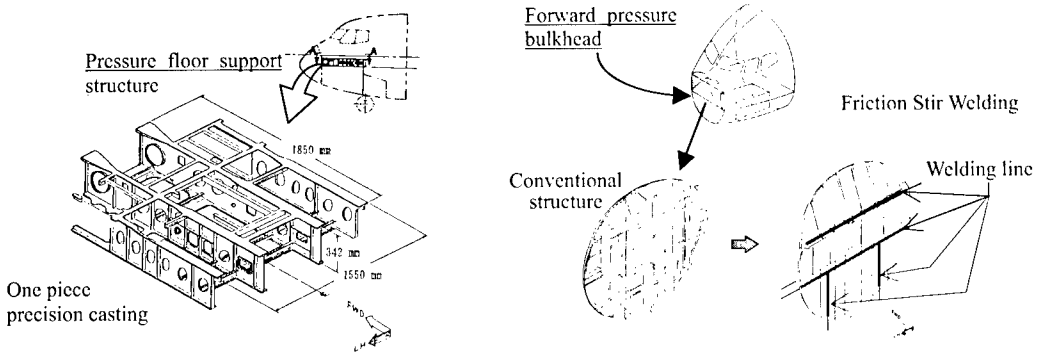

Fig. 3-1 Candidate Structures

A conventional pressure floor panel support structure is a built up of sheet metal parts and has many open holes for control cables and piping. Therefore, the application of a composite material is not suitable, but the application of precision casting technology will be most suitable for such a one-piece large structure.

The conventional forward pressure bulkhead is a built up component and has to sustain structural loads and maintain structural integrity. Therefore, a casting structure is not suitable due to its low ductility and also a composite structure is unsuited due to many open holes for system installations. In order to reduce its parts count, the application of the FSW with the integral panel is expected to be suitable.

3.2 FEM Analysis

Considering the above applications, the FEM analysis was conducted based on the conceptual design to determine the critical loading conditions due to pressurization and landing loads. Through this analysis, internal loads for each part were obtained. It was confirmed that the pressurization load and the local bending moment due to open sections for windows were sustained. (See Fig.3-2)

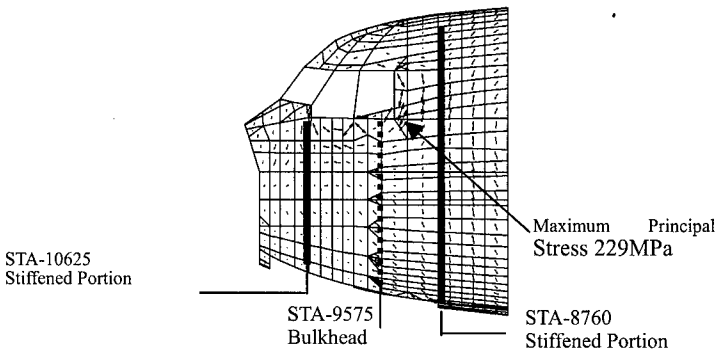

Fig.3-2 FEM Analysis Result (Pressure Load ULT)

3.3 Stress Analyses

Based on the internal loads obtained by the FEM analysis, stress analyses were carried out. The analyses of all parts of the nose structure had enough margin of safety and the minimum figure was 0.03 at the corner of an open section.

4. EXPERIMENTAL RESULTS

4.1 Precision Casting Structure

The objective of this test is to obtain the mechanical properties of a casting material and to gain the prospects of the production of the large size precision casting structures.

In order to estimate the dispersion of thin casting material, tests for D357 aluminum alloy and fabrication of the sub-component of the pressure floor support structure were conducted.

4.1.1 Material Test

Through the various coupon tests, such as tension, compression, bearing, fatigue and crack propagation tests, small dispersion and good mechanical properties of D357 alloy were confirmed. Tensile test results are shown in Fig. 4-1.

The CV(Coefficient of Variation) values of test data are less than 3%.

This figure shows that the tension strength is higher than the value specified in MIL-handbook-5.

The prospects of the application of D357 alloy to the aircraft structures are thus confirmed.

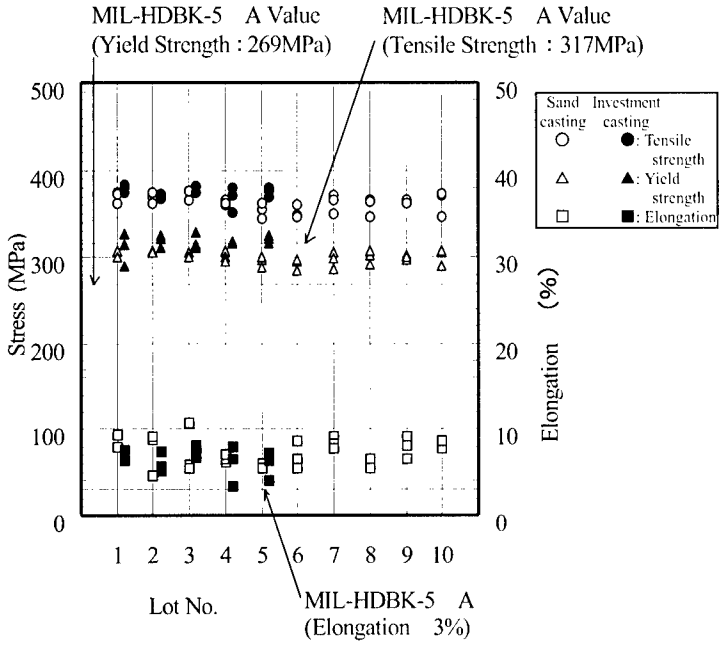

Fig.4-1 D357 Material Test Results

4.1.2 Fabrication of The Sub-component

The sub-component test article of the pressure floor support structure (1.85m × 1.55m) was fabricated by the sand casting method using D357 alloy.

In order to evaluate the casting quality, the destructive test and non-destructive inspection were conducted.

As for the destruction test, test specimens were cut from the article. Using these specimens, tension, compression and fatigue tests were conducted. These tests have shown the mechanical properties equivalent to those of base material.

As for the quality assurance, the following inspections were conducted.

- Dimensional Inspection
- X-ray inspection
- Microstructure analysis

These inspection results showed that there were little gas porosities in the article and the dendrite arm spacing were small.

The uniform thickness distribution and the improvement of heats treat distortion were achieved due to the improvement of casting method and heat treatment method (See Fig.4-2).

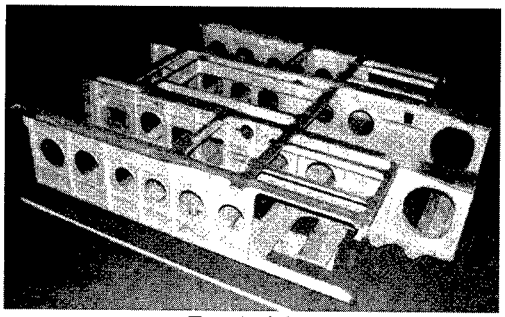

Test Article

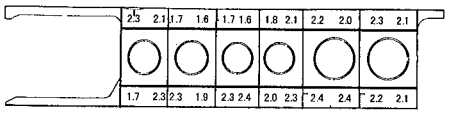

unit:mm

Typical thickness distribution

Fig. 4-2 Pressure Floor Support Structure

4.2 Friction Stir Welding Joint

In order to obtain the perspectives of the application of FSW technology, appropriate welding conditions should be established and mechanical properties of welded portion should be evaluated as a first step.

4.2.1 Material Characterization Test of FSW Joints

For the FSW, welding conditions, i.e., rotation speed, welding speed and the shape of tool, should be decided for 2024 alloy and 7075 alloy, respectively through the laboratory tests.

Using these conditions, welded joint coupon specimens were fabricated and the mechanical characterization tests were conducted for static strength, fatigue strength, crack propagation and corrosion resistance.

Through these tests the following results were obtained;

For static tests;

- 2024 alloy FSW joints have 93%～85% tensile strength of the base metal.
- 7075 alloy FSW joints have 83%～68% tensile strength of the base metal.

For fatigue test;

- 2024 alloy FSW joints have about 80% fatigue strength of the base metal at 10^6 cycles.
- 7075 alloy FSW joints have about 60% fatigue strength of the base metal at 10^6 cycles.

For crack propagation tests, the crack propagation rate of FSW joint was a little greater than that of the base metal.

For corrosion resistance tests, it was revealed that 2024 joints have a tendency of faster corrosion spread and 7075 joints have tendency of lower spread, compared with the base metal.

Through these tests, basic mechanical properties of FSW joints were obtained. This data can be used for the further improvement of the FSW technology and preliminary design.

4.2.2 Subcomponent Test

Based on the material characterization test, welding condition for the subcomponent test article of the forward pressure bulkhead structure was established and subcomponent test were conducted as shown in Fig. 4-3.

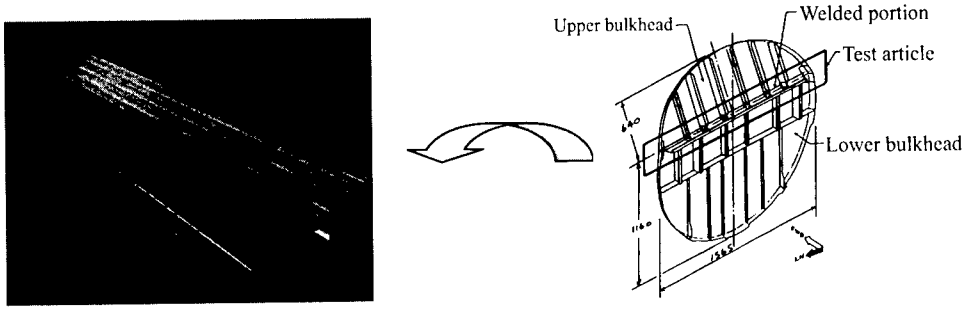

Fig. 4-3 Subcomponent Test Article

Tension test specimens were cut from the welded portion. Tension test and microstructure analysis were conducted. Through these tests, it was confirmed that FSW was successfully performed.

5. CONCLUSION

Through the research activities in 1999 and 2000 the bare bone of our research plan has been established. Fundamental research and tests were conducted. Through these activities, the prospects of the weight reduction by 10% and the parts count reduction by 80% were obtained. Based on these results as a step stone, the research activities will continue towards the final goal. The full-scale test of the nose structure will be performed in the final year for the substantiation.

6. ACKNOWLEDEMENT

The authors would like to note their appreciation for NEDO and JADC, especially Mr.Itoh, Dr.Kikukawa and Mr.Yahata.

REFERENCES

1. FAR Part 25, revised as January 1.1999
2. FAA AC25-571-1C, Damage Tolerance and Fatigue Evaluation of Structure, April 29, 1998
3. Hirose, Y., Maekawa, S., Imuta, M., Tajima, N., and Kikukawa, H. : Technology Development for Innovative Cockpit Structure of a Transport Aircraft, Presented at Thermec 2000, Las Vegas, USA, Dec. 2000

APPLICATION OF MANUFACTURING PROCESSES FOR MONOLITHIC STRUCTURE TO WING LEADING EDGE

T. Jinishi, M. Matoba, S. Ohashi, M. Ochi and A. Yahata*

Aerospace Div., Japan Aircraft Mfg. Co., Ltd
3175 Showa-machi, Kanazawa-ku, Yokohama, 236-8540, Japan
*Japan Aircraft Development Co., Tokyo, 105-0001, Japan

ABSTRACT

To achieve cost saving product and lightweight design on wing leading edge, it is significant to apply monolithic structure. Superplastic forming, precision casting and advanced welding are applied to a new concept leading edge that has been designed with the requirements of endurance to bird strike and anti-icing. This structure consists of a panel made from 5083 superplastic forming Al alloy sheets and a support cast made from high strength Al alloy D357. The panel constructed from two sheets lapped with ultrasonic bonding, has a corrugated inner skin that forms hot air flow ducts for anti-icing. The support is a monolithic casting made from investment method, and has thin complex shells. The panels and supports, separately welded span-wise using TIG welding with magnetic stirring, have been assembled finally with fasteners. Coupon tests were conducted to obtain basic properties of these welded materials. To verify the design concept, fabrication trials were performed. As a result, the new wing leading edge is verified to reduce parts count approximately to one eighth, and to reduce weight 5% lighter than conventional ones. The bird strike test and its FEM analysis were executed to obtain design data and evaluate structural properties.

1. INTRODUCTION

For requirements of low manufacturing cost and lightweight structure on new generation aircraft, there is a major effort to reduce parts count. This will result in an increased use of monolithic structure, e.g. forgings, castings and machined parts. In this situation, a study on a structure of wing leading edge for commercial airplane was approached to satisfy these requirements. Superplastic forming (SPF), precision casting and advanced welding are especially appropriate processes for wing leading edge. The leading edge with a new concept that involves those processes has been designed for the requirements of endurance to bird strike and anti-icing. To verify the design concept, manufacturing articles that modeled a part of the leading edge, were produced as fabrication trials. Bird strike tests and its FEM analysis were executed to obtain design data and to evaluate structural properties.

2. DESIGN CONCEPT

Leading edge structures on conventional airplane are built-up structures consists of many sheet metal and machined parts, assembled using a lot of fasteners. That conventional structure cannot reduce parts count to satisfy requirements of low manufacturing cost and

lightweight structure. On the other hand, it is important to satisfy the toughness against hail/bird strike and anti-icing requirements to be certified as an airplane structure. So the new concept wing leading edge has been designed with metal processes shown in Fig.1. This structure consists of a skin panel, a support frame and an anti-icing duct. The skin panel consists of only two sheets, an outer skin and an inner skin. These skins are both made of 5083 superplastic aluminum alloy sheets. The inner skin has many formed corrugations that work as hot air passages for anti-icing. SPF process is applied for the forming of passages, at the same time with bending into a shape of wing section. Before forming, the two skins are lap joined by using ultrasonic spot bonding. The support frame, which has skin, stiffeners, ribs and support fitting for anti-icing duct, is a single piece unit made by precision casting process. This frame is made from D357, high strength aluminum casting alloy. A process of precision castings, called "lost wax method", is applied to shape this support frame which has thin complex ribs. For a lightweight design, minimum thickness of the support frame is 1.5mm. The skin panels and support frames are separately welded span-wise using TIG welding with magnetic stirring. A titanium tube with many small holes is installed in front of the support frame to supply hot air to the duct in the skin panel. The skin panel and support frame are fastened with rivets. This structure is expected to endure bird strike impact with energy absorption due to its large deformation. As a result, the new wing leading edge is expected to reduce parts count to approximately 1/8, and to reduce weight 5% lighter than conventional structures.

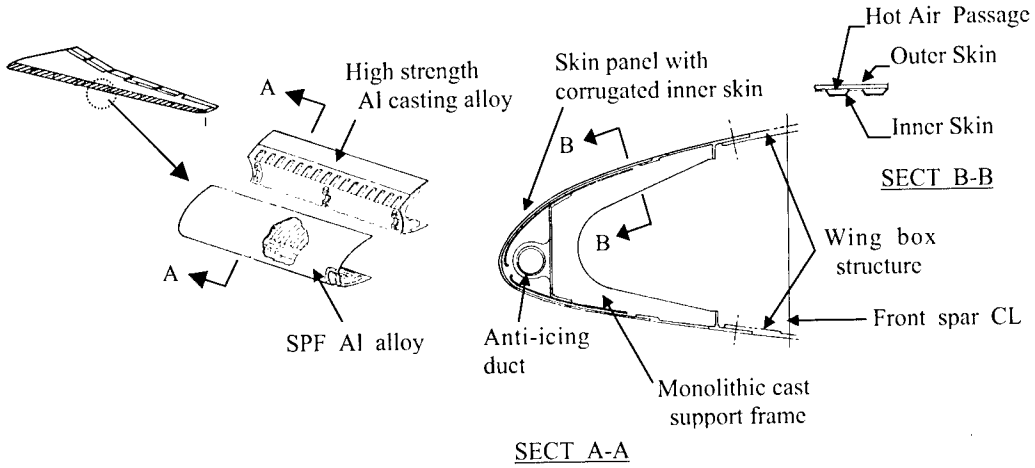

Fig.1 Structure of a new concept wing leading edge

3. FABRICATION TRIALS

To verify the design concept and its productivity, manufacturing articles that modeled a part of leading edge, were produced as fabrication trials.

3.1 Skin panel

3.1.1 Ultrasonic bonding

The inner and outer skins are lap joined by using ultrasonic spot bonding before their forming. The features of the ultrasonic bonding are solid-state metallurgical bonds, a smoother surface compared with electrical resistance spot welding and its formability at bonded point. For a wing leading edge, it is significant to keep smooth surface on its outer skin. At fabrication trials, 0.8mm and 1.6mm thickness 5083 aluminum alloy sheets were used as inner and outer skins, respectively. Ultrasonic bonding is carried out by putting work between the bonding tip and anvil, while the inner skin side faces bonding tip. The surface

after bonding is shown in Fig.2. On bonding tip side view of the surface shown in Fig.2 (a), there are many impressions caused by the bonding. To improve bonding marks on the surface, it is necessary to devise shape of the bonding tip face. On the outer skin shown in Fig.2 (b), only light tool marks can be observed. Some polishing will eliminate these marks from the surface. Observation with an optical microscope shows that the solid-state bond is accomplished in good condition.

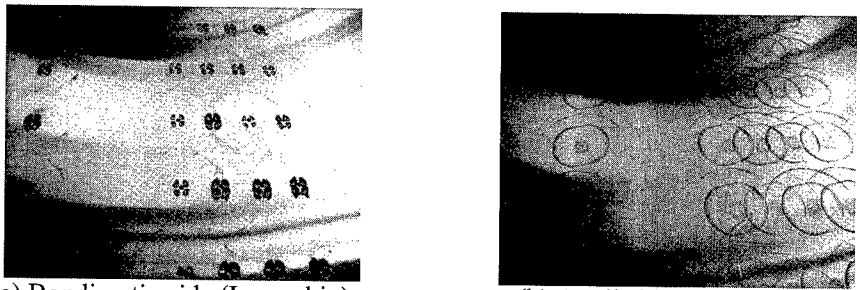

(a) Bonding tip side (Inner skin) (b) Anvil side (Outer skin)

Fig.2 Zoom up view of the surface after ultrasonic bonding

3.1.2 Superplastic forming

An aluminum tube for supplying forming gas was welded on the skin after bonding, as shown in Fig.3. A SPF die for the experiment was designed, and was made of steel, as shown in Fig.4. BN powder lubricant was applied to the die surface. The die was set in a press machine with hot platens, and heated up and kept at approximately 800K. A commonly used strain rate was utilized for the superplastic forming was given [1]. Argon gas was supplied according to a pressurization schedule for the forming.

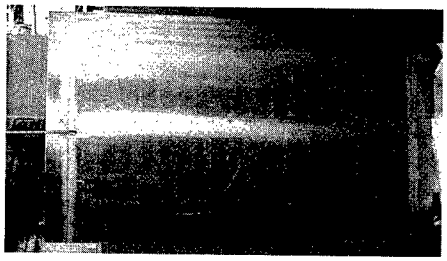

Fig.3 View of blank sheet

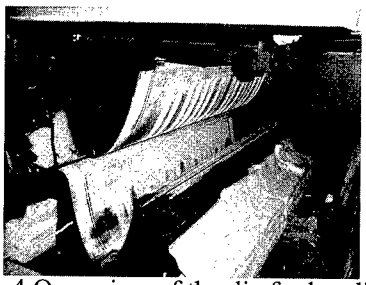

Fig.4 Over view of the die for bending and SPF set in a hot press

At first, a blank sheet was formed to the shape of the leading edge. Fig.5 shows the bending process of blank sheet in the heated die. It was bent gradually between upper and lower dies. Finally, blank sheet was clamped between the dies and was pressed with a counter load. As the dies were closing in, blank sheet was clamped easily between the dies due to degrease in stiffness under heated condition.

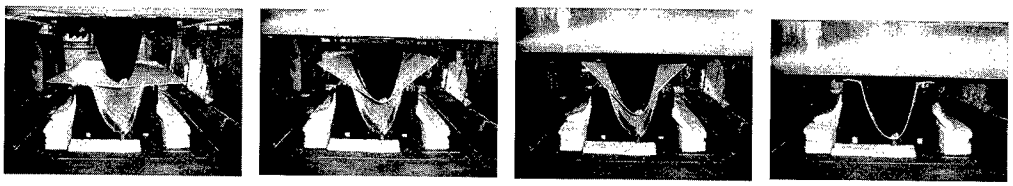

(a) (b) (c) (d)

Fig.5 Continuous views of bending process before SPF

After recovering to temperature suitable for SPF, forming pressure was loaded through the tube with an adequate pressurization schedule. It took approximately 30 minutes to form small hot air ducts on the inner skin. After completion of SPF, the dies were opened and formed panel was taken out. With this experiment, it was shown that the forming process was feasible and easy for production. An outside view of the formed skin panel is shown in Fig.6(a). Outer skin of the panel was formed smoothly without influence of SPF on the inner skin. Each duct on the inner skin, as shown in Fig.6(b) was formed superplastically without breakage or undesirable wrinkle. Fig.6(c) shows a zoom up view of superplastic formed ducts on inner skin of the panel. Although this process is a bulge forming to inner side, the ducts were formed along die surface in good condition.

(a) Outer skin side (b) Inner skin side (c) Superplastic formed duct on inner skin

Fig.6 Views of superplastic formed panel

3.2 Support frame

The support frame, which consists of skin, stiffeners, ribs and support fitting for anti-icing duct, is integrated into a single piece structure by using a precision casting process called "lost wax method". Since it is a small quantity production, master model for the support frame was made using rapid prototyping method. The rapid prototype model shown in Fig. 7 is based on CAD data, and produced taking account of the shrinkage after casting. Fig. 8 shows the support frame after casting and heat treatment, and it looks as same as the master model. There was no large distortion hindering subsequent assembly. With sandblast treatment, roughness of surface became satisfactory to the design requirement. Thickness of parts was a little greater than design, because estimation of shrinkage in thickness was not enough. But many data were obtained by this trial. Monolithic structure of the support frame was cast in good shape condition by applying the "lost wax method".

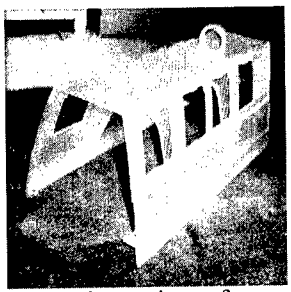

Fig.7 Over view of a rapid prototype model

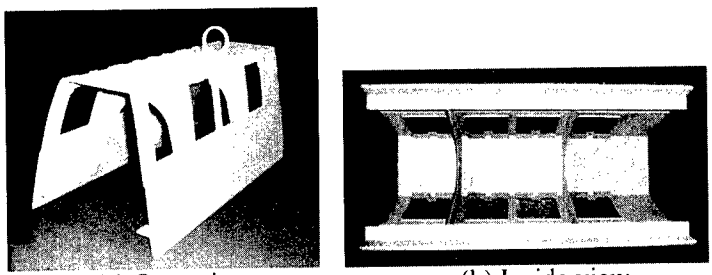

(a) Over view (b) Inside view

Fig.8 Precision casting support frame

3.3 Assembly

TIG welding with magnetic stirring was used on skin panels and support frames, in joining them span-wise, respectively. By stirring the molten pool with electromagnetic force, this welding method makes it possible to prevent hot cracking due to reduced grain size, and to

prevent generation of blowholes, and to prevent discrepant fusion by flattening bead shape. Fig. 9 shows over views of skin panel and support frame after the span-wise welding. Their weld lines had been finished in good condition with fine surface appearance. Therefore, it was verified that this welding method could be applied effectively to skin panels with large curvature, and to support frames made from casting aluminum alloy.

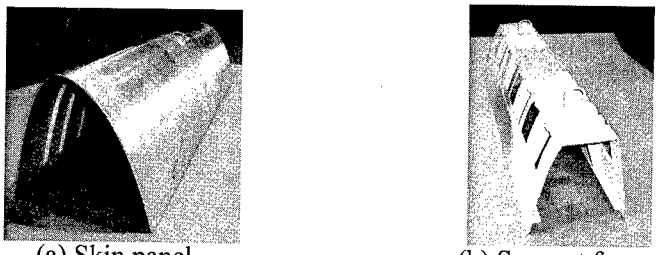

(a) Skin panel (b) Support frame

Fig.9 Over views of test articles after welding

After installing anti-icing duct made of titanium tube, the skin panel and the support frame were fastened using flash head rivets. Fig.10 shows over views of the leading edge. There was no difficulty in assembly, and it satisfied design requirements. As a result, it was verified that productivity of the wing leading edge structure was sufficiently established.

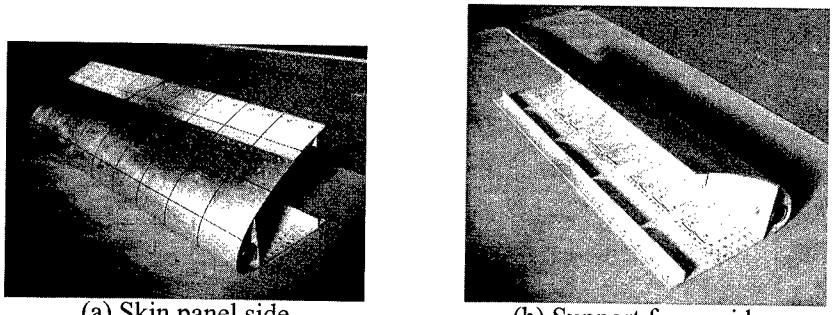

(a) Skin panel side (b) Support frame side

Fig.10 Over views of the wing leading edge

4. BIRD STRIKE TEST

4.1 Analysis with FEM

A dynamic analysis of bird strike on the wing leading edge was performed using nonlinear dynamic FEM code, LS-DYNA[2], in the case of a 4 lb. bird traveling at velocity of 320 knots. Detailed analysis model was created, and basic material properties[3] were input, and additionally weld properties were taking into account. Result of analysis, shown in Fig. 11, indicates that bird will penetrate through the leading edge.

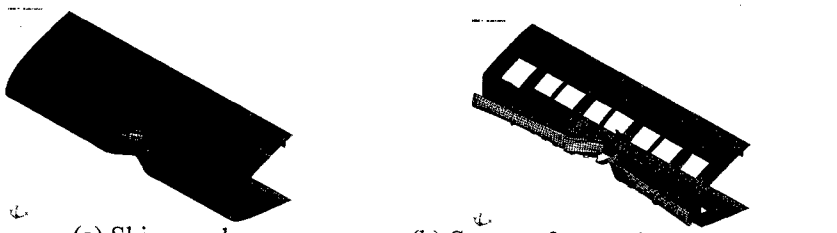

(a) Skin panel (b) Support frame with anti-icing duct

Fig.11 Analysis result

4.2 Experiment

To check accuracy of the analysis, a bird strike test was planned using artificial bird to impact test article, in the same condition as the FEM analysis. The artificial bird was made from mixture of water and gelatin, and its density was adjusted to simulate a bird, by adding phenolic micro balloons. This test was conducted on a range with large compressed-gas gun. As a result, the artificial bird penetrated through leading edge structure, as shown in Fig. 12. This showed that the FEM analysis had been accurate. Additionally, residual velocity of the bird after penetration was measured. It represented the energy absorption with this new design concept was better than with conventional one.

(a) Skin panel side (b) Support frame side

Fig.12 Post impact views of the leading edge

5. SUMMARY

To achieve cost saving product and lightweight design on wing leading edge, it is significant to apply monolithic structure. Superplastic forming, precision casting and advanced welding are applied to production of a new concept leading edge that designed with requirements of endurance to bird strike and anti-icing. To verify the design concept, fabrication trials that modeled a part of leading edge were performed. They have verified that the design based on new conception, is feasible for a wing leading edge, and these manufacturing processes are suitable for production. As a result, the new wing leading edge is verified to reduce parts count approximately to 1/8, and weight to 5% lighter compared with conventional ones. FEM analysis of a bird strike was executed with extreme accuracy, and through bird strike test, design data was obtained and structural properties were evaluated.

ACKNOWLEDGEMENTS

This work has been sponsored by New Energy and Industrial Technology Development Organization, and led by Japan Aircraft Development Corporation.

REFERENCES

1. N. Suzuki, H. Kohzu, S. Tanabe and K. Higashi, Materials Science Forum (1999), pp. 304-306
2. James s. Wilbeck, Impact Behavior of Low Strength Projectiles, Technical report, AFML-TR-77-134 (1977)
3. Military Standardization Handbook Metallic Materials and Elements for Aerospace Vehicle Structure

AUTHOR INDEX

A

Abe, T., 869
Adachi, H., 597
Adachi, K., 1121
Aghion, E., 175
Ahn, H.J., 671
Ahn, J.H., 247
Ahn, J.K., 675
Ahn, S.H., 695
Ahn, S.H., 701
An, C.W., 503
Ankem, S., 153
Asahina, T., 457

B

Bae, Y.I., 1067
Baeck, S.M., 621
Balmuth, E.S., 589
Bardi, F., 361
Bieler, T.R., 79
Blackburn, M.J., 721
Bong, H.H., 469
Boot, D.A., 1037
Burvill, C., 281, 287
Byeon, J.W., 823

C

Cantor, B., 1055
Cavaliere, P., 361
Ceschini, L., 361
Cha, S.I., 469
Chandrasekaran, V., 1133
Chang, S.N., 105
Chang, S.Y., 627, 863
Chang, Y.W., 423, 695
Chatterjee, U. K., 571
Chen, L.H., 547, 689
Chen, Y., 857
Cheon, J.H., 905
Cho, D.C., 1101
Cho, K.M., 675, 851, 929
Cho, W.S., 3
Choe, B.H., 65
Choh, T., 411
Choi, C.J., 615
Choi, D.C., 671
Choi, I.D., 675, 851, 929
Choi, N.B., 851
Choi, Y., 247
Choi, Y.S., 331
Choi, Y.S., 977
Chung, C.S., 503
Chung, I.S., 943
Chung, S.W., 417

D

Das, K., 571
Davila, G., 559
Dimiduk, D.M., 721
Ding, H., 857
Doraiswamy, D., 153
Dutkiewicz, J., 387

E

Eliezer, D., 175
Emura, S., 817
Eom, J.P., 221
Es-Said, O.S., 305, 559
Euh, K.J., 1027
Eum, C.Y., 875
Evangelista, E., 361
Eylon, D., 111, 127, 133, 141

F

Fagaraseanu, D., 793
Fang, W., 805
Fisher, P., 1037
Fleck, P., 559
Fountain, C., 305
Fox, S., 57
Foyos, J., 559
Frazier, W. E., 5

Fromer, E., 559
Frouin, J., 141
Fujishiro, S., 111, 127
Fujita, K., 961
Fukagawa, H., 489
Fukunaga, K., 111, 127
Furukawa, M., 399, 647
Furukawa, T., 923

G

Gao, M.C., 509
Gariboldi, E., 375, 1115
Garmestani, H., 305
Ghosh, K.S., 571
Gunawarman, 127

H

Ha, C.S., 675, 929
Ha, T.K., 423, 695
Ha, W., 1109
Hackenberg, R.E., 509
Hagiwara, M., 817
Han, C.H., 881
Han, D.S., 1055
Han, J.H., 317
Han, S.W., 665, 707
Han, Y.H., 405
Hanada, S., 31
Hao, H., 659
Hashimoto, H., 869
Hashimoto, K., 799
Higashi, K., 255, 451
Hilpert, M., 205
Hino, M., 893
Hiraga, K., 1093
Hirano, M., 603
Hiroki, F., 991
Hirose, Y., 489
Hoeppner, D.W., 1133
Hoffmann, J., 1021
Hokamoto, K., 811
Hong, S.H., 469
Hong, T.W., 1067, 1109
Hong, W.P., 167
Horita, Z., 399, 647
Horng, J.H., 689
Hu, J.L., 689
Hur, B.Y., 221, 671
Hur, S.M., 97
Hwang, J.I., 851
Hwang, S.K., 729, 769
Hwang, Y.H., 1133
Hyun, Y.T., 41, 91

I

Igarashi, A., 235
Ikeda, M., 73
Ikenaga, K., 787
Ikenaga, M., 787
Ikeno, S., 535
Im, H.B., 675
Im, Y.R., 583
Imai, T., 411
Imose, T., 73
Imuta, M., 489
Inagaki, Y., 337
Inoue, A., 609
Inoue, K., 73
Isui, H., 911
Ito, Y., 477
Ivanov, E., 261
Ivasishin, O.M., 57
Iwamoto, N., 961
Iwata, S., 949
Izui, H., 923

J

Jang, W.K., 681
Jata, K.V., 15
Jeong, H.W., 41, 91
Jeong, Y.G., 829
Jin, H.W., 517
Jin, J.Z., 659
Jinishi, T., 495
Jo, Y.J., 343
Ju, D., 147
Jung, B.G., 65
Jung, B.H., 1081

Jung, D.J., 983
Jung, H.C., 215
Jung, H.G., 983
Jung, H.K., 1049

K

Kadoya, M., 483
Kalidindi, S. R., 305
Kamio, A., 875
Kang, C.G., 1043, 1049
Kang, S.B., 641, 875
Kankawa, Y., 275
Kato, M., 1009
Katoh, K., 445, 457
Kawai, G., 1121, 1127
Kawai, H., 603
Kawamoto, M., 893
Kikukawa, H., 483
Kim, B.K., 615
Kim, B.S., 1139
Kim, C.G., 905
Kim, D.H., 199
Kim, D.I., 621
Kim, G.Y., 973
Kim, H.C., 167
Kim, H.J., 775
Kim, H.J., 905, 1081
Kim, H.S., 355
Kim, H.W., 641
Kim, J., 695
Kim, J.G., 967, 977
Kim, J.H., 755
Kim, J.H., 997
Kim, J.H., 1003
Kim, J.K., 503
Kim, J.S., 743
Kim, K.B., 381
Kim, K.B., 1061
Kim, K.H., 297
Kim, K.Y., 983
Kim, M.G., 1067
Kim, M.H., 943
Kim, M.K., 1081
Kim, Nack J., 225, 529, 553
Kim, S.E., 41, 91, 1075
Kim, S.H., 119
Kim, S.H., 297
Kim, S.H., 463
Kim, S.H., 529
Kim, S.H., 713
Kim, S.H., 899
Kim, S.I., 881
Kim, S.J., 65
Kim, S.K., 743
Kim, S.K., 1109
Kim, S.S., 681
Kim, S.W., 439
Kim, S.W., 565, 659,665
Kim, S.W., 1003
Kim, S.Y., 671
Kim, W.J., 381, 417, 503
Kim, W.T., 199
Kim, Y.H., 823
Kim, Y.J., 1067, 1109
Kim, Y.S., 241, 343
Kim, Y.S., 899
Kim, Y.Y., 463
Kimm, K.W., 221
Kimura, H.M., 609
Ko, M.W., 1101
Ko, S.H., 805
Kobayashi, S., 577
Kobayashi, T., 653
Kohyama, M., 255
Kohzu, M., 255, 451
Koike, J., 111
Komatsu, S., 73
Konishi, H., 349
Konstanchuk, I.G., 261
Kosugi, K., 489
Koziar, K., 559
Kuan, S.L., 547
Kumai, S., 541, 665, 707
Kumar, K.S., 811
Kurozawa, T., 1127
Ku?nierz, J., 387
Kusui, J., 597
Kwon, D., 247

Kwon, H., 845, 899
Kwon, S.C., 463
Kwon, S.W., 583
Kwun, S.I., 823

L

Langdon, T.G., 399, 647
Lavernia, E.J., 523
Leal, M., 559
Leary, M., 281, 287
Lee, B.H., 65
Lee, B.Y., 1139
Lee, C.C., 911
Lee, C.G., 65
Lee, C.H., 439
Lee, C.H., 1101
Lee, C.S., 119, 269,755,775
Lee, C.-S., 119
Lee, D., 729
Lee, D.B., 955, 973
Lee, D.G., 119
Lee, D.J., 167
Lee, D.N., 297
Lee, D.Y., 1061
Lee, E.S., 695
Lee, E.W., 5, 305, 559
Lee, H.C., 583, 621
Lee, H.I., 317, 881, 887, 1061
Lee, H.J., 1139
Lee, H.K., 829
Lee, J., 317
Lee, J.C., 621, 837, 887
Lee, J.G., 627
Lee, J.H., 331
Lee, J.H., 823
Lee, J.M., 641, 875
Lee, J.M., 1027
Lee, J.S., 565
Lee, J.S., 811
Lee, K.B., 845
Lee, K.H., 1093
Lee, M.Y., 343
Lee, S.B., 529
Lee, S.G., 1109
Lee, S.H., 119, 1027
Lee, S.H., 191
Lee, S.H., 311, 635
Lee, S.W., 399, 647
Lee, S.Y., 343, 1139
Lee, S.-Y., 1139
Lee, T.H., 65
Lee, U.J., 659
Lee, W.S., 823
Lee, Y.H., 247
Lee, Y.H., 1093
Lee, Y.J., 1093
Lee, Y.S., 331
Lee, Y.T., 41, 65, 91, 1075
Lei, C. S. C., 5
Lesuer, D.R., 369
Lian, Z., 23, 917
Lim, C.Y., 641, 875
Lim, H.K., 199
Lim, H.T., 423
Lim, K.M., 517
Lim, S.G., 221
Lim, S.W., 411
Lindemann, J., 793
Lipsitt, H.A., 721
Liying, Z., 917
Locati, P., 1115
Lui, T.S., 547, 689
Luo, G.Z., 737

M

Mal, A.K., 701
Malczewski, P., 387
Mao, J., 411
Matoba, M., 495
Matsuda, K., 535
Matsui, H., 535
Matsuura, Y., 577
Maurer, J.L., 141
Meletis, E.I., 1015
Meng, X., 857
Meyendorf, N., 1021
Mishra, R.S., 405
Miyauchi, H., 431

Moon, I.G., 393
Moon, J.J., 955
Morri, A., 361
Mosneaga, V.A., 653
Motegi, T., 185
Mukherjee, A.K., 405
Muraishi, S., 541

N

Nagura, Y., 235
Nakai, K., 577
Nakasa, K., 1009
Nakata, J., 431
Nam, K.W., 701
Nam, S.W., 749, 761, 769
Nieh, T.G., 387
Niinomi, M., 111, 127
Nishida, Y., 411
Nishikawa, N., 185
Niwa, N., 991
Noda, K., 349
Nomura, N., 31
Nozue, A., 781

O

O'Brien, M.J., 369
Ochi, M., 495
Ogawa, K., 1121, 1127
Oh, K.H., 621
Oh, L.S., 905
Ohashi, S., 495
Ohmori, Y., 577
Osamura, K., 597
Ouchi, C., 127

P

Park, C.G., 517, 997
Park, E.S., 199
Park, H.C., 565
Park, H.C., 899
Park, H.L., 105
Park, H.S., 729
Park, I.M., 675, 851, 929
Park, J.K., 615, 743
Park, J.M., 675
Park, J.S., 97
Park, J.S., 269
Park, J.W., 393
Park, K.B., 955
Park, K.T., 627
Park, S.H., 269
Park, S.J., 829
Park, S.S., 225
Park, T.Y., 503
Park, W.J., 695
Park, W.W., 943
Park, Y., 729
Park, Y.H., 393, 805, 869
Park, Y.S., 225, 553
Park, Y.S., 749, 761
Park, Y.W., 1087
Pech, H., 559

Q

Qu, H.L., 161

R

Rhee, K.H., 713
Rhyim, Y.M., 997
Ryu, K.H., 583
Ryu, S.K., 863

S

Saito, Y., 311, 325,635
Sakai, T., 311, 635
Sakurai, K., 1121
Sarkar, B., 559
Sasamori, K., 609
Sathish, S., 141, 1021
Sato, A., 541, 665, 707
Sato, T., 863, 875
Sawai, T., 1127
Semiatin, S.L., 79
Senda, T., 275
Seo, M.H., 355
Seo, P.K., 1043
Seok, H.K., 317, 621, 887
Seon, Y.K., 1061

Seri, O., 937
Shan, A., 393
Shell, E.B., 133
Sherby, O.D., 369
Shiflet, G.J., 509
Shim, W.S., 973
Shimamoto, A., 911
Shin, C.H., 1003
Shin, D.H., 523, 627, 755, 863
Shin, D.S., 887, 1061
Shin, H.H., 105
Shin, K.S., 191, 215, 681
Shin, K.S., 1101
Shin, S.Y., 1101
Shinoda, T., 431
Shiota , I., 991
Sim, H.S., 845
Sohn, S.M., 343
Sohn, W.H., 469
Somekawa, H., 451
Son, J.Y., 1087
Son, K.J., 1081
Son, Y.I., 1043
Song, J.H., 423
Song, J.M., 547
Souba, R., 325
Spigarelli, S., 361
Stone, I.C., 1055
Suh, D.W., 583
Suh, J.Y., 317, 887
Sun, F., 1075
Sun, Z., 869
Sung, S.Y., 1067
Suryanarayana, C., 261
Suzuki, H., 781
Suzuki, H., 787
Suzuki, H.G., 49
Suzuki, K., 275
Suzuki, T., 31
Syn, C.K., 369

T

Tada, A., 923
Takaki, Y., 349
Takeda, M., 235
Tamin, M.N., 781
Tanaka, S.I., 949
Tanaka, T., 665
Tang, F., 817
Taniguchi, S., 961
Terayama, K., 535
Tezuka, H., 863, 875
Toda, H., 653
Tokisue, H., 445, 457
Tono, G., 111
Tsuji, N., 635
Tsujikawa, M., 893
Tsujimoto, T., 489

U

Ueda, M., 73
Uesugi, T., 255
Uetani, Y., 535
Ueyama, M., 325
Utsunomiya, H., 325, 635

V

Vassel, A., 917
Vedani, M., 375, 1115

W

Wagner, L., 205, 793
Wang, Q., 869
Wang, W.S., 737
Watanabe, Y., 787
Wen, J., 857
Wendt, J., 205
Williams, L., 305
Won, S.Y., 241
Woo, K.D., 565, 659
Wu, H., 161
Wu, Y., 729

X

Xiaonan, M., 917

Y

Yahata, A., 483, 495

Yamaguchi, H., 1127
Yamaguchi, M., 1075
Yamamoto, Y., 1127
Yan, X., 1009
Yan, Y.Q., 737
Yang, C.H., 565
Yang, J.K., 583
Yang, S.J., 761, 769
Yano, E., 185
Yim, C.D., 191
Yim, H.J., 463
Yokoe, K., 597
Yongqing, Z., 917
Yoo, Y.C., 881
Yoon, Y.I., 1133
Yoshimi, K., 31
You, B.S., 943
Yu, Y.J., 967
Yumoto, A., 991

Z

Zhao, Y.Q., 161
Zhentao, Y., 147
Zhou, F., 523
Zhou, L., 161, 737
Zhu, K.Y., 161
Zhu, Y.C., 961